

**EVALUATION OF THE PERFORMANCE OF A MAGNESIUM RICH,  
NON-CHROMATE PRIMER WITH/WITHOUT TOPCOAT ON 2024-T351:  
THE ROLE OF VARIOUS SUBSTRATE PRETREATMENTS**

---

A Dissertation

Presented to  
the Faculty of the School of Engineering and Applied Science  
University of Virginia

---

In partial Fulfilment  
of the requirements for the degree  
Doctor of Philosophy in Materials Science and Engineering

by

Balaji Kannan  
April 2017

## **APPROVAL SHEET**

The dissertation  
is submitted in partial fulfillment of the requirements  
for the degree of  
Doctor of Philosophy (Materials Science and Engineering)

---

Balaji Kannan  
(Author)

The dissertation has been read and approved by the examining committee:

---

Dr. John R. Scully  
(Dissertation Advisor)

---

Dr. Robert. G. Kelly  
(Committee Chairmen)

---

Dr. Elizabeth J. Opila  
(Committee Member)

---

Dr. William. C. Keene  
(Committee Member)

---

Dr. Jason. S. Lee  
(Committee Member)

Accepted for the School of Engineering and Applied Science:

---

Craig H. Benson, Dean, School of Engineering and Applied Science  
April 2017

## Executive Summary

Many aerospace structures utilize precipitation age hardened aluminum alloys which heavily rely on the use of chromated primers and pretreatments to provide active corrosion protection. Carcinogenicity, high handling cost and lack of environmental safety have necessitated an accelerated phase-out of hexavalent chromium, concurrent with initiatives to find effective alternatives.

The sacrificial anode-based cathodic and barrier protection capabilities of a non-chromate magnesium rich primer (MgRP) with a non-film forming pretreatment, in both a topcoated and non-topcoated conditions is an emerging, promising corrosion mitigation strategy for precipitation age hardened aluminum alloy, 2024-T351. However, little is known about the effect of surface pretreatments upon which most coatings will be deposited. This work addresses how resistive surface pretreatments (such as chromate conversion coating (CCC), trivalent chromium pretreatment (TCP), non-chromate pretreatment (NCP), anodization without sealing (ANS), anodization with hexavalent chromium sealing (ACS) and anodized with trivalent chromium pretreatment (ATS)) affect the overall corrosion protection functions of MgRP-based systems. The effect of pretreatment properties on sacrificial protection function, barrier degradation, and scribe protection by MgRP was examined. In addition, alternate modes of corrosion protection by chemical species leaching from the pretreatment and primer were also investigated.

The pretreatment chemistry and thickness was characterized using X-ray photoelectron spectroscopy (XPS) and scanning electron microscopy/energy dispersive spectroscopy (SEM/EDS) while initial electrochemical properties were examined using electrochemical impedance spectroscopy (EIS). Anodization based pretreatment especially added a significantly resistive surface layer while conversion coatings have moderate barrier properties.

An accelerated electrochemical cycle test was adopted to evaluate the evolution of sacrificial protection function and barrier degradation of the coating in full immersion conditions. A finite full immersion exposure time was required for degradation of more electrically insulating pretreatment layers. The pretreatment degradation lowered the resistance between the MgRP and the 2024-T351 substrate and enabled delayed activation and triggered sacrificial anode-based cathodic protection by MgRP. In contrast, MgRP was galvanically coupled immediately and functioned as a sacrificial anode for the non-film forming (NFF) pretreatment.

This work has further illuminated and verified test methods which assess coating degradation and scribe protection that could be used in both the laboratory and the field. A suite of test methods was utilized to track the elemental Mg depletion, galvanic protection potential, barrier degradation, Mg corrosion products formation and corrosion volume loss at the scribe throughout exposure in field as well as laboratory accelerated life environments. In the case of systems without a topcoat, significant depletion of Mg pigment and coating degradation were observed in all environments but at different rates. In the case of NFF pretreated AA2024-T351 with MgRP, magnesium was galvanically coupled to AA2024-T351 immediately and was available for cathodic protection from the beginning of the exposure. In the case of trivalent chromium pretreatment (TCP) and other similar conversion coating pretreated AA2024-T351, initially there was limited galvanic coupling with the MgRP due to high pretreatment resistance. Upon prolonged exposure in full immersion, the global galvanic protection potential decreased to more negative potentials below the open circuit potential (OCP) of AA2024-T351 indicative of galvanic coupling. In anodized systems with chromate sealing (ACS), Mg pigment was not electrically connected to the AA2024-T351 until after long environmental exposure times because of the resistive nature of the pretreatment and improved sealing with increasing exposure time.

The barrier properties of the MgRP pigmented coating also degraded with time at a higher rate in systems in the absence of topcoat. This result was attributed to UV degradation of the pigmented coating resin and which was reduced by the UV resistant polyurethane topcoat. SEM/EDS characterization of the scribe after different ASTM B117/field exposure times indicated that the protective throwing power increased as a function of exposure time in all MgRP-based systems. Moreover, a secondary protection mode enabled by  $Mg(OH)_2$  redeposition was identified.

In addition, the galvanic throwing power of the MgRP was studied via the scanning vibrating electrode technique (SVET), which enabled the spatial analysis of net anodic and cathodic current densities for a MgRP on pretreated 2024-T351 coupled with a bare 2024-T351 scribe to be mapped. The effect of pretreatment resistance, coating to scribe area ratio and topcoat polymer properties on galvanic protection was elucidated. For NFF/MgRP, anodic current densities in the scribe indicative of local sites of pitting were lowered by 2-3 orders of magnitude. This result was attributed to sacrificial anode-based cathodic prevention. TCP and ACS pretreated systems did not exhibit galvanic protection in lower coating to scribe area ratios. However, at higher coating to scribe area ratio, improved scribe protection with time was observed for these pretreatments. Alternate modes of corrosion protection attributed to chemical species leaching from the primer and pretreatments were elucidated as the cause of this effect.

The outcome of this research provided a scientific foundation for understanding how utilization of resistive pretreatments along with MgRP enables development of a multi-functional corrosion protection system which includes delayed cathodic/sacrificial protection of Mg, barrier protection by pretreatments/primer/topcoat and corrosion inhibition by chemical species leaching from the MgRP. The throwing power of the Mg in the primer was heavily limited by topcoat polymer properties in addition to high pretreatment resistances. The work performed herein

suggests that a pretreatment with high resistance that does not degrade significantly with time may not be suitable for use with MgRP because the substrate is decoupled from the sacrificial anode.

## **Bibliography**

The publication that either will result/resulted from or related to this dissertation with author's significant contribution are listed below:

1. **B. Kannan**, A.D. King and J.R. Scully, "Effect of Pretreatments on 2024-T351 Corrosion Protection by a Magnesium Rich, Non-Chromium Primer (MgRP): Laboratory Characterization in Full Immersion", *Corrosion* 71: pp. 1093-1109 (2015).
2. **B. Kannan**, A.D. King and J.R. Scully, "Impact of Pretreatments on AA2024-T351 Corrosion Protection by a Magnesium Rich, Non-Chrome Primer (MgRP)", *NACE DoD Corrosion Conference Paper*, November 15-19, 2015, Pittsburgh, PA.
3. **B. Kannan** and J.R. Scully, "Performance of a Magnesium Rich Primer on Pretreated 2024-T351 in Selected Laboratory and Field Environments - Conversion Coatings Pretreatment", *Corrosion* 72: pp. 1363-1384 (2016).
4. **B. Kannan**, D.M. Wolanski and J.R. Scully, "Performance of a Magnesium Rich Primer on Pretreated 2024-T351 in Selected Laboratory and Field Environments: Anodization Pretreatment", *Corrosion, In Review* (2017).
5. **B. Kannan**, D.M. Wolanski and J.R. Scully, "Environmental Degradation of Pretreatments and Role of Pretreatments in Corrosion Protection of AA2024-T351", to be submitted to *Materials and Corrosion*, 2017.

6. **B. Kannan**, C. F. Glover, N. McMurray, G. Williams and J. R. Scully, "Performance of a Magnesium Rich Primer on Pretreated 2024-T351 in Full Immersion: Throwing Power Investigation Using Scanning Vibrating Electrode Technique," In Progress.

7. A.D. King, **B. Kannan**, and J.R. Scully, "Environmental Degradation of a Mg-Rich Primer in Selected Field and Laboratory Environments – Part I. Without a Topcoat" *Corrosion*: 70 (5), 2013, 512-535.

8. A.D. King, **B. Kannan**, and J.R. Scully, "Environmental Degradation of a Mg-Rich Primer in Selected Field and Laboratory Environments – Part II. Primer and Topcoat" *Corrosion*: 70 (5), 2013, 536-557.

## **Acknowledgements**

I would like to first thank my research advisor, Prof. John. R. Scully, for providing me opportunity and continual support to pursue research under his guidance. His mentorship and guidance has helped me concretize my academic foundations and realize my long cherished dream of making original contributions to science and technology. I would also like to thank the members of my thesis committee: Dr. Robert. G. Kelly, Dr. Elizabeth. J. Opila, Dr. William. C. Keene and Dr. Jason. S. Lee for their valuable inputs on my research.

I would like to recognize everyone at the CESE and MSE department for all their help over several years. Particularly would like to specially thank Andrew, Brendy, RJ and Matt for coatings and pretreatments related discussions. I would also like to thank other members of my group and CESE specially, Katie Fleming, Hung Ha, Ai, Arwen, Merrill, Sam, Eric, Mara, Marylyn, Rebecca, Mike W, Jay, Piyush, Marybeth, Leslie, Taylor, Mike H, Veronica, Kat, Gilbert, Lindsey, Katie, Ian and Drew who all have provided a lot of help around the labs. Also around the department, I would like to thank Richard White, Dr. Sabat, Tanner, Joe, Eric, Kim, Jeannie, Shelley, Sherri, Ashley, Kari, Mike Melia, Noelle, Bonnie, Joe, Matt Schneider, Bernard, Proloy, Jishnu, Joha, Begum, Zach (s), Gopal and Ehsan for all help. Outside of UVA, I would like to acknowledge the help from Dr. Jason Lee, Carol, Klomjit, Dr. Hommel, Bill Abbott, Dr. Matzdorf, Mr. Pepe and John Kolody who provided technical advice, help with experiments, materials and field exposures.

I would like to than my research mentors from undergrad, work and MS (notably Dr. Scherson, Dr. Kalaiselvi, Dr. Sergi, and Dr. N. G. Renganathan) for encouraging me to pursue a research career. Finally, I would like to thank my family and friends (CECRI, Fosroc, Case, Richmond and UVA/Charlottesville) for being my support system throughout this incredible journey.

## Table of Contents

<b>1</b>	<b>Introduction .....</b>	<b>50</b>
1.1	Metallurgy and Microstructure of AA2024-T351 .....	50
1.2	Corrosion Susceptibility of AA2024-T351 .....	51
1.3	Anticorrosion Coatings. ....	51
1.3.1	Barrier Protection.....	52
1.3.2	Corrosion Inhibitors .....	53
1.3.3	Sacrificial Coatings.....	57
1.4	Corrosion Protection of AA2024-T351 by a Mg Rich Primer – An Overview .....	58
1.5	Surface Pretreatments for Aluminum Alloys .....	65
1.5.1	Non-film Forming Surface Pretreatment .....	65
1.5.2	Conversion Coatings.....	65
1.5.3	Anodization.....	68
1.6	Possible Impacts of Resistive Pretreatments on the Corrosion Protection of 2024-T351 by a Magnesium Rich Primer.....	69
1.7	Specific Surface Pretreatments, Magnesium Rich Primer and Topcoat Systems of Interest.....	70
1.8	Critical Unresolved Issues.....	71
1.9	Objective .....	73
1.10	Experimental Approach.....	75

1.10.1	Preliminary Characterization of the Pretreatments .....	75
1.10.2	Post-exposure Characterization of Intact Region of Coating/Pretreatment: .....	75
1.10.3	Post-exposure Characterization of 2024-T351 Scribe Adjacent to Coating/Pretreatment: .....	76
1.10.4	Throwing Power Investigation:.....	76
1.11	Thesis Organization.....	76
1.12	References .....	81
1.13	Tables .....	88
1.14	Figures .....	89
<b>2</b>	<b>Effect of Pretreatments on 2024-T351 Corrosion Protection by Magnesium Rich, Non- Chromium Primer (MgRP): Laboratory Characterization in Full Immersion.....</b>	<b>95</b>
2.1	Abstract .....	95
2.2	Introduction .....	97
2.3	Experimental Procedure .....	100
2.3.1	Materials .....	100
2.3.2	Full-Immersion Electrochemical Analysis .....	100
2.3.3	Electrochemical Impedance Spectroscopy .....	101
2.3.4	Potentiodynamic Polarization Scans.....	101
2.3.5	Full-Immersion Electrochemical Testing Protocol (Cycle Test) .....	102
2.3.6	X-ray Photoelectron Spectroscopy .....	102

2.3.7	X-ray Diffraction .....	103
2.3.8	Scanning Electron Microscopy and Energy Dispersive Spectroscopy .....	104
2.4	Results .....	104
2.4.1	Preliminary Studies of Chemistry of Chosen Pretreatments.....	104
2.4.2	Characterization of Thickness of the Pretreatments .....	105
2.4.3	Laboratory Assessment of Electrochemical Behavior of Pretreated 2024-T351/MgRP/Topcoat in the As-Received Condition .....	105
2.4.4	Diagnostic Electrochemical Cycle Test to Assess the Charge Capacity Associated With Mg Oxidation in MgRP Without a Topcoat .....	108
2.4.5	Diagnostic Electrochemical Cycle Test to Assess Charge Capacity of Mg in MgRP With a Topcoat .....	110
2.5	Discussion .....	111
2.5.1	The Role of Pretreatments in Cathodic Protection .....	111
2.5.2	Delayed Galvanic Protection by MgRP in Presence of Resistive Pretreatments .	113
2.5.3	Role of Topcoat in Cathodic Protection of 2024-T351 by Mg Rich Primer .....	113
2.5.4	The Need for Lab vs. Field Assessment With Macro Scale Defects .....	114
2.6	Conclusions .....	115
2.7	References:.....	116
2.8	Tables .....	119
2.9	Figures .....	122

<b>3</b>	<b>Performance of a Magnesium Rich Primer on Pretreated AA2024-T351 in Selected Laboratory and Field Environments: Conversion Coating Pretreatments .....</b>	<b>137</b>
3.1	Abstract .....	137
3.2	Introduction .....	139
3.3	Experimental Procedure .....	143
3.3.1	Materials .....	143
3.3.2	Laboratory and Field Exposures of Pretreated AA2024-T351 coated with MgRP and Topcoat .....	144
3.3.3	Post-mortem Surface Analysis of the Intact Coating and the Scribe.....	145
3.4	Results .....	147
3.4.1	Evaluation of the Performance of a MgRP without Topcoat on Pretreated AA2024-T351 after Exposure in Selected Lab and Field Environments: Global Protection.....	147
3.4.2	Evaluation of the Performance of a MgRP without Topcoat on Pretreated AA2024-T351 after Exposure in Selected Lab and Field Environments: Scribe Protection .....	151
3.4.3	Evaluation of the Performance of a MgRP with Topcoat on Pretreated AA2024-T351 after Exposure in Selected Lab and Field Environments: Global Protection.....	153
3.4.4	Evaluation of the Performance of a MgRP with Topcoat on Pretreated AA2024-T351 after Exposure in Selected Lab and Field Environments: Scribe Protection .....	155
3.4.5	Summary of Observations made after Environmental Exposure in Various Environments.....	157
3.5	Discussion .....	158

3.5.1	Understanding Residual Protection Mechanisms by Mg Corrosion Products:.....	158
3.5.2	Summary of Corrosion Protection Mechanisms: .....	158
3.5.3	Understanding Performance of the Coating in LALT vs Field: .....	159
3.5.4	Throwing Power Analysis.....	160
3.6	Conclusions .....	162
3.7	References .....	165
3.8	Tables .....	168
3.9	Figures .....	171
<b>4</b>	<b>Performance of a Magnesium Rich Primer on Pretreated 2024-T351 in Selected Laboratory and Field Environments: Anodization Pretreatment .....</b>	<b>191</b>
4.1	Abstract .....	191
4.2	Introduction .....	193
4.3	Experimental Procedure .....	196
4.3.1	Materials .....	196
4.3.2	Laboratory and Field Exposures of Pretreated AA2024-T351 coated with MgRP and Topcoat .....	196
4.3.3	Post-mortem Surface Analysis of the Coating and the Scribe .....	197
4.4	Results .....	199
4.4.1	Evaluation of the Performance of a MgRP without Topcoat on Pretreated 2024-T351 after Exposure in Selected Lab and Field Environments: Global Protection.....	199

4.4.2	Evaluation of the Performance of a MgRP without Topcoat on Pretreated AA2024-T351 after Exposure in Selected Lab and Field Environments: Scribe Protection .....	203
4.4.3	Evaluation of the Performance of a MgRP with Topcoat on Pretreated AA2024-T351 after Exposure in Selected Lab and Field Environments: Global Protection.....	205
4.4.4	Evaluation of the Performance of a MgRP with Topcoat on Pretreated AA2024-T351 after Exposure in Selected Lab and Field Environments: Scribe Protection .....	206
4.5	Discussion .....	207
4.5.1	Understanding the Effect of Sealing in Global and Scribe Protection of Anodized MgRP Systems .....	207
4.5.2	Comparison of Anodization with Conversion Coating and Non-film Forming Pretreatment:.....	208
4.5.3	Future Work .....	210
4.6	Conclusions .....	211
4.7	References .....	215
4.8	Figures .....	219
<b>5</b>	<b>Environmental Degradation of Pretreatments and Role of Pretreatments in Corrosion Protection of AA2024-T351.....</b>	<b>235</b>
5.1	Abstract .....	235
5.2	Introduction .....	237
5.3	Experimental Procedure .....	239
5.3.1	Materials .....	239

5.3.2	Laboratory and Field Exposures of Pretreated AA2024-T351 .....	239
5.3.3	Post-mortem Surface Analysis of the Pretreatment and the Scribe .....	240
5.3.4	Chemical Species Leaching Studies: .....	242
5.3.5	Potentiodynamic Polarization: .....	242
5.4	Results .....	243
5.4.1	Barrier Degradation of Pretreated AA2024-T351 after Exposure in Selected Lab and Field Environments: .....	243
5.4.2	Scribe Protection of Pretreated 2024-T351 after Exposure in Selected Lab and Field Environments: .....	246
5.4.3	Electrochemical Kinetics of AA2024-T351: Role of Pretreatments .....	248
5.5	Discussion .....	250
5.5.1	Summary of Protection Mechanisms .....	250
5.5.2	Effect on Pretreatment Degradation on Sacrificial Protection Function of MgRP systems	252
1.1.1	Influence of Pretreatments on Electrochemical Throwing Power of Mg .....	252
5.6	Conclusions .....	253
5.7	References .....	255
5.8	Tables .....	260
5.9	Figures .....	262

## **6 Performance of a Magnesium Rich Primer on Pretreated 2024-T351 in Full**

### **Immersion: Throwing Power Investigation Using Scanning Vibrating Electrode Technique**

**279**

6.1	Abstract .....	279
6.2	Introduction .....	281
6.3	Experimental Procedure .....	284
6.3.1	Materials .....	284
6.3.2	Sample Preparation .....	284
6.3.3	Laboratory Full Immersion Exposures of Pretreated AA2024-T351 Coated with MgRP and Topcoat.....	285
6.3.4	Scanning Vibration Electrode Technique (SVET) Measurements .....	286
6.4	Results .....	287
6.4.1	Laboratory Full Immersion Exposures of Pretreated AA2024-T351 Coated with MgRP and Topcoat.....	287
6.4.2	Localized Corrosion of AA2024-T351:.....	288
6.4.3	Galvanic Protection of Bare 2024-T351 Coupled to Bare Mg .....	289
6.4.4	Galvanic Protection of Bare 2024-T351 Coupled to 2024-T351/Pretreatment/MgRP.....	290
6.4.5	Galvanic Protection of Bare 2024-T351 Coupled to 2024-T351/Pretreatment/MgRP/TC.....	295
6.5	Discussion .....	296

6.5.1	Correlation of Galvanic Currents from SVET to FEA Results.....	296
6.5.2	Need for Long Term Full Immersion Exposures .....	296
6.6	Conclusion.....	297
6.7	References .....	299
6.8	Tables .....	309
6.9	Figures.....	310
<b>7</b>	<b>Thesis Conclusions and Suggested Future Work .....</b>	<b>334</b>
7.1	Conclusions .....	334
7.2	Suggested Future Work.....	338
7.2.1	Suggested Future Work to Investigate Throwing Power .....	338
7.2.2	Suggested Future Work to Investigate Desirable Topcoat Properties .....	341
7.2.3	Suggested Future Work to Investigate Corrosion Protection Function of Mg depleted or MgO primer .....	342
7.2.4	Suggested Future Work to Investigation of Other Metal Rich Primers for Galvanic Protection of Aluminum Alloys .....	343
7.3	Technological/Scientific Impact .....	343
7.4	Economic Summary .....	344
<b>8</b>	<b>APPENDIX A: Finite Element Analysis of the Galvanic Couple Current and Potential Distribution between Mg and 2024-T351 in a Mg Rich Primer Configuration: Effect of Resistive Pretreatments – FIGURES ONLY .....</b>	<b>345</b>
8.1	Abstract .....	345

8.2	Experimental Procedure .....	345
8.2.1	Materials .....	345
8.2.2	Full Immersion Electrochemical Analysis to Establish Boundary Condition .....	346
8.3	Results .....	347
8.3.1	Phenomenological Model .....	347
8.3.2	Ionic Effects of Pretreatments.....	348
8.3.3	Resistive Effects of Pretreatments .....	350
8.3.4	Mixed Effects of Pretreatments .....	352
8.3.5	Solution Conductivity (Based on OLI calculations).....	356
8.4	Future Work .....	358
<b>9</b>	<b>APPENDIX B: Performance of a Magnesium Rich Primer on Pretreated 2024-T351 in Full Immersion: Throwing Power Investigation Using Optical Profilometry – FIGURES ONLY .....</b>	<b>359</b>
9.1	Abstract .....	359
9.2	Experimental Procedures.....	360
9.2.1	Materials .....	360
9.2.2	Sample Preparation .....	360
9.2.3	Laboratory Full Immersion Exposures Studies.....	361
9.2.4	Post-mortem Surface Analysis of the Scribe .....	361
9.3	Results .....	362

9.3.1	Sample Design .....	362
9.3.2	Optical Profilometry Maps .....	363
9.3.3	Effect of Distance from Coating and Coating to scribe area ratio .....	366
9.4	Summary and Future Work .....	367
<b>10</b>	<b>APPENDIX C: Preliminary Investigation of Throwing Power of a Magnesium Rich Primer on 2024-T351 under Thin Films Using Scanning Kelvin Probe – FIGURES ONLY</b>	
	<b>369</b>	
10.1	Introduction .....	369
10.2	Experimental Procedures.....	369
10.2.1	Materials .....	369
10.2.2	Surface Analysis of the Intermetallics .....	370
10.2.3	Sample Preparation for Scribed Coating.....	370
10.2.4	Scanning Kelvin Probe Experiments .....	371
10.3	Results .....	372
10.3.1	Chemical Characterization of Intermetallic in 2024-T351 .....	372
10.3.2	Characterization of Volta Potentials of Intermetallic Phases .....	376
10.3.3	Galvanic Couple Experiments .....	378
10.4	Summary and Future Work .....	381
<b>11</b>	<b>APPENDIX D: Extensions of Environmental Degradation of a Mg-rich Primer in Selected Laboratory Environments – Part III. In ASTM B117 Modified with UV Light and</b>	

**Acidified Artificial Sea Water and Selected Full Immersion Exposures – FIGURES ONLY**

**382**

11.1 Introduction ..... 382

11.2 Experimental Procedure ..... 382

    11.2.1 Materials ..... 382

    11.2.2 Laboratory and Field Exposures of Pretreated AA2024-T351 coated with MgRP  
and Topcoat ..... 383

    11.2.3 Post-mortem Surface Analysis of the Coating and the Scribe ..... 384

11.3 Tables ..... 385

11.4 Figures ..... 386

11.5 Summary and Future Work ..... 396

## LIST OF TABLES

Table 1.1. Composition of Aluminium alloy 2024-T351 on a weight percent basis.....	88
Table 2.1. Diagnostic electrochemical cycle test to assess sacrificial anode-based cathodic protection, potentiostatic hold times for charge capacity of MgRP determination. ....	119
Table 2.2. Quantitative analysis (atomic percent) of surface chemistry of pretreated 2024-T351 through XPS after 5 minutes argon ion sputtering.....	120
Table 2.3. Thickness of pretreatments (based on cross-sectional EDS line profile analysis). ...	120
Table 2.4. Values of parameters estimated by EIS fitting procedure discussed in Figure 6. ....	121
Table 3.1. Exposure conditions in field and lab accelerated life testing environments.....	168
Table 3.2. Reference Peaks for Magnesium Corrosion Products. ....	169
Table 3.3. AA2024-T351/Pretreatment/MgRP: Summary of observations made after environmental exposure in various environments. ....	170
Table 3.4. AA2024-T351/Pretreatment/MgRP/TC: Summary of observations made after environmental exposure in various environments. ....	170
Table 5.1. Experimental protocol for modified ASTM B117 environmental exposure. ....	260
Table 5.2. Summary of pretreatment degradation trends after exposure in different LALT/field exposures. Pretreatments were ranked from 1-4 based on visual appearances. 1 indicates minimal corrosion and 4 indicates severe corrosion. ....	260
Table 5.3. Summary of scribe protection trends (SEM/EDS) after exposure in different LALT/field exposures. Pretreatments were ranked from 1-4 based on SEM images and oxygen elemental maps. 1 indicates excellent scribe protection and 4 indicates severe corrosion at scribe. ....	261
Table 5.4. Summary of scribe protection trends (optical profilometry) after exposure in different LALT/field exposures. Pretreatments were ranked from 1-4 based on corrosion volume loss. 1 low pit volume densities and 4 indicates high pit volume densities. ....	261

Table 6.1. Thickness of pretreatments (based on cross-sectional EDS line profile analysis). ...	309
Table 6.2. Comparison of SVET analysis to FEA modelling of Galvanic Current distribution of Mg and AA2024-T351.....	309
Table 8.1. Solution conductivity for various bulk solutions of NaCl with and without Na <sub>2</sub> CrO <sub>4</sub>	356
Table 8.2. Solution conductivity for various bulk solutions of MgCl <sub>2</sub> with and without Na <sub>2</sub> CrO <sub>4</sub> .....	357
Table 11.1. Experimental protocol for modified ASTM B117 environmental exposure. ....	385

## LIST OF FIGURES

Figure 1.1. Schematics of Al alloy surface with electrode potential of different constituent phases .....	89
Figure 1.2. Mixed potential model depicting $E_{\text{surface}}$ and $E_{\text{couple}}$ as they pertain to a galvanic couple between AA2024-T351 and polymer coated Mg.....	89
Figure 1.3. Schematic of AA2024-T351 coated with MgRP and advanced performance topcoat under full immersion depicting MgRP function under situation without cathodic corrosion in the case of MgRP/topcoat.....	90
Figure 1.4. Hypothetical schematic of AA2024-T351 coated with MgRP depicting MgRP sacrificial cathodic protection function under (a) full immersion (b) thin-layer electrolyte and (c) droplet electrolyte conditions.....	90
Figure 1.5. (a) Schematic cross section of microelectrode array to assess throwing power of Mg over a representative bare AA2024-T4 scratch in an RH controlled cabinet. (b) Optical image of a the bare Mg/AA2024-T4 microelectrode <sup>[52]</sup> (c) Schematic of geometric model developed in finite element computational modeling software (COMSOL).....	
Figure 1.6. Current, RH, and time-lapse optical images of the bare Mg/AA2024-T4 microelectrode array(a)/ acrylic polymer coated Mg/AA2024-T4 microelectrode array(b) during an episodic wetting and drying event under 5 %(wt) NaCl solution. In the color map dark red indicates an anodic current $\geq 1 \times 10^{-7}$ A and dark blue indicates a cathodic current of $\leq -1 \times 10^{-7}$ A. White color indicates a net current of zero.....	
Figure 1.7. Comparison of FEA modelling to micro-electrode array measurements during drying (a) I measured by Micro-electrode Array, (b) I predicted by COMSOL FEA model (c) Schematic	

of multi-electrode array(cross sectional view), (d) Optical Image of multi-electrode array(planar view) .....

Figure 1.8. Schematic of scribed coating system showing two regions of interest for post exposure characterization, intact coating and scribe. .... 94

Figure 2.1. EDS layered cross sectional SEM image of 2024-T351/MgRP/topcoat systems .....

Figure 2.2. EDS line profile of the characteristic elements of different pretreatments, (a) chromate conversion coating (CCC), (b) trivalent chromium pretreatment (TCP), (c) non chromium pretreatment (NCP), (d) anodized without sealing, (e) anodized with chromate sealing and (f) anodized with TCP sealing. ....

Figure 2.3. Electrical description of pretreated 2024-T351/MgRP/Topcoat. The dotted line indicates galvanic couple potential measured for an intact coating without a scratch. Polarization of this intact coating galvanically coupled to a scratch is simulated by the -0.8 V potentiostatic hold. ....

Figure 2.4. (a) E-log (i) data for bare/pretreated AA2024-T351 in quiescent 5 % (wt) NaCl solution (b) mixed potential model (E vs log I) depicting a galvanic couple between bare or pretreated 2024-T351 and bare Mg.  $A_{\text{cathode}} = A_{\text{anode}} = 1 \text{ cm}^2$ . when there is direct contact between Mg and bare or pretreated 2024-T351 and negligible ohmic drop through solution:  $E_{2024}^{\text{couple}} = E_{\text{Mg}}^{\text{couple}}$  (A) and  $E_{2024/\text{Anod Chromate Seal}}^{\text{couple}} = E_{\text{Mg}}^{\text{couple}}$  (B) and (c) galvanic couple potential of bare/pretreated 2024-T351 as function of ohmic resistance imposed between Mg and 2024-T351. The couple potential sensed by the 2024-351 surface is indicated in (c). In this case of anodized pretreatment low resistances that indicated are not accessible. ....

Figure 2.5. Initial impedance profiles of (a) bare/pretreated 2024-T351, (b) bare/pretreated 2024-T351 coated with Akzo Nobel† MgRP and (c) bare/pretreated AA2024-T351 coated with Akzo

Nobel† MgRP and Akzo Nobel (ANAC) Aerodur 5000 exposed in quiescent 5 % (wt) NaCl solution, after 1 h (bare/pretreated 2024-T351 with/without MgRP) or 12 h (MgRPTC) at OCP. Abraded (■), Prekote™ (◻), CCC (△), TCP (▽), NCP (⊕), Anodized no seal (⌘), Anodized chromate seal (⌘) and Anodized TCP seal (⊕).....

Figure 2.6. Equivalent circuit models for EIS fitting, (a) Abraded/Prekote™ and (b) other resistive pretreatments.  $R_{sol}$  is resistance of the electrolyte.  $R_{po}$  and  $R_{Cor}$  represents the resistance of the pretreatment layer and the resistance corresponding to charge transfer.  $CPE_c$  and  $CPE_{cor}$  are constant phase elements representing the capacitance of intact pretreatment and the double layer capacitance.....

Figure 2.7. Initial impedance profiles: Comparison of (a) Prekote™, (b) CCC and (c) anodized with chromate sealing exposed in quiescent 5 % (wt) NaCl solution, after 1 h (pretreated 2024-T351/MgRP) or 12 h (MgRP/TC) at OCP. 2024-T351/pretreatment (■), 2024-T351/pretreatment/MgRP (△) and 2024-T351/pretreatment/MgRP/TC (◻)..... 128

Figure 2.8. (a) Average OCP (of last 1 h of exposure) and (b) Low frequency impedance Z modulus (at 0.01 Hz) of 2024-T351 with different pretreatments (■) and coated with Akzo Nobel† Mg-rich primer (●), coated with Akzo Nobel† Mg-rich primer and Akzo Nobel (ANAC) Aerodur 5000 (▲), during exposure in quiescent 5 % (wt) NaCl solution, for 1 hour (AA2024-T351/MgRP) or 12 hours (Topcoat)..... 129

Figure 2.9. E-log (i) data for of Bare Mg and bare/pretreated 2024-T351 in quiescent 5 % (wt) NaCl..... 130

Figure 2.10. Cycle test results: OCP vs. time, Z modulus vs. time and anodic charge vs. time for the pretreated 2024-T351/ MgRP in quiescent 5 % (wt) NaCl, (a-c) Prekote™ (d-f) TCP and (g-i)

Anodized TCP Seal. Time in legend refers to elapsed time. Listed Table 1 for the diagnostic electrochemical cycle test. .... 131

Figure 2.11. Cycle test results: anodic charge density (of the indicated intact 2024-T351/pretreatment/MgRP systems) at -0.8 V (vs SCE) for each individual cycle test step indicated in Table 1 vs total elapsed cycle test time in the cycle test protocol ..... 132

Figure 2.12. Cycle test results: OCP (of the indicated intact 2024-T351/pretreatment/MgRP systems) for each individual cycle test step indicated in Table 1 vs total elapsed cycle test time in the cycle test protocol ..... 133

Figure 2.13. Cycle test results: complex impedance Z Modulus at 0.01 Hz (of the indicated intact 2024-T351/pretreatment/MgRP systems) for each individual cycle test step indicated in Table 1 vs total elapsed cycle test time in the cycle test protocol. .... 133

Figure 2.14. Cycle test results: (a) Mod. Z vs time for 2024-T351/anodized with chromate seal/MgRP in quiescent 5 % (wt) NaCl, Time in legend refers to elapsed time in Table 1 in the diagnostic electrochemical cycle test. (b) complex impedance Z modulus at 10 Hz (of the indicated intact 2024-T351/pretreatment/MgRP systems) for each individual cycle test step indicated in Table 1 vs total elapsed cycle test time in cycle test protocol (for the indicated pretreatment/MgRP systems).....

Figure 2.15. Cycle test results (XRD): The normalized integral intensity for Mg<101> (of the indicated intact 2024-T351/pretreatment/MgRP systems) for each individual cycle test step indicated in Table 1 vs total elapsed cycle test time in the cycle test protocol..... 135

Figure 2.16. Cycle test results: OCP (of the indicated intact 2024-T351/pretreatment/MgRP/Topcoat systems) for each individual cycle test step indicated in Table 1 vs total elapsed cycle test time in the cycle test protocol. .... 135

Figure 2.17. Cycle test results: cumulative anodic charge density (of the indicated intact 2024-T351/pretreatment/MgRP/Topcoat systems) at -0.8 V (vs SCE) for the sum of cycles added up to the time indicated in Table 1 vs total elapsed cycle test time in the cycle test protocol..... 136

Figure 2.18. Cycle test results: complex impedance Z modulus at 0.01 Hz (of the indicated intact 2024-T351/pretreatment/MgRP/Topcoat systems) for each individual cycle test step indicated in Table 1 vs total elapsed cycle test time in the cycle test protocol. .... 136

Figure 3.1. Low frequency impedance IZI modulus of intact AA2024-T351/Pretreatment/MgRP at 0.01 Hz vs time in the environments indicated for (a) NFF/MgRP (b) CCC/MgRP (c) TCP/MgRP and (d) NCP/MgRP..... 171

Figure 3.2. High breakpoint frequency ( $F_{bpt}$ ) of intact AA2024-T351/Pretreatment/MgRP systems vs time in in the environments indicated for (a) NFF/MgRP (b) CCC/MgRP (c) TCP/MgRP and (d) NCP/MgRP..... 172

Figure 3.3. Selected XRD spectra of intact AA2024-T351/Pretreatment/MgRP systems after exposure in the LALT/field environments for (a) NFF/MgRP and (b) TCP/MgRP. .... 173

Figure 3.4. The normalized integral XRD intensity for Mg<101> XRD peak of intact AA2024-T351/Pretreatment/MgRP systems vs time in the environments indicated for (a) NFF/MgRP (b) CCC/MgRP (c) TCP/MgRP and (d) NCP/MgRP..... 174

Figure 3.5. Average global galvanic protection potential of intact coating for the last 1 h exposure in 5 % wt NaCl vs the normalized integral XRD intensity for Mg<101>. The time indicates total exposure time in different LALT/Field environments indicated, (a) AA2024-T351/NFF/MgRP after exposure, in Full immersion in 5 % wt NaCl and Field at CHO and (b) AA2024-T351/TCP/MgRP after exposure, in Full immersion in 5 % wt NaCl, ASTM B-117 in 5 % wt NaCl and Field at CHO. ....

Figure 3.6. High breakpoint frequency of intact coating after 1 h exposure in 5 % wt NaCl vs The normalized integral intensity for Mg<101>. The time indicates total exposure time in different LALT/Field environments indicated, (a) AA2024-T351/NFF/MgRP after exposure, in Full immersion in 5 % wt NaCl, ASTM B-117 in 5 % wt NaCl, Modified ASTM B-117 with acidified SOW and UV and Field exposure at CHO. ....

Figure 3.7. Raman spectra for AA2024-T351/NFF/MgRP systems (a) Standard ASTM B-117 exposure – 400 h and (b) At field, CHO for 24 weeks. .... 177

Figure 3.8. EDS maps of elemental Mg across scribe and adjacent coating a) NFF pretreated 2024-T351/MgRP before exposure, b) NFF pretreated 2024-T351/MgRP after 1000 h exposure in ASTM B-117, c) TCP pretreated 2024-T351/MgRP after 1000 h exposure in ASTM B-117. (Red dash lines indicates the borders of the scribe in the figure). .... 178

Figure 3.9. a) EDS line profile of NFF/TCP pretreated AA2024-T351/MgRP systems without a topcoat after 1000 h exposure time in ASTM B-117 testing (red dash line indicates the borders of the scribe in the figure). Integral intensity of Mg EDS line profile in scribe/MgRP as a function of exposure time in (b) ASTM B-117 testing for 1000 h (c) Modified ASTM B-117 with acidified ASTM SOW/UV testing for 1000 h and (d) KSC for 8736 h. .... 179

Figure 3.10. Optical profilometry maps of scribe exposing AA2024-T351 in NFF(a)/TCP(b) pretreated AA2024-T351/MgRP without topcoat after exposure in ASTM B-117 for 1000 h. The 0 μm position (white) on the scale is indicative of the starting material condition before corrosion. .... 180

Figure 3.11. Corrosion volume loss of scribe exposing AA2024-T351 in AA2024-T351/Pretreatment/MgRP systems without topcoat as a function of exposure time in in different

LALT/field environments indicated. The baseline data is for uncoated AA2024-T351. (a) NFF/MgRP and (b) TCP/MgRP. .... 181

Figure 3.12. Low frequency impedance IZI modulus of AA2024-T351/Pretreatment/MgRP/TC systems at 0.01 Hz vs time in the environments indicated for (a) NFF/MgRP/TC (b) CCC/MgRP/TC (c) TCP/MgRP/TC and (d) NCP/MgRP/TC. .... 182

Figure 3.13. High breakpoint frequency ( $F_{bpt}$ ) of AA2024-T351/Pretreatment/MgRP/TC systems vs time in the environments indicated for (a) NFF/MgRP/TC (b) CCC/MgRP/TC (c) TCP/MgRP/TC and (d) NCP/MgRP/TC. .... 183

Figure 3.14. Selected XRD spectra of AA2024-T351/Pretreatment/MgRP/TC systems after exposure in the LALT/field environments for (a) NFF/MgRP/TC and (b) TCP/MgRP/TC. .... 184

Figure 3.15. The normalized integral XRD intensity for Mg<101> XRD peak of AA2024-T351/Pretreatment/MgRP/TC systems vs time in the environments indicated for (a) NFF/MgRP/TC (b) CCC/MgRP/TC (c) TCP/MgRP/TC and (d) NCP/MgRP/TC. .... 185

Figure 3.16. Breakpoint Frequency of intact coating after 1 h exposure in 5 % wt NaCl vs The normalized integral intensity for Mg<101>. The time indicates total exposure time in different LALT/Field environments indicated, AA2024-T351/NFF/MgRP/TC after exposure, in Full immersion in 5 % wt NaCl, ASTM B-117 in 5 % wt NaCl, Modified ASTM B-117 with Acidified SOW and UV and Field exposure at CHO and KSC. ....

Figure 3.17. Optical profilometry maps of scribe exposing AA2024-T351 in NFF(a)/TCP(b) pretreated AA2024-T351/MgRP/TC after exposure in ASTM B-117 for 1000 h. The 0  $\mu\text{m}$  position (white) on the scale is indicative of the starting material condition before corrosion. .... 187

Figure 3.18. Corrosion volume loss of scribe exposing AA2024-T351 in NFF(a)/TCP(b) pretreated AA2024-T351/MgRP/TC as a function of exposure time in in different LALT/field environments

indicated. The baseline data is for uncoated AA2024-T351. (c) comparison of non-coated, primer only and primer/topcoat systems for NFF pretreated 2024-T351 in standard ASTM B117 exposure environment. .... 188

Figure 3.19. Schematics of coating breakdown and galvanic coupling process between AA2024-T351/Pretreatment/MgRP systems and a bare AA2024-T351 scratch (a) Coating degradation of AA2024-T351/Pretreatment/MgRP and (b) Coating degradation of AA2024-T351/Pretreatment/MgRP/TC after long exposure times. .... 190

Figure 4.1. Low frequency impedance IZI modulus of intact AA2024-T351/Pretreatment/MgRP systems at 0.01 Hz vs time in the environments indicated for (a) ANS/MgRP (b) ACS/MgRP and (c) ATS/MgRP. .... 219

Figure 4.2. High Breakpoint Frequency ( $F_{bpt}$ ) of intact AA2024-T351/Pretreatment/MgRP systems vs time in in the environments indicated for (a) ANS/MgRP (b) ACS/MgRP and (c) ATS/MgRP. .... 220

Figure 4.3. Selected XRD spectra of intact AA2024-T351/ACS/MgRP system after exposure in the LALT/field environments ..... 221

Figure 4.4. The normalized integral XRD intensity for Mg<101> XRD peak of intact AA2024-T351/Pretreatment/MgRP systems vs time in the environments indicated for (a) ANS/MgRP, (b) ACS/MgRP and (c) ATS/MgRP. .... 222

Figure 4.5. Average global galvanic protection potential of intact coating for the last 1 h of exposure in 5 % wt NaCl vs the normalized integral XRD intensity for Mg<101>. The time indicates total exposure time in different LALT/Field environments indicated, AA2024-T351/Pretreatment/MgRP after exposure, in Full immersion in 5 % wt NaCl, ASTM B-117 in 5 % wt NaCl and Field at CHO. (a) ANS/MgRP and (b) ACS/MgRP ..... 223

Figure 4.6. Breakpoint Frequency of intact coating after 1 h exposure in 5 % wt NaCl vs The normalized integral intensity for Mg<101>. The time indicates total exposure time in different LALT/Field environments indicated, (a) AA2024-T351/ACS/MgRP after exposure, in Full immersion in 5 % wt NaCl, ASTM B-117 in 5 % wt NaCl, and Field exposure at CHO.....

Figure 4.7. Raman spectra for AA2024-T351/ACS/MgRP) (a) Standard ASTM B-117 exposure – 1000 h and (b) At field, KSC for 24 weeks ..... 224

Figure 4.8. EDS maps of elemental Mg across scribe and adjacent coating a) ACS pretreated 2024-T351/MgRP before environmental exposure, b) ACS pretreated 2024-T351/MgRP after 400 h exposure in ASTM B-117, c) ACS pretreated 2024-T351/MgRP after 1000 h exposure in ASTM B-117. (red dash lines indicates the borders of the scribe in the figure) ..... 225

Figure 4.9. a) EDS line profile of ACS pretreated AA2024-T351/MgRP without a topcoat after 1000 h exposure time in ASTM B-117 testing (red dash line indicates the borders of the scribe in the figure). Integral intensity of Mg EDS line profile in scribe/MgRP as a function of exposure time in (b) ASTM B-117 testing for 1000 h (c) KSC for 8736 h and (d) ASTM B-117 modified with acidified ASTM SOW/UV testing for 1000 h. .... 226

Figure 4.10. Optical profilometry maps of scribe exposing AA2024-T351 in pretreated AA2024-T351/MgRP without topcoat after exposure in ASTM B-117 for 1000 h. (a) AA2024-T351/ANS/MgRP, (b) AA2024-T351/ACS/MgRP and (c) AA2024-T351/ATS/MgRP. The 0 μm position (white) on the scale is indicative of the starting material condition before corrosion. . 227

Figure 4.11. Corrosion volume loss of scribe exposing AA2024-T351 in AA2024-T351/Pretreatment/MgRP without topcoat as a function of exposure time in in different LALT/field environments indicated. The baseline data is for uncoated AA2024-T351. (a)

AA2024-T351/ANS/MgRP, (b) AA2024-T351/ACS/MgRP and (c) AA2024-T351/ATS/MgRP .....	228
Figure 4.12. Low frequency impedance IZI modulus of AA2024-T351/Pretreatment/MgRP/TC systems at 0.01 Hz vs time in the environments indicated for (a) ANS/MgRP/TC (b) ACS/MgRP/TC and (c) ATS/MgRP/TC. ....	229
Figure 4.13. High breakpoint frequency ( $F_{bpt}$ ) of AA2024-T351/Pretreatment/MgRP/TC systems vs time in the environments indicated for (a) ANS/MgRP/TC (b) ACS/MgRP/TC and (c) ATS/MgRP/TC .....	230
Figure 4.14. Selected XRD spectra of AA2024-T351/ACS/MgRP/TC system after exposure in the LALT/field environments. ....	231
Figure 4.15. The normalized integral XRD intensity for Mg<101> XRD peak of AA2024-T351/Pretreatment/MgRP/TC systems vs time in the environments indicated for (a) ANS/MgRP/TC (b) ACS/MgRP/TC and (c)ATS/MgRP/TC.....	232
Figure 4.16. Optical profilometry maps of scribe exposing 2024-T351 in pretreated 2024-T351/MgRP systems with topcoat after exposure in indicated LALT environments. (a) AA2024-T351/ANS/MgRP/TC, (b) AA2024-T351/ACS/MgRP/TC and (c) AA2024-T351/ATS/MgRP/TC. The 0 $\mu\text{m}$ position (white) on the scale is indicative of the starting material condition before corrosion. ....	233
Figure 4.17. Corrosion volume loss of scribe exposing AA2024-T351 in pretreated AA2024-T351/MgRP with and without topcoat as a function of exposure time in in different LALT/field environments indicated. (a) AA2024-T351/ANS/MgRP/TC, (b) AA2024-T351/ACS/MgRP/TC and (c) AA2024-T351/ATS/MgRP/TC. The baseline data is for uncoated AA2024-T351. ....	234

Figure 5.1. Macroscopic morphology of AA2024-T351/Pretreat after different LALT/field exposures. (a) AA2024-T351/NFF after 1000 h in ASTM B117 (b) AA2024-T351/CCC after 1000 h in ASTM B117 (c) AA2024-T351/ACS after 1440 h in ASTM B117 (d) AA2024-T351/NFF after 1440 h in Modified ASTM B117 (e) AA2024-T351/CCC after 1440 h in Modified ASTM B117 (f) AA2024-T351/ACS after 1440 h in Modified ASTM B117 and (g) AA2024-T351/NFF after 4032 h in CHO..... 262

Figure 5.2. Low frequency impedance IZI modulus of AA2024-T351/Pretreatment systems at 0.01 Hz vs time in the environments indicated for (a) Standard ASTM B117 (b) At field, CHO (c) Modified ASTM B117 with SOW and UV and (d) Full immersion in 5 % (wt) NaCl solution. 263

Figure 5.3. Average open circuit potential (1 hour) of AA2024-T351/Pretreatment systems vs time in the environments indicated for (a) Standard ASTM B117 (b) At field, CHO (c) Modified ASTM B117 with SOW and UV and (d) Full immersion in 5 % (wt) NaCl solution..... 264

Figure 5.4. Optical profilometry maps of AA2024-T351/Pretreatment after exposure in standard ASTM B117 for 400 h. (a) AA2024-T351/NFF, (b) AA2024-T351/CCC, (c) AA2024-T351/TCP, (d) AA2024-T351/NCP, (e) AA2024-T351/ANS, (f) AA2024-T351/ACS and (g) AA2024-T351/ATS. The 0  $\mu\text{m}$  position (white) on the scale is indicative of the starting material condition before corrosion. .... 265

Figure 5.5. Corrosion volume loss of AA2024-T351/Pretreatment as a function of exposure time in in different LALT/field environments indicated. (a) NFF vs conversion coating in standard ASTM B117, (b) NFF vs anodization in standard ASTM B117, (c) NFF vs conversion coating in modified ASTM B117, (d) NFF vs anodization in modified ASTM B117, (e) NFF vs conversion coating at CHO, and (f) NFF vs anodization at CHO..... 266

Figure 5.6. SEM morphology of 2024-T351/Pretreat after exposure in standard ASTM B117 environment for 1000 h. (a) AA2024-T351/NFF, (b) AA2024-T351/CCC, (c) AA2024-T351/TCP, (d) AA2024-T351/NCP, (e) AA2024-T351/ANS, (f) AA2024-T351/ACS and (g) AA2024-T351/ATS. .... 267

Figure 5.7. EDS maps of oxygen across scribe and adjacent pretreatment after exposure in standard ASTM B117 environment for 1000 h. (a) AA2024-T351/NFF, (b) AA2024-T351/CCC, (c) AA2024-T351/TCP, (d) AA2024-T351/NCP, (e) AA2024-T351/ANS, (f) AA2024-T351/ACS and (g) AA2024-T351/ATS..... 268

Figure 5.8. EDS maps of oxygen across scribe and adjacent pretreatment after exposure in LALT/field environment for selected pretreatments. (a) AA2024-T351/NFF after 1440 h in modified ASTM B117, (b) AA2024-T351/TCP after 1440 h in modified ASTM B117, (c) AA2024-T351/ACS after 1440 h in modified ASTM B117, (d) AA2024-T351/NFF after 4032 h in CHO, (e) AA2024-T351/TCP after 4032 h in CHO and (f) AA2024-T351/ACS after 4032 h in CHO ..... 269

Figure 5.9. Optical profilometry maps of AA2024-T351 scribe in AA2024-T351/Pretreatment after exposure in standard ASTM B117 environment for 1000 h. (a) AA2024-T351/NFF, (b) AA2024-T351/CCC, (c) AA2024-T351/TCP, (d) AA2024-T351/NCP, (e) AA2024-T351/ANS, (f) AA2024-T351/ACS and (g) AA2024-T351/ATS. The 0  $\mu\text{m}$  position (white) on the scale is indicative of the starting material condition before corrosion. .... 270

Figure 5.10. Corrosion volume loss of bare AA2024-T351 scribe in AA2024-T351/Pretreatment panel as a function of exposure time in different LALT/field environments indicated. (a) Standard ASTM B117 (b) Modified ASTM B117 with SOW and UV and (c) At field, CHO..... 271

Figure 5.11. Raman spectra for AA2024-T351/Pretreatment after different LALT exposure times (a) AA2024-T351/CCC, pristine conditions, (b) AA2024-T351/ACS, pristine conditions, (c) AA2024-T351/ACS after 48 h exposure in standard ASTM B117 environment and (d) AA2024-T351/ACS after 1000 h exposure in standard ASTM B117 environment.....	272
Figure 5.12. Raman spectra for of AA2024-T351 scribe in AA2024-T351/Pretreatment after exposure in standard ASTM B117 environment (a) AA2024-T351/CCC, 48 h in ASTM B117, (b) AA2024-T351/ACS, after different exposure times in ASTM B117 .....	273
Figure 5.13. Cathodic polarization of bare/pretreated AA2024-T351 in quiescent 1 M NaCl (a)/ 1 M MgCl <sub>2</sub> solution (b).....	274
Figure 5.14. Anodic polarization of bare/pretreated AA2024-T351 in quiescent 1 M NaCl (a)/ 1 M MgCl <sub>2</sub> solution (b) .....	275
Figure 5.15. Leaching kinetics of bare/pretreated AA2024-T351 as a function of controlled relative humidity exposure time. (a) Al <sup>3+</sup> leaching kinetics of 2024-T351/Pretreatment after different exposure time as a function of pretreatment and (b) Leaching kinetics of Cr or Zr in selected pretreatments after different exposure time. ....	276
Figure 5.16. Cathodic polarization of bare AA2024-T351 in quiescent 1 M NaCl (a)/ 1 M MgCl <sub>2</sub> solution (b) as a function of CrO <sub>4</sub> <sup>2-</sup> concentration. ....	277
Figure 5.17. Anodic polarization of bare AA2024-T351 in quiescent 1 M NaCl (a)/ 1 M MgCl <sub>2</sub> solution (b) as a function of CrO <sub>4</sub> <sup>2-</sup> concentration. ....	278
Figure 6.1. Sample design for SVET experiments. (a) coating/scribe ratio (0.3) and (b) coating/scribe ratio (5) .....	310

Figure 6.2. Average OCP of last 1 hour of exposure (a)/ Low Frequency Mod. Z (b) vs full immersion exposure time for selected 2024-T351/Pretreatment/MgRP with/without topcoat indicated..... 312

Figure 6.3. Mixed potential model depicting  $E_{\text{surface}}$  and  $E_{\text{couple}}$  as they pertain to a galvanic couple between bare and pretreated 2024-T351 and polymer coated Mg.  $R_{\text{polymer}}$ ,  $R_{\text{pretreat}}$  and  $R_s$  indicates polymer resistance, pretreatment resistance and solution resistance, respectively.  $E_{\text{corr}2024}$ ,  $E_{\text{corr}Mg}$  indicate corrosion potential of bare 2024-T351 and bare Mg, respectively.  $E_{\text{couple}2024}$ ,  $E_{\text{couple}Mg}$  indicate galvanic couple potential at surface for bare 2024-T351 and bare Mg, respectively.  $E_{\text{surface}polymer}$ ,  $E_{\text{surface}pretreat}$  indicate Galvanic couple potential at surface of 2024-T351/pretreatment and 2024-T351/pretreatment/MgRP, respectively..... 313

Figure 6.4. OCP of bare 2024-T351 galvanically coupled to 2024-T351/Pretreatment/MgRP with/without topcoat for for two coating to scribe area ratios, 0.3 (a) and 5 (b) ..... 314

Figure 6.5. Surface plots showing the distribution of normal current density  $j_z$  above a 2024-T351 alloy sample freely corroding in aerated 2 M NaCl solution. Data were obtained from SVET scans carried out (a) 0 h, (b) 4 h, (c) 14 h, (d) 26 h and (e) 36 h after sample immersion. (f) shows the visual appearance of the sample after 38 h immersion. .... 315

Figure 6.6. (a) Surface plots showing the distribution of normal current density  $j_z$  above a 2024-T351 alloy sample galvanically coupled to Mg in aerated 2 M NaCl solution. (b) Representative SVET line scan of 2024-T351/Mg couple (c) shows the visual appearance of the sample after 1 h immersion. .... 316

Figure 6.7. Surface plots showing the distribution of normal current density  $j_z$  above a 2024-T351 alloy adjacent to 2024-T351/NFF/MgRP in aerated 2 M NaCl solution. Data were obtained from SVET scans carried out (a) 0 h, (b) 4 h, (c) 14 h, (d) 26 h and (e) 36 h after sample immersion. (f)

shows the visual appearance of the sample after 38 h immersion. Coating to scribe area ratio (CSR) – 0.3..... 317

Figure 6.8. Surface plots showing the distribution of normal current density  $j_z$  above a 2024-T351 alloy adjacent to 2024-T351/TCP/MgRP in aerated 2 M NaCl solution. Data were obtained from SVET scans carried out (a) 0 h, (b) 4 h, (c) 14 h, (d) 26 h and (e) 36 h after sample immersion. (f) shows the visual appearance of the sample after 38 h immersion. Coating to scribe area ratio (CSR)

– 0.3..... 318

Figure 6.9. Surface plots showing the distribution of normal current density  $j_z$  above an 2024-T351 alloy adjacent to 2024-T351/ACS/MgRP in aerated 2 M NaCl solution. Data were obtained from SVET scans carried out (a) 0 h, (b) 4 h, (c) 14 h, (d) 26 h and (e) 36 h after sample immersion. (f)

shows the visual appearance of the sample after 38 h immersion. Coating to scribe area ratio (CSR) – 0.3..... 319

Figure 6.10. (a) Representative SVET line scans showing the distribution of normal current density  $j_z$  above freely corroding bare 2024-T351 alloy (a) and 2024-T351 alloy adjacent to 2024-T351/Pretreat/MgRP (b-d) in aerated 2 M NaCl solution ..... 320

Figure 6.11. Schematic for SVET analysis. The dotted lines indicates the separation of regions of interest to determine throwing power from local anodic/cathodic current densities in SVET maps.

Regions of interest (a) MgRP coating. (b) Scribe – 0 -2 mm away from the coating edge (c) Scribe - 2 – 4 mm away from the coating edge (d) Scribe – 4 – 6 mm away from the coating edge (e) Scribe – 6 – 8 mm away from the coating edge (f) Scribe – 8 – 10 mm away from the coating edge ..... 321

Figure 6.12. Total anodic current density as a function of exposure time for selected 2024-T351/Pretreatment/MgRP systems; (a) NFF/MgRP, (b) TCP/MgRP and (c) ACS/MgRP. Anodic

current density was calculated in scribe at five different regions with various distance away from coating interface as indicated in legend. Anodic current density from control (bare 2024-T351) was also provided for comparison. .... 322

Figure 6.13. Total cathodic current density as a function of exposure time for selected 2024-T351/Pretreatment/MgRP systems; (a) NFF/MgRP, (b) TCP/MgRP and (c) ACS/MgRP. Cathodic current density was calculated in scribe at five different regions with various distance away from coating interface. Cathodic current density from control (bare 2024-T351) was also provided for comparison..... 323

Figure 6.14. Mixed potential model of a galvanic couple between various area ratios of bare Mg to bare AA2024-T351 in 1.0 M NaCl solution.<sup>10</sup> ..... 324

Figure 6.15. Surface plots showing the distribution of normal current density  $j_z$  above a 2024-T351 alloy adjacent to 2024-T351/NFF/MgRP in aerated 2 M NaCl solution. Data were obtained from SVET scans carried out (a) 0 h, (b) 4 h, (c) 14 h, (d) 24 h and (e) shows the visual appearance of the sample after 24 h immersion. Coating to scribe area ratio (CSR) – 5 ..... 325

Figure 6.16. Surface plots showing the distribution of normal current density  $j_z$  above a 2024-T351 alloy adjacent to 2024-T351/TCP/MgRP in aerated 2 M NaCl solution. Data were obtained from SVET scans carried out (a) 0 h, (b) 4 h, (c) 14 h, (d) 24 h and (e) shows the visual appearance of the sample after 24 h immersion. Coating to scribe area ratio (CSR) – 5 ..... 326

Figure 6.17. Surface plots showing the distribution of normal current density  $j_z$  above a 2024-T351 alloy adjacent to 2024-T351/ACS/MgRP in aerated 2 M NaCl solution. Data were obtained from SVET scans carried out (a) 0 h, (b) 4 h, (c) 14 h, (d) 24 h and (e) shows the visual appearance of the sample after 24 h immersion. Coating to scribe area ratio (CSR) – 5 ..... 327

Figure 6.18. (a) Representative SVET line scans showing the distribution of normal current density  $j_z$  2024-T351 alloy adjacent to 2024-T351/Pretreat/MgRP in aerated 2 M NaCl solution (a) NFF/MgRP, (b) TCP/MgRP and (c) ACS/MgRP. Coating to scribe area ratio (CSR) – 5 ..... 328

Figure 6.19. Total anodic (a) and cathodic (b) current density as a function of exposure time for selected 2024-T351/Pretreatment/MgRP systems for 2024-T351/Pretreatment/MgRP with different coating to scribe area ratio. Anodic and cathodic current density from control (bare 2024-T351) was also provided for comparison..... 329

Figure 6.20. Surface plots showing the distribution of normal current density  $j_z$  above an 2024-T351 alloy adjacent to 2024-T351/NFF/MgRP/TC in aerated 2 M NaCl solution. Data were obtained from SVET scans carried out (a) 0 h, (b) 4 h, (c) 14 h, (d) 24 h and (e) shows the visual appearance of the sample after 24 h immersion..... 330

Figure 6.21. Surface plots showing the distribution of normal current density  $j_z$  above an 2024-T351 alloy adjacent to 2024-T351/NFF/MgRP/TC in aerated 2 M NaCl solution. Data were obtained from SVET scans carried out (a) 0 h, (b) 4 h, (c) 14 h, (d) 24 h and (e) shows the visual appearance of the sample after 38 h immersion..... 331

Figure 6.22. Representative SVET line scans showing the distribution of normal current density  $j_z$  2024-T351 alloy adjacent to 2024-T351/Pretreat/MgRP/TC in aerated 2 M NaCl solution (a) NFF/MgRP/TC (CSR: 0.3), (b) NFF/MgRP/TC (CSR: 5)..... 332

Figure 6.23. Total anodic (a) and cathodic (b) current density as a function of exposure time at 2024-T351 scribe adjacent to 2024-T351/NFF/MgRPTC with different coating to scribe area ratio. Anodic and cathodic current density from control (bare 2024-T351) and 2024-T351 coupled to NFF/MgRP (CSR: 0.3) was also provided for comparison. .... 333

Figure 8.1. Phenomenological model to understand effect of (a) anionic species leaching from pretreatments on cathodic kinetics of bare 2024-T351 and anodic kinetics of Mg (b) resistive effects of pretreatments on cathodic kinetics of bare/pretreated 2024-T3351 and (c) pretreatment degradation on cathodic kinetics of pretreated 2024-T351..... 347

Figure 8.2. E-log (i) data for bare AA2024-T351 in quiescent NaCl solution of different concentration (a) 5 M, (b) 1 M, (c) 0.1 M, (d) 0.01 M and (e) 0.001 M NaCl at 4 inhibitor concentrations ..... 348

Figure 8.3. E-log (i) data for bare AA2024-T351 in quiescent MgCl<sub>2</sub> solution of different concentration (a) 5 M, (b) 1 M, (c) 0.1 M, (d) 0.01 M and (e) 0.001 M MgCl<sub>2</sub> at 4 inhibitor concentrations ..... 349

Figure 8.4. E-log (i) data for bare and pretreated AA2024-T351 in quiescent MgCl<sub>2</sub> solution of different concentration (a) 5 M, (b) 1 M, (c) 0.1 M, (d) 0.01 M and (e) 0.001 M MgCl<sub>2</sub> The pretreatments indicated are (a) non-film forming (NFF), (b) chromate conversion coating (CCC), (c) trivalent chromium pretreatment (TCP), (d) non-chromium pretreatment (NCP), (e) anodized no seal (ANS), (f) anodized chromate seal (ACS) and (g) anodized TCP seal (ATS). ..... 350

Figure 8.5. E-log (i) data for bare and pretreated AA2024-T351 in quiescent NaCl solution of different concentration (a) 5 M, (b) 1 M, (c) 0.1 M, (d) 0.01 M and (e) 0.001 M NaCl. The pretreatments indicated are (a) non-film forming (NFF), (b) chromate conversion coating (CCC), (c) trivalent chromium pretreatment (TCP), (d) non-chromium pretreatment (NCP), (e) anodized no seal (ANS), (f) anodized chromate seal (ACS) and (g) anodized TCP seal (ATS). ..... 351

Figure 8.6. E-log (i) data for pretreated AA2024-T351 in quiescent 1 M NaCl solution after different full immersion exposure times for (a) CCC, (b) TCP and (c) NCP ..... 352

Figure 8.7. E-log (i) data for pretreated AA2024-T351 in quiescent 1 M NaCl solution after different full immersion exposure times for (a) ANS, (b) ACS and (c) ATS..... 353

Figure 8.8. E-log (i) data for Mg in quiescent NaCl solution of different concentration (a) 5 M, (b) 1 M, (c) 0.1 M, (d) 0.01 M and (e) 0.001 M NaCl at 4 inhibitor concentrations..... 354

Figure 8.9. E-log (i) data for Mg in quiescent MgCl<sub>2</sub> solution of different concentration (a) 5 M, (b) 1 M, (c) 0.1 M, (d) 0.01 M and (e) 0.001 M MgCl<sub>2</sub> at 4 inhibitor concentrations..... 355

Figure 8.10. Schematic of geometric model developed in FEA software (COMSOL) (a) material and electrolyte conditions studied where the polymer resistance is given and (b) Significant difference in existing model used for throwing power determination ..... 358

Figure 9.1. Sample design for SVET and optical profilometry measurements. (a) coating/scribe ratio (0.3) and (b) coating/scribe ratio (5)..... 362

Figure 9.2. Optical profilometry maps indicating depth perpendicular to the plan of the surface for scribe exposing bare 2024-T351 adjacent to the coating (< 2 mm) for selected coating systems indicated after exposure in full immersion for 275 h. (a) no coating, (b) 2024-T351/NFF/MgRP, (c) 2024-T351/TCP/MgRP, (d) 2024-T351/ACS/MgRP and (e) 2024-T351/NFF/MgRP/TC. Coating to scribe area ratio: 0.3. .... 363

Figure 9.3. Optical profilometry maps indicating depth perpendicular to the plan of the surface for scribe exposing bare 2024-T351 adjacent to the coating (< 8 mm) for selected coating systems indicated after exposure in full immersion for 275 h. (a) no coating, (b) 2024-T351/NFF/MgRP, (c) 2024-T351/TCP/MgRP, (d) 2024-T351/ACS/MgRP and (e) 2024-T351/NFF/MgRP/TC. Coating to scribe area ratio: 0.3. .... 364

Figure 9.4. Optical profilometry maps indicating depth perpendicular to the plan of the surface of scribe exposing bare 2024-T351 adjacent to the coating (< 2 mm) in selected coating systems

indicated after exposure in full immersion for 275 h. (a) no coating, (b) 2024-T351/NFF/MgRP, (c) 2024-T351/TCP/MgRP, (d) 2024-T351/ACS/MgRP and (e) 2024-T351/NFF/MgRP/TC.

Coating to scribe area ratio: 5. .... 365

Figure 9.5. Corrosion volume loss of scribe exposing AA2024-T351 adjacent to the coating (< 2 mm) in selected coating systems indicated after exposure in full immersion for 275 h. (a) corrosion volume loss as a function of distance from coating interface. (b) corrosion volume loss as a function of coating to scribe area ratio (CSR) ..... 366

Figure 10.1. Secondary electron image (a) and elemental maps of Al (b), Mg (c) and Cu (d) of bulk synthesized S phase ( $Al_2CuMg$ ) intermetallic particle, as cast..... 372

Figure 10.2. Secondary electron image (a) and elemental maps of Al (b), Fe (c) and Cu (d) of bulk synthesized  $Al_7Cu_2Fe$  intermetallic particle, as cast..... 373

Figure 10.3. Secondary electron image (a) and elemental maps of Al (b), and Cu (c) of bulk synthesized Al – 4 wt % Cu alloy, as cast. .... 374

Figure 10.4. Secondary electron image (a) and elemental maps of Al (b), and Cu (c) of bulk synthesized  $\theta$  phase ( $Al_2Cu$ ) intermetallic particle, as cast. .... 375

Figure 10.5. Volta potential maps without electrolyte at 95 % RH, ambient temperature for (a) 2024-T351, (b) Al-4 wt. % Cu, (c)  $Al_7Cu_2Fe$ , (d)  $Al_2CuMg$  and (e)  $Al_2Cu$  of bulk synthesized S phase ( $Al_2CuMg$ ) intermetallic particle ..... 376

Figure 10.6. Volta potential for bare metals, alloys and bulk synthesized intermetallic phases indicated without electrolyte at 95 % RH, ambient temperature as a function of exposure time (a) and average Volta potential for bare metals, alloys and bulk synthesized intermetallic phases indicated (obtained from Volta potential maps). .... 377

Figure 10.7. Initial Volta potential maps (0-15 min) for 2024-T351/NFF/MgRP exposing a bare scribe (2024-T351) under 5 M NaCl electrolyte at 95 % RH, ambient temperature. The red region in the map indicates the scribe whereas the blue regions indicate the MgRP region. The sample design utilized for the above experiments is same as one utilized for LALT and field exposures (~ 650 μm machine drilled scribe). ..... 378

Figure 10.8. Initial Volta potential line profiles (0 – 360 min) (a) and surface topography (b) for 2024-T351/NFF/MgRP exposing a bare scribe (2024-T351) under NaCl electrolyte air dried prior to environmental exposure. Relative humidity was increased in steps from 45 % and held at 95 % RH for 6 h. .... 379

Figure 10.9. Initial Volta potential line profiles for samples indicated under 650 μl of 5 M NaCl electrolyte at 95 % RH, ambient temperature. (a) Mg ribbon coupled to bare 2024-T351, (b) 2024-T351/NFF/MgRP coupled to bare 2024-T351 and (c) 2024-T351/NFF/MgRP/TC coupled to bare 2024-T351..... 380

Figure 11.1. Low frequency impedance IZI modulus of intact AA2024-T351/Pretreatment/MgRP at 0.01 Hz vs time in the environments indicated for (a) 2024-T351/Pretreatment/MgRP (b) 2024-T351/Pretreatment/MgRP/TC..... 386

Figure 11.2. High breakpoint frequency ( $F_{bpt}$ ) of intact AA2024-T351/Pretreatment/MgRP at 0.01 Hz vs time in the environments indicated for (a) 2024-T351/Pretreatment/MgRP (b) 2024-T351/Pretreatment/MgRP/TC..... 387

Figure 11.3. The normalized integral XRD intensity for Mg<101> XRD peak of intact AA2024-T351/Pretreatment/MgRP at 0.01 Hz vs time in the environments indicated for (a) 2024-T351/Pretreatment/MgRP (b) 2024-T351/Pretreatment/MgRP/TC ..... 388

Figure 11.4. Average global galvanic protection potential of intact coating for the last 1 h exposure in 5 % wt NaCl vs the normalized integral XRD intensity for Mg<101>. The time indicates total exposure time in different LALT/Field environments indicated, (a) AA2024-T351/NFF/MgRP after exposure, in Full immersion in 5 % wt NaCl and Field at CHO and (b) AA2024-T351/TCP/MgRP after exposure, in Full immersion in 5 % wt NaCl, ASTM B-117 in 5 % wt NaCl and Field at CHO. .... 389

Figure 11.5. High breakpoint frequency of intact coating after 1 h exposure in 5 % wt NaCl vs The normalized integral intensity for Mg<101>. The time indicates total exposure time in different LALT/Field environments indicated, (a) AA2024-T351/NFF/MgRP after exposure, in Full immersion in 5 % wt NaCl, ASTM B-117 in 5 % wt NaCl, Modified ASTM B-117 with acidified SOW and UV and Field exposure at CHO. .... 390

Figure 11.6. EDS maps of elemental Mg and Ca across scribe and adjacent coating pretreated 2024-T351/MgRP after 1440 h exposure in modified ASTM B117 with ASTM SOW and UV (a/b) NFF/MgRP, (c/d) TCP/MgRP and (e/f) ACS/MgRP. (red dash line indicates the borders of the scribe in the figure). .... 391

Figure 11.7. Optical profilometry maps of selected AA2024-T351/Pretreatment/MgRP with/without topcoat after exposure in modified ASTM B117 for 1440 h. (a) AA2024-T351/NFF/MgRP, (b) AA2024-T351/NFF/MgRP/TC, (c) AA2024-T351/TCP/MgRP, (d) AA2024-T351/TCP/MgRP/TC, (e) AA2024-T351/ACS/MgRP and (f) AA2024-T351/ACS/MgRPTC. The 0 μm position (white) on the scale is indicative of the starting material condition before corrosion. .... 392

Figure 11.8. Corrosion volume loss of scribe exposing AA2024-T351 in AA2024-T351/Pretreatment/MgRP systems with/without topcoat as a function of exposure time in modified

ASTM B117 with ASTM SOW and UV. The baseline data is for uncoated AA2024-T351. (a) 2024-T351/Pretreatment/MgRP and (b) 2024-T351/Pretreatment/MgRP/TC..... 393

Figure 11.9. Low frequency impedance IZI modulus at 0.01 Hz (a)/High breakpoint frequency ( $F_{bpt}$ ) (b) of intact AA2024-T351/Pretreatment/MgRP vs time in the environments indicated.. 394

Figure 11.10. Average open circuit potential of last 1 hour of exposure for intact AA2024-T351/Pretreatment/MgRP vs time in the environments indicated..... 395

## List of Symbols and Acronyms

ACS – Anodization, chromate sealing

ANS – Anodization, No Sealing

ATS – Anodization, TCP Sealing

$\beta_a$  anodic Tafel slope

$\beta_c$  cathodic Tafel slope

C capacitance

CCC Chromate Conversion Coating

CPE constant phase element

CSR coating to scribe area ratio

$E_{app}$  applied potential

$E_{couple}$  galvanic couple potential

EDS Energy Dispersive Spectroscopy

EIS Electrochemical impedance spectroscopy

$E_{SCE}$  potential measured vs. SCE

$E^0$  equilibrium half-cell potential

$E_{corr}^{2024}$  corrosion potential of bare 2024-T351

$E_{corr}^{Mg}$  corrosion potential of bare Mg

$E_{couple}^{2024}$  galvanic couple potential at surface for bare 2024-T351

$E_{couple}^{Mg}$  galvanic couple potential at surface

$E_{surface}^{polymer}$  Galvanic couple potential at surface of 2024-T351/pretreatment

$E_{surface}^{pretreat}$  Galvanic couple potential at surface of 2024-T351/pretreatment/MgRP

F frequency

F Faraday's constant

F atomic sensitivity factor

$i$  current density (A/cm<sup>2</sup>)

$i^0$  exchange current density

I current (Amps)

I intensity of photoelectron peak

$i_{lim}$  limited current density

$n$  number of electrons transferred in a reaction

OCP Open Circuit Potential

PVC Pigment volume concentration

MgRP Magnesium Rich Primer

NFF Non-Film Forming

NCP Non-Chromium Pretreatment

R resistance ( $\Omega$ )

$R_p$  polarization resistance

$R_{pore}$  pore resistance

$R_{polymer}$  polymer resistance

$R_{pretreat}$  pretreatment resistance

$R_s$  solution resistance

$C_{coat}$  coating capacitance

$\sigma$  conductivity (S/m)

$\rho$  resistivity ( $\Omega \cdot m$ )

Q charge

$t$  time

TCP Trivalent Chromium Pretreatment

$\eta$  over-potential

SEM Scanning Electron Microscopy

SKP Scanning Kelvin Probe

SVET Scanning Vibrating Electrode Technique

$V_{pp}$  SVET voltage signal

XRD X-ray Diffraction

XPS X-ray Photoelectron Spectroscopy

# 1 Introduction

## 1.1 Metallurgy and Microstructure of AA2024-T351

Aluminum metal has numerous favorable properties such as high electrical and thermal conductivity, high reflectivity, non-toxic corrosion products and high strength to weight ratio. However, aluminum metal is soft for engineering applications.<sup>1</sup> Its mechanical properties can be improved by adding alloying elements such as copper, magnesium, manganese, zinc and silicon.<sup>1</sup> In general, aluminum alloys are classified into two groups based on thermomechanical processing procedure; wrought and cast aluminum alloy.<sup>1</sup> Wrought aluminum alloys are further classified into numerous groups based on heat-treatability and major alloying elements.<sup>1</sup>

AA2xxx series alloys have Cu and Mg as major alloying elements (Table 1.1) and they are heat treatable and strengthened by quenching or rapid cooling and aging. They have high strength to weight ratio, high damage tolerance and fatigue resistance and are used for aerospace application. Coarse intermetallic compounds (IMC), dispersoids and fine hardening precipitates are generated during the thermomechanical processes and some of them contribute to improved mechanical properties. Major second phase particles in AA2xxx series alloys includes  $\text{Al}_2\text{CuMg}$  (S phase),  $\text{Al}_2\text{Cu}$  ( $\theta$  phase),  $\text{Mg}_2\text{Si}$ ,  $\text{Al}_{12}\text{Si}$  (Mn, Fe),  $\text{Al}_3$  (Mn, Fe) and  $\text{Al}_6$  (Mn, Fe).<sup>2</sup> 60 % of intermetallic particles with dimensions greater than  $0.2 \mu\text{m}$  correspond to S-phase particles and their fraction correspond to 2.7 % of total surface area.<sup>2</sup> The remaining 40 % of intermetallic comprises of a wide range of Al-Cu-Fe-Mn containing phases. In addition submicron size dispersoid particles such as  $\text{Al}_{20}\text{Mn}_3\text{Fe}$ ,  $\text{Al}_{12}\text{Mg}_2\text{Cr}$  and  $\text{Al}_3\text{Zr}$  are also present in the microstructure.<sup>2</sup> At the finest

scale, there are lenticular precipitates around 100 nm in length which comprise the S-phase and the  $\theta$  phase and they both contribute to hardening.<sup>2</sup>

## **1.2 Corrosion Susceptibility of AA2024-T351**

AA2024-T351 forms aluminum oxide films which are thermodynamically stable in water, under ambient conditions in the pH range of 4 to 8.5. The oxide film functions as a barrier layer and lowers the uniform corrosion of Al-rich matrix. However in service, the oxide film breaks down due to the presence of chloride or other anions. This results in a non-uniform localized pitting corrosion. Copper is one of the noblest alloying elements added to aluminum alloys and its distribution has a major impact on the corrosion process.<sup>3,4</sup> Copper-containing intermetallics which are more cathodic compared to Al matrix have high cathodic reaction rates and they assist pit initiation in the surrounding matrix in the form of trenches.<sup>5,6</sup> S-phase particles are more anodic compared to Al matrix and initially undergo preferential dissolution of Al and Mg.<sup>2,7</sup> This results in a copper-rich surface which further enhances the cathodic reaction rates. In addition to this, any soluble copper ions from dissolution of matrix<sup>8</sup> result in intermetallic redeposition as metallic Cu which also results in very high cathodic reaction rates on the surface. The extent of localized corrosion also depends on pH. A schematic of Al alloy surface and electrode potentials of different constituent phases is shown in Figure 1.1.

## **1.3 Anticorrosion Coatings.**

Many different methods are employed to minimize corrosion of metallic structures in service. Based on overall mechanism, protection methods can be classified into two different categories; passive protection and active corrosion protection. While passive

protection mechanisms involve corrosion protection by a barrier layer, active corrosion protection provides additional corrosion protection to remote defects in barrier layer by different corrosion protection mechanisms. In service, a combination of balanced barrier protection along with active corrosion protection is necessary to improve the corrosion protection of underlying substrate.

### **1.3.1 Barrier Protection**

The primary mode of corrosion protection for earlier generation coatings is barrier protection. The electrochemical reactions between the local anodes and cathodes in the substrate can be reduced by protective coatings which function as a barrier.<sup>9-11</sup> Coatings decrease the corrosion by reducing access to ion(s), water and oxygen.<sup>10,11</sup> One mechanism of barrier protection relies on ionic impermeability of the coatings.<sup>10</sup> The ionic impermeability ensures that moisture at the interface of coating and substrate has very high electrical resistance. They do not necessarily keep the water from getting into the substrate. Thus, the conductivity of the electrolyte in the underlying substrate is less and corrosion current between local anodes and cathodes is very minimal.<sup>10</sup> Protective coatings are usually organic polymers and they reduce the weathering, oxidation and corrosion of the underlying substrate. The coating systems consist of a primer (which is usually epoxy based) and a topcoat (polyurethane) which both provide barrier protection.<sup>12</sup> Pretreatments are applied to underlying substrate to improve the adhesion between metal and polymer layers. Some pretreatments also provide additional corrosion protection.<sup>13-43</sup> The degree of protection offered by a barrier coating as well as its adhesion to substrate is dependent on the thickness of the coating system as well as the

generic type and nature of the binder system. In service, however defects in the organic coating are formed by various factors such as abrasion, UV degradation of coating, fretting, chemical attack by aerosol deposition and wetting.<sup>12</sup> One of the significant limitations in barrier coating is that it cannot provide corrosion protection in the place where defects are created.<sup>12</sup> Therefore, active corrosion protection schemes are necessary for long term corrosion protection. Active corrosion protection uses different electrochemical protection mechanisms to protect a remote defect from corrosion.<sup>42</sup> Two most common active corrosion protection systems are corrosion protection by leaching of chemical inhibitor species stored in the pretreatments or the organic primer and sacrificial anode-based cathodic protection.<sup>42</sup>

### **1.3.2 Corrosion Inhibitors**

Corrosion protection by leaching of inhibitor species from the pretreatments or the organic primer has been one of the key approaches for corrosion protection of aerospace aluminum alloys.<sup>42</sup> Hexavalent chromates are currently recognized as one of the most effective inhibitor species for corrosion mitigation of 2024 aluminum alloys.<sup>42</sup> Unfortunately, due to their carcinogenic effects, non-chromate alternatives have been explored for corrosion protection.<sup>42</sup> This section briefly reviews chromates and other non-chromate corrosion inhibitors and their corrosion protection mechanisms.<sup>42</sup>

#### ***Chromates:***

The inhibition of corrosion of 2024 by chromate has been extensively reported.<sup>22-26,42,44-47</sup> Chromate is included in anticorrosion coatings by incorporation in a primer or pretreatment (conversion coatings or sealings in anodization based pretreatments). Chromate functions as an excellent cathodic inhibitor with chloride to chromate ratio as high as  $10^5$  to 1.<sup>44</sup>

Cathodic polarization of 2024-T3 with additions as low as  $10^{-5}$  M showed an order of magnitude decrease in limiting current for oxygen reduction reaction (ORR).<sup>44</sup> The mechanism for corrosion protection is suppression of the ORR at copper rich intermetallics by adsorption of  $\text{Cr}^{6+}$  oxoanions and then reduction of these anions to form an irreversible trivalent chromium based hydroxide that is strongly bonding and inhibiting the electron transfer. Co-adsorbed  $\text{Cr}^{6+}$  anions were seen in the robust  $\text{Cr}^{3+}$  hydroxide.<sup>47</sup> The anodic inhibition by chromate on Al has been thoroughly studied and chromates provide modest anodic inhibition.<sup>44</sup> It reduces the pit nucleation occurrence and pit growth kinetics. This reduction in pitting is attributed to its ability to stabilize barrier oxides through either electrochemical reduction or incorporation into the oxide film or through competitive adsorption with  $\text{Cl}^-$  as an adsorbing ion without a three dimensional oxide.<sup>44</sup>

***Permanganate:***

The manganese system has multiple valence states between +7 and +2 which, in a similar way to chromate system, can provide mechanisms for transport of the soluble oxidizing inhibiting species to sites for electrochemical reduction leading to the potential for self-healing.<sup>48-53</sup> Low concentration pretreatment with permanganate leads to a slight increase in pitting potential ( $E_{\text{pit}}$ ) of 2024 but only when partially oxidized manganese oxides were electrochemically deposited over 2024 matrix. Permanganate increases cathodic reaction rates when present in solution. However, when permanganate was used as a pretreatment and was electrochemically deposited as a lower valence oxide on the IMCs, it decreased cathodic reaction rates.<sup>52,53</sup> Moreover, OCP was greatly reduced after pretreatment as copper rich sites were covered with manganese oxides.<sup>48</sup> The slow reduction of high valence manganese oxides may account for the gradual decrease in OCP.<sup>48</sup> Copper

replating during NaCl exposure also decreased after pretreatments. In summary,  $\text{MnO}_4^{2-}$  is a complex ionic inhibitor that is more beneficial when present as pretreatment compared to an ionic species addition.

***Cerium:***

Cerium has been studied as a corrosion inhibitor for precipitation age-hardened aluminium alloys.<sup>54-62</sup> Cerium forms protective barrier hydroxide film in high pH region by chemical reaction of  $\text{Ce}^{3+}$  ions with hydroxyl ions in the solution.<sup>62</sup> This lowers the cathodic reaction rates in intermetallic region. Cerium has also be found to be a potent inhibitor for copper replating.<sup>62</sup> Anodic inhibition of cerium ions has not been reported in literature.

***Molybdate:***

Molybdate is an oxyanion with a similar structure as chromate,  $\text{MoO}_4^{2-}$  with a valence of +6. Molybdate has been found to be a potent anodic inhibitor increasing the pitting potentials of 2024 significantly.<sup>56,62,63</sup> Competitive adsorption of  $\text{MoO}_4^{2-}$  into barrier films block the adsorption of  $\text{Cl}^-$ . Molybdates have also been found to be a potent inhibitor for ORR and copper replating.<sup>62</sup> Molybdates have been effective cathodic inhibitor only if it was present in solution suggesting no physically precipitated species were present in the film or a film was not effective in blocking the ORR.<sup>62</sup> Anionic addition of molybdate to chloride containing solutions showed inhibition of cathodic reaction and increasing pitting potential.<sup>62</sup> High throughput analysis of binary combinations of inhibitors  $\text{CeCl}_3$  and  $\text{Na}_2\text{MoO}_4$  and  $\text{LaCl}_3/\text{Na}_2\text{MoO}_4$  demonstrated synergy and excellent corrosion inhibition in wide range of concentrations.<sup>64,65</sup>

### ***Vanadates:***

Vanadates operate by mixed inhibition mechanism, inhibiting both the ORR as well as anodic kinetics. The inhibition characteristics of vanadate compounds may be related to their complex aqueous chemistry.<sup>66-68</sup> Depending on the pH of the solution, they exist forms such as ortho-vanadate( $\text{VO}_4^{3-}$ ), pyro-vanadate( $\text{V}_2\text{O}_7^{4-}$ ), meta-vanadate( $\text{VO}_3^-$ ), or poly-vanadate ( $\text{H}_2\text{V}_{10}\text{O}_{28}^{4-}$ ).<sup>66</sup> Sodium metavanadate improved corrosion resistance of 2024-T3 making it comparable to other non-chromate inhibitors.<sup>64</sup> Salt spray tests of decavanadate incorporated coatings/pretreatments showed improved corrosion resistance.<sup>64</sup>

In addition to above mentioned corrosion inhibitors, selected inhibitors such as metaborates, metatungstanates, phosphates and rare earth metals were also investigated for use in synergistic combination.<sup>69</sup>

### ***Organic Inhibitors:***

Organic inhibitors has been studied alongside inorganic inhibitors as possible alternative for chromium based inhibitors. Most organic inhibitors come in the form of weak acids and their derivatives that form insoluble salts at the metal surface.<sup>70</sup> Chelating inhibitors form an intermediate between an organic complex and the metal surface or its oxide.<sup>70</sup> Their effectiveness can be correlated to thin but tenacious passive layer.<sup>70</sup> The potentiokinetic studies of inhibitors such as sodium benzoate, sodium acetate and thioglycolic acid on Al and Al-Cu/Al-Mg alloys showed that these inhibitors are effective only to prevent pit initiation as pit growth occurs inspite of the presence of these selected inhibitors.<sup>70</sup>

$\text{CrO}_4^{2-}$ , a redox active anodic inhibitor operates quite independent of environmental parameters such as oxygen, pH and substrate. <sup>71</sup> Anionic species that are non-chromate

systems such as  $\text{MoO}_4^{2-}$  operate according to action mechanisms that are still dependent on parameters of the environment and hence are less effective compared to chromates.<sup>71</sup> Due to significant performance gap between chromate and non-chromate system, chromates still play an active role for inhibitor based protection system.<sup>71</sup>

### 1.3.3 Sacrificial Coatings

One of the protection schemes utilized for protection of aerospace aluminum alloys and steel is sacrificial anode-based cathodic protection by metallic coatings.<sup>16,19,32,72-96</sup> In this protection scheme a material that is more active than the Al alloy substrate is applied as a coating and it is galvanically coupled to the substrate in the presence of an electrolyte. Some sacrificial coatings commonly used on Al alloys are Al-cladding<sup>96</sup>, Al-Co-Ce metallic coatings<sup>91-93</sup>, Mg rich primer<sup>72,73,75-77,81-85,87,88</sup>, Al rich primer and Zn rich primer. The cladding layer consists of a roll-bonded layer that is usually pure aluminum which is more anodic compared to underlying substrate. Usually, the thickness of the cladding is approximately 1.5-10 % of that of the base metal depending on the characteristics of the cladding alloy, base metal and the environment. The more active, sacrificial coating material preferentially corrodes and provides current to the cathodic, Al-alloy substrate.<sup>96</sup> This cathodic polarization of the substrate, ideally, is sufficiently enough below the threshold potentials of the matrix phase and any constituent particles which make up the AA2024-T351 substrate to decrease both localized and uniform attack. Moreover, coatings which utilize the sacrificial galvanic protection mechanism have the ability to protect bare areas of the substrate that are both ionically and electrically well-connected to the anodic material in the coating.

The distance over which the coating system can protect a defect by sacrificial anode-based cathodic protection, is termed the “galvanic throwing power”. The cathodic protection, as measured by galvanic throwing power, available to a defect depends on many things such as the electrochemical driving force ( $\Delta E_{OCP}$ ) between anodes and cathodes, the area ratios between anodes and cathodes, electrolyte geometry and chemistry, electrical resistances between anodes and cathodes, as well as others. In the case of Al-cladding, which has been used for many decades, the galvanic couple potential that is achieved is often only 80 – 100 mV below the OCP of the substrate alloy it is being used to protect. This modest cathodic polarization of the substrate provides limited driving force for galvanic throwing power to protect bare defects or scratches. Additionally, this galvanic couple potential is often above the critical pitting potential of the cladding material, resulting in non-uniform degradation of the cladding and inefficient anode utilization.

#### **1.4 Corrosion Protection of AA2024-T351 by a Mg Rich Primer – An Overview**

Study of corrosion protection technology which would replace the chromate based inhibitor coatings technology has been of significant interest for research in corrosion control of aerospace aluminum alloys such as AA2024-T351 <sup>72,73,80,81,84,88</sup>. Since Mg would offer cathodic protection to aluminum alloys in a manner similar to Zn pigments used in zinc rich coatings for cathodic corrosion protection of steel <sup>78,79,86,89,90</sup>, Mg-rich coatings formulation would serve the interest of corrosion control of Al alloys. If the coating system is designed properly, the open circuit potential (OCP) also called as galvanic couple potential will take a mixed potential value between the OCPs of the two metal systems involved in the system as shown in Figure 1.2.

The sacrificial anode-based cathodic and barrier protection capabilities of non-chromate magnesium rich primer (MgRP), in both a topcoated and non-topcoated condition, for the corrosion protection of Prekote™ pretreated AA2024-T351 has been extensively studied<sup>72,73,80,81,84,88</sup>. Barrier protection is afforded to the AA2024-T351 substrate by the continuous physical barrier consisting of organic epoxy polymer matrix of the MgRP, the Mg pigment particles and any other insoluble pigments in the primer or corrosion products which may have formed within defects in the coating. Also, an organic polyurethane polymer topcoat is often applied to add additional barrier protection and greatly decrease the coating system's susceptibility to UV degradation. When coupled to AA2024-T351 substrate, the galvanically coupled Mg pigment becomes an electron donor via Mg oxidation to  $Mg^{2+}$ , and mixed potential theory can be used to explain the open circuit of the system when exposed to full immersion. This has been verified with open circuit and anodic polarization measurement of AA2024-T351 coated with experimental formulations of MgRP.<sup>84</sup>

Two possible modes of protection; long range protection of remote defects by global galvanic protection potential afforded to the substrate and local or short range Mg pigment-based protection of local and buried defects are observed.<sup>84</sup> A schematic of the same is shown in the Figure 1.3. Both modes of protection are mediated by the high ionic and electrical resistance of the coating systems as a function of MgPVC, substrate pretreatments, primer polymer and topcoat properties.<sup>84</sup> The mediation of cathodic protection abilities is important in the application of MgRP. It is important for the coating system to provide adequate cathodic protection to AA2024-T351 substrate, but also avoid the detrimental effects of cathodic

corrosion of the amphoteric AA2024-T351 substrate which can be caused by increased localized pH due to severe cathodic polarization and/or excessive Mg pigment dissolution.<sup>84</sup>

Past lab and field exposure studies were conducted to determine an optimal primer formulation with respect to Mg pigment volume concentration along with optimal coating system stack-ups.<sup>84</sup> Most of these studies have pointed to an optimal Mg pigment volume concentration of approximately 45 % which is at, or just below, the calculated theoretical pigment concentration.<sup>84</sup> This formulation is speculated to provide a balance of moderated sacrificial cathodic protection, long term barrier protection, and the beneficial characteristics of preserved, isolated clusters of Mg pigment available for the protection of future defects as they occur throughout a coating lifetime in a given exposure environment.<sup>84</sup>

Also test methods were developed to assess MgRP in the laboratory and in the field. Mg pigment depletion rate, galvanic couple potential and coating barrier properties were tracked throughout exposure periods in both field and laboratory accelerated life environments.<sup>80,81</sup> Preliminary acceleration factors with respect to pigment depletion and residual barrier properties were developed in field vs lab exposures.<sup>80,81</sup> Post-mortem characterization with SEM/EDS was conducted to elucidate coating and scribe morphology, corrosion products present, corrosion of the AA2024-T351 substrate, as well as in an attempt to determine the galvanic throwing power of the MgRP coating system based on cathodic protection of a scratch exposing bare AA2024-T351.<sup>80,81</sup>

The "galvanic throwing power" (TP) of the MgRP coating system pertains to the distance extending perpendicularly away from the edge of a scribe in the MgRP coating exposing bare AA 2024-T351 by sacrificial anode-based cathodic protection.<sup>81</sup> Conversely, the "inverse

throwing power" is the distance extending perpendicularly away from the scribe back into the MgRP coating in which Mg pigment is anodically polarized within a polymer resin while actively galvanically coupled to the AA 2024-T351 scribe, scratch or defect<sup>81</sup>. A sacrificial coating can protect a defect which is electrically and ionically connected to Mg. In lab accelerated life cycle tests (LALT) such as salt fog, a continuous layer of electrolyte is formed over the scribe as well as adjacent coating.<sup>81</sup> In this system, the throwing power is limited by secondary and tertiary current distribution based on mixed potential theory.<sup>81</sup> Previous LALT exposure experiments conducted showed the effectiveness of the Mg to protect the whole scribe.<sup>81</sup> However in field environments, electrolyte layer is tortuous as thin film electrolyte might shrink to small disconnected droplets due to relative humidity change with respect to efflorescent point of deposited salts.<sup>82</sup> A hypothetical RH cycle which could be observed in an environment changes with time, so does the equilibrium salt concentration and geometry of the electrolyte layer, playing an important role in dictating galvanic throwing power and subsequent cathodic protection vs scratch distance afforded by the MgRP coating system.<sup>82</sup> The drying characteristics of individual salts was also shown to have an effect on evolution of throwing power as MgCl<sub>2</sub> was shown to be less susceptible to drying at low RH, thus extending the time of which the galvanic couple was active compared to pure NaCl or ASTM Artificial Sea Water. Corrosion will occur in these local droplet regions while the Mg would not be able to provide cathodic protection as it would not be ionically connected to the defect.<sup>82</sup> A hypothetical schematic of AA 2024-T351 coated with MgRP is shown in Figure 1.4, which shows how electrolyte thickness varies as a function of environment in which it is exposed. A definitive determination of throwing power from post-mortem sample evaluation is difficult due to factors in the field such as drying or wetting event which makes the Mg-Al

alloy ionic contact tortuous which could temporarily increase or diminish the throwing power of the MgRP.<sup>82</sup> These limitations emphasize a need for alternate methods to predict throwing power or spatial current-potential relationship distribution of the physical AA 2024-T351 system.<sup>82</sup> Understanding and predicting throwing power and inverse throwing power of MgRP is quite complicated and depends on various factors such as scribe size, coating formulation, electrolyte compositions, electrolyte geometry and bare/coated area ratios can limit the throwing power of the coating that provides sacrificial anode based galvanic protection.<sup>82</sup> So, in addition to post-mortem sample evaluation, the galvanic throwing power of the MgRP was studied via finite element analysis modelling in conjunction with diagnostic multi-electrode arrays (MEAs), which enable the spatial distribution of cathodic protection to be elucidated in wet/dry conditions, under thin layers, or droplets.<sup>82</sup>

A microelectrode array consisting of one 500  $\mu\text{m}$  diameter, flush mounted 99.9 % Mg electrode and twenty isolated, 254  $\mu\text{m}$  diameter, flush mounted AA2024-T4 electrodes arranged in a single ribbon was mounted in epoxy thin resin to diagnostically represent the MgRP/AA2024 galvanic couple system next to a scribe or scratch.<sup>82</sup> A Scribner Model MMA910B was used to provide graphical interface and data acquisition of each micro-electrode current. A schematic cross section and planar optical image of microelectrode array is shown in the Figure 1.5.<sup>82</sup> The throwing power of the Mg across the AA 2024-T4 is depicted spatially by a blue- red color map at various times of interest (Figure 1.6). In each map, dark red indicates an anodic current greater than or equal to  $10^{-7}$  A and blue indicates a cathodic current less than or equal to  $10^{-7}$  A.<sup>82</sup> Microelectrodes which are freely corroding pass a net current of zero and coded white. Different electrolytes chosen for studies were deposited as thin electrolyte over the surface of the electrode.<sup>82</sup> The array was then place in the relative

humidity controlled cabinet and connected to the MMA. The effect of wet/dry cycle on the throwing power of Mg electrode was studied. Similar experiments were also done with a thin layer of polymer above the surface of the Mg.<sup>82</sup>

During drying, the net cathodic current density on the AA2024-T4 electrode closest to the Mg electrode was observed to increase to a peak due to the combined effects of the increasing electrolyte concentration and the decreasing area of the active cathode.<sup>82</sup> Upon further drying, the net cathodic current density on the AA2024-T4 electrodes closest to the Mg electrode was then observed to decrease in magnitude to zero as the effect of increasingly thin and tortuous electrolyte geometry reduced the ionic conductive path despite the increased in concentration of NaCl as shown in Figure 1.6(a).<sup>82</sup> The chemical species in the electrolyte also dictate the efflorescent and equilibrium behavior of the electrolyte later exposed to various ambient RH and temperature. When the microelectrode array was exposed under continuous thin electrolyte layers of pure MgCl<sub>2</sub>, in contrast to NaCl or ASTM Artificial Sea Water, the electrolyte layer did not completely dry at low RH. In case of coated Mg, RH the was kept high to keep the sample wet in order to observe mediation in throwing power by polymer only.<sup>82</sup> The added ionic resistance of the polymer over the Mg anode mediates the protection until either the polymer wets or a defect is formed in the coating.<sup>82</sup>

Finite element analysis, or similar spatially resolved computation methods, of potential and current distribution in galvanic systems has long been reported in the literature. Such studies are often carried out to investigate fundamental effects of electrolyte geometry<sup>97-99</sup>, electrode kinetics<sup>98-100</sup>, unique part geometries<sup>101</sup>, crevice corrosion<sup>98,102</sup> and sacrificial anode based, cathodic protection schemes<sup>93</sup>. A finite elemental analysis approach was also attempted to study the throwing power of Mg in MgRP/AA2024 galvanic couple system next to a scribe

or scratch. The model geometry is shown schematically in Figure. 1.6. The electrochemical boundary conditions utilized for AA2024-T351 and Mg were based on best fit approximations of experimentally obtained, full immersion polarization data previously done in different electrolytes. Increasing the NaCl concentration by an order of magnitude results in increase in the galvanic current by almost an order of magnitude.<sup>83</sup> Thicker electrolyte layers results in less ohmic drop throughout the electrolyte and allows for the Mg to cathodically polarize AA2024-T351 to a lower  $E_{\text{couple}}$  at the far geometrical limit of the AA2024-T351 of the model. Ionic resistance of the added polymer layer over the Mg electrode strongly mediate the galvanic current passing between anodes and cathodes and when large enough, impeded galvanic coupling all together.<sup>83</sup> The most uniform current distribution was observed under high polymer resistance albeit at low currents.<sup>83</sup> The galvanic protection capabilities of the coating in various full immersion, thin layer and the droplet electrolyte geometries relevant to field service explain long misunderstood field behavior.<sup>83</sup> Effect of additional resistances (polymer coating), drying characteristics of individual salts, and dry-wet cycle in throwing power of Mg is elucidated by combination of finite elemental analysis spatial modelling and diagnostic multi-electrode arrays.<sup>83</sup> In general, the magnitude and distribution of cathodic and anodic current densities predicted by the finite element computational model throughout a wet/dry cycle are in same order to the current densities measured by the microelectrode galvanic array on the coupled electrodes. However the finite element model assumes, infinitely long, thin electrolyte layer and does not take into account the shrinking geometric boundaries of the electrolyte layer or droplets of variable electrolyte height as it dries.<sup>83</sup> 40  $\mu\text{L}$  of 0.9 M NaCl solution was applied to the microelectrode array and the RH was then studied below 20 % to dry the electrolyte layer.<sup>83</sup> In previous work, specific current profiles

produced by the FEA studies were selected to closely match the electrolyte layer thickness and concentration assuming the same initial conditions as the array. The galvanic current from micro-electrode array and FEA modelling are summarized in Figure 1.7(a) and (b).<sup>83</sup> The schematics of micro-electrode array are shown in Figure 1.7(c) and (d).

## **1.5 Surface Pretreatments for Aluminum Alloys**

### **1.5.1 Non-film Forming Surface Pretreatment**

Prekote™ is chromate free surface pretreatment. It contains approximately 95% water and less than 3 % each of Diethylene Glycol Monobutyl Ether and N-Methyl-2-Pyrrolidone (NMP).<sup>103</sup> Unlike other pretreatments, Prekote™ does not form a visible layer between substrate and primer that adds to resistance of the full-up coating. Prekote™ is proven to improve the adhesion properties of substrate with primer with AA2024-T351.<sup>85</sup> It does not impart any additional corrosion resistance as in the case of other pretreatments.

### **1.5.2 Conversion Coatings**

Chromate conversion coatings (CCC) are widely used as pretreatment in coating systems for aluminum alloys in aerospace applications. CCC is known to be a highly corrosion-resistant coating for light alloys since it provides a good barrier to the substrate and active corrosion protection. The CCC layer is characterized by an oxy-hydroxide mixture of  $\text{Cr}^{3+}$  and  $\text{Cr}^{6+}$ .<sup>37,104</sup> During layer formation,  $\text{Cr}^{6+}$  is reduced to  $\text{Cr}^{3+}$ , then polycondensation reactions takes place resulting in a hydrated  $\text{Cr}^{3+}$  oxy-hydroxide<sup>104-107</sup>.  $\text{Cr}^{6+}$  is covalently bonded to this network through  $\text{Cr}^{3+}\text{-O-Cr}^{6+}$  bonds. The Cr present in this layer is

composed of 75 %  $\text{Cr}^{3+}$  and 25 %  $\text{Cr}^{6+}$ . This  $\text{Cr}^{6+}$  can be released when exposed to water or salt solution and migrate to bare substrate location to be reduced to  $\text{Cr}^{3+}$ , the release is favored in low  $\text{Cr}^{6+}$  concentrations and high pH. This type of corrosion protection is referred to as self-healing.<sup>104</sup> Self-healing refers to the ability of the coating to resist corrosion from scribes or defects in the coatings at remote sites wherein inhibitor species must be transported. CCC offers anodic and strong cathodic inhibition.<sup>22-26,42,44-47</sup> This layer decreases the electrochemical activity of anodic and cathodic sites on AA 2024-T351. Regarding cathodic inhibition, a decrease in the oxygen reduction reaction kinetics was observed when  $\text{Na}_2\text{Cr}_2\text{O}_7$  (0.1 mM) was added to 1 M NaCl solution.<sup>108</sup> The anodic inhibition reflects the localized corrosion initiation.<sup>109</sup> The effect of  $\text{Na}_2\text{Cr}_2\text{O}_7$  on S phase particles ( $\text{Al}_2\text{CuMg}$ ) dissolution was studied using AFM scratching. In presence of chromate, no localized corrosion was observed. The breakdown potential was found to increase by 200 mV for AA2024-T351 in 0.005 M NaCl + 0.1 M  $\text{Na}_2\text{SO}_4$  when substrate is coated with CCC for 3 seconds<sup>26</sup>. This increase in potential in CCC could possibly be correlate to the film stabilization and additional resistance added to system in presence of conversion coating. The threshold values for  $R_{\text{coat}}$  on AA2024-T3 as measured by EIS and are in the range of  $2 \times 10^6 \Omega\text{-cm}^2$  to  $5 \times 10^6 \Omega\text{-cm}^2$ .<sup>109</sup> EIS data were collected after 24 h exposure to 0.5 M NaCl solution and were subjected to CNLS fitting to a generalized equivalent-circuit model from which  $R_{\text{coat}}$  was extracted<sup>109</sup>

Trivalent chromium pretreatment (TCP) is a leading replacement for CCC.<sup>19</sup> This coating is a fluozirconate based conversion coating with an enrichment in  $\text{Cr}^{3+}$  compounds such as  $\text{Cr}_2\text{O}_3$  and  $\text{Cr}(\text{OH})_3$ . The solution bath does not contain  $\text{Cr}^{6+}$ . However there is evidence of self-healing mechanism like CCC, through Cr release from TCP into solution and also

transport to bare AA2024-T351 surfaces.<sup>19,110,111</sup> Evidence of  $\text{Cr}^{6+}$  through Raman spectroscopy has been found on TCP surfaces during oxygen reduction reaction on Cu rich intermetallics where a strong oxidizer such as  $\text{H}_2\text{O}_2$  can be produced as ORR intermediary.<sup>19</sup> This strong oxidant is thought to diffuse to  $\text{Cr}^{3+}$  sites and oxidize it to  $\text{Cr}^{6+}$ .<sup>19</sup> Evidence of  $\text{Cr}^{6+}$  in TCP has also been found on TCP treated galvanized metal exposed to ASTM B-117 for 24h.<sup>112</sup> Therefore TCP does not represent any risk during application, but it does provide the self-healing mechanism exhibited by CCC. The TCP formation includes two stages. During the first one, the fluoride alkalization promotes hydrolysis of  $\text{ZrF}_6^{2-}$  resulting in hydrated zirconia. Also  $\text{Cr}^{3+}$  precipitation takes place simultaneously. A three layered structure of zirconia,  $\text{Cr}_2\text{O}_3$  and hydrated Zr/Cr oxide covered with  $\text{Cr}^{3+}/\text{Zr}/\text{O}/\text{F}$  is formed<sup>110</sup>. TCP protects AA2024-T351 from corrosion. Evidence of anodic and slight cathodic inhibition have been found.<sup>113</sup> The polarization resistance increased by one order of magnitude when the sample is TCP coated compared to bare substrate in 0.5 M  $\text{Na}_2\text{SO}_4$  which reveals corrosion protection.<sup>113</sup> Potentiodynamic polarization studies exhibited a decrease in passive current density and increased breakdown potential when the sample is TCP coated.<sup>112</sup> In terms of cathodic inhibition, the current density is suppressed at potentials near to the OCP. As explained previously,  $\text{Cr}^{6+}$  can be formed in TCP layers.<sup>113</sup> This can lead to a self-healing mechanism.<sup>113</sup> This mechanism was proven by the increase of polarization resistance of bare substrate in close proximity to TCP coated substrate when compared to bare substrate.<sup>113</sup> The low frequency impedance value of the TCP coated surface proves the barrier properties offered by TCP coating. The low frequency impedance value of TCP coated surface exposed to dilute Harrison's solution (0.05 wt %  $\text{NaCl}$  + 0.35 wt %  $(\text{NH}_4)_2\text{SO}_4$ ) in an artificial scratch cell indicates that low

frequency impedance increased steadily with time initially until 528 h ( $2 \times 10^6 \Omega\text{-cm}^2$  to  $5 \times 10^6 \Omega\text{-cm}^2$ ) and after 692 h, the impedance value decreased ( $2 \times 10^6 \Omega\text{-cm}^2$ ) suggesting commencement of attack of the TCP surface.<sup>19</sup>

Non-chromate pretreatment baths commonly include hexafluorometal complexes of Zr or Ti, oxyfluor compounds, fluoride and polymeric material. The polymer is added to enhance adhesion and corrosion resistance.<sup>16</sup> These layers are thin ( $< 25$  nm, depending on application) and are characterized by multiple layers. When there was no polymer addition, the constituent layers are defined in the following manner: next to aluminum surface, an aluminum oxide layer is formed followed by zirconium oxide layer and finally topped with a mixture of Zr/O/F. If polymeric material is present, the two outer layers are replaced by a polymeric material containing Al/O/Zr/F, where the polymeric material is concentrated towards the Aluminum surface<sup>16</sup>. During the layer formation, fluoride ion activates the native aluminum oxide, which becomes hydrated. Then the hydroxide-aluminum bonds are substituted by the more stable fluoride aluminum bonds aided by the very acidic pH and the positive nature of the alumina.<sup>32</sup> Finally, the Zr oxyfluoride layer forms. This conversion layer does not offer strong corrosion resistance<sup>32,43</sup>. There is no previous literature pertinent to this conversion coating which discusses the resistive properties of these coating on aluminum alloys.

### **1.5.3 Anodization**

Anodization is a common pretreatment process in which anodic polarization of aluminum alloy in acidic environment results in formation and growth of anodic oxide film.<sup>33</sup> The oxide film is characterized by inner thin barrier layer and outer thick porous layer.<sup>33</sup> The

porous nature of the oxide makes alloys susceptible to corrosion and to improve corrosion resistance; pretreated samples need to be sealed after anodizing.<sup>14,15,17,20,21,27-31,34,38,39,41</sup> The pores are often sealed by active inhibitors such as chromic acid or other active inhibitors to help with corrosion protection.<sup>41</sup> TCP is explored as an alternate for chromic acid for sealing due to its corrosion resistance and adhesion.<sup>35</sup> TCP is also easy in terms of application as it can be applied in ambient conditions for shorter exposure time whereas chromate or water seals require exposure at 190° F to 200° F for longer exposure times.<sup>35</sup> The electrochemically grown oxide layer provides extra barrier protection due to the highly capacitive behavior of Al<sub>2</sub>O<sub>3</sub>.<sup>33</sup> Enhanced sealing might occur during exposure while corrosion progressed.<sup>18,40</sup> The adhesion strength of anodized aluminum to polymers is directly related to size and density of pores created by anodization process as mechanical interlocking directly correlates with adhesion strength.<sup>114</sup>

## **1.6 Possible Impacts of Resistive Pretreatments on the Corrosion Protection of 2024-T351 by a Magnesium Rich Primer**

The sacrificial anode-based cathodic and barrier protection capabilities of a non-chromate magnesium rich primer (MgRP) with a non-film forming pretreatment, in both a topcoated and non-topcoated conditions has validated it as an emerging, promising corrosion mitigation strategy for precipitation age hardened aluminum alloy, 2024-T351.<sup>72,73,81-83,85,87,88</sup> However in service, there is an interest by end-users to apply Mg-rich primers above many different surface pretreatments which are more resistive than non-film forming pretreatment. Two significant surface pretreatment systems of interest are conversion coatings and anodization. In addition to improving the adhesion of substrate to the primer polymer, the above

pretreatments also provide additional modes of corrosion protection in the form of barrier protection as well as active corrosion protection.<sup>15,18-20,22-27,34-42</sup> While individually their corrosion protection mechanisms has been reported, a comparative study of barrier degradation characteristics and efficacy of corrosion protection of different resistive pretreatments has not been reported previously. The barrier characteristics of resistive pretreatments might reduce detrimental cathodic corrosion by providing a barrier layer between 2024-T351 and MgRP. On the other hand, the resistive layer might limit sacrificial anode-based cathodic protection by mediating the galvanic protection potential. There is a significant knowledge gap in understanding of the factors controlling the coating/pretreatment performance, and limiting the function and functional lifetime of the sacrificial corrosion protection function associated with Mg as a protection scheme when a resistive pretreatment is used.

### **1.7 Specific Surface Pretreatments, Magnesium Rich Primer and Topcoat Systems of Interest**

99.9 % pure magnesium rod (8.0 mm dia) and 1.6 mm thick AA 2024-T351 sheet were utilized for investigations. Chemical analysis showed that Mg rod and wire had purity which are substantially similar to the powder used in commercial Mg-rich Primer (MgRP) products. The panels studied comprised a 1.6 mm thickness AA2024-T351 sheet bare and pretreated with 7 different pretreatments for comparison including i) Prekote™ ii) Chromium Conversion Coating (CCC) iii) Trivalent Chromium Pretreatment (TCP) iv) Non Chromium Pretreatment (NCP) v) Anodized without Sealing vi) Anodized with Chromate Seal vii) Anodized with TCP Seal. A 30 µm primer layer of Mg-rich primer (45 % PVC) produced by Akzo Nobel Coatings (Waukegan, Illinois) and a 50 µm –thick topcoat of Aerodur 5000 high-performance advanced coating also produced by Akzo Nobel Coatings were applied over

pretreated panels chosen for studies. All tested panels were provided and pretreated/painted by our collaborators in NAVAIR.

Prekote™ is chromate free surface pretreatment. It contains approximately 95% water and less than 3 % each of Diethylene Glycol Monobutyl Ether and N-Methyl-2-Pyrrolidone (NMP) from Pantheon. Chromate Conversion coating (Alodine 1200s) and Non-Chromate Pretreatment (Alodine 5200) are products from Henkel Corporation. Trivalent Chromium Pretreatment (Surtec 650) is a product from SurTec. For anodization pretreatments, Thin Sulfuric Acid Anodizing-MIL-A-8625F: Type II pretreatment procedure was followed. A dilute chromic acid sealing and TCP sealing was performed for anodized samples and compared to anodized samples with no sealing. The Mg rich primer consists of one part epoxy matrix with Mg metal flake pigment (D~20µm) with pigment volume concentration of 45 %. Aerodur 5000 is a two component polyurethane topcoat developed by Akzo Nobel for military application in variety of exposure environments.

### **1.8 Critical Unresolved Issues**

- The addition of the resistance of the pretreatment to the coating system stack up is presumed to mediate the sacrificial galvanic protection function afforded by the MgRP through the added electrical and ionic resistance. The role of pretreatments, their thickness, chemistry and electrical properties on galvanic couple mediation needs to be understood.
- Chosen pretreatments might also provide additional corrosion resistance through other modes of corrosion protection such as chemical inhibition via release of a chemical corrosion inhibitor. Chemical leaching of different species from chosen pretreatment or MgRP need to be quantified to understand the role of inhibitor ions and so as to not confuse sacrificial protection with other sources of corrosion protection.

- Effect of inhibitor ions on the cathodic protection function needs to be studied. The mixed potential model for galvanic protection needs to be modified to take into account both the resistive properties of pretreatments as well as ionic effects of inhibitor release on both the cathodic and the anodic kinetics of AA2024-T351 and Mg, respectively.
- The performance of AA2024-T351/MgRP and AA2024-T351/MgRP/Topcoat systems with the chosen pretreatments in lab and field need to be studied. LALT and field exposed samples need to be characterized for Mg depletion, the global cathodic protection potential, chemical species in the scribe leaching from the coating or pretreatment as well as scribe protection.
- The effect of pretreatment resistance, coating/scribe ratio, topcoat, inhibitor leaching, soluble  $Mg^{2+}$  species on corrosion protection of scribe and throwing power needs to be understood. Therefore, in addition to post-exposure SEM/EDS examination, use of local probe techniques to understand effect of each of these variables on corrosion protection need to be undertaken.
- A holistic understanding of the effects of pretreatments discussed above should be attempted to understand functionality and balance between added resistance to restrict galvanic protection vs species release.

## 1.9 Objective

The research outlines four tasks which will help establish a baseline of understanding for role of different surface pretreatments on the time dependent sacrificial anode-based cathodic and barrier protection mechanisms afforded by the MgRP. Further studies on coating degradation mechanism and performance on different pretreatments would help us develop a multi-function system which would include cathodic/sacrificial protection of Mg, barrier protection by pretreatments/primer/topcoat and corrosion inhibition of pretreatments.

- 1 The primary objective of Task - 1 is to first perform chemical characterization and then develop a detailed understanding of role of different surface pretreatments in galvanic couple mediation through laboratory full immersion tests. The influence of thickness of pretreatment, its chemistry and electrical properties imparted by pretreatments will be examined first. This would give some preliminary understanding to aid our second objective which is to understand the role played by pretreatments in regulating galvanic couple potential mediation in chosen system. Degradation of coatings as a function of time for different pretreatments will be studied by diagnostic tests including accelerated electrochemical cycle test with ex-situ Mg depletion studies using X-ray diffraction.
- 2 Performance of different pretreated AA2024-T351 with MgRP and with and without topcoat in relevant lab and field environments needs to be studied to further expand the knowledge of role of pretreatments in corrosion protection function. This would further the understanding of discrepancies between coating performances in the laboratory compared to the field. Coating degradation will be tracked in various environments by utilizing electrochemical techniques described

in Task 1 and non-electrochemical post-mortem analysis techniques including x-ray diffraction, Raman spectroscopy, scanning electron microscopy/energy dispersive spectroscopy and optical profilometry. Degradation in various environments would then be compared.

3 Conversion coatings/anodized coating (with hexavalent chromium/TCP sealing) may also provide additional modes of corrosion protection by chemical inhibition. Chemical species dissolution of ions due to pretreatment degradation after exposure in relevant environments will be quantified by ICP-OES technique. The impact of any release of ionic species such as  $\text{CrO}_4^{2-}$  on E-i behavior will be rationalized in the context of galvanic couple mixed potential model. The effect of chemical dissolution of inhibitor species from pretreatments on anodic and cathodic kinetics of 2024-T351 and anodic kinetics of Mg need to be understood. These objectives will be accomplished by Task – 3 of this dissertation. In addition, pretreatment degradation will be tracked in various environments by utilizing electrochemical techniques and non-electrochemical post-mortem analysis techniques including Raman spectroscopy, scanning electron microscopy/energy dispersive spectroscopy and optical profilometry.

4 The objective of Task 4 is to utilize scanning vibrating electrode technique (SVET) to quantitatively observe the spatial distribution of current density over coated 2024-T351 with a controlled defect exposing bare substrate. Effect of pretreatment resistance, barrier properties of the coating, Mg self-corrosion, chemical species release and cathode to anode ratio on sacrificial protection function as well as other modes of corrosion protection will be elucidated using SVET studies in aqueous

sodium chloride solution under full immersion conditions. Correlation of local anodic/cathodic current to corrosion volume loss will be conducted by post-exposure studies of cleaned surface using optical profilometry.

## **1.10 Experimental Approach**

### **1.10.1 Preliminary Characterization of the Pretreatments**

The chemistry and thickness of the pretreatments were characterized using X-ray photoelectron spectroscopy and energy dispersive spectroscopy, respectively.

### **1.10.2 Post-exposure Characterization of Intact Region of Coating/Pretreatment:**

Initial electrochemical properties of the pretreatments/coating was characterized by diagnostic electrochemical measurements such as open circuit potential (OCP) and electrochemical impedance spectroscopy (EIS). The amount of the global Mg present in the coating was characterized using X-ray diffraction. The amount of electrochemically active Mg present in the coating or anodic capacity was calculated by potentiostatic polarization based cumulative anodic charge density analysis. The cathodic and anodic kinetics of bare/pretreated 2024-T351 and Mg were characterized using potentiodynamic polarization measurements. The anionic species leaching after controlled relative humidity droplet exposure was quantified using inductively coupled plasma – optical emission spectrometry (ICP-OES). The corrosion products and pretreatment degradation were monitored using Raman spectroscopy. Schematic of a MgRP coating system with a scribe showing regions of interest for post-exposure characterization is shown in Figure 1.8.

### **1.10.3 Post-exposure Characterization of 2024-T351 Scribe Adjacent to**

#### **Coating/Pretreatment:**

The corrosion product present in the scribe were characterized using scanning electron spectroscopy, energy dispersive spectroscopy and Raman spectroscopy. The corrosion volume loss was characterized using optical profilometry.

### **1.10.4 Throwing Power Investigation:**

The spatial current distribution of AA2024-T351 scribe and adjacent coating region were characterized using scanning vibration electrode technique. The galvanic couple protection potential of coating with scribe exposed was characterized using open circuit potential measurements. The spatial potential distribution was characterized using scanning Kelvin probe. The corrosion volume loss in scribe was characterized using optical profilometry. Preliminary experiments for full immersion electrochemical boundary conditions was conducted to model the spatial distribution of galvanic current and galvanic protection potential for a representative pretreated 2024-T351/Mg systems by finite element analysis modelling.

## **1.11 Thesis Organization**

This thesis is organized by these tasks and/or critical issues pertaining to role of pretreatments in corrosion protection of 2024-T351 by MgRP.

Chapter 2 elucidates the effect of pretreatments on 2024-T351 corrosion protection by a Mg rich primer in laboratory full immersion NaCl solution. The chemistry and thickness of the pretreatments were characterized using X-ray photoelectron spectroscopy and energy dispersive spectroscopy line profiles, respectively. The initial electrochemical properties of the pretreatments was characterized by diagnostic electrochemical measurements such as

open circuit potential (OCP) and electrochemical impedance spectroscopy (EIS). A laboratory full immersion test methodology called the accelerated electrochemical cycle test was adopted from prior work and utilized to understand how pretreatments effects the overall coating degradation and sacrificial protection functions for MgRP in topcoated and non-topcoated conditions. OCP, EIS, potentiostatic polarization and ex-situ X-ray diffraction techniques were utilized to assess the performance of the coating in accelerated electrochemical cycle test. A mixed potential model was developed and utilized to account for the effects of pretreatments which add a resistive element to the galvanic couple and various other electrical and ionic resistances that exist between the 2024-T351 substrate and Mg pigment in the primer. Preliminary potentiodynamic polarization experiments were conducted to understand how the pretreatment resistances affect the cathodic kinetics of the oxygen reduction reaction which was subsequently incorporated into a mixed potential electrochemical model.

Chapter 3 and 4 focus on environmental degradation of MgRP with different pretreatments, with and without topcoat using a suite of high level surveillance methods in various field, laboratory salt fog and full immersion exposures. The environmental degradation of intact coating, Mg pigment depletion and modification of its sacrificial protection capabilities as a function of exposure time in different environments was elucidated by combination of diagnostic electrochemical tests (OCP/EIS) and material characterization techniques ( X-ray diffraction and Raman spectroscopy). In addition, the ability of a coating to protect a defect exposing underlying bare 2024-T351 was studied by exposing a scribed sample in the above stated environments. The scribe protection was elucidated by scanning electron microscopy/energy dispersive spectroscopy, Raman spectroscopy in scratch and optical

profilometry. Chapter 3 focuses on comparison of the effects of conversion coating to non-film forming surface pretreatment which have low to moderate electrical resistance on MgRP function and Chapter 4 which focuses on comparison of the effects of different anodization based pretreatments which have high resistance on MgRP function.

Chapter 5 focus on pretreatment degradation and role of pretreatment in residual corrosion protection of 2024-T351. All the experiments pertinent to this chapter were conducted for 2024-T351/Pretreatments without any organic coating. The pretreatment degradation was tracked in various environments such as laboratory full immersion, laboratory salt-fog exposures, field and a controlled relative humidity (droplet) environment. Pretreatment barrier degradation was characterized using diagnostic electrochemical measurements (OCP/EIS). The scratch protection of 2024-T351 by inhibitor species from pretreatment after various environment exposures was characterized using scanning electron microscopy/energy dispersive spectroscopy, Raman spectroscopy and optical profilometry. The chemical species leaching after controlled relative humidity droplet exposure was quantified using inductively coupled plasma – optical emission spectrometry (ICP-OES). Effects of pretreatment resistance and chemical species release on anodic/cathodic kinetics of 2024-T351 was characterized using potentiodynamic polarization measurements. The experiments were conducted for pretreated 2024-T351 in as received condition, pretreated 2024-T351 after different full immersion exposure times, and bare 2024-T351 with anionic species in solution.

Chapter 6 focus on the galvanic throwing power of the MgRP on pretreated 2024-T351 using scanning vibrating electrode technique (SVET) which enable the spatial mapping of local net galvanic current. Major emphasis of this work lies on studying the impact of pretreatment

resistance, topcoat resistance, coating/scribe ratio, soluble species leaching into solution from pretreatment/primer on throwing power and scribe protection as assessed by local net anodic current on scratches with and without galvanic coupling to a MgRP.

Chapter 7 presents the conclusion of this work and highlight key lessons learned relevant to utilizing MgRP in service with different surface pretreatments. Remaining questions and discussion of ongoing and future work are also detailed.

Appendix A has been included to report the boundary condition information for finite element analysis modelling of spatial distribution of galvanic current and potential for model systems of 2024-T351 and MgRP. The modelling experiments will be conducted in different conditions to study the effect of pretreatment resistances, anionic species leaching and combined effect of pretreatment degradation and anionic species leaching. The results obtained from here would be used to elucidate and rationalize the experimental results from chapter 6 which would help further improvement in experimental design and finite elemental analysis modelling for galvanic throwing power analysis.

Appendix B summarizes preliminary results for the spatial distribution of corrosion volume loss for bare 2024-T351 coupled with a MgRP coated and pretreated 2024-T351 studied using optical profilometry. Optical profilometry experiments were conducted after long term full immersion exposure. The effect of distance from coating, pretreatment resistance, top coat and coating to scribe area ratio on pit volume densities or corrosion volume loss was investigated.

Appendix C summarizes preliminary results for spatial distribution of cathodic protection potential (Volta potential) as a function of distance from coating for selected system by utilizing scanning Kelvin probe (SKP). In addition the Volta potential for different micro

constituent particles present in 2024-T351 was characterized using bulk synthesized secondary phase particles such as  $\text{Al}_2\text{CuMg}$  (S phase),  $\text{Al}_2\text{Cu}$  ( $\theta$  phase),  $\text{Mg}_2\text{Si}$ ,  $\text{Al}_7\text{Cu}_2\text{Fe}$  and compared with volta potential of bare Al, Cu, Mg and 2024-T351. The results obtained herein demonstrate SKP as technique to characterize galvanic interaction and future experiments could validate the finite elemental analysis model's spatial potential distribution data with experimental results.

Appendix D extends the laboratory environmental exposures studied in chapter 4 and 5 to include cyclic tests in ASTM B-117 modified with ASTM sea water and ASTM D-4587. In addition full immersion exposure studies were conducted for selected pretreatment in the presence of other aerosol deposits chemicals such as oxalate and nitrate on Mg depletion and barrier degradation.

The thesis concludes with a summary and future work. Some results pertinent to future work suggested are reported in appendix chapters A-D.

## 1.12 References

1. I.J. Polmear, *Light Alloys*. 4 ed: Butterworth-Heinemann, Oxford, 2005.
2. R.G. Buchheit, R.P. Grant, P.F. Hlava, B. Mckenzie, and G.L. Zender, "Local dissolution phenomena associated with S phase (Al<sub>2</sub>CuMg) particles in aluminum alloy 2024-T3," *Journal of the Electrochemical Society* 144, 8 (1997): p. 2621-2628.
3. A.M. Glenn, T.H. Muster, C. Luo, X. Zhou, G.E. Thompson, A. Boag, and A.E. Hughes, "Corrosion of AA2024-T3 Part III: Propagation," *Corrosion Science* 53, 1 (2011): p. 40-50.
4. A.E. Hughes, A. Boag, A.M. Glenn, D. McCulloch, T.H. Muster, C. Ryan, C. Luo, X. Zhou, and G.E. Thompson, "Corrosion of AA2024-T3 Part II Co-operative corrosion," *Corrosion Science* 53, 1 (2011): p. 27-39.
5. G.O. Ilevbare, O. Schneider, R.G. Kelly, and J.R. Scully, "In situ confocal laser scanning microscopy of AA 2024-T3 corrosion metrology - I. Localized corrosion of particles," *Journal of the Electrochemical Society* 151, 8 (2004): p. B453-B464.
6. O. Schneider, G.O. Ilevbare, J.R. Scully, and R.G. Kelly, "In situ confocal laser scanning microscopy of AA 2024-T3 corrosion metrology - II. Trench formation around particles," *Journal of the Electrochemical Society* 151, 8 (2004): p. B465-B472.
7. R.G. Buchheit, L.P. Montes, M.A. Martinez, J. Michael, and P.F. Hlava, "The electrochemical characteristics of bulk-synthesized Al<sub>2</sub>CuMg," *Journal of the Electrochemical Society* 146, 12 (1999): p. 4424-4428.
8. R.G. Buchheit, M.A. Martinez, and L.P. Montes, "Evidence for Cu ion formation by dissolution and dealloying the Al<sub>2</sub>CuMg intermetallic compound in rotating ring-disk collection experiments," *Journal of the Electrochemical Society* 147, 1 (2000): p. 119-124.
9. R.C. Bacon, J.J. Smith, and F.M. Rugg, "Electrolytic Resistance in Evaluating Protective Merit of Coatings on Metals," *Industrial & Engineering Chemistry* 40, 1 (1948): p. 161-167.
10. N.L. Thomas, "The barrier properties of paint coatings," *Progress in Organic Coatings* 19, 2 (1991): p. 101-121.
11. G.W. Walter, "A critical review of the protection of metals by paints," *Corrosion Science* 26, 1 (1986): p. 27-38.
12. P.A. Sørensen, S. Kiil, K. Dam-Johansen, and C.E. Weinell, "Anticorrosive coatings: a review," *Journal of Coatings Technology and Research* 6, 2 (2009): p. 135-176.
13. ASM International Handbook Committee., *ASM Handbook Corrosion: Materials*. Vol. 13A (Materials Park, OH: ASM International, 2003).
14. A. Bautista, R. Lizarbe, E. Otero, V. Lopez, and J.A. Gonzalez, "New alternatives to the industrially introduced methods for the sealing of anodized aluminium," *Revista De Metalurgia* 35, 3 (1999): p. 195-202.
15. N. Chahboun, E. Rocca, D. Veys-Renaux, M. Augros, M. Boutoba, and N. Caldeira, "Sealing of Anodized Multiphase Aluminum Alloys with Cr( plus III)/Zr( plus IV) Salts: Characterization and Corrosion Behavior," *Journal of the Electrochemical Society* 163, 3 (2016): p. C69-C75.
16. P.D. Deck and D. Reichgott, "Characterization of chromium-free no-rinse prepaint coatings on aluminum and galvanized steel," *Metal Fin.* 90, 9 (1992): p. 29-35.
17. J.A. Gonzalez, V. Lopez, E. Otero, A. Bautista, R. Lizarbe, C. Barba, and J.L. Baldonado, "Overaging of sealed and unsealed aluminium oxide films," *Corrosion Science* 39, 6 (1997): p. 1109-1118.
18. J.A. Gonzalez, M. Morcillo, E. Escudero, V. Lopez, A. Bautista, and E. Otero, "Self-sealing of unsealed aluminium anodic oxide films in very different atmospheres," *Revista De Metalurgia* (2003): p. 110-115.

19. Y. Guo and G.S. Frankel, "Active Corrosion Inhibition of AA2024-T3 by Trivalent Chrome Process Treatment," *Corrosion* 68, 4 (2012).
20. N.P. Hu, X.C. Dong, X.Y. He, J.F. Browning, and D.W. Schaefer, "Effect of sealing on the morphology of anodized aluminum oxide," *Corrosion Science* 97, (2015): p. 17-24.
21. Y.L. Huang, H. Shih, H.C. Huang, S. Wu, S. Ramanathan, C. Chang, and F. Mansfeld, "Evaluation of the corrosion resistance of anodized aluminum 6061 using electrochemical impedance spectroscopy (EIS)," *Corrosion Science* 50, 12 (2008): p. 3569-3575.
22. G.O. Ilevbare, C.S. Jeffcoate, and J.R. Scully, "Mass transport limited oxygen reduction kinetics on chromate conversion coated Al-Cu, Al-Cu-Mg and Al-Cu-Mn-Fe intermetallic compounds.," *Passivity and Localized Corrosion* 99, 27 (1999): p. 269-279.
23. G.O. Ilevbare and J.R. Scully, "Mass-Transport-Limited oxygen reduction reaction on AA2024-T3 and selected intermetallic compounds in chromate-containing solutions (vol 57, pg 134, 2001)," *Corrosion* 57, 5 (2001): p. 480-480.
24. G.O. Ilevbare and J.R. Scully, "Oxygen reduction reaction kinetics on chromate conversion coated Al-Cu, Al-Cu-Mg, and Al-Cu-Mn-Fe intermetallic compounds," *Journal of the Electrochemical Society* 148, 5 (2001): p. B196-B207.
25. G.O. Ilevbare and J.R. Scully, "Mass-transport-limited oxygen reduction reaction on AA2024-T3 and selected intermetallic compounds in chromate-containing solutions," *Corrosion* 57, 2 (2001): p. 134-152.
26. G.O. Ilevbare, J.R. Scully, J. Yuan, and R.G. Kelly, "Inhibition of pitting corrosion on aluminum alloy 2024-T3: Effect of soluble chromate additions vs chromate conversion coating," *Corrosion* 56, 3 (2000): p. 227-242.
27. D. Kanagaraj, S. Mohan, N.G. Renganathan, R.V. Raman, and S.V. Iyer, "Evaluation of anodized aluminum surface obtained from a sulfanic acid bath using electrochemical impedance spectroscopy," *Plating and Surface Finishing* 86, 7 (1999): p. 58-61.
28. J. Lee, Y. Kim, H. Jang, and W. Chung, "Cr<sub>2</sub>O<sub>3</sub> sealing of anodized aluminum alloy by heat treatment," *Surface & Coatings Technology* 243, (2014): p. 34-38.
29. Y. Li and Z.F. Zhu, "Cold Sealing Mechanism of Anodic Oxide-Films on Aluminum .2. Cold Sealing Models of Oxide-Films," *Plating and Surface Finishing* 80, 10 (1993): p. 77-80.
30. Y. Li, Z.F. Zhu, Z.Y. Jiang, and M.M. Yan, "Cold Sealing Mechanism of Anodic Oxide-Films on Aluminum .1. Composition and Structure of Cold-Sealed Oxide-Films," *Plating and Surface Finishing* 80, 9 (1993): p. 79-82.
31. D. Liu, G.Y. Wei, and P.L. He, "The Effect of Sealing and Trivalent Chromium Passivating on Anodized Aluminum," *International Journal of Electrochemical Science* 11, 3 (2016): p. 2097-2105.
32. O. Lunder, C. Simensen, Y. Yu, and K. Nisancioglu, "Formation and characterisation of Ti-Zr based conversion layers on AA6060 aluminium," *Surface and Coatings Technology* 184, 2 (2004): p. 278-290.
33. F. Mansfeld and M.W. Kendig, "Evaluation of Anodized Aluminum Surfaces with Electrochemical Impedance Spectroscopy," *Journal of the Electrochemical Society* 135, 4 (1988): p. 828-833.
34. F. Mansfeld, G. Zhang, and C. Chen, "Evaluation of sealing methods for anodized aluminum alloys with electrochemical impedance spectroscopy (EIS)," *Plating and Surface Finishing* 84, 12 (1997): p. 72-81.
35. C. Matzdorf, Beck, Erin., Hilgeman, Amy., Prado, Ruben. , *Trivalent Chromium Process as a Sealer for MIL-A-8625 Type II, IIB and IC Anodic Coatings*. 2008, NAVAIR. p. 50.
36. L. Xia, E. Akiyama, G. Frankel, and R. McCreery, "Storage and release of soluble hexavalent chromium from chromate conversion coatings - Equilibrium aspects of Cr-VI concentration," *Journal of the Electrochemical Society* 147, 7 (2000): p. 2556-2562.

37. J. Zhao, G. Frankel, and R.L. McCreery, "Corrosion protection of untreated AA-2024-T3 in chloride solution by a chromate conversion coating monitored with Raman spectroscopy," *Journal of the Electrochemical Society* 145, 7 (1998): p. 2258-2264.
38. J.M. Zhao, H.X. Liu, S.L. Chen, and X.H. Zhao, "EIS evolution of anodised aluminium by cerium salt sealing in NaCl solution with exposure time," *Corrosion Engineering Science and Technology* 48, 1 (2013): p. 44-47.
39. X. Zhao, L. Tian, J. Zhao, and Y. Zuo, "Electrochemical properties of anodized and sealed aluminum films," *Aicam* 2005 11-12, (2006): p. 433-436.
40. X.H. Zhao, Y. Zuo, J.M. Zhao, J.P. Xiong, and Y.M. Tang, "A study on the self-sealing process of anodic films on aluminum by EIS," *Surface & Coatings Technology* 200, 24 (2006): p. 6846-6853.
41. Y. Zuo, P.H. Zhao, and J.M. Zhao, "The influences of sealing methods on corrosion behavior of anodized aluminum alloys in NaCl solutions," *Surface & Coatings Technology* 166, 2-3 (2003): p. 237-242.
42. M.W. Kendig and R.G. Buchheit, "Corrosion Inhibition of Aluminum and Aluminum Alloys by Soluble Chromates, Chromate Coatings, and Chromate-Free Coatings," *CORROSION* 59, 5 (2003): p. 379-400.
43. H. Leidheiser, "Corrosion control by organic coatings," (1981).
44. L. Gáncs, A.S. Besing, R. Buják, A. Kolics, Z. Németh, and A. Wieckowski, "Interaction of Chromate with Aluminum in NaCl Solutions," *Electrochemical and Solid-State Letters* 5, 4 (2002): p. B16-B19.
45. M. Kendig, R. Addison, and S. Jeanjaquet, "The Influence of Adsorbed Oxo-Cr(VI) Species on the Zeta Potential in the Porous Oxide of Anodized Aluminum," *Journal of The Electrochemical Society* 146, 12 (1999): p. 4419-4423.
46. J.D. Ramsey and R.L. McCreery, "In Situ Raman Microscopy of Chromate Effects on Corrosion Pits in Aluminum Alloy," *Journal of The Electrochemical Society* 146, 11 (1999): p. 4076-4081.
47. W.J. Clark and R.L. McCreery, "Inhibition of Corrosion-Related Reduction Processes via Chromium Monolayer Formation," *Journal of The Electrochemical Society* 149, 9 (2002): p. B379-B386.
48. S.B. Madden and J.R. Scully, "Inhibition of AA2024-T351 Corrosion Using Permanganate," *Journal of The Electrochemical Society* 161, 3 (2014): p. C162-C175.
49. S.A. Kulinich, M. Farzaneh, and X.W. Du, "Growth of corrosion-resistant manganese oxide coatings on an aluminum alloy," *Inorganic Materials* 43, 9 (2007): p. 956-963.
50. M. Crouse, A.E. Miller, M.G. Pujar, and K.L. Vasanth, *Evaluation of Potassium Permanganate (KMnO4) as a Green Corrosion Inhibitor/Sealant for Anodized Al 2024 and Al 6061 at Different pH Values*, NACE International.
51. J.W. Bibber, *A Chrome Free Conversion Coating and Sealant for Aluminum and Its Alloys*, NACE International.
52. I. Danilidis, J. Hunter, G.M. Scamans, and J.M. Sykes, "Effects of inorganic additions on the performance of manganese-based conversion treatments," *Corrosion Science* 49, 3 (2007): p. 1559-1569.
53. I. Danilidis, A.J. Davenport, and J.M. Sykes, "Characterisation by X-ray absorption near-edge spectroscopy of KMnO4-based no-rinse conversion coatings on Al and Al alloys," *Corrosion Science* 49, 4 (2007): p. 1981-1991.
54. S.A. Hayes, P. Yu, T.J. O'Keefe, M.J. O'Keefe, and J.O. Stoffer "The Phase Stability of Cerium Species in Aqueous Systems: I. E-pH Diagram for the Ce - HClO<sub>4</sub> - H<sub>2</sub>O System," *Journal of The Electrochemical Society* 149, 12 (2002): p. C623-C630.

55. A.S. Hamdy, A.M. Beccaria, and P. Traverso, "Corrosion protection of aluminium metal–matrix composites by cerium conversion coatings," *Surface and Interface Analysis* 34, 1 (2002): p. 171-175.
56. F.J. Presuel-Moreno, M.A. Jakab, and J.R. Scully, "Inhibition of the Oxygen Reduction Reaction on Copper with Cobalt, Cerium, and Molybdate Ions," *Journal of The Electrochemical Society* 152, 9 (2005): p. B376-B387.
57. M.L. Zheludkevich, R. Serra, M.F. Montemor, K.A. Yasakau, I.M.M. Salvado, and M.G.S. Ferreira, "Nanostructured sol–gel coatings doped with cerium nitrate as pre-treatments for AA2024-T3: Corrosion protection performance," *Electrochimica Acta* 51, 2 (2005): p. 208-217.
58. X. Yu and G. Li, "XPS study of cerium conversion coating on the anodized 2024 aluminum alloy," *Journal of Alloys and Compounds* 364, 1–2 (2004): p. 193-198.
59. A.J. Aldykiewicz, A.J. Davenport, and H.S. Isaacs, "Studies of the Formation of Cerium-Rich Protective Films Using X-Ray Absorption Near-Edge Spectroscopy and Rotating Disk Electrode Methods," *Journal of The Electrochemical Society* 143, 1 (1996): p. 147-154.
60. D. Ho, N. Brack, J. Scully, T. Markley, M. Forsyth, and B. Hinton, "Cerium Dibutylphosphate as a Corrosion Inhibitor for AA2024-T3 Aluminum Alloys," *Journal of The Electrochemical Society* 153, 9 (2006): p. B392-B401.
61. F. Andreatta, M.E. Druart, A. Lanzutti, M. Lekka, D. Cossement, M.G. Olivier, and L. Fedrizzi, "Localized corrosion inhibition by cerium species on clad AA2024 aluminium alloy investigated by means of electrochemical micro-cell," *Corrosion Science* 65, (2012): p. 376-386.
62. M.A. Jakab, F. Presuel-Moreno, and J.R. Scully, "Critical Concentrations Associated with Cobalt, Cerium, and Molybdenum Inhibition of AA2024-T3 Corrosion: Delivery from Al-Co-Ce(-Mo) Alloys," *CORROSION* 61, 3 (2005): p. 246-263.
63. E.A. Lizlovs, "Molybdates as Corrosion Inhibitors in the Presence of Chlorides," *CORROSION* 32, 7 (1976): p. 263-266.
64. R.L. Cook and S.R. Taylor, "Pigment-Derived Inhibitors for Aluminum Alloy 2024-T3," *CORROSION* 56, 3 (2000): p. 321-333.
65. B.D. Chambers and S.R. Taylor, "The high throughput assessment of aluminium alloy corrosion using fluorometric methods. Part II – A combinatorial study of corrosion inhibitors and synergistic combinations," *Corrosion Science* 49, 3 (2007): p. 1597-1609.
66. S. Prasad, S.I.B. Gonçalves, and J.B. Brito, "Electrometric studies on the system acid-vanadate and the formation of heavy metal vanadates," *Catalysis Today* 57, 3–4 (2000): p. 339-348.
67. R.G. Buchheit, H. Guan, S. Mahajanam, and F. Wong, "Active corrosion protection and corrosion sensing in chromate-free organic coatings," *Progress in Organic Coatings* 47, 3–4 (2003): p. 174-182.
68. H. Guan and R.G. Buchheit, "Corrosion Protection of Aluminum Alloy 2024-T3 by Vanadate Conversion Coatings," *CORROSION* 60, 3 (2004): p. 284-296.
69. B.D. Chambers and S.R. Taylor, "High-Throughput Assessment of Inhibitor Synergies on Aluminum Alloy 2024-T3 through Measurement of Surface Copper Enrichment," *CORROSION* 63, 3 (2007): p. 268-276.
70. R.L. Twite and G.P. Bierwagen, "Review of alternatives to chromate for corrosion protection of aluminum aerospace alloys," *Progress in Organic Coatings* 33, 2 (1998): p. 91-100.
71. D. Battocchi, A.M. Simoes, D.E. Tallman, and G.P. Bierwagen, "Electrochemical behaviour of a Mg-rich primer in the protection of Al alloys," *Corrosion Science* 48, 5 (2006): p. 1292-1306.
72. G. Bierwagen, D. Battocchi, A. Simoes, A. Stamness, and D. Tallman, "The use of multiple electrochemical techniques to characterize Mg-rich primers for Al alloys," *Progress in Organic Coatings* 59, 3 (2007): p. 172-178.

73. D.E.T. G. P. Bierwagen, M. Nannan, D. Battocchi, A. Stamness and V. J. Gelling, *New developments in Cr-Free primers for aerospace alloys*, in *American Chemical Society*. 2004. p. U360.
74. B. Kannan, Scully, J. R, "Performance of a Magnesium Rich Primer on Pretreated AA2024-T351 in Selected Laboratory and Field Environments: Conversion Coating Pretreatments," *Corrosion* (2016).
75. B. Kannan, A. King, and J. Scully, *Impact of Surface Pretreatments on AA2024-T351 Corrosion Protection by a Magnesium Rich, Non-Chrome Primer (MgRP)*, in *NACE DoD 2015*. 2015, NACE: Pittsburgh, PA.
76. B. Kannan, A. King, and J. Scully, "Effect of Pretreatments on 2024-T351 Corrosion Protection by Magnesium Rich, Non-Chromium Primer (MgRP): Laboratory Characterization in Full Immersion," *Corrosion* doi:10.5006/1700, (2015).
77. C.M. Abreu, M. Izquierdo, P. Merino, X.R. Novoa, and C. Perez, "A new approach to the determination of the cathodic protection period in zinc-rich paints," *Corrosion* 55, 12 (1999): p. 1173-1181.
78. R.A. Armas, C.A. Gervasi, A. Disarli, S.G. Real, and J.R. Vilche, "Zinc-Rich Paints on Steels in Artificial Seawater by Electrochemical Impedance Spectroscopy," *Corrosion* 48, 5 (1992): p. 379-383.
79. A.D. King, B. Kannan, and J.R. Scully, "Environmental Degradation of a Mg-Rich Primer in Selected Field and Laboratory Environments – Part II. Primer and Topcoat," *Corrosion* 70, 5 (2014).
80. A.D. King, B. Kannan, and J.R. Scully, "Environmental Degradation of a Mg-Rich Primer in Selected Field and Laboratory Environments – Part I. Without a Topcoat," *Corrosion* 70, 5 (2014).
81. A.D. King, J.S. Lee, and J.R. Scully, "Galvanic Couple Current and Potential Distribution between a Mg Electrode and 2024-T351 under Droplets Analyzed by Microelectrode Arrays," *Journal of the Electrochemical Society* 162, 1 (2015): p. C12-C23.
82. A.D. King, J.S. Lee, and J.R. Scully, "Finite Element Analysis of the Galvanic Couple Current and Potential Distribution between Mg and 2024-T351 in a Mg Rich Primer Configuration," *Journal of The Electrochemical Society* 163, 7 (2016): p. C342-C356.
83. A.D. King and J.R. Scully, "Sacrificial Anode-Based Galvanic and Barrier Corrosion Protection of 2024-T351 by a Mg-Rich Primer and Development of Test Methods for Remaining Life Assessment," *Corrosion* 67, 5 (2011): p. 05500401-05500422.
84. A.D. King and J.R. Scully. *Blistering Phenomena in Early Generation Mg-Rich Primer Coatings on AA2024-T351 and the Effects of CO<sub>2</sub>*. in *NACE DoD 2011 Conference Proceedings*. 2011. Palm Springs, CA.
85. O.O. Knudsen, U. Steinsmo, and M. Bjordal, "Zinc-rich primers - Test performance and electrochemical properties," *Progress in Organic Coatings* 54, 3 (2005): p. 224-229.
86. M.J. Lin, D.D. Battocchi, and P.G. Bierwagen, "Degradation of Magnesium Rich Primers over AA2024-T3 during Constant Immersion in Different Solutions," *CORROSION* 0, 0: p. null.
87. B. Maier and G.S. Frankel, "Behavior of Magnesium-Rich Primers on AA2024-T3," *Corrosion* 67, 5 (2011): p. 055001.
88. H. Marchebois, M. Keddou, C. Savall, J. Bernard, and S. Touzain, "Zinc-rich powder coatings characterisation in artificial sea water - EIS analysis of the galvanic action," *Electrochimica Acta* 49, 11 (2004): p. 1719-1729.
89. M. Morcillo, R. Barajas, S. Feliu, and J.M. Bastidas, "A-Sem Study on the Galvanic Protection of Zinc-Rich Paints," *Journal of Materials Science* 25, 5 (1990): p. 2441-2446.

90. M.A. Jakab and J.R. Scully, "On-demand release of corrosion-inhibiting ions from amorphous Al-Co-Ce alloys," *Nat Mater* 4, 9 (2005): p. 667-670.
91. F. Presuel-Moreno, M.A. Jakab, N. Tailleart, M. Goldman, and J.R. Scully, "Corrosion-resistant metallic coatings," *Materials Today* 11, 10 (2008): p. 14-23.
92. F.J. Presuel-Moreno, M.E. Goldman, R.G. Kelly, and J.R. Scully, "Electrochemical Sacrificial Cathodic Prevention Provided by an Al-Co-Ce Metal Coating Coupled to AA2024-T3," *Journal of The Electrochemical Society* 152, 8 (2005): p. B302-B310.
93. Y. Cubides, S.S. Su, and H. Castaneda, "Influence of Zinc Content and Chloride Concentration on the Corrosion Protection Performance of Zinc-Rich Epoxy Coatings Containing Carbon Nanotubes on Carbon Steel in Simulated Concrete Pore Environments," *Corrosion* 72, 11 (2016): p. 1397-1423.
94. Y. Cubides and H. Castaneda, "Corrosion protection mechanisms of carbon nanotube and zinc-rich epoxy primers on carbon steel in simulated concrete pore solutions in the presence of chloride ions," *Corrosion Science* 109, (2016): p. 145-161.
95. F. Cui, F.J. Presuel-Moreno, and R.G. Kelly, "Experimental and Computational Evaluation of the Protection Provided by an Aluminum Cladding to AA2024-T3 Exposed at a Seacoast Environment," *CORROSION* 62, 3 (2006): p. 251-263.
96. F.S. Cui, F.J. Presuel-Moreno, and R.G. Kelly, "Computational modeling of cathodic limitations on localized corrosion of wetted SS 316L at room temperature," *Corrosion Science* 47, 12 (2005): p. 2987-3005.
97. S.M. Sharland, C.P. Jackson, and A.J. Diver, "A finite-element model of the propagation of corrosion crevices and pits," *Corrosion Science* 29, 9 (1989): p. 1149-1166.
98. J.T. Waber, "Mathematical Studies of Galvanic Corrosion: VI. . Limiting Case of Very Thin Films," *Journal of the Electrochemical Society* 103, 10 (1956): p. 567-570.
99. J.T. Waber, "Mathematical Studies of Galvanic Corrosion: III . Semi-infinite Coplanar Electrodes with Equal Constant Polarization Parameters," *Journal of the Electrochemical Society* 102, 7 (1955): p. 420-429.
100. J.T. Waber and M. Rosenbluth, "Mathematical Studies of Galvanic Corrosion: II . Coplanar Electrodes with One Electrode Infinitely Large and with Equal Polarization Parameters," *Journal of the Electrochemical Society* 102, 6 (1955): p. 344-353.
101. J.S. Lee, M.L. Reed, and R.G. Kelly, "Combining rigorously controlled crevice geometry and computational modeling for study of crevice corrosion scaling factors," *Journal of the Electrochemical Society* 151, 7 (2004): p. B423-B433.
102. Henkel, *Surface Pretreatment - Technical Data Sheet* (2014).
103. G.S. Frankel and R.L. McCreery, "Inhibition of Al alloy corrosion by chromates," *Interface-Electrochemical Society* 10, 4 (2001): p. 34-39.
104. F.W. Lytle, R.B. Gregor, G.L. Bibbins, K.Y. Blohowiak, R.E. Smith, and G.D. Tuss, "An Investigation of the Structure and Chemistry of a Chromium-Conversion Surface-Layer on Aluminum," *Corrosion Science* 37, 3 (1995): p. 349-369.
105. L. Xia and R.L. McCreery, "Chemistry of a chromate conversion coating on aluminum alloy AA2024-T3 probed by vibrational spectroscopy," *Journal of the Electrochemical Society* 145, 9 (1998): p. 3083-3089.
106. L. Xia and R.L. McCreery, "Structure and function of ferricyanide in the formation of chromate conversion coatings on aluminum aircraft alloy," *Journal of the Electrochemical Society* 146, 10 (1999): p. 3696-3701.
107. A. Sehgal, G.S. Frankel, B. Zoofan, and S. Rokhlin, "Pit growth study in Al alloys by the foil penetration technique," *Journal of the Electrochemical Society* 147, 1 (2000): p. 140-148.

108. R.G. Buchheit, M. Cunningham, H. Jensen, M.W. Kendig, and M.A. Martinez, "A Correlation Between Salt Spray and Electrochemical Impedance Spectroscopy Test Results for Conversion-Coated Aluminum Alloys," *CORROSION* 54, 1 (1998): p. 61-72.
109. L.L. Li, D.Y. Kim, and G.M. Swain, "Transient Formation of Chromate in Trivalent Chromium Process (TCP) Coatings on AA2024 as Probed by Raman Spectroscopy," *Journal of the Electrochemical Society* 159, 8 (2012): p. C326-C333.
110. P. Schmutz and G.S. Frankel, "Influence of dichromate ions on corrosion of pure aluminum and AA2024-T3 in NaCl solution studied by AFM scratching," *Journal of the Electrochemical Society* 146, 12 (1999): p. 4461-4472.
111. T. Rochester and Z.W. Kennedy, "Unexpected results from corrosion testing of trivalent passivates," *Plating and surface finishing* 94, 10 (2007): p. 14.
112. L.L. Li, G.P. Swain, A. Howell, D. Woodbury, and G.M. Swain, "The Formation, Structure, Electrochemical Properties and Stability of Trivalent Chrome Process (TCP) Coatings on AA2024," *Journal of the Electrochemical Society* 158, 9 (2011): p. C274-C283.
113. D.E. Packham, *Handbook of Adhesion*. 2 ed.

### 1.13 Tables

Table 1.1. Composition of Aluminium alloy 2024-T351 on a weight percent basis.

Element	Limit (Wt % )
Cu	3.8 to 4.9
Mg	1.2 to 1.8
Mn	0.3 to 0.9
Si	0.5
Fe	0.5
Zn	0.15
Ti	0.15
Cr	0.1
Al	Rest

## 1.14 Figures

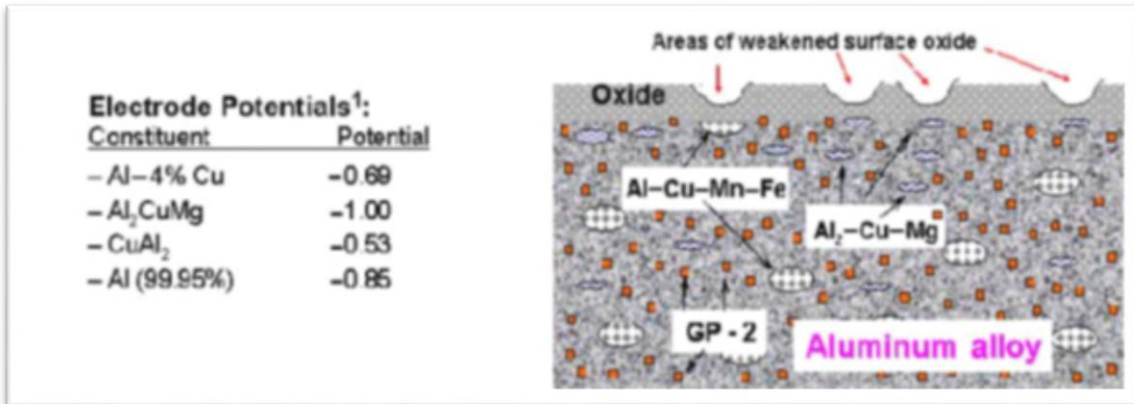


Figure 1.1. Schematics of Al alloy surface with electrode potential of different constituent phases

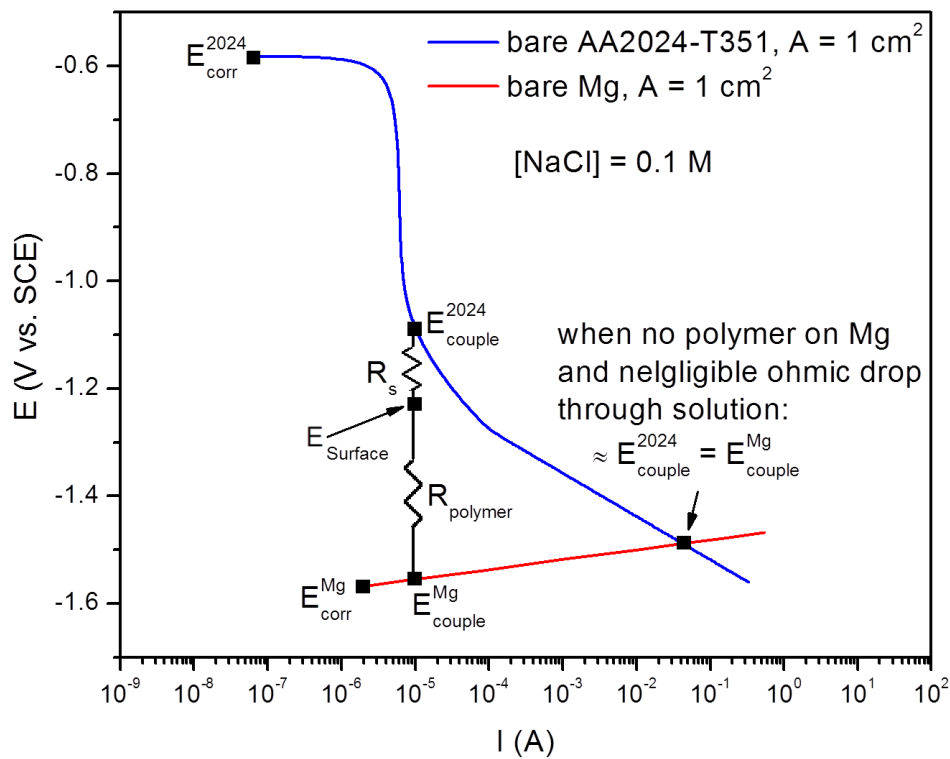


Figure 1.2. Mixed potential model depicting  $E_{surface}$  and  $E_{couple}$  as they pertain to a galvanic couple between AA2024-T351 and polymer coated Mg.

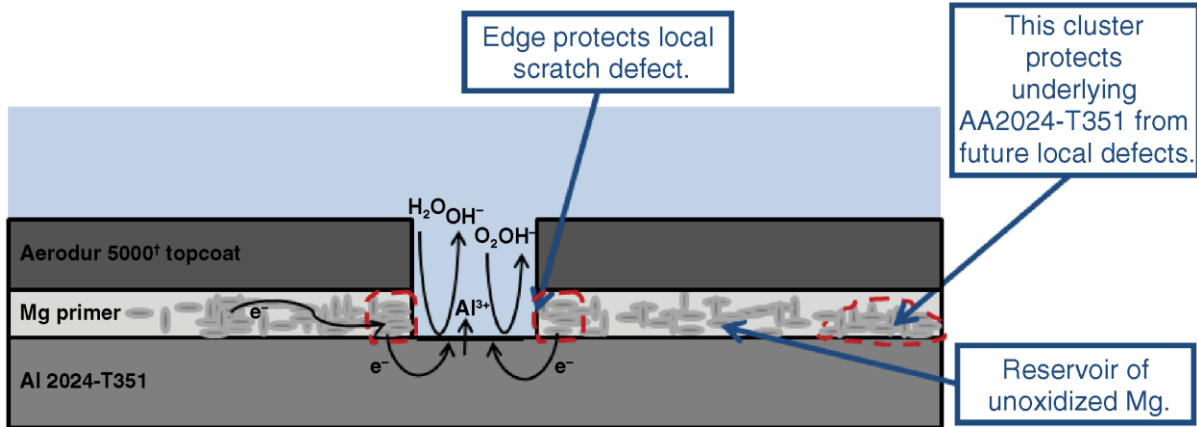


Figure 1.3. Schematic of AA2024-T351 coated with MgRP and advanced performance topcoat under full immersion depicting MgRP function under situation without cathodic corrosion in the case of MgRP/topcoat

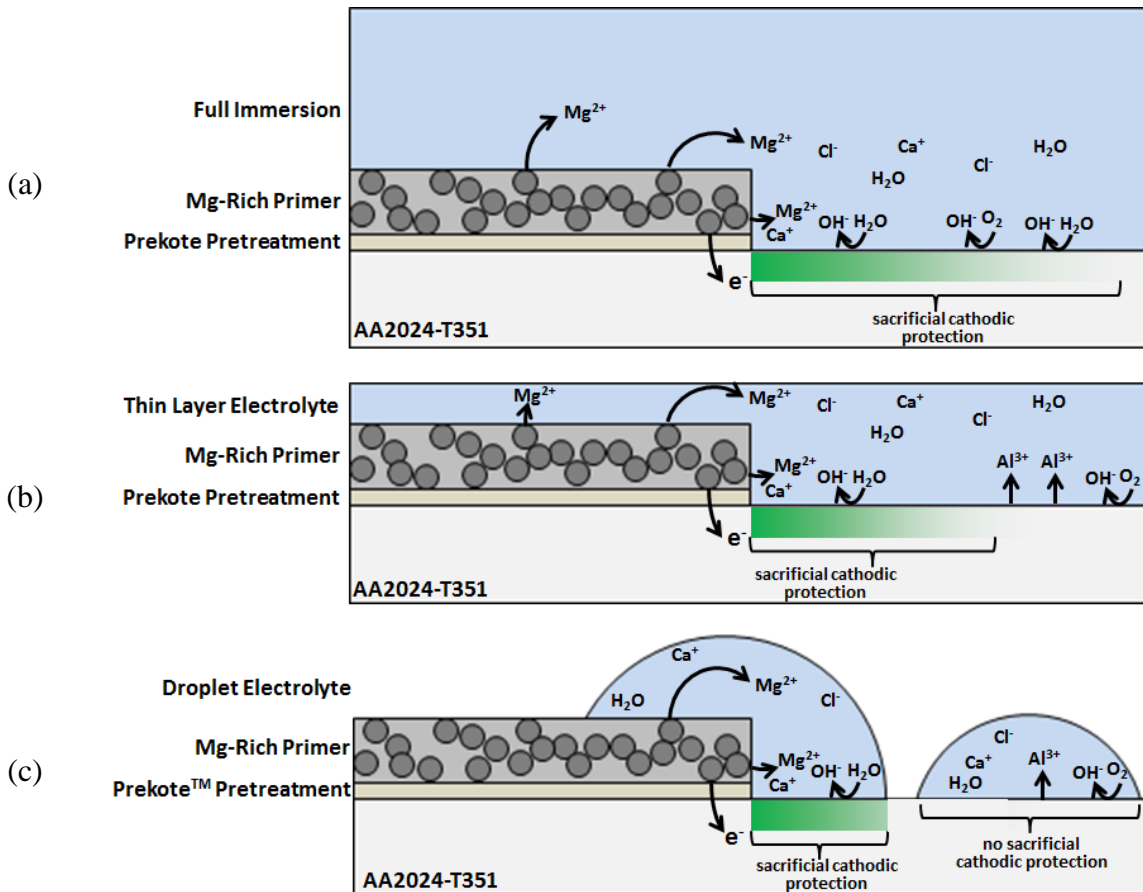


Figure 1.4. Hypothetical schematic of AA2024-T351 coated with MgRP depicting MgRP sacrificial cathodic protection function under (a) full immersion (b) thin-layer electrolyte and (c) droplet electrolyte conditions

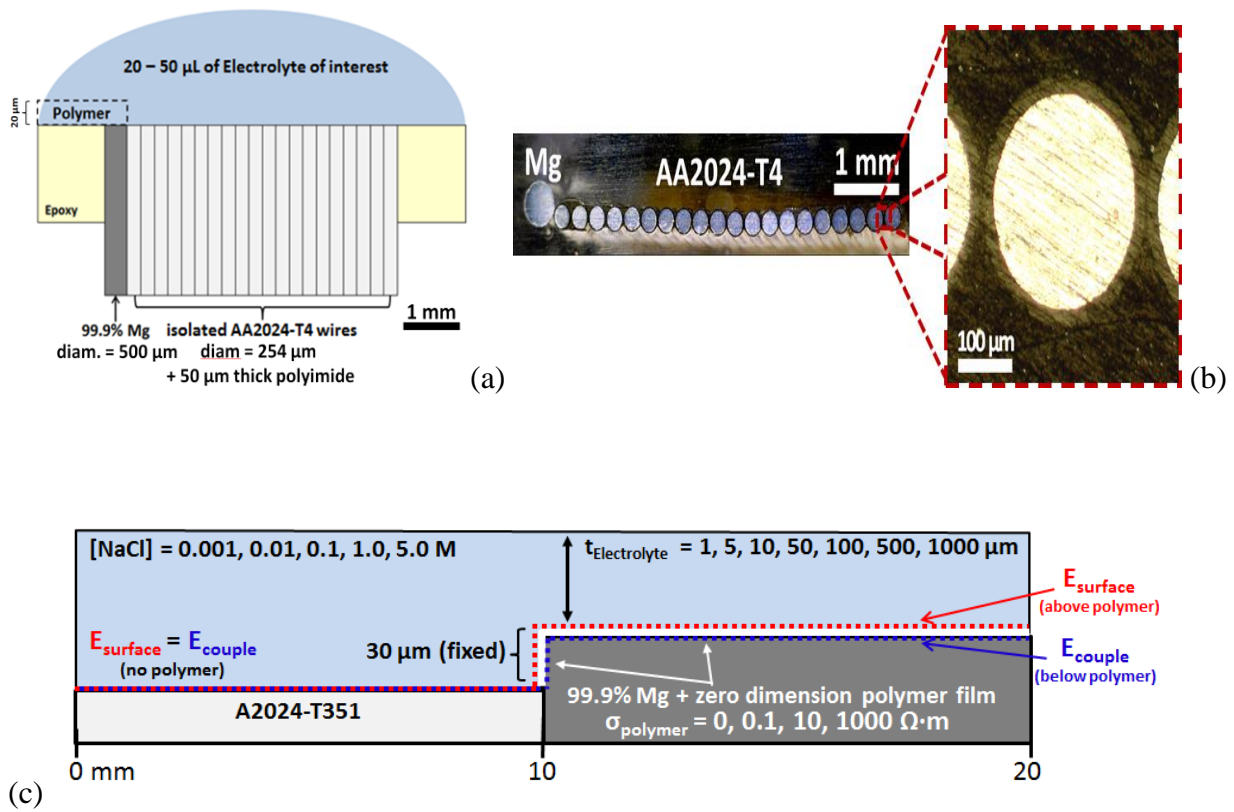
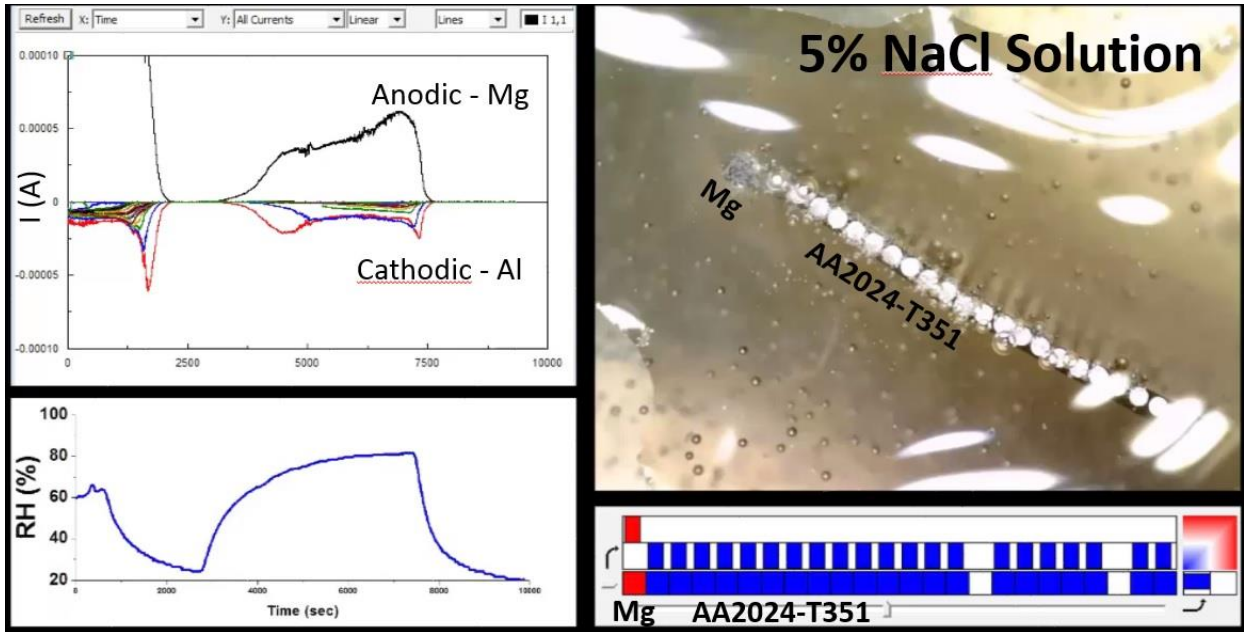
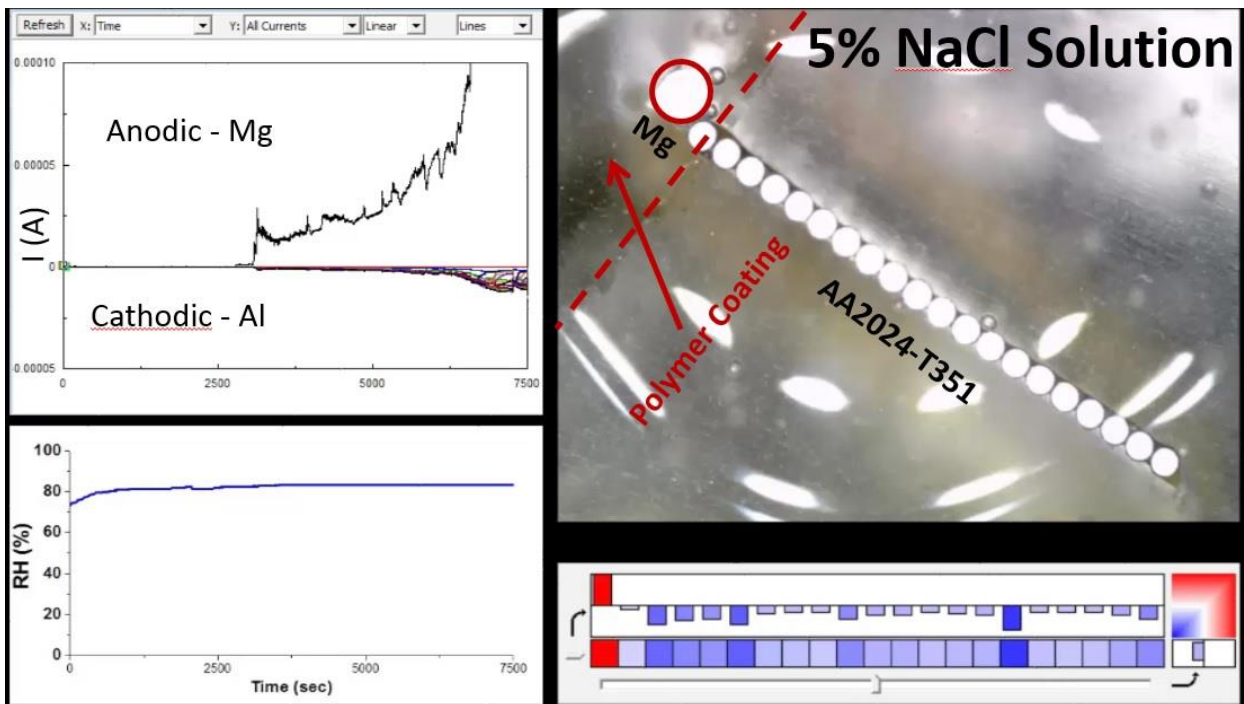


Figure 1.5. (a) Schematic cross section of microelectrode array to assess throwing power of Mg over a representative bare AA2024-T4 scratch in an RH controlled cabinet. (b) Optical image of a the bare Mg/AA2024-T4 microelectrode<sup>[52]</sup> (c) Schematic of geometric model developed in finite element computational modeling software (COMSOL)



(a)



(b)

Figure 1.6. Current, RH, and time-lapse optical images of the bare Mg/AA2024-T4 microelectrode array(a)/ acrylic polymer coated Mg/AA2024-T4 microelectrode array(b) during an episodic wetting and drying event under 5 % (wt) NaCl solution. In the color map dark red indicates an anodic current  $\geq 1 \times 10^{-7}$  A and dark blue indicates a cathodic current of  $\leq -1 \times 10^{-7}$  A. White color indicates a net current of zero

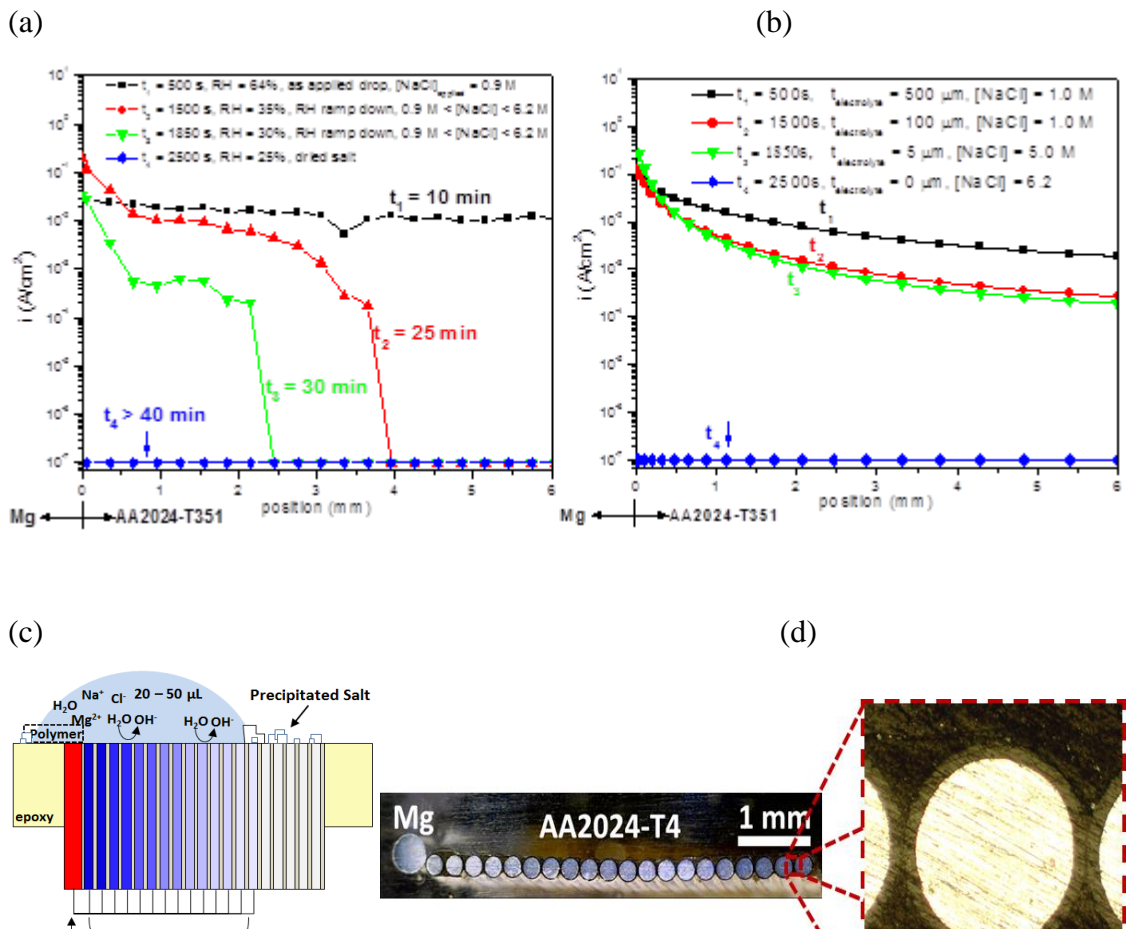


Figure 1.7. Comparison of FEA modelling to micro-electrode array measurements during drying (a)  $I$  measured by Micro-electrode Array, (b)  $I$  predicted by COMSOL FEA model (c) Schematic of multi-electrode array(cross sectional view), (d) Optical Image of multi-electrode array(planar view)

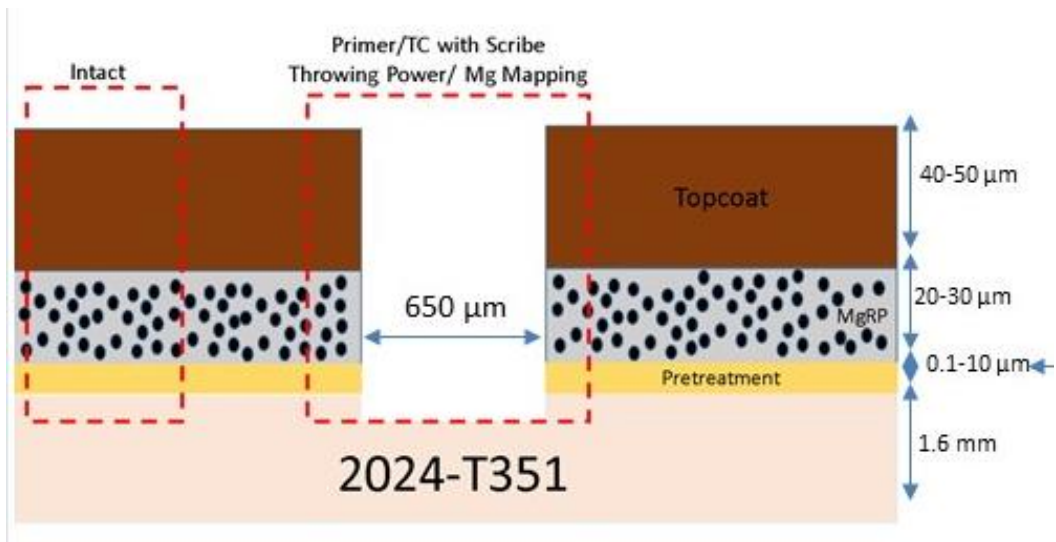


Figure 1.8. Schematic of scribed coating system showing two regions of interest for post exposure characterization, intact coating and scribe.

## **2 Effect of Pretreatments on 2024-T351 Corrosion Protection by Magnesium Rich, Non-Chromium Primer (MgRP): Laboratory Characterization in Full Immersion**

### **2.1 Abstract**

The role of different surface pretreatments on the sacrificial anode-based cathodic as well as barrier protection mechanisms afforded by Magnesium Rich, Non-Chromium Primer (MgRP) with and without topcoat (TC) has been investigated. Conversion coatings (chromate conversion coating, trivalent chromium based pretreatment, non-chromium pretreatment) and anodized coatings (without sealing, with chromate sealing and trivalent chromium pretreatment sealing) were compared to clean and desmuted surfaces and those with a non-film forming surface pretreatment (Prekote™) with and without MgRP/TC. In preliminary studies, pretreatment chemistry and thickness were characterized using X-ray Photoelectron Spectroscopy (XPS) and Scanning Electron Microscopy/Energy Dispersive Spectroscopy (SEM/EDS) while electrical properties were examined with Electrochemical Impedance Spectroscopy (EIS). Full immersion tests in 5 % (wt) NaCl were conducted to evaluate the degradation characteristics of the coating and the subsequent evolution of the sacrificial anode-based cathodic protection as well as barrier protection attributes. A finite full immersion exposure time was required to breakdown the more electrically insulating pretreatment layers. This process lowered the resistance between the MgRP and the 2024-T351 substrate and enabled sacrificial anode-based cathodic protection afforded by the MgRP to commence. In contrast, MgRP was galvanically coupled immediately and functioned from the start as a sacrificial anode for the non-film forming Prekote™ and abrasion-only pretreatments.

A manuscript based on this chapter has been published in Corrosion Journal as a Full Research Paper, “Effect of Pretreatments on 2024-T351 Corrosion Protection by Magnesium Rich, Non-Chromium Primer (MgRP): Laboratory Characterization in Full Immersion.”

Representative author contributions:

B. Kannan: experiments, analysis and interpretation

A. D. King: analysis and interpretation

J. R. Scully: Advisor, analysis and interpretation

## 2.2 Introduction

Corrosion control strategies to replace the chromate based inhibitor coatings technology have been of significant interest for research for corrosion control in Aerospace aluminum alloys such as 2024-T351.<sup>72,73,80,81,84,85,88,115-117</sup> Mg may offer cathodic protection to aluminum alloys in a manner similar to Zn pigments used in zinc rich coatings for cathodic corrosion protection of steel.<sup>78,79,86,89,90</sup> Barrier protection is afforded to the 2024-T351 substrate by the continuous physical barrier consisting of organic epoxy polymer matrix of the MgRP, the Mg pigment particles and any other insoluble pigments in the primer or corrosion products which may have formed within defects in the coating.<sup>84</sup> Also, an organic polyurethane polymer topcoat which greatly decreases the coating system's susceptibility to UV degradation is often applied for additional barrier protection.<sup>84</sup> Field results for precipitation hardened aluminum alloys coated with MgRP indicates that even after the elemental Mg is all converted to corrosion products, the system still provides sufficient barrier protection.<sup>117</sup> Other protection mechanisms have been proposed.<sup>117</sup>

Previous laboratory accelerated lifecycle tests (LALT) and field exposure studies were conducted to determine an optimal primer formulation with respect to Mg pigment volume concentration (PVC) along with optimal coating system stack-ups.<sup>88</sup> Most of these studies have pointed to an optimal Mg pigment volume concentration of approximately 45 % which is at, or just below, the calculated theoretical pigment concentration.<sup>84,88</sup> This formulation is speculated to provide a balance of moderated sacrificial anode-based cathodic protection mediated by the electrical resistance of the resin-MgRP composite, long term barrier protection by the polymers in primer and topcoat, and the beneficial characteristics of preserved, isolated clusters of buried Mg pigment available for the protection of future defects as they occur throughout the protection system's

lifetime in a given exposure environment.<sup>84</sup> Two possible modes of galvanic protection have been proposed; long range protection of remote defects by global galvanic protection potential afforded to the substrate and local or short range Mg pigment-based protection of local as well as buried defects in close proximity to buried pigment particle.<sup>84</sup> Both modes of protection are mediated by the high ionic and electrical resistance of the coating systems as a function of Mg PVC, substrate pretreatments, primer polymer, and topcoat properties. The regulation of cathodic protection abilities is an important aspect for optimization of the MgRP. In addition, the throwing power of polymer coated Mg galvanically coupled to a simulated bare 2024-T351 scribe was studied using multi-electrode arrays.<sup>82</sup>

However, these studies have all been conducted with a MgRP over a bare or Prekote™ pretreated 2024-T351. In practical applications, several pretreatments may be used with aerospace aluminum alloys to improve the adhesion between the substrate and polymer and also to impart corrosion protection.<sup>118</sup> Chromate conversion coatings (CCC) offer strong corrosion resistance properties<sup>36,104,106</sup> and are noted for their ability to self-heal.<sup>104</sup> This phenomenon is attributed to the release of hexavalent chromium from the coating into the corrosive solution in contact with the surface.<sup>104</sup> Due to environmental hazards posed by hexavalent chromium, non-chromium process (NCP) and trivalent chromium process (TCP) coatings have been explored as alternatives for CCCs.<sup>16,19,110,112,113,119,120</sup> NCP conversion coatings are based on titanium/zirconium oxides<sup>16</sup> whereas TCP conversion coatings are trivalent chromium enriched zirconium oxide coatings.<sup>113</sup> Corrosion resistance of Al alloys can also be enhanced by anodization,<sup>33,121-123</sup> where the oxide film is characterized by an inner thin barrier layer on the substrate and an outer thick porous layer.<sup>33</sup> Sealing is often performed following the anodization.<sup>33</sup> The pores are sealed by chromic acid or

other active inhibitors to improve corrosion protection.<sup>33,121-123</sup> These effects of these pretreatments on MgRP performance has not been investigated.

A fundamental understanding of the role of surface pretreatments such as chromate conversion coatings, and anodization on MgRP cathodic protection potential mediation and protection processes has not been previously reported for the MgRP system. A pretreatment might function in several roles. Pretreatments could suppress detrimental blistering and cathodic corrosion by providing a corrosion resistant layer,<sup>16,19,33,36,104,106,110,112,113,118-123</sup> as well as act as source of chemical inhibitor.<sup>19,36,104,106,110,112</sup> The electrical resistance imparted by the pretreatment might mediate the galvanic couple potential by mixed potential theory, suppressing cathodic corrosion and/or limiting or delaying sacrificial anode-based cathodic protection. A pretreatment layer has the potential to delay the onset of Mg depletion by sacrificial protection and could also increase the residual life once Mg is depleted. However these functions clearly depend on the details of the pretreatment used and its properties.

The objective of this chapter is to provide insight into the role of different surface pretreatments on the sacrificial anode-based cathodic and barrier protection mechanisms afforded by an overlaying Magnesium Rich Primer (MgRP). This work focuses on initial laboratory testing of 2024-T351/pretreatment/MgRP and 2024-T351/pretreatment/MgRP/TC in 5 % (wt) NaCl solution. Subsequent chapters will compare the performance of the pretreated 2024-T351/MgRP in laboratory accelerated test environments and at well-established field exposure sites and will address the throwing power of MgRP in atmospheric environments.

## **2.3 Experimental Procedure**

### **2.3.1 Materials**

Test panels were comprised of a 1.6 mm thickness 2024-T351 sheet bare and pretreated with 7 different pretreatments for comparison including (i) Non-film Forming Surface Pretreatment (Prekote™), (ii) Chromate Conversion Coating (CCC), (iii) Trivalent Chromium Pretreatment (TCP), (iv) Non Chromium Pretreatment (NCP), (v) Anodized without Sealing, (vi) Anodized with Chromate Seal, and (vii) Anodized with TCP Seal. Prekote™ is a non-film forming chromium free surface pretreatment from Pantheon. It contains approximately 95% water and less than 3 % each of diethylene glycol monobutyl ether and N-methyl-2-pyrrolidone.<sup>124</sup> Chromate conversion coating (Alodine 1200s),<sup>103</sup> non-chromium pretreatment (Alodine 5200),<sup>125</sup> and trivalent chromium pretreatment (Surtec 650)<sup>126</sup> are also commercial products. For anodization pretreatments, a thin-film sulfuric acid anodizing, MIL-A-8625F: Type II pretreatment procedure was followed.<sup>127</sup>

A 40 µm primer layer of Mg-rich primer and a 50 µm thick topcoat of Aerodur 5000 high-performance advanced coating, both produced by Akzo Nobel Coatings (Waukegan, Illinois) were applied. The Mg rich primer consist of one part epoxy matrix with Mg metal flake pigment of a diameter 20 µm with pigment volume concentration of 45 % (3rd generation 2100P003, Lot: 493-190). Aerodur 5000 (Gloss white finish product: ECM-G7875) is a two component polyurethane topcoat developed for military application in variety of exposure environments.<sup>128</sup>

### **2.3.2 Full-Immersion Electrochemical Analysis**

All full-immersion studies reported herein were conducted in quiescent 5 % (wt) NaCl (pH: 6.9±0.4) open to laboratory air. Potential control during electrochemical experiments was maintained using a Gamry Potentiostat (Ref 600/ PCI4) with computer interface software.

Saturated calomel electrode (SCE) and Pt mesh were used as reference and counter electrode, respectively. All current values reported herein are area normalized. Exposed sample area is 0.825 cm<sup>2</sup> for electrochemical measurements and 19.625 cm<sup>2</sup> for XRD measurements.

### **2.3.3 Electrochemical Impedance Spectroscopy**

Electrochemical impedance spectroscopy (EIS) was conducted on bare Mg, bare/pretreated 2024-T351, and Akzo Nobel based, Mg-rich primer/topcoat coated 2024-T351 panels using a three electrode cell. A typical EIS scan was acquired in swept sine mode from 100 kHz to 0.01 Hz with 6 points per decade. Bare/pretreated electrodes were scanned with an AC amplitude range of 50 mV while coated panels were scanned with an AC amplitude of 80-100 mV to reduce noise. The tests were conducted in quiescent 5 % (wt) NaCl, as discussed above, after 1 hour exposure at open circuit for bare/pretreated/MgRP coated panels and 12 hour exposure for MgRP/Topcoat coated panels. EIS fits to equivalent electrical circuit of the coating/metal interface was performed using Gamry Echem Analyst software.

### **2.3.4 Potentiodynamic Polarization Scans**

Cathodic potentiodynamic polarization scans were conducted on bare 2024-T351 as well as pretreated 2024-T351 in the as-received condition. A typical cathodic scan started at 0.005 V vs. OCP and scanned to -1.0 V vs. OCP at 0.1667 mV/s.<sup>129</sup> Anodic potentiodynamic polarization scans were conducted on 99.9 % pure, 8.00 mm diameter bare Mg electrodes. The bare Mg electrodes were polished with 1200-grit SiC paper. A typical anodic scan started at -0.005 V vs. OCP and scanned to 0.5 V vs. OCP at 0.1667 mV/s.<sup>129</sup> All tests were conducted in 5 % (wt) NaCl solution at quiescent conditions.

### **2.3.5 Full-Immersion Electrochemical Testing Protocol (Cycle Test)**

A full-immersion electrochemical testing regimen was used. This protocol was discussed elsewhere.<sup>84</sup> This test included 1 hour at OCP (2 hours for the first cycle) followed by EIS measurement. The protocol then assessed the MgRP charge supplied at a simulated galvanic couple potential where polarization by galvanic coupling with an infinite cathode is sensed. A potentiostatic hold at -0.8 V (vs. SCE) accelerated the Mg dissolution in MgRP, and the anodic charge supplied by the electrically connected MgRP was measured in a situation simulating polarization by contact with a large electrode area of bare 2024-T351. This potential was indicative of the cathodic protection afforded by the coating when galvanically coupled to a remote defect exposing 2024-T351. This approach simulated a remote infinite cathode of 2024-T351. This approach does not examine galvanic coupling between buried MgRP and 2024-T351 locally. The potential chosen for potentiostatic hold (-0.8 V vs SCE) did not reduce or damage pretreatments. The protocol also assessed the residual barrier properties of the coating with EIS. These steps were repeated for a specific number of cycles (as indicated in Table 2.1) to assay remaining electrically connected Mg pigment in the MgRP while sampling the OCP and residual barrier properties by EIS. If Mg in MgRP was not electrically connected to the 2024-T351 substrate or consumed, anodic currents were not registered during this potentiostatic hold as bare 2024-T351 would be slightly cathodically polarized at a potential of -0.8 V.

### **2.3.6 X-ray Photoelectron Spectroscopy**

X-ray photoelectron spectroscopy (XPS) was conducted on pretreated 2024-T351 to analyze the surface chemistry of respective pretreatments. A Kraton AXIS Ultra instrument with a 9 channeltron multi-detector controlled by a VISION data system was used. A monochromatic Al-K $\alpha$  X-ray sources was used with a voltage of 1486.6 eV and 120 W. The data were acquired using

a spectrum analyzer with a hybrid lens mode. The operating pressure during analysis was approximately  $1 \times 10^{-8}$  Torr. All spectra were corrected by C 1s peak at 284.5 eV. To minimize the carbon contamination of pre-aged samples, Argon ion sputtering was conducted intermediately between the XPS measurements. All spectra were analyzed using CasaXPS™ software (version 2.3.16). The atomic fraction of an element in multi-component system was determined by using the following expression;

$$\text{Atomic (\% Element 1)} = (I_1 F_1) / \sum_{n=1}^n (I_n F(n)) \quad (1)$$

where I is the intensity of corresponding photoelectron peak, F is the atomic sensitivity factor and n is the number of elements.  $I_1$  corresponds to intensity of element 1. Elements, 1 to n are summed in the denominator. The inelastic mean-free-path (IMFP or  $\lambda$ ) of photoelectrons, with kinetic energy between 10 to 1000 eV, ranges from about 1 to 3 nm.<sup>130</sup>

### 2.3.7 X-ray Diffraction

X-ray Diffraction (XRD) was conducted to characterize global Mg depletion as a function of exposure time in cycle tests. A Panalytical X'pert powder diffractometer utilizing a Cu-K $\alpha$  source was utilized for measurements. All samples were scanned continuously from 30 degrees to 50 degrees at 5 degrees per minute. Both fresh Mg-rich-coated panels and panels exposed in the full immersion cycle test were examined using XRD to detect elemental Mg or Mg corrosion products. XRD measurements of pristine and environmentally exposed samples were made on panels without any scribe, presumed to be representative of global coating degradation. XRD obtained from Mg-rich-coated panels were normalized against the face-centered cubic (fcc) Al <200>  $2\theta = 44.74^\circ$  peak from the underlying substrate. Peak normalization and integration was performed with

Origin Lab 7.5 software. The lower detection limit for crystalline phases was approximately 3-5 % of the sample by volume.<sup>131</sup>

### **2.3.8 Scanning Electron Microscopy and Energy Dispersive Spectroscopy**

Scanning electron microscopy (SEM) and energy dispersive spectroscopy (EDS) were used for characterization of thickness and chemistry of chosen pretreatments, MgRP and Topcoat. A field emission Quanta 650 SEM was used to conduct these investigations. For EDS, Oxford XMax 150 detector was utilized. A working distance of 15 mm and an accelerating voltage of at least 3 times the energy of the maximum characteristic peak of interest were used (~15 kV). At an accelerating voltage of 15 kV, EDS has a penetration depth of roughly 2 to 5  $\mu\text{m}$  into the materials investigated in this study. Elemental maps and line profiles were collected and EDS analysis was performed using Aztec analysis software. Cross sectional EDS were performed for all chosen pretreatments on surface of 2024-T351 at low vacuum mode. Before characterization, each sample was ground to 0.05  $\mu\text{m}$ . To prevent abrasion of conversion coatings and preserve interface during polishing, the conversion coatings from two planar specimen were stacked facing each other using Gatan G-1 epoxy resin.

## **2.4 Results**

### **2.4.1 Preliminary Studies of Chemistry of Chosen Pretreatments**

Survey XPS scans for the CCC, TCP and NCP were acquired at different ion etching times after 0, 3, and 5 minutes. High resolution XPS experiments were conducted for chosen identified elements in their photoelectron energy ranges after survey scans. The results of the quantitative analysis of the spectra are summarized in Table 2.2. CCC was characterized by strong peaks for chromium and oxygen. TCP had strong zirconium and oxygen peaks and a small peak indicative of presence of chromium. NCP showed characteristic peaks for zirconium, titanium and carbon.

The carbon peak did not decrease as a function of etching time, indicating that the NCP is enriched with carbon. Fluorine was detected in all conversion coatings as fluoride was added to all pretreat baths for surface activation of substrate. A small amount of silicon was detected in both bare and pretreated samples which could have been introduced through cleaning/desmutting process.

#### **2.4.2 Characterization of Thickness of the Pretreatments**

EDS compositional map of 2024-T351/Prekote<sup>TM</sup>/MgRP/Topcoat is shown in Figure 2.1. The average thickness of MgRP and topcoat are  $40\pm 10$   $\mu\text{m}$  and  $50\pm 10$   $\mu\text{m}$ , respectively. The thickness of pretreatments were calculated from cross-sectional EDS line profile of pretreated 2024-T351 without any primer/topcoat. Based on previous XPS measurements, Cr, Zr and Ti were used as EDS markers for CCC, TCP and NCP, respectively. Oxygen was used as EDS marker for anodized coatings. EDS line spectra of corresponding elements (Figure 2.2) showed that due to the significant interaction volume, the peaks have a characteristic bell curve instead of a sharp interface. Therefore, thickness was calculated by approximating the interface at a position where half of the peak height was achieved. The thickness of different pretreatments as measured using EDS line profiles are summarized in Table 2.3. Based on the EDS data, the thickness of the pretreatments are assigned in the following order, Anodized coating > CCC ~NCP > TCP.

#### **2.4.3 Laboratory Assessment of Electrochemical Behavior of Pretreated 2024-T351/MgRP/Topcoat in the As-Received Condition**

The various resistances between the MgRP, the buried 2024-T351 and 2024-T351 scratch are depicted in Figure 2.3. Significant electrical resistance was introduced between the MgRP and the 2024-T351 substrate by inserting the pretreatments. The electrolyte path between the MgRP and

2024-T351 includes ionic conducting phases such as the primer and topcoat resins and electrolyte. Intact coatings without a scratch were examined in 5 % (wt) NaCl. Figure 2.4a shows the effect of different pretreatments on cathodic kinetics of 2024-T351 in quiescent 5 % (wt) NaCl solution. Pretreatments raise the OCP, and lower the ORR and HER reaction rates at potentials between -0.4 V to -1.8 V. As the pretreatment resistance between the 2024-T351 and buried Mg pigment increases, the predicted galvanic couple potential sensed by the coated 2024-T351 also increases. This occurs in accordance with mixed potential model as indicated in Figure 2.4b and 4c. In order to characterize this resistance, impedance spectroscopy was applied to intact coatings. Impedance spectra (Bode magnitude/phase angle) of bare/pretreated 2024-T351 with and without primer/topcoat are summarized in Figure 2.5. Anodized 2024-T351 had very high impedance at all frequencies, typical of the insulating behavior of the highly resistive oxide layer. Conversion coatings had intermediate impedance whereas bare/Prekote™ 2024-T351 had lowest overall impedance. Equivalent circuits shown in Figures 2.6a and 2.6b were chosen for EIS fitting of bare/Prekote™ pretreated 2024-T351 and conversion coatings/anodization pretreated 2024-T351, respectively. Resulting circuit parameters estimated by EIS fitting procedure are summarized in Table 2.4. The effects of MgRP as well as an organic topcoat on EIS behavior for three selected pretreatments are elucidated in Figure 2.7. The lowest impedance was for bare 2024-T351. MgRP coated samples had higher impedance than uncoated 2024-T351 which implies that Mg pigment did not form a continuous network and that separated metallic particles were encapsulated in moderately high resistance polymer.<sup>84</sup> The presence of polyurethane topcoat increased the barrier impedance properties of the system by two orders of magnitude (Figure 2.7). The low frequency impedances and phase angle indicate that barrier properties were highest for topcoated samples. MgRP primer based samples have intermediate impedance behavior in comparison to pretreated

samples without any MgRP as the MgRP becomes decoupled and the pretreatment becomes more insulating (Figure 2.7). The galvanic couple potential sensed by the bare 2024-T351 coupled to Mg given intermediate ionic and electrical resistances, was measured by monitoring the global open circuit potential (OCP) of the chosen intact coating system with no scratch. In Figure 2.4, the potential sensed by 2024-T351 is noted in the context of the galvanic couple formed for an intact coating. In Figure 2.3, the remote reference electrode position is noted. Figure 2.4c summarizes the effect of imposing a resistance between the Mg in MgRP and the 2024-T351 on the galvanic couple potential at the 2024-T351 surface. The galvanic couple potential at low resistances cannot be accessed by the more resistive layers of same pretreatment.

Preliminary electrochemical measurements (OCP and EIS) for chosen pretreatments with and without MgRP and Topcoat have been summarized in Figure 2.8. The OCP values of bare 2024-T351 and bare Mg are included in Figure 2.8a for comparison. The error bars indicate the mean and the standard deviation for three experimental runs conducted for each system (Figure 2.8). When 2024-T351 is galvanically coupled to bare Mg the galvanic couple potential of 2024-T351 was approximately -1.4 V (vs. SCE) as shown in Figure 2.9.<sup>84</sup> Bare 2024-T351/MgRP and Prekote™ pretreated MgRP achieved galvanic couple potential closer to that of bare Mg (-1.4 V vs. SCE). Conversion coating pretreated 2024-T351/MgRP system achieved a galvanic couple potential of approximately -0.8 V (vs. SCE). The anodized 2024-T351/MgRP based systems achieved very high galvanic couple potentials (-0.4 V vs. SCE) in comparison to other pretreatments.

#### **2.4.4 Diagnostic Electrochemical Cycle Test to Assess the Charge Capacity Associated With Mg Oxidation in MgRP Without a Topcoat**

Figure 2.10 compares the electrochemical cycle test performance of Prekote™ pretreated 2024-T351/MgRP to TCP pretreated 2024-T351/MgRP. The OCP of the Prekote™ pretreated 2024-T351/MgRP shifted from -1.49 V (vs. SCE) to -0.95 V (vs. SCE) as a function of potentiostatic hold (at -0.8 V vs. SCE) cycles indicating that Mg was depleted as function of time. The net anodic charge in the potentiostatic hold also decreased with each additional cycle indicating that some amount of Mg in the MgRP that had exposure to both electrolyte, and had some electric conductivity with substrate, had been converted to magnesium corrosion products during simulated galvanic coupling (Figure 2.10). These trends in galvanic couple potential and anodic charge confirm that, magnesium was galvanically coupled to 2024-T351 immediately and Mg was available for cathodic protection of a remote scratch from the beginning of exposure. In the case of TCP pretreated 2024-T351/MgRP, the open circuit potential of intact coating shifted from -0.67 V (vs. SCE) to -1.0 V (vs. SCE) as shown in Figure 2.10. The net charge for the initial cycles was cathodic but after prolonged exposure it became anodic. In the anodized TCP sealing system (Figure 2.10), the anodic charge was heavily mediated by the resistive nature of the anodized coating. Similar to the TCP pretreatment, the anodized TCP sealing system was initially cathodic at -0.8 V (vs. SCE) indicative of the cathodic reactions on uncoupled 2024-T351. Also there was a cathodic to anodic transition towards anodic charge supplied by MgRP with the increasing number of cycles indicating the breakdown of pretreatment or at least decreased resistance of the pretreatment enabling galvanic coupling. The open circuit potential of intact coating shifted from -0.60 V (vs. SCE) to -0.86 V (vs. SCE) as cycles accumulated (Figure 2.10). Barrier properties of all three systems decreased as a function of exposure time (Figures 2.10). There was an initial large

drop in low frequency impedance that could be correlated to the initial time required for wetting of underlying substrate. Similar experiments were conducted in other pretreated 2024-T351/MgRP systems. The initial cathodic charge was followed by anodic charge when held at -0.8 V (vs. SCE) in selected pretreatments (CCC, TCP and anodized TCP Seal) as shown in Figure 2.11. This trend indicates that initially no galvanic coupling occurs between 2024-T351 and MgRP because of the high resistance between the anode and cathode given the various resistive pretreatments (Figure 2.8b). However, prolonged exposure brought about lowering in the resistance of these pretreatment layers enabling galvanic coupling (Figure 2.11). The OCP of pretreated systems also shifted to more negative potentials during this process signaling improved galvanic coupling over time, which correlates well with cathodic to anodic charge transition in chosen pretreated system. In other MgRP systems with pretreatments such as NCP, anodized without sealing and anodized chromate seal, there was no galvanic coupling enabled in the time frame of the electrochemical cycle test protocol. This is with respect to a remote defect. It does not mean that local galvanic coupling between a buried MgRP pigment particle and 2024-T351 just beneath it would not be coupled. A summary of OCP as a function of elapsed time for chosen pretreatments is shown in Figure 2.12. Figure 2.13 shows the impedance magnitude at 0.01 Hz for all the bare/pretreated 2024-T351 system coated with MgRP over the lifetime of the full-immersion electrochemical testing regimen. The highest impedance was observed in the anodized systems as indicated by an order of magnitude increase in Z modulus values (Figure 2.13). Due to the complex nature of impedance curves, low frequency EIS could not be directly correlated with coating degradation (Figure 2.14a). Intermediate frequency EIS at 10 Hz gave a better correlation to coating degradation for anodized coating with no sealing and with TCP sealing (Figure 2.14b).

XRD spectra of each sample was also taken after each individual cycle in the full-immersion electrochemical regimen. The normalized integral intensity of the Mg <101> peak plotted as a function of elapsed time is shown in Figure 2.15. The intensity of the Mg in the primer dropped as a function of exposure time in the cycle test regimen. Only 30 - 50 % of the Mg present in the MgRP depleted at the end of cycle test. Note that there is a difference between the total Mg sensed by XRD and Mg utilization in the cycle test. Potentiostatic hold experiments during cycle test were indicative of amount of Mg that was electrically and ionically well-connected and was available for cathodic protection when an external potentiostat is used. XRD measurements are indicative of total amount of buried Mg present in the coating. Some of this Mg might be buried and isolated beneath the coating and might not be available for cathodic protection initially. Also Mg depletion occurs as a function of time irrespective of galvanic coupling, because Mg in MgRP is susceptible to high rates of self-corrosion in the absence of a topcoat.

#### **2.4.5 Diagnostic Electrochemical Cycle Test to Assess Charge Capacity of Mg in MgRP**

##### **With a Topcoat**

Intact bare/pretreated 2024-T351 panels coated with MgRP and an advance performance polyurethane topcoat were also exposed to the full-immersion electrochemical testing regimen discussed above. Cycle test protocol was applied after 12 hours of exposure in full immersion conditions. The anodic charge (at -0.8 V vs. SCE) was 2-3 orders of magnitude lower for topcoated systems compared to non-topcoated systems as indicated in Figure 2.16. The anodic capacity of Mg available for protection of a remote defect was limited by the larger ionic resistance added to the electrolyte ionic resistance path between the anode and the cathode by the topcoat (Figure 2.8b). The galvanic couple potential as a function of the cycle times in the electrochemical cycle test are indicated in Figure 2.17. The galvanic couple potential was significantly regulated and

moderated by presence of the topcoat. The galvanic couple potential of the intact system was very high (-0.1 V (vs. SCE) for the anodized system with no sealing). Most pretreated systems had a galvanic couple potential in the range of -0.4 V (vs. SCE) to -0.8 V (vs. SCE) reflective of well passivated 2024-T351 with a metallic substrate uncoupled to MgRP. The Prekote™ pretreated system had a galvanic couple potential around -1.0 V (vs. SCE) with the topcoat. The anodized systems had 2 orders of magnitude higher impedance compared to the other pretreated systems (Figure 2.18). Figure 2.18 indicates that the low frequency EIS did not change appreciably as a function of time which is indicative of the excellent barrier properties of the topcoat.

XRD spectra of each type of pretreatment was taken after selected cycles in the full-immersion electrochemical regimen. It showed no substantial decrease in Mg pigment intensity confirming that the presence of topcoat lowers the self-corrosion of Mg in MgRP.

## **2.5 Discussion**

### **2.5.1 The Role of Pretreatments in Cathodic Protection**

The electrical resistance imparted by the pretreatments, high OCP of pretreated 2024-T351 and the polarizability of the pretreated 2024-T351 with respect to ORR and low HER rates all play an important role in determining the sacrificial cathodic protection capabilities of the overlaying MgRP as indicated in Figure 2.4b. When a bare 2024-T351 is coupled to bare Mg, the potential at which 2024-T351 senses protection is approximately -1.4 V as shown in Figure 2.9. As the ohmic resistance between the 2024-T351 and MgRP increases due to pretreatments, this potential sensed by remote reference electrode coupled shifts to more positive direction as indicated in Figure 2.8a. This potential at which 2024-T351 senses protection is called galvanic couple potential of the 2024-T351. However, the high IR drop between the MgRP and the 2024-T351 brought about by the primer resin and the pretreatment means that the 2024-T351 is not polarized to the galvanic

couple potential of the Mg. These two potentials are separated by a large ohmic resistance. The chemistry as well as thickness of pretreatment determines the resistance imparted by the pretreatments to the system. The galvanic couple potential of the intact coating stack up can hence be regulated and controlled by pretreatments. This can be seen in mixed potential model of Figure 2.4b. The anodization with chromate sealing pretreatment not only had a high IR drop, but is also very sensitive to ohmic resistance given its restriction in both ORR and HER cathodic kinetics as shown in Figure 2.4a and b. The galvanic couple potential of the bare 2024-T351 and the anodized 2024-T351 with chromate seal as a function of ohmic resistance between 2024-T351 and MgRP are shown in Figure 2.4c. The galvanic couple potential is more positive at all resistances due to the E-log (i) behavior of anodized 2024-T351 (Figure 2.4c). Anodized coatings have thickness of approximately 5 to 9  $\mu\text{m}$ , whereas conversion coatings have thicknesses in the range of 0.4  $\mu\text{m}$  to 0.8  $\mu\text{m}$  as shown in Table 2.3. The low ORR current density on pretreated 2024-T351, the high OCP and high resistance which all depend on the chemistry and thickness of the pretreatment, can be correlated to the galvanic couple potential as shown in Figure 2.8a. Anodized pretreatment have a more positive galvanic couple potential for 2024-T351/pretreatment/MgRP system compared to bare or Prekote<sup>TM</sup> pretreated 2024-T351/MgRP. In contrast, conversion coatings have intermediate galvanic couple potentials. These results indicate that the galvanic couple potential shifts to relatively more positive potentials when 2024-T351 is pretreated with different protective systems such as conversion coatings or anodized coatings. This implies that metallic 2024-T351 is buried under the pretreatments and the resistance of pretreatment layer is great enough to decouple the MgRP from the 2024-T351 substrate. Given the low oxygen reduction reaction (ORR) rate on pretreated 2024-T351 (Figure 2.4b), polarization of the 2024-T351 substrate towards Mg is easier. However, this is not the overriding factor. The

positive shift in the OCP of the uncoupled pretreated 2024-T351 indicates additional resistive effects due to the pretreatments. Due to the insulating aluminum oxide layer the OCP is shifted to more positive potentials as predicted by mixed potential model (Figure 2.4c).

### **2.5.2 Delayed Galvanic Protection by MgRP in Presence of Resistive Pretreatments**

Clusters of buried magnesium pigment that lack electrical connection to the substrate would be anodically polarized if actively polarized to a true interfacial potential of -0.8 V vs. SCE (i.e. free of IR drop). In case of bare and Prekote™ pretreated 2024-T351, the absence of a pretreatment layer (which imparts additional resistance) resulted in polarization of connected MgRP pigment to -0.8 V (vs. SCE) from the beginning of the exposure. In this case Mg corrosion is accelerated.

The onset of galvanic coupling and cumulative anodic charge as function of exposure time in cycle test for pretreated 2024-T351/MgRP are summarized in Figures 2.19. In systems with resistive pretreatment layer, no anodic charge was sensed initially during exposure. However, upon prolonged exposure, apparently degradation of pretreatment overtime led to lowering of resistance between 2024-T351 and Mg in the MgRP. This is suggested to enable polarization of MgRP in the cycle test and galvanic coupling during subsequent exposure (Figure 2.13 and 2.14).

### **2.5.3 Role of Topcoat in Cathodic Protection of 2024-T351 by Mg Rich Primer**

The polyurethane topcoat used in our current study had considerably greater thickness and impedance compared to the topcoat used in our previous MgRP studies.<sup>80,84</sup> This higher impedance directly correlates to excellent barrier properties afforded by the pretreatment/MgRP/TC (Figure 2.8b). The anodic charge at -0.8 V (vs. SCE) from diagnostic electrochemical cycle test experiments were 2-3 orders lower in comparison to the 2024-T351/Pretreatment/MgRP with no

topcoat (Figure 2.11). This is interpreted as due to the high resistance of the topcoat which would regulate galvanic coupling to a remote scratch exposing 2024-T351. In this case, MgRP is not polarized to -0.8 V (vs. SCE). Moreover, the barrier properties of the intact topcoated system did not change appreciably as a function of cycle test regimen exposure times (Figure 2.18). X-ray diffraction studies after cycle test exposures also indicate that the topcoat prevented the self-corrosion of Mg pigment in the primer thereby preserving it for cathodic protection of future defects. Therefore, the topcoat is an excellent resistive barrier, and a barrier to moisture ingress. In the presence of the topcoat, MgRP likely protects the buried local substrate underneath the MgRP but would have difficulty protecting remote scratches exposing 2024-T351 galvanically coupled above the topcoat except at edges of scratches or coatings where the primer is exposed directly. This aspect was investigated in detail recently.<sup>82</sup>

#### **2.5.4 The Need for Lab vs. Field Assessment With Macro Scale Defects**

The MgRP degradation rate herein were performed in accordance with diagnostic electrochemical cycle test protocol in 5 % (wt) NaCl solution.<sup>84</sup> However, there is a critical need to study the MgRP degradation characteristics in presence of pretreatments in various relevant exposure environments in order to identify the pertinent field environmental factors that are significant to MgRP depletion and rationalize the differences in performances of MgRP in presence of different surface pretreatments. Field exposures have been reported for Prekote<sup>TM</sup> based systems.<sup>80,81</sup> In future work to be reported, results of exposures studies conducted in the field at a coastal marine site; Kennedy Space Center, FL (KSC), at an inland rural site; Birdwood Golf Course in Charlottesville, VA, and compared to ASTM B-117 with 5% NaCl, and full immersion in quiescent 5 % (wt) NaCl solution will be reported. Mg pigment depletion rate, global galvanic protection potential, and

coating barrier properties will be tracked throughout exposure periods in both field and laboratory environments.

## **2.6 Conclusions**

The role of different surface pretreatments on the sacrificial anode-based cathodic as well as barrier protection mechanisms afforded by Magnesium Rich, Non-Chromium Primer (MgRP) with and without topcoat (TC) has been investigated. Anodized coatings were characterized by thick resistive layer (5 to 9  $\mu\text{m}$ ) whereas conversion coating thickness was in the range of 0.4 to 0.8  $\mu\text{m}$ . The thickness and chemistry of pretreatments are directly correlated to the resistances between a MgRP and 2024-T351 substrate. These resistance must be added to model galvanic coupling accurately by a mixed potential theory model. The galvanic couple sensed by intact 2024-T351 is regulated by the pretreatment which operates through its resistance and effects on E-log (i) kinetics. The cycle test conducted to simulate a remote defect consisting of bare 2024-T351 indicated that in case of coating systems with no resistive pretreatment layer (bare/Prekote™ pretreated), galvanic coupling of bare 2024-T351 to the MgRP was enabled immediately upon exposure. In case of a resistive pretreatment such as CCC, TCP and anodized TCP seal, there was delayed galvanic coupling of bare 2024-T351 with the 2024-T351/pretreatment/MgRP system. Delayed galvanic coupling was correlated with the time dependent lowering of the resistance of the pretreatment layers which enabled more facile electrical connection between 2024-T351 and MgRP. Cumulative charge at the simulated galvanic couple potential of -0.8 V (vs. SCE) was still less owing to greater resistance and less polarization of the MgRP. In NCP, anodized without sealing and anodized with chromate sealing pretreatments, no protection was afforded to a remote defect as detected by the cycle test. Lastly, the topcoat significantly mediates the galvanic couple

potential, prevents self-corrosion of Mg pigment and also provides excellent barrier properties in all cases.

## 2.7 References:

1. D. Battocchi, A.M. Simoes, D.E. Tallman, and G.P. Bierwagen, "Electrochemical behaviour of a Mg-rich primer in the protection of Al alloys," *Corrosion Science* 48, 5 (2006): p. 1292-1306.
2. G. Bierwagen, D. Battocchi, A. Simoes, A. Stanness, and D. Tallman, "The use of multiple electrochemical techniques to characterize Mg-rich primers for Al alloys," *Progress in Organic Coatings* 59, 3 (2007): p. 172-178.
3. G. Bierwagen, R. Brown, D. Battocchi, and S. Hayes. *Observations on the testing of Mg-Rich Primers for Totally Chromate-free Corrosion Protection of Aerospace Alloys. in NACE DoD 2009 Conference Proceedings*. 2009. Washing, DC.
4. A.D. King, B. Kannan, and J.R. Scully, "Environmental Degradation of a Mg-Rich Primer in Selected Field and Laboratory Environments – Part II. Primer and Topcoat," *Corrosion* 70, 5 (2014).
5. A.D. King, B. Kannan, and J.R. Scully, "Environmental Degradation of a Mg-Rich Primer in Selected Field and Laboratory Environments – Part I. Without a Topcoat," *Corrosion* 70, 5 (2014).
6. A.D. King and J.R. Scully, "Sacrificial Anode-Based Galvanic and Barrier Corrosion Protection of 2024-T351 by a Mg-Rich Primer and Development of Test Methods for Remaining Life Assessment," *Corrosion* 67, 5 (2011): p. 05500401-05500422.
7. A.D. King and J.R. Scully. *Blistering Phenomena in Early Generation Mg-Rich Primer Coatings on AA2024-T351 and the Effects of CO<sub>2</sub>*. in *NACE DoD 2011 Conference Proceedings*. 2011. Palm Springs, CA.
8. B. Maier and G.S. Frankel, "Behavior of Magnesium-Rich Primers on AA2024-T3," *Corrosion* 67, 5 (2011): p. 055001.
9. H. Xu, D. Battocchi, D.E. Tallman, and G.P. Bierwagen, "Use of Magnesium Alloys as Pigments in Magnesium-Rich Primers for Protecting Aluminum Alloys," *Corrosion* 65, 5 (2009): p. 318-325.
10. S.S. Pathak, M.D. Blanton, S.K. Mendon, and J.W. Rawlins, "Investigation on dual corrosion performance of magnesium-rich primer for aluminum alloys under salt spray test (ASTM B117) and natural exposure," *Corrosion Science* 52, 4 (2010): p. 1453-1463.
11. C.M. Abreu, M. Izquierdo, P. Merino, X.R. Novoa, and C. Perez, "A new approach to the determination of the cathodic protection period in zinc-rich paints," *Corrosion* 55, 12 (1999): p. 1173-1181.
12. R.A. Armas, C.A. Gervasi, A. Disarli, S.G. Real, and J.R. Vilche, "Zinc-Rich Paints on Steels in Artificial Seawater by Electrochemical Impedance Spectroscopy," *Corrosion* 48, 5 (1992): p. 379-383.
13. O.O. Knudsen, U. Steinsmo, and M. Bjordal, "Zinc-rich primers - Test performance and electrochemical properties," *Progress in Organic Coatings* 54, 3 (2005): p. 224-229.

14. H. Marchebois, M. Keddam, C. Savall, J. Bernard, and S. Touzain, "Zinc-rich powder coatings characterisation in artificial sea water - EIS analysis of the galvanic action," *Electrochimica Acta* 49, 11 (2004): p. 1719-1729.
15. M. Morcillo, R. Barajas, S. Feliu, and J.M. Bastidas, "A-Sem Study on the Galvanic Protection of Zinc-Rich Paints," *Journal of Materials Science* 25, 5 (1990): p. 2441-2446.
16. A.D. King, J.S. Lee, and J.R. Scully, "Galvanic Couple Current and Potential Distribution between a Mg Electrode and 2024-T351 under Droplets Analyzed by Microelectrode Arrays," *Journal of the Electrochemical Society* 162, 1 (2015): p. C12-C23.
17. B.C.R. Troconis and G.S. Frankel, "Effects of Pretreatments on the Adhesion of Acetoacetate to AA2024-T3 Using the Blister Test," *Corrosion* 70, 5 (2014): p. 483-495.
18. G.S. Frankel and R.L. McCreery, "Inhibition of Al alloy corrosion by chromates," *Interface-Electrochemical Society* 10, 4 (2001): p. 34-39.
19. L. Xia, E. Akiyama, G. Frankel, and R. McCreery, "Storage and release of soluble hexavalent chromium from chromate conversion coatings - Equilibrium aspects of Cr-VI concentration," *Journal of the Electrochemical Society* 147, 7 (2000): p. 2556-2562.
20. L. Xia and R.L. McCreery, "Chemistry of a chromate conversion coating on aluminum alloy AA2024-T3 probed by vibrational spectroscopy," *J Electrochem Soc* 145, 9 (1998): p. 3083-3089.
21. P.D. Deck and D. Reichgott, "Characterization of chromium-free no-rinse prepaint coatings on aluminum and galvanized steel," *Metal Fin.* 90, 9 (1992): p. 29-35.
22. Y. Guo and G.S. Frankel, "Active Corrosion Inhibition of AA2024-T3 by Trivalent Chrome Process Treatment," *Corrosion* 68, 4 (2012).
23. H. Leidheiser, *Corrosion control by organic coatings*, 1981.
24. L.L. Li, K.P. Doran, and G.M. Swain, "Electrochemical Characterization of Trivalent Chromium Process (TCP) Coatings on Aluminum Alloys 6061 and 7075," *J Electrochem Soc* 160, 8 (2013): p. C396-C401.
25. L.L. Li, D.Y. Kim, and G.M. Swain, "Transient Formation of Chromate in Trivalent Chromium Process (TCP) Coatings on AA2024 as Probed by Raman Spectroscopy," *J Electrochem Soc* 159, 8 (2012): p. C326-C333.
26. L.L. Li, G.P. Swain, A. Howell, D. Woodbury, and G.M. Swain, "The Formation, Structure, Electrochemical Properties and Stability of Trivalent Chrome Process (TCP) Coatings on AA2024," *J Electrochem Soc* 158, 9 (2011): p. C274-C283.
27. T. Rochester and Z.W. Kennedy, "Unexpected results from corrosion testing of trivalent passivates," *Plating and Surface Finishing* 94, 10 (2007): p. 14.
28. F. Mansfeld and M.W. Kendig, "Evaluation of Anodized Aluminum Surfaces with Electrochemical Impedance Spectroscopy," *Journal of the Electrochemical Society* 135, 4 (1988): p. 828-833.
29. M. Saeedikhani, M. Javidi, and A. Yazdani, "Anodizing of 2024-T3 aluminum alloy in sulfuric-boric-phosphoric acids and its corrosion behavior," *T Nonferr Metal Soc* 23, 9 (2013): p. 2551-2559.
30. D. Chidambaram, C.R. Clayton, and G.P. Halada, "A duplex mechanism-based model for the interaction between chromate ions and the hydrated oxide film on aluminum alloys," *J Electrochem Soc* 150, 5 (2003): p. B224-B237.
31. E. Beck, "Performance validation of Thin-film sulfuric acid anodization(TFSAA) on aluminum alloys," *Metal Finishing* 101, 1 (2003): p. 28-31, 33-40.
32. Pantheon, *Surface Pretreatment - Technical Data Sheet* (2009).

33. Henkel, Surface Pretreatment - Technical Data Sheet (2014).
34. Henkel, Surface Pretreatment - Technical Data Sheet (2006).
35. Surtec, Surface Pretreatment - Technical Data Sheet (2012).
36. MIL-A-8625, "Anodic coatings for aluminum and aluminum alloys," Military Specification (1993).
37. AkzoNobel, "Aerodur5000," Topcoat - Technical Data Sheet (2013).
38. *Standard Reference Test Method for Making Potentiostatic and Potentiodynamic Anodic Polarization Measurements*, in *Annual Book of ASTM Standards*. 1197, ASTM: West Conshohocken, PA. p. 1-12.
39. Z. Ye, X-Ray Photoelectron Spectroscopy Demonstrations (2014): p. 9.
40. V.K. Pecharsky and P.Y. Zavalij, *Fundamentals of powder diffraction and structural characterization of materials*. 2nd ed (New York: Springer, 2009). p. xxiii, 741 p.

## 2.8 Tables

Table 2.1. Diagnostic electrochemical cycle test to assess sacrificial anode-based cathodic protection, potentiostatic hold times for charge capacity of MgRP determination.

Cycle	Test	Test Duration (mins)	Total Cycle Test Time (mins)
<b>A</b>	OCP	120	0
	EIS	30	120
	Potentiostatic hold	10	150
<b>B</b>	OCP	60	160
	EIS	30	220
	Potentiostatic hold	20	250
<b>C</b>	OCP	60	270
	EIS	30	330
	Potentiostatic hold	40	360
<b>D</b>	OCP	60	400
	EIS	30	460
	Potentiostatic hold	60	490
<b>E</b>	OCP	60	550
	EIS	30	610
	Potentiostatic hold	120	640
<b>F</b>	OCP	60	760
	EIS	30	820
	Potentiostatic hold	300	850
<b>G</b>	OCP	60	1150
	EIS	30	1210
	Potentiostatic hold	600	1240
<b>H</b>	OCP	60	1840
	EIS	30	1900
	Potentiostatic hold	600	1930
<b>I</b>	OCP	60	2530
	EIS	30	2590
	Potentiostatic hold	600	2620
<b>J</b>	OCP	60	3220
	EIS	30	3280
	Potentiostatic hold	600	3310

Table 2.2. Quantitative analysis (atomic percent) of surface chemistry of pretreated 2024-T351 through XPS after 5 minutes argon ion sputtering.

Pretreatments	Cr	Zr	Ti	O	Al	Mg	Cu	Fe	F	N	C	Si	Na
Chromate Conversion Coating (CCC)	22.4	0	0	32.3	19.1	0.9	0.1	2.4	0.8	5.4	16.6	0	0
Trivalent Chromium Pretreatment (TCP)	5.9	18.6	0	48.8	15.6	2.9	0.1	0	8.1	0	0	0	0
Non-Chromium Pretreatment (NCP)	0	0.5	7.0	15.5	27.7	0.2	0.7	1.3	4.0	1.2	39.3	1.0	1.5

Table 2.3. Thickness of pretreatments (based on cross-sectional EDS line profile analysis).

Pretreatment	Thickness of pretreatments characterized by cross-sectional EDS line profile ( $\mu\text{m}$ )
Chromate Conversion Coating (CCC)	0.8
Trivalent Chromium Pretreatment (TCP)	0.4
Non-Chromium Pretreatment (NCP)	0.8
Anodized without sealing	5.6
Anodized with chromate sealing	8.9
Anodized with TCP Sealing	6.8

\*thickness was calculated from intensities corresponding to half the peak intensity.

Table 2.4. Values of parameters estimated by EIS fitting procedure discussed in Figure 6.

Pretreatment	$R_{soln}$ ( $\Omega\text{-cm}^2$ )	$R_{cor}$ ( $\Omega\text{-cm}^2$ )	$R_{po}$ ( $\Omega\text{-cm}^2$ )	$C_{cor}$ ( $S\text{-s}^n\text{-cm}^{-2}$ )	n	$C_c$ ( $S\text{-s}^m\text{-cm}^{-2}$ )	m
Abraded	11	$2.2 \times 10^5$	NA	$1.3 \times 10^{-5}$	0.9	NA	NA
NFF	11	$1.4 \times 10^4$	NA	$1.3 \times 10^{-5}$	1.0	NA	NA
CCC	16	$1.2 \times 10^5$	$6.6 \times 10^3$	$9.0 \times 10^{-6}$	0.2	$5.5 \times 10^{-6}$	0.9
NCP	12	$9 \times 10^3$	393	$2.3 \times 10^{-6}$	0.6	$6.1 \times 10^{-6}$	0.8
TCP	11	$9 \times 10^4$	188	$8.7 \times 10^{-6}$	0.8	$1.9 \times 10^{-6}$	0.9
Anodized without sealing	21	$1.1 \times 10^6$	$9 \times 10^3$	$2.2 \times 10^{-6}$	0.5	$1.8 \times 10^{-7}$	0.8
Anodized with chromate sealing	20	$1.3 \times 10^7$	$2.5 \times 10^4$	$6.8 \times 10^{-7}$	0.8	$5.5 \times 10^{-7}$	0.9
Anodized with TCP sealing	39	$3.9 \times 10^5$	$2.9 \times 10^4$	$2.9 \times 10^{-5}$	0.6	$2.3 \times 10^{-7}$	0.9

## 2.9 Figures

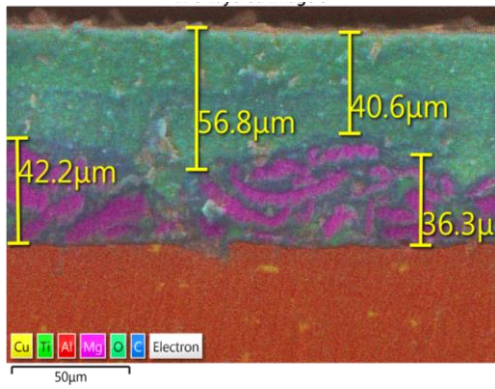


Figure 2.1. EDS layered cross sectional SEM image of 2024-T351/MgRP/topcoat systems

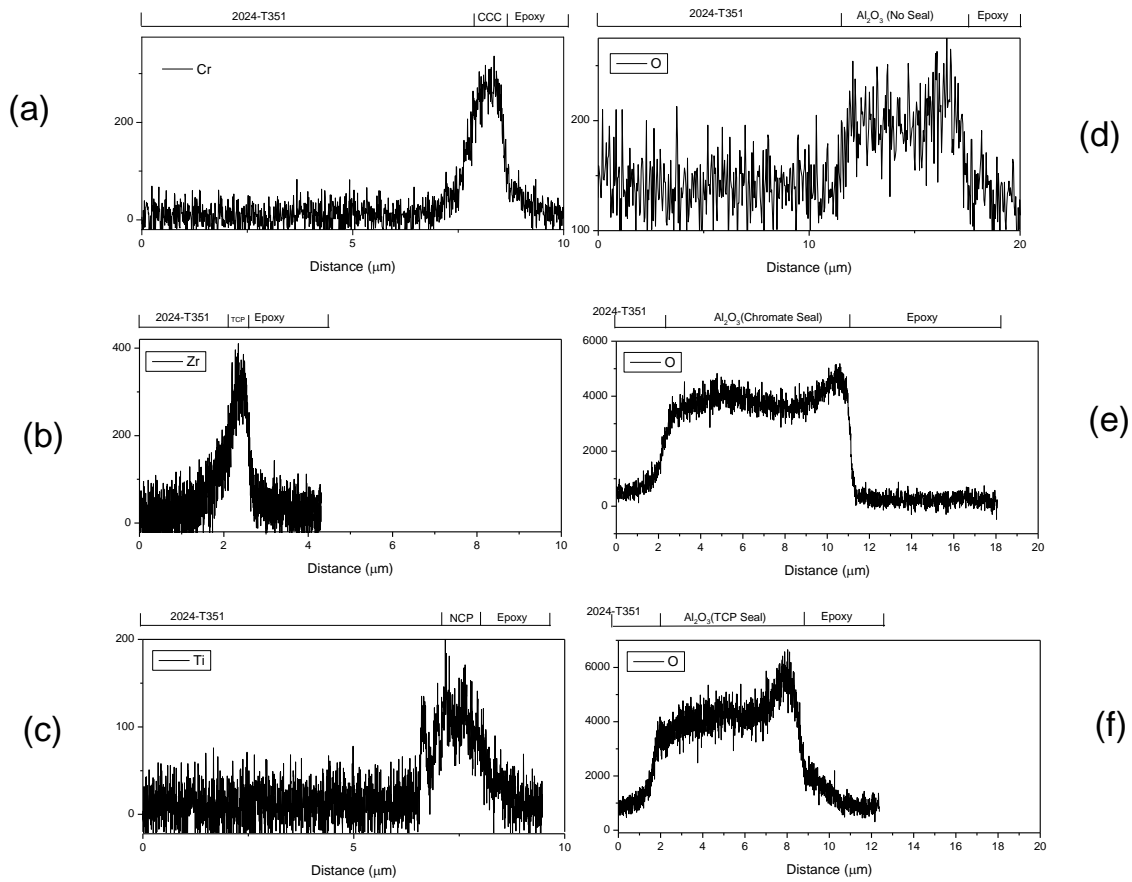


Figure 2.2. EDS line profile of the characteristic elements of different pretreatments, (a) chromate conversion coating (CCC), (b) trivalent chromium pretreatment (TCP), (c) non chromium pretreatment (NCP), (d) anodized without sealing, (e) anodized with chromate sealing and (f) anodized with TCP sealing.

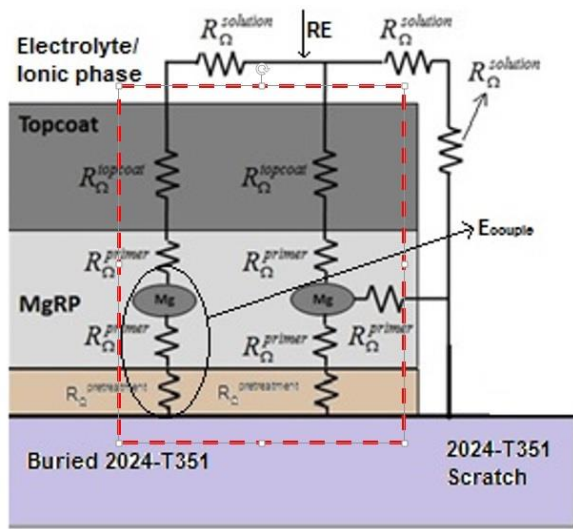


Figure 2.3. Electrical description of pretreated 2024-T351/MgRP/Topcoat. The dotted line indicates galvanic couple potential measured for an intact coating without a scratch. Polarization of this intact coating galvanically coupled to a scratch is simulated by the -0.8 V potentiostatic hold.

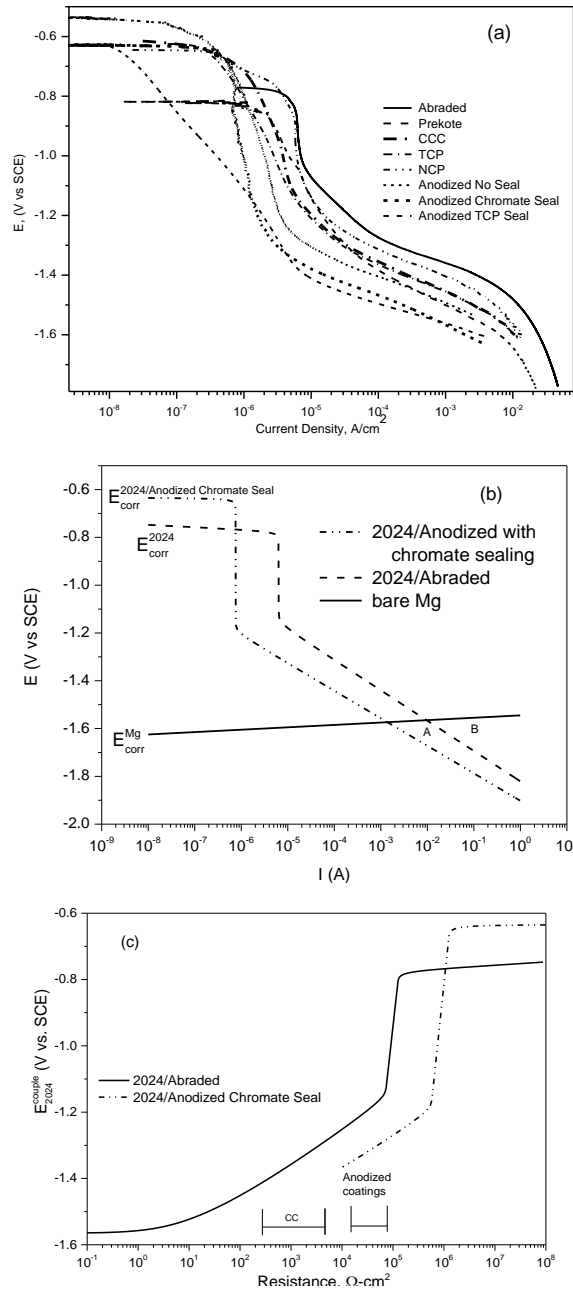


Figure 2.4. (a) E-log (i) data for bare/pretreated AA2024-T351 in quiescent 5 % (wt) NaCl solution (b) mixed potential model (E vs log I) depicting a galvanic couple between bare or pretreated 2024-T351 and bare Mg.  $A_{\text{cathode}} = A_{\text{anode}} = 1 \text{ cm}^2$ . when there is direct contact between Mg and bare or pretreated 2024-T351 and negligible ohmic drop through solution:  $E_{2024}^{\text{couple}} = E_{\text{Mg}}^{\text{couple}}$  (A) and  $E_{2024/\text{Anod Chromate Seal}}^{\text{couple}} = E_{\text{Mg}}^{\text{couple}}$  (B) and (c) galvanic couple potential of bare/pretreated 2024-T351 as function of ohmic resistance imposed between Mg and 2024-T351. The couple potential sensed by the 2024-351 surface is indicated in (c). In this case of anodized pretreatment low resistances that indicated are not accessible.

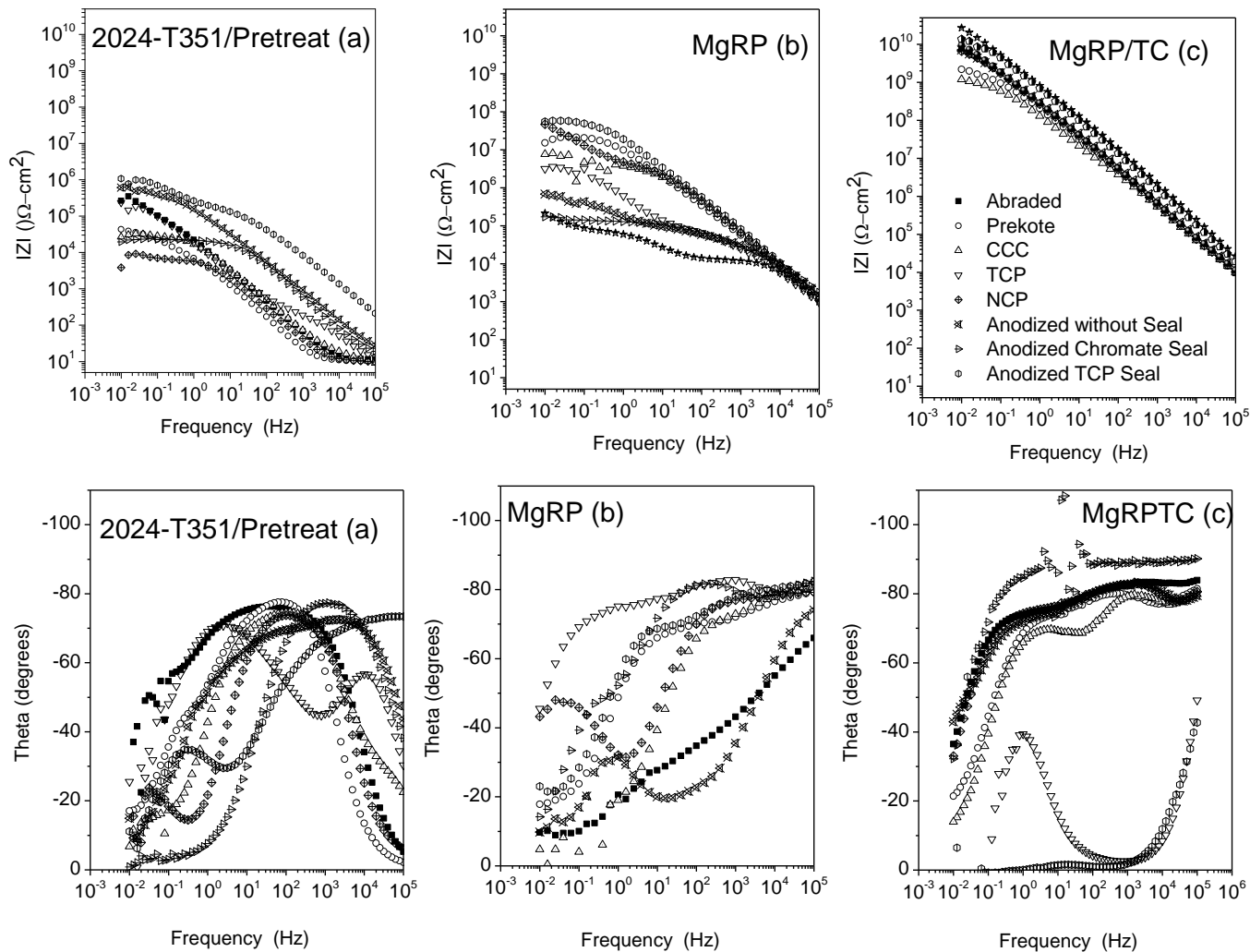
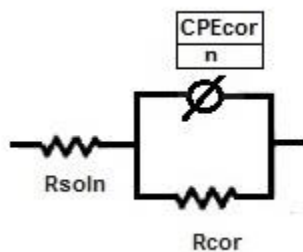
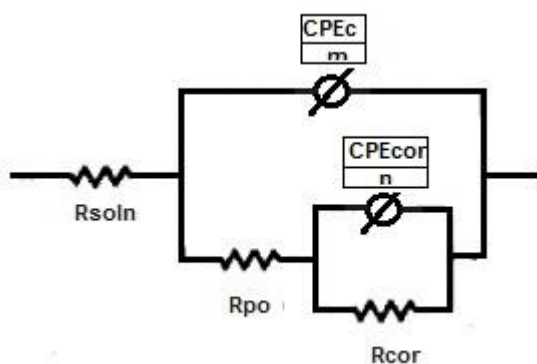


Figure 2.5. Initial impedance profiles of (a) bare/pretreated 2024-T351, (b) bare/pretreated 2024-T351 coated with Akzo Nobel<sup>†</sup> MgRP and (c) bare/pretreated AA2024-T351 coated with Akzo Nobel<sup>†</sup> MgRP and Akzo Nobel (ANAC) Aerodur 5000 exposed in quiescent 5 % (wt) NaCl solution, after 1 h (bare/pretreated 2024-T351 with/without MgRP) or 12 h (MgRPTC) at OCP. Abraded (■), Prekote<sup>TM</sup> (○), CCC (△), TCP (▽), NCP (⊕), Anodized no seal (⊗), Anodized chromate seal (⊞) and Anodized TCP seal (⊕).



(a)



(b)

Figure 2.6. Equivalent circuit models for EIS fitting, (a) Abraded/Prekote™ and (b) other resistive pretreatments.  $R_{soln}$  is resistance of the electrolyte.  $R_{po}$  and  $R_{Cor}$  represents the resistance of the pretreatment layer and the resistance corresponding to charge transfer.  $CPE_c$  and  $CPE_{cor}$  are constant phase elements representing the capacitance of intact pretreatment and the double layer capacitance.

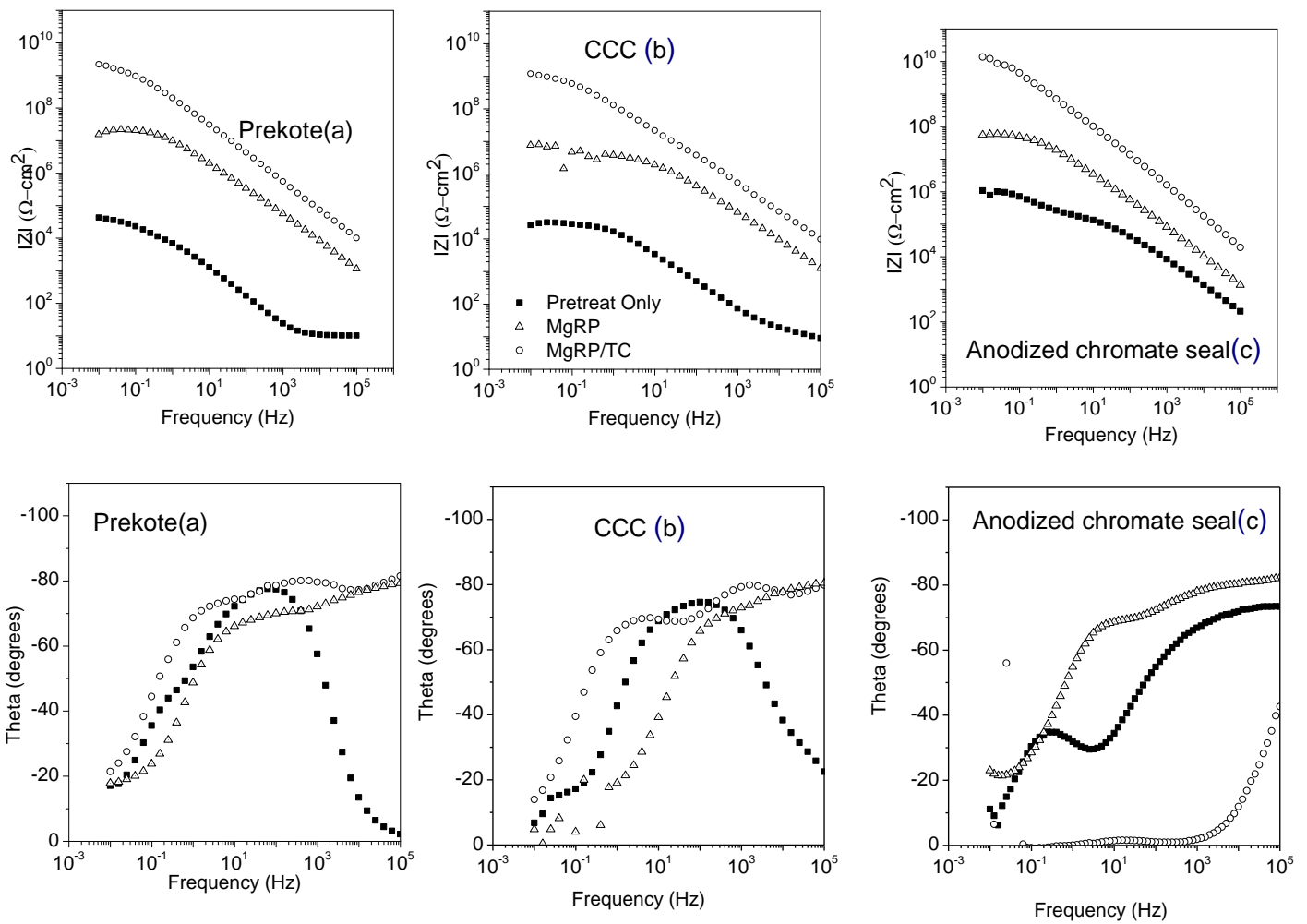


Figure 2.7. Initial impedance profiles: Comparison of (a) Prekote<sup>TM</sup>, (b) CCC and (c) anodized with chromate sealing exposed in quiescent 5 % (wt) NaCl solution, after 1 h (pretreated 2024-T351/MgRP) or 12 h (MgRP/TC) at OCP. 2024-T351/pretreatment (■), 2024-T351/pretreatment/MgRP (△) and 2024-T351/pretreatment/MgRP/TC (○).

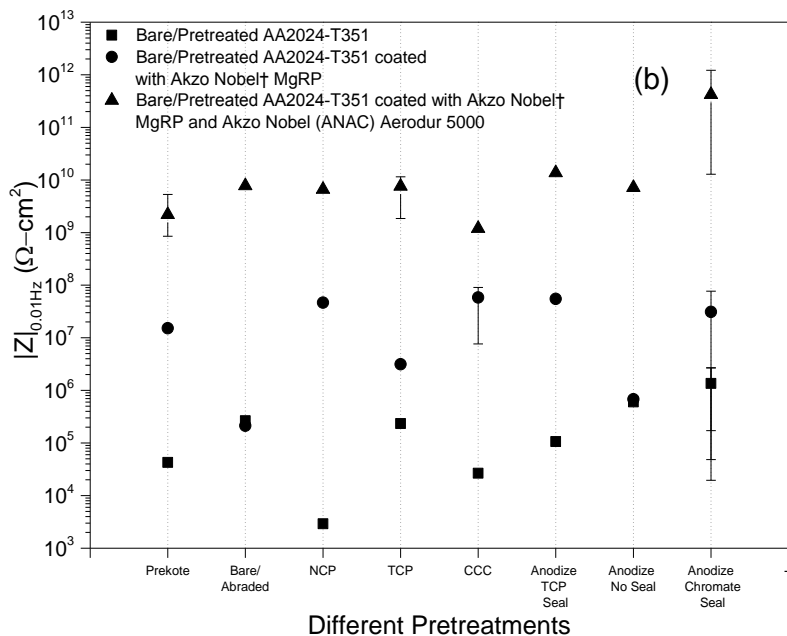
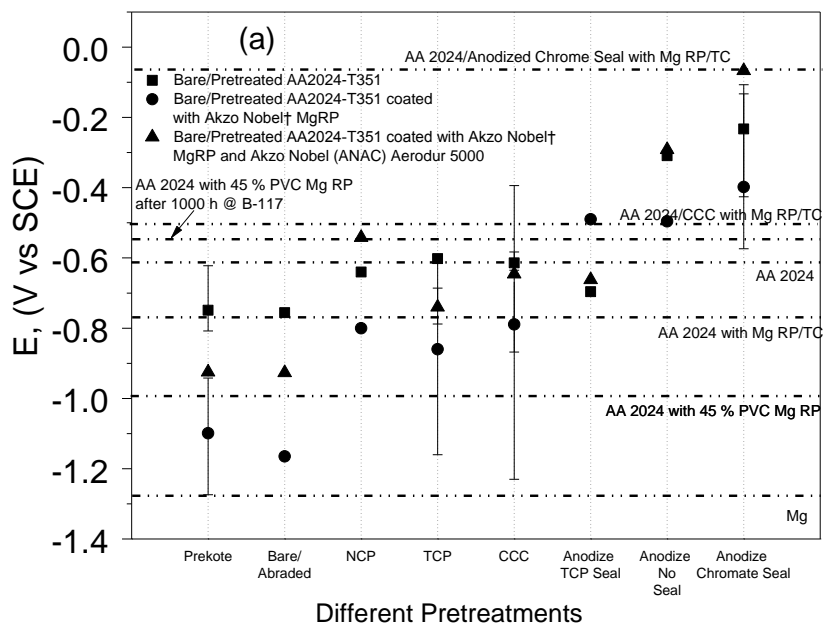


Figure 2.8. (a) Average OCP (of last 1 h of exposure) and (b) Low frequency impedance Z modulus (at 0.01 Hz) of 2024-T351 with different pretreatments (■) and coated with Akzo Nobel† Mg-rich primer (●), coated with Akzo Nobel† Mg-rich primer and Akzo Nobel (ANAC) Aerodur 5000 (▲), during exposure in quiescent 5 % (wt) NaCl solution, for 1 hour (AA2024-T351/MgRP) or 12 hours (Topcoat).

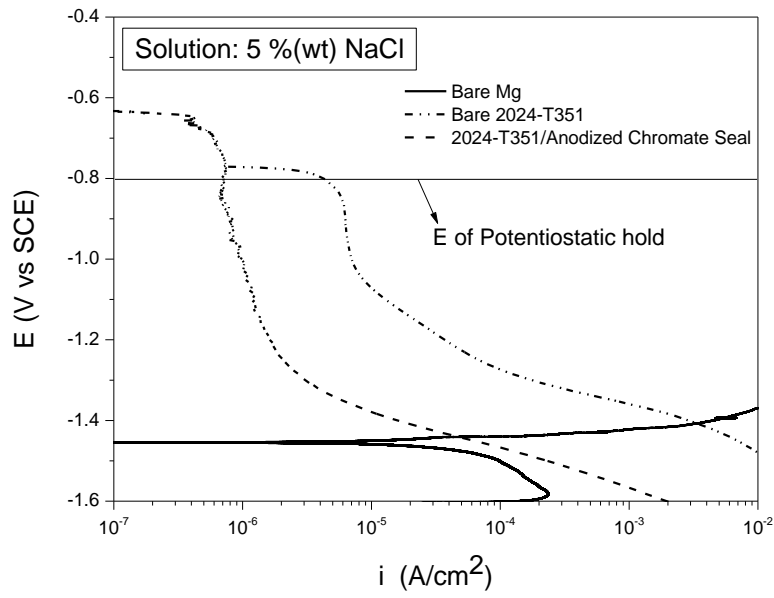


Figure 2.9. E-log ( $i$ ) data for of Bare Mg and bare/pretreated 2024-T351 in quiescent 5 % (wt) NaCl.

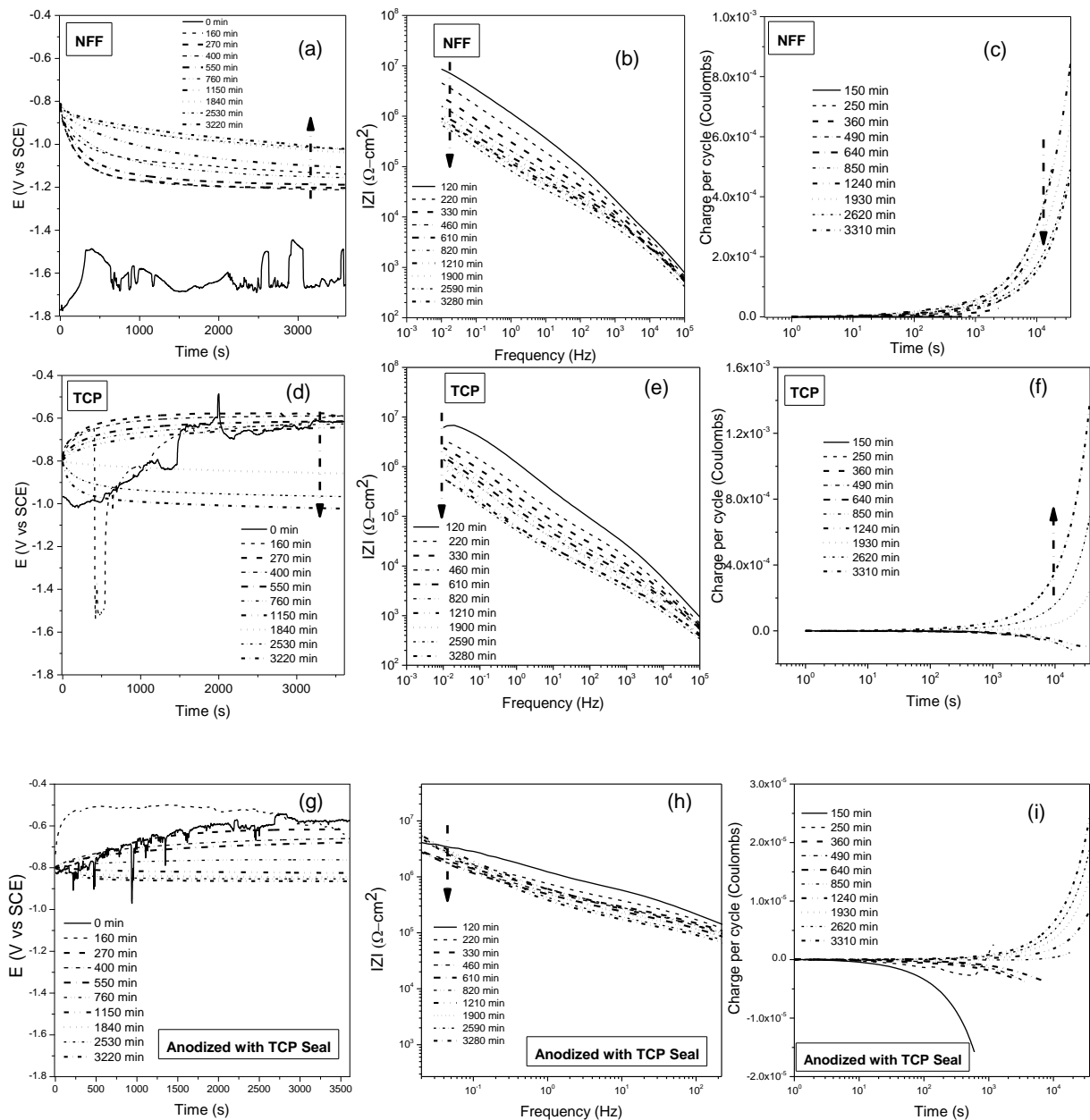


Figure 2.10. Cycle test results: OCP vs. time, Z modulus vs. time and anodic charge vs. time for the pretreated 2024-T351/MgRP in quiescent 5 % (wt) NaCl, (a-c) Prekote™ (d-f) TCP and (g-i) Anodized TCP Seal. Time in legend refers to elapsed time. Listed Table 1 for the diagnostic electrochemical cycle test.

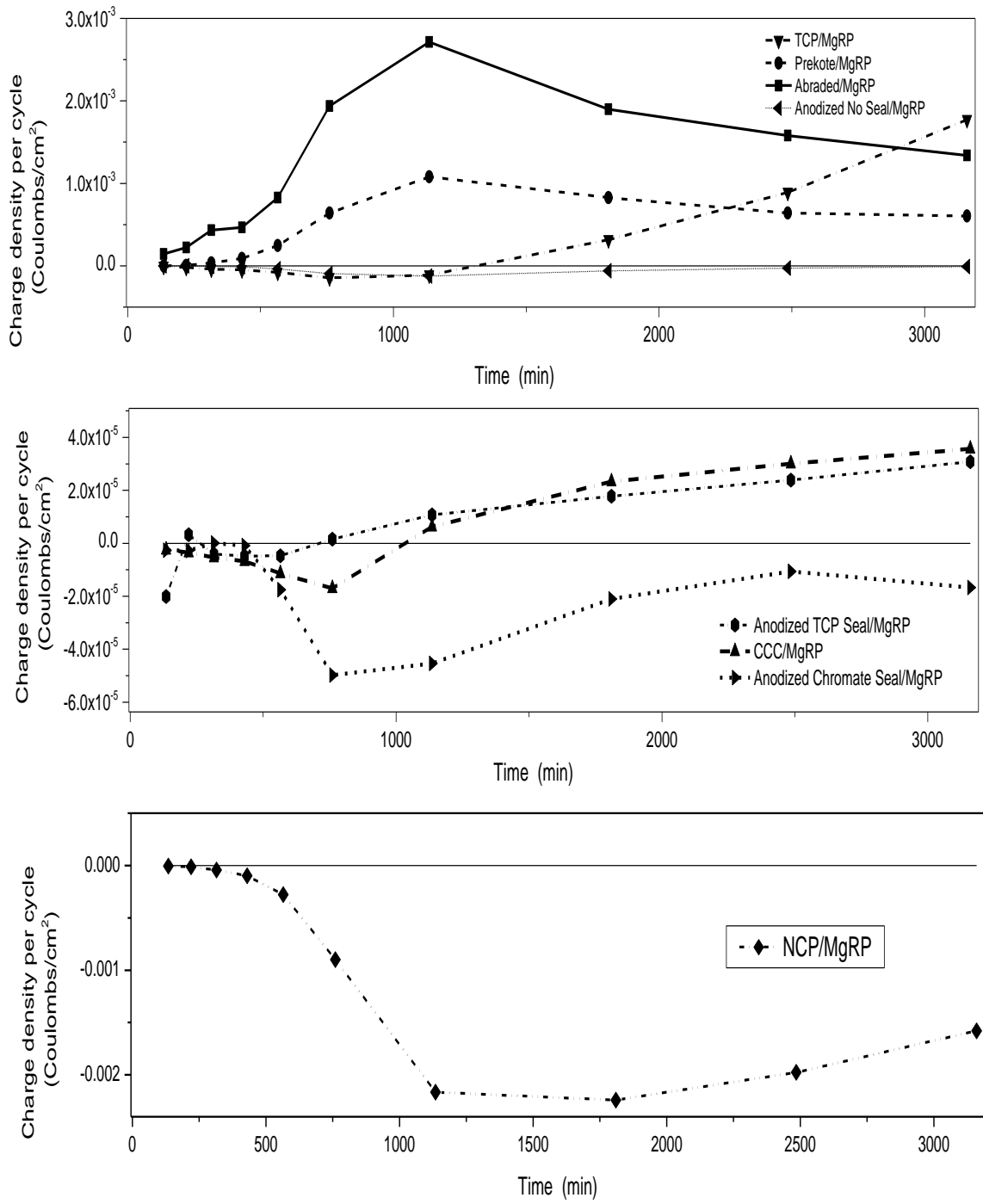


Figure 2.11. Cycle test results: anodic charge density (of the indicated intact 2024-T351/pretreatment/MgRP systems) at -0.8 V (vs SCE) for each individual cycle test step indicated in Table 1 vs total elapsed cycle test time in the cycle test protocol

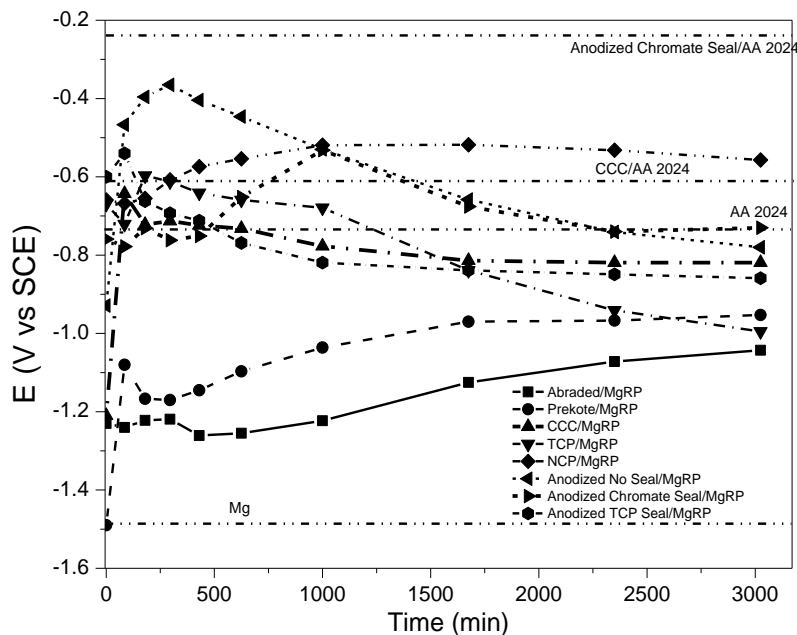


Figure 2.12. Cycle test results: OCP (of the indicated intact 2024-T351/pretreatment/MgRP systems) for each individual cycle test step indicated in Table 1 vs total elapsed cycle test time in the cycle test protocol

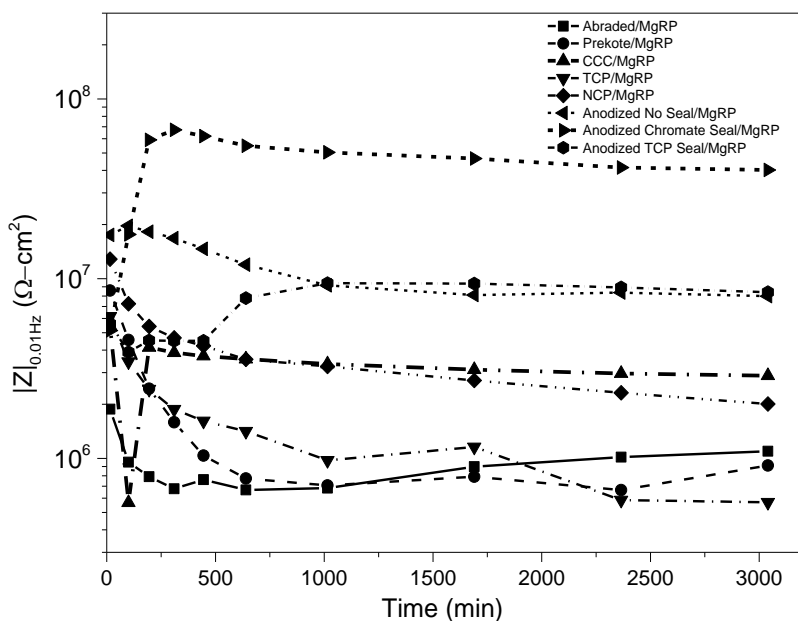


Figure 2.13. Cycle test results: complex impedance Z Modulus at 0.01 Hz (of the indicated intact 2024-T351/pretreatment/MgRP systems) for each individual cycle test step indicated in Table 1 vs total elapsed cycle test time in the cycle test protocol.

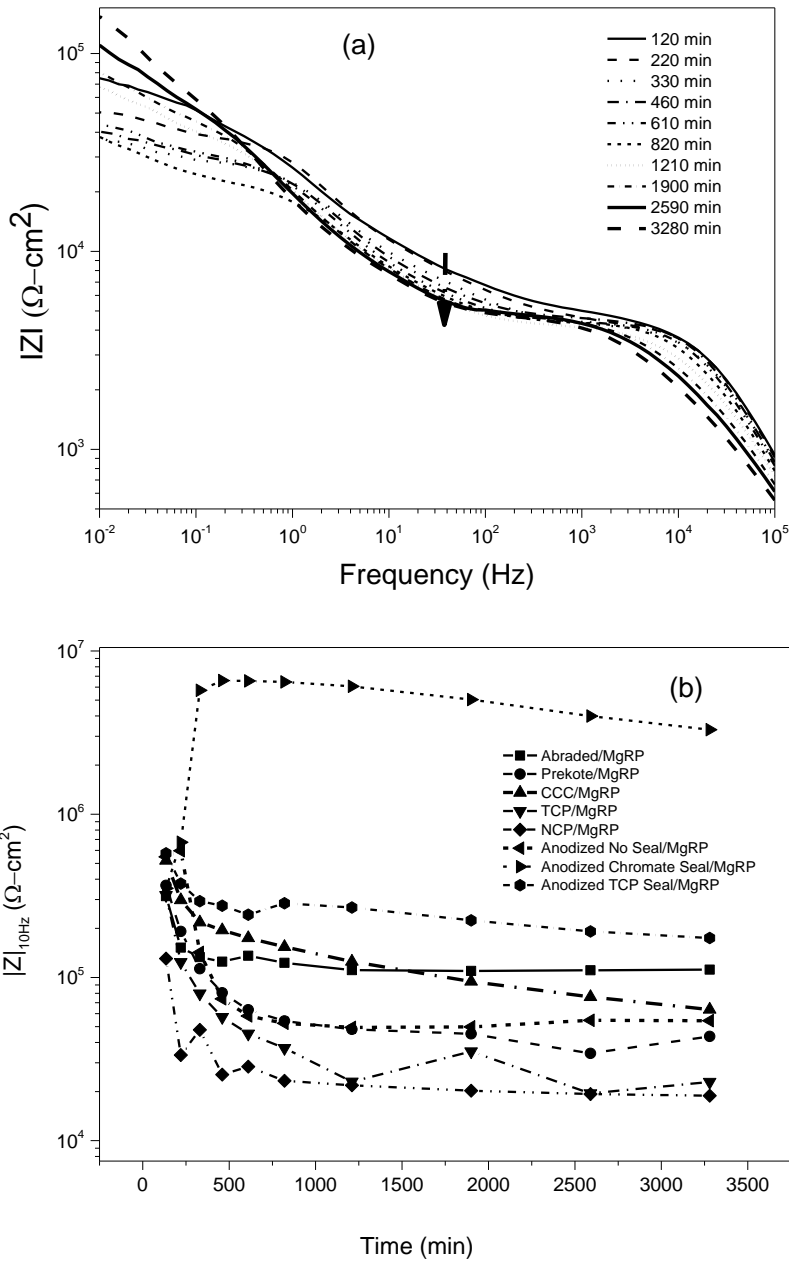


Figure 2.14. Cycle test results: (a) Mod. Z vs time for 2024-T351/anodized with chromate seal/MgRP in quiescent 5 % (wt) NaCl, Time in legend refers to elapsed time in Table 1 in the diagnostic electrochemical cycle test. (b) complex impedance Z modulus at 10 Hz (of the indicated intact 2024-T351/pretreatment/MgRP systems) for each individual cycle test step indicated in Table 1 vs total elapsed cycle test time in cycle test protocol (for the indicated pretreatment/MgRP systems).

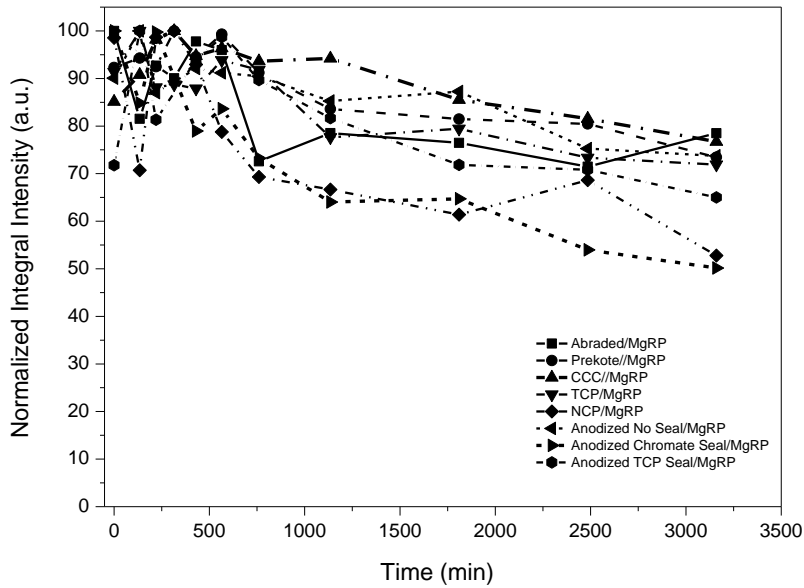


Figure 2.15. Cycle test results (XRD): The normalized integral intensity for Mg<101> (of the indicated intact 2024-T351/pretreatment/MgRP systems) for each individual cycle test step indicated in Table 1 vs total elapsed cycle test time in the cycle test protocol.

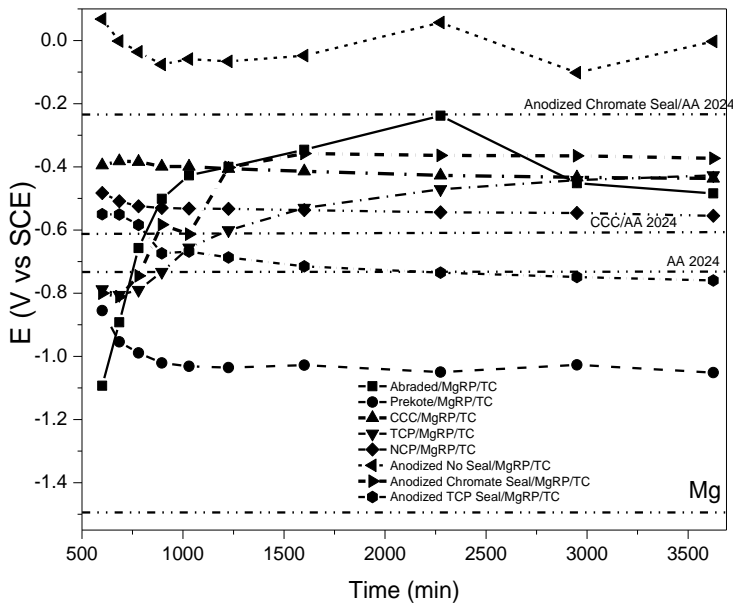


Figure 2.16. Cycle test results: OCP (of the indicated intact 2024-T351/pretreatment/MgRP/Topcoat systems) for each individual cycle test step indicated in Table 1 vs total elapsed cycle test time in the cycle test protocol.

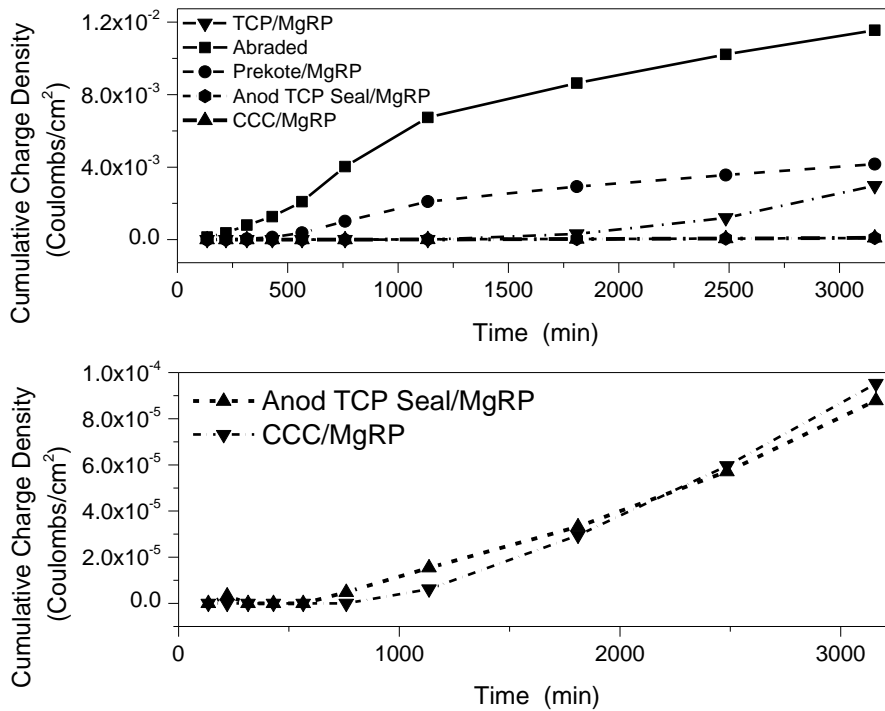


Figure 2.17. Cycle test results: cumulative anodic charge density (of the indicated intact 2024-T351/pretreatment/MgRP/Topcoat systems) at -0.8 V (vs SCE) for the sum of cycles added up to the time indicated in Table 1 vs total elapsed cycle test time in the cycle test protocol.

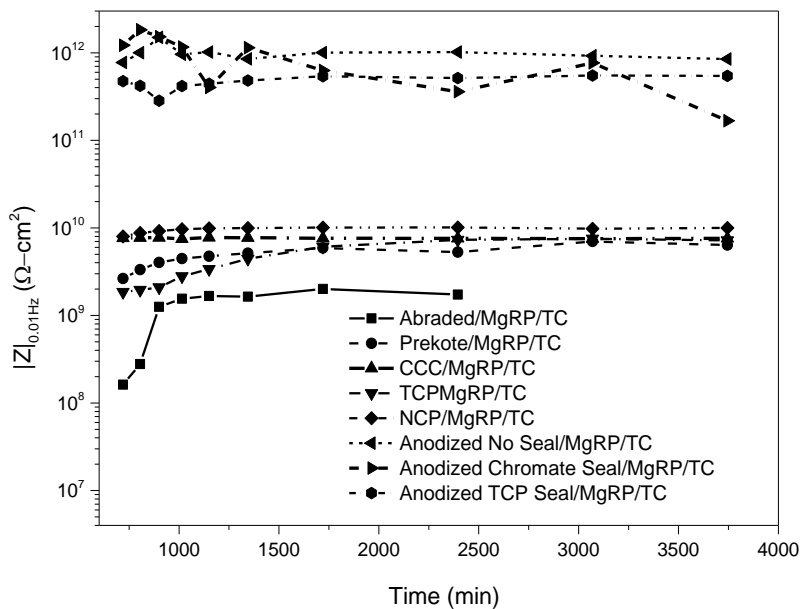


Figure 2.18. Cycle test results: complex impedance  $Z$  modulus at 0.01 Hz (of the indicated intact 2024-T351/pretreatment/MgRP/Topcoat systems) for each individual cycle test step indicated in Table 1 vs total elapsed cycle test time in the cycle test protocol.

### **3 Performance of a Magnesium Rich Primer on Pretreated AA2024-T351 in Selected Laboratory and Field Environments: Conversion Coating Pretreatments**

#### **3.1 Abstract**

The effect of conversion coatings on the corrosion protection of AA2024-T351 by Magnesium-rich primer (MgRP) was evaluated in topcoated (TC) and non-topcoated, scribed conditions. Protection of remote scratches and global protection by the coating after exposure in selected laboratory and field environments was investigated. Exposure studies focused on chromate conversion coating (CCC), trivalent chromium pretreatment (TCP) and non-chromium pretreatment (NCP) and compared to non-film forming (NFF) surface pretreatment. Exposures were conducted in the field under two different environments; at a coastal marine site, Kennedy Space Center (KSC), Florida; and at an inland rural site, Birdwood Golf Course in Charlottesville (CHO), Virginia. ASTM B-117 with 5 % (wt) NaCl, modified ASTM B-117 with acidified ASTM substitute ocean water (SOW) and UV light as well as full immersion in ambiently aerated 5 % (wt) NaCl solution were compared to field environments. Mg pigment depletion rate, global galvanic protection potential, coating barrier properties and scribe protection were investigated. In systems without a topcoat, full immersion studies resulted in significant depletion of Mg and all other environments lead to depletion of Mg at different rates. In contrast, a polyurethane topcoat limited the Mg metallic pigment depletion resulting in only partial Mg depletion in all chosen environments. In NFF pretreated AA2024-T351 with MgRP, magnesium was galvanically coupled to AA2024-T351 immediately and was available for cathodic protection from the beginning of exposure. This is indicated by a shift in global galvanic protection potential from -1.4 V (vs SCE) to more positive potentials with increasing exposure time. In case of conversion coatings pretreated

AA2024-T351, there was limited galvanic coupling with the MgRP. Upon prolonged exposure in full immersion, the global galvanic protection potential decreased to more negative potentials below the open circuit potential (OCP) of AA2024-T351 indicative of galvanic coupling. In case of systems with topcoat, the global galvanic protection potential was heavily regulated by the polyurethane topcoat and there was no significant global galvanic coupling between AA2024-T351 and Mg in the timeframe over which experiments were conducted. Mg was preserved and available for any future sacrificial anode-based cathodic protection and local protection. The barrier properties of the MgRP pigmented coating also degraded with time at a higher rate in systems in the absence of topcoat. This result was attributed to UV degradation of the pigmented coating resin and could be reduced with the polyurethane topcoat. SEM/EDS characterization of scribe after different B-117/field exposure times indicated that the protective throwing power increased as a function of exposure time in both AA2024-T351/NFF/MgRP and AA2024-T351/TCP/MgRP systems. Moreover, a secondary protection mode by  $Mg(OH)_2$  redeposition was identified.

A manuscript based on this chapter has been published in Corrosion Journal as a Full Research Paper, “Performance of a Magnesium Rich Primer on Pretreated AA2024-T351 in Selected Laboratory and Field Environments: Conversion Coating Pretreatments.”

Representative author contributions:

B. Kannan: experiments, analysis and interpretation

J. R. Scully: Advisor, analysis and interpretation

### 3.2 Introduction

Aerospace structures using precipitation age hardened aluminum alloys rely on the use of multilayered coatings to provide corrosion resistance, improved adhesion and other specialized functions.<sup>13</sup> The most commonly used active protection system includes corrosion inhibition by hexavalent chromium.<sup>13,74</sup> Typical formulations consists of chromated pigments enveloped in epoxy resin.<sup>13,74</sup> Carcinogenicity, high handling costs and lack of environmental safety required an accelerated phase-out of hexavalent chromium, concurrent with a push to find effective alternatives.<sup>13,74</sup> Over the past few years, a commercial organic coating system containing a Mg-pigmented polymer primer (MgRP) has been developed for the active corrosion protection of aluminum alloys.<sup>72,73,76,77,80-85,88,117,132,133</sup> The commercial MgRP coating consists of a surface pretreatment, an epoxy resin with Mg pigment and a polyurethane based topcoat. The primary function of the pretreatment is to provide good adhesion between substrate and primer.<sup>13</sup> Pretreatments also provide additional functions such as improved corrosion resistance by acting as a barrier layer and/or enabling inhibitor ion release.<sup>13</sup> The metal pigment system is designed to galvanically couple the relatively more active, metallic Mg pigment in the primer to the AA2024-T351 substrate thereby providing sacrificial anode-based cathodic protection.<sup>84</sup> This approach has been well established previously in the design of zinc-rich primers for use on various steel.<sup>78,79,86,89,90</sup> The organic resin in the epoxy based primer mediates the global galvanic protection potential and also provides barrier protection to the substrate.<sup>84</sup> A topcoat functions as main barrier for environmental influences such as extreme climate, ultra-violet rays and can also serve additional purposes.<sup>13</sup> A systematic evaluation of each of these components and their effect

on overall performance of coating systems in different lab-accelerated life testing environments and different environmental exposures needs to be understood.

Previous laboratory accelerated life cycle (LALT) and field exposures conducted to determine optimal primer formulation concluded that, approximately 45 % pigment volume concentration Mg provides a balance between moderated sacrificial anode-based cathodic protection, long term barrier protection, and the beneficial characteristics of preserved, isolated clusters of Mg pigment available for the future protection of defects.<sup>84</sup> Two possible modes of galvanic protection were proposed; long range protection of remote defects by global galvanic corrosion protection afforded to the substrate and local or short range Mg pigment-based protection of local as well as buried defects in close proximity to buried pigment particle.<sup>84</sup> Both modes of protection are mediated by the high ionic and electrical resistances of the coating systems as a function of Mg pigment volume concentration (PVC), surface pretreatments, primer polymer and topcoat properties. The regulation of cathodic protection abilities is an important aspect in optimizing the MgRP performance.<sup>84</sup>

Environmental degradation of MgRP on NFF pretreated AA2024-T351 in selected field and laboratory environment in the presence and absence of topcoat has been extensively studied.<sup>76,80,81</sup> Full immersion in ambiently aerated 5 % NaCl solution, ASTM B-117 in 5 % NaCl, and ASTM B-117 in ASTM artificial seawater all resulted in significant depletion of metallic Mg pigment in the MgRP (without topcoat) far from the scribe after 1000 hours.<sup>81</sup> Field exposures in Charlottesville, VA and Kennedy Space Center, FL also resulted in similar levels of Mg pigment depletion far from the scribe after 2000 h and 4000 h of exposure.<sup>81</sup> This implies magnesium loss via self-corrosion. The global galvanic protection potential of the coating system, with respect to remote scratches, became more positive with exposure time in each environment, from values approximately equal to that of bare Mg (-1.6 V vs. SCE) to those approximately equal to that of

bare AA2024-T351 (-0.7 V vs. SCE). It was found that this rise took approximately 300 hours in full immersion in ambiently aerated 5% NaCl solution, ASTM B-117 in 5% NaCl, and in ASTM B-117 with ASTM artificial seawater and approximately 1000 h in the field at CHO and KSC. These times does not represent actual service times on accounts of periods of drying and wetting. Residual barrier properties of the MgRP with an initial MgPVC of 45% coating system also degrade with time in each environment.<sup>81</sup> However, corrosion was not observed under the residual coating polymer after Mg pigment depletion.<sup>81</sup> Therefore, the primer provides some residual barrier protection.<sup>81</sup> The Aerodur 5000™ topcoat significantly regulated the depletion of Mg pigment from the MgRP in all exposure environments as compared to identical environmental exposures of non-topcoated samples as measured by XRD.<sup>80</sup> Full immersion in ambiently aerated 5% NaCl solution, ASTM B-117 using 5% NaCl, and ASTM B-117 modified with ASTM artificial seawater and UV all resulted in very limited depletion of metallic Mg pigment in the MgRP far from the scribe after 1000 hours.<sup>80</sup> Field exposures in CHO and KSC also resulted in partial Mg pigment depletion far from the scribe after 1 year of exposure.<sup>80</sup> The global galvanic protection potential of the coating system, with respect to remote scratches, increased slightly with exposure time in each environment, from initial values of approximately -1.0 V to -0.7 V vs. SCE after extensive environmental exposure. These values fall between the open circuit potentials of bare AA2024-T351 (-0.6 V vs. SCE) and bare Mg (-1.6 V vs. SCE) and are predicted by mixed potential theory.<sup>80,81</sup> This suggests that Mg pigment that is both electrically and ionically connected to the AA2024-T351 can provide sacrificial galvanic protection of the AA2024-T351 substrate in extended time-of-wetness events.<sup>80,81</sup> Barrier properties of the MgRP primer coating, as assessed by electrochemical impedance, also only slightly degrade with time in each environment but,

overall, remain very high ( $\geq 10^9 \Omega\text{-cm}^2$  at 0.01 Hz) throughout exposure in each environment indicating significant barrier protection remains after all environmental exposures studied.<sup>80,81</sup>

However all of these studies investigated MgRP over a bare or NFF pretreated AA2024-T351. In practical applications, several pretreatments are of interest to improve adhesion between the substrate and the polymer and also to impart additional corrosion protection.<sup>16,19,32,33,36,37,118,121,122</sup>

Chromate conversion coatings (CCC) offer strong corrosion resistance properties and are noted for their ability to self-heal.<sup>22-26,36,37</sup> This phenomenon is attributed to the release of hexavalent chromium from the coating into the corrosive solution in contact with the surface.<sup>36,37</sup> Due to environmental hazards posed by hexavalent chromium, non-chromium process (NCP)<sup>16,32</sup> and trivalent chromium process (TCP)<sup>19</sup> coatings have been explored as alternatives for CCC. NCP conversion coatings are based on titanium/zirconium oxides<sup>16,32</sup> whereas TCP conversion coatings are trivalent chromium enriched zirconium oxide coatings.<sup>19</sup>

A systematic evaluation of each of these coating system components, including the conversion coatings previously mentioned, and their effect on the overall performance of coating systems containing MgRP in different lab-accelerated life testing environments and different environmental exposures is of interest. The objective of this study was to investigate MgRP system on 2024-T351 with various pretreatments. The thickness of the pretreatment, its chemistry and electrical properties imparted by the pretreatments were examined to understand the role of pretreatment in global galvanic protection potential mediation.<sup>76,77</sup> Degradation of pretreatment, MgRP and topcoat as a function of time for different pretreatments were studied using diagnostic tests including accelerated electrochemical cycle test with ex-situ Mg depletion studies using X-ray diffraction.<sup>76,77</sup> Environmental degradation of different pretreated AA2024-T351 with MgRP and with and without topcoat in relevant lab and field environments need to be understood to

expand the knowledge of the role of pretreatments in corrosion protection function. Comparison of environmental degradation of conversion coatings to non-film forming pretreatment based coating systems are discussed in this work. The sacrificial anode protection function, barrier properties and alternative protection modes afforded by AA2024-T351/Pretreatment/MgRP and AA2024-T351/Pretreatment/MgRP/Topcoat were characterized by utilizing electrochemical techniques and non-electrochemical post-mortem analysis techniques including X-ray diffraction, Raman spectroscopy, optical profilometry and scanning electron microscopy/energy dispersive spectroscopy after pertinent lab and field exposures. The behavior in field is particularly pertinent based on the lack of applicability of Standard ASTM B-117<sup>28</sup> (5 % (wt) NaCl) to assessments of field performance due to discrepancies between lab and field exposures.<sup>80,81</sup> Effect of pretreatment on Mg depletion, self-corrosion of Mg and scratch protection are reported herein.

### **3.3 Experimental Procedure**

#### **3.3.1 Materials**

AA2024-T351 sheet (1.6 mm thickness) pretreated with 4 different pretreatments for comparison including (i) Non-film Forming Surface Pretreatment (NFF), (ii) Chromate Conversion Coating (CCC), (iii) Trivalent Chromium Pretreatment (TCP), (iv) Non Chromium Pretreatment (NCP). Prekote<sup>TM</sup> is a non-film forming chromium free surface pretreatment. It contains approximately 95% water and less than 3 % each of diethylene glycol monobutyl ether and N-methyl-2-pyrrolidone.<sup>124</sup> CCC (Alodine 1200s),<sup>125</sup> NCP (Alodine 5200),<sup>103</sup> and TCP (Surtec 650)<sup>126</sup> are also commercial products.

A 40  $\mu\text{m}$  primer layer of MgRP and a 50  $\mu\text{m}$  thick topcoat of Aerodur 5000 high-performance advanced coating, both produced by Akzo Nobel Coatings (Waukegan, Illinois) were applied. The

MgRP consist of one part epoxy matrix with Mg metal flake pigment of a diameter 20  $\mu\text{m}$  with PVC of 45 % (3rd generation 2100P003, Lot: 493-190). Aerodur 5000 (Gloss white finish product: ECM-G7875) is a two component polyurethane topcoat developed for military application in variety of exposure environments.<sup>128</sup>

### **3.3.2 Laboratory and Field Exposures of Pretreated AA2024-T351 coated with MgRP and Topcoat**

MgRP coated AA2024-T351 panels (3' x 2') were exposed to salt spray in a QFog Cyclic Corrosion Tester (QFog model CCT 1100†) according to ASTM B-117<sup>134</sup> “with neutral 5 % (wt) NaCl solution (pH =  $6.9 \pm 0.4$ ) as the electrolyte at a temperature of 35°C for at least 1000 hours. During a second exposure, the standard ASTM B-117 salt fog was altered such that the standard 5 % (wt) NaCl solution electrolyte was replaced with acidified ASTM substitute ocean water<sup>135</sup> ([SOW] pH =  $3.2 \pm 0.2$ ) and ultraviolet radiation. The salt fog exposure cabinet was modified to include four hanging ultraviolet A (UVA), fluorescent lights. The UVA lamps (Q-Lab Corporation model UVA-340) were chosen to simulate sunlight in the critical short-wave UV region from 365 nm down to the solar cutoff of 295 nm. The ASTM artificial seawater was produced according to ASTM D-1141<sup>135</sup> and acidified by the addition of 10 mL of glacial acetic acid per 1 L of salt solution following ASTM G85 A3.<sup>136</sup> In all salt fog exposures reported herein, ambient air was supplied to the chamber and to the atomizer for fog production. Ambient concentrations of CO<sub>2</sub> were measured in-situ and were found to be approximately 425 ppm. Other ambient gas concentrations were not measured. Natural weathering exposures of MgRP-coated AA2024-T351 panels were conducted in two different environments: at a coastal marine site 30 m from the high tide line at Kennedy Space Center Corrosion Technology Lab in Titusville, FL (28.6°N, 80.6°W, elevation = 0 m) and a rural inland site at Birdwood Golf Course in Charlottesville, VA

(38.0402°N, 78.54.27°W, elevation = 172 m). The sample test racks at Kennedy Space Center face the ocean and the one in Birdwood Golf Course face south. During exposure, panels were mounted on unsheltered atmospheric test racks with full exposure to natural elements according to ASTM G-4.<sup>137</sup> Pertinent environmental parameters such as mean temperature, mean relative humidity, mean dew point, mean precipitation rate, precipitation pH and dry chloride deposition rate were measured in all LALT/field environments. These parameters are summarized in Table 3.1.

### **3.3.3 Post-mortem Surface Analysis of the Intact Coating and the Scribe**

All full-immersion studies as well as post-mortem analysis after salt fog and field exposures reported herein were conducted in quiescent 5 % (wt) NaCl (pH: 6.9±0.4) open to laboratory air. Electrochemical experiments were performed using a Gamry Potentiostat (Ref 600/ PCI4)<sup>†</sup> with computer interface software. Saturated calomel electrode (SCE) and Pt mesh were used as the reference and counter electrode, respectively. The intact coating area tested was far away ( $\geq 2$  cm away) from scribe. A typical EIS scan was acquired in sine sweep mode from 100 kHz to 0.01 Hz with 6 points per decade. MgRP and MgRP/TC coated panels were scanned with an AC amplitude of 80-100 mV to reduce noise. The tests were conducted in quiescent 5 % (wt) NaCl, as discussed above, after 1 hour exposure at open circuit for MgRP coated panels and 12 hour exposure for MgRP/TC coated panels.

X-ray diffraction (XRD) was conducted to characterize global Mg depletion as a function of exposure time in different lab and field environments as described elsewhere.<sup>80,81,84</sup> A Panalytical X'pert powder diffractometer utilizing a Cu-K $\alpha$  source was utilized for measurements. All samples were scanned continuously from 30 degrees to 50 degrees at 5 degrees per minute. XRD measurements of pristine and environmentally exposed samples were made on panels far away ( $\geq 2$  cm away) from any edge or scribe. These measurements were confirmed to be representative of

global coating degradation. XRD obtained from MgRP panels were normalized against the face-centered cubic (fcc) Al  $\langle 200 \rangle$   $2\theta = 44.74^\circ$  peak from the underlying substrate. Peak normalization and integration was performed with Origin Lab 7.5 software. The lower detection limit for crystalline phases was approximately 3-5 % of the sample by volume.

Corrosion products formed after environmental exposure were characterized using Raman spectroscopy. Raman spectroscopy was conducted using a Renishaw InVia Raman Microscope. Measurements were conducted using a 514 nm laser at 1 – 50 % power under the 20x objective with a 3000 1/mm (vis) grating. Scans with 15 second exposure time were taken with 2 accumulations under standard confocality. If Raman spectra showed heavy fluorescence then a pre-measurement sample bleaching was conducted where the sample was subjected to laser exposure under the aforementioned conditions for 450 to 600 seconds prior to taking the spectra. For all measurements, prior calibration of Raman spectroscopy was performed using a silicon standard.

Scanning electron microscopy (SEM) and energy dispersive spectroscopy (EDS) were used for post-mortem analysis of corrosion products in the scribe. A field emission Quanta 650 SEM was used to conduct these investigations. For EDS, Oxford XMax 150 detector was utilized. A working distance of 15 mm and an accelerating voltage of at least 3 times the energy of the maximum characteristic peak of interest were used (~15 kV). At an accelerating voltage of 15 kV, EDS has a penetration depth of roughly 2 to 5  $\mu\text{m}$  into the materials investigated in this study. Elemental maps and line profiles were collected and the analysis was performed using the Aztec software.

Optical profilometry of scribe was conducted using a Zygo optical profilometer (Newview 7200/7300 model). The environmentally exposed samples were first exposed to concentrated nitric acid for 20 minutes to remove corrosion products present in the scribe as per the ASTM G1

Standard.<sup>138</sup> Image refinement and corrosion volume loss calculation was performed using MountainsMaps<sup>139</sup> imaging topography software.

### **3.4 Results**

#### **3.4.1 Evaluation of the Performance of a MgRP without Topcoat on Pretreated AA2024-T351 after Exposure in Selected Lab and Field Environments: Global Protection Assessment of Global Barrier Degradation**

The low frequency EIS and break point frequency data for the AA2024-T351/Pretreatment/MgRP system as a function of exposure time in different LALT and field environments are summarized in Figures 3.1 and 3.2, respectively. The approximate barrier low frequency EIS at 0.01 Hz did indicate significant coating degradation of AA2024-T351/NFF/MgRP in full immersion. Similar full immersion exposure led to lowering of low frequency impedance by 1-2 orders of magnitude for all chosen conversion coatings based system indicating degradation of conversion coatings. However, there is substantial degradation in barrier properties of AA2024-T351/Pretreatment/MgRP after exposure in standard and modified ASTM B-117 environment. After 1000 h exposure in standard/modified ASTM B-117, the low frequency EIS lowered by 2-3 orders of magnitude indicating rapid coating degradation. Barrier properties slightly improved at longer exposure times indicating sealing of pores by conversion of Mg pigment to magnesium hydroxide. Similar exposure conducted in field (KSC/Birdwood) showed moderate coating degradation in initial and intermediate exposure times (2 – 24 weeks) and significant coating degradation after 52 weeks. There is significant degradation of primer polymer by UV exposure eventually exposing the underlying substrate after 52 weeks. This can be correlated to the significant degradation in barrier properties of AA2024-T351/Pretreatment/MgRP after 52 weeks. The breakpoint frequency increased with time in chosen LALT/field exposures

suggesting porosity development. This could be due to combination of corrosion of metallic Mg pigment and degradation of primer polymer. However in selected LALT environments corrosion of metallic Mg pigments leads to formation of Mg corrosion products which seal the pores and improved the barrier properties. Breakpoint frequency analysis indicate that severity of coating degradation as a function of exposure environment is in the following order, Full Immersion (5 % NaCl) < KSC ~ CHO < ASTM B-117 < Modified ASTM B-117.

### **Assessment of Global Magnesium Depletion**

X-ray spectra of AA2024-T351/NFF/MgRP after exposure in selected LALT/Field environments are shown in Figure 3.3. Elemental Mg HCP (001), (002) and (101) peaks and FCC Al (111) and (200) peaks were observed in initial spectra. The integral intensity of (200) peaks was normalized so as to compare the elemental Mg depletion as a function of exposure time in all chosen environments. Partial depletion (~ 80 %) of Mg occurred after 550 h exposure in full immersion. Mg in MgRP was completely depleted after 96 h, 1000 h and 8736 h in Modified ASTM B-117, ASTM B-117 and field exposure (KSC/Birdwood), respectively. This indicates that self-corrosion of Mg occurs in all chosen environments but only in absence of a topcoat. Mg depletion was not complemented by detection of any crystalline Mg corrosion products as indicated in Figure 3.3. Similar Mg depletion trends were observed in other chosen AA2024-T351/Pretreatment/MgRP systems which were conversion coatings based. The results are summarized in Figure 3.4. Irrespective of the nature of the pretreatments, the Mg depletion trends were similar indicating self-corrosion is predominant factor in Mg depletion in chosen environments since these studies involved intact coating. Mg depletion trends indicate that Mg depletion as a function of exposure environment is in the following order, Full Immersion (5 % NaCl) < KSC ~ CHO < ASTM B-117 < Modified ASTM B-117.

## **Correlation of Global Mg depletion to Global Galvanic Protection Potential and Barrier Properties of Coating**

The global galvanic protection potential of the AA2024-T351/NFF/MgRP system as a function of amount of Mg available is shown in the Figure 3.5a. The average open circuit potential of AA2024-T351 and Mg in ambiently aerated 5 % (wt) NaCl solution are -0.71 V and -1.48 V respectively. In NFF pretreatment, magnesium is galvanically coupled to AA2024-T351 immediately as evident from more negative potential and Mg is available for cathodic protection from the beginning of exposure as indicated in Figure 3.5a. In field exposures, the global galvanic protection potential rises to the OCP of AA2024-T351 after 24 weeks. This could be correlated to visual inspection of samples wherein coating has completely degraded by UV exposure and the bare substrate was exposed. The global galvanic protection potential of the AA2024-T351/TCP/MgRP system as a function of amount of Mg available in three different environments including full immersion, ASTM B-117 and field exposure (at Charlottesville) is shown in the Figure 3.5b. In TCP pretreatment, the global galvanic protection potential is initially more positive compared to OCP of bare AA2024-T351. This indicates that initially no galvanic coupling occurs between AA2024-T351 and MgRP because of the high resistance between the anode and cathode given the resistive nature of conversion coating. However, prolonged exposure up to 85 h, brought about lowering in the resistance enabling galvanic coupling. The OCP shifted to more negative potentials during this process signaling improved galvanic coupling over time. In field exposures, the global galvanic protection potential reaches the OCP of AA2024-T351 after 52 weeks. This could be correlated to visual inspection of samples wherein coating has completely degraded by UV exposure and the bare substrate was exposed. A similar trend of delayed galvanic coupling was observed in CCC

and NCP based conversion coatings. In modified ASTM B-117 (Acidified SOW and UV), Mg is completely depleted within 96 h of exposure and there is no galvanic coupling as it could be inferred from much higher potentials. Similar behavior of rapid Mg degradation was seen in all chosen AA2024-T351/Pretreatment/MgRP systems. The acidic pH ( $3.2 \pm 0.2$ ) resulted in immediate depletion of Mg by self-corrosion.

The global breakpoint frequency of the AA2024-T351/NFF/MgRP system as a function of amount of Mg available is shown in the Figure 3.6. The coating degradation as a function of exposure time is similar in full immersion and field exposures. The ASTM B-117 environments resulted in rapid degradation of MgRP. Acidified SOW/UV modified ASTM B-117 environment had even more rapid depletion of Mg in addition to the coating degradation due to highly acidic environments. As the Mg was depleted extensive porosity development occurred as indicated by the rapid raise of  $F_{bpt}$ . Similar behavior was seen in all chosen pretreatments.

### **Characterization of Corrosion Products**

Raman Spectroscopy was conducted for pristine as well as field exposed AA2024-T351/NFF/MgRP samples to study the nature of different corrosion products formed in pertinent lab and field environments. For pristine samples, the Raman studies indicated that Mg present on surface of MgRP is immediately converted to magnesium oxide. After LALT exposure in Standard ASTM B-117 for 400 h, the peaks corresponding to Mg-O bonds disappeared and a more prominent peak corresponding to  $MgCO_3$  appears at  $1090\text{ cm}^{-1}$  as shown in Figure 3.7a. Similar trends were observed in field exposures at KSC and CHO after 24 weeks. The Raman spectra of samples exposed at CHO for 24 weeks is shown in Figure 3.7b. This indicates that Mg in the MgRP is converted to  $MgCO_3$  at the surface due to ambient concentration of carbon dioxide present in the environments. The reference peaks for magnesite ( $MgCO_3$ ) and brucite ( $Mg(OH)_2$ )

are summarized in Table 3.2. Numerous additional peaks also appears in the range of  $1200\text{ cm}^{-1}$  to  $2200\text{ cm}^{-1}$  after pertinent lab and field exposures. This may be due to degradation of polymer and further work on change in polymer chemistry is out of the scope of our current work.

### **3.4.2 Evaluation of the Performance of a MgRP without Topcoat on Pretreated AA2024-T351 after Exposure in Selected Lab and Field Environments: Scribe Protection**

#### **Assessment of Scribe Protection: Mg Corrosion Products Redeposition**

In the ASTM B-117 salt fog exposures (LALT) the electrolyte layer is subject to continuous wetting enabling a fairly accurate determination of throwing power across the scribe as indicated. This means that Mg depleted from the primer can be transported over the scratch and precipitated in the scratch. Figure 3.8 shows EDS elemental Mg maps of NFF/TCP pretreated AA2024-T351/MgRP after different ASTM B-117 exposure times. Mg EDS intensity in the scribe increased with exposure time and corresponding intensity of Mg in the primer near to scribe edge decreased as indicated in EDS line profiles (Figure 3.9a). Integral intensity of Mg EDS line profiles across scribe and primer as a function of exposure time in ASTM B-117, KSC and Modified ASTM B-117 are summarized in Figure 3.9b-d. Preliminary results indicate that throwing power for Mg redeposition is not greatly inhibited by the presence of additional resistance due to pretreatments. The presence of  $\text{Mg}(\text{OH})_2$  in the scribe indicates production of hydroxide resulting in change of equilibrium pH from 6.9 to 10.45 via oxygen reduction reaction as well as  $\text{Mg}^{2+}/\text{Mg}(\text{OH})_2/\text{H}_2\text{O}$  equilibrium and also transport and deposition of Mg to scribe.<sup>140</sup> The alkaline pH suppresses the chemical dissolution of species used to identify zones of cathodic protection. The increase in Mg EDS intensity as a function of exposure time in ASTM B-117 and KSC environment could be exploited to investigate the transfer of Mg and its chemical precipitation. The modified ASTM B-117 environment (acid) indicated initial deposition of  $\text{Mg}(\text{OH})_2$  after 48 h followed by dissolution

of Mg corrosion products as well as leaching of Mg from AA2024-T351 substrate on prolonged exposure as shown in Figure 3.9d. This is due to dissolution of Mg corrosion products in the low pH solution. Field exposures studies conducted at CHO indicated no presence of Mg corrosion products. The acidic nature of CHO environment resulted in dissolution of Mg corrosion products. The Mg corrosion products in addition to being chemical markers could also provide secondary form of AA2024-T351 protection. The mode of protection will be examined in future work.

#### **Assessment of Scribe Protection: Corrosion Volume Loss Analysis**

Optical profilometry maps of scribe exposing AA2024-T351 in NFF and TCP pretreated AA2024-T351/MgRP after exposure in ASTM B-117 for 1000 h is indicated in Figure 3.10. The optical profilometry map of AA2024-T351/NFF/MgRP after exposure for 1000 h in ASTM B-117 is indicative of the sacrificial corrosion protection or other corrosion mitigation processes provided by Mg across the scribe as indicated by presence of fewer and less deep pits. Similar behavior was exhibited by AA2024-T351/TCP/MgRP after exposure for 1000 h in ASTM B-117 indicating that any detriment due to delayed galvanic protection of 2024-T351 scribe was minimal. The sacrificial protection is enabled immediately after breakdown of pretreatments and the localized corrosion damage during the initial delay in galvanic coupling is minimal. Due to low pH ( $3.2 \pm 0.2$ ), the acidified ASTM SOW/UV environment exposed scribe suffered a very large amount of localized corrosion exhibiting pits as deep as 60 – 70  $\mu\text{m}$ . Irrespective of nature of pretreatment, this behavior was prominent in acidified ASTM B-117 environment. Figure 3.11a-b summarizes the corrosion volume loss for AA2024-T351/NFF/MgRP and AA2024-T351/TCP/MgRP without topcoat in the various environments indicated. Corrosion volume loss increased as a function of exposure time in all environments. The rate of loss of corrosion volume was higher in acidified ASTM B-117 modified with SOW/UV environment and the least in field environments with

moderate protection in ASTM B-117. Non topcoated conditions with both pretreatments perform better than control experiments conducted on bare AA2024-T351 without any coating in ASTM B-117 environment as shown in Figure 3.11a-b indicating that MgRP provides scribe protection in all environments except for Modified ASTM B-117 environment. This indicates that these results can be correlated to the observations during post-exposure scribe chemical analysis using EDS and hence could be effective to determine scribe protection in environments such as CHO in which chemical markers approach is not feasible due to dissolution of corrosion products in scribe.

### **3.4.3 Evaluation of the Performance of a MgRP with Topcoat on Pretreated AA2024-T351 after Exposure in Selected Lab and Field Environments: Global Protection Assessment of Global Barrier Degradation**

The low frequency EIS and break point frequency of AA2024-T351/Pretreatment/MgRP/TC as a function of exposure time in different LALT/field environments are summarized in Figure 3.12 and Figure 3.13, respectively. Irrespective of the nature of the pretreatment, the barrier low frequency EIS at 0.01 Hz did not indicate significant coating degradation of AA2024-T351/Pretreatment/MgRP/TC in full immersion and standard ASTM B-117. After 5000 h exposure in field, the low frequency EIS lowered by 1-2 orders of magnitude indicative of moderate coating degradation. Substantial degradation in barrier properties of the coating was observed in Modified ASTM B-117 environment. Breakpoint frequency increased with time in chosen LALT/field exposures suggesting porosity development. This could be primarily due to degradation of topcoat polymer. Breakpoint frequency analysis indicate that severity of coating degradation as a function of exposure environment is in the following order, Full Immersion (5 % NaCl) < ASTM B-117 < KSC ~ CHO < Modified ASTM B-117.

## **Assessment of Global Magnesium Depletion**

X-ray spectra of AA2024-T351/NFF/MgRP/TC after exposure in selected LALT/Field environments are shown in Figure 3.14. Elemental Mg HCP (001), (002) and (101) peaks, Rutile  $\text{TiO}_2$  hcp (101), (200), (111) and (210) peaks and FCC Al (111) and (200) peaks were observed in initial spectra. The integral intensity of (200) peaks was normalized so as to compare the elemental Mg depletion as a function of exposure time in all chosen environments. There is no significant depletion of Mg in full immersion, ASTM B-117 and field exposures. However, there is a partial depletion of Mg in Modified ASTM B-117 environment. This indicates that self-corrosion of Mg is minimized in the presence of topcoat. Mg depletion was not complemented by detection of any crystalline corrosion products as indicated in Figure 3.14. Similar Mg depletion trends were observed in other chosen AA2024-T351/Pretreatment/MgRP/TC systems which were conversion coatings based. The results are summarized in Figure 3.15. Irrespective of the nature of the pretreatments, the Mg depletion trends were similar indicating degradation of topcoat polymer is predominant factor for subsequent Mg depletion in chosen environments.

## **Correlation of Global Mg depletion to Global Galvanic Protection Potential and Barrier Properties of Coating**

The average open circuit potential of AA2024-T351 and Mg in naturally aerated 5 % (wt) NaCl solution are -0.71 V and -1.48 V respectively. In TCP pretreatment, the global galvanic protection potential is heavily mediated by the presence of resistive topcoat layers. Mg pigment remains in the MgRP coating and is not coupled to AA2024-T351 substrate and hence not used up and the global galvanic couple potential was above the open circuit potential of AA2024-T351. Similar behavior of limited galvanic coupling and minimal depletion of Mg was observed all through the lifetime of coating for all chosen AA2024-T351/Pretreatment/MgRP/TC systems.

The global breakpoint frequency of the AA2024-T351/NFF/MgRP/TC system as a function of amount of Mg available is shown in the Figure 3.16. There is neither appreciable coating degradation nor Mg depletion in full immersion, Standard ASTM B-117 and field environment. Modified ASTM B-117 showed partial depletion of Mg and substantial degradation of coating barrier properties.

#### **3.4.4 Evaluation of the Performance of a MgRP with Topcoat on Pretreated AA2024-T351 after Exposure in Selected Lab and Field Environments: Scribe Protection Assessment of Scribe Protection: Mg Corrosion Products Redeposition**

EDS elemental Mg maps of NFF/TCP pretreated AA2024-T351/MgRP/TC after different ASTM B-117 exposure times showed no significant Mg presence in the scribe. The limited scratch protection is due to resistive layers of topcoat which render galvanic coupling and Mg transport to the scribe more difficult. Similar observations were made for AA2024-T351/Pretreatment/MgRP/TC exposed to other LALT and field exposures. Since no appreciable amount of Mg was observed in the scribe or coating adjacent to scribe, further line profiles to quantify the amount of Mg in and near scribe region was not conducted. It is to be noted that, from previous global Mg depletion trends by XRD (Figure 3.15), elemental Mg is still preserved beneath the topcoat polymers and it would be available for sacrificial protection and Mg transport to scribe once further degradation of topcoat occurs.

### **Assessment of Scribe Protection: Corrosion Volume Loss Analysis**

Optical profilometry maps of scribe exposing AA2024-T351 in NFF and TCP pretreated AA2024-T351/MgRP/TC after exposure in ASTM B-117 for 1000 h are indicated in Figure 3.17. All corrosion volume loss maps were representative of regions less than 50 micrometers from coating edge to scribe center. The optical profilometry map of AA2024-T351/NFF/MgRP/TC after exposure for 1000 h in ASTM B-117 is indicative of the moderate sacrificial corrosion protection provided by Mg across the scribe as indicated by presence of fewer and less deep pits in comparison to control experiments run for bare AA2024-T351. Similar behavior was exhibited by AA2024-T351/TCP/MgRP/TC after exposure for 1000 h in ASTM B-117 indicating that any detriment in galvanic protection of 2024-T351 scribe is minimal. Due to low pH ( $3.2 \pm 0.2$ ), the acidified ASTM SOW/UV environment exposed scribe suffered a very large amount of localized corrosion exhibiting pits as deep as 60 – 70  $\mu\text{m}$ . Irrespective of nature of pretreatment, this behavior was prominent in acidified ASTM B-117 environment. Figure 3.18a-b summarizes the corrosion volume loss for AA2024-T351/NFF/MgRP/TC and AA2024-T351/TCP/MgRP/TC with topcoat in the various environments indicated. Corrosion volume loss increased as a function of exposure time in all environments. The rate of increase of corrosion volume loss was higher in acidified ASTM B-117 modified with SOW/UV environment and the least in field environments with intermediate protection in ASTM B-117. However topcoated conditions with both pretreatments perform better than control experiments conducted for bare AA2024-T351 without any coating in ASTM B-117 environment as shown in Figure 3.18a-b indicating that MgRP provides scribe protection in all environments except for modified ASTM B-117 environment. In spite of no substantial corrosion product redeposition in scribe as evident from EDS, in topcoated condition there is moderate sacrificial protection indicative of galvanic protection at scribe after

topcoat polymer degradation. Higher corrosion volume loss densities for MgRP coated system with topcoat in comparison to non-topcoated condition is indication of topcoat limiting the sacrificial protection due to the additional resistance and need for an optimized topcoat barrier properties in a way that both scribe protection by cathodic protection and global barrier protection are balanced (Figure 3.18 c).

### **3.4.5 Summary of Observations made after Environmental Exposure in Various Environments**

Table 3.3 and 3.4 summarize observations concerning degradation times for global Mg and barrier properties for AA2024-T351 panels coated with MgRP and MgRP/polyurethane topcoat, respectively. The threshold value for  $IZI_{0.01 \text{ Hz}}$  and breakpoint frequency changes was approximated to be  $1/100^{\text{th}}$  of low frequency impedance at 0 h and  $10^3 \text{ Hz}$ , respectively to assess the performance of the coating in selected LALT and field exposures. These values corresponds to significant coating degradation and were utilized to compare the performance of the coating. There was no significant macroscopic blistering and coating delamination due to underpaint corrosion in coating system exposed to standard ASTM B-117 and field exposures. However, the modified ASTM B-117 with acidified SOW and UV showed significant blisters formation. Global Mg depletion from XRD measurements (Figure 3.3) can be correlated to self-corrosion of Mg. Mg self-corrosion is minimized in systems with a topcoat (Figure 3.14). The coating degradation trends (Figures 3.1 and 3.2) for systems with MgRP and without a topcoat indicates that there is rapid degradation in barrier properties of coatings after exposure in ASTM B-117 and modified ASTM B-117 environments. The barrier properties degradation in field environments are similar, moderately severe initially and substantially high at the end of 1 year due to UV degradation of polymer (Figures 3.1 and 3.2). The coating degradation rate is relatively low in systems with a

topcoat, indicative of the excellent barrier properties of polyurethane topcoat (Figures 3.12 and 3.13).

### **3.5 Discussion**

#### **3.5.1 Understanding Residual Protection Mechanisms by Mg Corrosion Products:**

The post-exposure characterization of AA2024-T351/Pretreatment/MgRP and AA2024-T351/Pretreatment/MgRP/TC after exposure in different LALT/field exposures indicated that initially there is no sacrificial protection mechanism because of high electrical resistance imparted by pretreatments. There was a delayed sacrificial protection mechanism in the bare scribe once the resistance drops (Figure 3.5b). The corrosion volume loss in the bare scribe was very minimal during this initial time and Mg corrosion products were seen in the scribe even though global galvanic protection potential indicates no initial sacrificial anode protection (Figure 3.5b). The protection could be due to self-corrosion of Mg and redeposition of  $Mg^{2+}$  ion in the scribe as  $Mg(OH)_2$  when local pH of the electrolyte in the scribe increased during Mg dissolution (Figure 3.8). The role of Mg corrosion products in residual protection of AA2024-T351 must be further investigated by electrochemically depositing these corrosion products on AA2024-T351 and studying the anodic and cathodic kinetics of AA2024-T351 in presence of  $Mg(OH)_2$  and  $MgCO_3$  rich films. This would be reported in our future work.

#### **3.5.2 Summary of Corrosion Protection Mechanisms:**

The NFF pretreated 2024-T351/MgRP exhibits galvanic protection from the beginning of exposure in both LALT and field as indicated by global galvanic protection potential trends (Figure 3.5a). The scribe protection could be due to combination of sacrificial anode cathodic protection by coupling with MgRP and protection of scratch by  $Mg(OH)_2$  redeposition (Figure 3.8b). The conversion coatings pretreated 2024-T351/MgRP had no galvanic protection at beginning of

exposure but exhibited delayed sacrificial protection in both LALT as well as field environments as indicated by global galvanic protection potential trends (Figure 3.5b). The scribe protection could be due to combination of delayed sacrificial anode cathodic protection by coupling with MgRP and protection of scratch by  $\text{Mg}(\text{OH})_2$  redeposition (Figure 3.8c). Two of the three conversion coatings examined are Cr based and they could provide some additional corrosion protection by leaching and supplying of  $\text{Cr}^{6+}$  species. However, EDS/Raman detected no presence of chromium based oxide redeposition on scribe. Moreover, further environmental exposure studies of pretreated 2024-T351 without any coating would be of interest to understand any residual additional corrosion protection provided by the pretreatments. In the topcoat based systems, both chemical analysis of the scribe as well as the global protection potential trends indicated limited scratch protection. However corrosion volume loss analysis by optical profilometry indicates that they still have better corrosion protection than non-topcoated samples indicating that in spite of limited ionic and Mg transport, they do provide moderate scratch protection (Figure 3.18). The protection trends of above mentioned systems are summarized in Figure 3.19a-b.

### **3.5.3 Understanding Performance of the Coating in LALT vs Field:**

Based on the threshold  $\text{IZI}_{0.01 \text{ Hz}}$  and threshold breakpoint frequency in Table 3.2, for non-topcoated systems, the time required for coating degradation in standard and modified ASTM B-117 environments is less than 48 h. In contrast, field exposure results indicated that substantial coating degradation occurs only after 1 year. Break point frequency trends of field exposures indicate significant pore development around 1344 h. LALT are generally not recommended especially acidified B-117 for a fairly accurate comparison to field exposures. Nevertheless acceleration factor with respect to time for equivalent degradation in LALT environment in comparison to field

is roughly 2 orders in magnitude. The Mg depletion trends showed different acceleration factors in comparison to coating degradation trends. Standard ASTM B-117 resulted in complete depletion of metallic Mg pigment after 1000 h. Similar exposure studies in Modified ASTM B-117 environments and field indicated that exposure time required for complete depletion of Mg are 48 h and 8736 h respectively. This translates to an acceleration factor of 10 and 100 for standard ASTM B-117 and modified ASTM B-117, respectively. In topcoated system, the coating degradation trends indicated that threshold breakpoint frequency was achieved only in Modified ASTM B-117. So quantitative definition of acceleration factor in topcoated systems cannot be accurately determined. The differences in environmental factors (Table 3.1) such as mean chloride ion concentration, pH, mean precipitation, relative humidity could explain the difference in acceleration factors. Extent of scribe protection in standard ASTM B-117 can be correlated to field environment with high chloride ion concentration such as KSC. Modified ASTM B-117 due to highly acidic environment cannot be directly correlated to the field exposures. To simulate an actual field environments which has episodes of drying and wetting, a modified ASTM B-117 exposure with substitute ocean water and accelerated UV testing would need to be conducted with cycling for better correlation with field environments.

#### **3.5.4 Throwing Power Analysis**

The “throwing power” pertains to the distance over which the MgRP coating system can protect bare AA2024-T351 by sacrificial anode-based cathodic protection or other means of corrosion mitigation. Optical profilometry analysis of corrosion volume loss after exposure in different environments for MgRP based systems in coated and uncoated conditions could be utilized to understand its efficacy in terms of scribe protection. Optical microscopy studies shows very low corrosion volume loss in all environments studied except for acidic environments (Figure 3.11 and

3.18). Comparison of corrosion volume loss densities to control experiments in bare 2024-T351 indicates that the corrosion volume loss densities are lowered by 2-3 orders of magnitude in non-topcoated conditions (Figure 3.11) and an order of magnitude for topcoated conditions (Figure 3.18) indicating they both provide corrosion protection to whole width of scribe. It should be noted that during a given episodic drying or wetting event, throwing power may be temporarily increased or diminished, making a definitive determination of throwing power difficult. At the end of the exposure, the definitive throwing power and inverse throwing power is complicated by corrosion during drying or isolated drop formation which leads to attack of those areas which were previously protected. Additional factors which complicate the determination of a throwing power via post mortem characterization of environmentally exposed panels result from the chemical dissolution of species stable at high pH used as markers indicative of zones of cathodic protection (such as  $\text{Mg}(\text{OH})_2$  and  $\text{CaCO}_3$ ) as well as difficulties in distinguishing between definitive regions of protection and of substrate corrosion in defect areas. Chemical dissolution of the precipitates that are common to zones of cathodic protection is likely in acidic, high TOW environments, like that of CHO, which is subject to regular acidic precipitation. EDS maps obtained throughout the width of the scribe after exposure at CHO showed very little indication of Mg or calcareous deposits ( $\text{CaCO}_3$ ) common to regions of cathodic protection, making observation for throwing power in this environment difficult. Moreover, it is likely that the throwing power of the MgRP could be detected in EDS maps obtained throughout the width of the scribe after exposure at KSC presumably due to the more alkaline exposure conditions (Figure 3.8c). Not only is the rain precipitation at KSC slightly alkaline as compared to CHO, but the proximity of the test racks to the ocean make the samples susceptible to spray from the ocean surf which has a pH of roughly 8.2. This alkaline pH suppresses the chemical dissolution of species (such as  $\text{Mg}(\text{OH})_2$  and  $\text{CaCO}_3$ )

used to identify zones of cathodic protection. Additionally, in most exposure environments and moderate pH ranges, aluminum is well known to form a barrier oxide film that reforms rapidly when damaged, leaving the primary form of attack in the scribe observed after exposure in most service environments to be non-uniform pitting corrosion.

### **3.6 Conclusions**

- Full immersion in ambiently aerated 5% NaCl solution resulted in partial depletion of metallic Mg pigment in the AA2024-T351/pretreatment/MgRP after 543 hours. Exposure in ASTM B-117 in 5% NaCl, and Modified ASTM B-117 in ASTM acidified artificial seawater with UV all resulted in complete depletion of metallic Mg pigment in the AA2024-T351/pretreatment/MgRP without a topcoat far from the scribe after 1000 hours and 96 hours, respectively. These harsh LALT environments are not necessarily recommended to assess field performance.
- Field exposures in CHO and KSC also resulted in complete depletion of metallic Mg pigment in the AA2024-T351/pretreatment/MgRP without a topcoat far from the scribe after 1 year of exposure. It also resulted in complete degradation of polymer by UV in field environments. Testing without a topcoat is also not recommended unless the specific application does not involve a topcoat.
- The global galvanic protection potential of the AA2024-T351/NFF/MgRP system, with respect to remote scratches, increased slightly with exposure time in each environment, from initial values of approximately -1.0 V vs. SCE to -0.7 V vs. SCE after extensive environmental exposure. These potential values fall between the open circuit potentials of bare AA2024-T351 (-0.7 V vs. SCE) and bare Mg (-1.6 V vs. SCE) and could be predicted by mixed potential theory. This suggests that Mg pigment is both electrically and ionically

connected to the AA2024-T351 can provide immediate sacrificial galvanic protection to the AA2024-T351 substrate.

- The global galvanic protection potential of the AA2024-T351/conversion coatings/MgRP system, with respect to remote scratches, was initially more positive and it decreased after initial exposure times and then shifted back to more positive values after longer exposure times. This suggests that Mg pigment that is not initially electrically connected to the AA2024-T351. A resistive pretreatment can provide delayed sacrificial galvanic protection to the AA2024-T351 substrate as the pretreatment degrades over time.
- The low frequency EIS measurement and breakpoint frequency analysis of AA2024-T351/pretreatment/MgRP indicate rapid degradation of coating barrier properties in ASTM B-117 and Modified ASTM B-117 in ASTM acidified artificial seawater with UV environments. The barrier properties degradation are relatively moderate in full immersion in ambiently aerated 5% NaCl solution and Field exposures in CHO and KSC.
- Raman spectroscopy of non-topcoated conditions indicate that Mg in the MgRP is converted to an outer layer of  $\text{MgCO}_3$  both in LALT and field exposures and possibly an inner layer of  $\text{Mg(OH)}_2$  due to presence of ambient concentration of  $\text{CO}_2$  in the environment.
- The throwing power measurements using SEM/EDS suggest that for all chosen pretreatments, AA2024-T351/pretreatment/MgRP system could protect the entire half width of the scribe ( $\sim 350 \mu\text{m}$ ) of the scribe in standard ASTM B-117 and Field exposures at KSC as indicated by magnesium hydroxide detection across the scribe. Modified ASTM B-117 in ASTM acidified artificial seawater with UV environment indicated initial

deposition of  $\text{Mg}(\text{OH})_2$  after 48 h followed by dissolution of Mg corrosion products as well as leaching of Mg from AA2024-T351 substrate. Field exposures studies conducted at CHO indicated no presence of Mg corrosion products. The acidic nature of CHO environment resulted in dissolution of Mg corrosion products.

- Corrosion volume loss measured using optical profilometry increased as a function of exposure time in all environments. The rate of increase of corrosion volume loss was higher in acidified ASTM B-117 modified with SOW/UV environment and the least in field environments with moderate protection in ASTM B-117. Compared to bare AA2024-T351, AA2024-T351/Pretreatment/MgRP had lower corrosion volume loss for all chosen pretreatments.
- The Aerodur 5000 topcoat was observed to significantly hinder the depletion of Mg pigment from the MgRP as well as the galvanic protection capabilities in all exposure environments studied as compared to identical environmental exposures of non-topcoated samples. The barrier properties degradation was also significantly reduced in presence of topcoat in all environments. Only the Modified ASTM B-117 in ASTM acidified artificial seawater with UV environment resulted in coating degradation of MgRP systems with topcoat due to acidic environment. The topcoat suppress the MgRP scribe protection by heavily mediating the galvanic protection capabilities and Mg transport. Therefore, topcoat systems have a lower fraction of corrosion products and relative higher corrosion volume loss in the scribe compared to AA2024-T351/Pretreatment/MgRP system in similar environments.

### 3.7 References

1. ASM International Handbook Committee., ASM Handbook Corrosion: Materials. Vol. 13A (Materials Park, OH: ASM International, 2003).
2. D.E.T. G. P. Bierwagen, M. Nannan, D. Battocchi, A. Stamness and V. J. Gelling, *New developments in Cr-Free primers for aerospace alloys*, in *American Chemical Society*. 2004. p. U360.
3. D. Battocchi, A.M. Simoes, D.E. Tallman, and G.P. Bierwagen, "Electrochemical behaviour of a Mg-rich primer in the protection of Al alloys," *Corrosion Science* 48, 5 (2006): p. 1292-1306.
4. G. Bierwagen, D. Battocchi, A. Simoes, A. Stamness, and D. Tallman, "The use of multiple electrochemical techniques to characterize Mg-rich primers for Al alloys," *Progress in Organic Coatings* 59, 3 (2007): p. 172-178.
5. B. Kannan, A. King, and J. Scully, "Effect of Pretreatments on 2024-T351 Corrosion Protection by Magnesium Rich, Non-Chromium Primer (MgRP): Laboratory Characterization in Full Immersion," *Corrosion* doi:10.5006/1700, (2015).
6. B. Kannan, A. King, and J. Scully, *Impact of Surface Pretreatments on AA2024-T351 Corrosion Protection by a Magnesium Rich, Non-Chrome Primer (MgRP)*, in *NACE DoD 2015*. 2015, NACE: Pittsburgh, PA.
7. A.D. King, B. Kannan, and J.R. Scully, "Environmental Degradation of a Mg-Rich Primer in Selected Field and Laboratory Environments – Part II. Primer and Topcoat," *Corrosion* 70, 5 (2014).
8. A.D. King, B. Kannan, and J.R. Scully, "Environmental Degradation of a Mg-Rich Primer in Selected Field and Laboratory Environments – Part I. Without a Topcoat," *Corrosion* 70, 5 (2014).
9. A.D. King, J.S. Lee, and J.R. Scully, "Galvanic Couple Current and Potential Distribution between a Mg Electrode and 2024-T351 under Droplets Analyzed by Microelectrode Arrays," *Journal of the Electrochemical Society* 162, 1 (2015): p. C12-C23.
10. A.D. King, J.S. Lee, and J.R. Scully, "Finite Element Analysis of the Galvanic Couple Current and Potential Distribution between Mg and 2024-T351 in a Mg Rich Primer Configuration," *Journal of The Electrochemical Society* 163, 7 (2016): p. C342-C356.
11. A.D. King and J.R. Scully, "Sacrificial Anode-Based Galvanic and Barrier Corrosion Protection of 2024-T351 by a Mg-Rich Primer and Development of Test Methods for Remaining Life Assessment," *Corrosion* 67, 5 (2011): p. 05500401-05500422.
12. A.D. King and J.R. Scully. *Blistering Phenomena in Early Generation Mg-Rich Primer Coatings on AA2024-T351 and the Effects of CO<sub>2</sub>*. in *NACE DoD 2011 Conference Proceedings*. 2011. Palm Springs, CA.
13. B. Maier and G.S. Frankel, "Behavior of Magnesium-Rich Primers on AA2024-T3," *Corrosion* 67, 5 (2011): p. 055001.
14. S.S. Pathak, M.D. Blanton, S.K. Mendon, and J.W. Rawlins, "Investigation on dual corrosion performance of magnesium-rich primer for aluminum alloys under salt spray test (ASTM B117) and natural exposure," *Corrosion Science* 52, 4 (2010): p. 1453-1463.

15. S.S. Pathak, M.D. Blanton, S.K. Mendon, and J.W. Rawlins, "Carbonation of Mg powder to enhance the corrosion resistance of Mg-rich primers," *Corrosion Science* 52, 11 (2010): p. 3782-3792.
16. S.S. Pathak, M.D. Blanton, S.K. Mendon, and J.W. Rawlins, "Mineralogical Transformation and Electrochemical Nature of Magnesium-Rich Primers during Natural Weathering," *Metals* 4, 3 (2014): p. 322-334.
17. C.M. Abreu, M. Izquierdo, P. Merino, X.R. Novoa, and C. Perez, "A new approach to the determination of the cathodic protection period in zinc-rich paints," *Corrosion* 55, 12 (1999): p. 1173-1181.
18. R.A. Armas, C.A. Gervasi, A. Disarli, S.G. Real, and J.R. Vilche, "Zinc-Rich Paints on Steels in Artificial Seawater by Electrochemical Impedance Spectroscopy," *Corrosion* 48, 5 (1992): p. 379-383.
19. O.O. Knudsen, U. Steinsmo, and M. Bjordal, "Zinc-rich primers - Test performance and electrochemical properties," *Progress in Organic Coatings* 54, 3 (2005): p. 224-229.
20. H. Marchebois, M. Keddam, C. Savall, J. Bernard, and S. Touzain, "Zinc-rich powder coatings characterisation in artificial sea water - EIS analysis of the galvanic action," *Electrochimica Acta* 49, 11 (2004): p. 1719-1729.
21. M. Morcillo, R. Barajas, S. Feliu, and J.M. Bastidas, "A-Sem Study on the Galvanic Protection of Zinc-Rich Paints," *Journal of Materials Science* 25, 5 (1990): p. 2441-2446.
22. D. Chidambaram, C.R. Clayton, and G.P. Halada, "A duplex mechanism-based model for the interaction between chromate ions and the hydrated oxide film on aluminum alloys," *Journal of the Electrochemical Society* 150, 5 (2003): p. B224-B237.
23. P.D. Deck and D. Reichgott, "Characterization of chromium-free no-rinse prepaint coatings on aluminum and galvanized steel," *Metal Fin.* 90, 9 (1992): p. 29-35.
24. Y. Guo and G.S. Frankel, "Active Corrosion Inhibition of AA2024-T3 by Trivalent Chrome Process Treatment," *Corrosion* 68, 4 (2012).
25. O. Lunder, C. Simensen, Y. Yu, and K. Nisancioglu, "Formation and characterisation of Ti-Zr based conversion layers on AA6060 aluminium," *Surface and Coatings Technology* 184, 2 (2004): p. 278-290.
26. F. Mansfeld and M.W. Kendig, "Evaluation of Anodized Aluminum Surfaces with Electrochemical Impedance Spectroscopy," *Journal of the Electrochemical Society* 135, 4 (1988): p. 828-833.
27. M. Saeedikhani, M. Javidi, and A. Yazdani, "Anodizing of 2024-T3 aluminum alloy in sulfuric-boric-phosphoric acids and its corrosion behavior," *Transactions of Nonferrous Metals Society of China* 23, 9 (2013): p. 2551-2559.
28. B.C.R. Troconis and G.S. Frankel, "Effects of Pretreatments on the Adhesion of Acetoacetate to AA2024-T3 Using the Blister Test," *Corrosion* 70, 5 (2014): p. 483-495.
29. L. Xia, E. Akiyama, G. Frankel, and R. McCreery, "Storage and release of soluble hexavalent chromium from chromate conversion coatings - Equilibrium aspects of Cr-VI concentration," *Journal of the Electrochemical Society* 147, 7 (2000): p. 2556-2562.
30. J. Zhao, G. Frankel, and R.L. McCreery, "Corrosion protection of untreated AA-2024-T3 in chloride solution by a chromate conversion coating monitored with Raman spectroscopy," *Journal of the Electrochemical Society* 145, 7 (1998): p. 2258-2264.
31. G.O. Ilevbare and J.R. Scully, "Mass-Transport-Limited oxygen reduction reaction on AA2024-T3 and selected intermetallic compounds in chromate-containing solutions (vol 57, pg 134, 2001)," *Corrosion* 57, 5 (2001): p. 480-480.

32. G.O. Ilevbare and J.R. Scully, "Oxygen reduction reaction kinetics on chromate conversion coated Al-Cu, Al-Cu-Mg, and Al-Cu-Mn-Fe intermetallic compounds," *Journal of the Electrochemical Society* 148, 5 (2001): p. B196-B207.
33. G.O. Ilevbare and J.R. Scully, "Mass-transport-limited oxygen reduction reaction on AA2024-T3 and selected intermetallic compounds in chromate-containing solutions," *Corrosion* 57, 2 (2001): p. 134-152.
34. G.O. Ilevbare, J.R. Scully, J. Yuan, and R.G. Kelly, "Inhibition of pitting corrosion on aluminum alloy 2024-T3: Effect of soluble chromate additions vs chromate conversion coating," *Corrosion* 56, 3 (2000): p. 227-242.
35. G.O. Ilevbare, C.S. Jeffcoate, and J.R. Scully, "Mass transport limited oxygen reduction kinetics on chromate conversion coated Al-Cu, Al-Cu-Mg and Al-Cu-Mn-Fe intermetallic compounds.," *Passivity and Localized Corrosion* 99, 27 (1999): p. 269-279.
36. Pantheon, *Surface Pretreatment - Technical Data Sheet* (2009).
37. Henkel, *Surface Pretreatment - Technical Data Sheet* (2006).
38. Henkel, *Surface Pretreatment - Technical Data Sheet* (2014).
39. Surtec, *Surface Pretreatment - Technical Data Sheet* (2012).
40. AkzoNobel, "Aerodur5000," *Topcoat - Technical Data Sheet* (2013).
41. *Standard Practice for Operating Salt Spray (Fog) Apparatus: B117*, in *Annual Book of ASTM Standards*. 1997, ASTM: West Conshohocken, PA. p. 1-8.
42. ASTM, "Standard Practice for the Preparation of Substitute Ocean Water," ASTM D1141 - 98 DOI: 10.1520/D1141-98R08 (1998).
43. ASTM, "Standard Practice for Modified Salt Spray Testing," ASTM G85 - A3 DOI: 10.1520/C0033-03, (2009).
44. ASTM, "Standard Guide for Conducting Corrosion Tests in Field Applications," ASTM G4 - 01 DOI: 10.1520/G0004-01R08, (2001).
45. ASTM, "Standard Practice for Preparing, Cleaning, and Evaluating Corrosion Test Specimens," ASTM G1 DOI: 10.1520/D1141-98R08 (2003).
46. S. Pommiers-Belin, J. Frayret, A. Uhart, J. Ledeuil, J.-C. Dupin, A. Castetbon, and M. Potin-Gautier, "Determination of the chemical mechanism of chromate conversion coating on magnesium alloys EV31A," *Applied Surface Science* 298, (2014): p. 199-207.
47. M. Pourbaix, *Atlas of Electrochemical Equilibria in Aqueous Solutions*: NACE, 1974.

### 3.8 Tables

Table 3.1. Exposure conditions in field and lab accelerated life testing environments.

Environment	Mean Temp (°C)				Mean RH (%)				Mean Dew Point (°C)			
	Win.	Spr.	Sum.	Fall	Win.	Spr.	Sum.	Fall	Win.	Spr.	Sum.	Fall
KSC	18.7	23.3	28.2	24.2	71.7	69.7	74	72.7	13.5	17.4	23.1	19
CHO	8.1	19.9	24	10.2	59.3	58.3	75.2	65.5	0.6	11	19.3	4
B-117	35				95				34			
B-117 w/ acidified ASW/UV	35				95				34			

Environment	Mean Precipitation (mm/hr)				Mean Precip. pH	Mean Cl <sup>-</sup> (µg/cm <sup>2</sup> /hr)
	Win.	Spr.	Sum.	Fall		
KSC	0.066	0.154	0.245	0.184	5.4 ± 0.4	0.8
CHO	0.102	0.102	0.135	0.139	4.9 ± 0.3	0.002
B-117	0.190				6.9 ± 0.4	600
B-117 w/ acidified ASW/UV	0.190				3.2±0.2	390

Table 3.2. Reference Peaks for Magnesium Corrosion Products.

Compound	Reference Peak	Vibration Mode
Mg(OH) <sub>2</sub>	278	Lattice vibration (E <sub>g</sub> )
Mg(OH) <sub>2</sub>	441	Mg-O stretching (A <sub>1g</sub> )
MgCO <sub>3</sub>	1097	CO <sub>3</sub> <sup>2-</sup> symmetric stretching (ν <sub>1</sub> )
MgCO <sub>3</sub>	1450	CO <sub>3</sub> <sup>2-</sup> antisymmetric stretching (ν <sub>1</sub> )
MgCO <sub>3</sub>	335	unassigned
MgCO <sub>3</sub>	218	unassigned
MgCO <sub>3</sub>	1764	unassigned
MgCO <sub>3</sub>	742	unassigned

Table 3.3. AA2024-T351/Pretreatment/MgRP: Summary of observations made after environmental exposure in various environments.

Environment	XRD – Mg	Breakpoint Frequency	IZI at 0.01 Hz
Full Immersion - Up to 550 h	Partial depletion ( ~ 80 %) in 550 h	Increase – slow coating degradation Time for $F_{bp-threshold}$ – 24 to 132 h	Drop – low Time for $IZI_{threshold} > 543$ h
Std. ASTM B-117 - up to 1000 h	Complete depletion in 1000 h	Increase – rapid coating degradation Time for $F_{bp-threshold} < 48$ h	Drop – high Time for $IZI_{threshold} < 48$ h
Mod ASTM B-117 Acidified SOW/UV - up to 1000 h	Complete depletion in 48 – 96 h	Increase – rapid coating degradation Time for $F_{bp-threshold} < 48$ h	Drop – very high Time for $IZI_{threshold} < 48$ h
Field – KSC - up to 8736 h	Complete depletion in 8736 h	Increase – moderate degradation initially and complete degradation after 1 year Time for $F_{bp-threshold}$ – 336 to 1344 h	Drop – moderate initially and significant after 1 year Time for $IZI_{threshold} \sim 8736$ h
Field – CHO - up to 8736 h	Complete depletion in 8736 h	Increase – moderate degradation initially and complete degradation in 1 year Time for $F_{bp-threshold}$ – 336 to 1344 h	Drop - moderate initially and significant after 1 year Time for $IZI_{threshold} \sim 8736$ h

Table 3.4. AA2024-T351/Pretreatment/MgRP/TC: Summary of observations made after environmental exposure in various environments.

Environment	XRD – Mg	Breakpoint Frequency	IZI at 0.01 Hz
Full Immersion - Up to 550 h	Partial depletion ( ~ 30 %)	No substantial increase Time for $F_{bp-threshold} > 275$ h	No significant drop Time for $IZI_{threshold} > 543$ h
Std. ASTM B-117 - up to 1000 h	Partial depletion ( ~ 30 %)	Increase – rapid coating degradation Time for $F_{bp-threshold} > 1000$ h	Drop – low Time for $IZI_{threshold} > 1000$ h
Mod ASTM B-117 Acidified ASW/UV - up to 1000 h	Partial depletion ( ~ 70 %)	Increase – rapid coating degradation Time for $F_{bp-threshold}$ – 384 to 684 h	Drop – high Time for $IZI_{threshold} \sim 192$ h
Field – KSC - up to 8736 h	Partial depletion ( ~ 30 %)	Increase – moderate coating degradation Time for $F_{bp-threshold} > 8736$ h	Drop – moderate Time for $IZI_{threshold} > 543$ h
Field – CHO - up to 8736 h	Partial depletion ( ~ 30 %)	Increase – moderate coating degradation Time for $F_{bp-threshold} > 8736$ h	Drop – moderate Time for $IZI_{threshold} > 543$ h

### 3.9 Figures

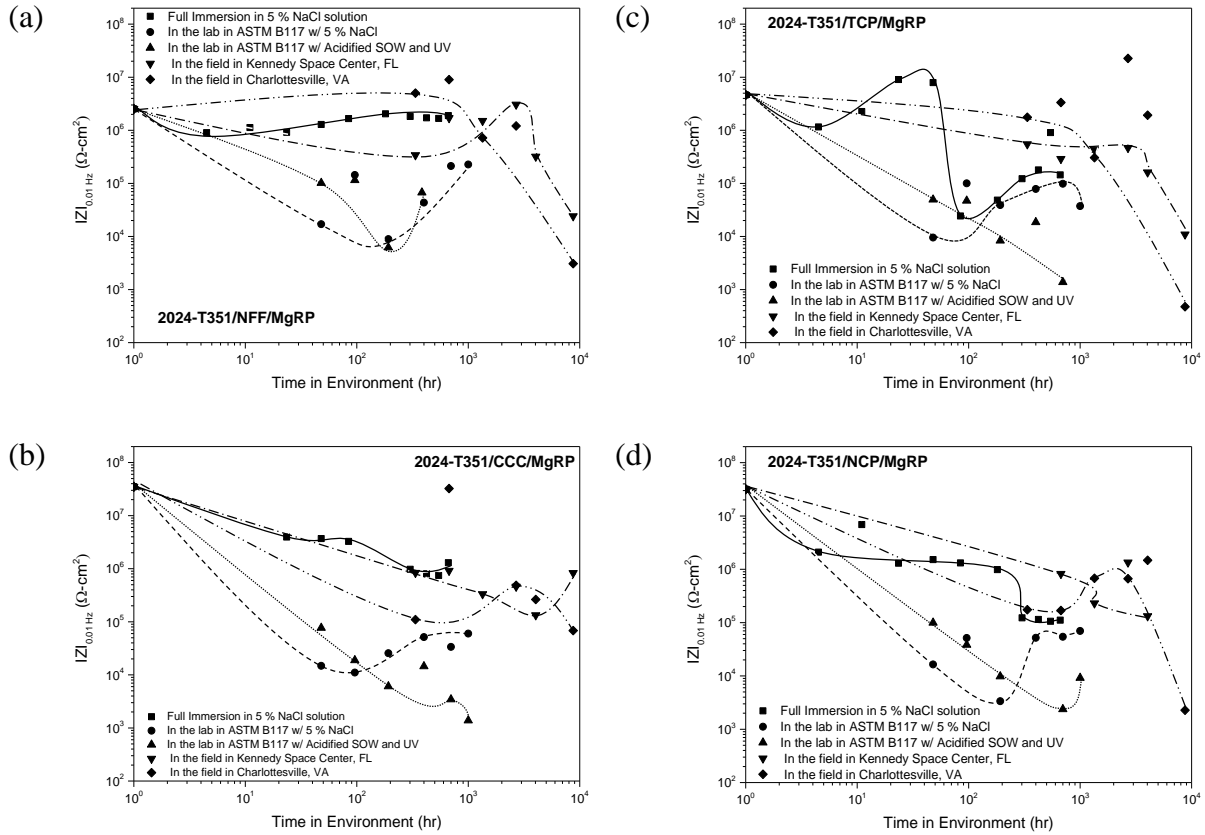
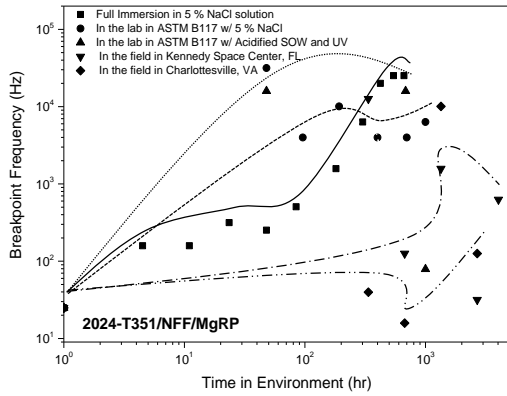
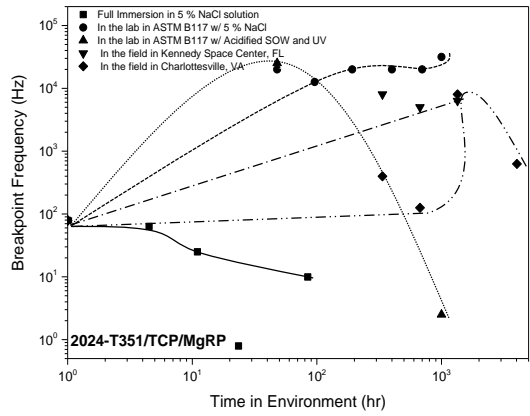


Figure 3.1. Low frequency impedance IZI modulus of intact AA2024-T351/Pretreatment/MgRP at 0.01 Hz vs time in the environments indicated for (a) NFF/MgRP (b) CCC/MgRP (c) TCP/MgRP and (d) NCP/MgRP.

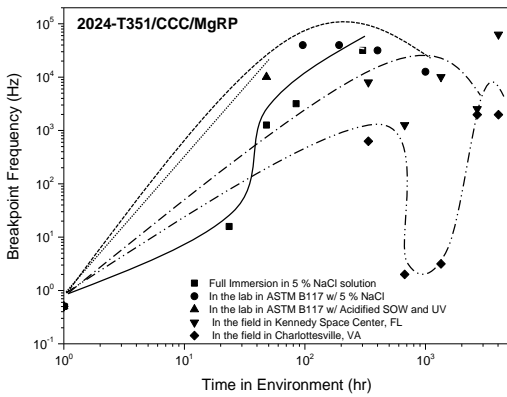
(a)



(c)



(b)



(d)

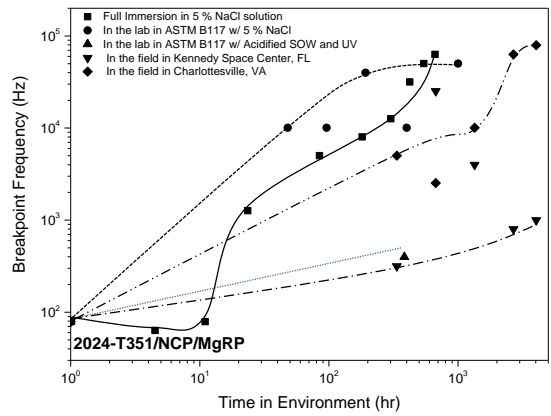


Figure 3.2. High breakpoint frequency ( $F_{bpt}$ ) of intact AA2024-T351/Pretreatment/MgRP systems vs time in the environments indicated for (a) NFF/MgRP (b) CCC/MgRP (c) TCP/MgRP and (d) NCP/MgRP.

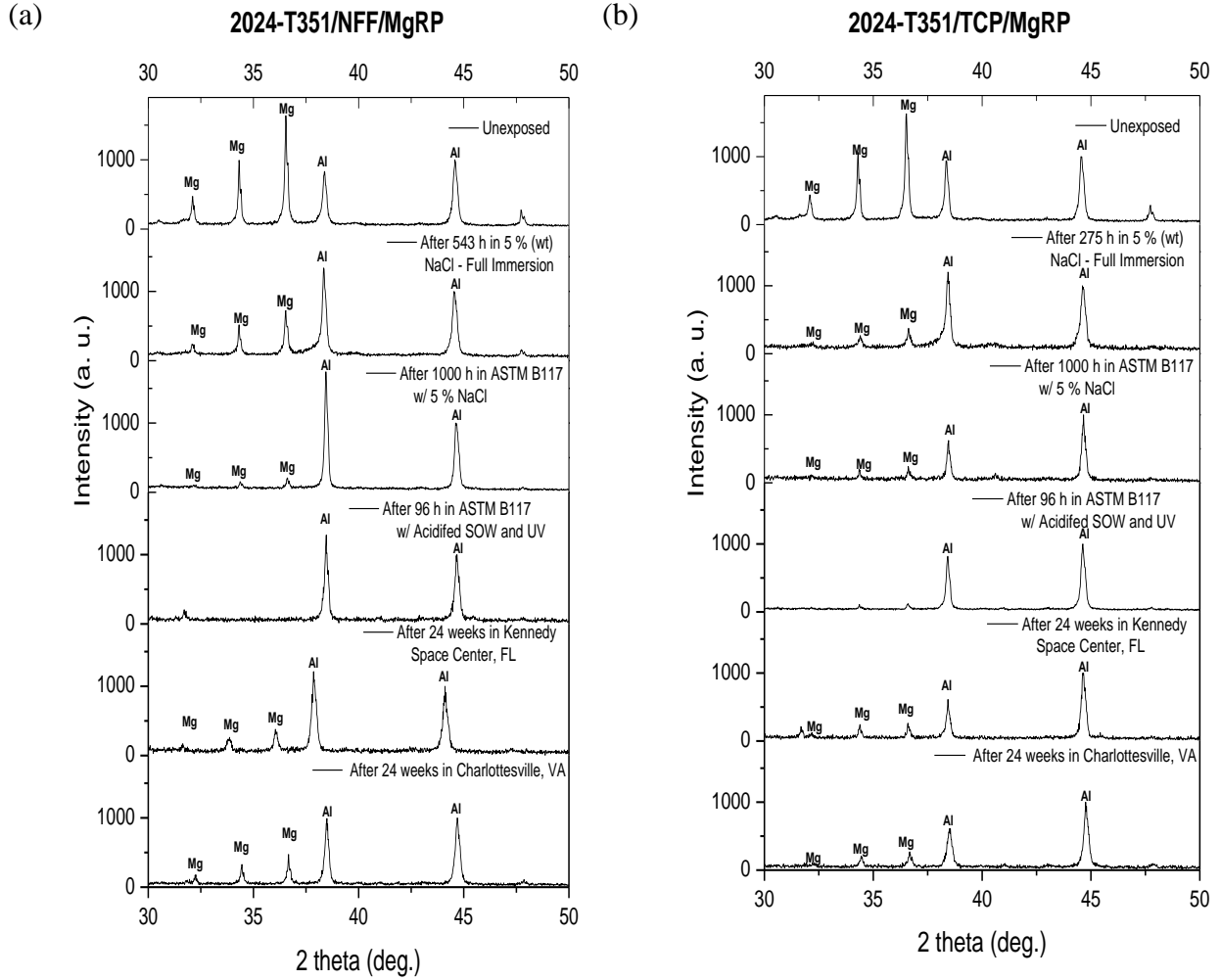
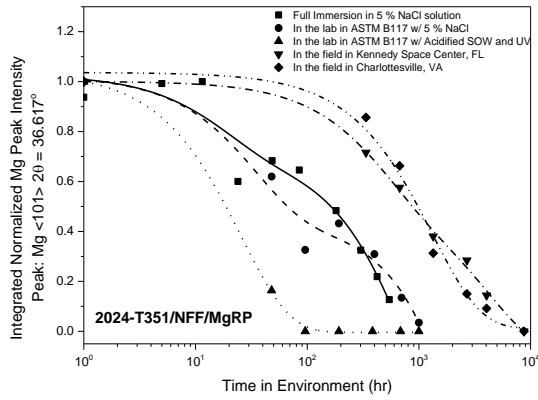
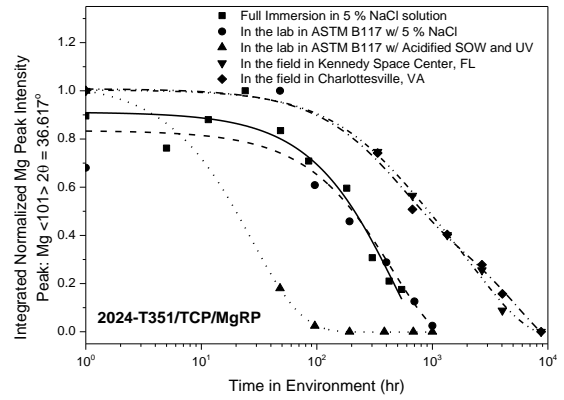


Figure 3.3. Selected XRD spectra of intact AA2024-T351/Pretreatment/MgRP systems after exposure in the LALT/field environments for (a) NFF/MgRP and (b) TCP/MgRP.

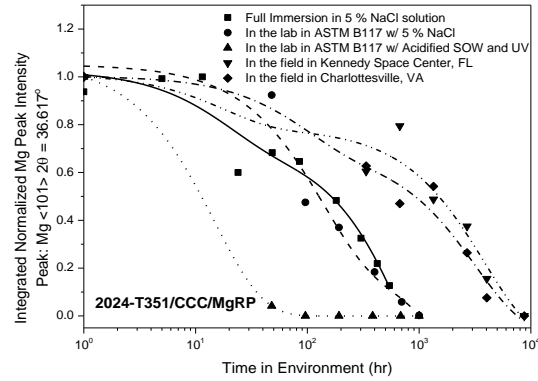
(a)



(c)



(b)



(d)

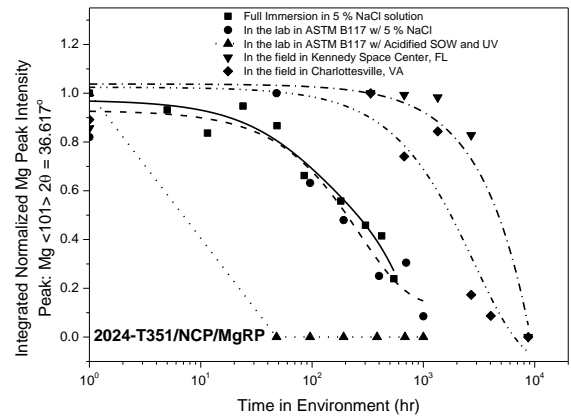


Figure 3.4. The normalized integral XRD intensity for Mg<101> XRD peak of intact AA2024-T351/Pretreatment/MgRP systems vs time in the environments indicated for (a) NFF/MgRP (b) CCC/MgRP (c) TCP/MgRP and (d) NCP/MgRP.

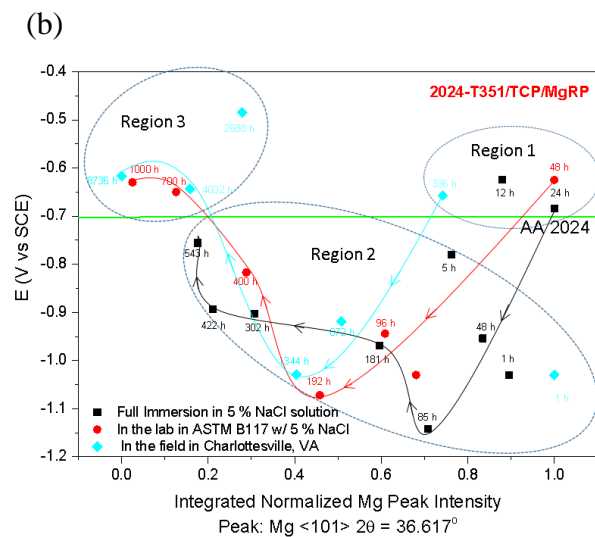
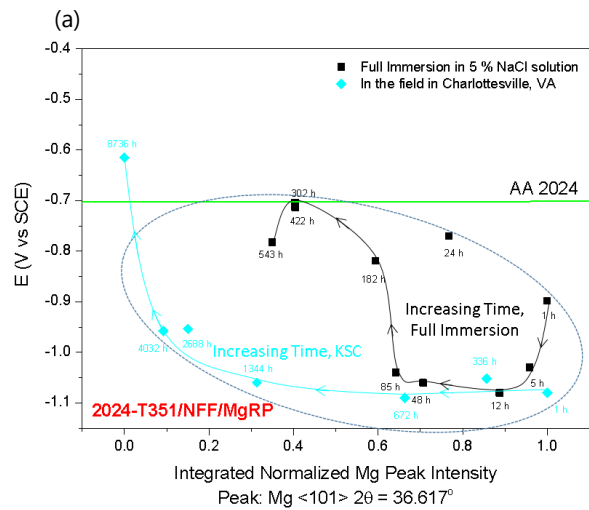


Figure 3.5. Average global galvanic protection potential of intact coating for the last 1 h exposure in 5 % wt NaCl vs the normalized integral XRD intensity for Mg<101>. The time indicates total exposure time in different LALT/Field environments indicated, (a) AA2024-T351/NFF/MgRP after exposure, in Full immersion in 5 % wt NaCl and Field at CHO and (b) AA2024-T351/TCP/MgRP after exposure, in Full immersion in 5 % wt NaCl, ASTM B-117 in 5 % wt NaCl and Field at CHO.

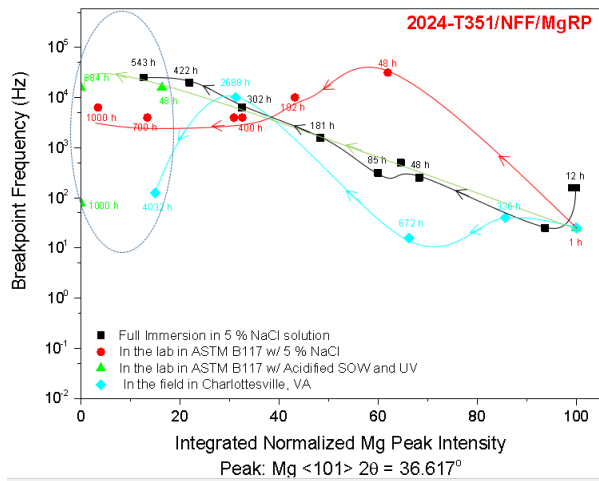
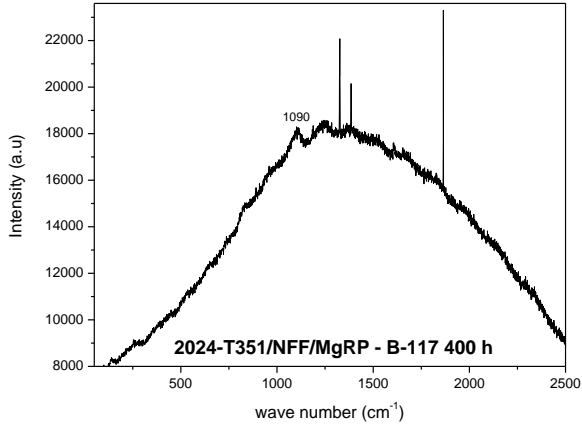


Figure 3.6. High breakpoint frequency of intact coating after 1 h exposure in 5 % wt NaCl vs The normalized integral intensity for Mg<101>. The time indicates total exposure time in different LALT/Field environments indicated,

(a) AA2024-T351/NFF/MgRP after exposure, in Full immersion in 5 % wt NaCl, ASTM B-117 in 5 % wt NaCl, Modified ASTM B-117 with acidified SOW and UV and Field exposure at CHO.

(a)



(b)

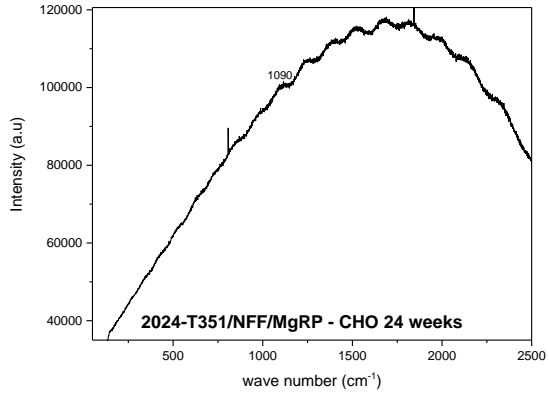


Figure 3.7. Raman spectra for AA2024-T351/NFF/MgRP systems (a) Standard ASTM B-117 exposure – 400 h and (b) At field, CHO for 24 weeks.

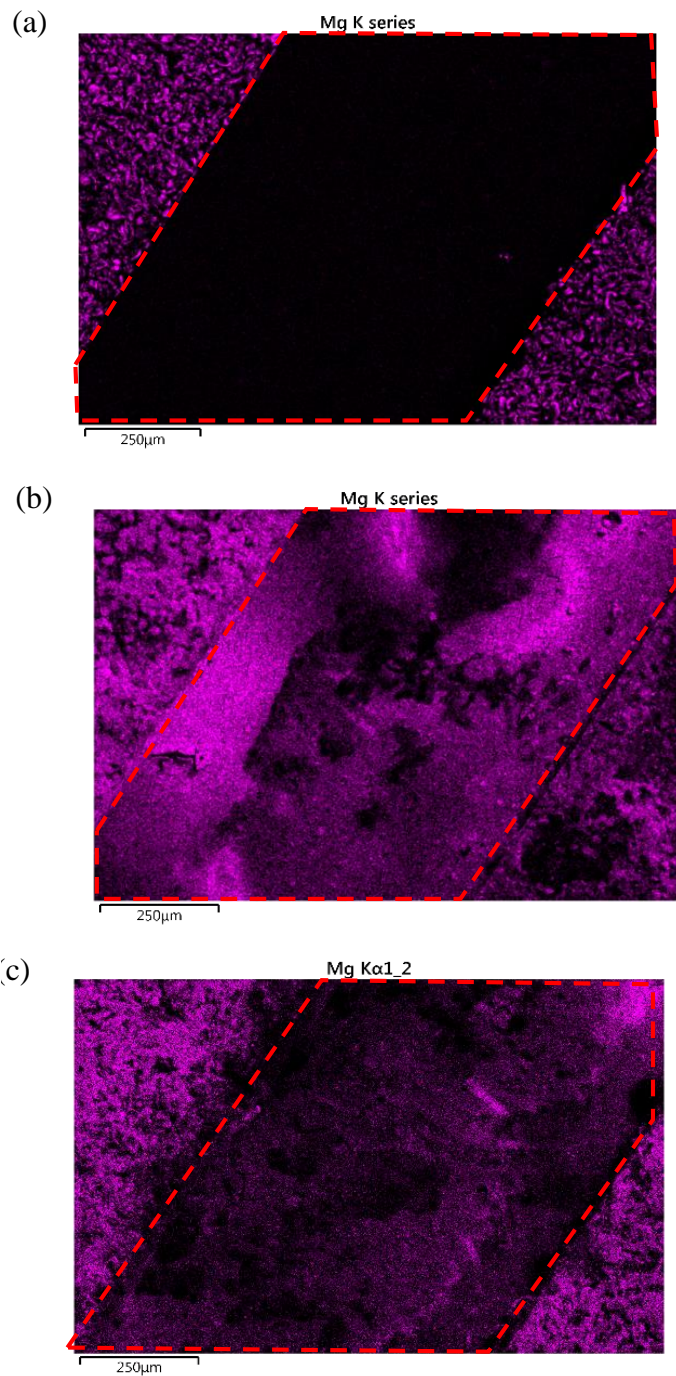


Figure 3.8. EDS maps of elemental Mg across scribe and adjacent coating a) NFF pretreated 2024-T351/MgRP before exposure, b) NFF pretreated 2024-T351/MgRP after 1000 h exposure in ASTM B-117, c) TCP pretreated 2024-T351/MgRP after 1000 h exposure in ASTM B-117. (Red dash lines indicates the borders of the scribe in the figure).

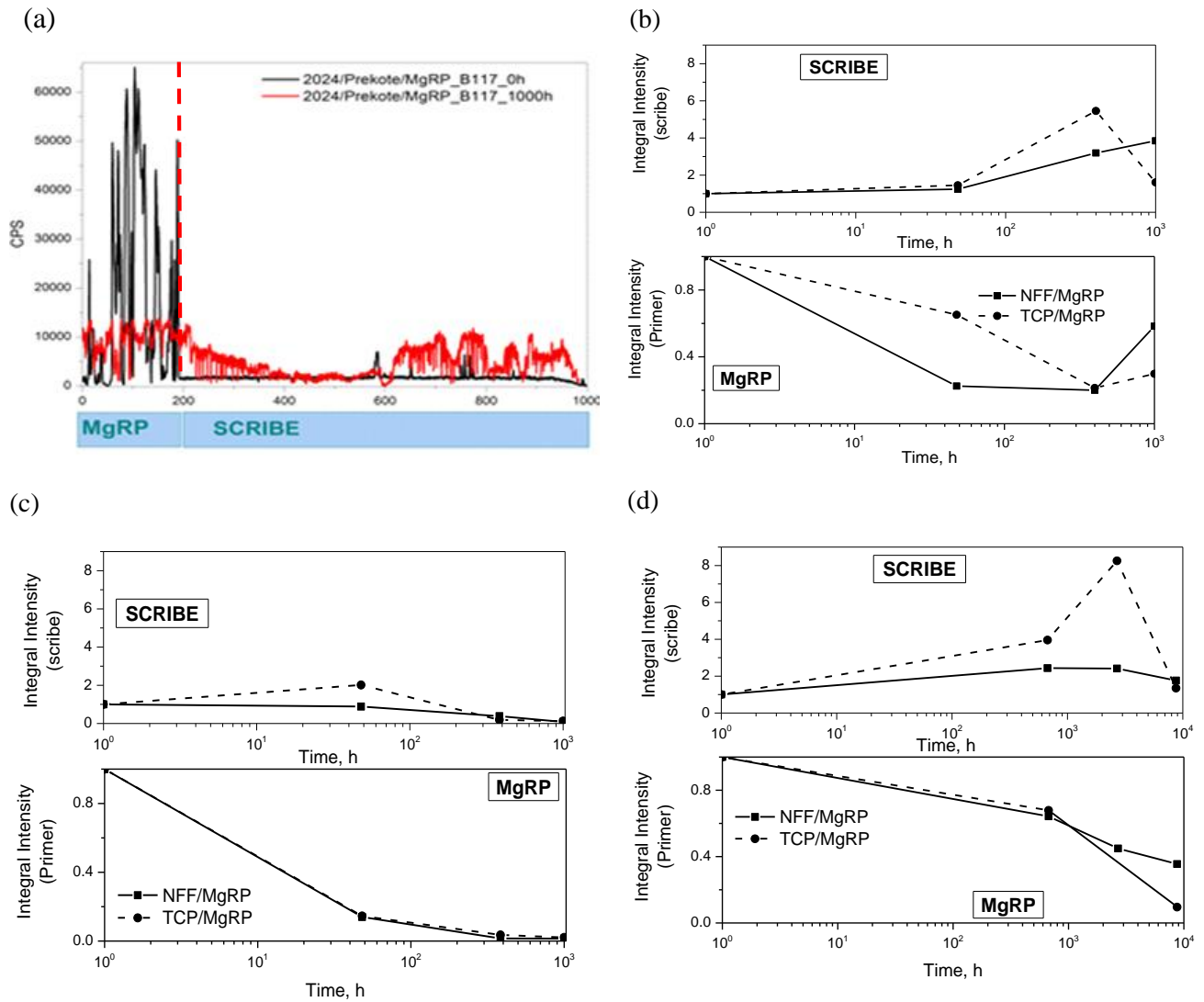


Figure 3.9. a) EDS line profile of NFF/TCP pretreated AA2024-T351/MgRP systems without a topcoat after 1000 h exposure time in ASTM B-117 testing (red dash line indicates the borders of the scribe in the figure). Integral intensity of Mg EDS line profile in scribe/MgRP as a function of exposure time in (b) ASTM B-117 testing for 1000 h (c) Modified ASTM B-117 with acidified ASTM SOW/UV testing for 1000 h and (d) KSC for 8736 h.

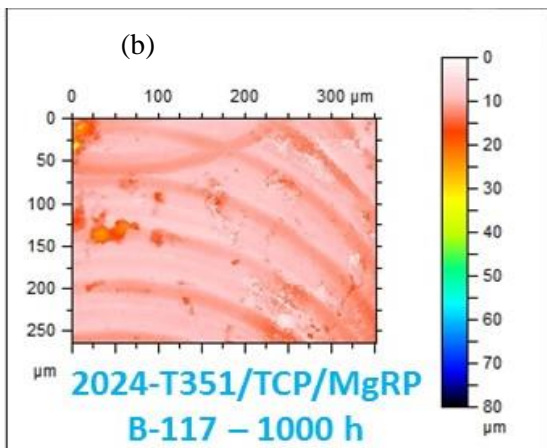
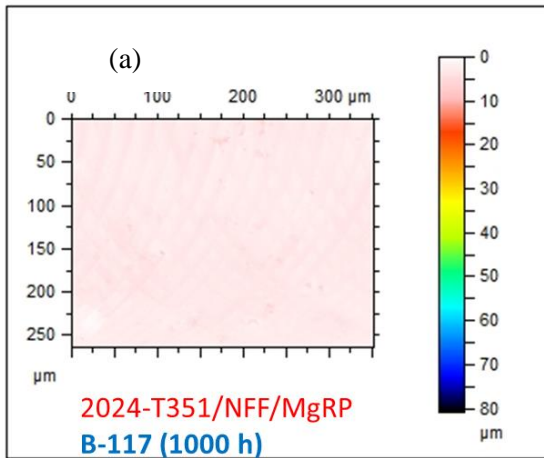


Figure 3.10. Optical profilometry maps of scribe exposing AA2024-T351 in NFF(a)/TCP(b) pretreated AA2024-T351/MgRP without topcoat after exposure in ASTM B-117 for 1000 h. The 0  $\mu\text{m}$  position (white) on the scale is indicative of the starting material condition before corrosion.

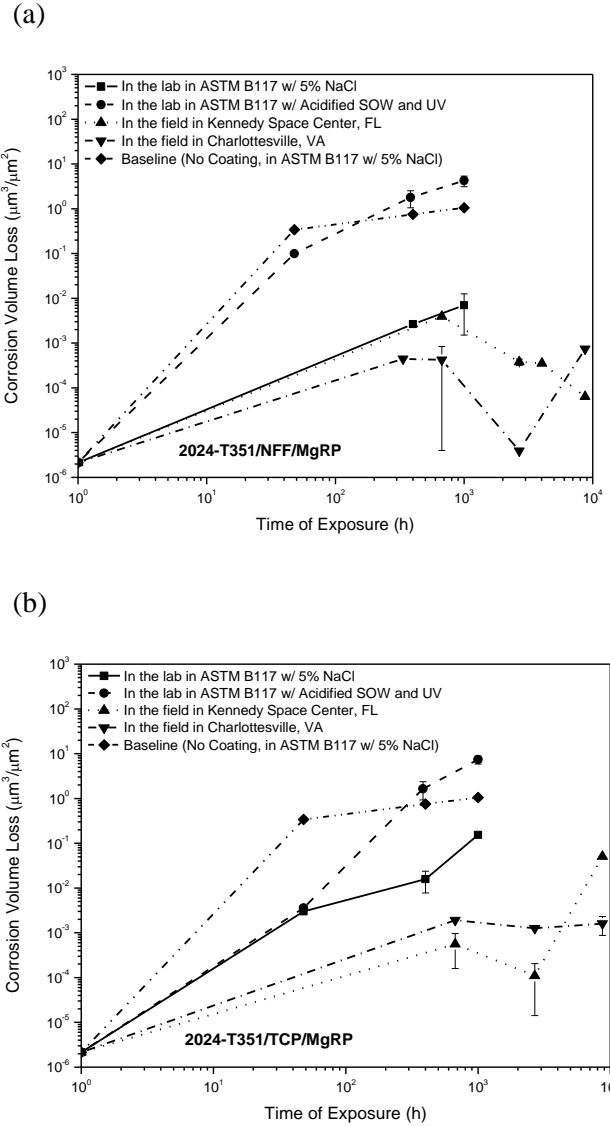


Figure 3.11. Corrosion volume loss of scribe exposing AA2024-T351 in AA2024-T351/Pretreatment/MgRP systems without topcoat as a function of exposure time in different LALT/field environments indicated. The baseline data is for uncoated AA2024-T351. (a) NFF/MgRP and (b) TCP/MgRP.

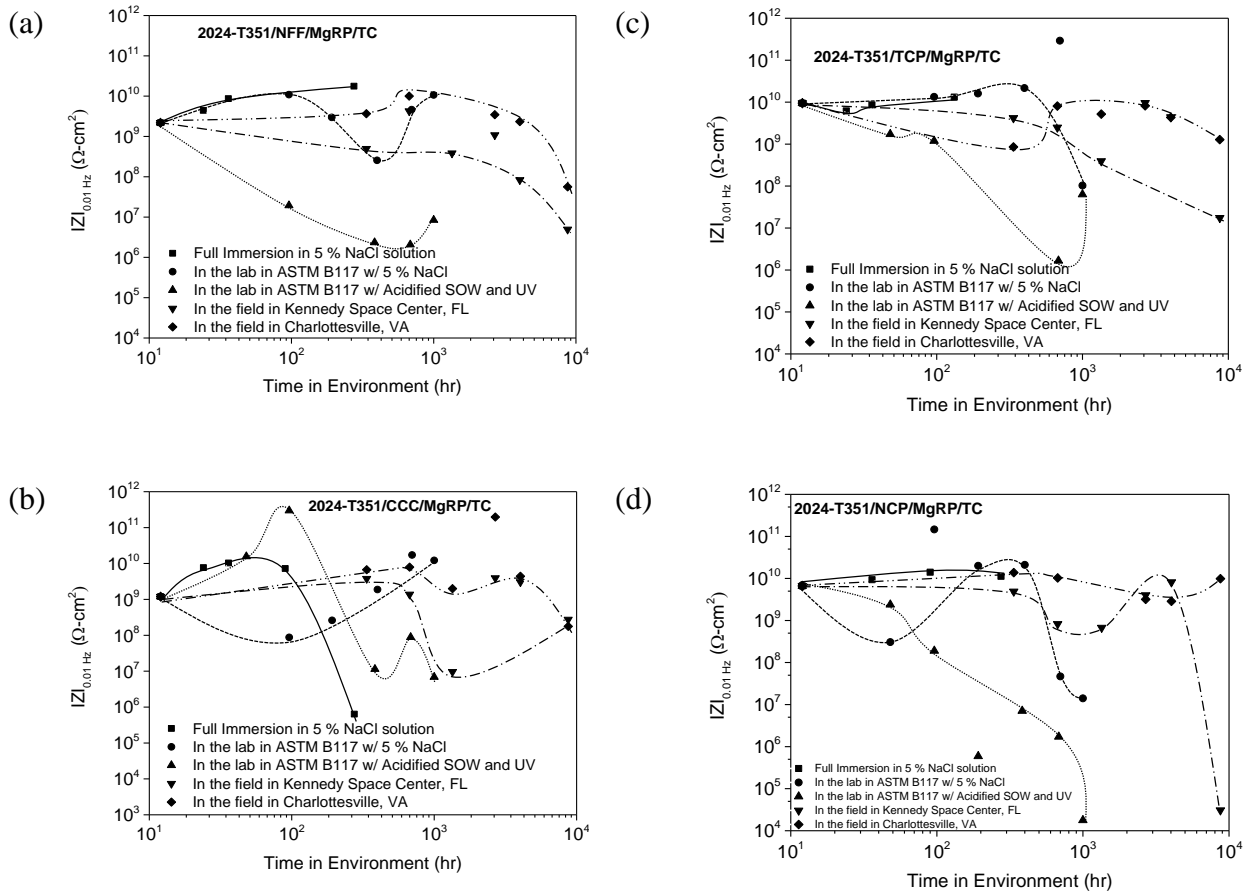
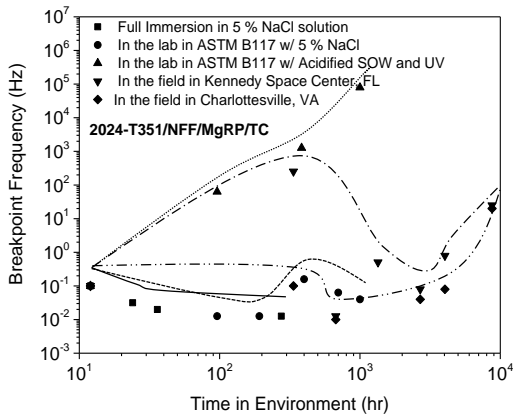
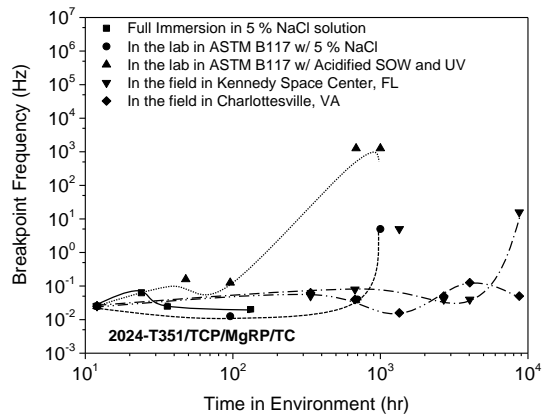


Figure 3.12. Low frequency impedance IZI modulus of AA2024-T351/Pretreatment/MgRP/TC systems at 0.01 Hz vs time in the environments indicated for (a) NFF/MgRP/TC (b) CCC/MgRP/TC (c) TCP/MgRP/TC and (d) NCP/MgRP/TC.

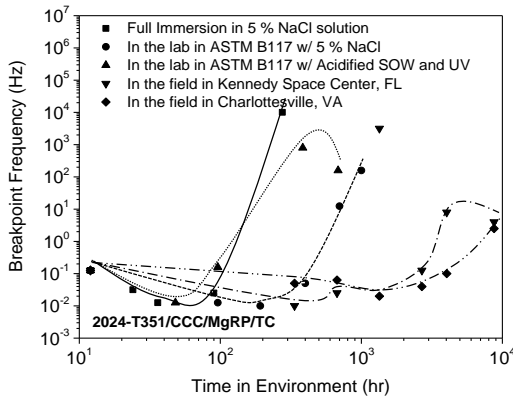
(a)



(c)



(b)



(d)

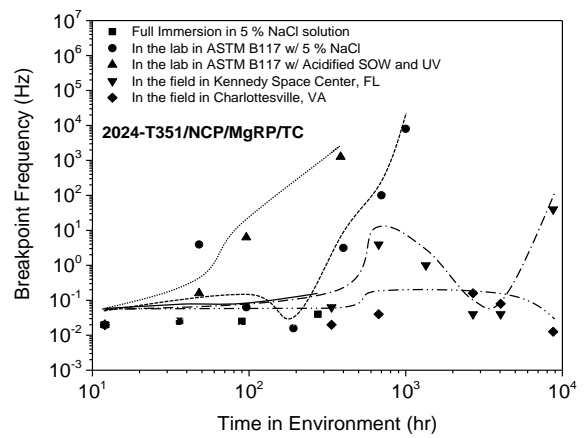
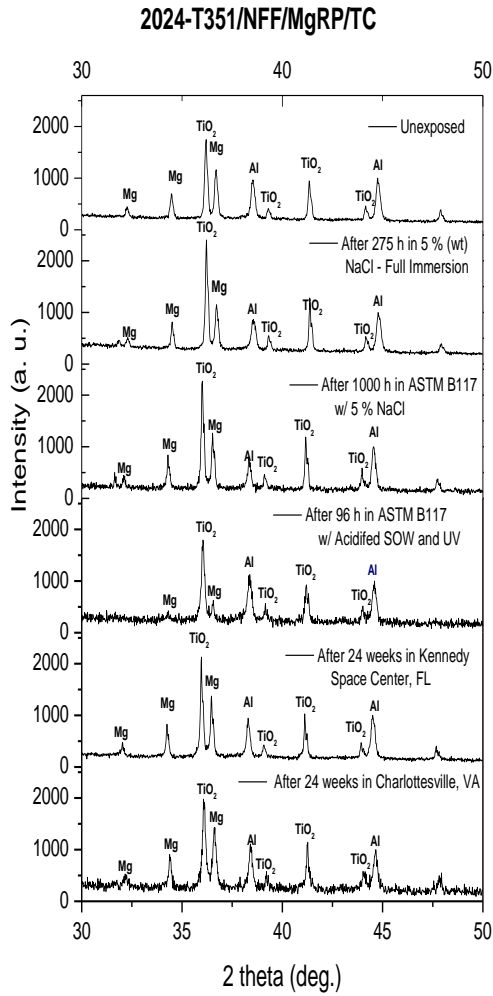


Figure 3.13. High breakpoint frequency ( $F_{bpt}$ ) of AA2024-T351/Pretreatment/MgRP/TC systems vs time in the environments indicated for (a) NFF/MgRP/TC (b) CCC/MgRP/TC (c) TCP/MgRP/TC and (d) NCP/MgRP/TC.

(a)



(b)

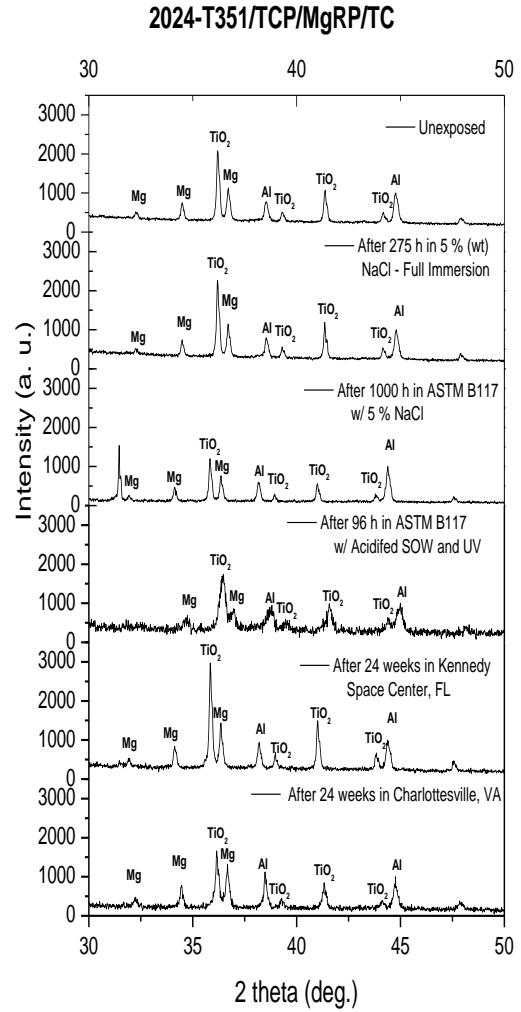
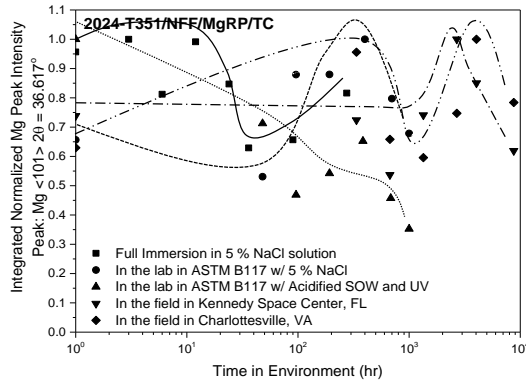
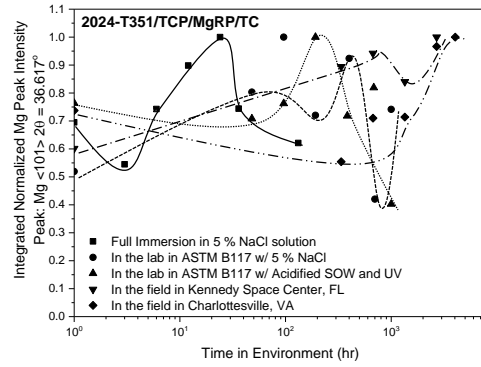


Figure 3.14. Selected XRD spectra of AA2024-T351/Pretreatment/MgRP/TC systems after exposure in the LALT/field environments for (a) NFF/MgRP/TC and (b) TCP/MgRP/TC.

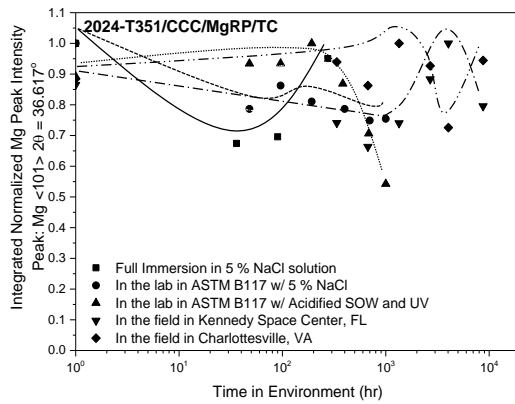
(a)



(c)



(b)



(d)

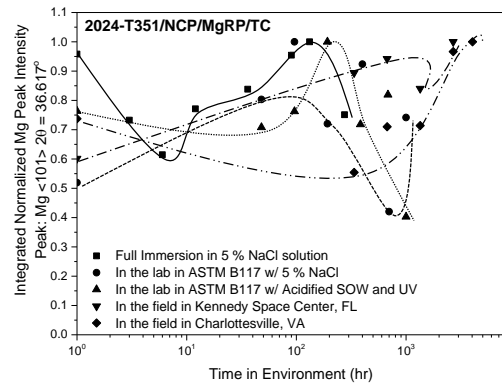


Figure 3.15. The normalized integral XRD intensity for Mg<101> XRD peak of AA2024-T351/Pretreatment/MgRP/TC systems vs time in the environments indicated for (a) NFF/MgRP/TC (b) CCC/MgRP/TC (c) TCP/MgRP/TC and (d) NCP/MgRP/TC.

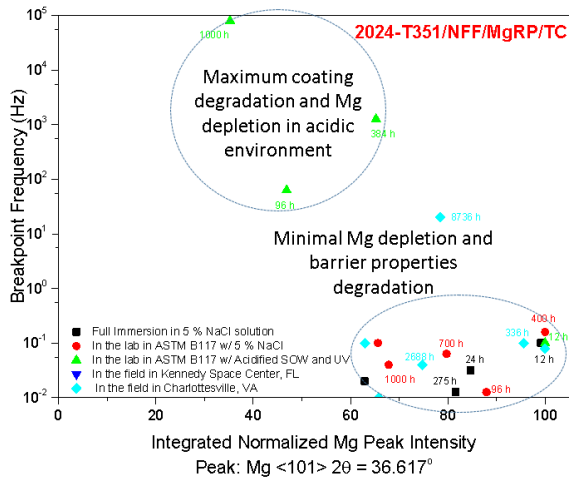
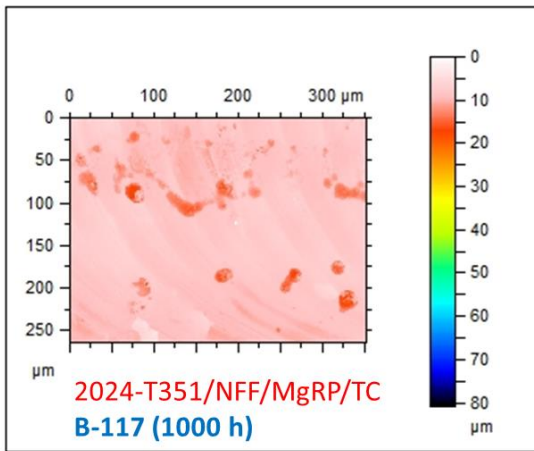


Figure 3.16. Breakpoint Frequency of intact coating after 1 h exposure in 5 % wt NaCl vs The normalized integral intensity for Mg<101>. The time indicates total exposure time in different LALT/Field environments indicated, AA2024-T351/NFF/MgRP/TC after exposure, in Full immersion in 5 % wt NaCl, ASTM B-117 in 5 % wt NaCl, Modified ASTM B-117 with Acidified SOW and UV and Field exposure at CHO and KSC.

(a)



(b)

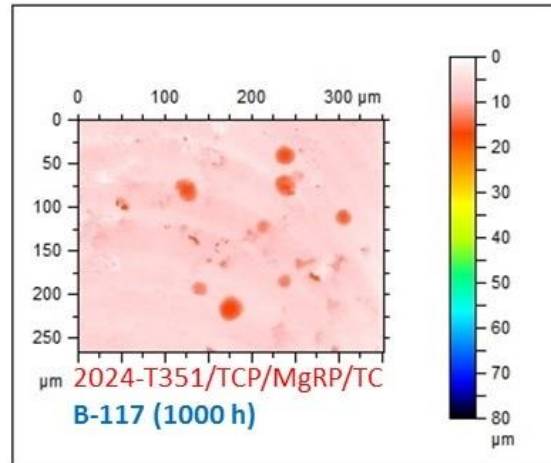


Figure 3.17. Optical profilometry maps of scribe exposing AA2024-T351 in NFF(a)/TCP(b) pretreated AA2024-T351/MgRP/TC after exposure in ASTM B-117 for 1000 h. The 0  $\mu\text{m}$  position (white) on the scale is indicative of the starting material condition before corrosion.

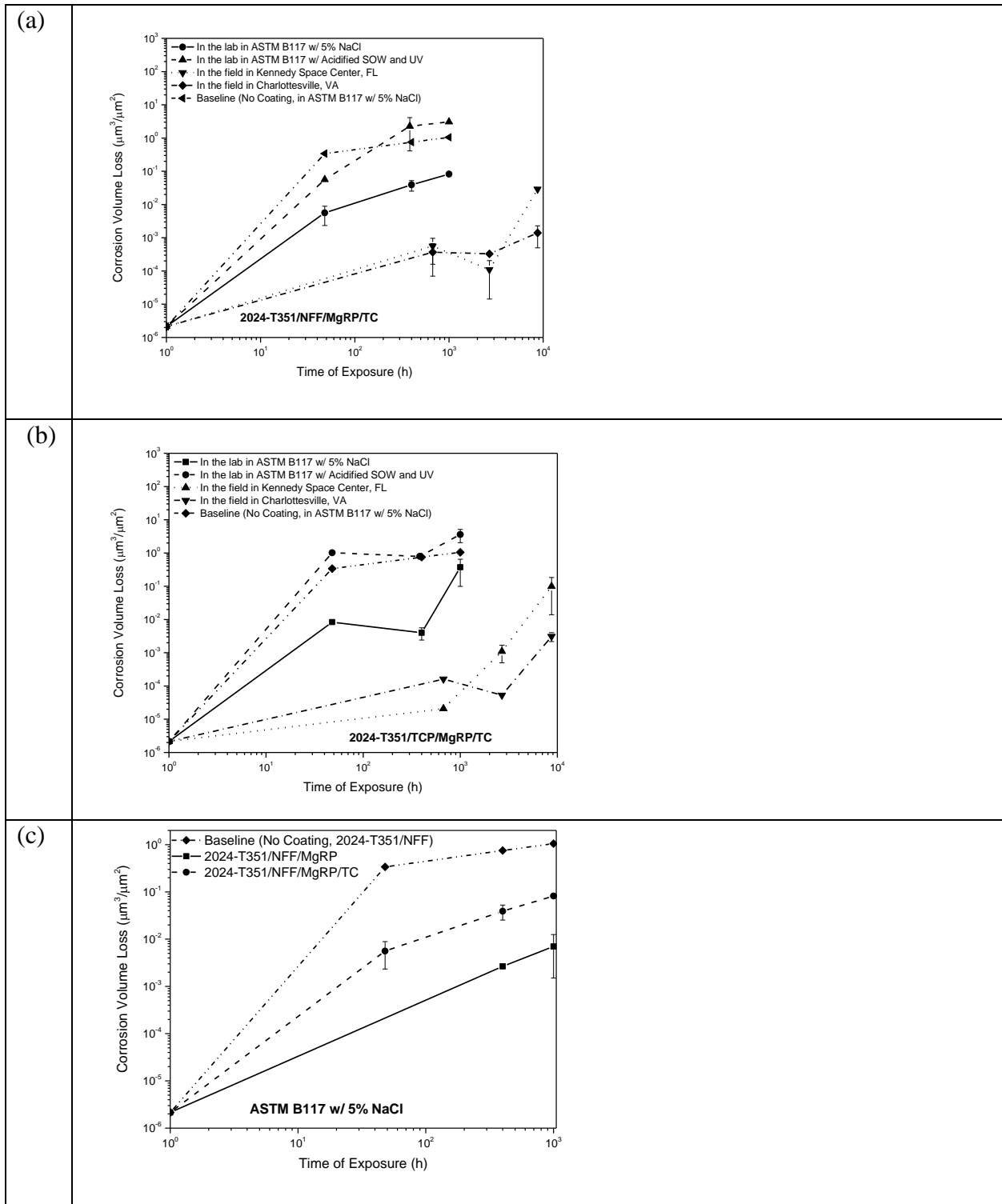


Figure 3.18. Corrosion volume loss of scribe exposing AA2024-T351 in NFF(a)/TCP(b) pretreated AA2024-T351/MgRP/TC as a function of exposure time in in different LALT/field environments indicated. The baseline data is for uncoated AA2024-T351. (c) comparison of non-coated, primer only and primer/topcoat systems for NFF pretreated 2024-T351 in standard ASTM B117 exposure environment.



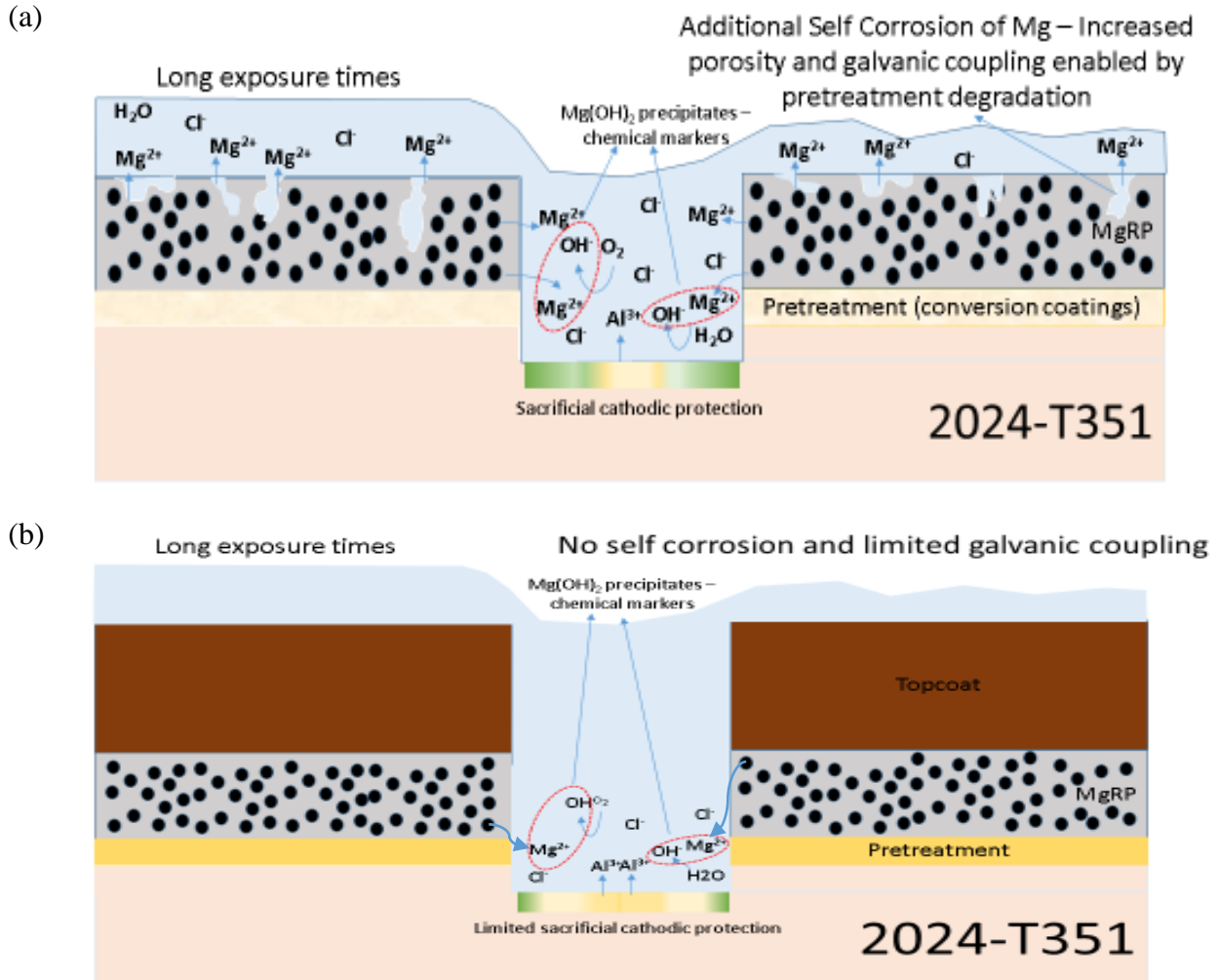


Figure 3.19. Schematics of coating breakdown and galvanic coupling process between AA2024-T351/Pretreatment/MgRP systems and a bare AA2024-T351 scratch (a) Coating degradation of AA2024-T351/Pretreatment/MgRP and (b) Coating degradation of AA2024-T351/Pretreatment/MgRP/TC after long exposure times.

## **4 Performance of a Magnesium Rich Primer on Pretreated 2024-T351 in Selected Laboratory and Field Environments: Anodization Pretreatment**

### **4.1 Abstract**

The effect of anodization on the corrosion protection of AA2024-T351 by Magnesium-rich primer (MgRP) was evaluated in topcoated (TC) and non-topcoated MgRP systems with and without scribes. Protection of remote scratches and global protection by the coating after exposure in selected laboratory and field environments was investigated. Exposure studies focused on the following pretreatments: anodization without sealing (ANS), anodization with hexavalent chromium sealing (ACS) and anodization with trivalent chromium pretreatment (TCP) sealing (ATS). Exposures were conducted in the field under two different environments; at coastal marine site, Kennedy Space Center (KSC), Florida; and at an inland rural site, Birdwood Golf Course in Charlottesville (CHO), Virginia. ASTM B117 with 5 % (wt) sodium chloride, modified ASTM B117 with acidified ASTM substitute ocean water and UV light as well as in full immersion in ambiently aerated 5 % (wt) NaCl solution were compared to field environments. Mg pigment depletion rate, global galvanic protection potential and coating barrier properties were investigated. In systems without a topcoat, all chosen environments except for full immersion resulted in complete depletion of Mg pigment by high self-corrosion rates. Polyurethane topcoats limited the Mg metallic pigment depletion resulting in only partial Mg depletion. In case of ANS and ATS pretreated 2024-T351 with MgRP, there is no initial galvanic coupling as inferred by a more positive global galvanic protection potential and predicted by high pretreatment resistances. Upon prolonged exposure in full immersion, the global galvanic protection potential decreased to more negative potentials with time indicative of galvanic coupling of the 2024-T351 substrate with MgRP. In case of ACS pretreated 2024-T351 with MgRP, there was no initial galvanic coupling.

After initial lowering of global galvanic protection potential, shift back to more positive potential occurred. In case of systems with a topcoat, the global galvanic protection potential is heavily mediated by the organic polymer and there was no significant galvanic coupling between 2024-T351 and Mg in the time frame over which experiments were conducted. Mg was preserved and available for any future sacrificial anode-based cathodic protection. The barrier properties of the MgRP pigmented coating also degraded with time at a higher rate in systems in the absence of topcoat. This result was correlated to UV degradation of the pigmented coating resin and could be reduced with the polyurethane topcoat. SEM/EDS characterization after different ASTM B117/field exposure times indicated that the chemical throwing power ( $Mg^{2+}$ ) increased as a function of exposure time in 2024-T351/ACS/MgRP systems. A topcoat limited the  $Mg^{2+}$  chemical throwing power by mediating both the global galvanic protection potential and Mg transport. Corrosion volume analysis by optical profilometry indicate that the scribe protection was better for sealed anodization pretreatments compared to the case of anodized without sealing based systems.

A manuscript based on this chapter has been submitted to Corrosion Journal as a Full Research Paper, “Performance of a Magnesium Rich Primer on Pretreated 2024-T351 in Selected Laboratory and Field Environments: Anodization Pretreatment.”

Representative author contributions:

B. Kannan: experiments, analysis and interpretation

D. M. Wolanski: SEM/EDS and optical profilometry characterization for selected pretreatments

J. R. Scully: Advisor, analysis and interpretation

## 4.2 Introduction

Precipitation age hardened aluminum alloys due to their heterogeneous microstructure are highly susceptible to localized corrosion and they rely on use of multilayered coatings to provide active corrosion protection, improved adhesion and other specialized functions.<sup>13</sup> The most commonly used active protection system includes corrosion inhibition by hexavalent chromium.<sup>13</sup> Typical formulations consists of chromated pigments enveloped in epoxy resin which release ionic inhibitor species that inhibit corrosion.<sup>13</sup> Carcinogenicity, high handling costs and lack of environmental safety required an accelerated phase-out of hexavalent chromium, concurrent with a push to find effective alternatives.<sup>13,72,74</sup> Over the past few years, a commercial organic coating system containing a Mg-pigmented polymer primer (MgRP) has been developed for the active corrosion protection of aluminum alloys.<sup>72,73,75-77,80,82-85,88</sup> The primary protection mechanisms provided by the MgRP are sacrificial anode-based cathodic protection by Mg metallic pigment in the primer and barrier protection by primer/topcoat polymers.<sup>84</sup> This approach has been well established previously in the design of zinc-rich primers for use on various steel.<sup>78,79,86,89,90</sup>

Previous laboratory accelerated lifecycle tests (LALT) and field exposure studies conducted to determine optimal primer formulation concluded that, approximately 45 % pigment volume concentration Mg provide a balance of moderated sacrificial anode-based cathodic protection, long term barrier protection, and the beneficial characteristics of preserved, isolated clusters of Mg pigment available for the future protection of defects.<sup>84</sup> Environmental degradation of Mg-rich primer on non-film forming (NFF) pretreated AA2024-T351 in selected field and laboratory environment in the presence and absence of the topcoat has been extensively studied.<sup>80,81</sup> Mg pigment depletion rate, galvanic protection potential, barrier properties and scribe protection of the coating were tracked through exposure period in both laboratory and field environments.<sup>80,81</sup>

In addition, the electrochemical throwing power of bare/polymer coated Mg over a simulated bare AA2024-T351 scribe was studied using diagnostic multi-electrode arrays<sup>82</sup> and finite element analysis.<sup>83</sup> In practical applications, several pretreatments are used with aerospace aluminum alloys to improve adhesion between the substrate and the polymer and also to impart additional corrosion protection.<sup>16,19,32,33,36,37,118,121,122</sup>

Anodization is a common pretreatment process in which anodic polarization of aluminum alloy in acidic environment results in formation and growth of anodic oxide film.<sup>33</sup> The oxide film is characterized by an inner thin barrier layer and an outer thick porous layer.<sup>33</sup> The porous nature of the oxide makes the alloy susceptible to corrosion and to improve corrosion resistance; pretreated samples need to be sealed after anodizing.<sup>14,15,17,20,21,27-31,34,38,39,41</sup> The pores are often sealed by active inhibitors such as chromic acid or other active inhibitors to help with corrosion protection.<sup>41</sup> TCP is explored as an alternate for chromic acid for sealing due to its corrosion resistance and adhesion.<sup>35</sup> TCP is also easy in terms of application as it can be applied in ambient conditions for shorter exposure time whereas chromate or water seals require exposure at 190° F to 200° F for longer exposure times.<sup>35</sup> The electrochemically grown oxide layer provides extra barrier protection due to the highly capacitive behavior of Al<sub>2</sub>O<sub>3</sub>.<sup>33</sup> Some sealing might occur during exposure while corrosion progresses.<sup>18,40</sup> The adhesion strength of anodized aluminum to polymers is directly related to the size and density of pores created by the anodization process as mechanical interlocking directly correlates with adhesion strength.<sup>114</sup>

A systematic evaluation of the effect of anodization on the overall performance of coating systems containing MgRP in different lab-accelerated life testing and environmental exposures is of significant interest for the further consideration of MgRP in aerospace applications. The objective of this study was to investigate the MgRP system on AA2024-T351 with various

anodization based pretreatments. The thickness, electrical properties and its role in global galvanic protection potential mediation were previously reported.<sup>77</sup> Degradation of pretreatment, MgRP and topcoat as function of time for different pretreatments were studied using diagnostic tests including accelerated electrochemical cycle test with ex-situ Mg depletion assessment by X-ray diffraction.<sup>77</sup> Environmental degradation of anodization pretreated AA2024-T351 with MgRP with as well as without topcoat in relevant lab and field environments is required to understand the influence of anodization on sacrificial protection and other modes of corrosion protection. Comparison of the behavior of a conversion coating to a non-film forming pretreatment based AA2024-T351/MgRP has been previously reported.<sup>75</sup> Results indicated that all conversion coating based pretreatment exhibited a delayed sacrificial protection due to their resistive nature.<sup>75</sup> The results also suggested that in addition to sacrificial protection, alternate mode of corrosion protection were observed.<sup>75</sup> Finally, chemical corrosion inhibition was also evident in pretreatments involving Cr species. Effect of these pretreatment on sacrificial protection function, global barrier protection and scratch protection are reported herein.

Environmental degradation of different pretreated AA2024-T351 with MgRP and with and without topcoat in relevant lab and field environments was investigated to study the role of anodization based pretreatments in corrosion protection function. Comparison of environmental degradation of conversion coatings to non-film forming pretreatment based coating systems are discussed in this work. The sacrificial anode protection function, barrier properties and alternative protection modes afforded by AA2024-T351/Pretreatment/MgRP and AA2024-T351/Pretreatment/MgRP/Topcoat were characterized by utilizing electrochemical techniques and non-electrochemical post-mortem analysis techniques including X-ray diffraction, Raman spectroscopy, optical profilometry and scanning electron microscopy/energy dispersive

spectroscopy after pertinent lab and field exposures. Effect of pretreatment on Mg depletion, self-corrosion of Mg and scratch protection are reported herein.

### **4.3 Experimental Procedure**

#### **4.3.1 Materials**

AA2024-T351 sheet (1.6 mm thickness) was pretreated with 3 different surface pretreatments for comparison including (i) Anodization – No Sealing (ANS), (ii) Anodization with hexavalent chromium sealing (ACS), (iii) Anodization with Trivalent Chromium Pretreatment (TCP) Sealing (ATS). For anodization pretreatments, a thin-film sulfuric acid anodizing, MIL-A-8625F: Type II pretreatment procedure was followed.<sup>36</sup> Anodized samples had 3 variants, one without sealing, one with hexavalent chromium sealing and one with trivalent chromium process sealing.

A 40 µm primer layer of Mg-rich primer and a 50 µm thick topcoat of Aerodur 5000 high-performance advanced coating, both produced by Akzo Nobel Coatings (Waukegan, Illinois) were applied. The Mg rich primer consist of one part epoxy matrix with Mg metal flake pigment of a diameter 20 µm with pigment volume concentration of 45 % (3rd generation 2100P003, Lot: 493-190). Aerodur 5000 (Gloss white finish product: ECM-G7875) is a two component polyurethane topcoat developed for military application in variety of exposure environments.<sup>128</sup>

#### **4.3.2 Laboratory and Field Exposures of Pretreated AA2024-T351 coated with MgRP and Topcoat**

Mg-rich primer-coated AA2024-T351 panels were exposed to salt spray in a QFog Cyclic Corrosion Tester (QFog model CCT 1100†) according to ASTM B117<sup>141</sup> for at least 1000 hours. During a second exposure, the standard ASTM B117 salt fog was altered such that the standard 5 % (wt) NaCl solution electrolyte was replaced with acidified ASTM substitute ocean water<sup>135,136</sup> ([SOW] pH = 3.2±0.2) and ultraviolet radiation. The salt fog exposure cabinet was modified to

include four hanging ultraviolet A (UVA), fluorescent lights. The UVA lamps (Q-Lab Corporation model UVA-340) were chosen to simulate sunlight in the critical short-wave UV region from 365 nm down to the solar cutoff of 295 nm. Artificial seawater was produced according to ASTM D-1141<sup>135</sup> and acidified by the addition of 10 mL of glacial acetic acid per 1 L of salt solution following ASTM G-85 A3.<sup>136</sup> In all salt fog exposures reported in this report, ambient air was supplied to the chamber and to the atomizer for fog production. Ambient concentrations of CO<sub>2</sub> were measured in-situ to be approximately 425 ppm. Other ambient gas concentrations were not measured. Natural weathering exposures of Mg-rich primer-coated AA2024-T351 panels were conducted at a coastal marine site 30 m from the high tide line at Kennedy Space Center (KSC) Corrosion Technology Lab in Titusville, FL (28.6°N, 80.6°W, elevation = 0 m) and a rural inland site at Birdwood Golf Course in Charlottesville (CHO), VA (38.0402°N, 78.54.27°W, elevation = 172 m). The sample test racks at KSC face the ocean and the one in CHO face south. During exposure, panels were mounted on unsheltered atmospheric test racks with full exposure to natural elements according to ASTM G-4.<sup>137</sup> Pertinent environmental parameters for KSC such as mean temperature, mean relative humidity, mean dew point, mean precipitation rate, precipitation pH and dry chloride deposition rate are reported elsewhere.<sup>75</sup>

#### **4.3.3 Post-mortem Surface Analysis of the Coating and the Scribe**

All full-immersion studies as well as post-mortem analysis after salt fog and field exposures reported herein were conducted in quiescent 5 % (wt) NaCl (pH: 6.9±0.4) open to laboratory air. Potential control during electrochemical experiments was maintained using a Gamry Potentiostat (Ref 600/ PCI4)† with computer interface software. A saturated calomel electrode (SCE) and a Pt mesh were used as the reference and counter electrode, respectively. The area tested was far away (≥ 2 cm away) from scribe. A typical EIS scan was acquired in sine sweep mode from 100 kHz to

0.01 Hz with 6 points per decade. MgRP and MgRP/TC coated panels were scanned with an AC amplitude of 80-100 mV to reduce noise. The tests were conducted in quiescent 5 % (wt) NaCl, as discussed above, after 1 hour exposure at open circuit for MgRP coated panels and 12 hour exposure for MgRP/TC coated panels.

X-ray diffraction (XRD) was conducted to characterize global Mg depletion as a function of exposure time in different lab and field environments. A Panalytical X'pert powder diffractometer utilizing a Cu-K $\alpha$  source was utilized for measurements. All samples were scanned continuously from 30 degrees to 50 degrees at 5 degrees per minute. XRD measurements of pristine and environmentally exposed samples were made on panels far away ( $\geq 2$  cm away) from any edge or scribe, presumed to be representative of global coating degradation. XRD obtained from Mg-rich-coated panels were normalized by the face-centered cubic (fcc) Al (200)  $2\theta = 44.74^\circ$  peak from the underlying substrate. Peak normalization and integration was performed with Origin Lab 7.5 software. The lower detection limit for crystalline phases was approximately 3-5 % of the sample by volume.

Corrosion products formed after environmental exposure were characterized using Raman spectroscopy. Raman spectroscopy was conducted using a Renishaw InVia Raman Microscope. Measurements were conducted using a 514 nm laser at 1 - 50% power under the 20x objective with a 3000 1/mm (vis) grating. Scans with 15 second exposure time were taken with 2 accumulations under standard confocality. If Raman spectra showed heavy fluorescence then a pre-measurement sample bleaching was conducted where the sample was subjected to laser exposure under the aforementioned conditions for 450 to 600 seconds prior to taking the spectra. For all measurements, prior calibration of Raman spectroscopy was performed using a silicon standard.

Scanning electron microscopy (SEM) and energy dispersive spectroscopy (EDS) were used for post-mortem analysis of corrosion products in the scribe. A field emission Quanta 650 SEM was used to conduct these investigations. For EDS, Oxford XMax 150 detector was utilized. A working distance of 15 mm and an accelerating voltage of at least 3 times the energy of the maximum characteristic peak of interest were used (~15 kV). At an accelerating voltage of 15 kV, EDS has a penetration depth of roughly 2 to 5  $\mu\text{m}$  into the materials investigated in this study. Elemental maps and line profiles were collected and EDS analysis was performed using Aztec image analysis software.

Optical profilometry was conducted using a Zygo optical profilometer (Newview 7200/7300 model). The environmentally exposed samples were first exposed to concentrated nitric acid for 15 minutes to remove corrosion products present in the scribe as per the ASTM G-1 Standard.<sup>138</sup> Image refinement and pit volume calculation was performed using MountainsMaps imaging topography software.<sup>142</sup>

## **4.4 Results**

### **4.4.1 Evaluation of the Performance of a MgRP without Topcoat on Pretreated 2024-T351 after Exposure in Selected Lab and Field Environments: Global Protection Assessment of Global Barrier Degradation**

The low frequency EIS at 0.01 Hz and high breakpoint frequency data for the AA2024-T351/Pretreatment/MgRP system as a function of exposure time in different laboratory and field environments are summarized in Figures 4.1 and 4.2. In AA2024-T351/ANS/MgRP systems, long terms exposure (1 year) in field led to lowering of low frequency impedance by 2 orders of magnitude (Figure 4.1a). Similarly, after 1000 h exposure in standard ASTM B117, the low frequency impedance decreased by 3-4 orders of magnitude indicative of significant barrier

degradation (Figure 4.1a). However, assessment of barrier degradation of AA2024-T351/ANS/MgRP was difficult in intermediate exposure times in LALT/Field environments and full immersion. Alternate increase and decrease in low frequency impedance values as a function of exposure time could be attributed to alternate sealing of highly porous oxide layer by corrosion products and creation of ionic pathway by quick degradation of oxide layers in pores (Figure 4.1a). Breakpoint frequency increased with exposure times in ASTM B117 indicative of pore development (Figure 4.2a). However, in field and full immersion, the break point frequency increased and decreased alternatively with exposure time (Figure 4.2a). In AA2024-T351/ACS/MgRP systems, low frequency impedance (Figure 4.1b) and high breakpoint frequency (Figure 4.2b) increased and decreased, respectively, with increasing exposure times in full immersion, LALT and field environments. This could be attributed to better sealing of anodized layers with increasing exposure times. After very long exposure times in field, barrier properties of coating degraded indicative of complete degradation of primer polymer by UV light exposing the underlying substrate (Figure 4.1b). AA2024-T351/ATS/MgRP systems exhibited lowering of low frequency impedance by 2-3 orders of magnitude in ASTM B117 and modified ASTM B117 environment and 1-2 order of magnitude in full immersion (5 % wt NaCl) and field exposures (Figure 4.1c). Breakpoint frequency increased with exposure time in ATS systems indicative of significant pore development (Figure 4.2c).

### **Assessment of Global Magnesium Depletion**

X-ray spectra of AA2024-T351/ACS/MgRP after exposure in selected LALT/field environments are shown in Figure 4.3. Elemental Mg (HCP) and Al (FCC) peaks were observed in initial spectra. The X-ray spectra indicates that Mg pigment in the MgRP was completely depleted after 96, 1000 h and 8736 h in modified ASTM B117, ASTM B117 and field exposure (KSC/CHO),

respectively (Figure 4.3). This indicates that self-corrosion of Mg occurs in all chosen environments in the absence of the topcoat. Absence of any additional XRD peaks after LALT/field environment indicate that either not enough corrosion products were produced to reach the detection limits of the diffractometer or the products formed are not crystalline (Figure 4.3). Elemental Mg depletion was tracked as a function of exposure in selected LALT/field environments and results are summarized in Figure 4.4. Mg depletion occurred at different rates in different environments and based on the rate of depletion, following ranking is obtained. Full immersion (5 % NaCl) < KSC~CHO < ASTM B117 < Modified ASTM B117.

### **Correlation of Global Mg depletion to Global Galvanic Protection Potential and Barrier Properties of the Coating**

The global galvanic protection potential of the AA2024-T351/ANS/MgRP as function of global Mg available after exposure in selected LALT/field environments is indicated in Figure 4.5a.

The average open circuit potential of AA2024-T351 and Mg in ambiently aerated 5 % (wt) NaCl solution are -0.71 V and -1.48 V respectively. For ANS pretreatment based MgRP systems, the global galvanic protection potential is initially more positive compared to the OCP of bare AA2024-T351 (Figure 4.5a). This indicates that no galvanic coupling initially occurs between AA2024-T351 and MgRP. However, upon prolonged exposure the global galvanic protection potential shifted to more negative values indicative of galvanic coupling. The porous nature of oxide films in the absence of sealing could bring about lowering of resistance thereby enabling galvanic coupling (Figure 4.5a). The global protection potential reached the OCP of AA2024-T351 after long exposure times which can be correlated to significant depletion of Mg (Figure 4.5a). The global galvanic protection potential of AA2024-T351/ACS/MgRP as a function of global Mg available after exposure in selected LALT/field environments is indicated in Figure

4.5b. For ACS pretreatment based MgRP systems, the global galvanic protection potential is initially more positive compared to the OCP of bare AA2024-T351. Upon prolonged exposure, the global protection potential initially decreased but shifted back to more positive potentials indicative of temporary galvanic coupling (Figure 4.5b). This could be due to improved sealing of anodized layers with increasing exposure times. This is further corroborated with high breakpoint frequency trends (Figure 4.6) which initially shifted to higher values and then decrease confirming improved barrier properties with increasing exposure time. Unlike the ASTM B117 and full immersion, this trend is not evident in field environments (Figure 4.6). This might be due to UV degradation of the epoxy polymer which resulted in exposure of underlying pretreatment directly to atmosphere.

#### **Characterization of Corrosion Products**

Raman spectroscopy was conducted for AA2024-T351/ACS/MgRP samples after exposure in pertinent lab and field environments to study the nature of the corrosion products formed. After LALT exposure in standard ASTM B117 for 1000 h, a prominent peak corresponding to  $\text{MgCO}_3$  appeared at  $1116\text{ cm}^{-1}$  (Figure 4.7a). Similar trends were observed in field exposures at KSC (Figure 4.7b). This indicates that due to ambient concentration of  $\text{CO}_2$  in atmosphere and ASTM B117 testing chamber, any Mg corrosion product that is formed on the surface of primer was converted into  $\text{MgCO}_3$ . It is to be noted that our previous reported work of MgRP with a non-resistive pretreatment indicated similar trends. The inner layers of the primer might still have  $\text{Mg(OH)}_2$  as another possible corrosion product as reported elsewhere.<sup>143</sup>

#### **4.4.2 Evaluation of the Performance of a MgRP without Topcoat on Pretreated AA2024-T351 after Exposure in Selected Lab and Field Environments: Scribe Protection**

##### **Assessment of Scribe Protection: Mg Corrosion Products Redeposition**

Figure 4.8a shows EDS map of a representative scribe and adjacent MgRP before exposure in any lab and field environments. During the exposure in LALT and field environment, the Mg depleted from primer can be transported over the scratch and precipitated in the scratch thereby providing additional modes of corrosion protection. Figure 4.8b and 8c showed EDS map of ACS pretreated AA2024-T351/MgRP after different ASTM B117 exposure times. Mg intensity in the scribe increased as function of exposure time and corresponding intensity of Mg in the primer near the scribe edge decreased as indicated in EDS line profiles (Figure 4.9a). Integral intensity of Mg EDS line profiles across scribe and primer as function of exposure time in ASTM B117, KSC and modified ASTM B117 are summarized in Figure 4.9b-d. Preliminary results indicate that Mg redeposition is not greatly inhibited by the presence of additional resistance due to the pretreatments. The presence of  $\text{Mg}(\text{OH})_2$  in the scribe indicate a shift in local pH upon Mg dissolution as well as  $\text{OH}^-$  production due to oxygen reduction reaction which all result in Mg deposition in the scribe. The increase in Mg EDS intensity as function of exposure time in ASTM B117 and KSC confirms the transfer of Mg to scribe and its chemical precipitation. Field exposure studies conducted at CHO did not detect Mg corrosion products in the scribe. The low pH which is characteristic of this environment, resulted in dissolution of Mg corrosion products. The additional modes of corrosion protection provided by the Mg corrosion products is reported elsewhere.<sup>143</sup>

### **Assessment of Scribe Protection: Corrosion Volume Loss Analysis**

Optical profilometry of scribes exposing AA2024-T351 in AA2024-T351/Anodization (ANS/ACS/ATS)/MgRP after exposure in ASTM B117 for 1000 h is indicated in Figure 4.10. All corrosion volume loss maps were representative of regions less than 50 micrometers from pretreatment edge to scribe center. Comparison of three anodization based pretreatments after exposure in ASTM B117 for 1000 h indicated that ACS provides very strong scribe protection indicated by fewer and less deep pits. ATS exhibit moderate scribe protection while ANS exhibited the least protection. ACS and ATS providing better corrosion protection than ANS could be explained by the leaching of anionic species from hexavalent chromium or trivalent chromium sealed layers. Corrosion volume loss increased as a function of exposure time in all chosen environments. Figure 4.11a-c summarizes the corrosion volume loss for AA2024-T351/MgRP with different anodization based pretreatments. Due to low pH ( $3.2 \pm 0.2$ ), the modified ASTM B117 environment exposed scribe suffered a very large amount of localized corrosion resulting in higher corrosion volume loss in comparison to control experiment performed using uncoated AA2024-T351 scribed panels exposed to standard ASTM B117. In all the other chosen environments including ASTM B117 and field, the coated samples perform better than control experiments indicative of corrosion protection. In terms of severity of the environment based on corrosion volume loss in scribes, the following rank was found. CHO~KSC < ASTM B117 < Control (ASTM B117 for AA2024-T351 without coating) < Modified ASTM B117.

#### **4.4.3 Evaluation of the Performance of a MgRP with Topcoat on Pretreated AA2024-T351 after Exposure in Selected Lab and Field Environments: Global Protection Assessment of Global Barrier Degradation**

The low frequency impedance and high breakpoint frequency of AA2024-T351/Anodization/MgRP/TC as function of exposure time in selected laboratory and field environments are indicated in Figure 4.12 and 4.13. Low frequency impedance at 0.01 Hz did not indicate significant coating degradation in full immersion and standard ASTM B117 exposure (Figure 4.12). There is slight degradation in barrier properties of MgRP/TC after 1 year in field exposures (Figure 4.12). Significant degradation in barrier properties of the coating was seen in the modified ASTM B117 environment as evident from both low frequency impedance (Figure 4.12) and high breakpoint frequency (Figure 4.13) trends.

##### **Assessment of Global Magnesium Depletion**

X-ray spectra of AA2024-T351/ACS/MgRP after exposure in selected LALT/field environments are shown in Figure 4.14. Elemental Mg (HCP), rutile TiO<sub>2</sub> (HCP) and Al (FCC) peaks were observed in initial spectra (Figure 4.14). There is no significant depletion of Mg in full immersion, ASTM B117 and field exposures (Figure 4.15). However, there is significant depletion of Mg in modified B117 environment (Figure 4.15). No crystalline corrosion products were detected for the time of exposure in different environments. Similar Mg depletion trends were observed in other variants of anodization pretreatments and the depletion trends are summarized in Figure 4.15.

## **Correlation of Global Mg depletion to Global Galvanic Protection Potential and Barrier Properties of the Coating**

The global galvanic protection potential anodization pretreated AA2024-T351/MgRP is heavily mediated by the presence of resistive topcoat layers. Mg pigment remains in the MgRP and is not coupled to AA2024-T351 substrate and hence not used up as could be inferred from global galvanic protection potential and Mg XRD intensity. The global breakpoint frequency of the anodization pretreated AA2024-T351/MgRP as a function of global Mg showed neither appreciable coating degradation nor Mg depletion in full immersion, standard ASTM B117 and field environments. Modified ASTM B117 showed significant depletion of Mg as well as barrier properties degradation.

### **4.4.4 Evaluation of the Performance of a MgRP with Topcoat on Pretreated AA2024-T351 after Exposure in Selected Lab and Field Environments: Scribe Protection Assessment of Scribe Protection: Mg Corrosion Products Redeposition**

EDS elemental Mg maps of ACS pretreated AA2024-T351/MgRP/TC after different B117 exposure times showed no significant Mg presence in the scribe. The limited scratch protection is due to topcoat polymers which suppress the Mg reaction, release and transport to the scribe. Similar observations were made for ACS pretreated AA2024-T351/MgRP/TC exposed to modified ASTM B117 and KSC. Although Mg transport is limited by topcoat polymers, Mg pigment is still preserved and available for sacrificial protection and Mg transport to scribe after significant degradation of topcoat.

#### **Assessment of Scribe Protection: Corrosion Volume Loss Analysis**

Optical Profilometry maps of scribe exposing AA2024-T351 in AA2024-T351/Anodization (ANS/ACS/ATS)/MgRP/TC after exposure in ASTM B117 for 1000 h are indicated in Figure

4.16. Comparison of three anodization based pretreatments after exposure in ASTM B117 for 1000 h indicated that ACS provides very strong protection indicated by fewer and less deep pits. ATS exhibit moderate corrosion protection while ANS exhibited the least protection. Better corrosion protection with ACS and ATS compared to ANS can be explained by the leaching of anionic species such as hexavalent chromium or trivalent chromium from the sealed layers. Figure 4.17a-c summarizes the corrosion volume loss for 2024-T351/MgRP with different anodization based pretreatments. Due to low pH ( $3.2 \pm 0.2$ ), the modified ASTM B117 environment exposed scribed produced a significant amount of localized corrosion resulting in higher corrosion volume in comparison to control experiment performed on uncoated AA2024-T351 scribed panels exposed to standard ASTM B117. ACS pretreated AA2024-T351/MgRP/TC performed slightly better than other anodization based pretreatments. However, the corrosion volume loss values are significantly higher in comparison to non-topcoated conditions indicating limited scribe protection. In terms of severity of the environment, they are ranked in the following order. CHO~KSC < ASTM B117 < Control (ASTM B117 for 2024-T351 without coating) < Modified ASTM B117.

## **4.5 Discussion**

### **4.5.1 Understanding the Effect of Sealing in Global and Scribe Protection of Anodized MgRP Systems**

MgRP systems without anodization sealing showed no galvanic protection at beginning of exposure but exhibited delayed sacrificial protection in both LALT and field environments as indicated by global galvanic protection potential trends (Figure 4.5a). At longer exposure times, the global galvanic protection potential shifted above the OCP of AA2024-T351 indicating no driving force for galvanic protection due to self-sealing of anodized layer by corrosion products. Anodized systems with hexavalent chromium sealing showed very limited galvanic protection for

the entire exposure time in different LALT and field environments as indicated by global protection potential trends (Figure 4.5b). This could be due to improved sealing by Cr inhibitors which then enhanced barrier properties and limited galvanic protection. The scribe protection could be due to combination of delayed sacrificial anode protection by slow resistance decreases followed by galvanic coupling with MgRP and protection of scratch by Mg(OH)<sub>2</sub> redeposition (Figure 4.8). Corrosion volume loss indicate that scribe protection is better in sealed systems compared to non-sealed coating stack-ups (Figure 4.10). This indicates that there could be some additional modes of protection due to leaching and supplying of Cr<sup>6+</sup> species. The hexavalent Cr based sealing exhibited better scratch protection compared to trivalent chromium based sealing. Topcoated systems are characterized by heavy mediation of galvanic protection potential, limited Mg self-corrosion (Figure 4.15), limited Mg transport to scribes and moderate scratch protection (Figure 4.17).

#### **4.5.2 Comparison of Anodization with Conversion Coating and Non-film Forming**

##### **Pretreatment:**

AA2024-T351/NFF/MgRP exhibited sacrificial protection from the beginning of exposure time in all chosen environments.<sup>75</sup> Similar studies conducted for AA2024-T351/TCP/MgRP indicated that due to presence of resistive layer, the system exhibited delayed sacrificial protection.<sup>75</sup> AA2024-T351/ANS/MgRP is characterized by initially high galvanic protection potential and delayed sacrificial protection in intermediate exposure times similar to TCP based systems. However, upon prolonged exposure the sacrificial protection capabilities were affected due to hypothesized self-sealing of anodized systems without sealing. Similar studies conducted for AA2024-T351/ACS/MgRP indicated very limited sacrificial protection as could be inferred from global galvanic protection potential trends. This might be due to improved sealing of anodized layers by

Cr<sup>6+</sup> which increases the barrier properties and henceforth produces a more positive global galvanic protection potential. In presence of topcoat, all system showed highly mediated galvanic protection potential and no global galvanic protection. Corrosion volume loss using optical profilometry was directly used to compare the performance of pretreatments. For non-topcoated systems, after 1000 h exposure time in ASTM B117, the corrosion volume loss showed below protection trends, NFF > ACS > TCP~ATS > ANS > Control.

There is no delayed sacrificial protection in NFF pretreated MgRP.<sup>75</sup> ACS showed limited sacrificial protection, but the hexavalent Cr based species leaching could provide significant corrosion protection (Figure 4.11b). TCP<sup>75</sup> and ATS which both have trivalent Cr based species showed moderate corrosion protection (Figure 4.11c). Whereas, ANS which exhibited a delayed sacrificial protection and no inhibitor species showed the least scribe protection (Figure 4.11a). All chosen systems performed better than control studies conducted for scribed AA2024-T351/NFF without coating exposed in ASTM B117 for 1000 h. While NFF and ACS showed 150 and 30 times lower corrosion volume loss, other chosen pretreatments had lowering of corrosion volume loss by a factor of 4-10 times.

Similar profilometry studies showed following protection trends for top-coated systems, NFF > ACS > TCP > ATS > ANS.

The corrosion volume loss in topcoated systems are higher in comparison to non-topcoated systems. It is to be noted that in topcoated systems, the transport of Mg to scribe is very limited due to excellent barrier properties of topcoated system. Hence only sacrificial protection and inhibitor release could play major roles in corrosion protection. In that context, it could be concluded that NFF and TCP based MgRP/TC systems have sacrificial protection as major protection mechanism for scribe protection, whereas ACS pretreated systems with MgRP/TC

might have inhibitor release from pretreatment as major mode for corrosion protection. ANS and ATS pretreated system performed poorly in comparison to control, hence may not have any active mode of corrosion protection.

### **4.5.3 Future Work**

In light of findings in the conversion coating pretreated MgRP systems reported elsewhere and anodized system pretreated MgRP systems reported here, three primary modes of corrosion protection of scribe could be inferred in addition to global barrier protection. Sacrificial protection by Mg pigment, corrosion inhibition by Mg corrosion products redeposition and corrosion inhibition by another inhibitor such as  $\text{CrO}_4^{2-}$  leaching from pretreatment all play major role in scribe protection. While the sacrificial protection aspects of MgRP including throwing power has been discussed in current and previous work, there is a need to explore other protection mechanisms. Role of Mg corrosion products in scribe protection can be studied by deposition of  $\text{Mg}(\text{OH})_2$  films on AA2024-T351 to study its effect on corrosion kinetics of scribe. The test methodologies developed for studying MgRP systems with and without topcoat will be utilized to study the performance of AA2024-T351/Pretreat in LALT and field environments without coating. Since the acidified ASTM B117 environment showed rapid coating degradation in comparison to ASTM B117 and field environments, this method is too harsh unless a high  $\text{Cl}^-$ , high acid environments is encountered. Future LALT studies should consider a different variation of modified ASTM B117 with SOW and UV. This modification should be compared with standard ASTM B117 and field environments. To further understand and predict the throwing power of Mg in presence of different pretreatments, finite element analysis should be modified to include the effect of corrosion inhibitors. Since the presence of topcoat largely mediate the global galvanic

protection potential and scribe protection capabilities, different topcoats with various chemistries and barrier properties also need to be explored.

#### **4.6 Conclusions**

- Full immersion in ambiently aerated 5% NaCl solution resulted in partial depletion of metallic Mg pigment in the AA2024-T351/pretreatment/MgRP after 543 hours. Exposure in ASTM B117 in 5% NaCl, and Modified ASTM B117 in ASTM acidified artificial seawater with UV all resulted in complete depletion of metallic Mg pigment in the AA2024-T351/pretreatment/MgRP far from the scribe after 1000 hours and 96 hours, respectively. Acidified ASW/UV environment is not recommended to assess field performance. Standard ASTM B117 environment might still be representative of more aggressive field environments such as Pt. Judith.
- Field exposures in CHO and KSC also resulted in complete depletion of metallic Mg pigment in the AA2024-T351/pretreatment/MgRP far from the scribe after 1 year of exposure. It also resulted in complete degradation of polymer by UV in field environments. Testing without a topcoat is also not recommended to assess field performance.
- The global galvanic protection potential of the AA2024-T351/NFF/MgRP system, with respect to remote scratches, increased slightly with exposure time in each environment, from initial values of approximately -1.0 V vs. SCE to -0.7 V vs. SCE after extensive environmental exposure. These values are between the open circuit potentials of bare AA2024-T351 (-0.7 V vs. SCE) and bare Mg (-1.6 V vs. SCE) and could be predicted by mixed potential theory. This suggests that Mg pigment is both electrically and ionically connected to the AA2024-T351 can provide immediate sacrificial galvanic protection to the AA2024-T351 substrate.

- The global galvanic protection potential of the AA2024-T351/ANS/MgRP and AA2024-T351/ATS/MgRP system, with respect to remote scratches, was initially more positive and it decreased after initial exposure times and then shifted back to more positive values after longer exposure times. This suggests that Mg pigment that is not initially electrically connected to the AA2024-T351 because of resistive pretreatments can provide delayed sacrificial galvanic protection to the AA2024-T351 substrate as the pretreatment degrades.
- The global galvanic protection potential of the AA2024-T351/ACS/MgRP system, with respect to remote scratches, was initially above the open circuit potential of AA2024-T351 and then it shifted back to more positive values after longer exposure times. This suggests that Mg pigment that is not electrically connected to the AA2024-T351 until long environmental exposure times because of resistive nature of the pretreatment and improved sealing with increasing exposure time. Henceforth there is very limited sacrificial galvanic protection to the AA2024-T351 substrate.
- The low frequency EIS measurement and breakpoint frequency analysis of AA2024-T351/ANS/MgRP indicate rapid degradation of coating barrier properties in ASTM B117 and Modified ASTM B117 in ASTM acidified artificial seawater with UV environments. The barrier properties degradation are relatively moderate in full immersion in ambiently aerated 5% NaCl solution and Field exposures in CHO and KSC.
- The low frequency EIS measurement and breakpoint frequency analysis of AA2024-T351/ACS/MgRP indicate improved barrier properties in ASTM B117 and full immersion in ambiently aerated 5% NaCl solution. Field exposures in CHO and KSC also showed similar trends although deposition rate of aerosol species and mean pH are very different

under those conditions. After very long exposure time the barrier properties degraded primarily due to UV weathering of primer polymer exposing underlying substrate.

- Raman spectroscopy of non-topcoated conditions indicate that Mg in the MgRP is converted to an outer layer of  $\text{MgCO}_3$  and possible inner layer of  $\text{Mg(OH)}_2$  both in LALT and field exposures. Role of solution chemistry on  $\text{Mg(OH)}_2$  vs  $\text{MgCO}_3$  deposition and their degree of protection would be of interest for future work.
- The chemical throwing power measurements using SEM/EDS suggest that for all chosen pretreatments, AA2024-T351/pretreatment/MgRP system could protect the entire half width of the scribe ( $\sim 350 \mu\text{m}$ ) of the scribe in standard ASTM B117 and field exposures at KSC as indicated by magnesium hydroxide detection across the scribe. Modified ASTM B117 in ASTM acidified artificial seawater with UV environment indicated initial deposition of  $\text{Mg(OH)}_2$  after 48 h followed by dissolution of Mg corrosion products as well as leaching of Mg from AA2024-T351 substrate. Field exposures studies conducted at CHO indicated no presence of Mg corrosion products. The acidic nature of CHO environment resulted in dissolution of Mg corrosion products.
- Corrosion volume loss measured using optical profilometry increased as a function of exposure time in all environments. The rate of increase of pit volume was higher in acidified ASTM B117 modified with SOW/UV environment and the least in field environments with moderate protection in ASTM B117. Compared to bare AA2024-T351, AA2024-T351/Anodization/MgRP has lower corrosion volume loss for all chosen environments. AA2024-T351/ACS/MgRP exhibited excellent scribe protection while ATS and ANS based systems exhibited moderate and poor protection, respectively.

- The Aerodur 5000 topcoat was observed to severely mediate the depletion of Mg pigment from the MgRP as well as the galvanic protection capabilities in all exposure environments studied as compared to identical environmental exposures of non-topcoated samples. The barrier properties degradation was also significantly reduced in presence of topcoat in all environments. Only the Modified ASTM B117 in ASTM acidified artificial seawater with UV environment resulted in coating degradation due to acidic environment. The topcoat suppress the scribe protection by heavily mediating the galvanic protection capabilities and Mg transport. Therefore, topcoat systems have a lower fraction of corrosion products and relative higher corrosion volume loss compared to AA2024-T351/Pretreatment/MgRP system in similar environments. Among topcoated systems, AA2024-T351/ACS/MgRP/TC exhibited excellent scribe protection while ATS and ANS based systems exhibited moderate and poor protection, respectively.

#### 4.7 References

1. ASM International Handbook Committee., ASM Handbook Corrosion: Materials. Vol. 13A (Materials Park, OH: ASM International, 2003).
2. D. Battocchi, A.M. Simoes, D.E. Tallman, and G.P. Bierwagen, "Electrochemical behaviour of a Mg-rich primer in the protection of Al alloys," *Corrosion Science* 48, 5 (2006): p. 1292-1306.
3. D.E.T. G. P. Bierwagen, M. Nannan, D. Battocchi, A. Stanness and V. J. Gelling, *New developments in Cr-Free primers for aerospace alloys*, in *American Chemical Society*. 2004. p. U360.
4. G. Bierwagen, D. Battocchi, A. Simoes, A. Stanness, and D. Tallman, "The use of multiple electrochemical techniques to characterize Mg-rich primers for Al alloys," *Progress in Organic Coatings* 59, 3 (2007): p. 172-178.
5. B. Kannan, Scully, J. R, "Performance of a Magnesium Rich Primer on Pretreated AA2024-T351 in Selected Laboratory and Field Environments: Conversion Coating Pretreatments," *Corrosion* (2016).
6. B. Kannan, A. King, and J. Scully, *Impact of Surface Pretreatments on AA2024-T351 Corrosion Protection by a Magnesium Rich, Non-Chrome Primer (MgRP)*, in *NACE DoD 2015*. 2015, NACE: Pittsburgh, PA.
7. B. Kannan, A. King, and J. Scully, "Effect of Pretreatments on 2024-T351 Corrosion Protection by Magnesium Rich, Non-Chromium Primer (MgRP): Laboratory Characterization in Full Immersion," *Corrosion* doi:10.5006/1700, (2015).
8. A.D. King, B. Kannan, and J.R. Scully, "Environmental Degradation of a Mg-Rich Primer in Selected Field and Laboratory Environments – Part II. Primer and Topcoat," *Corrosion* 70, 5 (2014).
9. A.D. King, J.S. Lee, and J.R. Scully, "Galvanic Couple Current and Potential Distribution between a Mg Electrode and 2024-T351 under Droplets Analyzed by Microelectrode Arrays," *Journal of the Electrochemical Society* 162, 1 (2015): p. C12-C23.
10. A.D. King, J.S. Lee, and J.R. Scully, "Finite Element Analysis of the Galvanic Couple Current and Potential Distribution between Mg and 2024-T351 in a Mg Rich Primer Configuration," *Journal of The Electrochemical Society* 163, 7 (2016): p. C342-C356.
11. A.D. King and J.R. Scully, "Sacrificial Anode-Based Galvanic and Barrier Corrosion Protection of 2024-T351 by a Mg-Rich Primer and Development of Test Methods for Remaining Life Assessment," *Corrosion* 67, 5 (2011): p. 05500401-05500422.
12. A.D. King and J.R. Scully. *Blistering Phenomena in Early Generation Mg-Rich Primer Coatings on AA2024-T351 and the Effects of CO<sub>2</sub>*. in *NACE DoD 2011 Conference Proceedings*. 2011. Palm Springs, CA.
13. B. Maier and G.S. Frankel, "Behavior of Magnesium-Rich Primers on AA2024-T3," *Corrosion* 67, 5 (2011): p. 055001.
14. C.M. Abreu, M. Izquierdo, P. Merino, X.R. Novoa, and C. Perez, "A new approach to the determination of the cathodic protection period in zinc-rich paints," *Corrosion* 55, 12 (1999): p. 1173-1181.
15. R.A. Armas, C.A. Gervasi, A. Disarli, S.G. Real, and J.R. Vilche, "Zinc-Rich Paints on Steels in Artificial Seawater by Electrochemical Impedance Spectroscopy," *Corrosion* 48, 5 (1992): p. 379-383.
16. O.O. Knudsen, U. Steinsmo, and M. Bjordal, "Zinc-rich primers - Test performance and electrochemical properties," *Progress in Organic Coatings* 54, 3 (2005): p. 224-229.

17. H. Marchebois, M. Keddam, C. Savall, J. Bernard, and S. Touzain, "Zinc-rich powder coatings characterisation in artificial sea water - EIS analysis of the galvanic action," *Electrochimica Acta* 49, 11 (2004): p. 1719-1729.
18. M. Morcillo, R. Barajas, S. Feliu, and J.M. Bastidas, "A-Sem Study on the Galvanic Protection of Zinc-Rich Paints," *Journal of Materials Science* 25, 5 (1990): p. 2441-2446.
19. A.D. King, B. Kannan, and J.R. Scully, "Environmental Degradation of a Mg-Rich Primer in Selected Field and Laboratory Environments – Part I. Without a Topcoat," *Corrosion* 70, 5 (2014).
20. P.D. Deck and D. Reichgott, "Characterization of chromium-free no-rinse prepaint coatings on aluminum and galvanized steel," *Metal Fin.* 90, 9 (1992): p. 29-35.
21. Y. Guo and G.S. Frankel, "Active Corrosion Inhibition of AA2024-T3 by Trivalent Chrome Process Treatment," *Corrosion* 68, 4 (2012).
22. O. Lunder, C. Simensen, Y. Yu, and K. Nisancioglu, "Formation and characterisation of Ti–Zr based conversion layers on AA6060 aluminium," *Surface and Coatings Technology* 184, 2 (2004): p. 278-290.
23. L. Xia, E. Akiyama, G. Frankel, and R. McCreery, "Storage and release of soluble hexavalent chromium from chromate conversion coatings - Equilibrium aspects of Cr-VI concentration," *Journal of the Electrochemical Society* 147, 7 (2000): p. 2556-2562.
24. J. Zhao, G. Frankel, and R.L. McCreery, "Corrosion protection of untreated AA-2024-T3 in chloride solution by a chromate conversion coating monitored with Raman spectroscopy," *Journal of the Electrochemical Society* 145, 7 (1998): p. 2258-2264.
25. F. Mansfeld and M.W. Kendig, "Evaluation of Anodized Aluminum Surfaces with Electrochemical Impedance Spectroscopy," *Journal of the Electrochemical Society* 135, 4 (1988): p. 828-833.
26. B.C.R. Troconis and G.S. Frankel, "Effects of Pretreatments on the Adhesion of Acetoacetate to AA2024-T3 Using the Blister Test," *Corrosion* 70, 5 (2014): p. 483-495.
27. D. Chidambaram, C.R. Clayton, and G.P. Halada, "A duplex mechanism-based model for the interaction between chromate ions and the hydrated oxide film on aluminum alloys," *Journal of the Electrochemical Society* 150, 5 (2003): p. B224-B237.
28. M. Saeedikhani, M. Javidi, and A. Yazdani, "Anodizing of 2024-T3 aluminum alloy in sulfuric-boric-phosphoric acids and its corrosion behavior," *Transactions of Nonferrous Metals Society of China* 23, 9 (2013): p. 2551-2559.
29. A. Bautista, R. Lizarbe, E. Otero, V. Lopez, and J.A. Gonzalez, "New alternatives to the industrially introduced methods for the sealing of anodized aluminium," *Revista De Metalurgia* 35, 3 (1999): p. 195-202.
30. N. Chahboun, E. Rocca, D. Veys-Renaux, M. Augros, M. Boutoba, and N. Caldeira, "Sealing of Anodized Multiphase Aluminum Alloys with Cr( plus III)/Zr( plus IV) Salts: Characterization and Corrosion Behavior," *Journal of the Electrochemical Society* 163, 3 (2016): p. C69-C75.
31. J.A. Gonzalez, V. Lopez, E. Otero, A. Bautista, R. Lizarbe, C. Barba, and J.L. Baldonado, "Overaging of sealed and unsealed aluminium oxide films," *Corrosion Science* 39, 6 (1997): p. 1109-1118.
32. N.P. Hu, X.C. Dong, X.Y. He, J.F. Browning, and D.W. Schaefer, "Effect of sealing on the morphology of anodized aluminum oxide," *Corrosion Science* 97, (2015): p. 17-24.

33. Y.L. Huang, H. Shih, H.C. Huang, S. Wu, S. Ramanathan, C. Chang, and F. Mansfeld, "Evaluation of the corrosion resistance of anodized aluminum 6061 using electrochemical impedance spectroscopy (EIS)," *Corrosion Science* 50, 12 (2008): p. 3569-3575.
34. D. Kanagaraj, S. Mohan, N.G. Renganathan, R.V. Raman, and S.V. Iyer, "Evaluation of anodized aluminum surface obtained from a sulfanic acid bath using electrochemical impedance spectroscopy," *Plating and Surface Finishing* 86, 7 (1999): p. 58-61.
35. J. Lee, Y. Kim, H. Jang, and W. Chung, "Cr<sub>2</sub>O<sub>3</sub> sealing of anodized aluminum alloy by heat treatment," *Surface & Coatings Technology* 243, (2014): p. 34-38.
36. Y. Li and Z.F. Zhu, "Cold Sealing Mechanism of Anodic Oxide-Films on Aluminum .2. Cold Sealing Models of Oxide-Films," *Plating and Surface Finishing* 80, 10 (1993): p. 77-80.
37. Y. Li, Z.F. Zhu, Z.Y. Jiang, and M.M. Yan, "Cold Sealing Mechanism of Anodic Oxide-Films on Aluminum .1. Composition and Structure of Cold-Sealed Oxide-Films," *Plating and Surface Finishing* 80, 9 (1993): p. 79-82.
38. D. Liu, G.Y. Wei, and P.L. He, "The Effect of Sealing and Trivalent Chromium Passivating on Anodized Aluminum," *International Journal of Electrochemical Science* 11, 3 (2016): p. 2097-2105.
39. F. Mansfeld, G. Zhang, and C. Chen, "Evaluation of sealing methods for anodized aluminum alloys with electrochemical impedance spectroscopy (EIS)," *Plating and Surface Finishing* 84, 12 (1997): p. 72-81.
40. J.M. Zhao, H.X. Liu, S.L. Chen, and X.H. Zhao, "EIS evolution of anodised aluminium by cerium salt sealing in NaCl solution with exposure time," *Corrosion Engineering Science and Technology* 48, 1 (2013): p. 44-47.
41. X. Zhao, L. Tian, J. Zhao, and Y. Zuo, "Electrochemical properties of anodized and sealed aluminum films," *Aicam* 2005 11-12, (2006): p. 433-436.
42. Y. Zuo, P.H. Zhao, and J.M. Zhao, "The influences of sealing methods on corrosion behavior of anodized aluminum alloys in NaCl solutions," *Surface & Coatings Technology* 166, 2-3 (2003): p. 237-242.
43. C. Matzdorf, Beck, Erin., Hilgeman, Amy., Prado, Ruben. , *Trivalent Chromium Process as a Sealer for MIL-A-8625 Type II, IIB and IC Anodic Coatings*. 2008, NAVAIR. p. 50.
44. J.A. Gonzalez, M. Morcillo, E. Escudero, V. Lopez, A. Bautista, and E. Otero, "Self-sealing of unsealed aluminium anodic oxide films in very different atmospheres," *Revista De Metalurgia* (2003): p. 110-115.
45. X.H. Zhao, Y. Zuo, J.M. Zhao, J.P. Xiong, and Y.M. Tang, "A study on the self-sealing process of anodic films on aluminum by EIS," *Surface & Coatings Technology* 200, 24 (2006): p. 6846-6853.
46. D.E. Packham, *Handbook of Adhesion*. 2 ed.
47. AkzoNobel, "Aerodur5000," *Topcoat - Technical Data Sheet* (2013).
48. ASTM, *Standard Practice for Operating Salt Spray (Fog) Apparatus: B117*, in *Annual Book of ASTM Standards*. 1997, ASTM: West Conshohocken, PA. p. 1-8.
49. ASTM, "Standard Practice for the Preparation of Substitute Ocean Water," *ASTM D1141 - 98* DOI: 10.1520/D1141-98R08 (1998).
50. ASTM, "Standard Practice for Modified Salt Spray Testing," *ASTM G85 - A3* DOI: 10.1520/C0033-03, (2009).
51. ASTM, "Standard Guide for Conducting Corrosion Tests in Field Applications," *ASTM G4 - 01* DOI: 10.1520/G0004-01R08, (2001).

52. ASTM, "Standard Practice for Preparing, Cleaning, and Evaluating Corrosion Test Specimens," ASTM G1 DOI: 10.1520/D1141-98R08 (2003).
53. M.T. Woldemedhin, M.E. Shedd, and R.G. Kelly, "Evaluation of the Maximum Pit Size Model on Stainless Steels under Thin Film Electrolyte Conditions," *Journal of the Electrochemical Society* 161, 8 (2014): p. E3216-E3224.
54. R.J. Santucci, Kannan, B., Scully, J. R, "Investigation of Magnesium Oxide Primer on 2024-T351: Assessment and Characterization of Magnesium Oxide Protection Mechanism," *Corrosion* (2016).

## 4.8 Figures

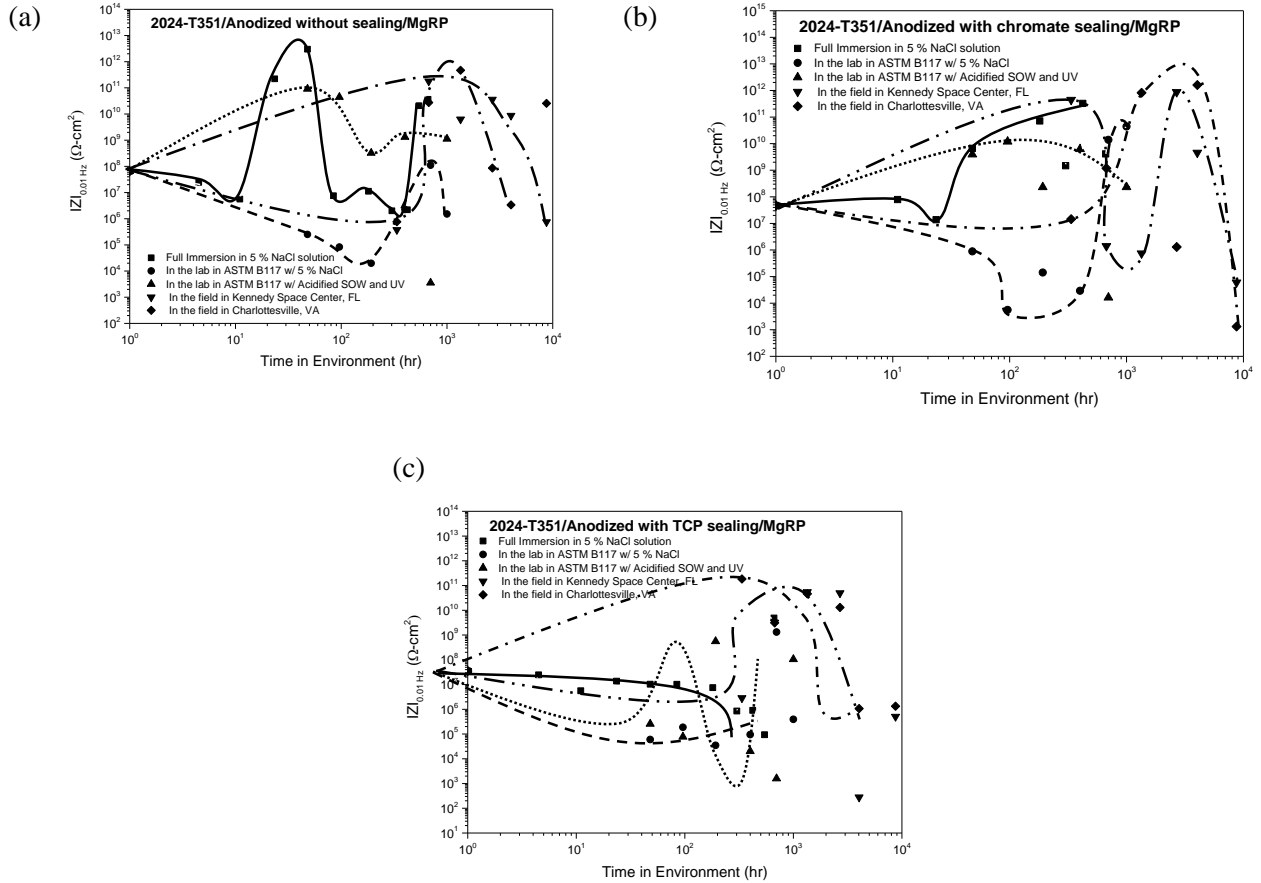


Figure 4.1. Low frequency impedance  $IZI$  modulus of intact AA2024-T351/Pretreatment/MgRP systems at 0.01 Hz vs time in the environments indicated for (a) ANS/MgRP (b) ACS/MgRP and (c) ATS/MgRP.

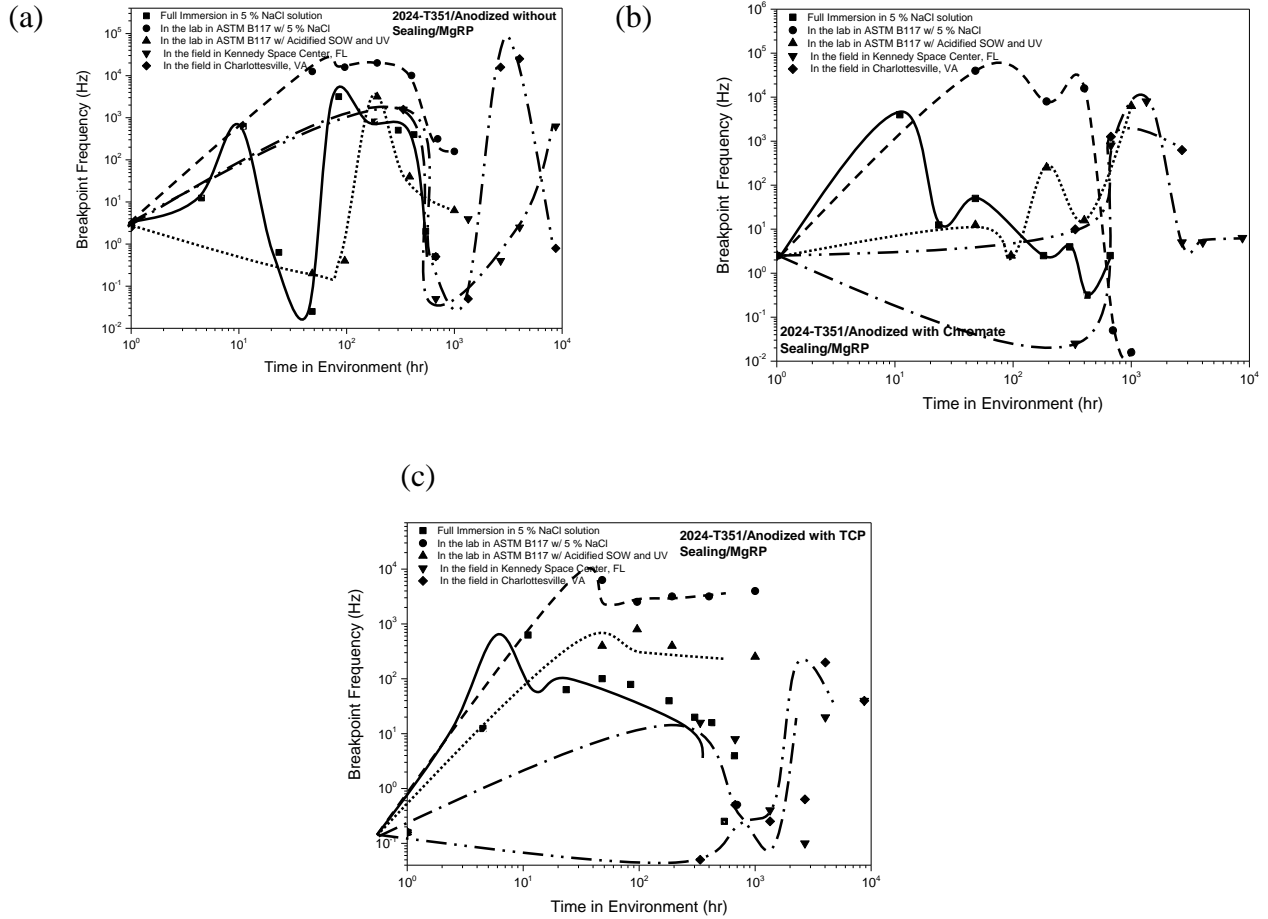


Figure 4.2. High Breakpoint Frequency ( $F_{bpt}$ ) of intact AA2024-T351/Pretreatment/MgRP systems vs time in the environments indicated for (a) ANS/MgRP (b) ACS/MgRP and (c) ATS/MgRP.

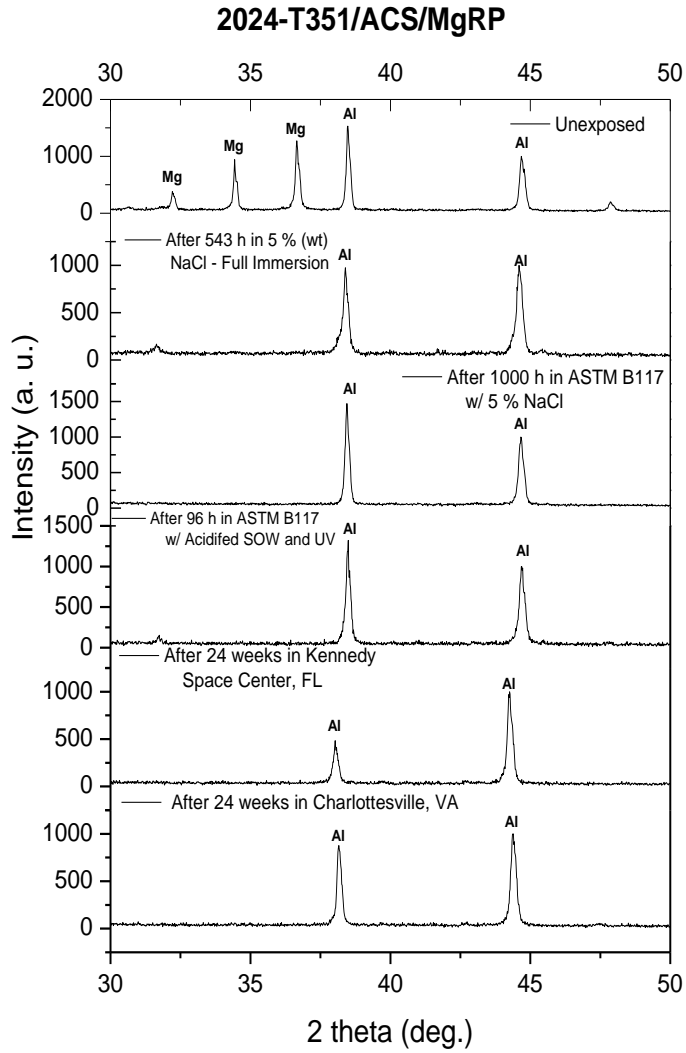


Figure 4.3. Selected XRD spectra of intact AA2024-T351/ACS/MgRP system after exposure in the LALT/field environments

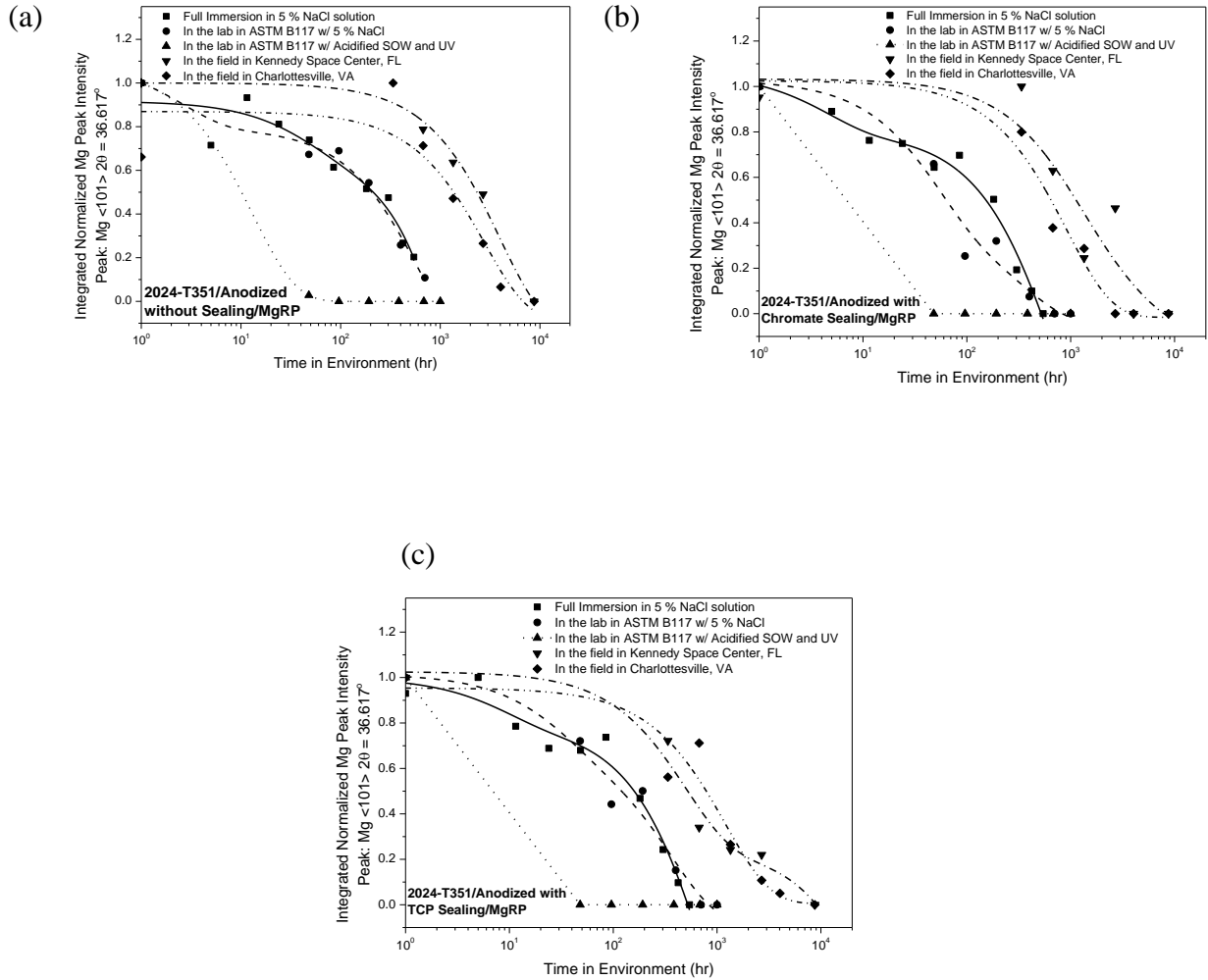


Figure 4.4. The normalized integral XRD intensity for Mg<101> XRD peak of intact AA2024-T351/Pretreatment/MgRP systems vs time in the environments indicated for (a) ANS/MgRP, (b) ACS/MgRP and (c) ATS/MgRP

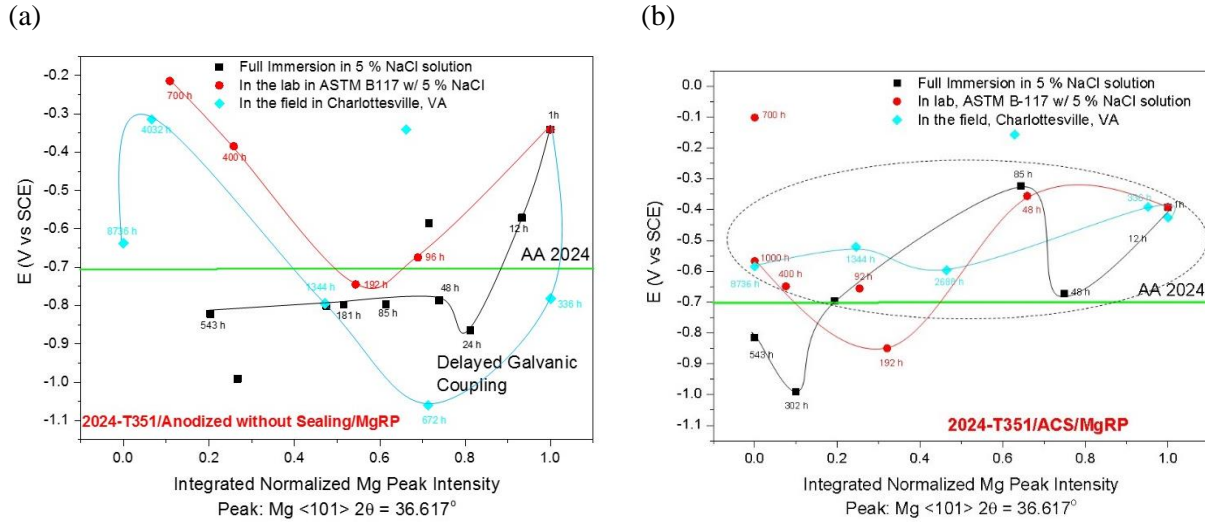


Figure 4.5. Average global galvanic protection potential of intact coating for the last 1 h of exposure in 5 % wt NaCl vs the normalized integral XRD intensity for Mg<101>. The time indicates total exposure time in different LALT/Field environments indicated, AA2024-T351/Pretreatment/MgRP after exposure, in Full immersion in 5 % wt NaCl, ASTM B-117 in 5 % wt NaCl and Field at CHO. (a) ANS/MgRP and (b) ACS/MgRP

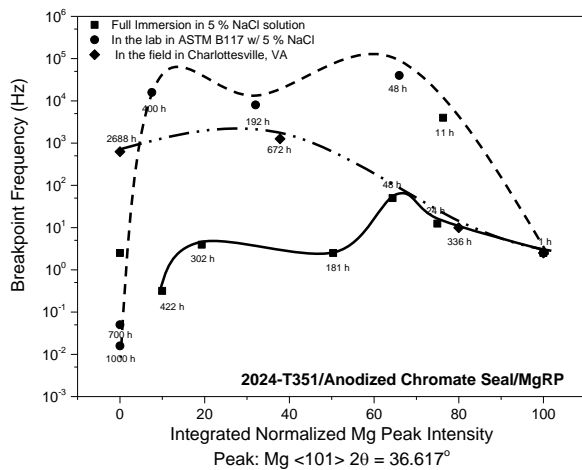


Figure 4.6. Breakpoint Frequency of intact coating after 1 h exposure in 5 % wt NaCl vs The normalized integral intensity for Mg<101>. The time indicates total exposure time in different LALT/Field environments indicated, (a) AA2024-T351/ACS/MgRP after exposure, in Full immersion in 5 % wt NaCl, ASTM B-117 in 5 % wt NaCl, and Field exposure at CHO.

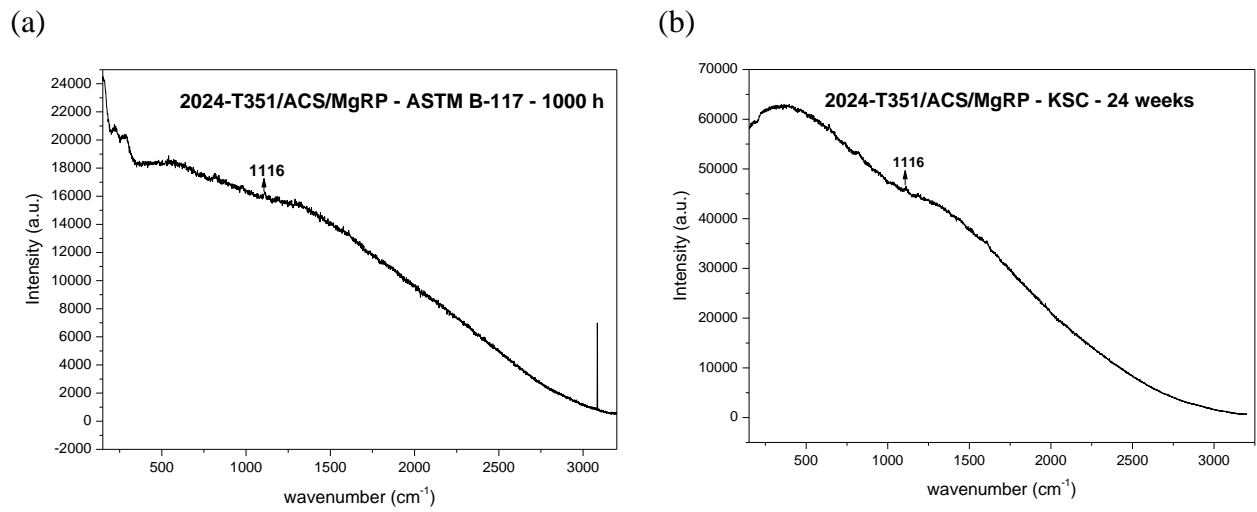


Figure 4.7. Raman spectra for AA2024-T351/ACS/MgRP) (a) Standard ASTM B-117 exposure – 1000 h and (b) At field, KSC for 24 weeks

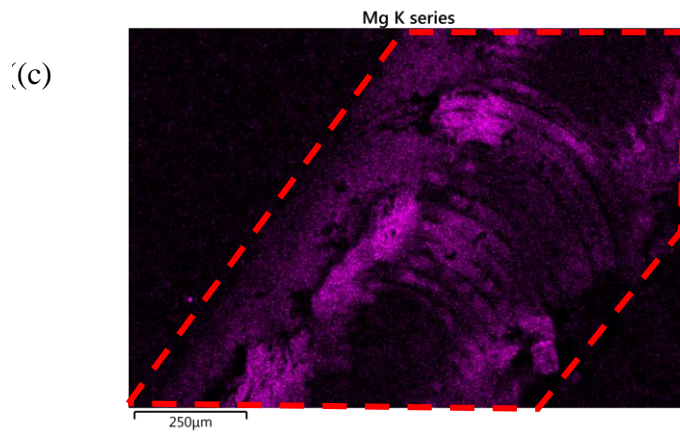
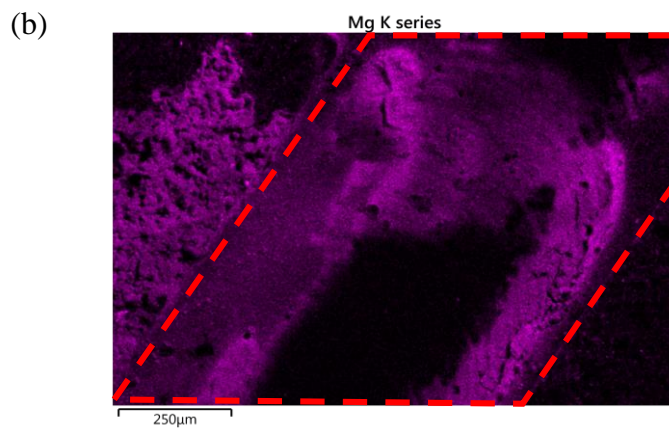
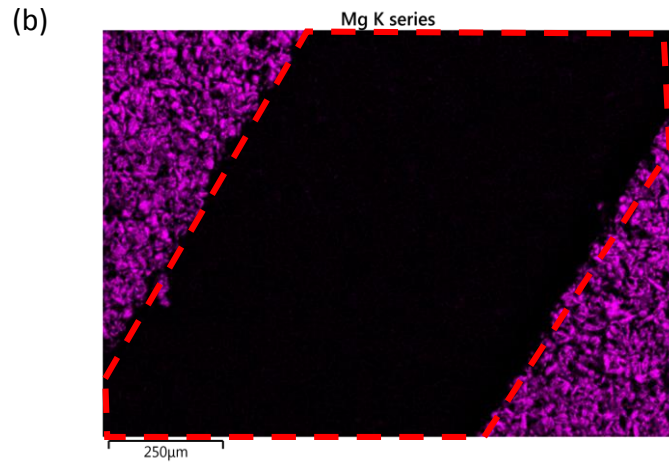


Figure 4.8. EDS maps of elemental Mg across scribe and adjacent coating a) ACS pretreated 2024-T351/MgRP before environmental exposure, b) ACS pretreated 2024-T351/MgRP after 400 h exposure in ASTM B-117, c) ACS pretreated 2024-T351/MgRP after 1000 h exposure in ASTM B-117. (red dash lines indicates the borders of the scribe in the figure)

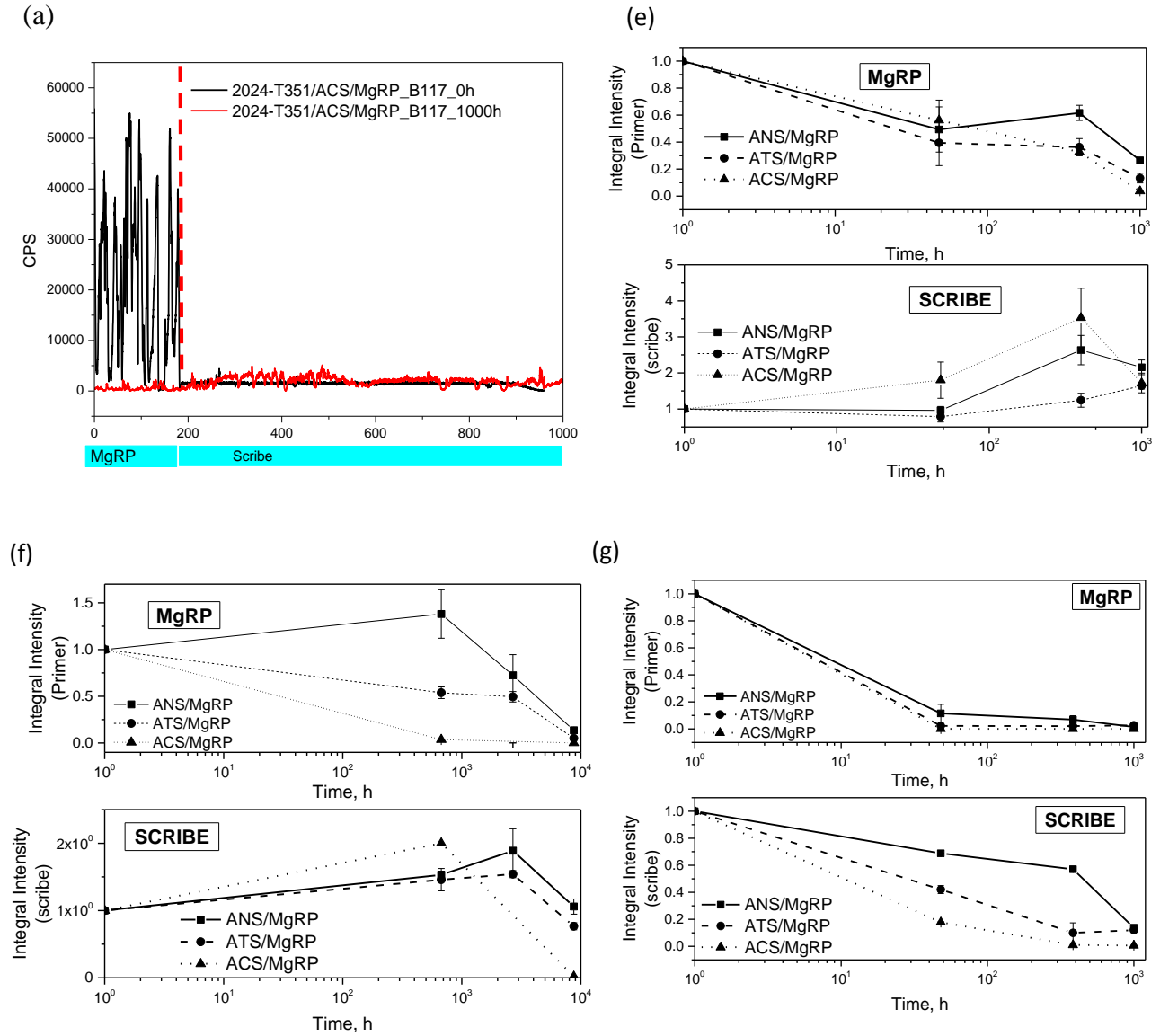


Figure 4.9. a) EDS line profile of ACS pretreated AA2024-T351/MgRP without a topcoat after 1000 h exposure time in ASTM B-117 testing (red dash line indicates the borders of the scribe in the figure). Integral intensity of Mg EDS line profile in scribe/MgRP as a function of exposure time in (b) ASTM B-117 testing for 1000 h (c) KSC for 8736 h and (d) ASTM B-117 modified with acidified ASTM SOW/UV testing for 1000 h.

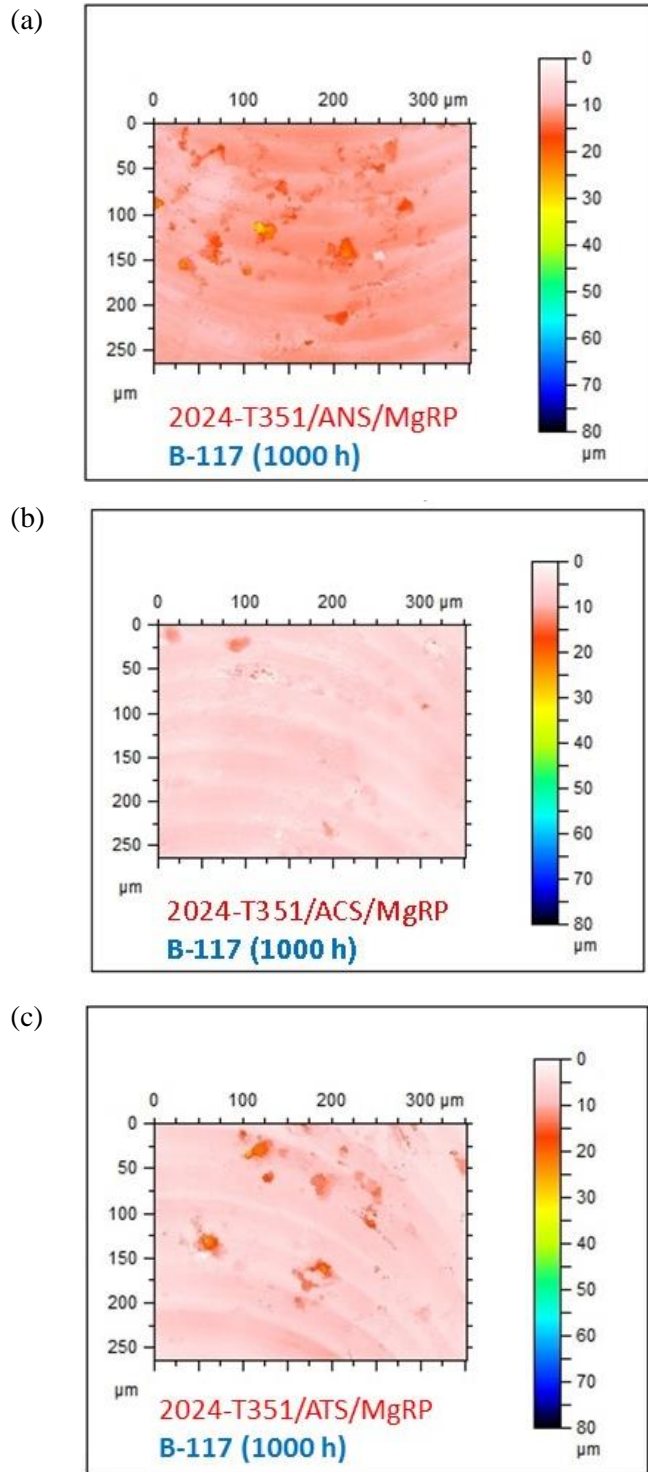


Figure 4.10. Optical profilometry maps of scribe exposing AA2024-T351 in pretreated AA2024-T351/MgRP without topcoat after exposure in ASTM B-117 for 1000 h. (a) AA2024-T351/ANS/MgRP, (b) AA2024-T351/ACS/MgRP and (c) AA2024-T351/ATS/MgRP. The 0  $\mu\text{m}$  position (white) on the scale is indicative of the starting material condition before corrosion.

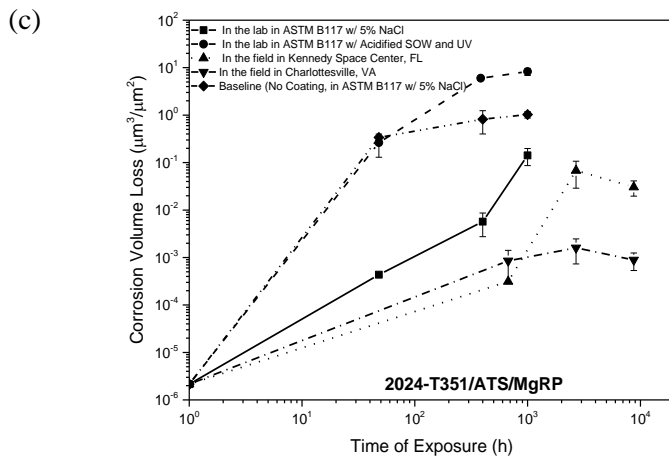
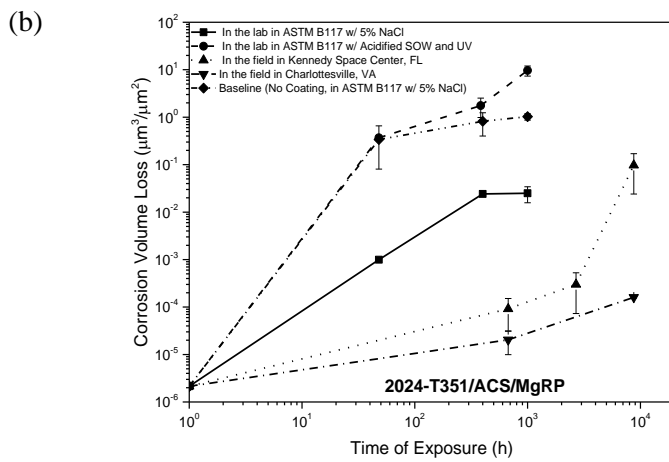
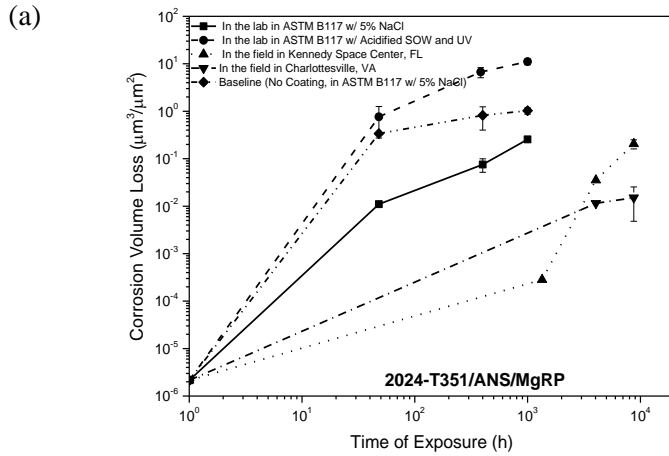


Figure 4.11. Corrosion volume loss of scribe exposing AA2024-T351 in AA2024-T351/Pretreatment/MgRP without topcoat as a function of exposure time in in different LALT/field environments indicated. The baseline data is for uncoated AA2024-T351. (a) AA2024-T351/ANS/MgRP, (b) AA2024-T351/ACS/MgRP and (c) AA2024-T351/ATS/MgRP

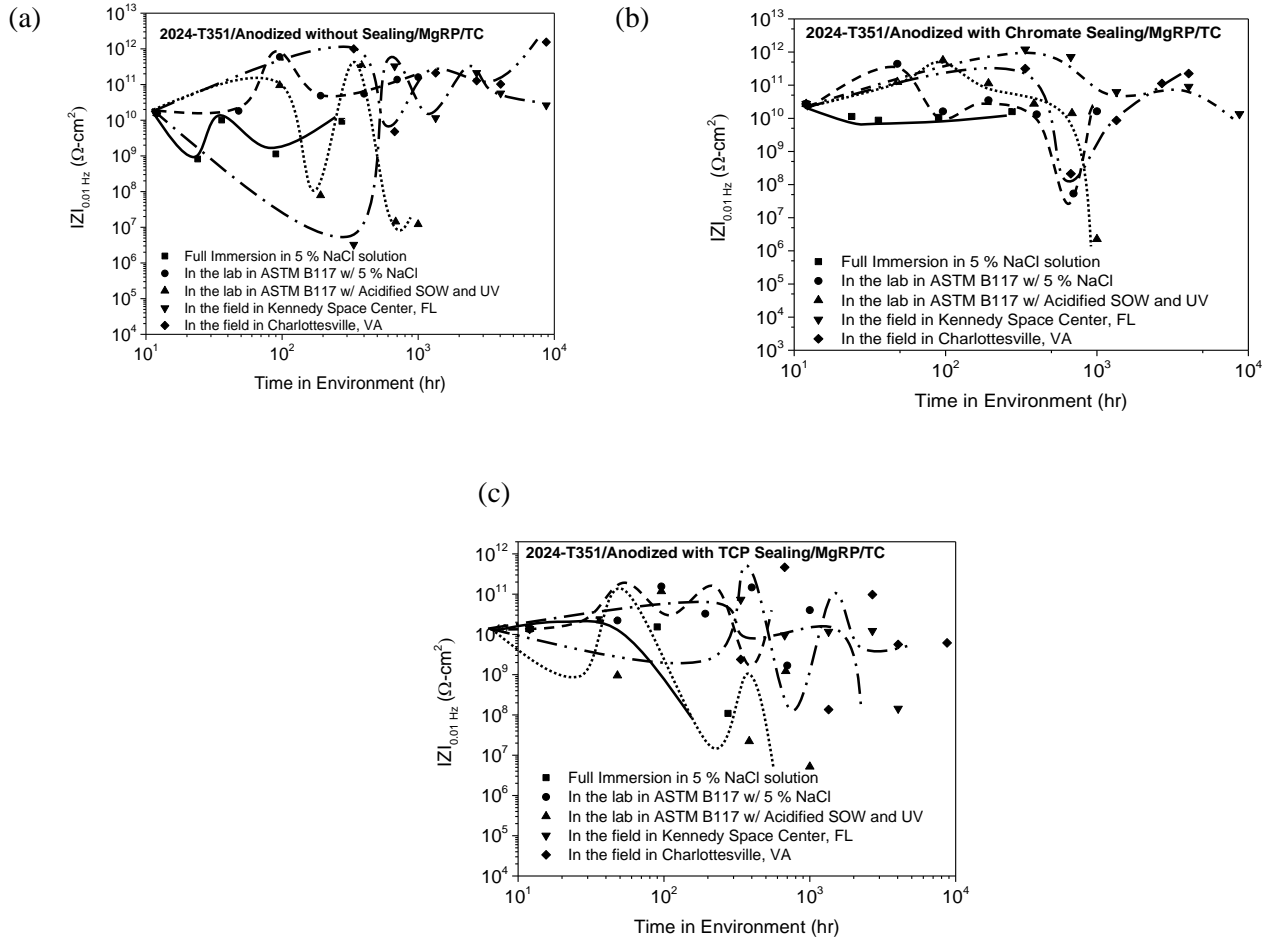


Figure 4.12. Low frequency impedance IZI modulus of AA2024-T351/Pretreatment/MgRP/TC systems at 0.01 Hz vs time in the environments indicated for (a) ANS/MgRP/TC (b) ACS/MgRP/TC and (c) ATS/MgRP/TC.

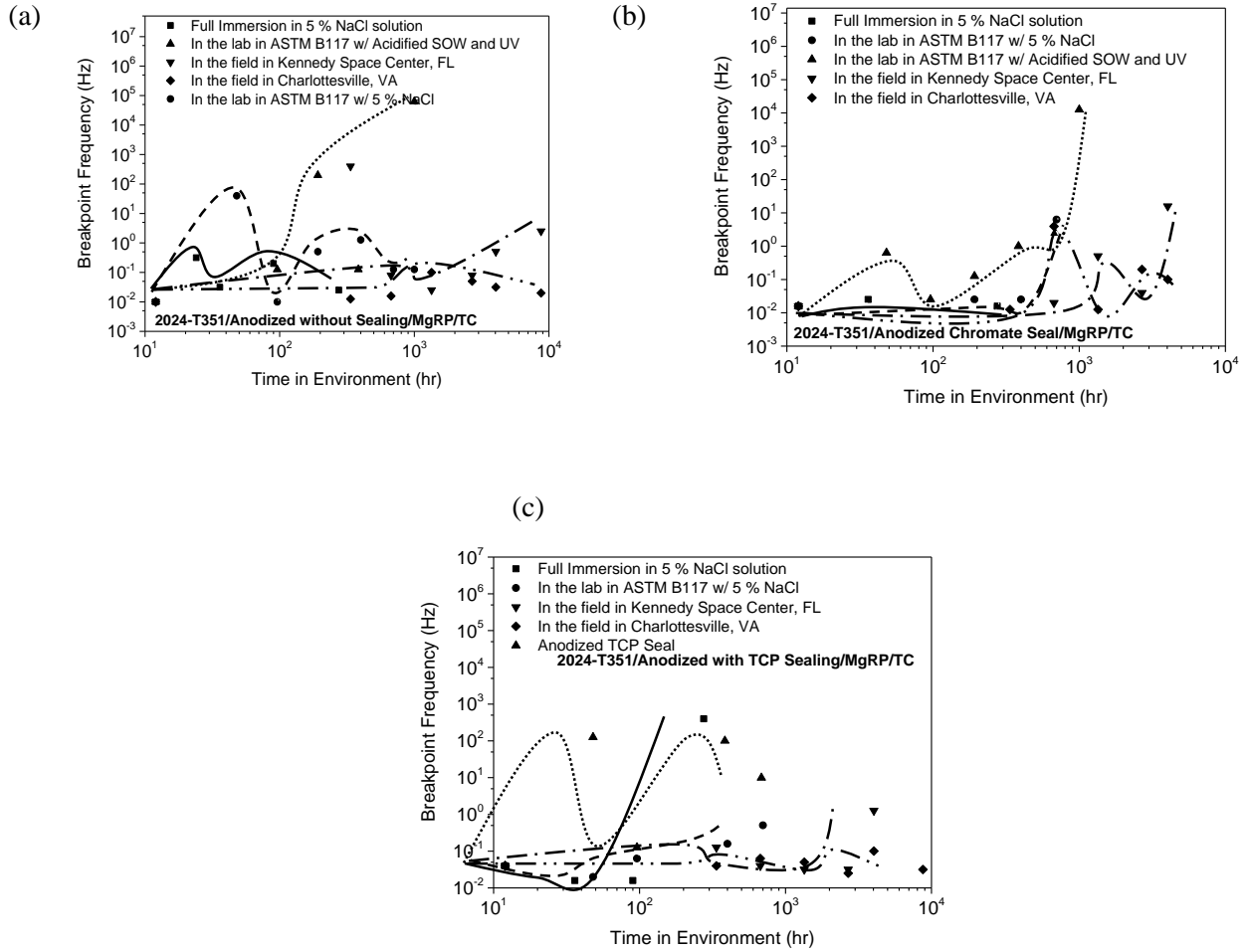


Figure 4.13. High breakpoint frequency ( $F_{bpt}$ ) of AA2024-T351/Pretreatment/MgRP/TC systems vs time in the environments indicated for (a) ANS/MgRP/TC (b) ACS/MgRP/TC and (c) ATS/MgRP/TC

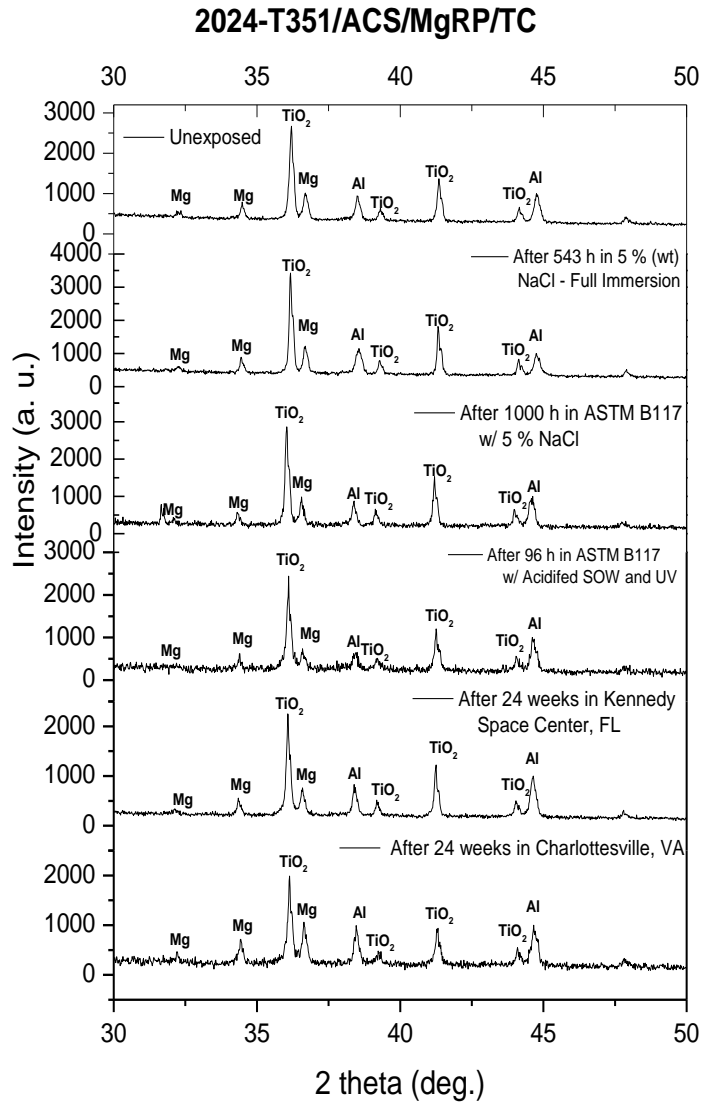


Figure 4.14. Selected XRD spectra of AA2024-T351/ACS/MgRP/TC system after exposure in the LALT/field environments.

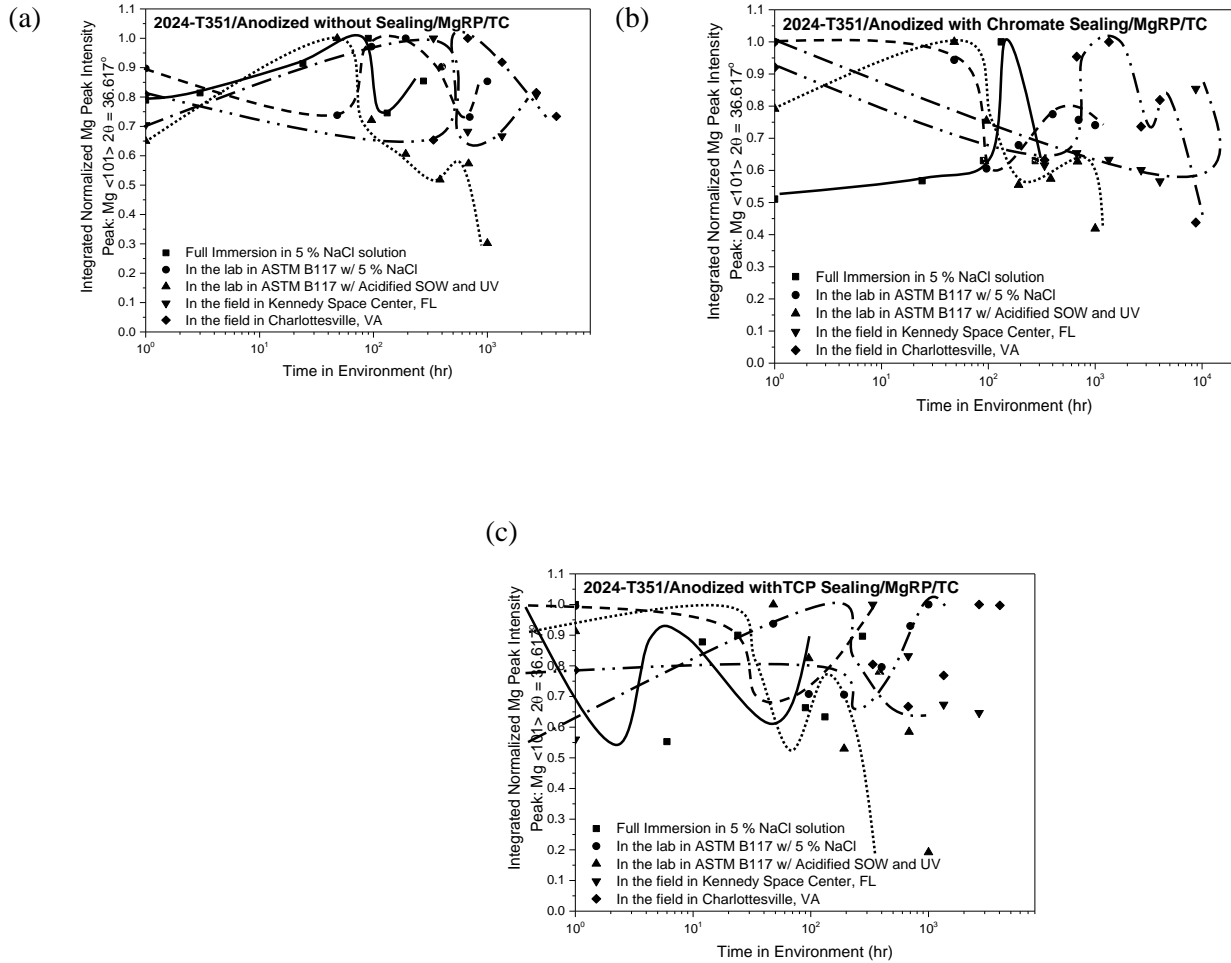


Figure 4.15. The normalized integral XRD intensity for Mg<101> XRD peak of AA2024-T351/Pretreatment/MgRP/TC systems vs time in the environments indicated for (a) ANS/MgRP/TC (b) ACS/MgRP/TC and (c)ATS/MgRP/TC.

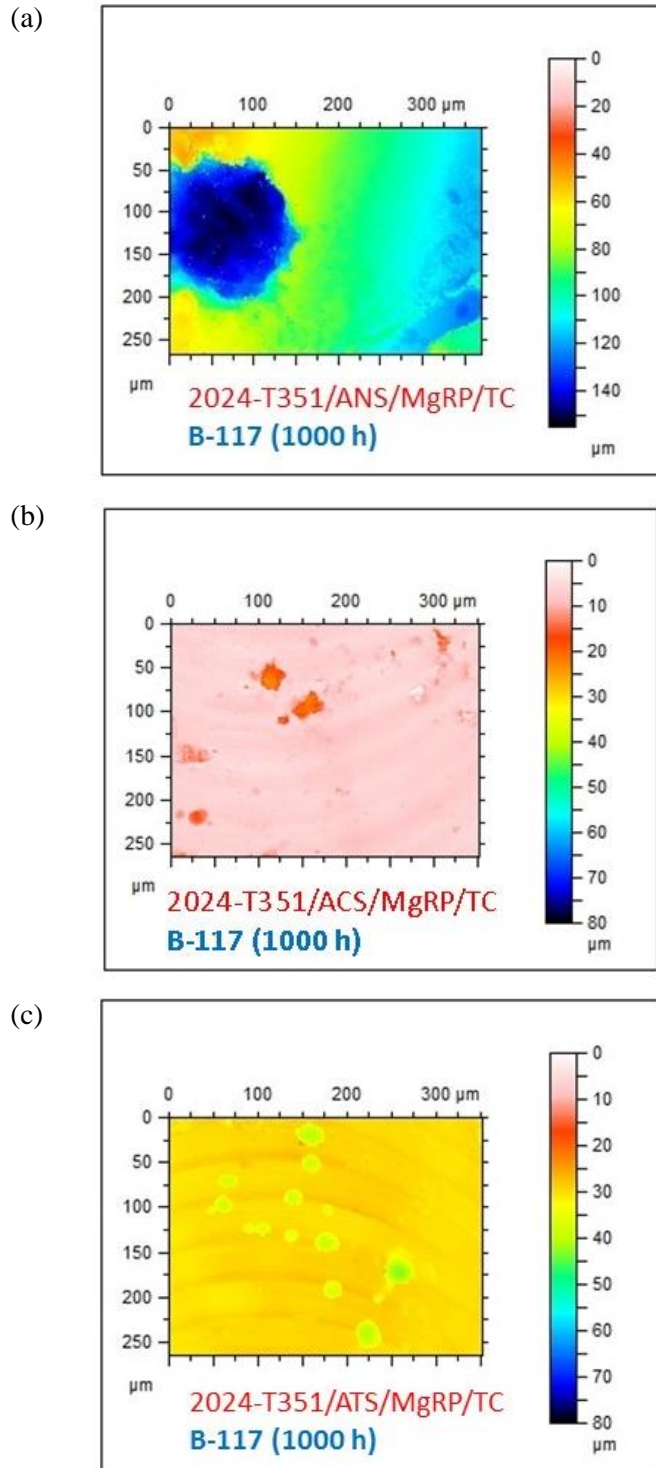


Figure 4.16. Optical profilometry maps of scribe exposing 2024-T351 in pretreated 2024-T351/MgRP systems with topcoat after exposure in indicated LALT environments. (a) AA2024-T351/ANS/MgRP/TC, (b) AA2024-T351/ACS/MgRP/TC and (c) AA2024-T351/ATS/MgRP/TC. The 0  $\mu\text{m}$  position (white) on the scale is indicative of the starting material condition before corrosion.

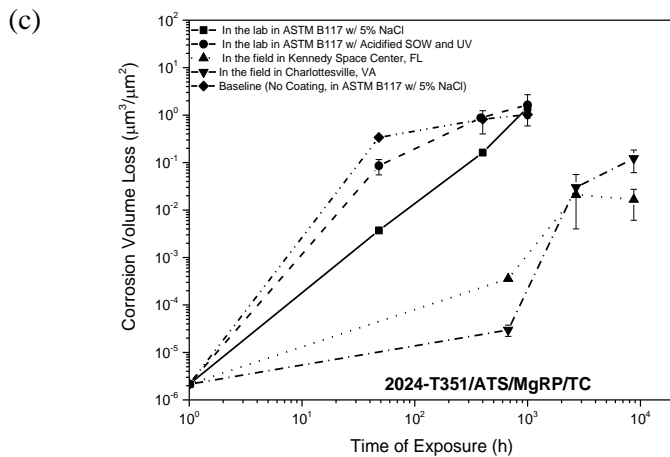
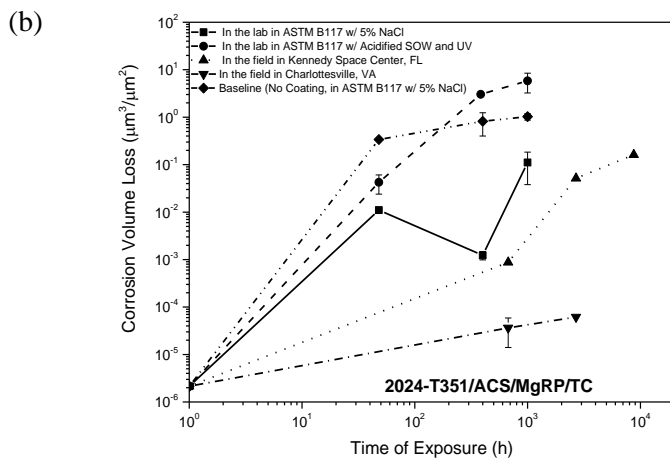
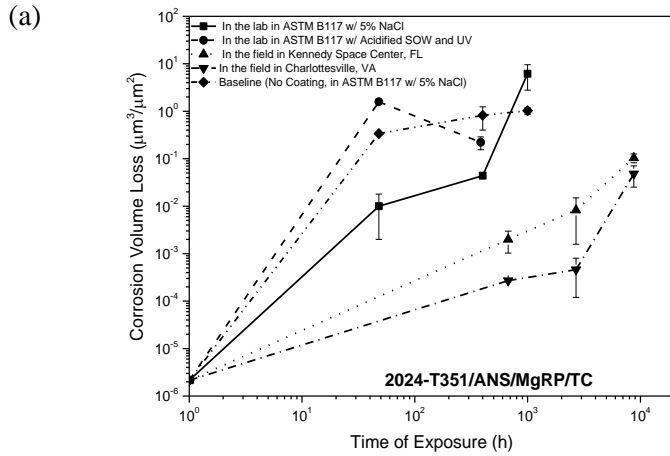


Figure 4.17. Corrosion volume loss of scribe exposing AA2024-T351 in pretreated AA2024-T351/MgRP with and without topcoat as a function of exposure time in in different LALT/field environments indicated. (a) AA2024-T351/ANS/MgRP/TC, (b) AA2024-T351/ACS/MgRP/TC and (c) AA2024-T351/ATS/MgRP/TC. The baseline data is for uncoated AA2024-T351.

## **5 Environmental Degradation of Pretreatments and Role of Pretreatments in Corrosion Protection of AA2024-T351**

### **5.1 Abstract**

This study compares the degradation of bare AA2024-T351 to surfaces protected with conversion coatings and anodization based pretreatments with and without sealing. Protection of remote scratches and global barrier degradation of the pretreatments after exposure in selected laboratory and field environments was investigated. Exposure studies focused on non-film forming pretreatment (NFF), chromate conversion coating (CCC), trivalent chromium pretreatment (TCP), non-chromium pretreatment (NCP), anodization without sealing (ANS), anodization with hexavalent chromium sealing (ACS) and anodization with trivalent chromium pretreatment (TCP) sealing (ATS). Exposures were conducted in the field at an inland rural site, Birdwood Golf Course in Charlottesville (CHO), Virginia. ASTM B117 with 5 % (wt) sodium chloride, modified ASTM B117 with ASTM substitute ocean water (SOW) and UV light as well as under full immersion in ambiently aerated 5 % (wt) NaCl solution. These conditions were compared to field. In addition, controlled relative humidity studies were conducted exposing NaCl droplets on bare/pretreated AA2024-T351 to quantify chemical species leaching. The effects of pretreatment resistance and chemical species release on cathodic kinetics of AA2024-T351 were characterized using potentiodynamic polarization measurements.

A manuscript based on this chapter will be submitted to Materials and Corrosion Journal as a Full Research Paper, “Environmental Degradation of Pretreatments and Role of Pretreatments in Corrosion Protection of AA2024-T351.”

Representative author contributions:

B. Kannan: experiments, analysis and interpretation

D. M. Wolanski: SEM/EDS and optical profilometry characterization for selected environments.

J. R. Scully: Advisor, analysis and interpretation

## 5.2 Introduction

Precipitation age hardened aluminum alloys, due to their heterogeneous microstructure, are highly susceptible to localized corrosion and they rely on use of multilayered coatings to provide active corrosion protection, improved adhesion and provide other specialized functions.<sup>13</sup> In practical applications, several pretreatments are of interest to improve adhesion between the substrate and the polymer and also to impart additional corrosion protection.<sup>14-41,114</sup>

Chromate conversion coatings (CCC) offer strong corrosion resistance properties and are noted for their ability to self-heal.<sup>22-26,36,37</sup> This phenomenon is attributed to the release of hexavalent chromium from the coating into the corrosive solution in contact with the surface.<sup>36,37</sup> Due to environmental hazards posed by hexavalent chromium, non-chromium process (NCP)<sup>16,32</sup> and trivalent chromium process (TCP)<sup>19</sup> coatings have been explored as alternatives for CCC. NCP conversion coatings are based on titanium/zirconium oxides<sup>16,32</sup> whereas TCP conversion coatings are trivalent chromium enriched zirconium oxide coatings.<sup>19</sup>

Anodization is a common pretreatment process in which anodic polarization of aluminum alloy in acidic environment result in formation and growth of anodic oxide film.<sup>33</sup> The oxide film is characterized by inner thin barrier layer and outer thick porous layer.<sup>33</sup> The porous nature of the oxide makes alloy susceptible to corrosion. In order to improve corrosion resistance, pretreated samples must be sealed after anodizing.<sup>14,15,17,20,21,27-31,34,38,39,41</sup> The pores are often sealed by active inhibitors such as chromic acid or other active inhibitors to add an additional feature to corrosion protection.<sup>41</sup> TCP has been explored as an alternate for chromic acid for sealing due to its corrosion resistance and adhesion.<sup>35</sup> TCP is also easy in terms of application as it can be applied in ambient conditions for shorter exposure time whereas chromate or water

seals require exposure at 190° F to 200° F for longer exposure times.<sup>35</sup> The electrochemically grown oxide layer provide extra barrier protection due to the highly capacitive behavior of Al<sub>2</sub>O<sub>3</sub>.<sup>33</sup> Some sealing might occur during exposure while corrosion progressed.<sup>18,40</sup> The adhesion strength of anodized aluminum to most polymers is directly related to size and density of pores created by anodization process as mechanical interlocking directly correlates to adhesion strength.<sup>114</sup>

These pretreatments are currently used for application in aerospace aluminum alloys along with chromate pigment primers. Carcinogenicity, high handling cost and environmental safety concerns push the need for developing new corrosion mitigation strategies. Over the past few years, a metallic Mg pigment based organic coating system was explored for active corrosion protection of aluminum alloys.<sup>72,73,75-77,80-85,88,117,132,143-145</sup> Mg is designed to provide sacrificial protection of an aluminum alloy while barrier protection is provided by organic polymer in primer and topcoat.<sup>84</sup> This approach has been well established previously in the design of zinc-rich primer for application with various steel.<sup>79,86,89,90</sup> A systematic evaluation of effect of various pretreatments on overall performance of coating systems containing MgRP in different lab-accelerated life testing and field environments has been previously reported elsewhere.<sup>75-77,80,81</sup> Results indicated that all conversion coatings pretreatment based MgRP systems provided a delayed sacrificial protection whereas anodization pretreated MgRP systems provided very limited galvanic protection.<sup>75-77</sup> In the light of these recent findings regarding conversion coating and anodization pretreatment based MgRP systems, three primary modes of corrosion protection of scribe could be inferred in addition to barrier protection. Sacrificial protection afforded by Mg pigment, corrosion inhibition by Mg corrosion products redeposition and possible corrosion inhibition by another inhibitor such as CrO<sub>4</sub><sup>2-</sup> leaching from the

pretreatment could all contribute towards corrosion protection. While the sacrificial protection aspects of MgRP including the throwing power or range of protection that has been discussed in our previous work<sup>75-77,80-85</sup>, this study aims at understanding the performance of pretreated AA2024-T351 in different lab-accelerated life testing and field environments in absence of any organic coating. In addition the leaching kinetics of chemical inhibitors from different pretreatment and their effect on cathodic kinetics of AA2024-T351 was explored to understand the role of pretreatments in overall corrosion protection.

### **5.3 Experimental Procedure**

#### **5.3.1 Materials**

AA2024-T351 sheet (1.6 mm thickness) was pretreated with 7 different surface pretreatments for comparison including (i) Non-film forming pretreatment (NFF), (ii) chromate conversion coating (CCC), (iii) trivalent chromium pretreatment (TCP), (iv) non-chromium pretreatment (NCP) (i) Anodization – No Sealing (ANS), (ii) Anodization with hexavalent chromium sealing (ACS), (iii) Anodization with Trivalent Chromium Pretreatment (TCP) Sealing (ATS). Prekote™ is a non-film forming chromium free surface pretreatment containing approximately 95% water and less than 3 % each of diethylene glycol monobutyl ether and N-methyl-2-pyrrolidone.<sup>124</sup> CCC (Alodine 1200s),<sup>125</sup> NCP (Alodine 5200),<sup>103</sup> and TCP (Surtec 650)<sup>126</sup> are also commercial products. For anodization pretreatments, a thin-film sulfuric acid anodizing, MIL-A-8625F: Type II pretreatment procedure was followed.<sup>36</sup>

#### **5.3.2 Laboratory and Field Exposures of Pretreated AA2024-T351**

Pretreated AA2024-T351 panels were exposed to salt spray in a QFog Cyclic Corrosion Tester (QFog model CCT 1100†) according to ASTM B117<sup>141</sup> for at least 1000 hours. During a second exposure, the standard ASTM B117 salt fog was altered such that the standard 5 % (wt) NaCl

solution electrolyte was replaced with ASTM substitute ocean water<sup>135,136</sup> ([SOW] pH = 8.2±0.3) and ultraviolet radiation. The details of the experiments are summarized in Table 5.1. Artificial seawater was produced according to ASTM D-1141<sup>135</sup> In all salt fog exposures reported in this report, ambient air was supplied to the chamber and to the atomizer for fog production. Ambient concentrations of CO<sub>2</sub> were measured in-situ to be approximately 425 ppm. Other ambient gas concentrations were not measured. Natural weathering exposures of pretreated AA2024-T351 panels were conducted at a rural inland site at Birdwood Golf Course in Charlottesville (CHO), VA (38.0402°N, 78.54.27°W, elevation = 172 m). The sample test racks face south. During exposure, panels were mounted on unsheltered atmospheric test racks with full exposure to natural elements according to ASTM G-4.<sup>137</sup> Pertinent environmental parameters for CHO such as mean temperature, mean relative humidity, mean dew point, mean precipitation rate, precipitation pH and dry chloride deposition rate are reported elsewhere.<sup>75</sup>

### **5.3.3 Post-mortem Surface Analysis of the Pretreatment and the Scribe**

All full-immersion studies as well as post-mortem analysis after salt fog and field exposures reported herein were conducted in quiescent 5 % (wt) NaCl (pH: 6.9±0.4) open to laboratory air. Potential control during electrochemical experiments was maintained using a Gamry Potentiostat (Ref 600/ PCI4)† with computer interface software. Saturated calomel electrode (SCE) and Pt mesh were used as the reference and counter electrode, respectively. The area tested was far away (≥ 2 cm away) from scribe. A typical EIS scan was acquired in sine sweep mode from 100 kHz to 0.01 Hz with 6 points per decade. NFF/conversion coatings pretreated and anodized panels were scanned with an AC amplitude of 20 mV and 60 mV, respectively. The tests were conducted in quiescent 5 % (wt) NaCl, as discussed above, after 1 hour exposure at open circuit for all pretreated panels.

Surface chemistry and corrosion products formed before and after environmental exposure were characterized using Raman spectroscopy. Raman spectroscopy was conducted using a Renishaw InVia Raman Microscope. Measurements were conducted using a 514 nm laser at 1 - 50% power under the 20x objective with a 3000 l/mm (vis) grating. Scans with 15 second exposure time were taken with 2 accumulations under standard confocality. If Raman spectra showed heavy fluorescence then a pre-measurement sample bleaching was conducted where the sample was subjected to laser exposure under the aforementioned conditions for 450 to 600 seconds prior to taking the spectra. For all measurements, prior calibration of Raman spectroscopy was performed using a silicon standard.

Scanning electron microscopy (SEM) and energy dispersive spectroscopy (EDS) were used for post-mortem analysis of corrosion products in the scribe. A field emission Quanta 650 SEM was used to conduct these investigations. For EDS, Oxford XMax 150 detector was utilized. A working distance of 15 mm and an accelerating voltage of at least 3 times the energy of the maximum characteristic peak of interest were used (~15 kV). At an accelerating voltage of 15 kV, EDS has a penetration depth of roughly 2 to 5  $\mu\text{m}$  into the materials investigated in this study. EDS analysis was performed using Aztec analysis software.

Optical profilometry was conducted using a Zygo optical profilometer (Newview 7200/7300 model). The environmentally exposed samples were first exposed to concentrated nitric acid for 15 minutes to remove corrosion products present in the scribe as per the ASTM G1 Standard.<sup>138</sup> Image refinement and corrosion volume loss analysis was performed using MountainsMaps imaging topography software.<sup>142,146</sup>

#### **5.3.4 Chemical Species Leaching Studies:**

Controlled relative humidity studies were conducted for droplet exposure to characterize the leaching of ionic species from the pretreatments. 250  $\mu\text{l}$  of 2 M NaCl solution was placed on pretreated AA2024-T351 for different exposure times at constant relative humidity of 95 %. Constant relative humidity was maintained in cabinets with a saturated solution of potassium nitrate to keep the size of droplet constant. After exposure, the surface is washed off with DI water and diluted to 7.5 ml. 0.5 ml of 5 M HCl was added to each of the samples to break up any potential corrosion products although there was no visible solid corrosion products in the solution. The post-exposure solution was characterized for ionic species by Inductively Coupled Plasma –Optical Emission Spectrometry.<sup>147-149</sup> Before analyzing, standards containing known amounts of Al, Cr, Zr, Ti as well as each of the alloying elements, were used to calibrate the instrument. In this work, the emission intensities of Mg (2795  $\text{nm}^{-1}$ ), Mg (2802  $\text{nm}^{-1}$ ), aluminum Al (3082  $\text{nm}^{-1}$ ), Al (3961  $\text{nm}^{-1}$ ), zirconium (Zr, 3273  $\text{nm}^{-1}$ ), Zr (3438  $\text{nm}^{-1}$ ), Titanium Ti (3234  $\text{nm}^{-1}$ ), Ti (3361  $\text{nm}^{-1}$ ), Chromium Cr (2677  $\text{nm}^{-1}$ ) and Cr (2835  $\text{nm}^{-1}$ ) were recorded and used for quantification of ionic species leaching.

#### **5.3.5 Potentiodynamic Polarization:**

Cathodic potentiodynamic polarization scans were conducted on bare AA2024-T351 as well as pretreated AA2024-T351 in the as-received condition and after different full immersion exposure times. A typical cathodic scan started at 0.005 V vs. OCP and scanned to -1.0 V vs. OCP at 0.1667 mV/s. Effect of anionic species leaching on cathodic kinetics of bare AA2024-T351 exposed by a defect in pretreatment was studied with presence of anionic species. Based on anionic species leaching studies conducted earlier, three different  $\text{CrO}_4^{2-}$  concentrations were chosen for

understanding effect of anionic species leaching in cathodic kinetics. All polarization studies were conducted in 1 M NaCl solution under quiescent conditions.

## **5.4 Results**

### **5.4.1 Barrier Degradation of Pretreated AA2024-T351 after Exposure in Selected Lab and Field Environments:**

#### **Macroscopic Morphology**

The performance of different pretreatments after exposure in selected LALT and field environments were assessed by visual inspection. The longest time of exposure for ASTM B117, modified ASTM B117 and field environment was 1000 h, 1440 h and 4032 h, respectively. These times were chosen for comparison. Figure 5. 1 shows representative samples which has degraded heavily, moderately and very minimally in chosen environments. In terms of severity of the environment, they are ranked in the following order, CHO < Modified ASTM B117 < ASTM B117. An arbitrary ranking metrics of 1-4, wherein 1 being the most protective and 4 being least protective were utilized to compare the performance of pretreatments in different environment and the results for different pretreatments are summarized in Table 5.2. Among chosen pretreatments, ACS provided excellent corrosion protection whereas NFF, NCP and ANS exhibited significant corrosion. Selected pretreatments provided moderate corrosion protection (Figure 5. 1). The better barrier protection of ACS can be correlated to thick and insulating barrier layer which was furthered enhanced by improved hexavalent chromium sealing.

## Assessment of Global Barrier Degradation

The low-frequency EIS at 0.01 Hz and average open circuit potential for the AA2024-T351/Pretreatment system as a function of exposure time in different laboratory and field environments are summarized in Figures 5.2 and 5.3, respectively. The initial barrier properties of NCP are similar to that of NFF. CCC and TCP had slightly better barrier characteristics while anodized systems have improved barrier properties due to high resistance oxide layer (Figure 5. 2). The barrier degradation trends of conversion coatings are similar to that of NFF. ANS barrier properties decreased with increasing exposure time. They showed improved barrier characteristics at intermittent exposure times and this can be correlated to the self-sealing of outer porous layer of by corrosion products. ATS showed no significant change in barrier properties with increasing exposure environment in full immersion, modified ASTM B117 and field environments (Figure 5. 2 b-d) indicating their improved barrier characteristics with sealing. In a highly aggressive environment like ASTM B117 there was significant degradation in barrier properties after long exposure time (Figure 5. 2a). For ACS pretreatment, the low frequency EIS showed improved barrier properties with increasing exposure time indicating the further sealing by hexavalent chromium. The low frequency Z modulus showed slight barrier degradation after long exposure time in standard/modified ASTM B117. However even after prolonged exposure, the barrier properties as assessed by low frequency modulus at 0.01 Hz were 2-3 orders of magnitude higher than other chosen pretreatments (Figure 5. 2). Conversion coatings had a slightly more positive potentials compared to NFF. ANS had initially high potential, which dropped to OCP of AA2024-T351 with increasing exposure time indicating barrier degradation due to porous nature of oxide layer (Figure 5. 3). Sealing improved the barrier characteristics as could be inferred from ATS degradation trends (Figure 5. 3). ACS OCP

shifted to more positive potentials with increasing exposure time indicating improved sealing (Figure 5. 3).

### **Corrosion Volume Loss Analysis**

Optical profilometry maps of bare/pretreated AA2024-T351 after 400 h exposure in standard ASTM B117 environment is indicated in Figure 5. 4. Among chosen pretreatments, NCP, NFF and ANS exhibited significant localized corrosion as indicated by a greater number of deeper pits (Figure 5. 4). Other pretreatments provided good corrosion protection and this can be correlated to the presence of inhibitor species in conversion coating and as sealants in anodization (Figure 5. 4). Similar studies were conducted for all chosen pretreatments in selected LALT/field environments and the corrosion volume loss trends are summarized in Figure 5. 5 a-f. Among conversion coatings, CCC provided good corrosion protection. TCP provided moderate protection whereas NCP suffered severe corrosion volume loss and was comparable to NFF in terms of corrosion protection (Figure 5. 5a). Pit volume densities of anodized surface are not directly comparable to conversion coatings. This is due to highly porous nature of the anodized systems which resulted in two orders of magnitude higher pit volume densities even before the beginning of exposure (Figure 5. 5b). Both ATS and ACS had better barrier protection compared to ANS as indicated by lower corrosion volume loss after 400 h in Standard ASTM B117 exposure (Figure 5. 4). Similar studies conducted for pretreatments in other environments showed following order for the severity of the environment, CHO < Modified ASTM B117 < ASTM B117 (Figure 5. 5 c-f). It is to be noted that all corrosion volume loss trends indicated here represent the global barrier properties and their degradation with different environments. Similar studies were conducted for scribed panels in order to study efficacy of inhibitor species present in pretreatments to protect a remote scratch and reported in next section.

## **5.4.2 Scribe Protection of Pretreated 2024-T351 after Exposure in Selected Lab and Field Environments:**

### **Surface Morphology and Elemental Mapping**

SEM images of bare/pretreated 2024-T351 after 1000 h exposure in standard ASTM B117 are shown in Figure 5.6. Visual inspection of scratch indicate that ACS provided better scratch protection as could be inferred from the minimal corrosion products (Figure 5. 6f). CCC provided moderate scratch protection whereas all other chosen pretreatments exhibited severe corrosion of bare 2024-T351 scribe (Figure 5.6). EDS elemental mapping was conducted to further understand the nature of corrosion products and the other chemical species present in scribe and pretreated surface adjacent to the scribe (Figure 5.7). No substantial Cr, Zr or Ti leaching and redeposition of conversion coatings was evident from EDS maps. Sulfur leaching and redeposition was observed in anodization based pretreatments. Increasing oxygen intensity with increasing exposure time was observed in scratch and this can be correlated to more corrosion products or minimal protection (Figure 5.7). SEM/Oxygen elemental map for NFF, CCC and ACS pretreated 2024-T351 after exposure in modified ASTM B117 (1440 h) and field environments (4032 h) are shown in Figure 5.8. The degree of severity of environment showed good correlation to visual observations and corrosion volume loss results discussed in previous section (Table 5.2). The scratch protection trends are summarized in Table 5.3 using similar metrics discussed in visual observation section.

### **Corrosion Volume Loss Analysis**

Optical profilometry of scribe exposing AA2024-T351 in 2024-T351/Pretreatment after exposure in ASTM B117 for 1000 h is indicated in Figure 5.9. All corrosion volume loss maps were

representative of regions less than 50 micrometers from coating edge to scribe center. Among chosen pretreatments, ACS provided excellent scratch protection, whereas TCP provided moderate scratch protection (Figure 5.9). All other chosen pretreatments exhibited larger and deeper pits indicating heavy localized corrosion (Figure 5.9). Figure 5.10 summarizes the corrosion volume loss trends as a function of exposure environment in standard ASTM B117, modified ASTM B117 and field. All pretreatments showed very minimal corrosion for field exposure at CHO (Figure 5.10c). Modified ASTM B117 showed moderate scribe degradation whereas standard ASTM B117 showed significant scribe degradation (Figure 5.10a and b). The scratch protection trends are summarized in Table 5.4 and it showed similar scratch protection trends compared to SEM/EDS observations made earlier.

### **Surface Characterization**

In spite of better scratch protection as evident from SEM/EDS and optical profilometry, no hexavalent chromium based species was observed in the scribe for all chosen Cr based pretreatments. This could be due to large interaction volume of EDS technique. So a more surface sensitive technique such as Raman spectroscopy was utilized to characterize the pretreated AA2024-T351 surface as well as scratch after different exposure times. All spectroscopic measurements were limited to only two selected pretreatments which are Cr based. Figure 5.11a and b showed the Raman spectra of CCC and ACS pretreated 2024-T351 prior to environmental exposure. Well defined Raman peaks at  $860 - 865 \text{ cm}^{-1}$  indicated presence of  $\text{Cr}_2\text{O}_5$  based species on pretreated surface.<sup>150</sup> After environmental exposure for 48 and 1000 h in ASTM B117 for ACS pretreatment the peaks were still observed with slight peak shifts to  $867-872 \text{ cm}^{-1}$  indicating that ACS provide good barrier protection. In contrast, the Raman characterization of scratch (Figure 5.12) indicated a significant peak at  $851-858 \text{ cm}^{-1}$  range which corresponds to  $\text{CrO}_4^{2-}$  species.<sup>151</sup> The

peak height decreased with increasing exposure time in ASTM B117 environment. There is significant degradation of Raman peaks after 400h and 1000 h in CCC and ACS, respectively. This indicate that ACS provided better Cr induced inhibition compared to CCC.

### 5.4.3 Electrochemical Kinetics of AA2024-T351: Role of Pretreatments

#### Electrochemical Kinetics of Pretreated AA2024-T351 in the As-Received Condition

Figure 5. 13a and b illustrate the effect of pretreatment in cathodic kinetics of AA2024-T351 after 1 h OCP in 1 M NaCl and 1 M MgCl<sub>2</sub>, respectively. The OCP of resistive pretreatments are more positive in comparison to that of NFF. While conversion coatings have barrier properties comparable to NFF, the anodized systems have higher resistance due to insulating oxide layer.<sup>77</sup> This could be used to rationalize with the mixed potential model wherein as resistance of pretreatment increases, the OCP shifts to more positive potential.<sup>77</sup> Cathodic kinetics was also largely suppressed by the barrier resistance of the pretreatments. The limiting current for oxygen reduction reaction was much lower for high resistive pretreatments compared to that of bare AA2024-T351 (Figure 5.13) interpreted through rate limitation.

Figure 5.14a and b illustrate the effect of the pretreatment on breakdown potential and anodic kinetics of AA2024-T351 after 1 h OCP in 1 M NaCl and 1 M MgCl<sub>2</sub>, respectively. Among chosen pretreatments, ACS provided excellent corrosion inhibition and strong passivation which can be correlated to thick and insulating barrier layer which was further enhanced by improved hexavalent sealing. ANS and ATS based pretreatments showed initial passivation and active corrosion at higher overpotentials due to breakdown of oxide layer due to its porous nature and less effective sealing. NFF exhibited pitting at very low anodic over potentials. NCP exhibited slightly higher overpotential for pitting initiation whereas TCP and CCC exhibited passive behavior for 50-100 mV before pitting initiation.

### **Chemical Species Release**

Figure 5.14a summarizes the amount of aluminum ion leached from the AA2024-T351 with different pretreatments as a function of exposure time in 2 M NaCl solution droplet. NFF exhibited significant amount of  $\text{Al}^{3+}$  leaching at all exposure times indicating the susceptibility of the alloy to localized corrosion. Conversion coatings had reduced  $\text{Al}^{3+}$  leaching due to slightly improved barrier properties (Figure 5. 14a). Among the conversion coatings, chromate based pretreatments did not show significant trends in Al leaching trends with increasing exposure time (Figure 5. 14a). This could be due to formation of passive layer of chromate on defects. NCP showed increasing Al leaching with increasing exposure time indicating the barrier properties degradation and no inhibiting action by any ionic species leached from pretreatment (Figure 5.14a). ACS exhibited almost 2 orders of magnitude lesser compared to other chosen pretreatments (Figure 5.14a). This could be due to presence of thick barrier layer that had enhanced barrier properties by hexavalent chromium sealing of the pores. Apart from  $\text{Al}^{3+}$  leaching of other ionic species was also monitored (Figure 5. 14b). CCC does not exhibit any appreciable amount of Cr leaching in the test environment and time. TCP and NCP released Zr and Ti (Figure 5.14b). ACS exhibited a significant amount of Cr leaching (Figure 5.14b). The amount of Cr in the solution could play a major role in mixed potential model as chromates as they inhibit both cathodic and anodic reactions on AA2024-T351.

## **Electrochemical Kinetics of bare AA2024-T351 in presence of Anionic Species**

Based on the Cr leaching kinetics which justify presence of  $\text{Cr}^{6+}$  in the thin electrolyte layer, three different chromium ion concentration were chosen to study the influence of  $\text{CrO}_4^{2-}$  ions on cathodic kinetics. Figure 5. 16a and b illustrate the E-logi behavior of bare AA2024-T351 after 1 h OCP in 1 M NaCl and 1 M  $\text{MgCl}_2$ , respectively, with different inhibitor concentrations. The open circuit potential of AA2024-T351 decreased with increasing concentration of chromate species (Figure 5.16a). The limiting current density for ORR was also reduced by almost 2 orders of magnitude (Figure 5.16a). This could be due to competitive adsorption of  $\text{CrO}_4^{2-}$  species at the sites for oxygen reduction.<sup>22</sup>

Figure 5.17a and b illustrate the effect of the soluble chromates on breakdown potential and anodic kinetics of AA2024-T351 after 1 h OCP in 1 M NaCl and 1 M  $\text{MgCl}_2$ , respectively. Presence of chromate species reduced the open circuit potential and passivation for anodic overpotentials of 150-250 mV before active corrosion. This can be correlated to formation of Al(III) and Cr(VI) complex which improve the passivation before active corrosion of AA2024-T351.<sup>152</sup>

## **5.5 Discussion**

### **5.5.1 Summary of Protection Mechanisms**

Post exposure characterization indicated two primary modes of corrosion protection. The barrier protection is afforded by all chosen pretreatments whereas the scribe protection was afforded only by pretreatments which had hexavalent chromium species. ACS provided excellent barrier protection which further improved with increasing exposure in different environments indicative of improved sealing (Figure 5. 2). Both ORR and HER reactions are limited by improved barrier characteristics in ACS pretreated systems (Figure 5. 16c). CCC, TCP and ATS exhibited moderate

barrier protection (Table 5.2). This can be correlated to initially low ORR rates which increased with increasing exposure time in full immersion conditions (Figure 5. 16). NFF, NCP and ANS showed significant localized corrosion indicative of very little barrier protection (Figure 5. 10). The scribe protection can be attributed to release of anionic species from hexavalent chromium based pretreatments. Non-chrome and trivalent chromium based systems provided limited and moderate scribe protection, respectively (Figure 5. 10). CCC provided slightly improved scribe protection (Figure 5. 10). In CCC, no chromium leaching was detected during controlled relative humidity studies. However, Raman peak corresponding to  $\text{CrO}_4^{2-}$  species was detected in scribe after exposure in ASTM B117 for 48 h (Figure 5. 12). In contrast, ACS based systems showed substantial amount of chromium leaching in controlled relative humidity studies (Figure 5. 14). Presence of hexavalent chromium species in solution decreased ORR rate by 2-3 orders of magnitude. In addition, re-deposition of  $\text{CrO}_4^{2-}$  species was observed after exposure in ASTM B117 for 1000 h as confirmed by Raman spectroscopy (Figure 5. 12). Both these trends confirmed that ACS provided improved corrosion protection compared to CCC due to leaching of substantial hexavalent Cr species for prolonged exposure time.

In addition to barrier protection, chromate based pretreatments renders active protection to AA2024-T351 by leaching of anionic species. Chromate species release is favored at high pH and they migrate to exposed area on the AA2024-T351 surface.<sup>42</sup> The hexavalent chromium species was reduced at active sites of the surface to form a monolayer of chromium (III) oxide.<sup>42</sup> This reduces the local galvanic interaction and results in a uniform potential distribution across the surface. This also acts as a barrier for diffusion of  $\text{Cl}^-$  species. This layer reduces the activity of cathodic sites such as Cu-rich intermetallic particles.<sup>22</sup> This layer also strongly retards the

dealloying of S-phase particles and significantly reduces the copper enrichment on surface which acts as cathodic sites. In addition,  $\text{CrO}_4^{2-}$  also inhibits pit initiation.<sup>26</sup>

### **5.5.2 Effect on Pretreatment Degradation on Sacrificial Protection Function of MgRP systems**

Current work which summarizes the efficacy of pretreatments for corrosion protection of AA2024-T351 and which also explains the barrier degradation of different pretreatments furthers the understanding of performance of MgRP along with pretreated AA2024-T351.<sup>75,76</sup> For MgRP systems without topcoat, NFF provided sacrificial protection to underlying AA2024-T351 substrate commencing immediately from the beginning of exposure time in different environments.<sup>75</sup> Conversion coatings provided a delayed sacrificial protection while anodized systems provided very limited galvanic protection attributed to high resistance.<sup>75,76</sup> Delayed protection can be explained by the pretreatment degradation trends in selected LALT and field environments. In addition, the scribe protection for ACS pretreated AA2024-T351/MgRP which exhibited very limited sacrificial protection can be attributed to leaching of hexavalent chromium based species.

#### **1.1.1 Influence of Pretreatments on Electrochemical Throwing Power of Mg**

In light of recent findings, the role of pretreatments in electrochemical throwing power between Mg and AA2024-T351 need to be rationalized to further the application of MgRP with different pretreatments. Previous work reported elsewhere has explored the usage of diagnostic multi-electrode arrays and finite elemental analysis numerical modelling for understanding effect of different variables in galvanic throwing power of bare Mg coupled with bare AA2024 scribe.<sup>82,83</sup> There is a need to understand the resistive effects and effects of anionic species leaching on electrochemical throwing power. Cathodic polarization measurements for bare/pretreated

AA2024-T351 in presence and absence of anionic species to understand the role of pretreatments in cathodic kinetics. Further studies will be conducted in solutions of NaCl and MgCl<sub>2</sub> at various concentrations with ambient aeration. Effects of anionic species leaching on anodic kinetics need to be considered and factored into analysis of bare Mg with similar solution chemistries. Along with this diagnostic multi-electrode array experiments need to be conducted for simulated environments with anionic species.

## **5.6 Conclusions**

- The low frequency EIS and OCP of AA2024-T351/Pretreatment indicated significant pretreatment degradation in Standard ASTM B117 and very minimal degradation in field environments. Modified ASTM B117 and full immersion exposure exhibited moderate pretreatment degradation.
- The macroscopic morphology observations, barrier degradation trends and corrosion volume loss showed similar pretreatment degradation trends. ACS provided excellent barrier properties which improved with increasing exposure time due to improved sealing. CCC, TCP and ATS exhibited moderate corrosion protection whereas NFF, NCP and ANS showed significant localized corrosion.
- The surface morphology characterization, elemental mapping and corrosion volume loss characterization indicated NCP and ANS did not exhibit any significant scribe protection. CCC, TCP and ATS provided moderate scratch protection whereas ACS provided excellent scratch protection. This can be correlated to anionic species leaching and redeposition to form a passive chromium oxide layer as confirmed using Raman spectroscopy.

- The cathodic kinetics of AA2024-T351 was studied for pretreated AA2024-T351 in as received conditions. The ORR limiting current decreases with increasing pretreatment resistance.
- ACS provided excellent corrosion inhibition and strong passivation which can be correlated to thick and insulating barrier layer which was further enhanced by improved hexavalent sealing. ANS and ATS based pretreatments showed initial passivation and active corrosion at higher overpotentials due to breakdown of oxide layer due to its porous nature and less effective sealing. NFF exhibited pitting at very low anodic over potentials. NCP exhibited slightly higher overpotential for pitting initiation whereas TCP and CCC exhibited passive behavior for 50-100 mV before pitting initiation.
- Chemical leaching studies were conducted for different pretreatments in controlled relative humidity cabinets with sodium chloride droplet for different exposure times. The solution was analyzed using ICP-OES and indicated leaching of Cr, Zr and Ti from pretreatments. Al, Cu and Mg from the substrate alloy also leached and the leaching kinetics confirmed similar corrosion protection trends as that after LALT/field exposure.
- The cathodic kinetics conducted for bare AA2024-T351 with  $\text{CrO}_4^{2-}$  species indicated that ORR rate is suppressed with increasing chromium species concentration.
- Presence of chromate species reduced the open circuit potential and passivation for anodic overpotentials of 150-250 mV before active corrosion. This can be correlated to formation of Al(III) and Cr(VI) complex which improve the passivation before active corrosion of AA2024-T351.

## 5.7 References

1. ASM International Handbook Committee., ASM Handbook Corrosion: Materials. Vol. 13A (Materials Park, OH: ASM International, 2003).
2. A. Bautista, R. Lizarbe, E. Otero, V. Lopez, and J.A. Gonzalez, "New alternatives to the industrially introduced methods for the sealing of anodized aluminium," *Revista De Metalurgia* 35, 3 (1999): p. 195-202.
3. N. Chahboun, E. Rocca, D. Veys-Renaux, M. Augros, M. Boutoba, and N. Caldeira, "Sealing of Anodized Multiphase Aluminum Alloys with Cr( plus III)/Zr( plus IV) Salts: Characterization and Corrosion Behavior," *Journal of the Electrochemical Society* 163, 3 (2016): p. C69-C75.
4. P.D. Deck and D. Reichgott, "Characterization of chromium-free no-rinse prepaint coatings on aluminum and galvanized steel," *Metal Fin.* 90, 9 (1992): p. 29-35.
5. J.A. Gonzalez, V. Lopez, E. Otero, A. Bautista, R. Lizarbe, C. Barba, and J.L. Baldonado, "Overaging of sealed and unsealed aluminium oxide films," *Corrosion Science* 39, 6 (1997): p. 1109-1118.
6. J.A. Gonzalez, M. Morcillo, E. Escudero, V. Lopez, A. Bautista, and E. Otero, "Self-sealing of unsealed aluminium anodic oxide films in very different atmospheres," *Revista De Metalurgia* (2003): p. 110-115.
7. Y. Guo and G.S. Frankel, "Active Corrosion Inhibition of AA2024-T3 by Trivalent Chrome Process Treatment," *Corrosion* 68, 4 (2012).
8. N.P. Hu, X.C. Dong, X.Y. He, J.F. Browning, and D.W. Schaefer, "Effect of sealing on the morphology of anodized aluminum oxide," *Corrosion Science* 97, (2015): p. 17-24.
9. Y.L. Huang, H. Shih, H.C. Huang, S. Wu, S. Ramanathan, C. Chang, and F. Mansfeld, "Evaluation of the corrosion resistance of anodized aluminum 6061 using electrochemical impedance spectroscopy (EIS)," *Corrosion Science* 50, 12 (2008): p. 3569-3575.
10. G.O. Ilevbare, C.S. Jeffcoate, and J.R. Scully, "Mass transport limited oxygen reduction kinetics on chromate conversion coated Al-Cu, Al-Cu-Mg and Al-Cu-Mn-Fe intermetallic compounds.," *Passivity and Localized Corrosion* 99, 27 (1999): p. 269-279.
11. G.O. Ilevbare and J.R. Scully, "Mass-Transport-Limited oxygen reduction reaction on AA2024-T3 and selected intermetallic compounds in chromate-containing solutions (vol 57, pg 134, 2001)," *Corrosion* 57, 5 (2001): p. 480-480.
12. G.O. Ilevbare and J.R. Scully, "Oxygen reduction reaction kinetics on chromate conversion coated Al-Cu, Al-Cu-Mg, and Al-Cu-Mn-Fe intermetallic compounds," *Journal of the Electrochemical Society* 148, 5 (2001): p. B196-B207.
13. G.O. Ilevbare and J.R. Scully, "Mass-transport-limited oxygen reduction reaction on AA2024-T3 and selected intermetallic compounds in chromate-containing solutions," *Corrosion* 57, 2 (2001): p. 134-152.

14. G.O. Ilevbare, J.R. Scully, J. Yuan, and R.G. Kelly, "Inhibition of pitting corrosion on aluminum alloy 2024-T3: Effect of soluble chromate additions vs chromate conversion coating," *Corrosion* 56, 3 (2000): p. 227-242.
15. D. Kanagaraj, S. Mohan, N.G. Renganathan, R.V. Raman, and S.V. Iyer, "Evaluation of anodized aluminum surface obtained from a sulfanic acid bath using electrochemical impedance spectroscopy," *Plating and Surface Finishing* 86, 7 (1999): p. 58-61.
16. J. Lee, Y. Kim, H. Jang, and W. Chung, "Cr<sub>2</sub>O<sub>3</sub> sealing of anodized aluminum alloy by heat treatment," *Surface & Coatings Technology* 243, (2014): p. 34-38.
17. Y. Li and Z.F. Zhu, "Cold Sealing Mechanism of Anodic Oxide-Films on Aluminum .2. Cold Sealing Models of Oxide-Films," *Plating and Surface Finishing* 80, 10 (1993): p. 77-80.
18. Y. Li, Z.F. Zhu, Z.Y. Jiang, and M.M. Yan, "Cold Sealing Mechanism of Anodic Oxide-Films on Aluminum .1. Composition and Structure of Cold-Sealed Oxide-Films," *Plating and Surface Finishing* 80, 9 (1993): p. 79-82.
19. D. Liu, G.Y. Wei, and P.L. He, "The Effect of Sealing and Trivalent Chromium Passivating on Anodized Aluminum," *International Journal of Electrochemical Science* 11, 3 (2016): p. 2097-2105.
20. O. Lunder, C. Simensen, Y. Yu, and K. Nisancioglu, "Formation and characterisation of Ti–Zr based conversion layers on AA6060 aluminium," *Surface and Coatings Technology* 184, 2 (2004): p. 278-290.
21. F. Mansfeld and M.W. Kendig, "Evaluation of Anodized Aluminum Surfaces with Electrochemical Impedance Spectroscopy," *Journal of the Electrochemical Society* 135, 4 (1988): p. 828-833.
22. F. Mansfeld, G. Zhang, and C. Chen, "Evaluation of sealing methods for anodized aluminum alloys with electrochemical impedance spectroscopy (EIS)," *Plating and Surface Finishing* 84, 12 (1997): p. 72-81.
23. C. Matzdorf, Beck, Erin., Hilgeman, Amy., Prado, Ruben. , *Trivalent Chromium Process as a Sealer for MIL-A-8625 Type II, IIB and IC Anodic Coatings*. 2008, NAVAIR. p. 50.
24. D.E. Packham, *Handbook of Adhesion*. 2 ed.
25. L. Xia, E. Akiyama, G. Frankel, and R. McCreery, "Storage and release of soluble hexavalent chromium from chromate conversion coatings - Equilibrium aspects of Cr-VI concentration," *Journal of the Electrochemical Society* 147, 7 (2000): p. 2556-2562.
26. J. Zhao, G. Frankel, and R.L. McCreery, "Corrosion protection of untreated AA-2024-T3 in chloride solution by a chromate conversion coating monitored with Raman spectroscopy," *Journal of the Electrochemical Society* 145, 7 (1998): p. 2258-2264.
27. J.M. Zhao, H.X. Liu, S.L. Chen, and X.H. Zhao, "EIS evolution of anodised aluminium by cerium salt sealing in NaCl solution with exposure time," *Corrosion Engineering Science and Technology* 48, 1 (2013): p. 44-47.
28. X. Zhao, L. Tian, J. Zhao, and Y. Zuo, "Electrochemical properties of anodized and sealed aluminum films," *Aicam* 2005 11-12, (2006): p. 433-436.
29. X.H. Zhao, Y. Zuo, J.M. Zhao, J.P. Xiong, and Y.M. Tang, "A study on the self-sealing process of anodic films on aluminum by EIS," *Surface & Coatings Technology* 200, 24 (2006): p. 6846-6853.

30. Y. Zuo, P.H. Zhao, and J.M. Zhao, "The influences of sealing methods on corrosion behavior of anodized aluminum alloys in NaCl solutions," *Surface & Coatings Technology* 166, 2-3 (2003): p. 237-242.
31. D. Battocchi, A.M. Simoes, D.E. Tallman, and G.P. Bierwagen, "Electrochemical behaviour of a Mg-rich primer in the protection of Al alloys," *Corrosion Science* 48, 5 (2006): p. 1292-1306.
32. G. Bierwagen, D. Battocchi, A. Simoes, A. Stanness, and D. Tallman, "The use of multiple electrochemical techniques to characterize Mg-rich primers for Al alloys," *Progress in Organic Coatings* 59, 3 (2007): p. 172-178.
33. B. Kannan, Scully, J. R, "Performance of a Magnesium Rich Primer on Pretreated AA2024-T351 in Selected Laboratory and Field Environments: Conversion Coating Pretreatments," *Corrosion* (2016).
34. B. Kannan, A. King, and J. Scully, *Impact of Surface Pretreatments on AA2024-T351 Corrosion Protection by a Magnesium Rich, Non-Chrome Primer (MgRP)*, in *NACE DoD 2015*. 2015, NACE: Pittsburgh, PA.
35. B. Kannan, A. King, and J. Scully, "Effect of Pretreatments on 2024-T351 Corrosion Protection by Magnesium Rich, Non-Chromium Primer (MgRP): Laboratory Characterization in Full Immersion," *Corrosion* doi:10.5006/1700, (2015).
36. A.D. King, B. Kannan, and J.R. Scully, "Environmental Degradation of a Mg-Rich Primer in Selected Field and Laboratory Environments – Part II. Primer and Topcoat," *Corrosion* 70, 5 (2014).
37. A.D. King, B. Kannan, and J.R. Scully, "Environmental Degradation of a Mg-Rich Primer in Selected Field and Laboratory Environments – Part I. Without a Topcoat," *Corrosion* 70, 5 (2014).
38. A.D. King, J.S. Lee, and J.R. Scully, "Galvanic Couple Current and Potential Distribution between a Mg Electrode and 2024-T351 under Droplets Analyzed by Microelectrode Arrays," *Journal of the Electrochemical Society* 162, 1 (2015): p. C12-C23.
39. A.D. King, J.S. Lee, and J.R. Scully, "Finite Element Analysis of the Galvanic Couple Current and Potential Distribution between Mg and 2024-T351 in a Mg Rich Primer Configuration," *Journal of The Electrochemical Society* 163, 7 (2016): p. C342-C356.
40. A.D. King and J.R. Scully, "Sacrificial Anode-Based Galvanic and Barrier Corrosion Protection of 2024-T351 by a Mg-Rich Primer and Development of Test Methods for Remaining Life Assessment," *Corrosion* 67, 5 (2011): p. 05500401-05500422.
41. A.D. King and J.R. Scully. *Blistering Phenomena in Early Generation Mg-Rich Primer Coatings on AA2024-T351 and the Effects of CO<sub>2</sub>*. in *NACE DoD 2011 Conference Proceedings*. 2011. Palm Springs, CA.
42. B. Maier and G.S. Frankel, "Behavior of Magnesium-Rich Primers on AA2024-T3," *Corrosion* 67, 5 (2011): p. 055001.
43. R.J. Santucci, Kannan, B., Scully, J. R, "Investigation of Magnesium Oxide Primer on 2024-T351: Assessment and Characterization of Magnesium Oxide Protection Mechanism," *Corrosion* (2016).
44. S. Pathak, M. Blanton, S. Mendon, and J. Rawlins, "Mineralogical Transformation and Electrochemical Nature of Magnesium-Rich Primers during Natural Weathering," *Metals* 4, 3 (2014): p. 322.

45. S.S. Pathak, M.D. Blanton, S.K. Mendon, and J.W. Rawlins, "Investigation on dual corrosion performance of magnesium-rich primer for aluminum alloys under salt spray test (ASTM B117) and natural exposure," *Corrosion Science* 52, 4 (2010): p. 1453-1463.
46. S.S. Pathak, M.D. Blanton, S.K. Mendon, and J.W. Rawlins, "Carbonation of Mg powder to enhance the corrosion resistance of Mg-rich primers," *Corrosion Science* 52, 11 (2010): p. 3782-3792.
47. N.D. Richter and D. Battocchi, "PMSE 332-Performance of Mg-rich primers in B117 salt fog," *Abstracts of Papers of the American Chemical Society* 235, (2008).
48. R.A. Armas, C.A. Gervasi, A. Disarli, S.G. Real, and J.R. Vilche, "Zinc-Rich Paints on Steels in Artificial Seawater by Electrochemical Impedance Spectroscopy," *Corrosion* 48, 5 (1992): p. 379-383.
49. O.O. Knudsen, U. Steinsmo, and M. Bjordal, "Zinc-rich primers - Test performance and electrochemical properties," *Progress in Organic Coatings* 54, 3 (2005): p. 224-229.
50. H. Marchebois, M. Keddam, C. Savall, J. Bernard, and S. Touzain, "Zinc-rich powder coatings characterisation in artificial sea water - EIS analysis of the galvanic action," *Electrochimica Acta* 49, 11 (2004): p. 1719-1729.
51. M. Morcillo, R. Barajas, S. Feliu, and J.M. Bastidas, "A-Sem Study on the Galvanic Protection of Zinc-Rich Paints," *Journal of Materials Science* 25, 5 (1990): p. 2441-2446.
52. Pantheon, *Surface Pretreatment - Technical Data Sheet* (2009).
53. Henkel, *Surface Pretreatment - Technical Data Sheet* (2006).
54. Henkel, *Surface Pretreatment - Technical Data Sheet* (2014).
55. Surtec, *Surface Pretreatment - Technical Data Sheet* (2012).
56. ASTM, *Standard Practice for Operating Salt Spray (Fog) Apparatus: B117*, in *Annual Book of ASTM Standards*. 1997, ASTM: West Conshohocken, PA. p. 1-8.
57. ASTM, "Standard Practice for the Preparation of Substitute Ocean Water," ASTM D1141 - 98 DOI: 10.1520/D1141-98R08 (1998).
58. ASTM, "Standard Practice for Modified Salt Spray Testing," ASTM G85 - A3 DOI: 10.1520/C0033-03, (2009).
59. ASTM, "Standard Guide for Conducting Corrosion Tests in Field Applications," ASTM G4 - 01 DOI: 10.1520/G0004-01R08, (2001).
60. ASTM, "Standard Practice for Preparing, Cleaning, and Evaluating Corrosion Test Specimens," ASTM G1 DOI: 10.1520/D1141-98R08 (2003).
61. M.T. Woldemedhin, M.E. Shedd, and R.G. Kelly, "Evaluation of the Maximum Pit Size Model on Stainless Steels under Thin Film Electrolyte Conditions," *Journal of the Electrochemical Society* 161, 8 (2014): p. E3216-E3224.
62. N.E.C. Co and J.T. Burns, "Galvanic Corrosion-Induced Fatigue Crack Initiation and Propagation Behavior in AA7050-T7451," *CORROSION* 72, 10 (2016): p. 1215-1219.
63. L. Bland, J. Fitz-Gerald, and J. Scully, "Metallurgical and Electrochemical Characterization of the Corrosion of AZ31B-H24 Tungsten Inert Gas Weld: Isolated Weld Zones," *Corrosion* (2015).
64. L.G. Bland, A.D. King, N. Birbilis, and J.R. Scully, "Assessing the Corrosion of Commercially Pure Magnesium and Commercial AZ31B by Electrochemical Impedance, Mass-Loss, Hydrogen Collection, and Inductively Coupled Plasma Optical Emission Spectrometry Solution Analysis," *CORROSION* 71, 2 (2015): p. 128-145.

65. L.G. Bland, B.C.R. Troconis, R.J.S. Jr., J.M. Fitz-Gerald, and J.R. Scully, "Metallurgical and Electrochemical Characterization of the Corrosion of a Mg-Al-Zn Alloy AZ31B-H24 Tungsten Inert Gas Weld: Galvanic Corrosion Between Weld Zones," *CORROSION* 72, 10 (2016): p. 1226-1242.
66. J.E. Maslar, W.S. Hurst, T.A. Vanderah, and I. Levin, "The Raman spectra of Cr<sub>3</sub>O<sub>8</sub> and Cr<sub>2</sub>O<sub>5</sub>," *Journal of Raman Spectroscopy* 32, 3 (2001): p. 201-206.
67. Y.-S. Li, K. Wang, P. He, B.X. Huang, and P. Kovacs, "Surface-enhanced Raman spectroelectrochemical studies of corrosion films on implant Co–Cr–Mo alloy in biosimulating solutions," *Journal of Raman Spectroscopy* 30, 2 (1999): p. 97-103.
68. D. Chidambaram, M. Jaime Vasquez, G.P. Halada, and C.R. Clayton, "Studies on the repassivation behavior of aluminum and aluminum alloy exposed to chromate solutions," *Surface and Interface Analysis* 35, 2 (2003): p. 226-230.
69. M.W. Kendig and R.G. Buchheit, "Corrosion inhibition of aluminum and aluminum alloys by soluble chromates, chromate coatings, and chromate-free coatings," *Corrosion* 59, 5 (2003): p. 379-400.

## 5.8 Tables

Table 5.1. Experimental protocol for modified ASTM B117 environmental exposure.

Total Exposure Time	UV exposure (h)	Cycles	ASTM B117 exposure (h)	Cycles
72	12	3	12	3
144	24	3	24	3
384	48	4	48	4
576	72	4	72	4
960	120	5	120	5
1440	120	6	120	6

Table 5.2. Summary of pretreatment degradation trends after exposure in different LALT/field exposures. Pretreatments were ranked from 1-4 based on visual appearances. 1 indicates minimal corrosion and 4 indicates severe corrosion.

Global	ASTM B-117	Modified ASTM B-117	Field, at Birdwood, CHO
NFF	4	3	1
CCC	2	2	1
TCP	3	2	1
NCP	4	3	1
ANS	4	1	1
ACS	1	1	1
ATS	3	1	1

Table 5.3. Summary of scribe protection trends (SEM/EDS) after exposure in different LALT/field exposures. Pretreatments were ranked from 1-4 based on SEM images and oxygen elemental maps. 1 indicates excellent scribe protection and 4 indicates severe corrosion at scribe.

<b>Scribe Protection (SEM/EDS)</b>	<b>ASTM B-117</b>	<b>Modified ASTM B-117</b>	<b>Field, at Birdwood, CHO</b>
NFF	4	3	1
CCC	2	3	2
TCP	3	2	2
NCP	4	3	1
ANS	4	2	1
ACS	1	1	1
ATS	3	3	2

Table 5.4. Summary of scribe protection trends (optical profilometry) after exposure in different LALT/field exposures. Pretreatments were ranked from 1-4 based on corrosion volume loss. 1 low pit volume densities and 4 indicates high pit volume densities.

<b>Scribe Protection (Optical Profilometry)</b>	<b>ASTM B-117</b>	<b>Modified ASTM B-117</b>	<b>Field, at Birdwood, CHO</b>
NFF	4	3	1
CCC	3	1	1
TCP	2	1	1
NCP	3	2	1
ANS	3	2	1
ACS	1	1	1
ATS	3	1	1

## 5.9 Figures

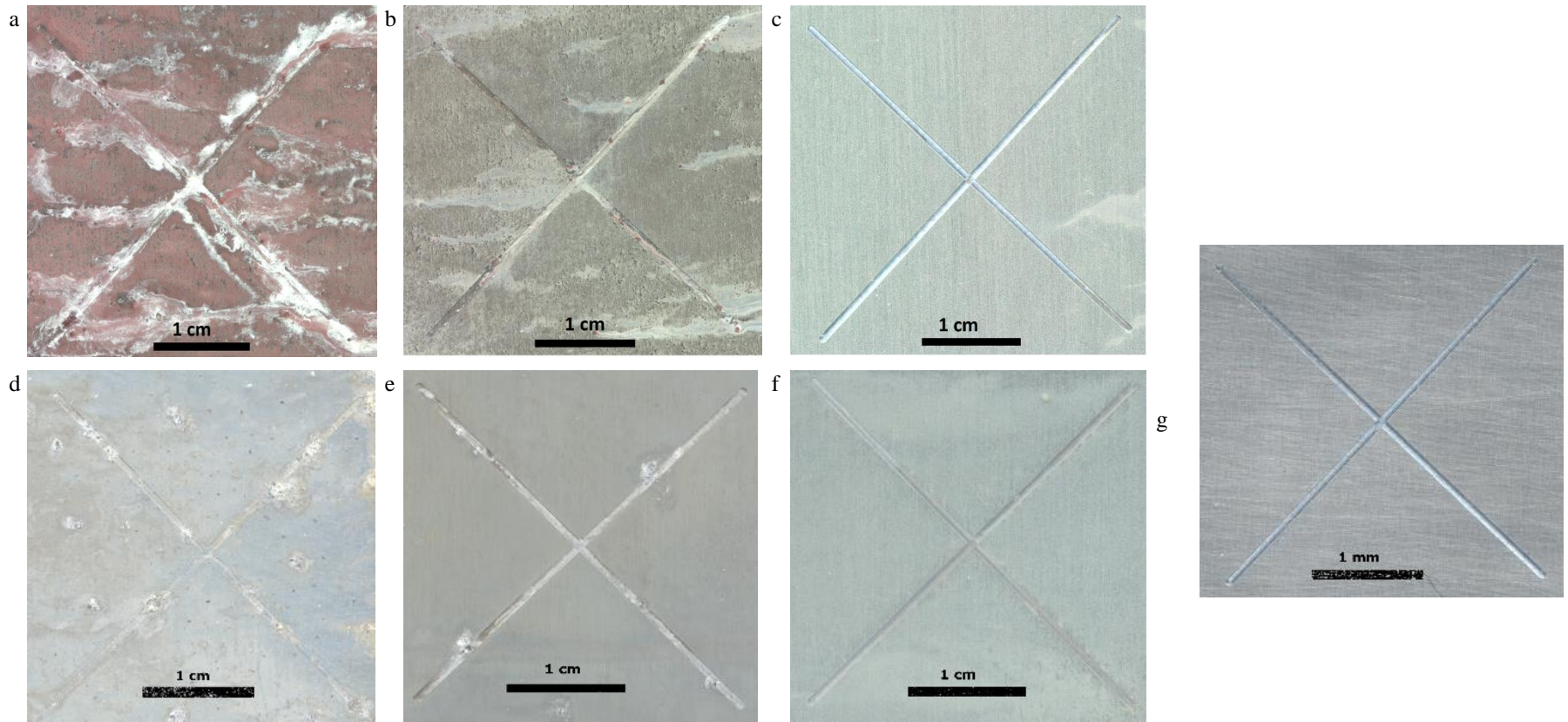


Figure 5.1. Macroscopic morphology of AA2024-T351/Pretreat after different LALT/field exposures. (a) AA2024-T351/NFF after 1000 h in ASTM B117 (b) AA2024-T351/CCC after 1000 h in ASTM B117 (c) AA2024-T351/ACS after 1440 h in ASTM B117 (d) AA2024-T351/NFF after 1440 h in Modified ASTM B117 (e) AA2024-T351/CCC after 1440 h in Modified ASTM B117 (f) AA2024-T351/ACS after 1440 h in Modified ASTM B117 and (g) AA2024-T351/NFF after 4032 h in CHO

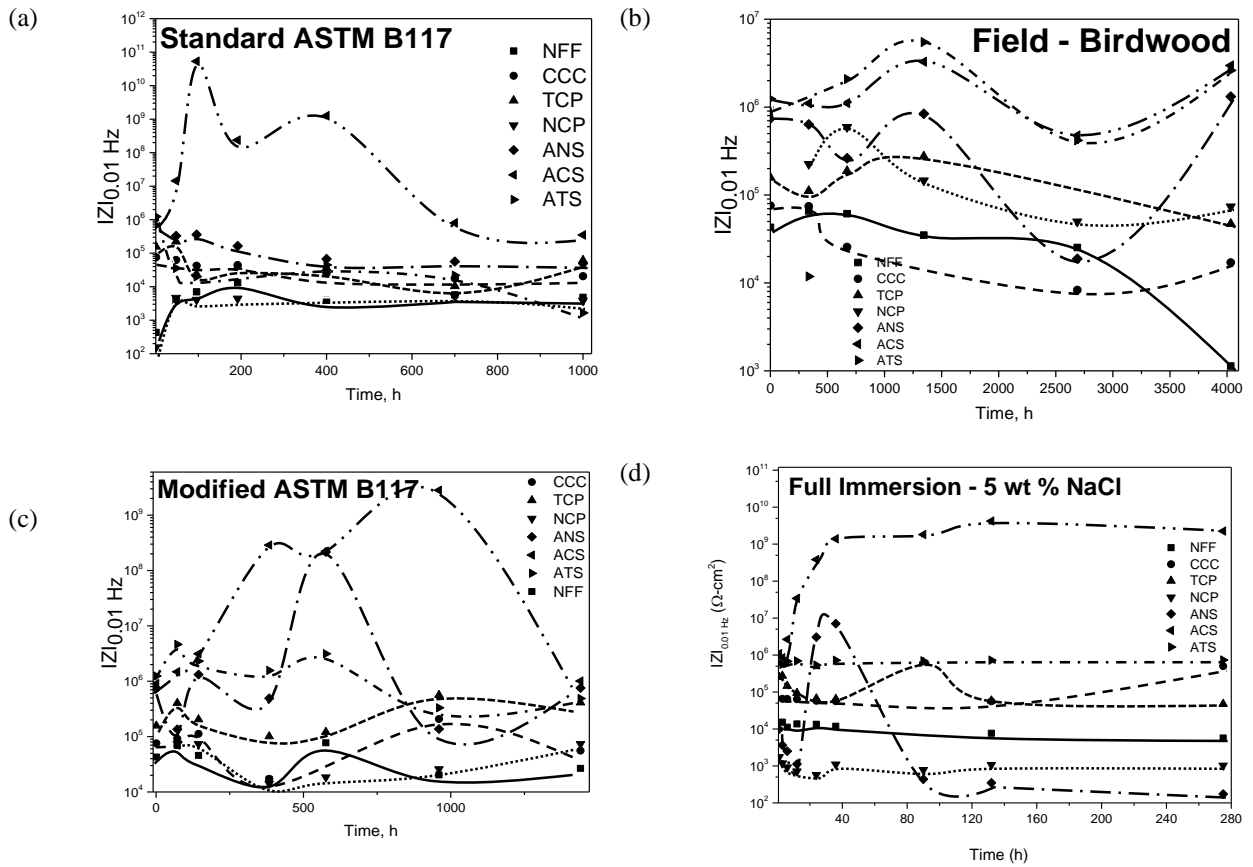


Figure 5.2. Low frequency impedance IZI modulus of AA2024-T351/Pretreatment systems at 0.01 Hz vs time in the environments indicated for (a) Standard ASTM B117 (b) At field, CHO (c) Modified ASTM B117 with SOW and UV and (d) Full immersion in 5 % (wt) NaCl solution.

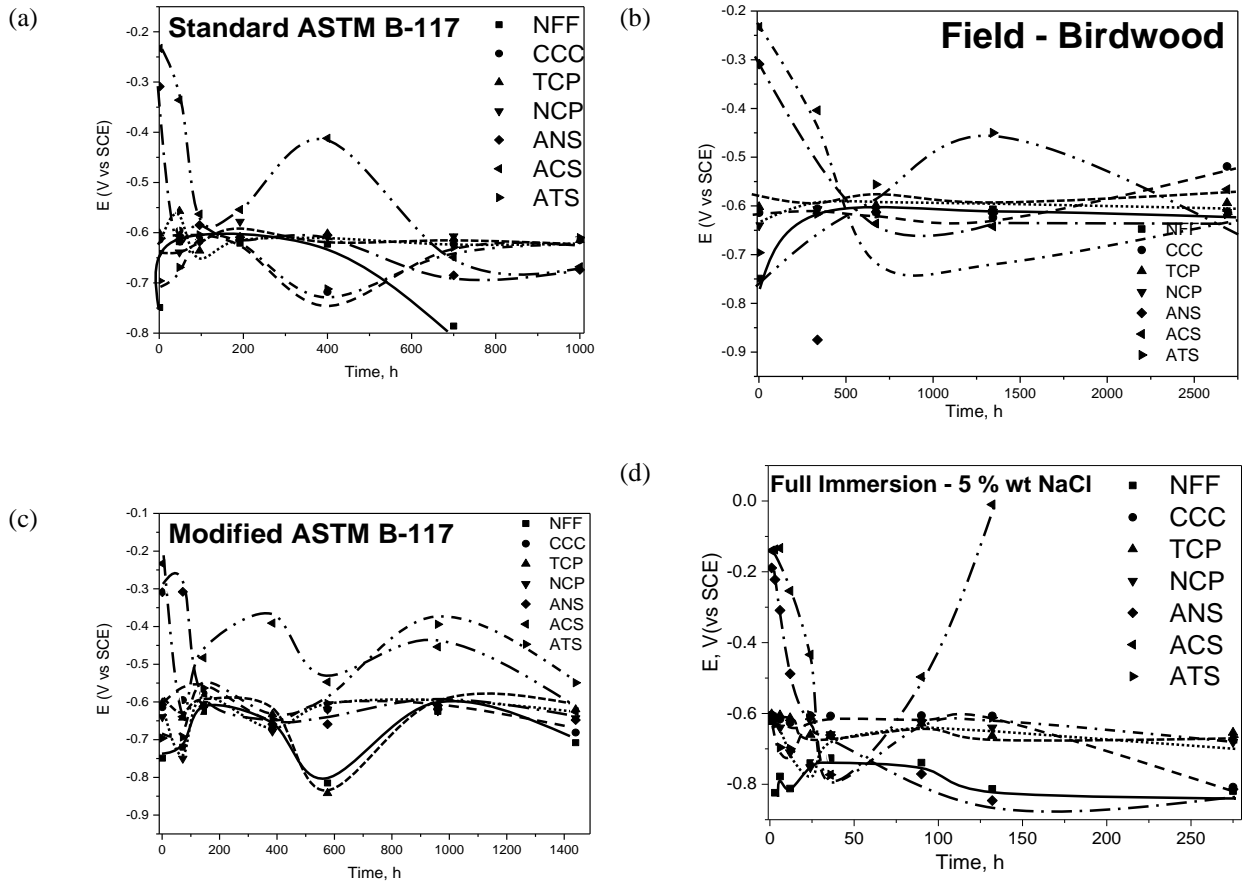


Figure 5.3. Average open circuit potential (1 hour) of AA2024-T351/Pretreatment systems vs time in the environments indicated for (a) Standard ASTM B117 (b) At field, CHO (c) Modified ASTM B117 with SOW and UV and (d) Full immersion in 5 % (wt) NaCl solution.

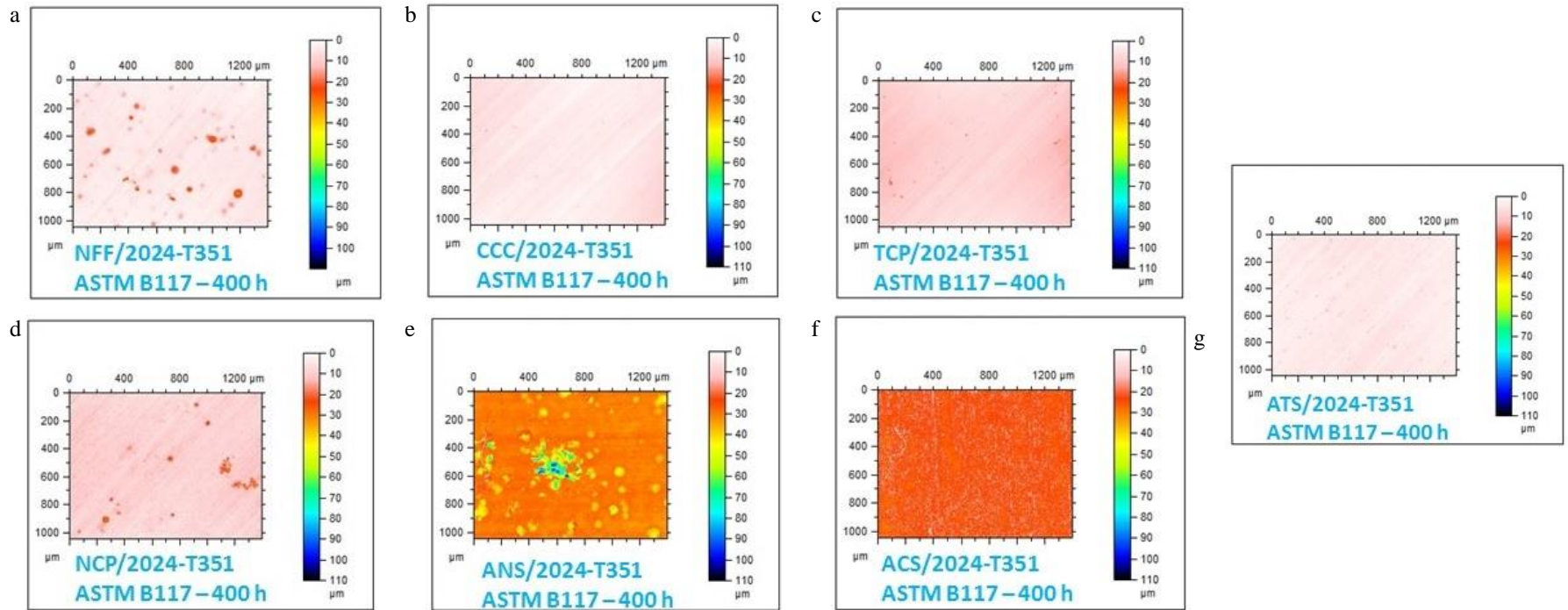


Figure 5.4. Optical profilometry maps of AA2024-T351/Pretreatment after exposure in standard ASTM B117 for 400 h. (a) AA2024-T351/NFF, (b) AA2024-T351/CCC, (c) AA2024-T351/TCP, (d) AA2024-T351/NCP, (e) AA2024-T351/ANS, (f) AA2024-T351/ACS and (g) AA2024-T351/ATS. The 0  $\mu\text{m}$  position (white) on the scale is indicative of the starting material condition before corrosion.

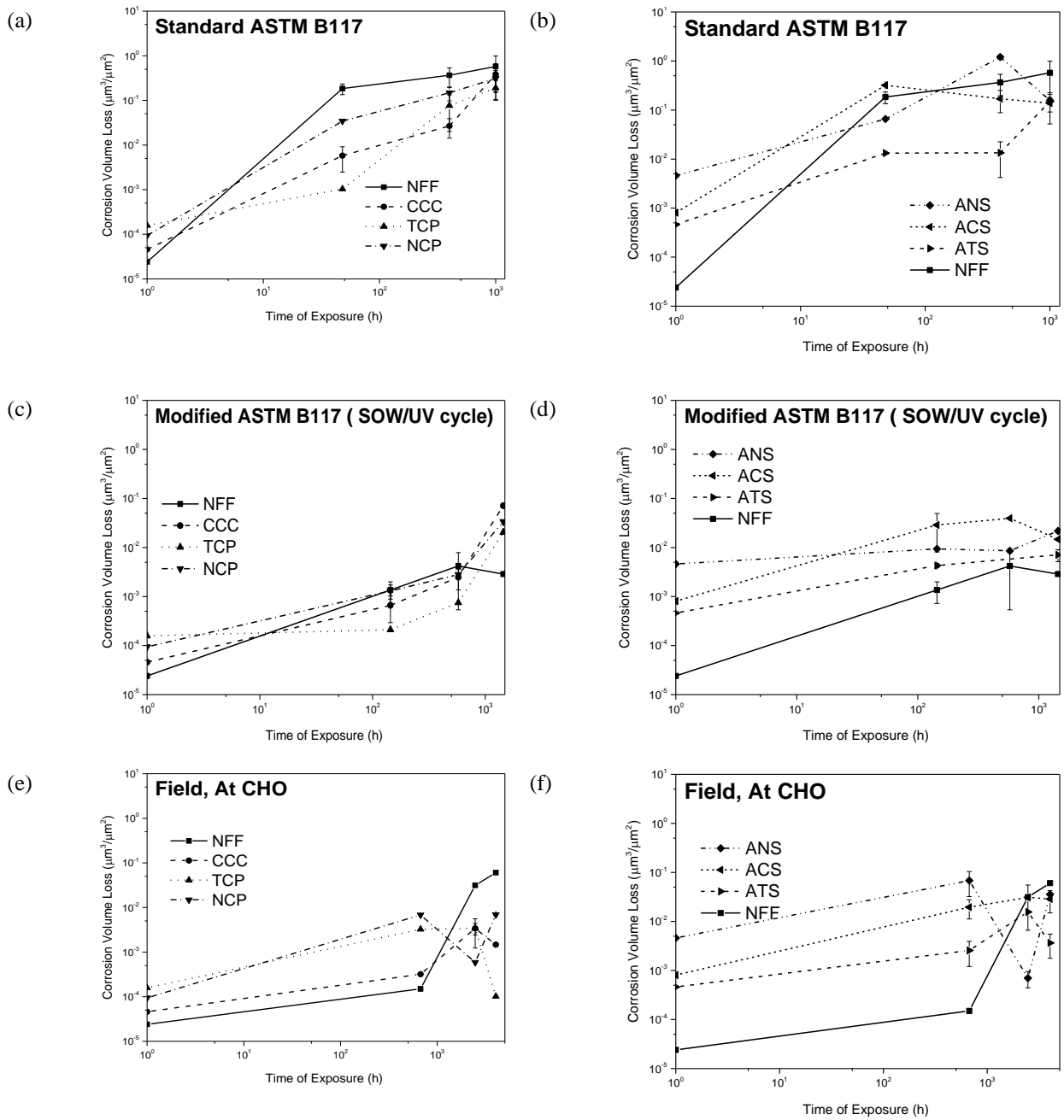


Figure 5.5. Corrosion volume loss of AA2024-T351/Pretreatment as a function of exposure time in in different LALT/field environments indicated. (a) NFF vs conversion coating in standard ASTM B117, (b) NFF vs anodization in standard ASTM B117, (c) NFF vs conversion coating in modified ASTM B117, (d) NFF vs anodization in modified ASTM B117, (e) NFF vs conversion coating at CHO, and (f) NFF vs anodization at CHO

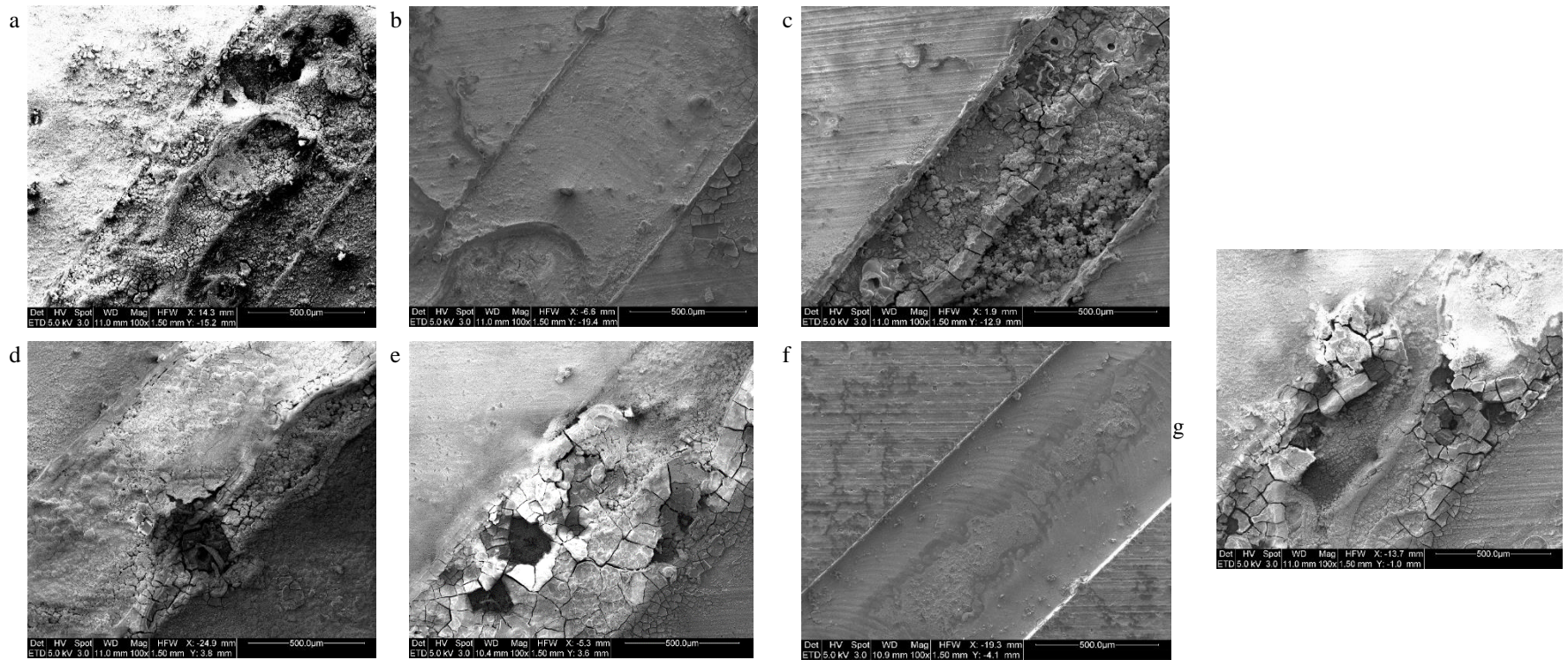


Figure 5.6. SEM morphology of 2024-T351/Pretreat after exposure in standard ASTM B117 environment for 1000 h. (a) AA2024-T351/NFF, (b) AA2024-T351/CCC, (c) AA2024-T351/TCP, (d) AA2024-T351/NCP, (e) AA2024-T351/ANS, (f) AA2024-T351/ACS and (g) AA2024-T351/ATS.

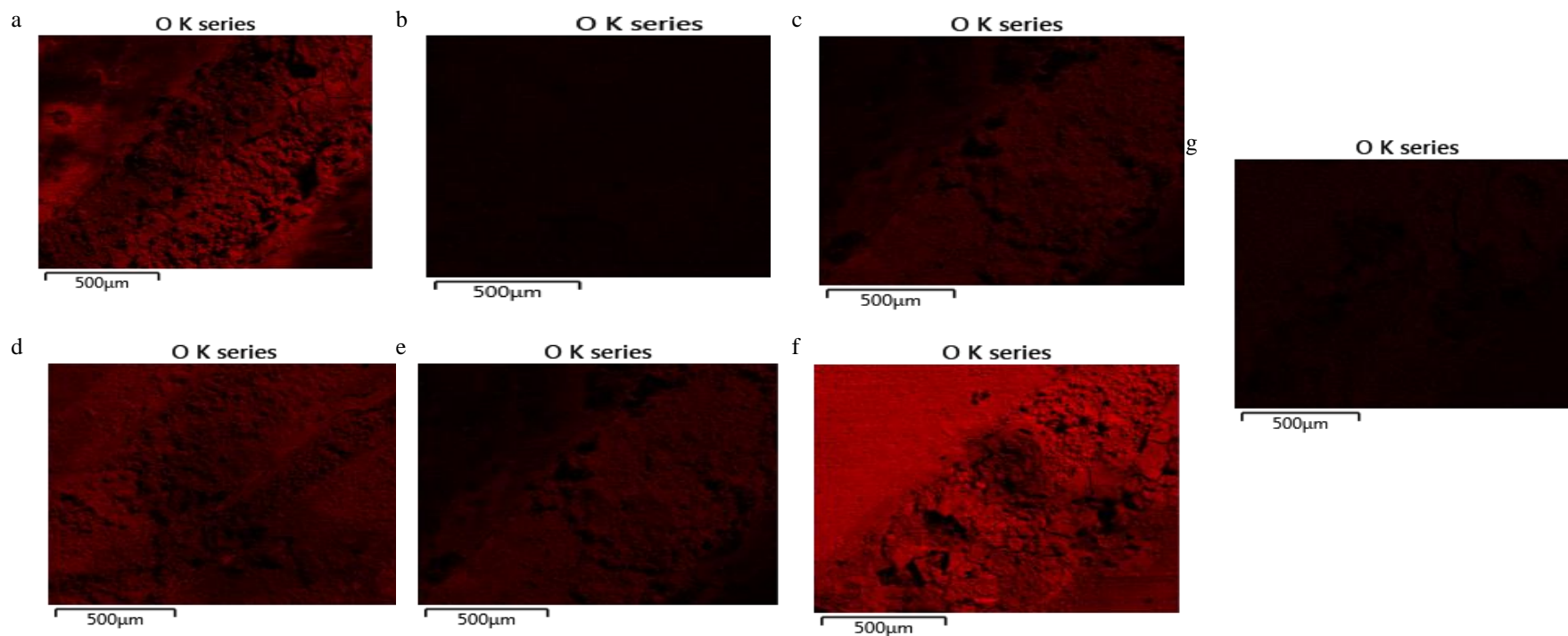


Figure 5.7. EDS maps of oxygen across scribe and adjacent pretreatment after exposure in standard ASTM B117 environment for 1000 h. (a) AA2024-T351/NFF, (b) AA2024-T351/CCC, (c) AA2024-T351/TCP, (d) AA2024-T351/NCP, (e) AA2024-T351/ANS, (f) AA2024-T351/ACS and (g) AA2024-T351/ATS.

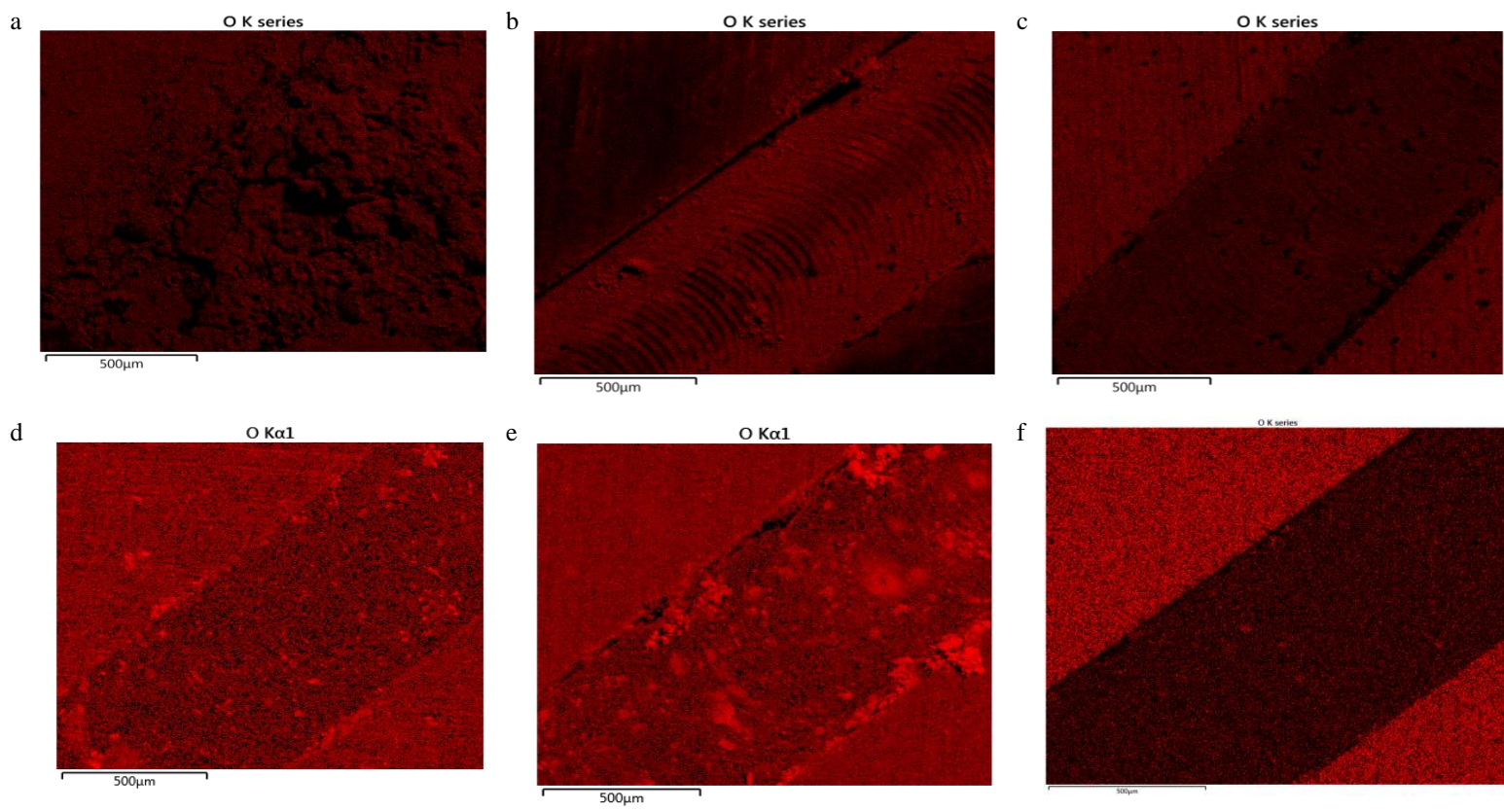


Figure 5.8. EDS maps of oxygen across scribe and adjacent pretreatment after exposure in LALT/field environment for selected pretreatments. (a) AA2024-T351/NFF after 1440 h in modified ASTM B117, (b) AA2024-T351/TCP after 1440 h in modified ASTM B117, (c) AA2024-T351/ACS after 1440 h in modified ASTM B117, (d) AA2024-T351/NFF after 4032 h in CHO, (e) AA2024-T351/TCP after 4032 h in CHO and (f) AA2024-T351/ACS after 4032 h in CHO

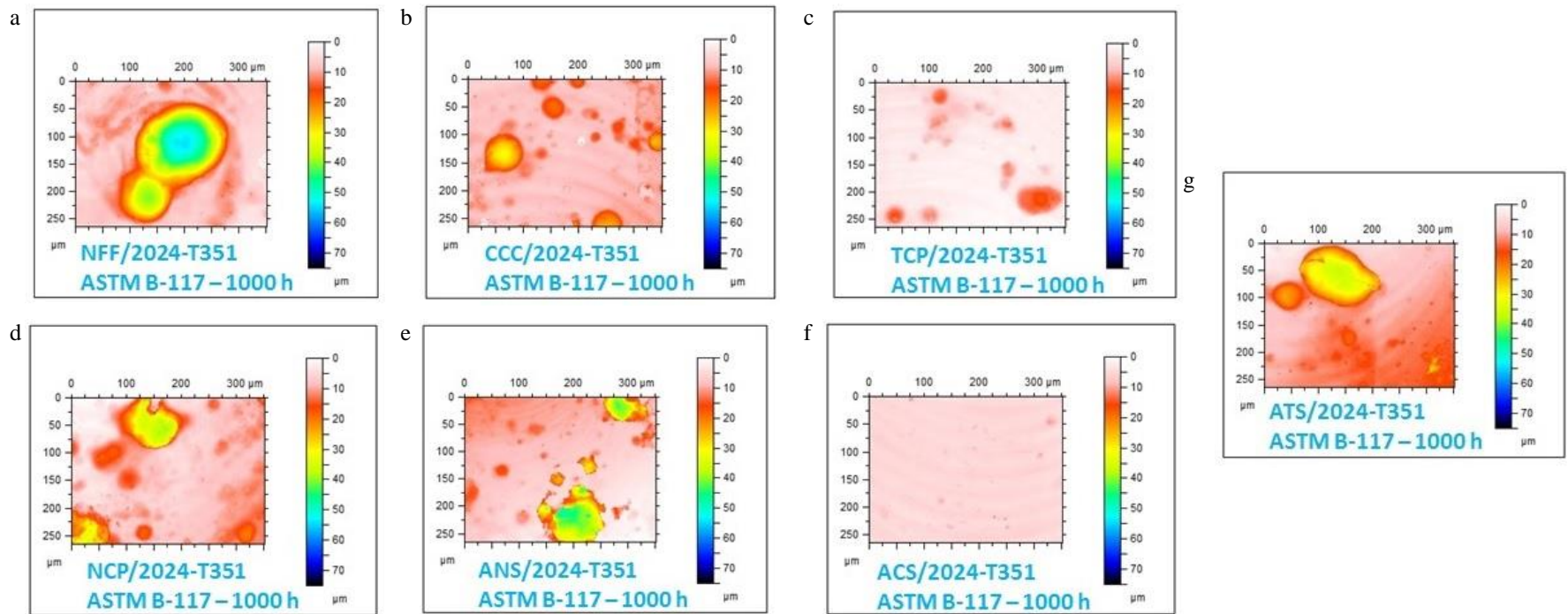


Figure 5.9. Optical profilometry maps of AA2024-T351 scribe in AA2024-T351/Pretreatment after exposure in standard ASTM B117 environment for 1000 h. (a) AA2024-T351/NFF, (b) AA2024-T351/CCC, (c) AA2024-T351/TCP, (d) AA2024-T351/NCP, (e) AA2024-T351/ANS, (f) AA2024-T351/ACS and (g) AA2024-T351/ATS. The 0  $\mu\text{m}$  position (white) on the scale is indicative of the starting material condition before corrosion.

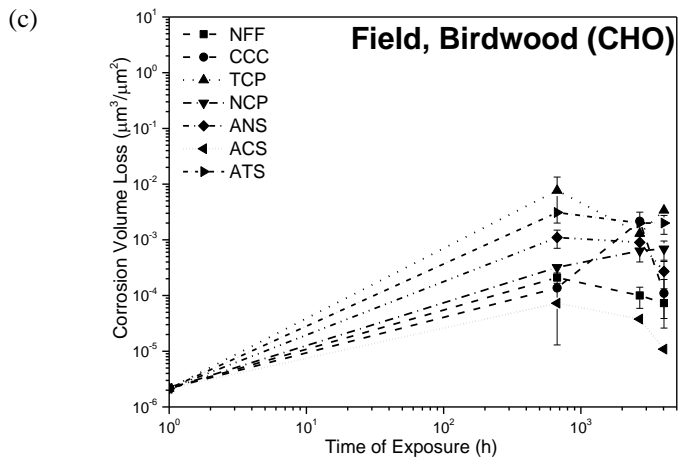
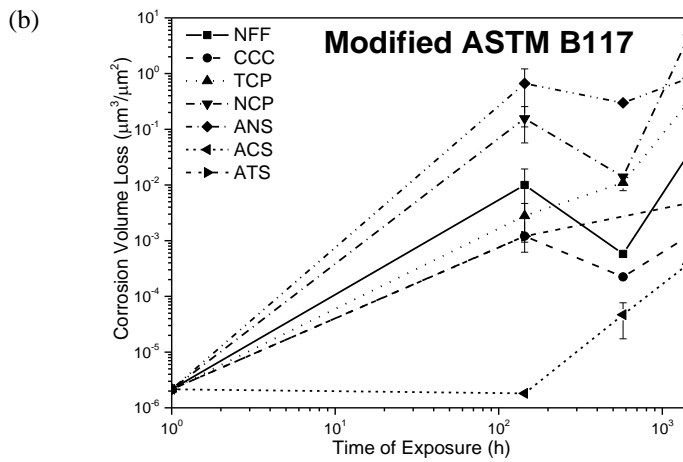
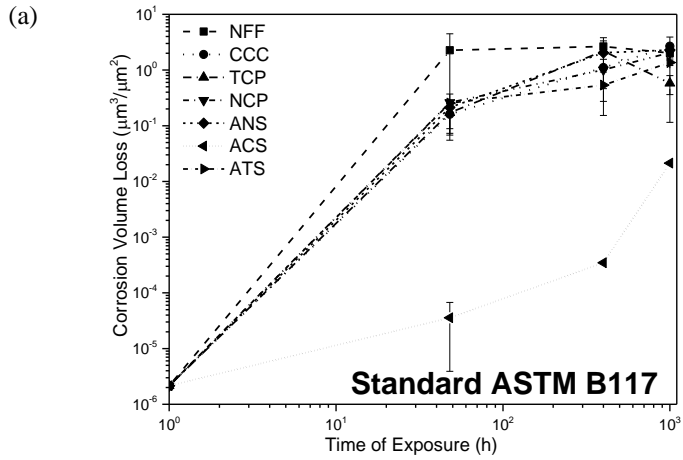


Figure 5.10. Corrosion volume loss of bare AA2024-T351 scribe in AA2024-T351/Pretreatment panel as a function of exposure time in different LALT/field environments indicated. (a) Standard ASTM B117 (b) Modified ASTM B117 with SOW and UV and (c) At field, CHO

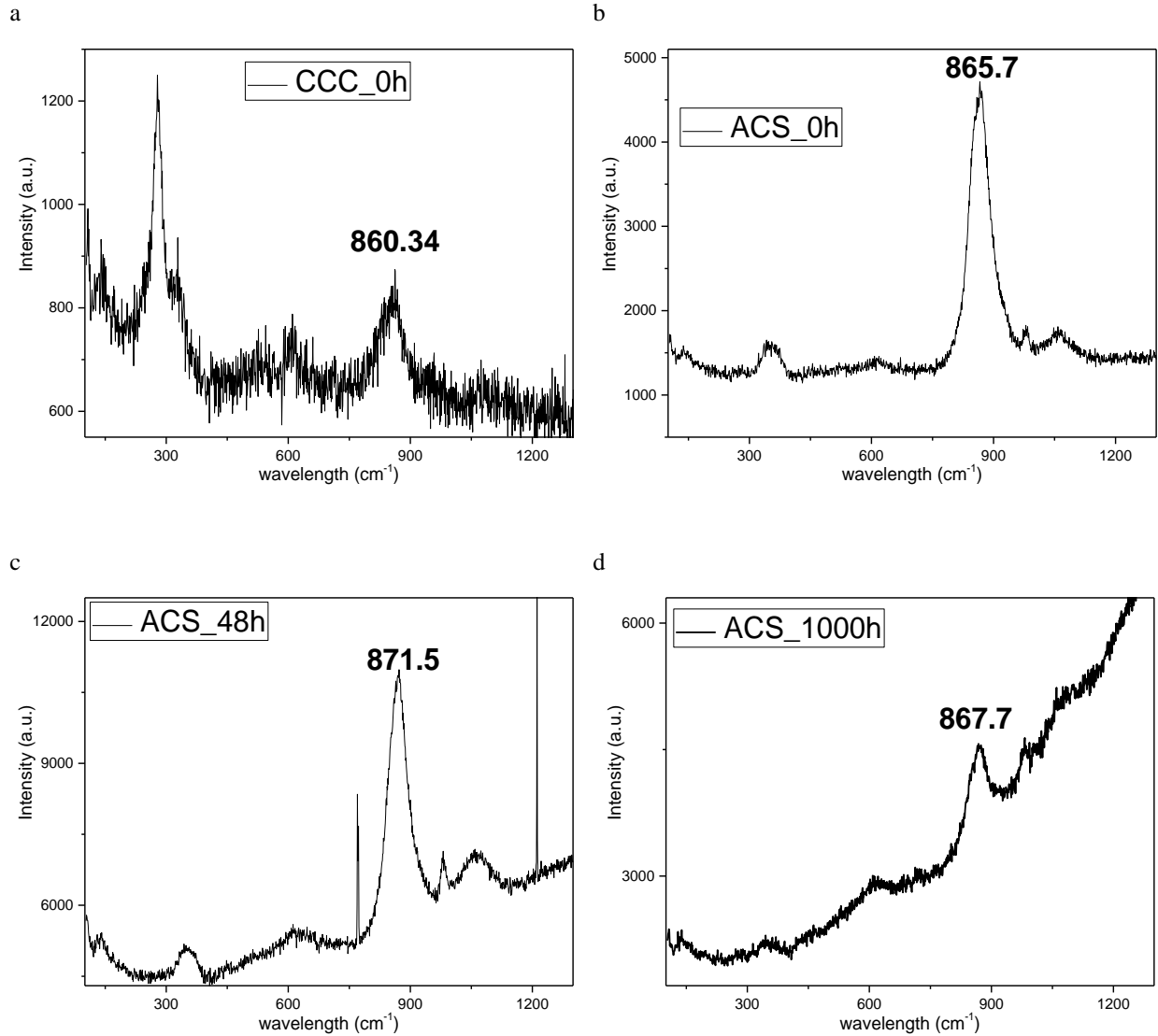
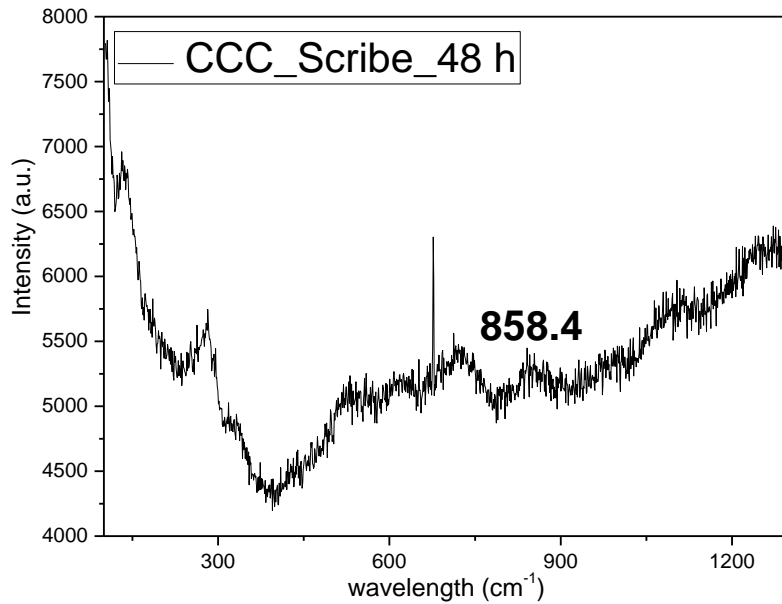


Figure 5.11. Raman spectra for AA2024-T351/Pretreatment after different LALT exposure times (a) AA2024-T351/CCC, pristine conditions, (b) AA2024-T351/ACS, pristine conditions, (c) AA2024-T351/ACS after 48 h exposure in standard ASTM B117 environment and (d) AA2024-T351/ACS after 1000 h exposure in standard ASTM B117 environment

a



b

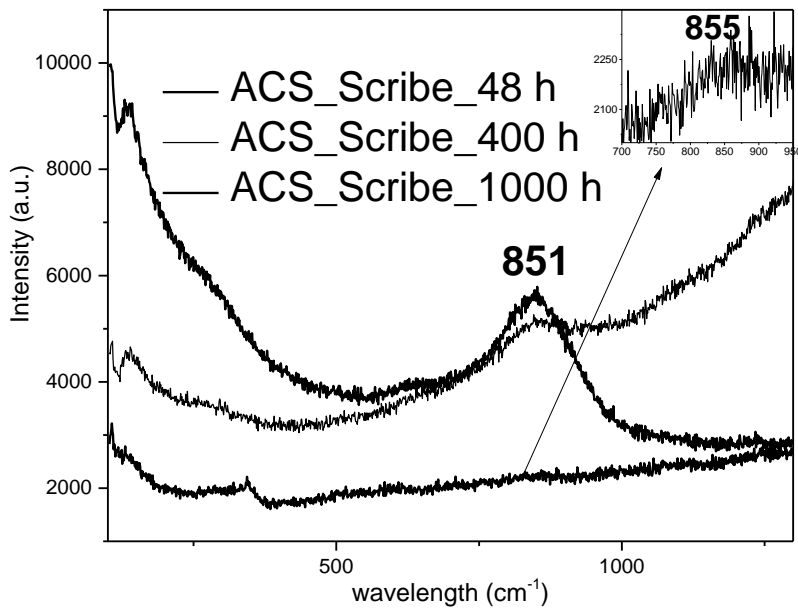
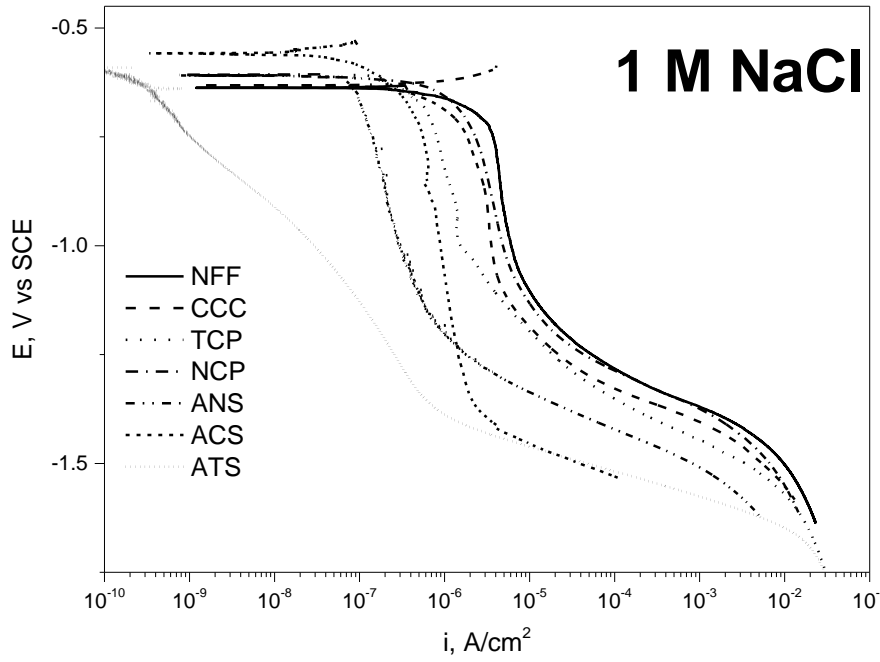


Figure 5.12. Raman spectra for of AA2024-T351 scribe in AA2024-T351/Pretreatment after exposure in standard ASTM B117 environment (a) AA2024-T351/CCC, 48 h in ASTM B117, (b) AA2024-T351/ACS, after different exposure times in ASTM B117

(a)



(b)

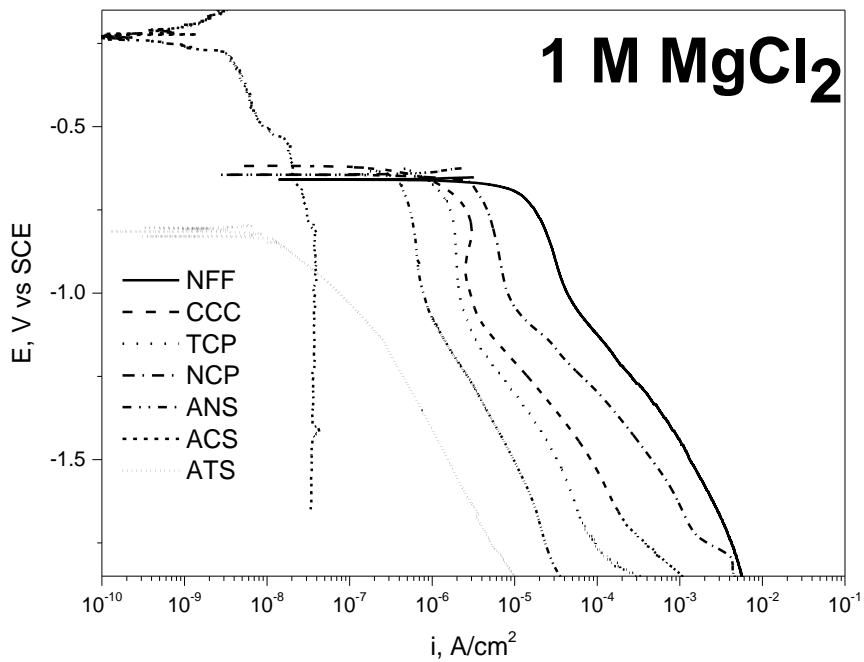


Figure 5.13. Cathodic polarization of bare/pretreated AA2024-T351 in quiescent 1 M NaCl (a)/ 1 M MgCl<sub>2</sub> solution (b)

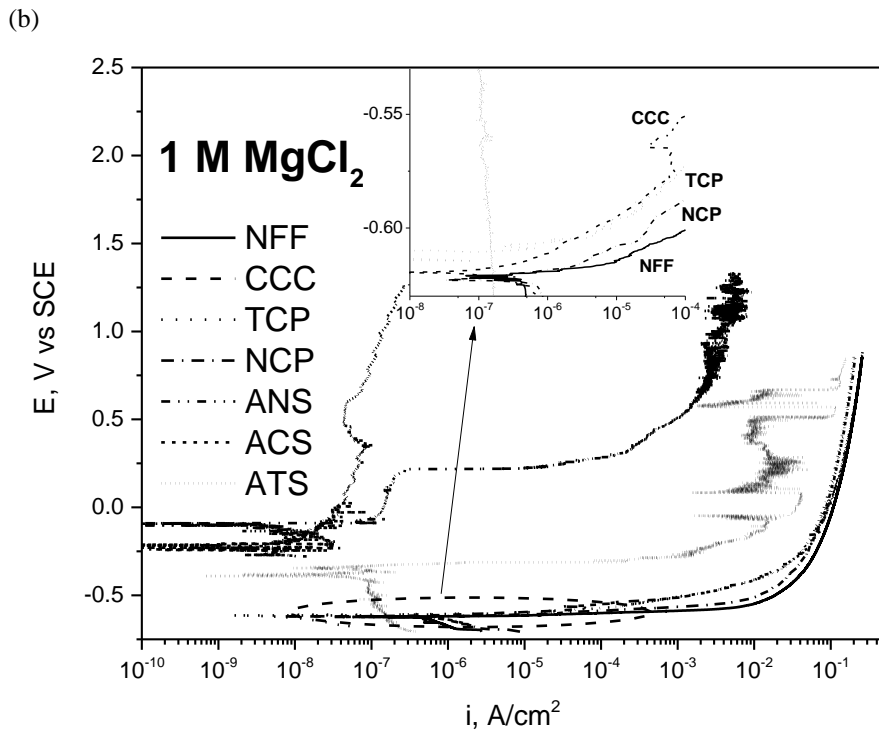
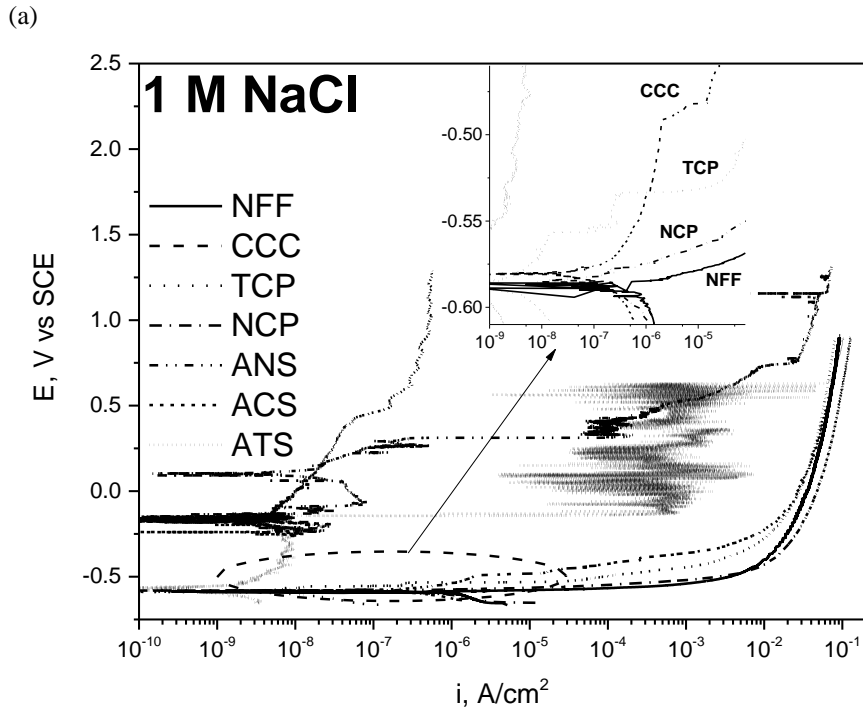


Figure 5.14. Anodic polarization of bare/pretreated AA2024-T351 in quiescent 1 M NaCl (a)/ 1 M MgCl<sub>2</sub> solution (b)

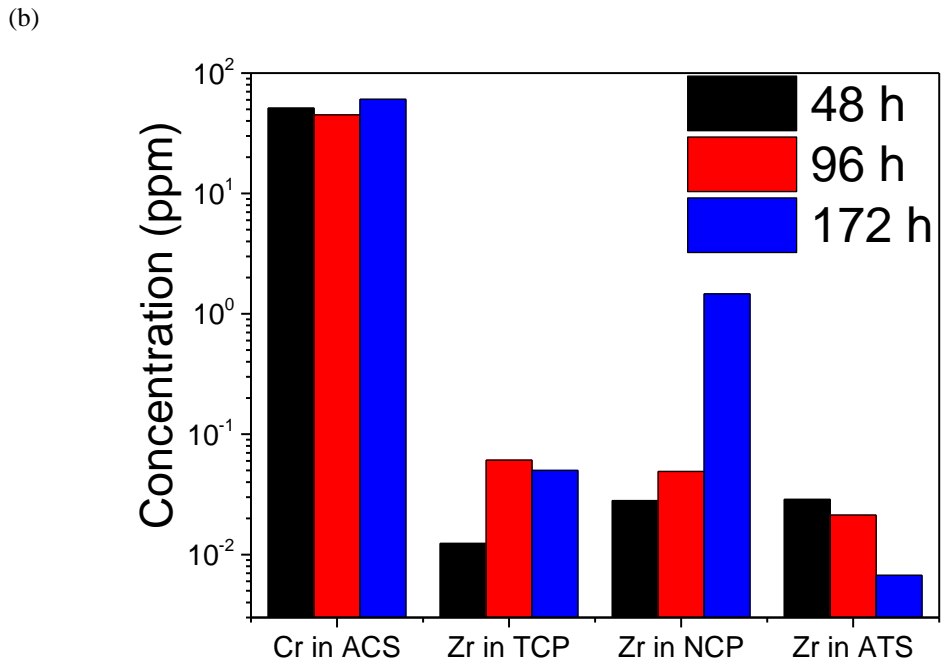
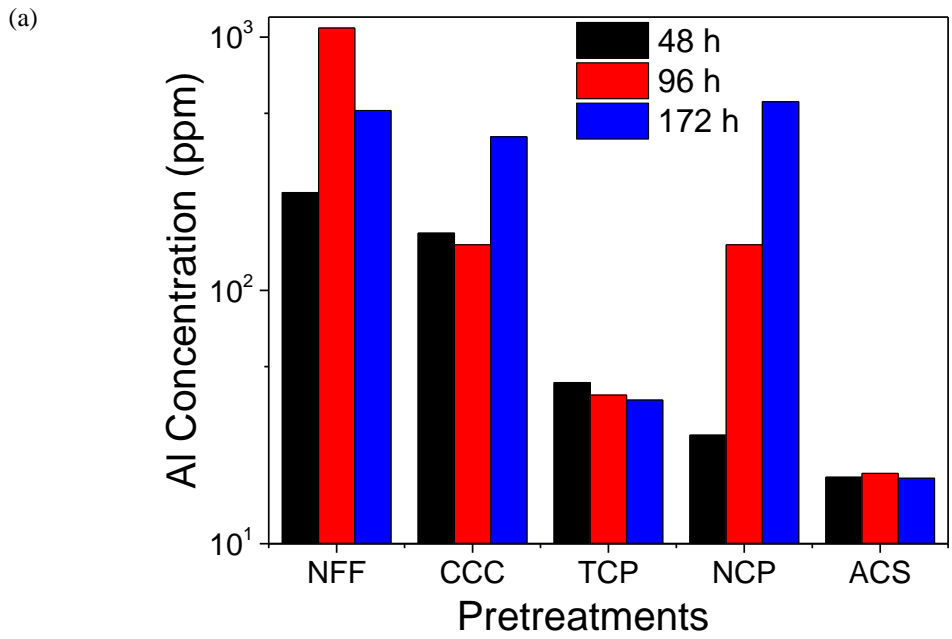


Figure 5.15. Leaching kinetics of bare/pretreated AA2024-T351 as a function of controlled relative humidity exposure time. (a)  $\text{Al}^{3+}$  leaching kinetics of 2024-T351/Pretreatment after different exposure time as a function of pretreatment and (b) Leaching kinetics of Cr or Zr in selected pretreatments after different exposure time.

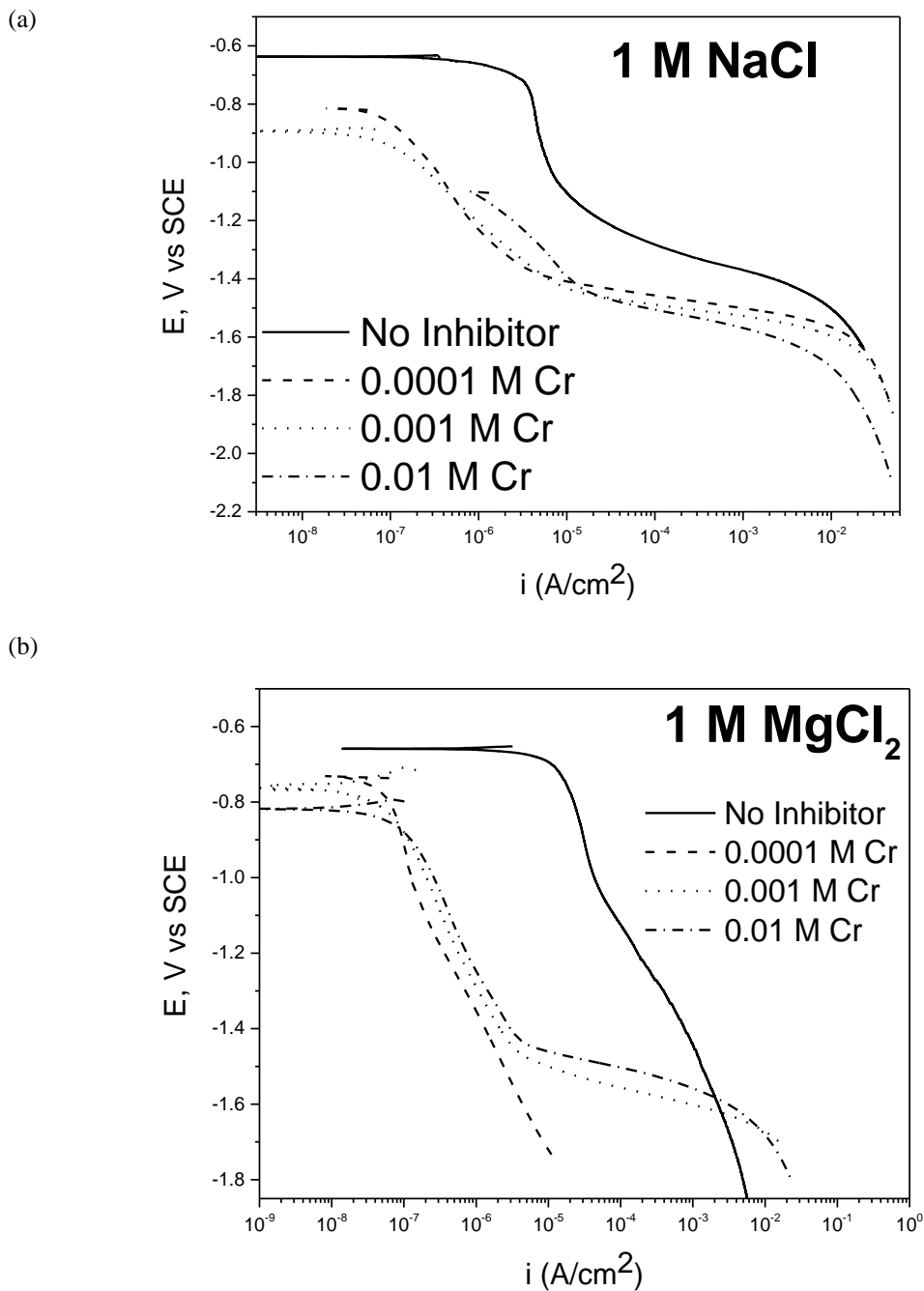


Figure 5.16. Cathodic polarization of bare AA2024-T351 in quiescent 1 M NaCl (a)/ 1 M MgCl<sub>2</sub> solution (b) as a function of CrO<sub>4</sub><sup>2-</sup> concentration.

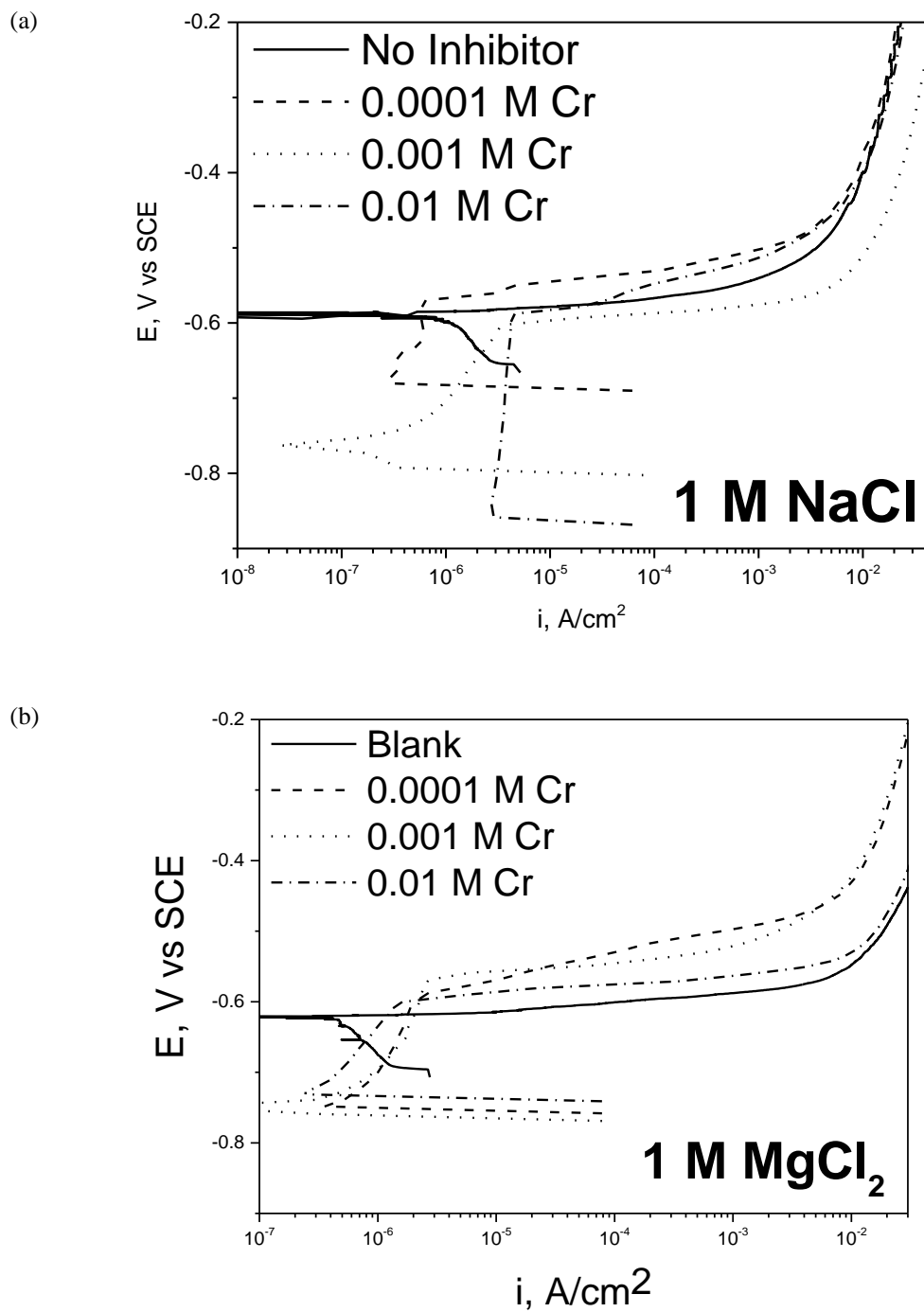


Figure 5.17. Anodic polarization of bare AA2024-T351 in quiescent 1 M NaCl (a)/ 1 M MgCl<sub>2</sub> solution (b) as a function of CrO<sub>4</sub><sup>2-</sup> concentration.

## **6 Performance of a Magnesium Rich Primer on Pretreated 2024-T351 in Full**

### **Immersion: Throwing Power Investigation Using Scanning Vibrating Electrode**

#### **Technique**

##### **6.1 Abstract**

The spatial distribution of net anodic and cathodic current densities for magnesium rich primer (MgRP) on pretreated 2024-T351 coupled with a bare 2024-T351 scribe was studied with scanning vibrating electrode technique (SVET). The galvanic current distribution over 2024-T351 scribe coupled to MgRP was studied in full immersion conditions with three different pretreatments (Non-film forming (NFF), trivalent chromium pretreatment (TCP) and anodization with chromate seal (ACS)) in two different area configurations with coating to scribe area ratios (0.3 and 5). In addition, similar studies were conducted for NFF/MgRP in presence of topcoat for above specified coating to scribe area ratios. Protection was measured by decreased pitting as well as quasi-steady state galvanic current distribution. For a coating to scribe area ratio of 0.3, NFF pretreated MgRP effectively inhibited pitting corrosion of 2024-T351 by lowering pitting below  $E_{pit}$ . This protection mechanism is called sacrificial anode-based cathodic prevention. In addition, quasi-steady state galvanic current distribution indicates enhanced cathodic activity adjacent to coating interface by galvanic coupling. Anodic current densities in the scribe which was indicative of local sites of pitting were lowered by 2-3 orders of magnitude adjacent to the coating in the presence of NFF/MgRP. Scratch protection decreased with increasing distance from the coating edge. Similar experiments conducted for TCP and ACS pretreated MgRP indicated moderate sacrificial protection and no significant scratch protection, respectively. However when the coating to bare 2024-T351 area ratio was increased to 5, a delayed scribe protection was observed in NFF, TCP and ACS pretreatment/MgRP indicative of alternate modes of scribe protection by anionic species

leaching from pretreatment and  $Mg^{2+}$  leaching from primer. In topcoated conditions, there was no significant sacrificial protection due to higher galvanic couple potential and limited conductive pathways for Mg to couple to 2024-T351 scribe.

A manuscript based on this chapter will be communicated as a Full Research Paper, “Performance of a Magnesium Rich Primer on Pretreated 2024-T351 in Full Immersion: Throwing Power Investigation Using Scanning Vibrating Electrode Technique.”

Representative author contributions:

B. Kannan: Sample preparation, experiments, analysis and interpretation

C. F. Glover: Scanning vibrating electrode technique experiments

J. R. Scully: Advisor, analysis and interpretation

G. Williams – Analysis and interpretation

N. McMurray – Analysis and interpretation

## 6.2 Introduction

Aerospace aluminum alloys are highly susceptible to localized corrosion due to their heterogeneous nature.<sup>13</sup> They rely on multilayered coatings to provide barrier protection, active corrosion protection and other specialized functions.<sup>13</sup> Over the past few years, a commercial organic coating system containing a Mg rich primer (MgRP) have been developed for the active corrosion protection of aerospace aluminum alloys.<sup>72,73,75-77,80-85,87,88,117,132,144</sup> The commercial MgRP coating system consists of a surface pretreatment, an epoxy resin with metallic Mg pigment and a polyurethane topcoat. The active corrosion protection of 2024-T351 is provided by galvanic coupling of more active Mg pigment in the primer to the 2024-T351 substrate. This approach has been well established previously in the design of zinc-rich primers for use on various steels.<sup>78,79,86,89,90,94,95</sup> The galvanic protection potential is usually dictated by mixed potential theory. The galvanic protection potential is mediated by various electrical/ionic resistances between the anode and cathode which might depend on polymer barrier properties, pretreatment resistances, electrolyte chemistry, electrolyte thickness and geometry, and anode/cathode ratio.<sup>82,83</sup> Barrier protection is afforded by pretreatment and polymer present in primer and topcoat.<sup>84</sup> Pretreatment might also provide additional corrosion protection by anionic species release which inhibit both anodic and cathodic kinetics of 2024-T351.<sup>22-26,35-37</sup> However the pretreatment may limit or delay sacrificial protection function of MgRP by adding electrical resistance between anode and cathode.<sup>75-77</sup>

Previous work on rare element based corrosion resistant metallic coatings has established how multi-function coatings with various modes of corrosion protection such as sacrificial anode protection function, inhibitor release function as well as barrier function can simultaneously provide barrier as well as active corrosion protection.<sup>91,153,154</sup> One critical issue in active protection

is the capacity of reservoir of chemical inhibitor and its release characteristics.<sup>91,153,154</sup> Another critical issue in active corrosion protection systems is determining the distance over which coating can provide corrosion protection.<sup>80-85</sup> The distance over which an active corrosion protection system can protect a scratch or a defect exposing bare 2024-T351 is called throwing power.<sup>82,83</sup> The corrosion protection of scribe might be either by galvanic (sacrificial protection) or chemical (inhibitor release/redeposition) and both have their own throwing power.

The galvanic throwing power of Mg on 2024-T351 has been previously studied using multi-electrode arrays and finite element analysis.<sup>82,83</sup> The role of electrolyte chemistry and thickness, environmental wet-dry cycling, polymer resistances and Mg pigment depletion on the galvanic throwing power has been elucidated by both approaches.<sup>82,83</sup> FEA successfully predicted that increasing the NaCl solution concentration by an order of magnitude increased the galvanic current density over the AA2024 by almost one order of magnitude. Increased electrolyte layer thickness resulted in less ohmic drop through the electrolyte and allows greater cathodic polarization of the AA2024-T351 to a lower  $E_{\text{couple}}$  which produced greater cathodic current densities at the far geometrical limit of the AA2024-T351 in the model.<sup>82,83</sup> This is an indication of increased throwing power under thicker electrolyte layers, when other conditions were held constant.<sup>82,83</sup> Regarding polymer resistance, it was found that the ionic resistance of the added polymer layer over the Mg electrode significantly mediated the galvanic current passing between anodes and cathodes and, when large enough, completely prevented the galvanic coupling of the electrodes altogether.<sup>82,83</sup>

An in-situ scanning vibrating electrode technique (SVET) was utilized to follow the kinetics of stable pitting of non-polarized 2024-T3 and effect of inhibitor concentration on corrosion inhibition in aqueous environments. SVET has been previously used to elucidate

localized corrosion and its inhibition for steel and aluminum alloy substrates using organic and inorganic inhibitors.<sup>155-162</sup> It has also been utilized to study filiform corrosion and cathodic delamination of galvanized steel and its protection by corrosion inhibitors.<sup>157-159</sup> Galvanic systems have been previously studied using multi-electrode arrays, finite element analysis and post-exposure corrosion volume loss characterization to study throwing power and scribe protection. In microelectrode arrays, wires of systems of interest are mounted in epoxy matrix and galvanic current distribution between the wires were studied using zero resistance ammeter (ZRAs). However limitations of it includes inability to study localized corrosion such as pitting in a continuous bare substrate as it is limited by wire dimensions. Effect of pretreatments on galvanic interaction between metal rich primer and the bare scribe might also be difficult to determine. The finite element analysis approach will not be able to account for transients as it calculates galvanic current and potential from steady state boundary conditions. Volume loss measurement would not be able to account for real time galvanic instruction. The main advantage of using in-situ SVET over conventional electrochemical and non-electrochemical techniques is that it provides spatial distribution of local net anodic and cathodic reactions happening in substrate occurring on local corroding surfaces which could provide information about pitting events as well as galvanic protection.

The objective of this current study is to utilize SVET to quantitatively observe the spatial distribution of current density over coated 2024-T351 with a defect exposing bare substrate. Effect of pretreatment resistance, barrier properties of the coating, Mg self-corrosion, anionic species release and cathode to anode ratio on sacrificial protection function as well as other modes of corrosion protection will be elucidated using SVET studies in aqueous sodium chloride solution in full immersion conditions.

## **6.3 Experimental Procedure**

### **6.3.1 Materials**

AA2024-T351 sheet (1.6 mm thickness) was pretreated with 3 different surface pretreatments for comparison including Non-film filming (NFF), trivalent chromium based pretreatment (TCP) and Anodization with hexavalent chromium sealing (ACS). Trivalent chromium pretreatment is a zirconium based conversion coating with trivalent chromium and is developed by NAVAIR. For anodization pretreatments, a thin-film sulfuric acid anodizing, MIL-A-8625F: Type II pretreatment procedure was followed.<sup>36</sup> Thickness of the pretreatments chosen for this studies is summarized in Table 6.1.

A 40  $\mu\text{m}$  primer layer of Mg-rich primer and a 50  $\mu\text{m}$  thick topcoat of Aerodur 5000 high-performance advanced coating, both produced by Akzo Nobel Coatings (Waukegan, Illinois) were applied. The Mg rich primer consist of one part epoxy matrix with Mg metal flake pigment of a diameter 20  $\mu\text{m}$  with pigment volume concentration of 45 % (3rd generation 2100P003, Lot: 493-190). Aerodur 5000 (Gloss white finish product: ECM-G7875) is a two component polyurethane topcoat developed for military application in variety of exposure environments.<sup>128</sup>

### **6.3.2 Sample Preparation**

A large size defect (2.5 cm x 2.5 cm) was created in coated samples by laser ablation. Samples were irradiated with a KrF excimer laser ( $\lambda = 248 \text{ nm}$ , 25 ns full width at half maximum) at a repetition rate of 10 Hz and a fluence of 2 J/cm<sup>2</sup>. All specimens were rastered using a Newport† linear actuator for a total irradiation of 8 PPA for ACS pretreatment only systems, 16-20 laser pulses per area (PPA) for primer only systems and 24-28 PPA for topcoated system and a 90% overlap with a cylindrical shaped spot size of 0.6 mm x 29 mm. The details of the equipment setup for laser ablation are reported elsewhere.<sup>163,164</sup> Any effect of laser ablation on microstructure

changes is minimal in chosen laser pulse intensity ( $< 10 \mu\text{m}$ ). To further minimize the effect the laser PPA were optimized for each system in such a way that intact coating is not completely removed. The final few microns of the coating and underlying substrate were removed by mechanical polishing so that original microstructure was exposed. The specimens were ground to a 240 grit finish to leave a rough sample to accelerate localized corrosion. An area of ca. 10 mm x10 mm (the exact size of which was noted in each case) was isolated in the center of the bare 2024-T351 for control experiments. The coating/scribe ratio design for coated systems are indicated in Figure 6.1. Two area ratios were chosen for studies. An insulating extruded PTFE self-adhesive tape was used to isolate the scan area for exposure. For any given test corrosion was observed on the scan area only and not anywhere else on the sample for the entire duration of experiment.

### **6.3.3 Laboratory Full Immersion Exposures of Pretreated AA2024-T351 Coated with MgRP and Topcoat**

The global galvanic protection potential of intact coating, galvanic couple potential at scribe and barrier properties of intact coating system are monitored using open circuit potential measurements and electrochemical impedance spectroscopy. All full-immersion studies reported herein were conducted in quiescent 2 M NaCl (pH:  $6.9 \pm 0.4$ ) open to laboratory air. Potential control during electrochemical experiments was maintained using a Gamry Potentiostat<sup>†</sup> (Ref 600/ PCI4) or Biologic Potentiostat with computer interface software. Saturated calomel electrode (SCE) and Pt mesh were used as reference and counter electrode, respectively. A typical EIS scan was acquired in swept sine mode from 100 kHz to 0.01 Hz with six points per decade. Coated panels were scanned with an AC amplitude of 80 mV to 100 mV to reduce noise. The tests were conducted in quiescent 2 M NaCl, as discussed, after 1 h

exposure at open circuit for bare/pretreated/MgRP coated panels and 12 h exposure for MgRP/TC-coated panels. The experiments were conducted for different full immersion exposure time for total time duration of 36 hours to track global galvanic protection potential and barrier properties of the coating. All these experiments were conducted in the intact region. In a separate experiment, the galvanic protection potential was also monitored for scribed samples (will be referred to as galvanic couple potential for scribed systems) for two different coating/scribe ratio indicated in Figure 6.1.

#### **6.3.4 Scanning Vibration Electrode Technique (SVET) Measurements**

Scanning vibrating electrode measurements were carried out using an SVET probe comprising a 125  $\mu\text{m}$  diameter platinum wire sealed in a glass sheath, so that the active portion of the probe tip consisted of a 125  $\mu\text{m}$  diameter platinum micro-disc electrode with a total tip diameter was  $\sim 250$   $\mu\text{m}$ . The probe vibration frequency was 140 Hz and the peak-to-peak vibration amplitude ( $A_{pp}$ ), as measured stroboscopically in air was  $30 \pm 5$   $\mu\text{m}$ . Movement of the SVET probe-vibrator assembly was achieved using three orthogonal linear bearings driven by stepper motors (Time and Precision Ltd). The SVET voltage signal was detected using a Perkin Elmer 7265 lock-in amplifier and subject to digital signal averaging (typically of 10 successive measurements) to further enhance signal-to-noise ratio. A full description of SVET probe/vibrator assembly design, along with details on probe surface preparation and reference electrode type are given elsewhere.<sup>162</sup> Details of SVET calibration are reported elsewhere.<sup>162</sup>

Bare and coated samples were completely immersed, exposed area uppermost, in an electrolyte bath containing 2 M aqueous sodium chloride at pH 6.5. Electrolyte thickness was kept constant at 10 mm for all chosen studies. The bath was left unstirred and in contact with room air at a nominal temperature of 20°C. The SVET probe was held vertically and scanned at a fixed height

(100  $\mu\text{m}$ ) above the metal surface. Each scan took ca. 30-45 minutes and produced a square matrix of 9000-12000  $V_{pp}$  data points. Individual  $V_{pp}$  values were converted to  $j_z$ , using the relevant calibration factor  $G$ .<sup>162</sup> Samples were scanned immediately following immersion, and continuously thereafter for a period of 24 – 36 hours. The spatial resolution of SVET in experiments conducted is 100  $\mu\text{m}$ .

## 6.4 **Results**

### 6.4.1 **Laboratory Full Immersion Exposures of Pretreated AA2024-T351 Coated with MgRP and Topcoat**

The open circuit potential or global galvanic protection potential and the low-frequency EIS of intact coating for selected 2024-T3351/Pretreatment/MgRP and 2024-T351/NFF/MgRP/TC at intact region are summarized in Figure 6.2a and b, respectively. 2024-T351/ NFF/MgRP exhibited initially more negative global galvanic protection potentials close to -1.4 V vs SCE and then stabilized at value of -1.2 V vs SCE for rest of the exposure time. This potential likely provided sacrificial anode-based cathodic protection. Similar experiments conducted for TCP and ACS based systems mediated by relative more positive potentials (-0.5 V to -0.8 V vs SCE) wherein the galvanic protection was very limited or negligible. The electrical resistance between the Mg in the primer and underlying 2024-T351 shifted the potential to more positive values which could be rationalized based on mixed potential theory applied to a galvanic corrosion cell (Figure 6.3). This might limit the sacrificial anode based galvanic protection. Similarly for topcoated system, due to high ionic resistance between the anode and the cathode limiting the extent of galvanic interaction, the global galvanic protection potential was initially more positive. With increase in exposure time, improved wetting of polymer reduced the ionic resistance which resulted in lowering of global galvanic protection potential. Figure 6.2b summarizes the change in low frequency EIS as a

function of exposure time in chosen coating systems. EIS indicated that barrier degradation occurs as a function of exposure time, but it was very minimal in the time frame of the experiment. Similar experiments conducted for ACS based systems (Figure 6.2 c-d) showed that the initial barrier properties of ACS based systems are 2 orders of magnitude higher than NFF based systems and showed very limited barrier degradation with increasing exposure time. The significantly higher barrier properties are due to thick and resistive oxide layer which is further sealed by hexavalent chromium as discussed in chapter 5. TCP based systems had intermediate resistances whereas topcoated systems exhibited 2-3 orders of magnitude higher coating resistance compared to non-topcoated systems (Figure 6.2).

The galvanic couple potential as function of exposure time was also monitored for scribed systems. Two coating to scribe area ratio (0.3 and 5) were chosen for galvanic couple experiments and the results are summarized in Figures 4a and b, respectively. In both chosen coating to scribe area ratios, NFF/MgRP showed initially more negative galvanic couple potentials and shift in potentials to more positive value with increasing exposure time. TCP exhibited intermediate galvanic couple potentials and they also indicated delayed but limited galvanic protection as could be inferred from lowering of galvanic couple potential with time. In both ACS based systems and topcoated systems, the galvanic couple potential was heavily mediated as could be inferred from relatively more positive galvanic couple potentials.

#### **6.4.2 Localized Corrosion of AA2024-T351:**

Localized corrosion of free corroding 2024-T351 was monitored in 2 M sodium chloride solution at ambient conditions. The net current density distribution was monitored as a function of exposure time by repetitive in-situ SVET scanning. Figure 6.5a-e shows representative current density maps obtained after 0 h, 4 h, 14 h, 26 h and 36 h, respectively. A SVET scan obtained

immediately after full immersion indicate that local anodic activity (Figure 6.5a) initiates within minutes of full immersion exposure in 2 M NaCl solution. First stable pit was formed after half an hour and further pit initiation in multiple sites was observed within 4 hours of full immersion as evidenced from Figure 6.5b. The time required for repassivation varied depending on individual pits with shortest one being 30 min and longest one being 1950 min. The total number of visible pits formed is 13 pits/cm<sup>2</sup> are and average life time of each pit of corroding area was 520 min. These deductions were made based on blue regions observed in the current density maps. Figure 6.5f shows the visual appearance of the sample after 38 h of full immersion wherein the physical pits can be correlated to the previously discussed electrochemical pits indicated by anodic current density SVET maps.

### **6.4.3 Galvanic Protection of Bare 2024-T351 Coupled to Bare Mg**

Figure 6.6a shows the surface plots of net local current density of bare 2024-T351 coupled to bare Mg. This experiment was conducted to simulate a condition wherein Mg with high surface area was coupled to 2024-T351 with negligible ohmic drop as shown in Figure 6.3. The surface current density maps show anodic and cathodic activity at bare Mg and bare 2024-T351, respectively (Figure 6.6a). A representative SVET line scan (Figure 6.6b) across the Mg/2024-T351 indicated that the net anodic and cathodic current density values in bare Mg and bare 2024-T351 are approximately the same and are in the order of 500 A/m<sup>2</sup>. Figure 6.6c shows the visual appearance of the galvanic couple after 1 h of full immersion. Significant corrosion occurred on both the Mg and 2024-T351. The corrosion of 2024-T351 as indicated by black layer on the surface can be correlated to enhanced cathodic activity the local pH of the cathodic region increases resulting in cathodic corrosion of amphoteric 2024-T351.

#### **6.4.4 Galvanic Protection of Bare 2024-T351 Coupled to 2024-T351/Pretreatment/MgRP Sacrificial Protection and Role of Pretreatments: Preliminary Trends**

Sample design as indicated in Figure 6.1a was chosen to study the galvanic protection in MgRP based systems and effect of pretreatment resistance in galvanic protection for NFF, TCP and ACS pretreated MgRP systems. For all experiments discussed herein a small coating to scribe area ratio (0.3) was chosen to understand the effect of distance from coating interface on galvanic protection. Figure 6.7, 6.8 and 6.9 shows representative current density maps as a function of exposure time and a post-exposure photograph for 2024-T351/NFF/MgRP, 2024-T351/TCP/MgRP and 2024-T351/ACS/MgRP, respectively. Irrespective of the nature of pretreatments, local anodic behavior was exhibited at scribe for all chosen systems, indicating that galvanic protection was not sufficient enough to completely suppress all the localized corrosion of 2024-T351 which is caused by microgalvanic coupling. Preliminary observation from SVET maps and post-exposure visual photographs indicated fewer and smaller pits in MgRP based systems compared to control indicative of corrosion protection. Figure 6.10 summarizes representative line SVET scans obtained from SVET maps for 2024-T351/Pretreatment/MgRP and bare 2024-T351. SVET line scan for bare 2024-T351 (Figure 6.10a) shows anodic regions as indicated by high anodic current densities and cathodic activity in rest of the surface as indicated by negative currents (Figure 6.10a). The anodic current density peaks increased with increasing exposure time. Representative SVET line scan for 2024-T351/NFF/MgRP coupled to bare 2024-T351 showed after different exposure times indicated that extent of galvanic coupling improved with exposure time indicative of degradation of barrier polymer or sufficient electrolyte ingress to activate galvanic coupling (Figure 6.10b). Two

distinct regions can be observed in the scribe (Figure 6.10 b). The region adjacent to coating interface exhibited cathodic protection and fewer and smaller anodic current spikes attributed to pitting activity. The quasi-steady state galvanic current also decreased as a function of distance from the interface. The region far away from the scribe ( $> 4\text{mm}$ ) exhibited significantly large anodic activity. The anodic peak current densities for 2024-T351/NFF/MgRP coupled 2024-T351 ( $6 - 10 \text{ A/m}^2$ ) are lower in comparison to bare 2024-T351 systems ( $20\text{-}30 \text{ A/m}^2$ ). Representative SVET line scans for 2024-T351/TCP/MgRP based systems (Figure 6.10 c) indicated a delayed and slightly enhanced anodic activity for 2024-T351 scribe adjacent to the interface. While the current densities were relatively lower and uniform, anodic activity occurred at regions as close as  $2 \text{ mm}$  from interface.

In the case of, 2024-T351/ACS/MgRP based systems, no galvanic protection was enabled in region adjacent to coating (Figure 6.10d). Due to inherently high electrical resistance between Mg in the primer and 2024-T351, galvanic couple potential was heavily mediated and no significant galvanic protection occurs (Figure 6.10 d). Peak anodic current densities occur as region as close as less than a mm from the coating interface. However the peak anodic current densities are an order of magnitude lower for ACS based systems compared to NFF based systems (Figure 6.10 d). This can be correlated to alternate modes of corrosion protection such as corrosion inhibition by leaching of anionic species from pretreatments and their redeposition in scribe lowering both the overall anodic and cathodic activity in the scribe which are reported elsewhere.<sup>4,29</sup>

### **Sacrificial Protection and Role of Pretreatments: Quantitative Analysis**

While line scan gives a preliminary trends on the effect of distance on galvanic protection, the region chosen for it accounts for only 1/100<sup>th</sup> of the total area for which the experiment was conducted. To account for corrosion phenomena in whole area of interest, further quantitative analysis was conducted as described below. For each representative surface map, there are 100\*100 data points for each 1cm<sup>2</sup> area of interest. Each surface map was first separated into two maps. An anodic map, wherein all current densities in anodic region are positive and all current densities in cathodic region are taken as zero. Similarly, in a cathodic map, anodic regions are taken as zero and cathodic regions are marked by negative current densities. The whole surface map was further divided into 6 regions of interest as shown in the Figure 6.11. Specifically, the scribe was divided into 5 different regions of identical area at different distances from the coating interface to study the effect of distance from coating interface on scribe protection. The net anodic current density and cathodic current density was calculated for each region of interest by calculating the sum of all data points in this region. Since the anodic and cathodic maps were separated in previous step, the net current density is either entirely anodic or cathodic and the local current densities does not cancel out each other. This step was repeated for different coating systems of interest after different exposure times.

The net anodic and cathodic current density for chosen 2024-T351/Pretreatment/MgRP of interest are summarized in Figures 6.12 and 6.13. The net anodic current density for NFF based systems (Figure 6.12a) remained almost constant away from the coating and was lowered after initial anodic activity near the coating indicative of the sacrificial protection near the coating edge. The net anodic current density was 2-3 orders of magnitude lower in the region 0-2 mm from coating area compared to the region 8-10 mm from coating (Figure 6.12a). Net anodic

current density trends for >4 mm from coating were similar to that of control indicative of very limited corrosion protection (Figure 6.12a).

In TCP based systems, there is moderate galvanic protection and no direct correlation between the distance from coating interface to anodic current densities (Figure 6.12b). In ACS based systems, the anodic current densities were similar to that of control systems and the variability of anodic current density as a function of distance was minimal, both indicating that there was little galvanic interaction (Figure 6.12c). The net cathodic current density was much higher for NFF and TCP based systems compared to ACS based systems indicating that sacrificial anode-based cathodic protection enhances the cathodic activity in the scribe (Figure 6.6b). Another possible reason for lower cathodic current densities in the scribe could arise from anionic species leaching and redeposition blocking the activity at copper rich cathodic sites. There was no significant distance effect as cathodic current over 2024-T351 (Figure 6.7 c-d) could arise from both anodic reactions of metallic Mg in the coatings as well as anodic reaction in the bare scribe and they cannot be differentiated by monitoring net cathodic current density.

### **Effect of Coating to scribe area ratio on Corrosion Protection**

Due to Mg pigment depletion during exposure or limited conductive pathways at various stages of barrier degradation, the active ratio of anode to cathode changes as a function of exposure time during environmental exposure. Figure 6.14 shows the effect of anode to cathode ratio on galvanic couple potential and galvanic current as explained by mixed potential model.<sup>10</sup> In addition to this effect, a higher ratio of 2024-T351/Pretreatment/MgRP to 2024-T351 would also facilitate alternate methods of corrosion inhibition by  $Mg^{2+}$  ions and/or anionic species leaching. To account for these phenomena, a higher coating to scribe area ratio (5) was chosen for further experiments. Figure 6.15, 6.16 and 6.17 shows representative current density maps as a function

of exposure time and a post-exposure photograph for 2024-T351/NFF/MgRP, 2024-T351/TCP/MgRP and 2024-T351/ACS/MgRP, respectively. Figure 6.18 summarizes representative SVET line scans obtained from SVET maps for chosen 2024-T351/Pretreatment/MgRP after different exposure times. Both NFF and TCP pretreated MgRP systems showed galvanic protection adjacent to the coating interface. ACS pretreated MgRP systems, due to heavy mediated galvanic couple potential, exhibited no galvanic protection. The results are consistent with previous trends observed with small coating to scribe area ratio. As discussed in previous section, the net anodic and cathodic current densities were calculated separately for 2 mm scratch. These results were compared to anodic and cathodic current density adjacent to 3 mm coating in first 2 mm scratch. The results are summarized in Figure 6.19. The net anodic current density indicate that ACS based systems performed significantly better with higher CSR (Figure 6.19). The NFF based systems performed almost similarly irrespective of CSR (Figure 6.19). Slightly higher anodic current densities at higher coating to scribe ratio can be correlated to enhanced anodic activity in scribe at high pH condition before  $Mg(OH)_2$  redeposition. The change in coating to scribe area ratio (CSR), simultaneously increases the area of anode while decreasing the area of active cathode. In addition, there was more active surface of Mg for self-corrosion. Both of these might contribute to increased amount of  $Mg^{2+}$  ion in the solution as well as increased pH. This result in chemical mechanism of redeposition of  $Mg^{2+}$  ions in scribe to form protective  $Mg(OH)_2$  in high pH conditions.<sup>5</sup> The  $Mg(OH)_2$  inhibit both anodic and cathodic reaction in scribe with time as could be inferred from Figure 6.19a and b. Anionic species leaching from the pretreatment might also bring down the anodic activity at scribe by acting as cathodic inhibitor.<sup>28</sup> The protection of scribe by  $Mg(OH)_2$  and anionic species leaching in both LALT and field exposures for pretreated systems has been previously reported.<sup>75,80,81</sup>

Further investigation of chemical protection mechanism and conditions required for chemical protection will be reported in our future work.

#### **6.4.5 Galvanic Protection of Bare 2024-T351 Coupled to 2024-T351/Pretreatment/MgRP/TC**

Polyurethane topcoat in addition to UV protection serves to limit Mg depletion by improved barrier protection and increased ionic resistance. However previous LALT/field exposures show that these coatings limit the active protection at scribe due to the increased ionic resistance in the presence of topcoat. To understand the effect of topcoat, 2024-T351/NFF/MgRP/TC was chosen for further studies. Two coating to scribe area ratio (0.3 and 5) as described in previous sections were utilized. The SVET experiments were conducted only for the scribe region instead of entirety of the coating as topcoat layer has very high resistance and very slow wetting characteristics. Figure 6.20 and 21 shows representative current density maps as a function of exposure time and a post-exposure photograph of 2024-T351/NFF/MgRP/TC for CSR ratio of 0.3 and 5, respectively. Both current maps as well as post-exposure photograph show significant localized corrosion in the scribe. Figure 6.22 summarizes representative SVET line scans obtained from SVET maps of 2024-T351/NFF/MgRP/TC for CSR ratio of 0.3 and 5, respectively. No region of cathodic protection was observed in adjacent to coating interface due to heavy mediation of galvanic couple potential by organic barrier layers. Figure 6.23 summarizes, the net anodic and cathodic current densities for up to 2 mm in scratch from the coating edge for topcoated, non-topcoated and bare 2024-T351 system. Except for NFF/MgRP all the other chosen systems, showed significantly high anodic current densities indicating that there was no significant corrosion protection.

## **6.5 Discussion**

### **6.5.1 Correlation of Galvanic Currents from SVET to FEA Results**

Previous work has utilized finite element analysis as a tool to predict the galvanic couple current and potential distribution between Mg and 2024-T351 in a MgRP configuration with zero pretreatment resistance. While the exact configurations such as electrolyte thickness, concentration and polymer resistances differ from this work, few similar configurations were chosen for comparison and the results are summarized in Table 6.2. The results shows good correlation. It is to be noted that while FEA predicts the galvanic current for fixed conditions such as fixed electrolyte chemistry and thickness, SVET as a tool can be utilized to predict the galvanic current distribution under evolving electrolyte chemistry which monitors changes in solution chemistry, pH and also surface modification such as formation of  $\text{Mg}(\text{OH})_2$  and chromate based barrier layer from pretreatment. The FEA model uses fixed E-logi boundary conditions and predicted the quasi-steady state galvanic current and galvanic couple potential distribution. In real systems, the slight suppression of galvanic couple potential significantly affected the microgalvanic coupling of intermetallic phases which result in local pitting. SVET experimental method was able to account for both quasi-steady state current distribution as well as role of galvanic couple potential suppression in reduction of local pitting. Future improvement of FEA model would involve considerations for barrier properties of pretreatment and its degradation, effect of anionic species leaching and  $\text{Mg}(\text{OH})_2$  redeposition on galvanic current and potential distribution to improve its correlation to environmental exposure.

### **6.5.2 Need for Long Term Full Immersion Exposures**

All the experiments conducted herein were done for 24-36 h of full immersion exposure. No significant degradation of barrier properties of the pretreatment is likely to occur in this time

frame. So for future experiments, long term full immersion experiments need to be conducted to understand how the galvanic protection function changes as a function of pretreatment degradation. This would also help us understand pretreatments that are desirable for sacrificial protection function to be enabled at delayed exposure time. This would also help the length of full immersion exposure time required for sufficient degradation of topcoat barrier properties to enable sacrificial protection function.

## **6.6 Conclusion**

- SVET revealed that the corrosion of bare 2024-T351 is dominated by microgalvanic coupling of intermetallic phases and the matrix. The quasi-steady state galvanic current distribution of non-film forming pretreatment with MgRP showed galvanic coupling near the interface of coating and bare 2024-T351. In addition, suppression of microgalvanic coupling by lowering of galvanic couple potential was also observed in the presence of non-film forming pretreatment with MgRP based system. Also the role of pretreatment and topcoat resistance on delayed or limited sacrificial protection function was demonstrated.
- In exposures of the bare 2024-T351 couple to bare Mg of identical areas, the galvanic current density for bare 2024-T351 was in the range of 500-1000 A/m<sup>2</sup>. The galvanic current density did not change as a function of distance from the Mg anode for a distance of 10 mm from the Mg anode.
- In exposures of the bare 2024-T351 coupled to MgRP with non-film forming pretreatment (CSR: 0.3), the galvanic current density was in the range of 0.1 – 0.2 A/m<sup>2</sup>. The galvanic current cease to be effective at longer distance from the coating interface

and the throwing power extended for a distance of 4 mm from the coating interface.

Galvanic current densities improved with increasing exposure times.

- Trivalent chromium pretreatment (TCP) and anodization with chromate sealing (ACS) pretreatment based MgRP systems (CSR: 0.3) exhibited a mediated galvanic couple potential. This resulted in either delayed or limited sacrificial anode based protection function in fresh coating and pretreatment. The throwing power extended for a distance of 2 mm for TCP based systems while no galvanic protection was evident in ACS based systems.
- The geometric area ratio of coverage of MgRP to a bare 2024-T351 scribe also affected the protection function. While NFF exhibited similar galvanic currents confirming cathodic protection, TCP and ACS exhibited no significant cathodic protection in fresh coatings as indicated by quasi steady state current distribution. However, lowered anodic currents with increasing exposure time indicate that other protection mechanisms such as  $\text{Mg}(\text{OH})_2$  redeposition and anionic species leaching might play a prominent role in corrosion protection in large coating to scribe area ratios.
- Highly resistive topcoat significantly mediated the galvanic couple potential as well as sacrificial protection function. No galvanic protection function was evident at the scribe for fresh coating for up to 36 h. The secondary modes of corrosion protection such as  $\text{Mg}(\text{OH})_2$  redeposition and anionic species leaching was also substantially lower even at large coating to scribe area ratio due to excellent barrier properties of the topcoat.

## 6.7 References

1. I.J. Polmear, *Light Alloys*. 4 ed: Butterworth-Heinemann, Oxford, 2005.
2. R.G. Buchheit, R.P. Grant, P.F. Hlava, B. Mckenzie, and G.L. Zender, "Local dissolution phenomena associated with S phase (Al<sub>2</sub>CuMg) particles in aluminum alloy 2024-T3," *Journal of the Electrochemical Society* 144, 8 (1997): p. 2621-2628.
3. A.M. Glenn, T.H. Muster, C. Luo, X. Zhou, G.E. Thompson, A. Boag, and A.E. Hughes, "Corrosion of AA2024-T3 Part III: Propagation," *Corrosion Science* 53, 1 (2011): p. 40-50.
4. A.E. Hughes, A. Boag, A.M. Glenn, D. McCulloch, T.H. Muster, C. Ryan, C. Luo, X. Zhou, and G.E. Thompson, "Corrosion of AA2024-T3 Part II Co-operative corrosion," *Corrosion Science* 53, 1 (2011): p. 27-39.
5. G.O. Ilevbare, O. Schneider, R.G. Kelly, and J.R. Scully, "In situ confocal laser scanning microscopy of AA 2024-T3 corrosion metrology - I. Localized corrosion of particles," *Journal of the Electrochemical Society* 151, 8 (2004): p. B453-B464.
6. O. Schneider, G.O. Ilevbare, J.R. Scully, and R.G. Kelly, "In situ confocal laser scanning microscopy of AA 2024-T3 corrosion metrology - II. Trench formation around particles," *Journal of the Electrochemical Society* 151, 8 (2004): p. B465-B472.
7. R.G. Buchheit, L.P. Montes, M.A. Martinez, J. Michael, and P.F. Hlava, "The electrochemical characteristics of bulk-synthesized Al<sub>2</sub>CuMg," *Journal of the Electrochemical Society* 146, 12 (1999): p. 4424-4428.
8. R.G. Buchheit, M.A. Martinez, and L.P. Montes, "Evidence for Cu ion formation by dissolution and dealloying the Al<sub>2</sub>CuMg intermetallic compound in rotating ring-disk collection experiments," *Journal of the Electrochemical Society* 147, 1 (2000): p. 119-124.
9. R.C. Bacon, J.J. Smith, and F.M. Rugg, "Electrolytic Resistance in Evaluating Protective Merit of Coatings on Metals," *Industrial & Engineering Chemistry* 40, 1 (1948): p. 161-167.
10. N.L. Thomas, "The barrier properties of paint coatings," *Progress in Organic Coatings* 19, 2 (1991): p. 101-121.
11. G.W. Walter, "A critical review of the protection of metals by paints," *Corrosion Science* 26, 1 (1986): p. 27-38.
12. P.A. Sørensen, S. Kiil, K. Dam-Johansen, and C.E. Weinell, "Anticorrosive coatings: a review," *Journal of Coatings Technology and Research* 6, 2 (2009): p. 135-176.
13. ASM International Handbook Committee., *ASM Handbook Corrosion: Materials*. Vol. 13A (Materials Park, OH: ASM International, 2003).

14. A. Bautista, R. Lizarbe, E. Otero, V. Lopez, and J.A. Gonzalez, "New alternatives to the industrially introduced methods for the sealing of anodized aluminium," *Revista De Metalurgia* 35, 3 (1999): p. 195-202.
15. N. Chahboun, E. Rocca, D. Veys-Renaux, M. Augros, M. Boutoba, and N. Caldeira, "Sealing of Anodized Multiphase Aluminum Alloys with Cr( plus III)/Zr( plus IV) Salts: Characterization and Corrosion Behavior," *Journal of the Electrochemical Society* 163, 3 (2016): p. C69-C75.
16. P.D. Deck and D. Reichgott, "Characterization of chromium-free no-rinse prepaint coatings on aluminum and galvanized steel," *Metal Fin.* 90, 9 (1992): p. 29-35.
17. J.A. Gonzalez, V. Lopez, E. Otero, A. Bautista, R. Lizarbe, C. Barba, and J.L. Baldonado, "Overaging of sealed and unsealed aluminium oxide films," *Corrosion Science* 39, 6 (1997): p. 1109-1118.
18. J.A. Gonzalez, M. Morcillo, E. Escudero, V. Lopez, A. Bautista, and E. Otero, "Self-sealing of unsealed aluminium anodic oxide films in very different atmospheres," *Revista De Metalurgia* (2003): p. 110-115.
19. Y. Guo and G.S. Frankel, "Active Corrosion Inhibition of AA2024-T3 by Trivalent Chrome Process Treatment," *Corrosion* 68, 4 (2012).
20. N.P. Hu, X.C. Dong, X.Y. He, J.F. Browning, and D.W. Schaefer, "Effect of sealing on the morphology of anodized aluminum oxide," *Corrosion Science* 97, (2015): p. 17-24.
21. Y.L. Huang, H. Shih, H.C. Huang, S. Wu, S. Ramanathan, C. Chang, and F. Mansfeld, "Evaluation of the corrosion resistance of anodized aluminum 6061 using electrochemical impedance spectroscopy (EIS)," *Corrosion Science* 50, 12 (2008): p. 3569-3575.
22. G.O. Ilevbare, C.S. Jeffcoate, and J.R. Scully, "Mass transport limited oxygen reduction kinetics on chromate conversion coated Al-Cu, Al-Cu-Mg and Al-Cu-Mn-Fe intermetallic compounds.," *Passivity and Localized Corrosion* 99, 27 (1999): p. 269-279.
23. G.O. Ilevbare and J.R. Scully, "Mass-Transport-Limited oxygen reduction reaction on AA2024-T3 and selected intermetallic compounds in chromate-containing solutions (vol 57, pg 134, 2001)," *Corrosion* 57, 5 (2001): p. 480-480.
24. G.O. Ilevbare and J.R. Scully, "Oxygen reduction reaction kinetics on chromate conversion coated Al-Cu, Al-Cu-Mg, and Al-Cu-Mn-Fe intermetallic compounds," *Journal of the Electrochemical Society* 148, 5 (2001): p. B196-B207.
25. G.O. Ilevbare and J.R. Scully, "Mass-transport-limited oxygen reduction reaction on AA2024-T3 and selected intermetallic compounds in chromate-containing solutions," *Corrosion* 57, 2 (2001): p. 134-152.
26. G.O. Ilevbare, J.R. Scully, J. Yuan, and R.G. Kelly, "Inhibition of pitting corrosion on aluminum alloy 2024-T3: Effect of soluble chromate additions vs chromate conversion coating," *Corrosion* 56, 3 (2000): p. 227-242.
27. D. Kanagaraj, S. Mohan, N.G. Renganathan, R.V. Raman, and S.V. Iyer, "Evaluation of anodized aluminum surface obtained from a sulfanic acid bath using electrochemical impedance spectroscopy," *Plating and Surface Finishing* 86, 7 (1999): p. 58-61.
28. J. Lee, Y. Kim, H. Jang, and W. Chung, "Cr<sub>2</sub>O<sub>3</sub> sealing of anodized aluminum alloy by heat treatment," *Surface & Coatings Technology* 243, (2014): p. 34-38.
29. Y. Li and Z.F. Zhu, "Cold Sealing Mechanism of Anodic Oxide-Films on Aluminum .2. Cold Sealing Models of Oxide-Films," *Plating and Surface Finishing* 80, 10 (1993): p. 77-80.

30. Y. Li, Z.F. Zhu, Z.Y. Jiang, and M.M. Yan, "Cold Sealing Mechanism of Anodic Oxide-Films on Aluminum .1. Composition and Structure of Cold-Sealed Oxide-Films," *Plating and Surface Finishing* 80, 9 (1993): p. 79-82.
31. D. Liu, G.Y. Wei, and P.L. He, "The Effect of Sealing and Trivalent Chromium Passivating on Anodized Aluminum," *International Journal of Electrochemical Science* 11, 3 (2016): p. 2097-2105.
32. O. Lunder, C. Simensen, Y. Yu, and K. Nisancioglu, "Formation and characterisation of Ti-Zr based conversion layers on AA6060 aluminium," *Surface and Coatings Technology* 184, 2 (2004): p. 278-290.
33. F. Mansfeld and M.W. Kendig, "Evaluation of Anodized Aluminum Surfaces with Electrochemical Impedance Spectroscopy," *Journal of the Electrochemical Society* 135, 4 (1988): p. 828-833.
34. F. Mansfeld, G. Zhang, and C. Chen, "Evaluation of sealing methods for anodized aluminum alloys with electrochemical impedance spectroscopy (EIS)," *Plating and Surface Finishing* 84, 12 (1997): p. 72-81.
35. C. Matzdorf, Beck, Erin., Hilgeman, Amy., Prado, Ruben. , *Trivalent Chromium Process as a Sealer for MIL-A-8625 Type II, IIB and IC Anodic Coatings*. 2008, NAVAIR. p. 50.
36. L. Xia, E. Akiyama, G. Frankel, and R. McCreery, "Storage and release of soluble hexavalent chromium from chromate conversion coatings - Equilibrium aspects of Cr-VI concentration," *Journal of the Electrochemical Society* 147, 7 (2000): p. 2556-2562.
37. J. Zhao, G. Frankel, and R.L. McCreery, "Corrosion protection of untreated AA-2024-T3 in chloride solution by a chromate conversion coating monitored with Raman spectroscopy," *Journal of the Electrochemical Society* 145, 7 (1998): p. 2258-2264.
38. J.M. Zhao, H.X. Liu, S.L. Chen, and X.H. Zhao, "EIS evolution of anodised aluminium by cerium salt sealing in NaCl solution with exposure time," *Corrosion Engineering Science and Technology* 48, 1 (2013): p. 44-47.
39. X. Zhao, L. Tian, J. Zhao, and Y. Zuo, "Electrochemical properties of anodized and sealed aluminum films," *Aicam* 2005 11-12, (2006): p. 433-436.
40. X.H. Zhao, Y. Zuo, J.M. Zhao, J.P. Xiong, and Y.M. Tang, "A study on the self-sealing process of anodic films on aluminum by EIS," *Surface & Coatings Technology* 200, 24 (2006): p. 6846-6853.
41. Y. Zuo, P.H. Zhao, and J.M. Zhao, "The influences of sealing methods on corrosion behavior of anodized aluminum alloys in NaCl solutions," *Surface & Coatings Technology* 166, 2-3 (2003): p. 237-242.
42. M.W. Kendig and R.G. Buchheit, "Corrosion Inhibition of Aluminum and Aluminum Alloys by Soluble Chromates, Chromate Coatings, and Chromate-Free Coatings," *CORROSION* 59, 5 (2003): p. 379-400.
43. H. Leidheiser, "Corrosion control by organic coatings," (1981).
44. L. Gáncs, A.S. Besing, R. Buják, A. Kolics, Z. Németh, and A. Wieckowski, "Interaction of Chromate with Aluminum in NaCl Solutions," *Electrochemical and Solid-State Letters* 5, 4 (2002): p. B16-B19.
45. M. Kendig, R. Addison, and S. Jeanjaquet, "The Influence of Adsorbed Oxo-Cr(VI) Species on the Zeta Potential in the Porous Oxide of Anodized Aluminum," *Journal of The Electrochemical Society* 146, 12 (1999): p. 4419-4423.

46. J.D. Ramsey and R.L. McCreery, "In Situ Raman Microscopy of Chromate Effects on Corrosion Pits in Aluminum Alloy," *Journal of The Electrochemical Society* 146, 11 (1999): p. 4076-4081.
47. W.J. Clark and R.L. McCreery, "Inhibition of Corrosion-Related Reduction Processes via Chromium Monolayer Formation," *Journal of The Electrochemical Society* 149, 9 (2002): p. B379-B386.
48. S.B. Madden and J.R. Scully, "Inhibition of AA2024-T351 Corrosion Using Permanganate," *Journal of The Electrochemical Society* 161, 3 (2014): p. C162-C175.
49. S.A. Kulinich, M. Farzaneh, and X.W. Du, "Growth of corrosion-resistant manganese oxide coatings on an aluminum alloy," *Inorganic Materials* 43, 9 (2007): p. 956-963.
50. M. Crouse, A.E. Miller, M.G. Pujar, and K.L. Vasanth, *Evaluation of Potassium Permanganate (KMnO<sub>4</sub>) as a Green Corrosion Inhibitor/Sealant for Anodized Al 2024 and Al 6061 at Different pH Values*, NACE International.
51. J.W. Bibber, *A Chrome Free Conversion Coating and Sealant for Aluminum and Its Alloys*, NACE International.
52. I. Danilidis, J. Hunter, G.M. Scamans, and J.M. Sykes, "Effects of inorganic additions on the performance of manganese-based conversion treatments," *Corrosion Science* 49, 3 (2007): p. 1559-1569.
53. I. Danilidis, A.J. Davenport, and J.M. Sykes, "Characterisation by X-ray absorption near-edge spectroscopy of KMnO<sub>4</sub>-based no-rinse conversion coatings on Al and Al alloys," *Corrosion Science* 49, 4 (2007): p. 1981-1991.
54. S.A. Hayes, P. Yu, T.J. O'Keefe, M.J. O'Keefe, and J.O. Stoffer "The Phase Stability of Cerium Species in Aqueous Systems: I. E-pH Diagram for the Ce - HClO<sub>4</sub> - H<sub>2</sub>O System," *Journal of The Electrochemical Society* 149, 12 (2002): p. C623-C630.
55. A.S. Hamdy, A.M. Beccaria, and P. Traverso, "Corrosion protection of aluminium metal-matrix composites by cerium conversion coatings," *Surface and Interface Analysis* 34, 1 (2002): p. 171-175.
56. F.J. Presuel-Moreno, M.A. Jakab, and J.R. Scully, "Inhibition of the Oxygen Reduction Reaction on Copper with Cobalt, Cerium, and Molybdate Ions," *Journal of The Electrochemical Society* 152, 9 (2005): p. B376-B387.
57. M.L. Zheludkevich, R. Serra, M.F. Montemor, K.A. Yasakau, I.M.M. Salvado, and M.G.S. Ferreira, "Nanostructured sol-gel coatings doped with cerium nitrate as pre-treatments for AA2024-T3: Corrosion protection performance," *Electrochimica Acta* 51, 2 (2005): p. 208-217.
58. X. Yu and G. Li, "XPS study of cerium conversion coating on the anodized 2024 aluminum alloy," *Journal of Alloys and Compounds* 364, 1-2 (2004): p. 193-198.
59. A.J. Aldykiewicz, A.J. Davenport, and H.S. Isaacs, "Studies of the Formation of Cerium-Rich Protective Films Using X-Ray Absorption Near-Edge Spectroscopy and Rotating Disk Electrode Methods," *Journal of The Electrochemical Society* 143, 1 (1996): p. 147-154.
60. D. Ho, N. Brack, J. Scully, T. Markley, M. Forsyth, and B. Hinton, "Cerium Dibutylphosphate as a Corrosion Inhibitor for AA2024-T3 Aluminum Alloys," *Journal of The Electrochemical Society* 153, 9 (2006): p. B392-B401.
61. F. Andreatta, M.E. Druart, A. Lanzutti, M. Lekka, D. Cossement, M.G. Olivier, and L. Fedrizzi, "Localized corrosion inhibition by cerium species on clad AA2024 aluminium

- alloy investigated by means of electrochemical micro-cell," *Corrosion Science* 65, (2012): p. 376-386.
62. M.A. Jakab, F. Presuel-Moreno, and J.R. Scully, "Critical Concentrations Associated with Cobalt, Cerium, and Molybdenum Inhibition of AA2024-T3 Corrosion: Delivery from Al-Co-Ce(-Mo) Alloys," *CORROSION* 61, 3 (2005): p. 246-263.
  63. E.A. Lizlovs, "Molybdates as Corrosion Inhibitors in the Presence of Chlorides," *CORROSION* 32, 7 (1976): p. 263-266.
  64. R.L. Cook and S.R. Taylor, "Pigment-Derived Inhibitors for Aluminum Alloy 2024-T3," *CORROSION* 56, 3 (2000): p. 321-333.
  65. B.D. Chambers and S.R. Taylor, "The high throughput assessment of aluminium alloy corrosion using fluorometric methods. Part II – A combinatorial study of corrosion inhibitors and synergistic combinations," *Corrosion Science* 49, 3 (2007): p. 1597-1609.
  66. S. Prasad, S.I.B. Gonçalves, and J.B. Brito, "Electrometric studies on the system acid-vanadate and the formation of heavy metal vanadates," *Catalysis Today* 57, 3–4 (2000): p. 339-348.
  67. R.G. Buchheit, H. Guan, S. Mahajanam, and F. Wong, "Active corrosion protection and corrosion sensing in chromate-free organic coatings," *Progress in Organic Coatings* 47, 3–4 (2003): p. 174-182.
  68. H. Guan and R.G. Buchheit, "Corrosion Protection of Aluminum Alloy 2024-T3 by Vanadate Conversion Coatings," *CORROSION* 60, 3 (2004): p. 284-296.
  69. B.D. Chambers and S.R. Taylor, "High-Throughput Assessment of Inhibitor Synergies on Aluminum Alloy 2024-T3 through Measurement of Surface Copper Enrichment," *CORROSION* 63, 3 (2007): p. 268-276.
  70. R.L. Twite and G.P. Bierwagen, "Review of alternatives to chromate for corrosion protection of aluminum aerospace alloys," *Progress in Organic Coatings* 33, 2 (1998): p. 91-100.
  71. J. Sinko, "Challenges of chromate inhibitor pigments replacement in organic coatings," *Progress in Organic Coatings* 42, 3–4 (2001): p. 267-282.
  72. D. Battocchi, A.M. Simoes, D.E. Tallman, and G.P. Bierwagen, "Electrochemical behaviour of a Mg-rich primer in the protection of Al alloys," *Corrosion Science* 48, 5 (2006): p. 1292-1306.
  73. G. Bierwagen, D. Battocchi, A. Simoes, A. Stamness, and D. Tallman, "The use of multiple electrochemical techniques to characterize Mg-rich primers for Al alloys," *Progress in Organic Coatings* 59, 3 (2007): p. 172-178.
  74. D.E.T. G. P. Bierwagen, M. Nannan, D. Battocchi, A. Stamness and V. J. Gelling, *New developments in Cr-Free primers for aerospace alloys*, in *American Chemical Society*. 2004. p. U360.
  75. B. Kannan, Scully, J. R, "Performance of a Magnesium Rich Primer on Pretreated AA2024-T351 in Selected Laboratory and Field Environments: Conversion Coating Pretreatments," *Corrosion* (2016).
  76. B. Kannan, A. King, and J. Scully, *Impact of Surface Pretreatments on AA2024-T351 Corrosion Protection by a Magnesium Rich, Non-Chrome Primer (MgRP)*, in *NACE DoD 2015*. 2015, NACE: Pittsburgh, PA.
  77. B. Kannan, A. King, and J. Scully, "Effect of Pretreatments on 2024-T351 Corrosion Protection by Magnesium Rich, Non-Chromium Primer (MgRP): Laboratory Characterization in Full Immersion," *Corrosion* doi:10.5006/1700, (2015).

78. C.M. Abreu, M. Izquierdo, P. Merino, X.R. Novoa, and C. Perez, "A new approach to the determination of the cathodic protection period in zinc-rich paints," *Corrosion* 55, 12 (1999): p. 1173-1181.
79. R.A. Armas, C.A. Gervasi, A. Disarli, S.G. Real, and J.R. Vilche, "Zinc-Rich Paints on Steels in Artificial Seawater by Electrochemical Impedance Spectroscopy," *Corrosion* 48, 5 (1992): p. 379-383.
80. A.D. King, B. Kannan, and J.R. Scully, "Environmental Degradation of a Mg-Rich Primer in Selected Field and Laboratory Environments – Part II. Primer and Topcoat," *Corrosion* 70, 5 (2014).
81. A.D. King, B. Kannan, and J.R. Scully, "Environmental Degradation of a Mg-Rich Primer in Selected Field and Laboratory Environments – Part I. Without a Topcoat," *Corrosion* 70, 5 (2014).
82. A.D. King, J.S. Lee, and J.R. Scully, "Galvanic Couple Current and Potential Distribution between a Mg Electrode and 2024-T351 under Droplets Analyzed by Microelectrode Arrays," *Journal of the Electrochemical Society* 162, 1 (2015): p. C12-C23.
83. A.D. King, J.S. Lee, and J.R. Scully, "Finite Element Analysis of the Galvanic Couple Current and Potential Distribution between Mg and 2024-T351 in a Mg Rich Primer Configuration," *Journal of The Electrochemical Society* 163, 7 (2016): p. C342-C356.
84. A.D. King and J.R. Scully, "Sacrificial Anode-Based Galvanic and Barrier Corrosion Protection of 2024-T351 by a Mg-Rich Primer and Development of Test Methods for Remaining Life Assessment," *Corrosion* 67, 5 (2011): p. 05500401-05500422.
85. A.D. King and J.R. Scully. *Blistering Phenomena in Early Generation Mg-Rich Primer Coatings on AA2024-T351 and the Effects of CO<sub>2</sub>*. in *NACE DoD 2011 Conference Proceedings*. 2011. Palm Springs, CA.
86. O.O. Knudsen, U. Steinsmo, and M. Bjordal, "Zinc-rich primers - Test performance and electrochemical properties," *Progress in Organic Coatings* 54, 3 (2005): p. 224-229.
87. M.J. Lin, D.D. Battocchi, and P.G. Bierwagen, "Degradation of Magnesium Rich Primers over AA2024-T3 during Constant Immersion in Different Solutions," *CORROSION* 0, 0: p. null.
88. B. Maier and G.S. Frankel, "Behavior of Magnesium-Rich Primers on AA2024-T3," *Corrosion* 67, 5 (2011): p. 055001.
89. H. Marchebois, M. Keddad, C. Savall, J. Bernard, and S. Touzain, "Zinc-rich powder coatings characterisation in artificial sea water - EIS analysis of the galvanic action," *Electrochimica Acta* 49, 11 (2004): p. 1719-1729.
90. M. Morcillo, R. Barajas, S. Feliu, and J.M. Bastidas, "A-Sem Study on the Galvanic Protection of Zinc-Rich Paints," *Journal of Materials Science* 25, 5 (1990): p. 2441-2446.
91. M.A. Jakab and J.R. Scully, "On-demand release of corrosion-inhibiting ions from amorphous Al-Co-Ce alloys," *Nat Mater* 4, 9 (2005): p. 667-670.
92. F. Presuel-Moreno, M.A. Jakab, N. Tailleart, M. Goldman, and J.R. Scully, "Corrosion-resistant metallic coatings," *Materials Today* 11, 10 (2008): p. 14-23.
93. F.J. Presuel-Moreno, M.E. Goldman, R.G. Kelly, and J.R. Scully, "Electrochemical Sacrificial Cathodic Prevention Provided by an Al-Co-Ce Metal Coating Coupled to AA2024-T3," *Journal of The Electrochemical Society* 152, 8 (2005): p. B302-B310.
94. Y. Cubides, S.S. Su, and H. Castaneda, "Influence of Zinc Content and Chloride Concentration on the Corrosion Protection Performance of Zinc-Rich Epoxy Coatings

- Containing Carbon Nanotubes on Carbon Steel in Simulated Concrete Pore Environments," *Corrosion* 72, 11 (2016): p. 1397-1423.
95. Y. Cubides and H. Castaneda, "Corrosion protection mechanisms of carbon nanotube and zinc-rich epoxy primers on carbon steel in simulated concrete pore solutions in the presence of chloride ions," *Corrosion Science* 109, (2016): p. 145-161.
  96. F. Cui, F.J. Presuel-Moreno, and R.G. Kelly, "Experimental and Computational Evaluation of the Protection Provided by an Aluminum Cladding to AA2024-T3 Exposed at a Seacoast Environment," *CORROSION* 62, 3 (2006): p. 251-263.
  97. F.S. Cui, F.J. Presuel-Moreno, and R.G. Kelly, "Computational modeling of cathodic limitations on localized corrosion of wetted SS 316L at room temperature," *Corrosion Science* 47, 12 (2005): p. 2987-3005.
  98. S.M. Sharland, C.P. Jackson, and A.J. Diver, "A finite-element model of the propagation of corrosion crevices and pits," *Corrosion Science* 29, 9 (1989): p. 1149-1166.
  99. J.T. Waber, "Mathematical Studies of Galvanic Corrosion: VI. . Limiting Case of Very Thin Films," *Journal of the Electrochemical Society* 103, 10 (1956): p. 567-570.
  100. J.T. Waber, "Mathematical Studies of Galvanic Corrosion: III . Semi-infinite Coplanar Electrodes with Equal Constant Polarization Parameters," *Journal of the Electrochemical Society* 102, 7 (1955): p. 420-429.
  101. J.T. Waber and M. Rosenbluth, "Mathematical Studies of Galvanic Corrosion: II . Coplanar Electrodes with One Electrode Infinitely Large and with Equal Polarization Parameters," *Journal of the Electrochemical Society* 102, 6 (1955): p. 344-353.
  102. J.S. Lee, M.L. Reed, and R.G. Kelly, "Combining rigorously controlled crevice geometry and computational modeling for study of crevice corrosion scaling factors," *Journal of the Electrochemical Society* 151, 7 (2004): p. B423-B433.
  103. Henkel, Surface Pretreatment - Technical Data Sheet (2014).
  104. G.S. Frankel and R.L. McCreery, "Inhibition of Al alloy corrosion by chromates," *Interface-Electrochemical Society* 10, 4 (2001): p. 34-39.
  105. F.W. Lytle, R.B. Gregor, G.L. Bibbins, K.Y. Blohowiak, R.E. Smith, and G.D. Tuss, "An Investigation of the Structure and Chemistry of a Chromium-Conversion Surface-Layer on Aluminum," *Corrosion Science* 37, 3 (1995): p. 349-369.
  106. L. Xia and R.L. McCreery, "Chemistry of a chromate conversion coating on aluminum alloy AA2024-T3 probed by vibrational spectroscopy," *Journal of the Electrochemical Society* 145, 9 (1998): p. 3083-3089.
  107. L. Xia and R.L. McCreery, "Structure and function of ferricyanide in the formation of chromate conversion coatings on aluminum aircraft alloy," *Journal of the Electrochemical Society* 146, 10 (1999): p. 3696-3701.
  108. A. Sehgal, G.S. Frankel, B. Zoofan, and S. Rokhlin, "Pit growth study in Al alloys by the foil penetration technique," *Journal of the Electrochemical Society* 147, 1 (2000): p. 140-148.
  109. R.G. Buchheit, M. Cunningham, H. Jensen, M.W. Kendig, and M.A. Martinez, "A Correlation Between Salt Spray and Electrochemical Impedance Spectroscopy Test Results for Conversion-Coated Aluminum Alloys," *CORROSION* 54, 1 (1998): p. 61-72.
  110. L.L. Li, D.Y. Kim, and G.M. Swain, "Transient Formation of Chromate in Trivalent Chromium Process (TCP) Coatings on AA2024 as Probed by Raman Spectroscopy," *Journal of the Electrochemical Society* 159, 8 (2012): p. C326-C333.

111. P. Schmutz and G.S. Frankel, "Influence of dichromate ions on corrosion of pure aluminum and AA2024-T3 in NaCl solution studied by AFM scratching," *Journal of the Electrochemical Society* 146, 12 (1999): p. 4461-4472.
112. T. Rochester and Z.W. Kennedy, "Unexpected results from corrosion testing of trivalent passivates," *Plating and surface finishing* 94, 10 (2007): p. 14.
113. L.L. Li, G.P. Swain, A. Howell, D. Woodbury, and G.M. Swain, "The Formation, Structure, Electrochemical Properties and Stability of Trivalent Chrome Process (TCP) Coatings on AA2024," *Journal of the Electrochemical Society* 158, 9 (2011): p. C274-C283.
114. D.E. Packham, *Handbook of Adhesion*. 2 ed.
115. G. Bierwagen, R. Brown, D. Battocchi, and S. Hayes. *Observations on the testing of Mg-Rich Primers for Totally Chromate-free Corrosion Protection of Aerospace Alloys*. in *NACE DoD 2009 Conference Proceedings*. 2009. Washing, DC.
116. H. Xu, D. Battocchi, D.E. Tallman, and G.P. Bierwagen, "Use of Magnesium Alloys as Pigments in Magnesium-Rich Primers for Protecting Aluminum Alloys," *Corrosion* 65, 5 (2009): p. 318-325.
117. S.S. Pathak, M.D. Blanton, S.K. Mendon, and J.W. Rawlins, "Investigation on dual corrosion performance of magnesium-rich primer for aluminum alloys under salt spray test (ASTM B117) and natural exposure," *Corrosion Science* 52, 4 (2010): p. 1453-1463.
118. B.C.R. Troconis and G.S. Frankel, "Effects of Pretreatments on the Adhesion of Acetoacetate to AA2024-T3 Using the Blister Test," *Corrosion* 70, 5 (2014): p. 483-495.
119. H. Leidheiser, *Corrosion control by organic coatings*, 1981.
120. L.L. Li, K.P. Doran, and G.M. Swain, "Electrochemical Characterization of Trivalent Chromium Process (TCP) Coatings on Aluminum Alloys 6061 and 7075," *J Electrochem Soc* 160, 8 (2013): p. C396-C401.
121. M. Saeedikhani, M. Javidi, and A. Yazdani, "Anodizing of 2024-T3 aluminum alloy in sulfuric-boric-phosphoric acids and its corrosion behavior," *Transactions of Nonferrous Metals Society of China* 23, 9 (2013): p. 2551-2559.
122. D. Chidambaram, C.R. Clayton, and G.P. Halada, "A duplex mechanism-based model for the interaction between chromate ions and the hydrated oxide film on aluminum alloys," *Journal of the Electrochemical Society* 150, 5 (2003): p. B224-B237.
123. E. Beck, "Performance validation of Thin-film sulfuric acid anodization(TFSAA) on aluminum alloys," *Metal Finishing* 101, 1 (2003): p. 28-31, 33-40.
124. Pantheon, *Surface Pretreatment - Technical Data Sheet* (2009).
125. Henkel, *Surface Pretreatment - Technical Data Sheet* (2006).
126. Surtec, *Surface Pretreatment - Technical Data Sheet* (2012).
127. MIL-A-8625, "Anodic coatings for aluminum and aluminum alloys," *Military Specification* (1993).
128. AkzoNobel, "Aerodur5000," *Topcoat - Technical Data Sheet* (2013).
129. *Standard Reference Test Method for Making Potentiostatic and Potentiodynamic Anodic Polarization Measurements*, in *Annual Book of ASTM Standards*. 1197, ASTM: West Conshohocken, PA. p. 1-12.
130. Z. Ye, *X-Ray Photoelectron Spectroscopy Demonstrations* (2014): p. 9.
131. V.K. Pecharsky and P.Y. Zavalij, *Fundamentals of powder diffraction and structural characterization of materials*. 2nd ed (New York: Springer, 2009). p. xxiii, 741 p.

132. S.S. Pathak, M.D. Blanton, S.K. Mendon, and J.W. Rawlins, "Carbonation of Mg powder to enhance the corrosion resistance of Mg-rich primers," *Corrosion Science* 52, 11 (2010): p. 3782-3792.
133. S.S. Pathak, M.D. Blanton, S.K. Mendon, and J.W. Rawlins, "Mineralogical Transformation and Electrochemical Nature of Magnesium-Rich Primers during Natural Weathering," *Metals* 4, 3 (2014): p. 322-334.
134. *Standard Practice for Operating Salt Spray (Fog) Apparatus: B117*, in *Annual Book of ASTM Standards*. 1997, ASTM: West Conshohocken, PA. p. 1-8.
135. ASTM, "Standard Practice for the Preparation of Substitute Ocean Water," ASTM D1141 - 98 DOI: 10.1520/D1141-98R08 (1998).
136. ASTM, "Standard Practice for Modified Salt Spray Testing," ASTM G85 - A3 DOI: 10.1520/C0033-03, (2009).
137. ASTM, "Standard Guide for Conducting Corrosion Tests in Field Applications," ASTM G4 - 01 DOI: 10.1520/G0004-01R08, (2001).
138. ASTM, "Standard Practice for Preparing, Cleaning, and Evaluating Corrosion Test Specimens," ASTM G1 DOI: 10.1520/D1141-98R08 (2003).
139. S. Pommiers-Belin, J. Frayret, A. Uhart, J. Ledeuil, J.-C. Dupin, A. Castetbon, and M. Potin-Gautier, "Determination of the chemical mechanism of chromate conversion coating on magnesium alloys EV31A," *Applied Surface Science* 298, (2014): p. 199-207.
140. M. Pourbaix, *Atlas of Electrochemical Equilibria in Aqueous Solutions*: NACE, 1974.
141. ASTM, *Standard Practice for Operating Salt Spray (Fog) Apparatus: B117*, in *Annual Book of ASTM Standards*. 1997, ASTM: West Conshohocken, PA. p. 1-8.
142. M.T. Woldemedhin, M.E. Shedd, and R.G. Kelly, "Evaluation of the Maximum Pit Size Model on Stainless Steels under Thin Film Electrolyte Conditions," *Journal of the Electrochemical Society* 161, 8 (2014): p. E3216-E3224.
143. R.J. Santucci, Kannan, B., Scully, J. R., "Investigation of Magnesium Oxide Primer on 2024-T351: Assessment and Characterization of Magnesium Oxide Protection Mechanism," *Corrosion* (2016).
144. S. Pathak, M. Blanton, S. Mendon, and J. Rawlins, "Mineralogical Transformation and Electrochemical Nature of Magnesium-Rich Primers during Natural Weathering," *Metals* 4, 3 (2014): p. 322.
145. N.D. Richter and D. Battocchi, "PMSE 332-Performance of Mg-rich primers in B117 salt fog," *Abstracts of Papers of the American Chemical Society* 235, (2008).
146. N.E.C. Co and J.T. Burns, "Galvanic Corrosion-Induced Fatigue Crack Initiation and Propagation Behavior in AA7050-T7451," *CORROSION* 72, 10 (2016): p. 1215-1219.
147. L. Bland, J. Fitz-Gerald, and J. Scully, "Metallurgical and Electrochemical Characterization of the Corrosion of AZ31B-H24 Tungsten Inert Gas Weld: Isolated Weld Zones," *Corrosion* (2015).
148. L.G. Bland, A.D. King, N. Birbilis, and J.R. Scully, "Assessing the Corrosion of Commercially Pure Magnesium and Commercial AZ31B by Electrochemical Impedance, Mass-Loss, Hydrogen Collection, and Inductively Coupled Plasma Optical Emission Spectrometry Solution Analysis," *CORROSION* 71, 2 (2015): p. 128-145.
149. L.G. Bland, B.C.R. Troconis, R.J.S. Jr., J.M. Fitz-Gerald, and J.R. Scully, "Metallurgical and Electrochemical Characterization of the Corrosion of a Mg-Al-Zn Alloy AZ31B-H24 Tungsten Inert Gas Weld: Galvanic Corrosion Between Weld Zones," *CORROSION* 72, 10 (2016): p. 1226-1242.

150. J.E. Maslar, W.S. Hurst, T.A. Vanderah, and I. Levin, "The Raman spectra of Cr<sub>3</sub>O<sub>8</sub> and Cr<sub>2</sub>O<sub>5</sub>," *Journal of Raman Spectroscopy* 32, 3 (2001): p. 201-206.
151. Y.-S. Li, K. Wang, P. He, B.X. Huang, and P. Kovacs, "Surface-enhanced Raman spectroelectrochemical studies of corrosion films on implant Co–Cr–Mo alloy in biosimulating solutions," *Journal of Raman Spectroscopy* 30, 2 (1999): p. 97-103.
152. D. Chidambaram, M. Jaime Vasquez, G.P. Halada, and C.R. Clayton, "Studies on the repassivation behavior of aluminum and aluminum alloy exposed to chromate solutions," *Surface and Interface Analysis* 35, 2 (2003): p. 226-230.
153. J.R. Scully, N. Tailleart, and F. Presuel-Moreno, *9 - Tunable multifunctional corrosion-resistant metallic coatings containing rare earth elements*, in *Rare Earth-Based Corrosion Inhibitors*. 2014, Woodhead Publishing, p. 267-290.
154. "User-Selectable Barrier, Sacrificial Anode, and Active Corrosion Inhibiting Properties of Al-Co-Ce Alloys for Coating Applications," *CORROSION* 64, 3 (2008): p. 210-229.
155. H.S. Isaacs, A.J. Davenport, and A. Shipley, "The Electrochemical Response of Steel to the Presence of Dissolved Cerium," *Journal of the Electrochemical Society* 138, 2 (1991): p. 390-393.
156. A.J. Aldykewicz, H.S. Isaacs, and A.J. Davenport, "The Investigation of Cerium as a Cathodic Inhibitor for Aluminum-Copper Alloys," *Journal of The Electrochemical Society* 142, 10 (1995): p. 3342-3350.
157. D. A. Worsley, H. N. McMurray, and A. Belghazi, "Determination of localised corrosion mechanisms using a scanning vibrating reference electrode technique," *Chemical Communications* 24 (1997): p. 2369-2370.
158. F. Thébault, B. Vuillemin, R. Oltra, K. Ogle, and C. Allely, "Investigation of self-healing mechanism on galvanized steels cut edges by coupling SVET and numerical modeling," *Electrochimica Acta* 53, 16 (2008): p. 5226-5234.
159. A.M. Simões, J. Torres, R. Picciochi, and J.C.S. Fernandes, "Corrosion inhibition at galvanized steel cut edges by phosphate pigments," *Electrochimica Acta* 54, 15 (2009): p. 3857-3865.
160. A.C. Bastos, M.G. Ferreira, and A.M. Simões, "Corrosion inhibition by chromate and phosphate extracts for iron substrates studied by EIS and SVET," *Corrosion Science* 48, 6 (2006): p. 1500-1512.
161. M.J. Franklin, D.C. White, and H.S. Isaacs, "A study of carbon steel corrosion inhibition by phosphate ions and by an organic buffer using a scanning vibrating electrode," *Corrosion Science* 33, 2 (1992): p. 251-260.
162. G. Williams, A.J. Coleman, and H.N. McMurray, "Inhibition of Aluminium Alloy AA2024-T3 pitting corrosion by copper complexing compounds," *Electrochimica Acta* 55, 20 (2010): p. 5947-5958.
163. M.A. Melia, M.L. Serron, D.C. Florian, J.P. Weiler, J.R. Scully, and J.M. Fitz-Gerald, "Excimer Laser Processing of Cast Mg-Al-Zn (AZ91D) and Mg-Al (AM60B) Alloys for Improved Corrosion Resistance," *CORROSION* 72, 12 (2016): p. 1580-1586.
164. M.A. Melia, P. Steiner, N. Birbilis, J.M. Fitz-Gerald, and J.R. Scully, "Excimer Laser Surface Modification of AZ31B-H24 for Improved Corrosion Resistance," *CORROSION* 72, 1 (2016): p. 95-109.

## 6.8 Tables

Table 6.1. Thickness of pretreatments (based on cross-sectional EDS line profile analysis).

Pretreatment	Thickness of pretreatments characterized by cross-sectional EDS line profile ( $\mu\text{m}$ )
Non-film forming pretreatment	0
Trivalent chromium pretreatment (TCP)	0.4
Anodization with chromate sealing	8.9

Table 6.2. Comparison of SVET analysis to FEA modelling of Galvanic Current distribution of Mg and AA2024-T351.

	Galvanic Current at Scribe (SVET), $\text{A}/\text{m}^2$	Galvanic Current at Scribe (FEA), $\text{A}/\text{m}^2$
Case 1 (2024-T351 and Mg couple) SVET: 2 M NaCl, 10 mm electrolyte thickness, $R_{\text{polymer}} : 0 \Omega\text{-m}^2$ FEA: 1 M NaCl, 0.5 mm electrolyte thickness, $R_{\text{polymer}} : 0 \Omega\text{-m}^2$	500 – 1000 $\text{A}/\text{m}^2$	100 – 1000 $\text{A}/\text{m}^2$
Case 2 (2024-T351 and NFF/MgRP couple) SVET: 2 M NaCl, 10 mm electrolyte thickness, $R_{\text{polymer}} : 100 \Omega\text{-m}^2$	0.1 - 0.2 $\text{A}/\text{m}^2$	0.09 $\text{A}/\text{m}^2$

FEA: 1 M NaCl, 0.1 mm electrolyte thickness, $R_{\text{polymer}} : 10 \Omega\text{-m}^2$		
--	--	--

## 6.9 Figures

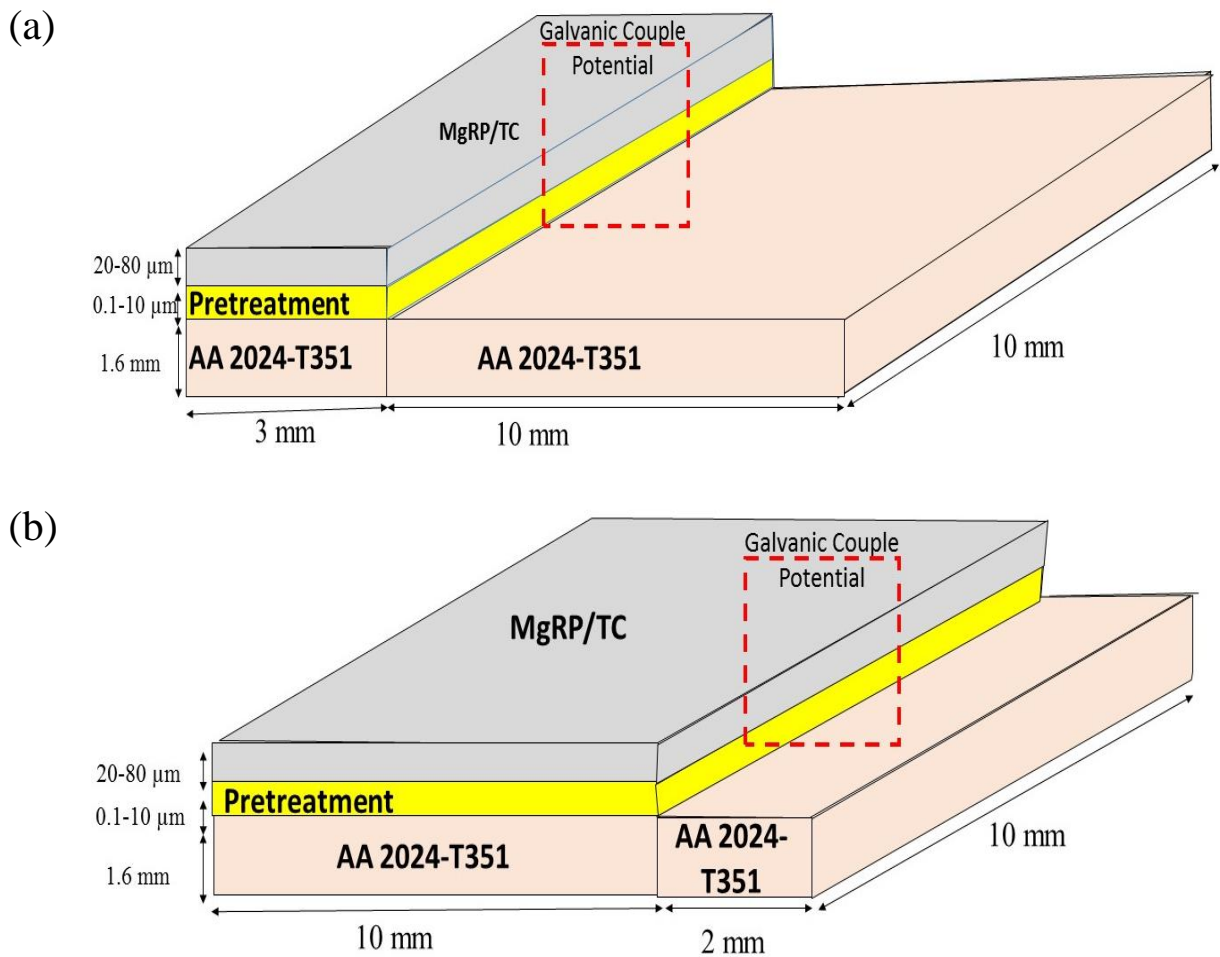
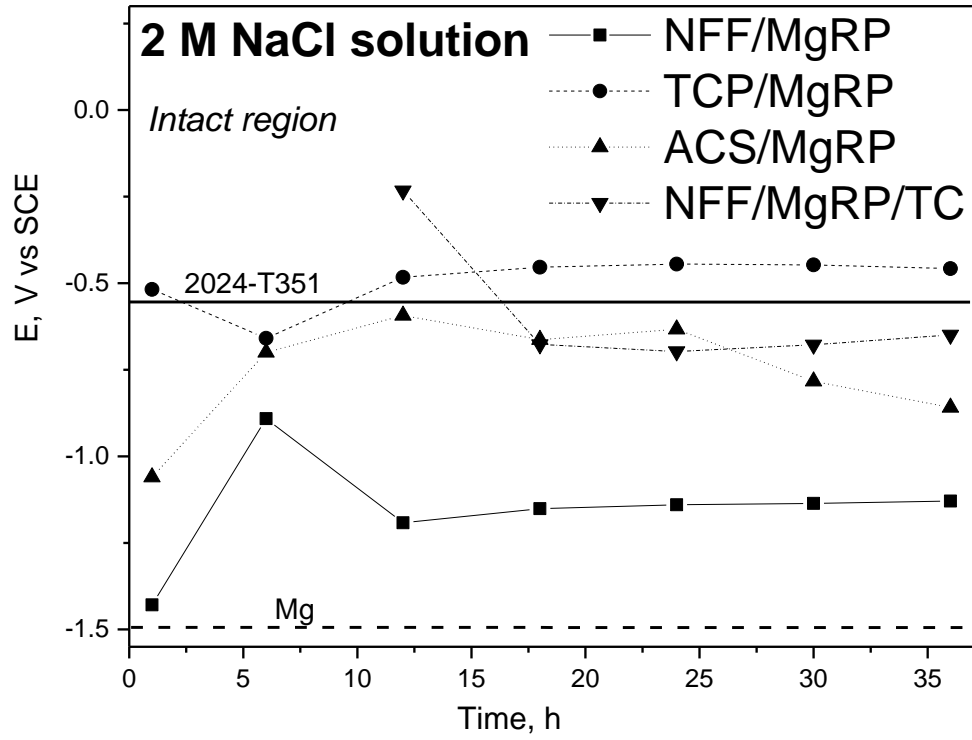


Figure 6.1. Sample design for SVET experiments. (a) coating/scribe ratio (0.3) and (b) coating/scribe ratio (5)

(a)



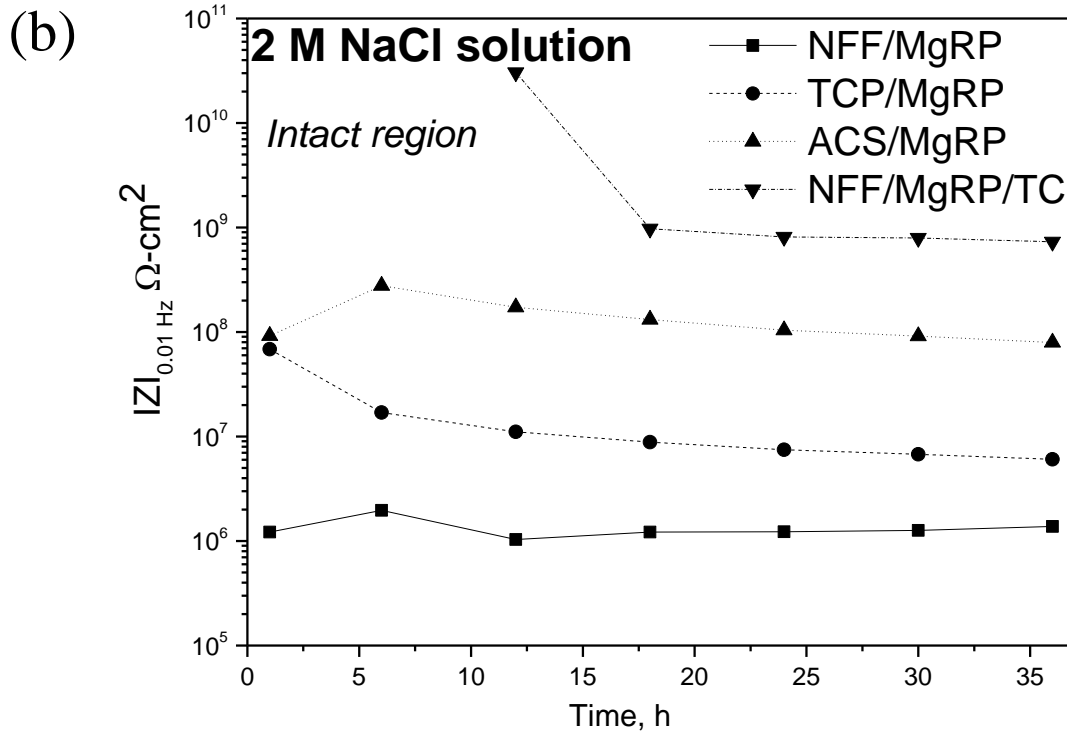


Figure 6.2. Average OCP of last 1 hour of exposure (a)/ Low Frequency Mod. Z (b) vs full immersion exposure time for selected 2024-T351/Pretreatment/MgRP with/without topcoat indicated.

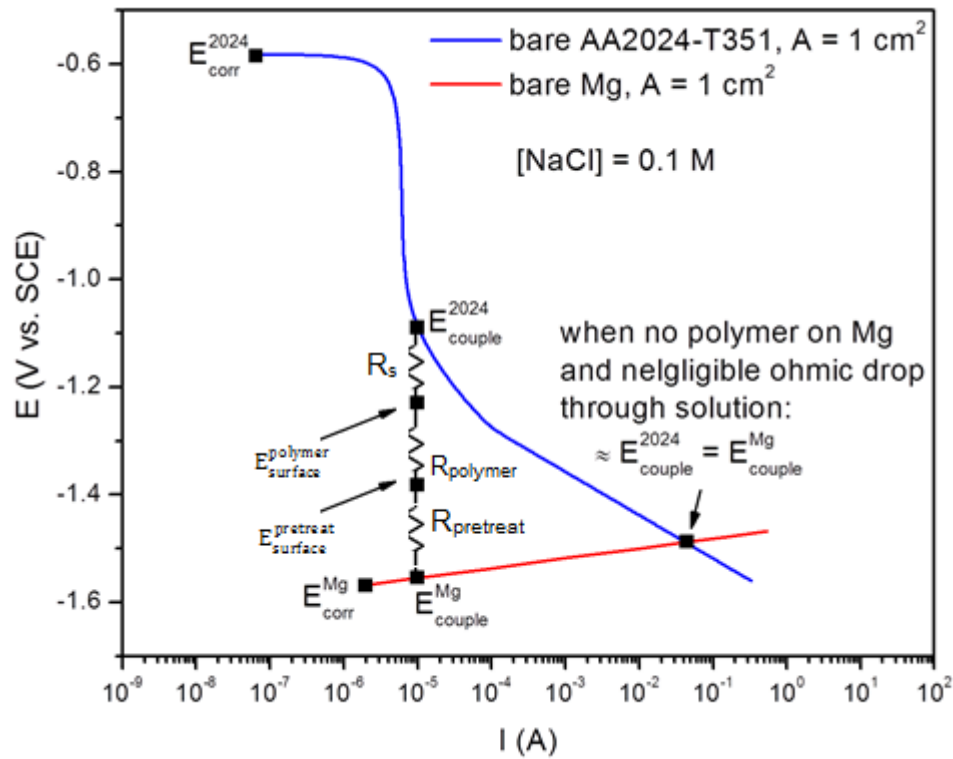


Figure 6.3. Mixed potential model depicting  $E_{\text{surface}}$  and  $E_{\text{couple}}$  as they pertain to a galvanic couple between bare and pretreated 2024-T351 and polymer coated Mg.  $R_{\text{polymer}}$ ,  $R_{\text{pretreat}}$  and  $R_s$  indicates polymer resistance, pretreatment resistance and solution resistance, respectively.  $E_{\text{corr}}^{2024}$ ,  $E_{\text{corr}}^{\text{Mg}}$  indicate corrosion potential of bare 2024-T351 and bare Mg, respectively.  $E_{\text{couple}}^{2024}$ ,  $E_{\text{couple}}^{\text{Mg}}$  indicate galvanic couple potential at surface for bare 2024-T351 and bare Mg, respectively.  $E_{\text{surface}}^{\text{polymer}}$ ,  $E_{\text{surface}}^{\text{pretreat}}$  indicate Galvanic couple potential at surface of 2024-T351/pretreatment and 2024-T351/pretreatment/MgRP, respectively.

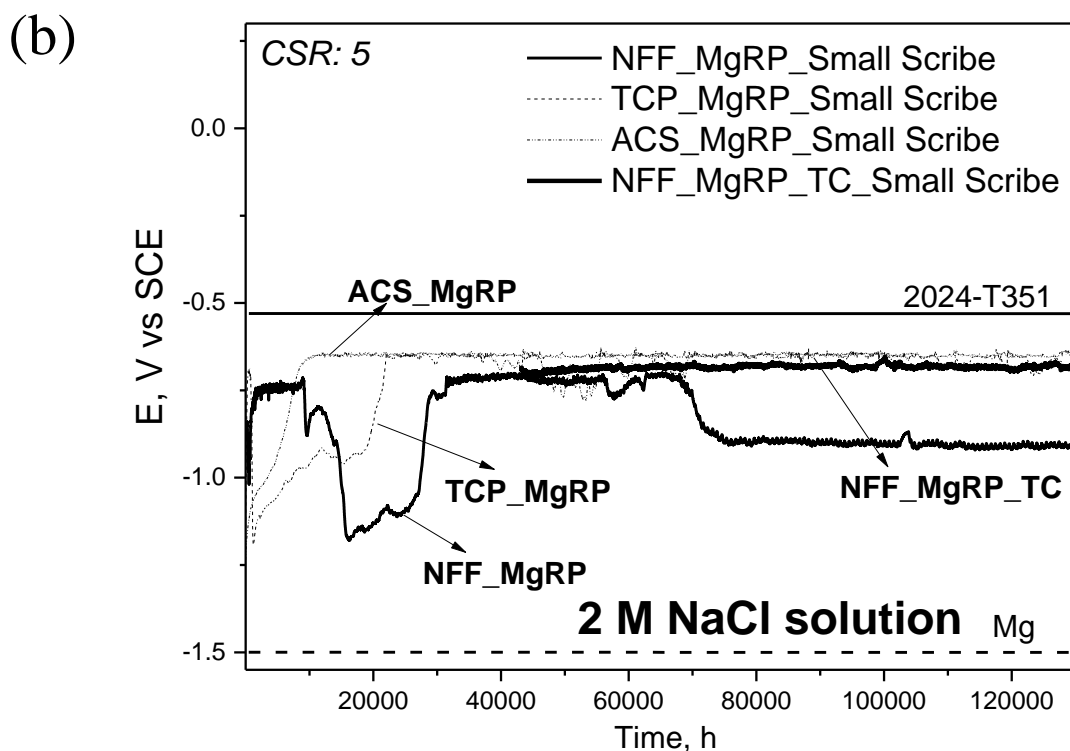
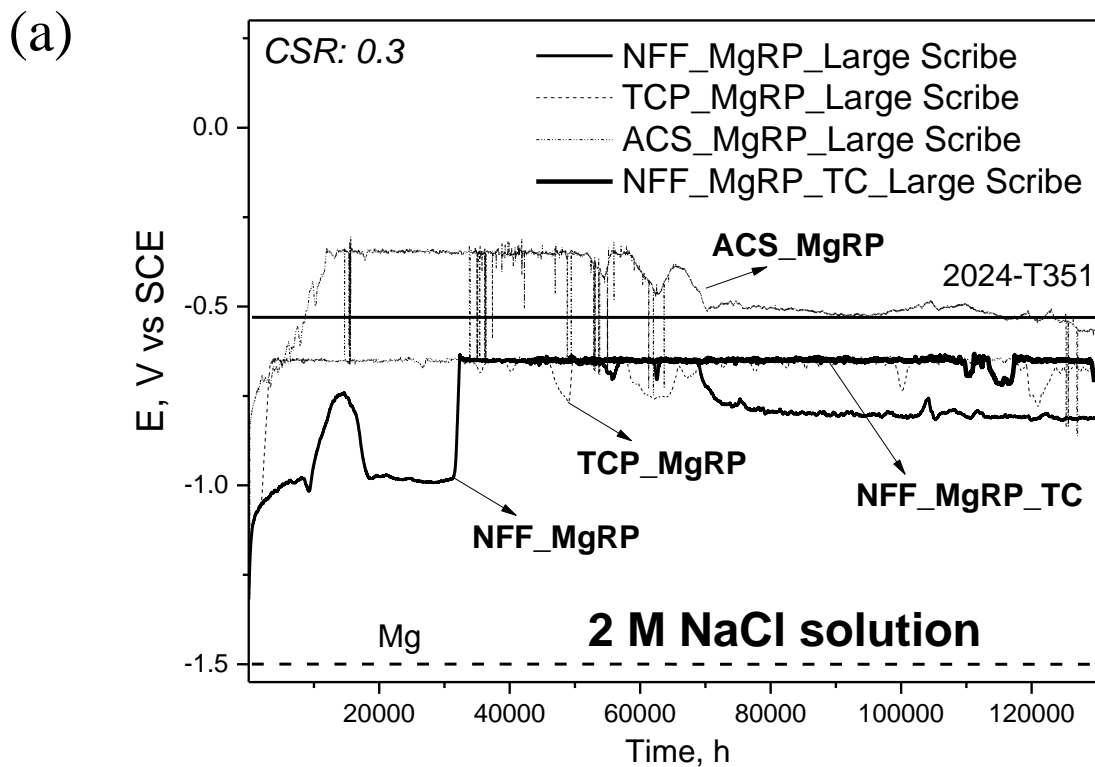


Figure 6.4. OCP of bare 2024-T351 galvanically coupled to 2024-T351/Pretreatment/MgRP with/without topcoat for for two coating to scribe area ratios, 0.3 (a) and 5 (b)

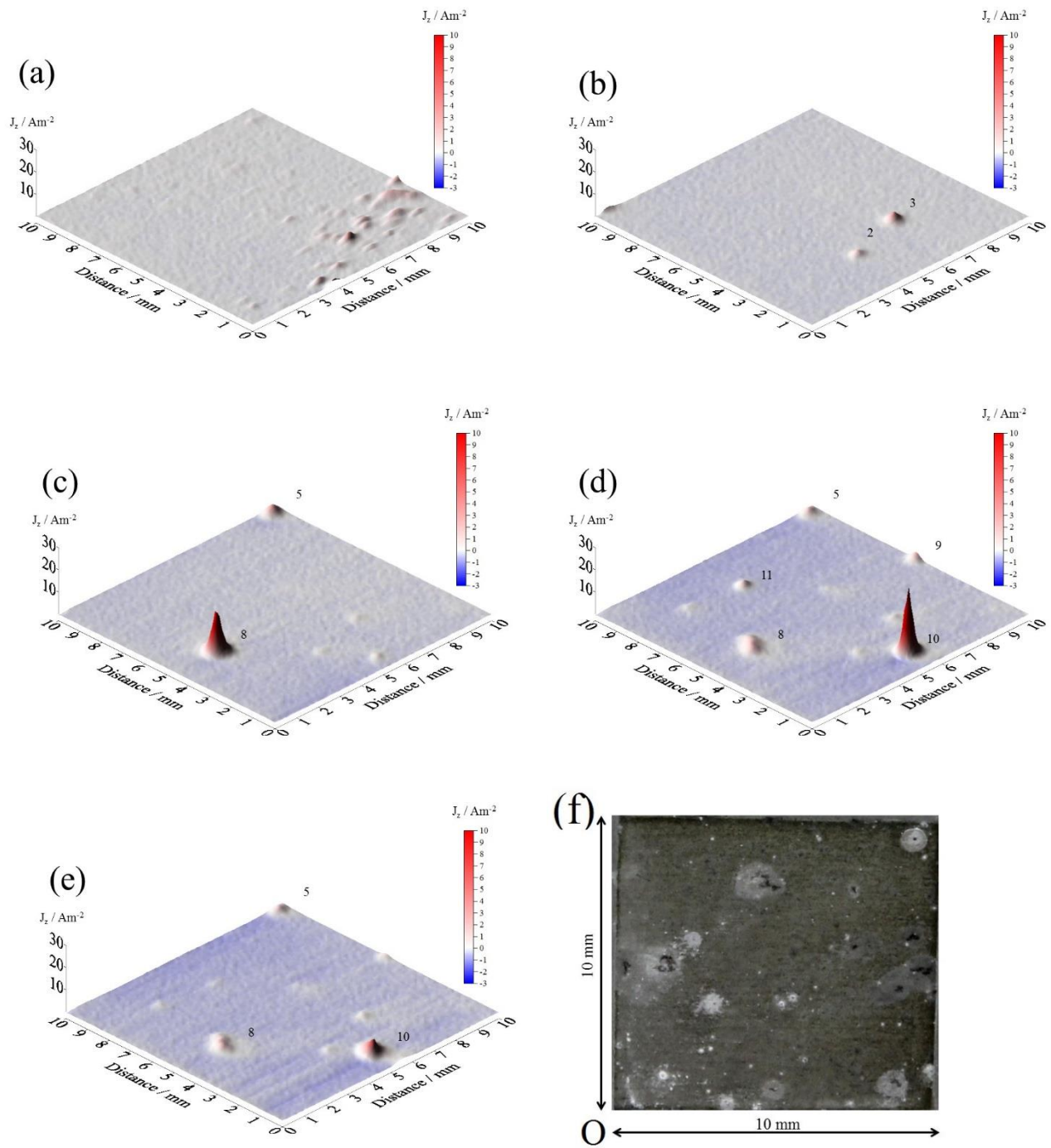


Figure 6.5. Surface plots showing the distribution of normal current density  $j_z$  above a 2024-T351 alloy sample freely corroding in aerated 2 M NaCl solution. Data were obtained from SVET scans carried out (a) 0 h, (b) 4 h, (c) 14 h, (d) 26 h and (e) 36 h after sample immersion. (f) shows the visual appearance of the sample after 38 h immersion.

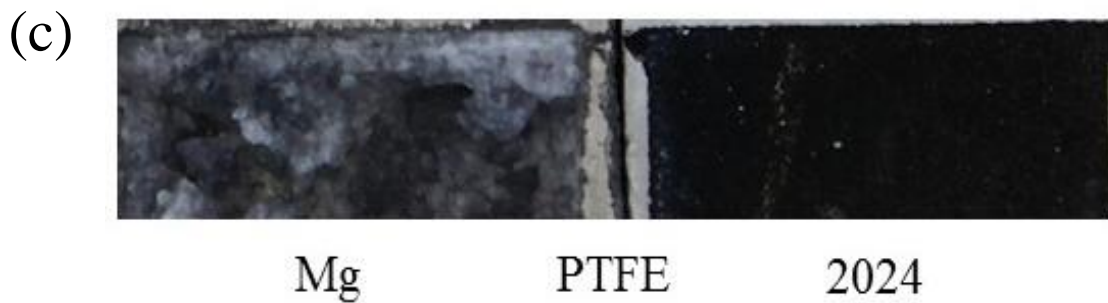
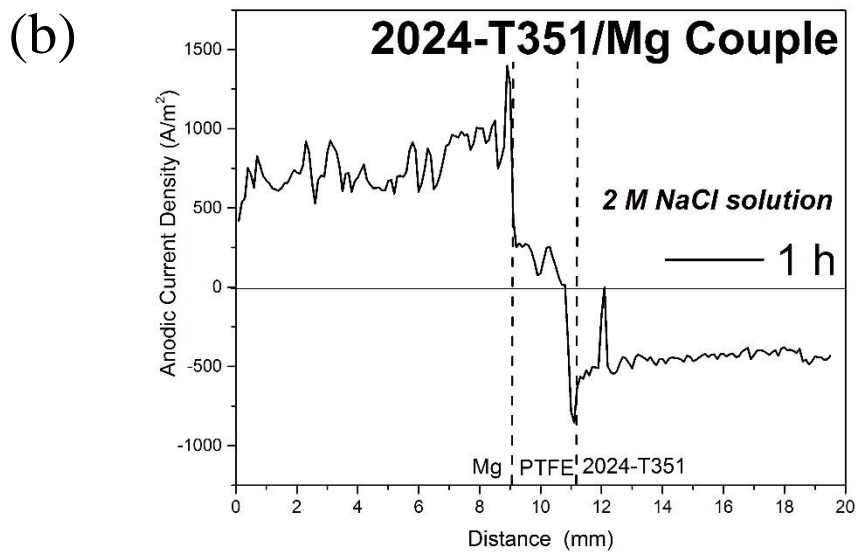
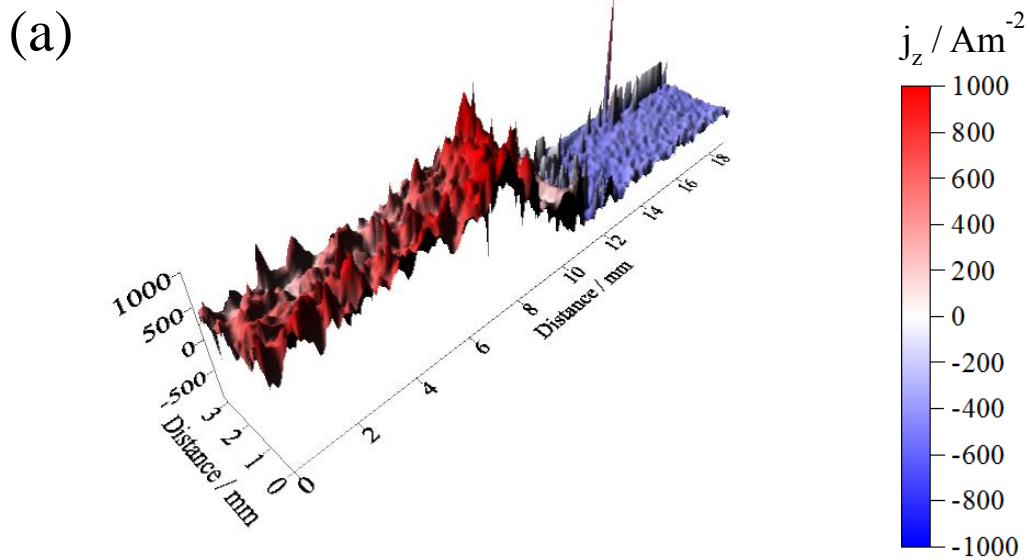


Figure 6.6. (a) Surface plots showing the distribution of normal current density  $j_z$  above a 2024-T351 alloy sample galvanically coupled to Mg in aerated 2 M NaCl solution. (b) Representative SVET line scan of 2024-T351/Mg couple (c) shows the visual appearance of the sample after 1 h immersion.

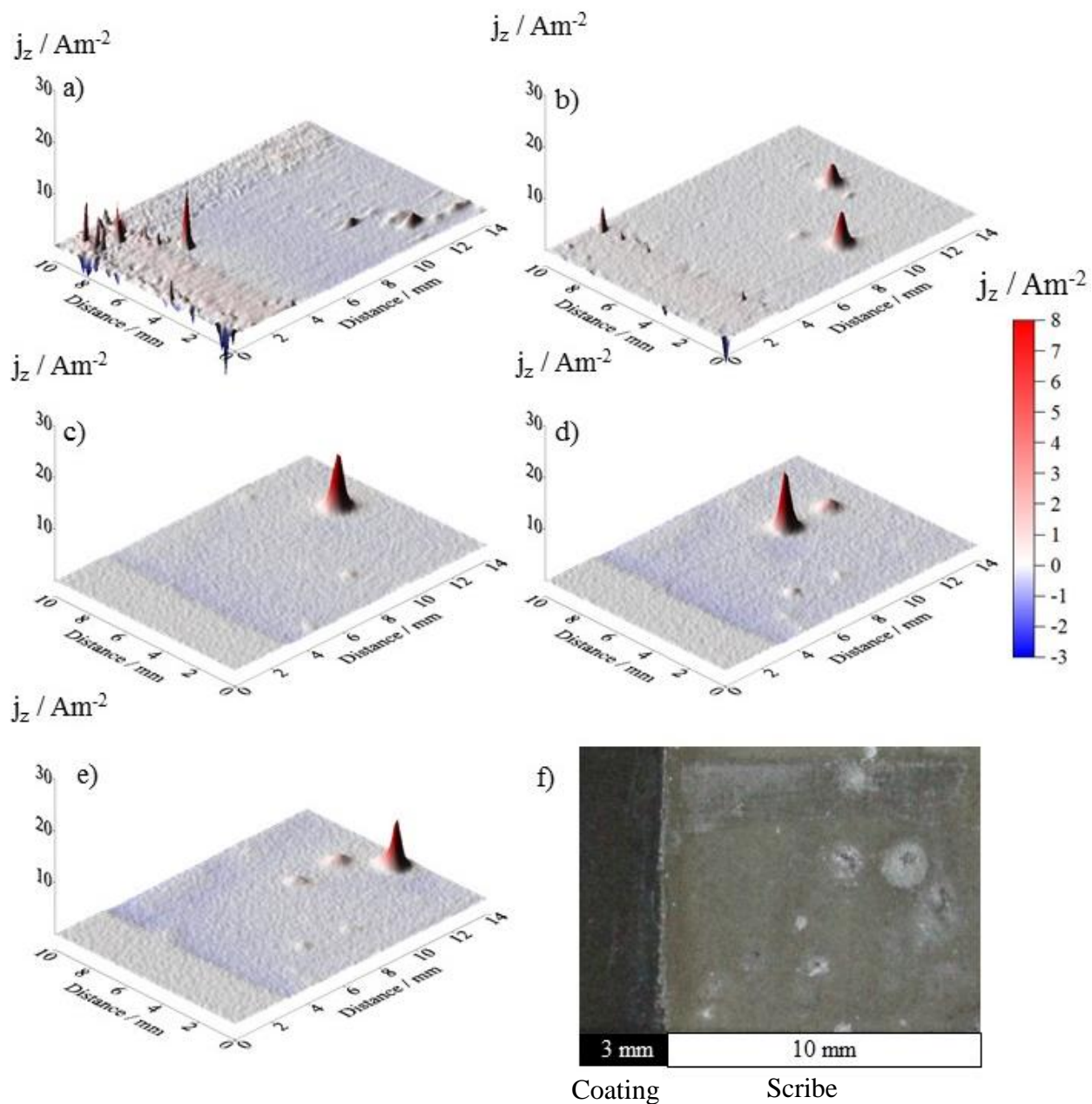


Figure 6.7. Surface plots showing the distribution of normal current density  $j_z$  above a 2024-T351 alloy adjacent to 2024-T351/NFF/MgRP in aerated 2 M NaCl solution. Data were obtained from SVET scans carried out (a) 0 h, (b) 4 h, (c) 14 h, (d) 26 h and (e) 36 h after sample immersion. (f) shows the visual appearance of the sample after 38 h immersion. Coating to scribe area ratio (CSR) – 0.3

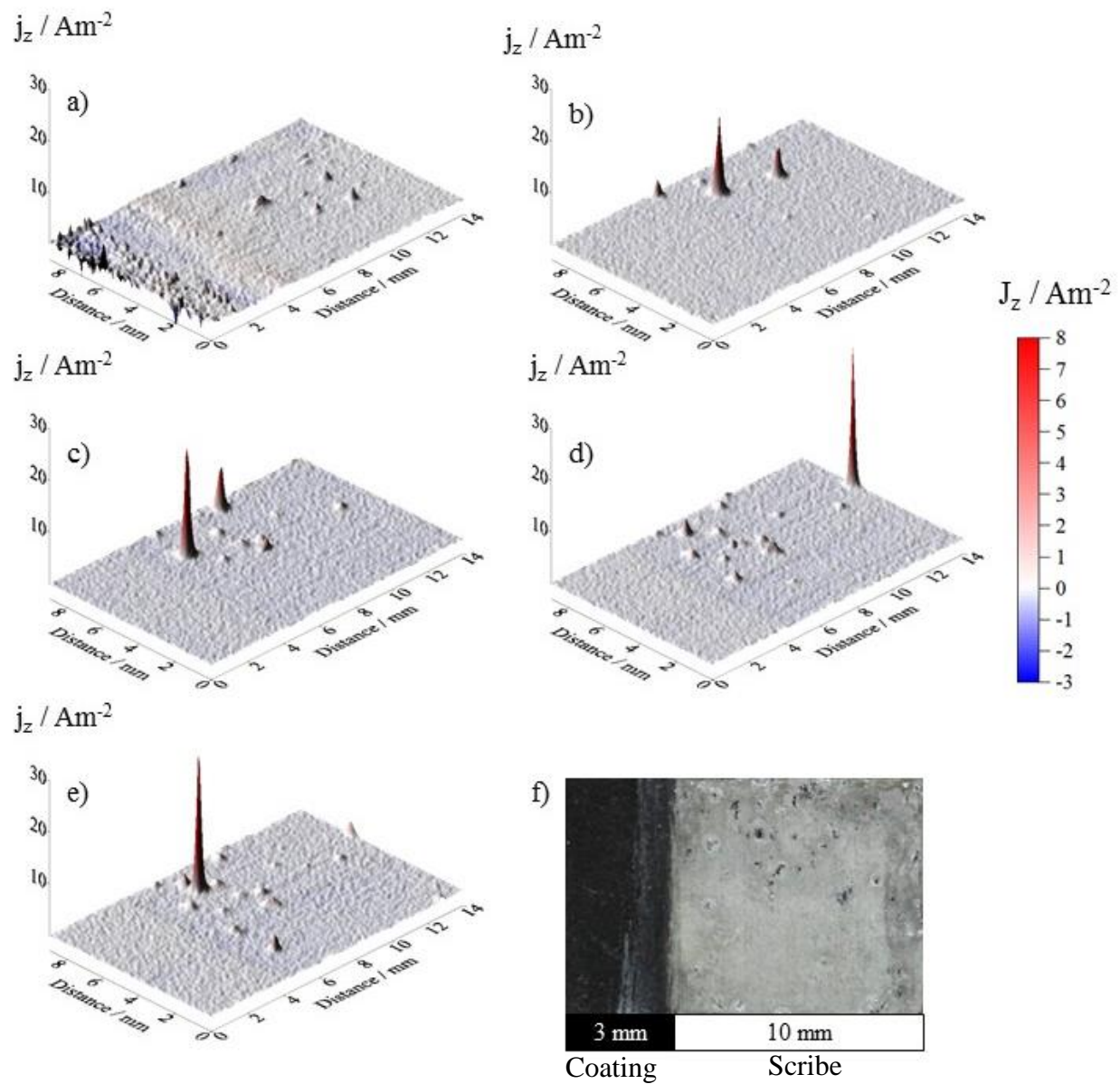


Figure 6.8. Surface plots showing the distribution of normal current density  $j_z$  above a 2024-T351 alloy adjacent to 2024-T351/TCP/MgRP in aerated 2 M NaCl solution. Data were obtained from SVET scans carried out (a) 0 h, (b) 4 h, (c) 14 h, (d) 26 h and (e) 36 h after sample immersion. (f) shows the visual appearance of the sample after 38 h immersion. Coating to scribe area ratio (CSR) – 0.3

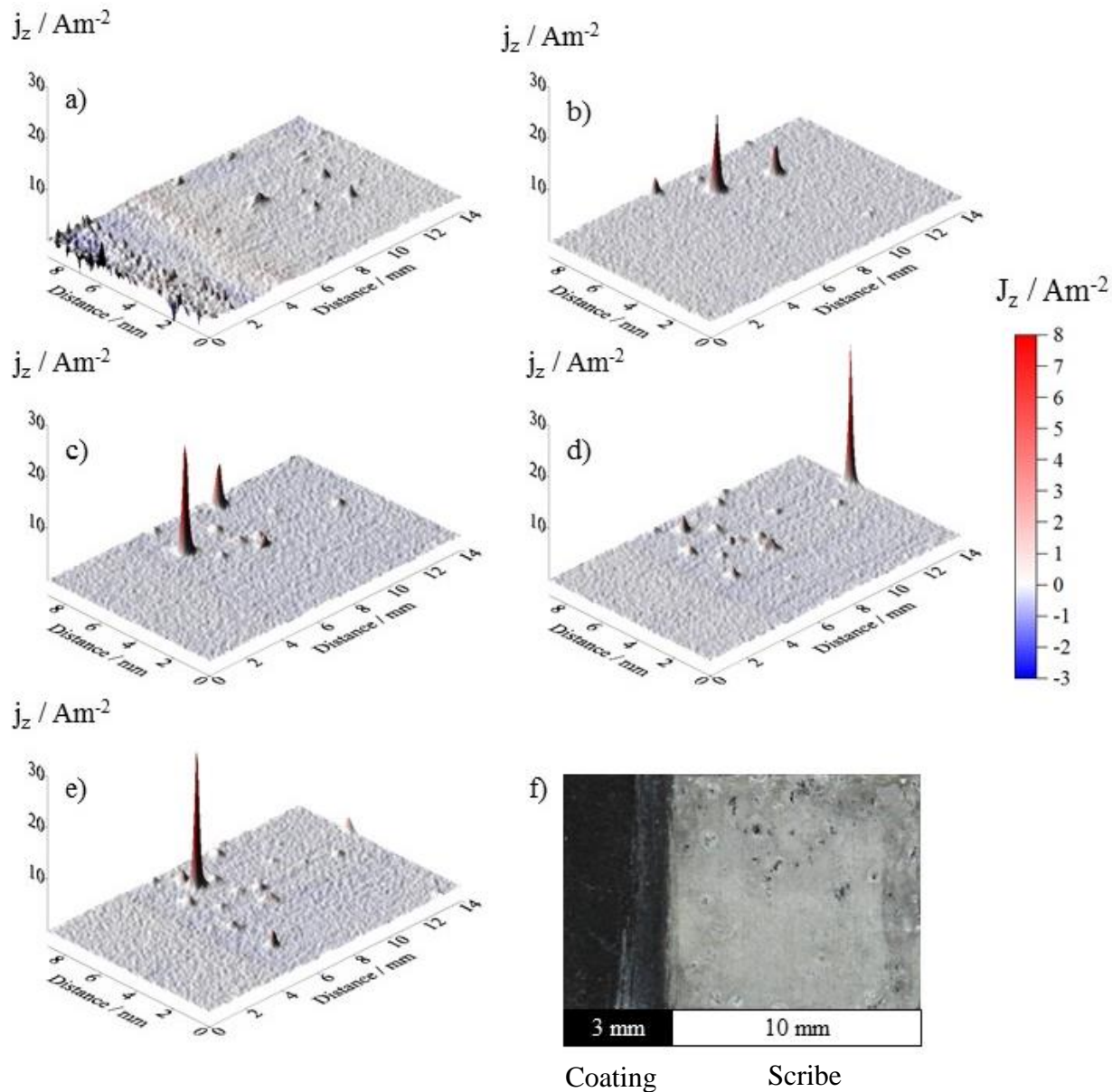


Figure 6.9. Surface plots showing the distribution of normal current density  $j_z$  above an 2024-T351 alloy adjacent to 2024-T351/ACS/MgRP in aerated 2 M NaCl solution. Data were obtained from SVET scans carried out (a) 0 h, (b) 4 h, (c) 14 h, (d) 26 h and (e) 36 h after sample immersion. (f) shows the visual appearance of the sample after 38 h immersion. Coating to scribe area ratio (CSR) – 0.3

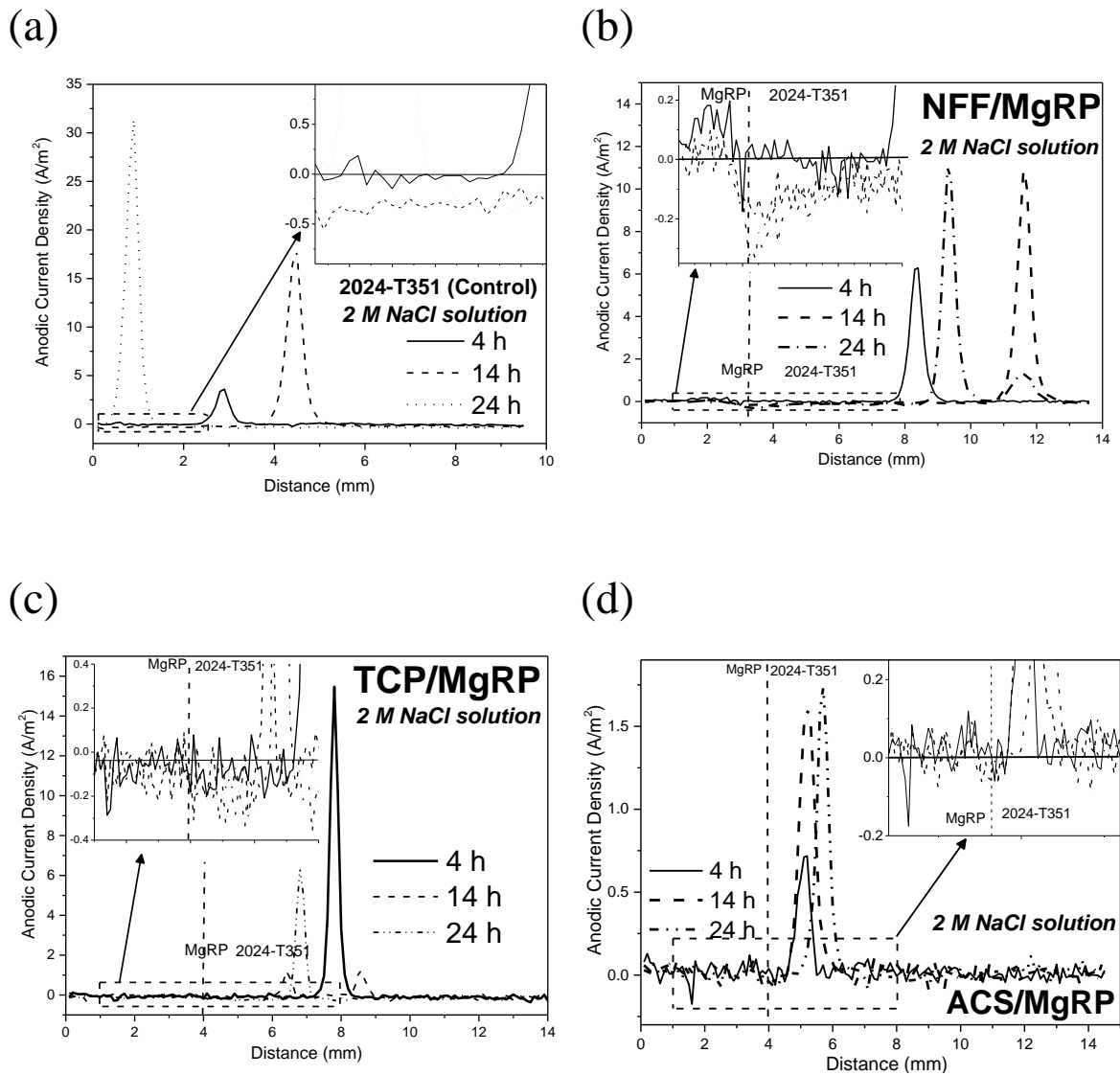


Figure 6.10. (a) Representative SVET line scans showing the distribution of normal current density  $j_z$  above freely corroding bare 2024-T351 alloy (a) and 2024-T351 alloy adjacent to 2024-T351/Pretreat/MgRP (b-d) in aerated 2 M NaCl solution

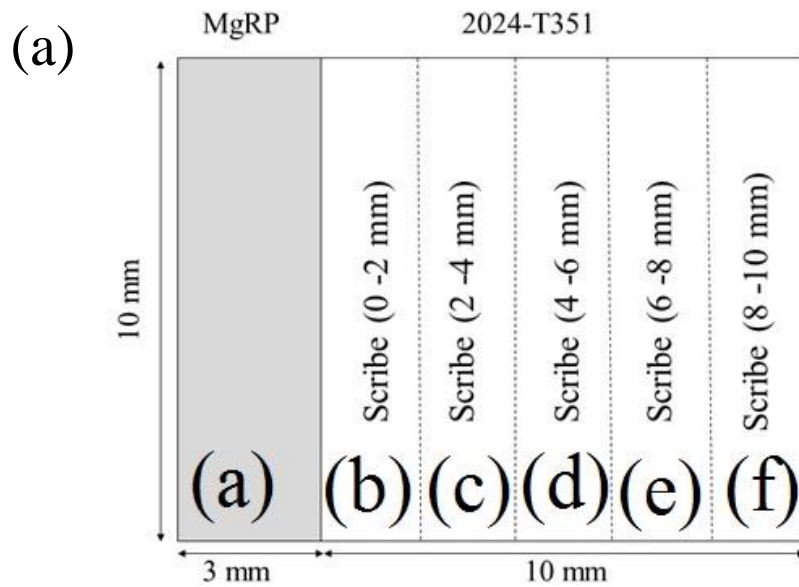


Figure 6.11. Schematic for SVET analysis. The dotted lines indicates the separation of regions of interest to determine throwing power from local anodic/cathodic current densities in SVET maps. Regions of interest

- (a) MgRP coating.
- (b) Scribe – 0 -2 mm away from the coating edge
- (c) Scribe - 2 – 4 mm away from the coating edge
- (d) Scribe – 4 – 6 mm away from the coating edge
- (e) Scribe – 6 – 8 mm away from the coating edge
- (f) Scribe – 8 – 10 mm away from the coating edge

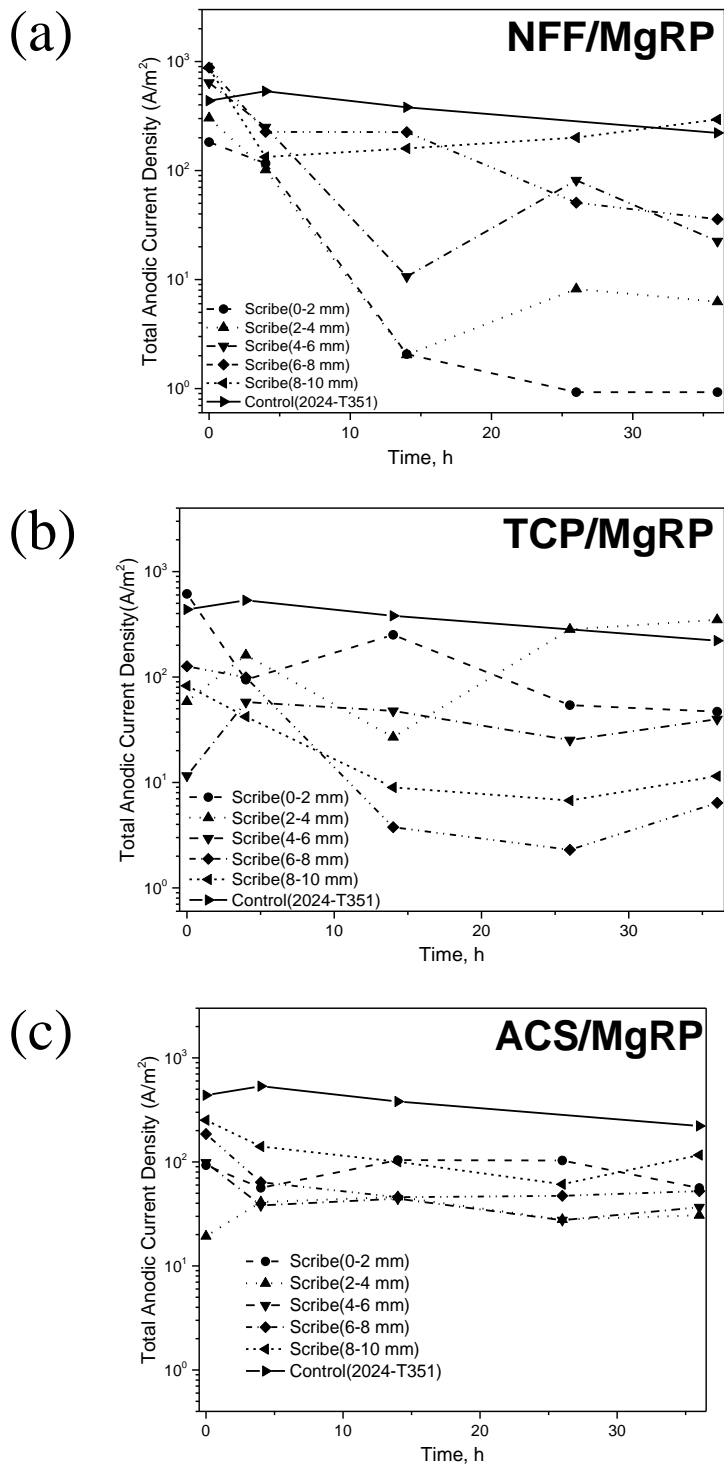


Figure 6.12. Total anodic current density as a function of exposure time for selected 2024-T351/Pretreatment/MgRP systems; (a) NFF/MgRP, (b) TCP/MgRP and (c) ACS/MgRP. Anodic current density was calculated in scribe at five different regions with various distance away from coating interface as indicated in legend. Anodic current density from control (bare 2024-T351) was also provided for comparison.

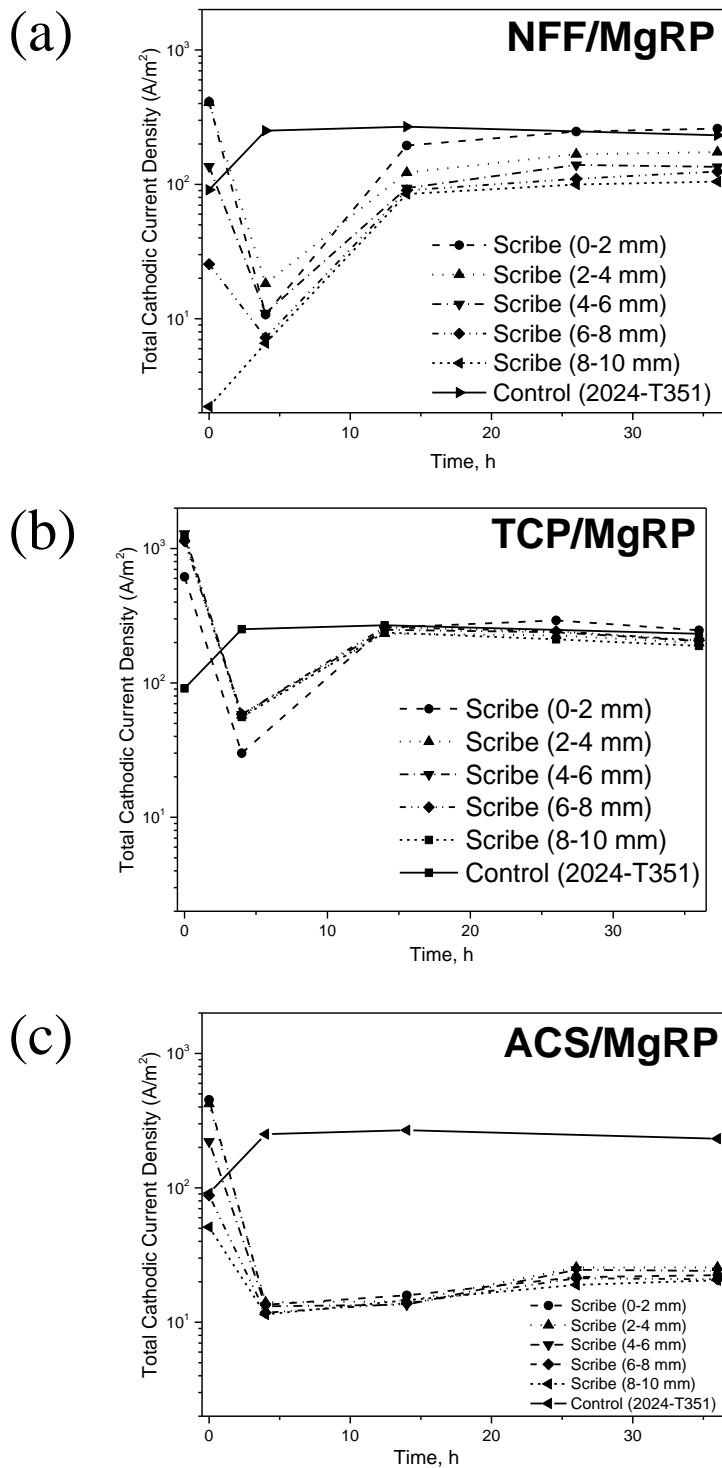


Figure 6.13. Total cathodic current density as a function of exposure time for selected 2024-T351/Pretreatment/MgRP systems; (a) NFF/MgRP, (b) TCP/MgRP and (c) ACS/MgRP. Cathodic current density was calculated in scribe at five different regions with various distance away from coating interface. Cathodic current density from control (bare 2024-T351) was also provided for comparison.

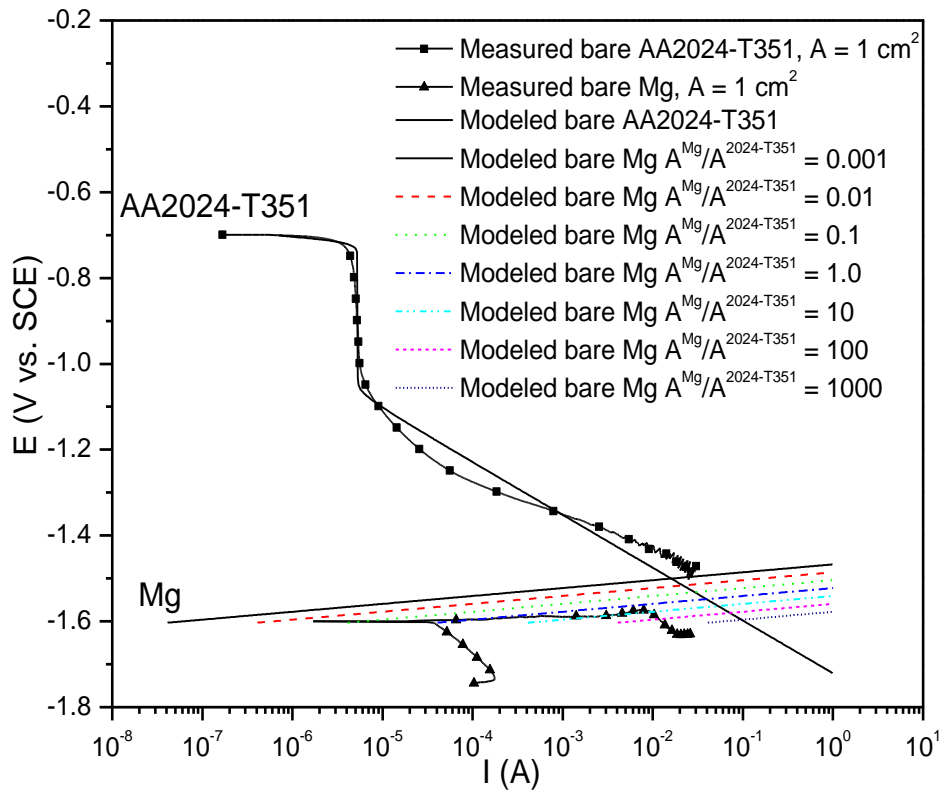


Figure 6.14. Mixed potential model of a galvanic couple between various area ratios of bare Mg to bare AA2024-T351 in 1.0 M NaCl solution.<sup>10</sup>

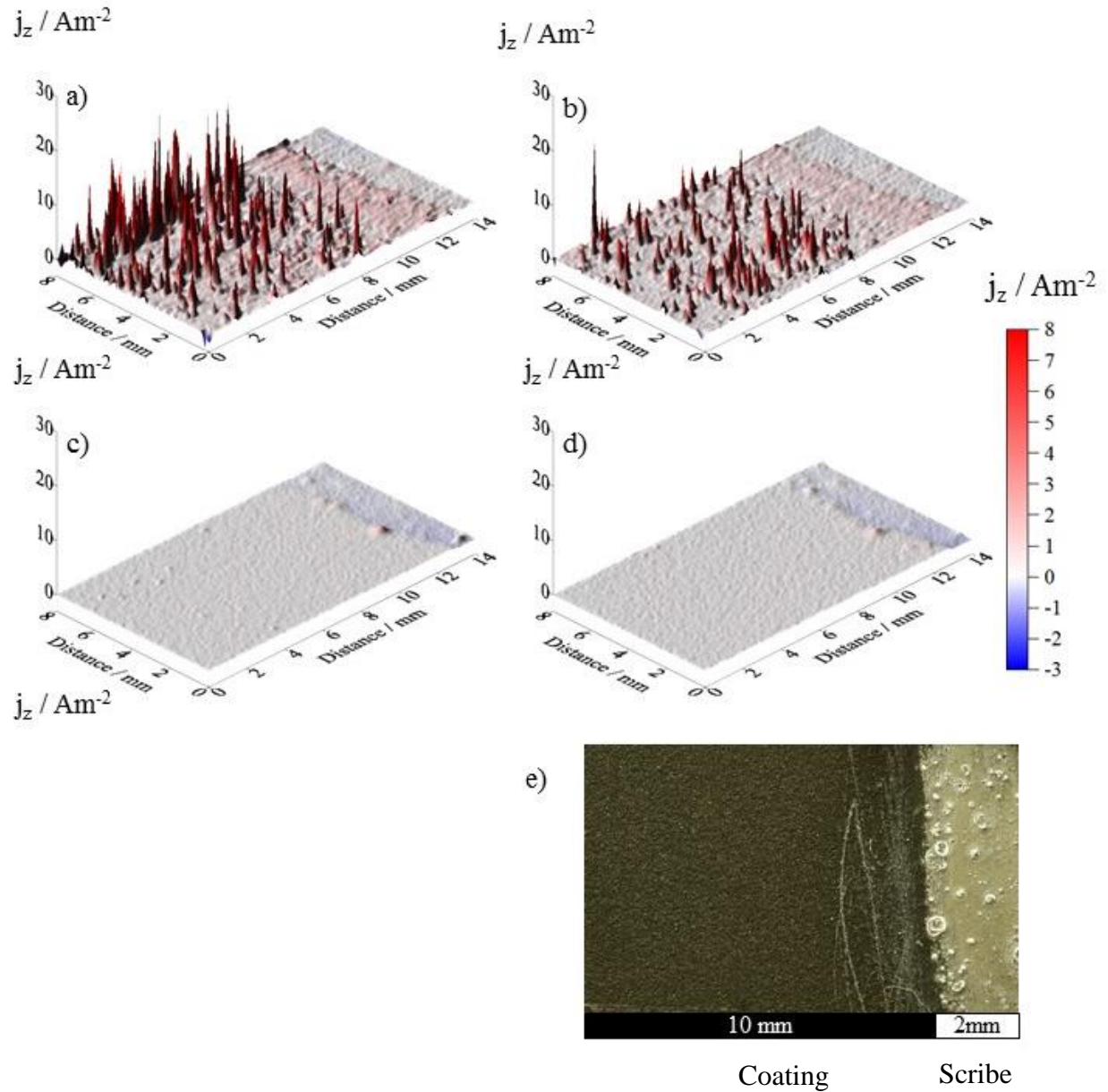


Figure 6.15. Surface plots showing the distribution of normal current density  $j_z$  above a 2024-T351 alloy adjacent to 2024-T351/NFF/MgRP in aerated 2 M NaCl solution. Data were obtained from SVET scans carried out (a) 0 h, (b) 4 h, (c) 14 h, (d) 24 h and (e) shows the visual appearance of the sample after 24 h immersion. Coating to scribe area ratio (CSR) – 5

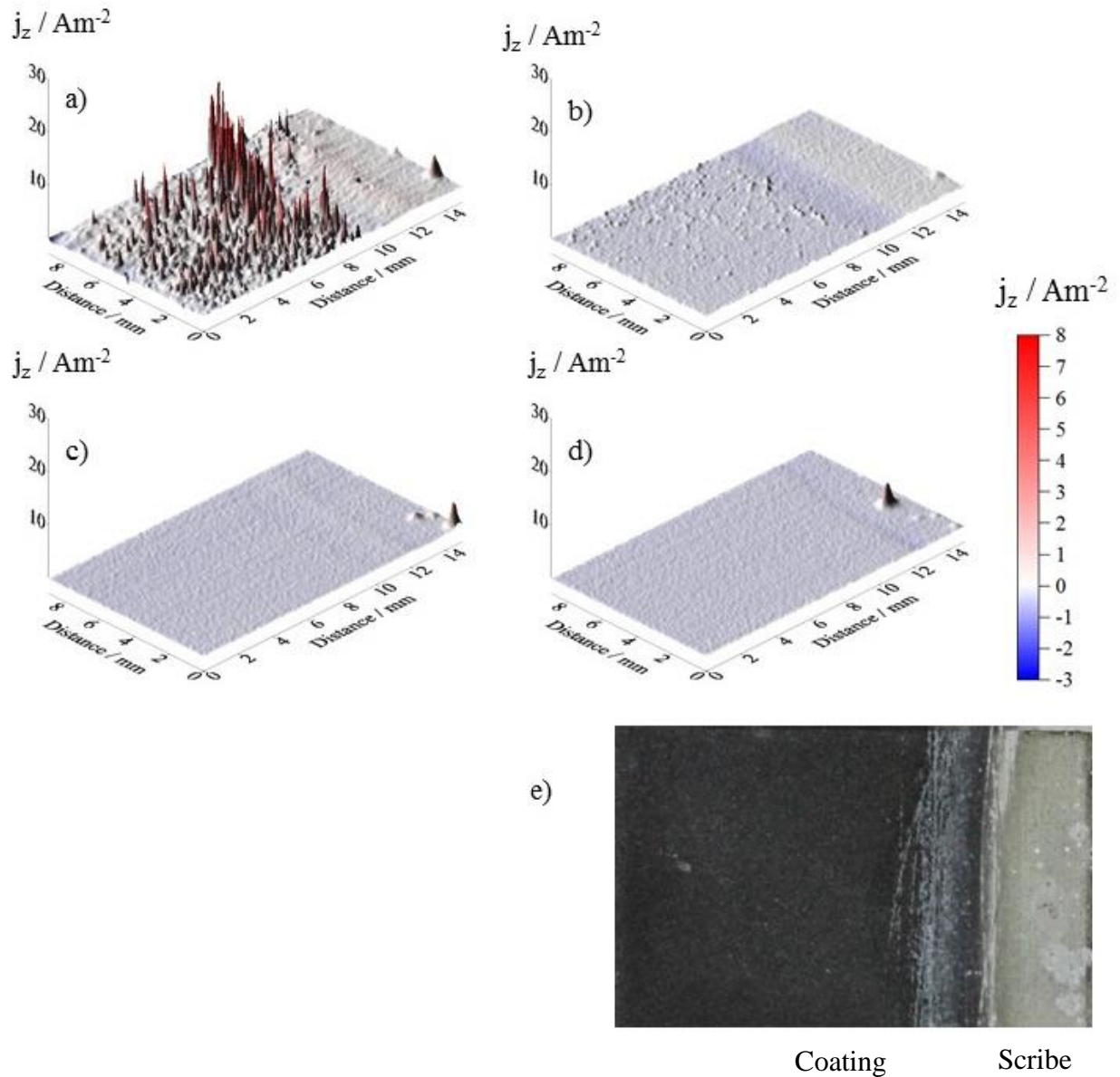


Figure 6.16. Surface plots showing the distribution of normal current density  $j_z$  above a 2024-T351 alloy adjacent to 2024-T351/TCP/MgRP in aerated 2 M NaCl solution. Data were obtained from SVET scans carried out (a) 0 h, (b) 4 h, (c) 14 h, (d) 24 h and (e) shows the visual appearance of the sample after 24 h immersion. Coating to scribe area ratio (CSR) – 5

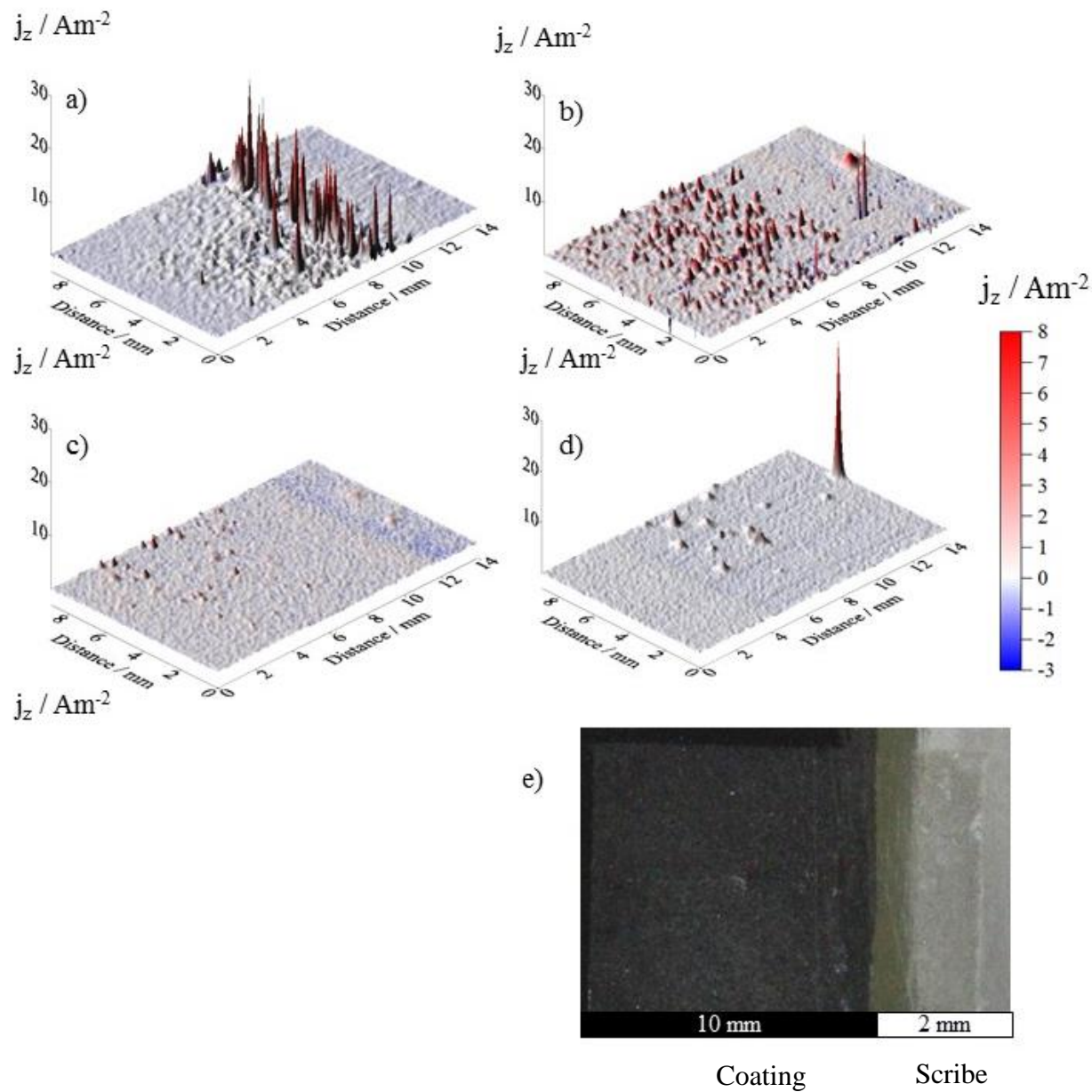


Figure 6.17. Surface plots showing the distribution of normal current density  $j_z$  above a 2024-T351 alloy adjacent to 2024-T351/ACS/MgRP in aerated 2 M NaCl solution. Data were obtained from SVET scans carried out (a) 0 h, (b) 4 h, (c) 14 h, (d) 24 h and (e) shows the visual appearance of the sample after 24 h immersion. Coating to scribe area ratio (CSR) – 5

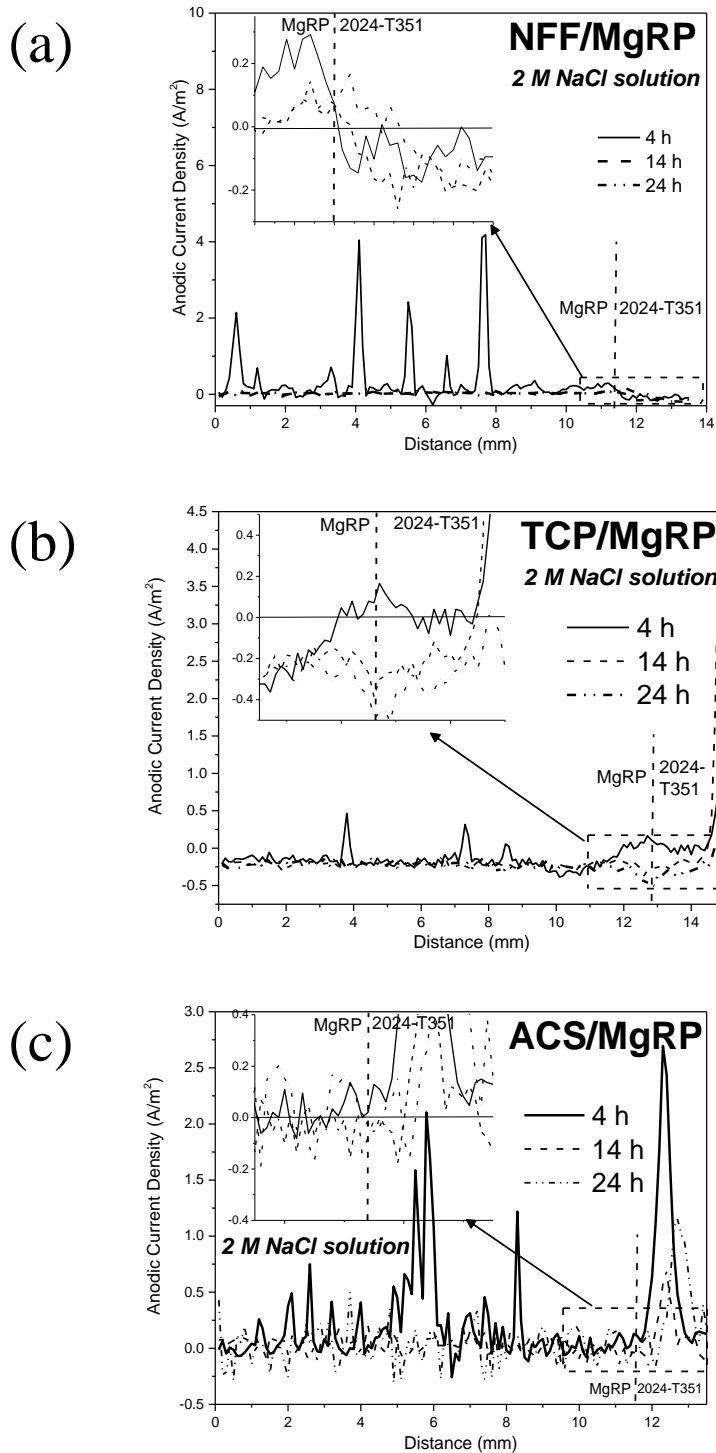


Figure 6.18. (a) Representative SVET line scans showing the distribution of normal current density  $j_z$  2024-T351 alloy adjacent to 2024-T351/Pretreat/MgRP in aerated 2 M NaCl solution (a) NFF/MgRP, (b) TCP/MgRP and (c) ACS/MgRP. Coating to scribe area ratio (CSR) – 5

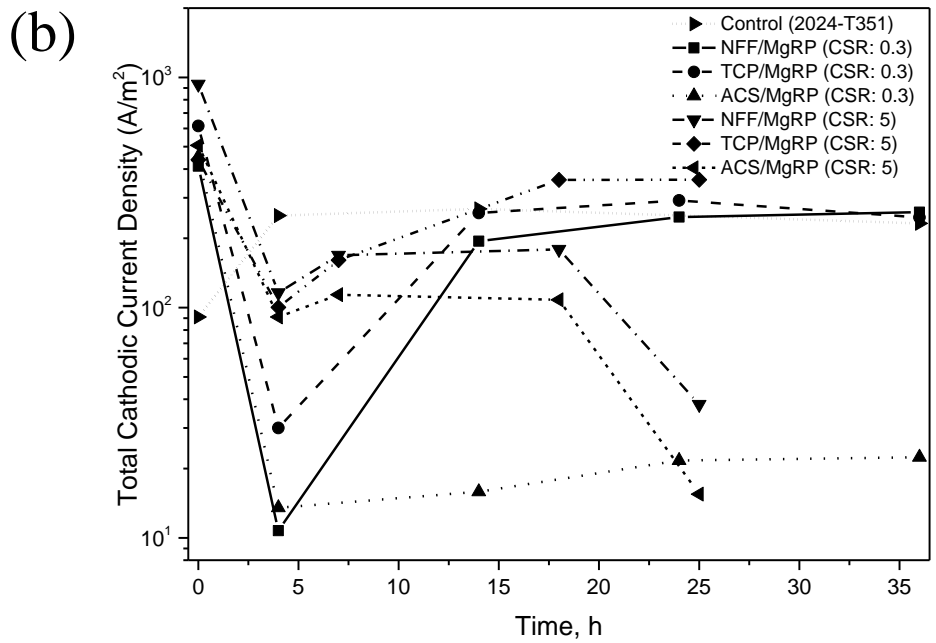
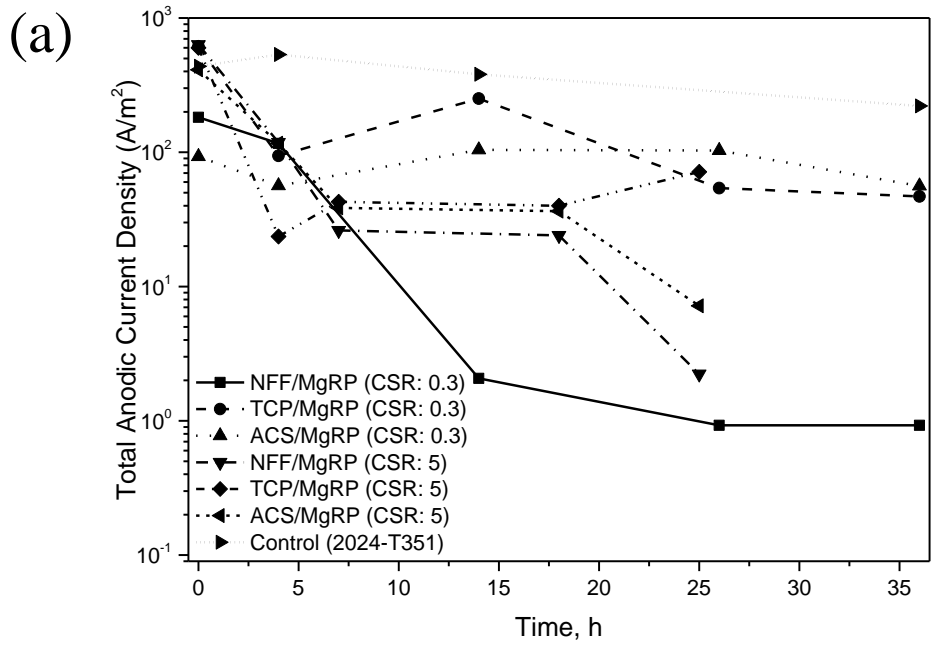


Figure 6.19. Total anodic (a) and cathodic (b) current density as a function of exposure time for selected 2024-T351/Pretreatment/MgRP systems for 2024-T351/Pretreatment/MgRP with different coating to scribe area ratio. Anodic and cathodic current density from control (bare 2024-T351) was also provided for comparison.

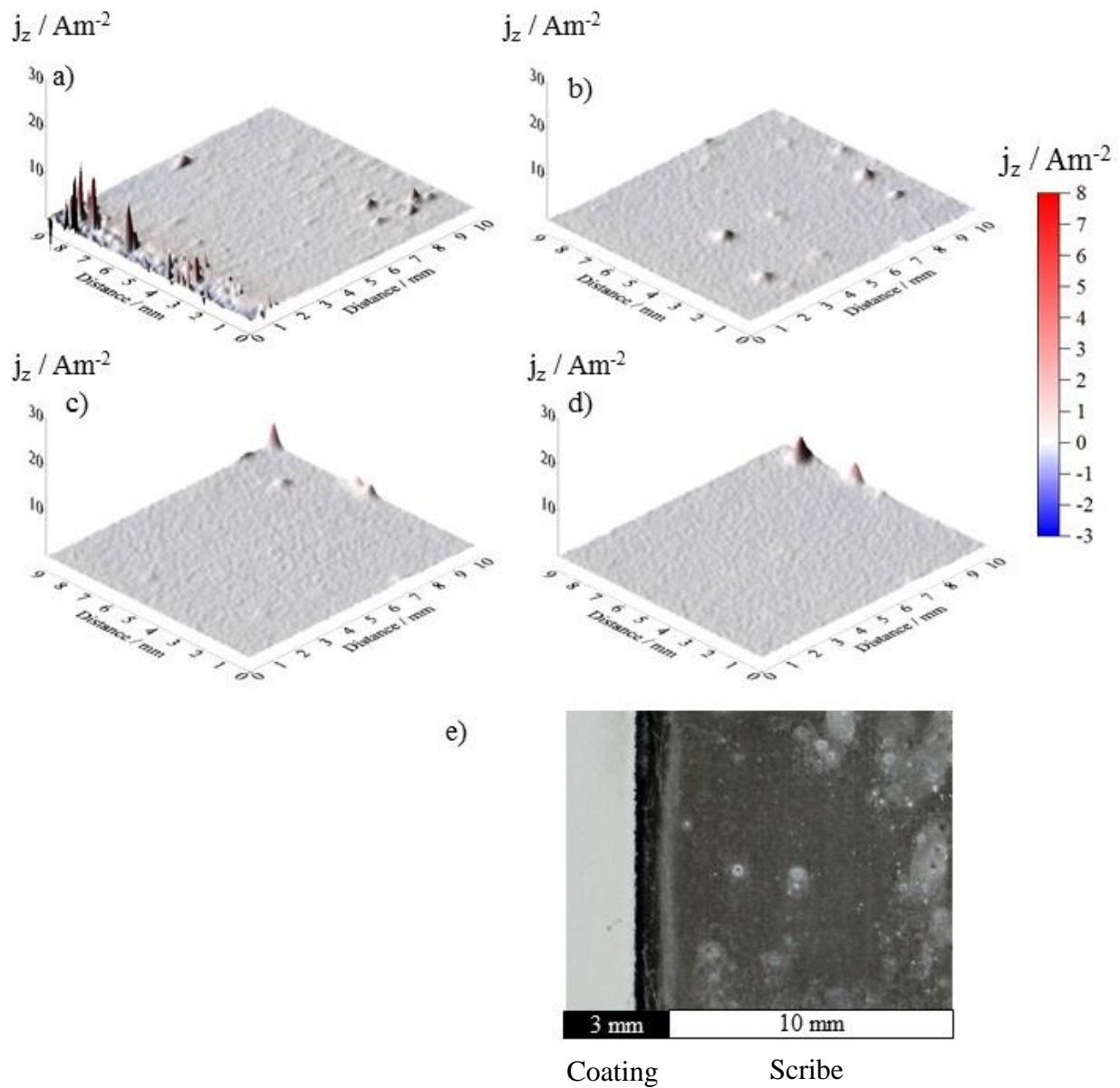


Figure 6.20. Surface plots showing the distribution of normal current density  $j_z$  above an 2024-T351 alloy adjacent to 2024-T351/NFF/MgRP/TC in aerated 2 M NaCl solution. Data were obtained from SVET scans carried out (a) 0 h, (b) 4 h, (c) 14 h, (d) 24 h and (e) shows the visual appearance of the sample after 24 h immersion.

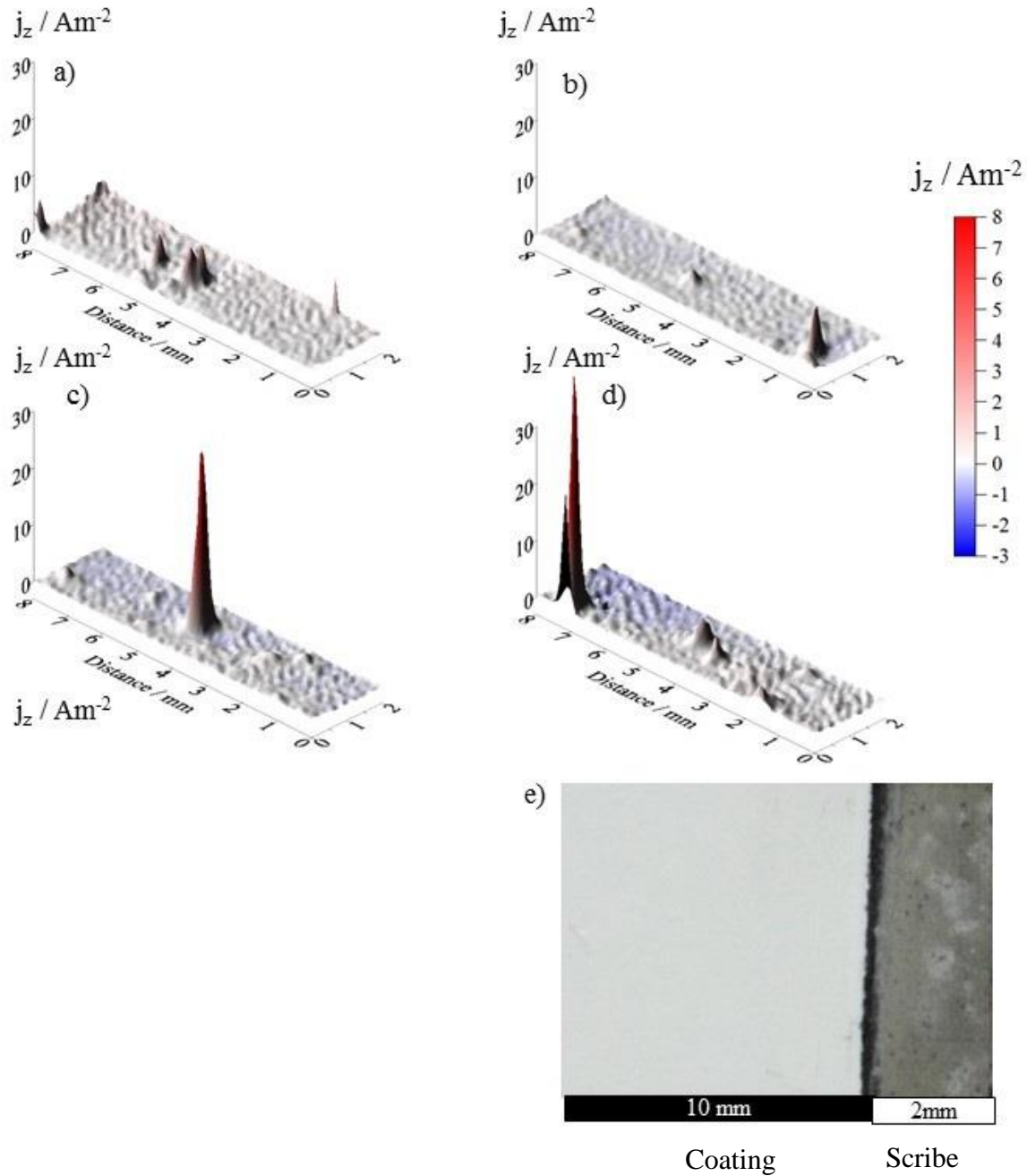


Figure 6.21. Surface plots showing the distribution of normal current density  $j_z$  above an 2024-T351 alloy adjacent to 2024-T351/NFF/MgRP/TC in aerated 2 M NaCl solution. Data were obtained from SVET scans carried out (a) 0 h, (b) 4 h, (c) 14 h, (d) 24 h and (e) shows the visual appearance of the sample after 38 h immersion.

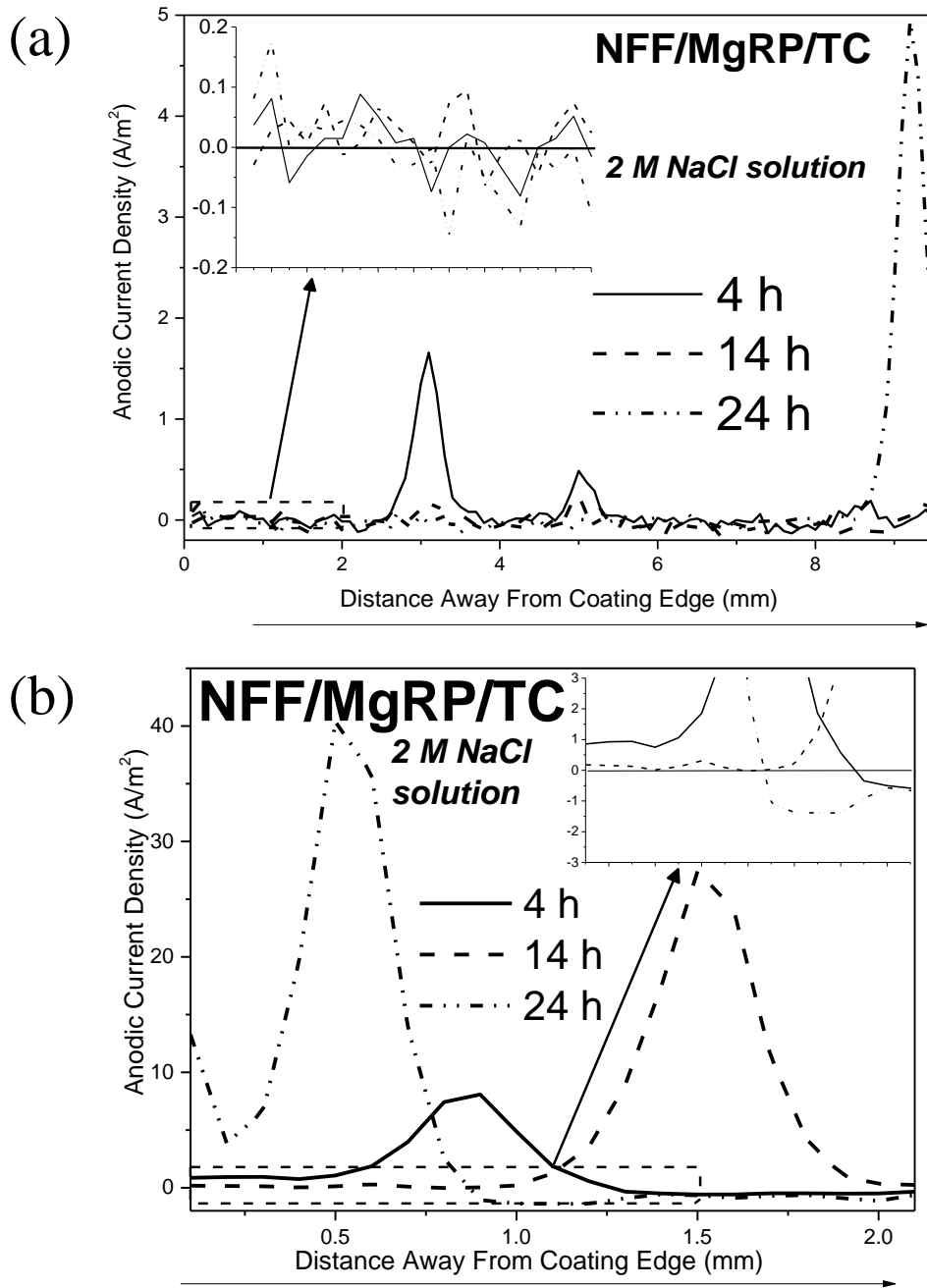


Figure 6.22. Representative SVET line scans showing the distribution of normal current density  $j_z$  2024-T351 alloy adjacent to 2024-T351/Pretreat/MgRP/TC in aerated 2 M NaCl solution (a) NFF/MgRP/TC (CSR: 0.3), (b) NFF/MgRP/TC (CSR: 5).

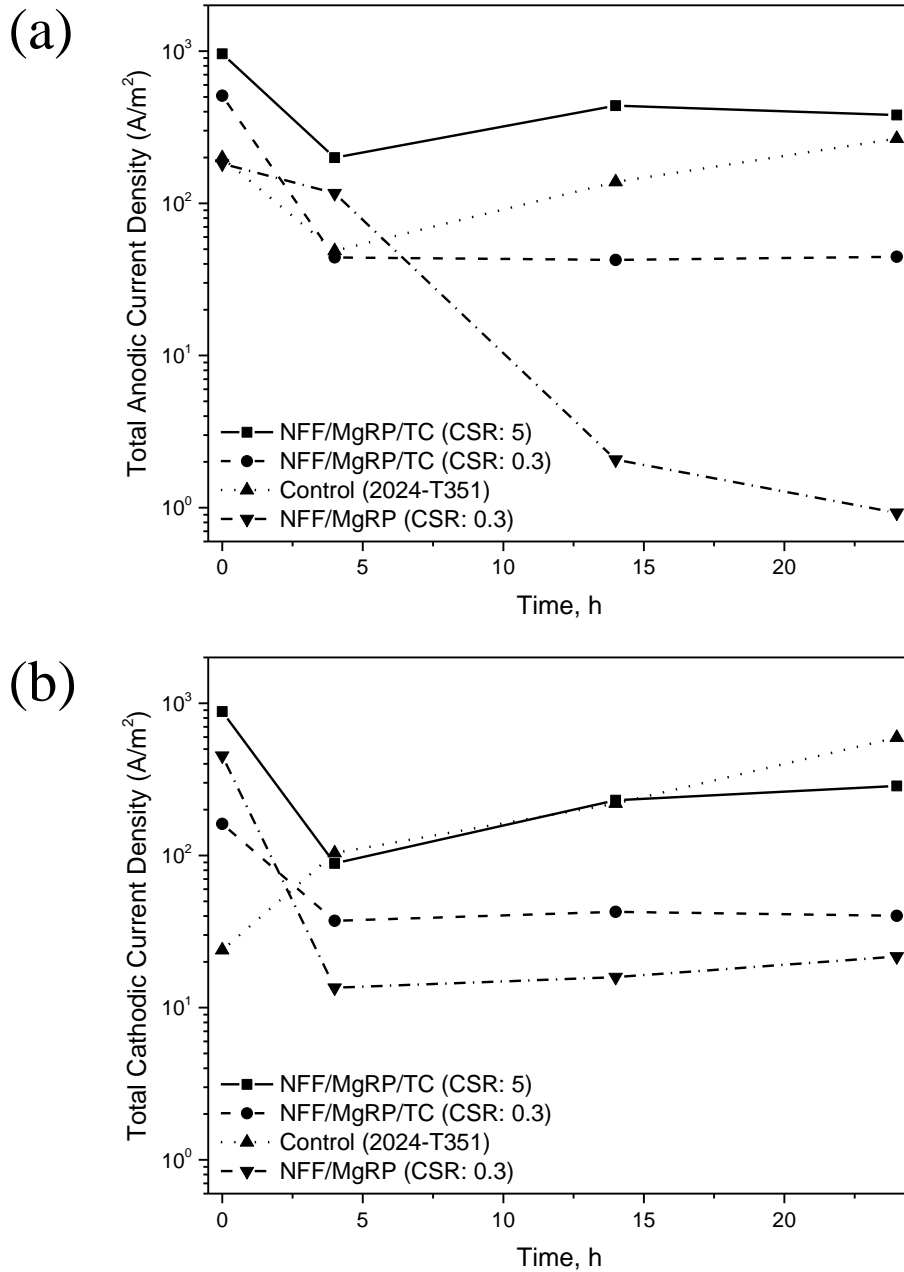


Figure 6.23. Total anodic (a) and cathodic (b) current density as a function of exposure time at 2024-T351 scribe adjacent to 2024-T351/NFF/MgRPTC with different coating to scribe area ratio. Anodic and cathodic current density from control (bare 2024-T351) and 2024-T351 coupled to NFF/MgRP (CSR: 0.3) was also provided for comparison.

## 7 Thesis Conclusions and Suggested Future Work

### 7.1 Conclusions

The role of different surface pretreatments on the sacrificial anode-based cathodic as well as barrier protection mechanism afforded by magnesium rich non-chromium primer (MgRP) with and without topcoat (TC) has been investigated. Anodized coatings were characterized by thick resistive layer (5 to 9  $\mu\text{m}$ ) whereas conversion coatings had thickness in the range of 0.4 to 0.8  $\mu\text{m}$ . The thickness and chemistry of the pretreatments showed good correlation to the barrier properties that they impart to the coating system. Anodization based pretreatment especially added a significantly resistive surface layer while conversion coatings had moderate barrier properties. These resistances mediate the galvanic protection potential and henceforth ability of the Mg pigment to protect a remote defect.

Preliminary investigations on role of pretreatments in sacrificial protection function was conducted using an accelerated electrochemical cycle test protocol that was adopted from our previous tests which was conducted for non-film forming pretreatment. The results suggest that for a non-film forming pretreatment, Mg in the primer is coupled to 2024-T351 immediately and is available for sacrificial anode-based cathodic protection from the beginning of environmental exposure. In contrast, a finite full immersion exposure time was required for degradation of more electrically insulating pretreatment layers. The pretreatment degradation lowered the resistance between the MgRP and the 2024-T351 substrate and enabled a delayed activation and triggered sacrificial anode-based cathodic protection by MgRP.

This work has further illuminated and verified test methods which assess coating degradation and scribe protection that could be used in both the laboratory as well as field. A suite of test methods was utilized to track the elemental Mg depletion, galvanic protection potential, barrier degradation,

Mg corrosion products formation and corrosion volume loss at the scribe throughout exposure in field as well as laboratory accelerated life environments. In the case of systems without a topcoat, significant depletion of Mg pigment was observed in all environments but at different rates. A polyurethane topcoat mediated the global Mg depletion by lowering the self-corrosion of Mg. In the case of NFF pretreated 2024-T351 with MgRP, magnesium was galvanically coupled to 2024-T351 immediately and was available for sacrificial anode-based cathodic protection from the beginning of environmental exposure. In the case of trivalent chromium pretreatment (TCP) and other similar conversion coating pretreated 2024-T351, initially there was limited galvanic coupling with the MgRP due to high pretreatment resistance. Upon prolonged exposure in full immersion, the global galvanic protection potential decreased to more negative potentials below the open circuit potential (OCP) of 2024-T351 indicative of galvanic coupling. In anodized systems with chromate sealing (ACS), Mg pigment was not electrically connected to the 2024-T351 until after long environmental exposure times because of the very high resistance of the pretreatment which further increased with improved sealing with environmental exposure. In the case of systems with topcoat, the global galvanic protection potential was heavily mediated by the ionic resistance of polyurethane topcoat and there was no significant global galvanic coupling between 2024-T351 and Mg pigment in the timeframe over which experiments were conducted. Mg was preserved and available for any future sacrificial anode-based cathodic protection and local protection. The barrier properties of the MgRP pigmented coating also degraded with time at a higher rate in the absence of topcoat. This result was attributed to UV degradation of the pigmented coating resin and which was reduced by the UV resistant polyurethane topcoat. SEM/EDS characterization of the scribe after different ASTM B117/field exposure times indicated that the protective throwing power increased as a function of exposure time in all MgRP-based

systems. Moreover, a secondary protection mode enabled by  $\text{Mg}(\text{OH})_2$  redeposition was identified. The topcoat suppressed the scribe protection by heavily mediating the galvanic protection capabilities and Mg transport. Therefore, topcoat systems have a lower fraction of corrosion products and relative higher corrosion volume loss compared to 2024-T351/Pretreatment/MgRP systems in similar environments.

In addition to performance of the pretreatments along with MgRP system, the corrosion protection mechanism of pretreatment-only systems was separately studied using a combination of lab accelerated lifecycle test, field exposures, controlled relative humidity exposures (to monitor anionic species leaching) and full immersion studies on bare/pretreated 2024-T351 to understand cathodic and anodic corrosion inhibition by anionic species from the pretreatment. ACS pretreated 2024-T351 exhibited enhanced barrier properties with increasing full immersion exposure time in NaCl. ACS also lowered the ORR kinetics on substrate alloy as expected in the case of more resistive pretreatments. Anionic species leaching from the pretreatments resulted in lowering of OCP and decreased the ORR kinetics by competitive adsorption of  $\text{CrO}_4^{2-}$  species.

In addition to post-mortem sample evaluation after laboratory accelerated life tests and field exposures, the galvanic throwing power of the MgRP was studied via the scanning vibrating electrode technique (SVET), which enabled spatial distribution analysis of net anodic and cathodic current densities for a MgRP on pretreated 2024-T351 coupled with a bare 2024-T351 scribe to be mapped. Two significant factors contribute to the scribe protection. The quasi-steady state galvanic current due to galvanic coupling of Mg in the primer with 2024-T351 is one indication of galvanic protection. SVET studies reveal that the galvanic current is not enough to completely shut down the localized corrosion which is dominated by microgalvanic coupling at the scribe. However, microgalvanic coupling is significantly affected by the MgRP. For NFF/MgRP, anodic current

densities in the scribe which are indicative of local sites of pitting were lowered by 2-3 orders of magnitude. It is hypothesized that this is achieved by lowering of galvanic protection potential below pitting potential attributed to sacrificial anode-based cathodic prevention. The effect of pretreatment resistance, coating to scribe area ratio and topcoat polymer properties on galvanic protection was elucidated. TCP and ACS pretreated systems did not exhibit significant galvanic protection in lower coating to scribe area ratios as indicated by quasi-steady state current distribution. However at higher coating to scribe area ratio, slightly improved scribe protection was observed with increasing exposure time. Alternate modes of corrosion protection attributed to chemical species leaching from the primer and pretreatments was elucidated as the cause of this effect. In the case of topcoated systems, there is no significant sacrificial or alternate modes of corrosion protection due to highly mediated galvanic couple potential and limited pathways for Mg transport for magnesium hydroxide redeposition.

The outcome of this research provided a scientific foundation for understanding how utilization of resistive pretreatments along with MgRP enables development of a multi-functional corrosion protection system which includes delayed cathodic/sacrificial protection of Mg, barrier protection by pretreatments/primer/topcoat and corrosion inhibition by chemical species leaching from the MgRP and the pretreatments. The throwing power of the Mg in the primer was heavily limited by topcoat polymer properties in addition to high pretreatment resistances. A coating that limits self-corrosion but that is less resistive may be of interest as it could function to balance galvanic protection potential mediation and preservation of Mg in MgRP against self-corrosion. The work performed herein suggests that a pretreatment with high resistance that does not degrade significantly with time may not be suitable for use with MgRP because the substrate is decoupled from the sacrificial anode.

## 7.2 Suggested Future Work

### 7.2.1 Suggested Future Work to Investigate Throwing Power

#### Finite Element Analysis

The previously developed FEA model for a representative Mg/2024-T351 couple without a resistive pretreatment must be modified to account for pretreatment resistance. Three different approaches are suggested to improve this model. For the first approach, it is assumed that the scribe exposes bare 2024-T351, but due to degradation of pretreatments, there are anionic species in the solution. The electrolyte boundary conditions are modified to account for this effect. Cathodic polarization experiments were conducted for bare 2024-T351 in various bulk solutions of quiescent NaCl and MgCl<sub>2</sub> with and without soluble chromates. Similarly anodic polarization experiments were conducted for bare Mg in various bulk solutions of quiescent NaCl and MgCl<sub>2</sub> with and without soluble chromates. The ionic effects of anionic species on spatial distribution of galvanic couple potential and galvanic current need to be investigated based on the above mentioned full immersion E-log i boundary conditions. In a second approach, it is assumed that pretreatment remains intact on the substrate in the defect and there is no significant anionic species leaching. Herein, the pretreatment acts as a resistive barrier on 2024-T351 and affects the mixed potential model and spatial galvanic current and galvanic couple potential distribution. Cathodic polarization experiments were conducted for pretreated 2024-T351 in various bulk solutions of quiescent NaCl and MgCl<sub>2</sub>. That along with boundary conditions for anodic kinetics of Mg in respective bulk solutions, will account for the effect of pretreatment resistance on galvanic current and galvanic couple potential distribution. For a third approach, both ionic effects from chemical species leaching and electrical resistance of pretreatments are accounted for in the FEA model. These effects can be deduced by conducting cathodic polarization experiments for pretreated 2024-T351 a representative solution, 1 M NaCl solution after different full immersion exposure times.

Based on the boundary conditions from E-log  $i$  data, the combined effect of soluble chromates from anionic species or pretreatment degradation and its electrical resistance on spatial distribution of galvanic couple potential and galvanic current distribution in representative Mg/2024-T351 is investigated. In the previously used model, few significant changes on the model geometry need to be made. The resistance over the top of coating and at the edge of the coating adjacent to scribe need to be differentiated from each other. While the resistance at the top of the Mg pigment in MgRP is dominated by topcoat resistance, the one at the scribe edge has a less resistive pathway which account for only electrical resistance of pretreatments and ionic resistance of the electrolyte during solution ingress into the primer polymer. Summary of significant results for E-log  $i$  boundary conditions and suggested geometry for the future model is presented in Chapter 8 (Appendix A). The modeling results are valid only for a constant and continuous electrolyte geometry such as full immersion or thin film conditions. A valuable addition to the future model development would be the ability to predict and account for this changing electrolyte geometry.

### **Corrosion Volume Loss Analysis**

As an extension of scribe protection characterization by corrosion volume loss analysis which was conducted for laboratory accelerated life and field exposures, spatial distribution of corrosion volume loss for bare 2024-T351 coupled with a MgRP coated and pretreated 2024-T351 must be studied using optical profilometry to investigate throwing power of Mg. Effect of pretreatment resistance, barrier properties of the coating, Mg self-corrosion, anionic species release and cathode to anode area ratio on corrosion volume loss at the scribe need to be elucidated using optical profilometry in full immersion conditions. The environmental exposure need to be further extended to thin film conditions or evolving electrolyte geometry, as in the case of wet/dry cycling to understand how the electrolyte geometry affects the corrosion volume loss at scribe and thereby

the throwing power. Some of preliminary results pertinent to this studies are summarized in Chapter 9 (Appendix B).

### **Scanning Kelvin Probe**

The spatial distribution of galvanic protection potential for a bare 2024-T351 coupled with a MgRP coated 2024-T351 under thin film conditions should be investigated using Scanning Kelvin Probe (SKP). The Volta potential can be correlated to the local galvanic couple potential at the scribe. The framework utilized for sample design for SVET and optical profilometry studies from previous chapters will be adopted for future SKP studies to study the effects of pretreatment resistance, topcoat polymer, coating to scribe area ratio as well as electrolyte layer thickness on spatially distribution of galvanic couple potential. Some preliminary investigation of Volta potential for different metal and bulk synthesized intermetallics which are pertinent for 2024-T351/Mg system were conducted. In addition, galvanic couple experiments were conducted for NFF/MgRP coupled to 2024-T351 for continuous thin film conditions and wet-dry cycle conditions as summarized in Chapter 10 (Appendix C).

### **Scanning Vibrating Electrode Technique Studies**

Long term full immersion experiments need to be conducted to understand how the galvanic protection function changes as a function of pretreatment degradation. This would also help determine pretreatments that are desirable for sacrificial protection function to be enabled at delayed exposure time. Such analysis would determine the length of full immersion exposure time required for sufficient degradation of topcoat barrier properties to enable sacrificial protection function. In additions, the effect of  $Mg^{2+}$  ions in the solution and anionic species (such as chromate) on corrosion protection for the scribe need to be conducted to study the efficacy of alternate modes of corrosion protection.

### **Multi-electrode Arrays**

A microelectrode galvanic array should be designed that would be more analogous to the real MgRP/ 2024-T351 system wherein the microelectrodes of AA2024-T3 wires are embedded in bare 2024-T351 to better simulate a scribe. In doing so, the galvanic current could be monitored between the coating and each wire at the bare edge at different distances from the coating edge to understand the effect of distance from the coating on galvanic current. Such a design as an alternative for 2024-T3 and Mg wires embedded in epoxy would improve the wettability of the surface and it would also help design experiments to understand the effect of pretreatment resistance and other factors such as coating to scribe area ratio on galvanic throwing power. Designing multiple local probe electrochemical and non-electrochemical techniques to investigate the throwing power would help validate the results from one technique through another and overcome the limitations of individual techniques while designing future experiments.

#### **7.2.2 Suggested Future Work to Investigate Desirable Topcoat Properties**

Significant barrier properties of the topcoat could adversely affect the scribe protection capabilities of the galvanic system, as established in our current topcoat studies. A desirable topcoat for future studies would involve coating systems with excellent UV resistance, but slightly lower barrier resistance so that the scribe protection capabilities can be improved. Factors such as thickness and chemistry of the topcoat need to be changed, as these factors might influence the ionic resistance and can be varied to improve the scribe protection. Future work conducted by fellow researchers at UVA will study the effects of utilizing MgRP for the corrosion protection of AA2024-T351 over various topcoats other than the currently investigated Aerodur 5000 polyurethane based coating.

### **7.2.3 Suggested Future Work to Investigate Corrosion Protection Function of Mg depleted or MgO primer**

Preliminary results from the LALT/field exposed MgRP samples indicate that in addition to sacrificial protection, a chemical mechanism which involves Mg dissolution and redeposition to the scribe area could also provide additional corrosion protection. Corrosion protection of this kind was confirmed in systems with resistive pretreatments such as anodization with chromate sealing (ACS) wherein no galvanic coupling occurred due to high resistance between Mg and 2024-T351, but which still showed magnesium hydroxide redeposition in the scribe. Independent work conducted by UVA for long term field exposed samples in collaboration with Battelle also suggested that MgRP provide long term corrosion protection even after the magnesium in MgRP is converted to a magnesium corrosion product such as magnesium hydroxide or magnesium carbonate. More investigation need to be conducted on this corrosion protection mechanism and its efficacy in comparison to the sacrificial protection mechanism. Some suggested approaches would include studying the Mg ion dissolution from its corrosion products such as magnesium hydroxide, magnesium carbonate as well as magnesium oxide. Galvanostatic deposition of magnesium corrosion products on bare 2024-T351 should be conducted, followed by study of their electrochemical kinetics. The suite of electrochemical and non-electrochemical techniques developed for MgRP can be utilized to compare the performance of magnesium oxide rich primer (MgORP) with magnesium rich primer (MgRP). Future work conducted by fellow researchers at UVA will study the effects of utilizing MgORP for the corrosion protection of AA2024-T351 over various topcoat system.

#### **7.2.4 Suggested Future Work to Investigation of Other Metal Rich Primers for Galvanic Protection of Aluminum Alloys**

The framework developed for current investigation of MgRP can be utilized to study the performance of other metal rich primers. Some significant systems of interest in addition to MgRP would include aluminum rich primers, zinc rich primers and mixed metal primers such as Al-Mg. The vehicle for pigment loading can be varied from organic (epoxy base) to inorganic systems. Future work conducted by fellow researchers at UVA will study the effects of utilizing different metal rich primers for the corrosion protection of 5000 series aluminum alloys.

#### **7.3 Technological/Scientific Impact**

- The Impact of the resistive layer on performance of non-chromate primer used in the sacrificial protection of aerospace aluminum alloys will be ascertained.
- Research focuses on surface modification technologies that improve coating corrosion resistance. Possible multi-function MgRP based coating systems will be elucidated due to multiple modes of corrosion resistance improvement such as barrier properties (Pretreatment/MgRP/Topcoat), sacrificial anode cathodic protection (Mg) and inhibitor based active protection imparted by pretreatments and MgRP.
- Field deployable test methods using electrochemical impedance spectroscopy and X-ray diffraction will be developed to analyze coatings integrity of aging aircraft. This would be a major outcome of coatings damage assessment tools research.
- Scanning vibrating electrode technique, scanning Kelvin probe, Optical profilometry, Microelectrode array and finite element model to study throwing power would be developed for different pretreatments on AA2024-T351/MgRP/Topcoat. These methods are transferable and applicable to other substrates and sacrificial anode coatings.

- Improved understanding of accelerated test methods to accurately reproduce the physical and chemical mechanisms that produce corrosion observed in the actual field applications would be enabled.
- The coating system as a whole provide alternatives (to chromate based primer) that are environment friendly.

#### **7.4 Economic Summary**

This project has further illuminated and verified test methods to assess MgRP that could be used in the laboratory and in the field and could be applied to the characterization and performance on other substrates. Since the test methods should be transferable and applicable to other materials, substrates, pretreatments, and field vs lab, the cost of unique test development for each and every case where a MgRP or other metal rich primer must be tested and might be deployed can be avoided. Assuming the cost of several scientist person years, this should save several hundred thousand dollars. Trial and error, guess-based development of field deployable test methods that may or may not work satisfactorily has also been avoided by using the suite of tests developed here in addition to our previous work done on MgRP. This should save an additional several hundred thousand dollars in test development costs for a field deployable MgRP assessment tool. This work further validates MgRP as an emerging, promising technology to replace chromated corrosion inhibiting technology. The savings to components during the use of MgRP and MgRP/Topcoat systems is a little more difficult to assess. The maturation of an effective non-chromated corrosion inhibiting technology stands to save financial resources dedicated to carcinogenic materials handling alone. If one single asset avoids an unscheduled repainting or repair due to proper coating degradation assessment or proper utilization of the MgRP, then several million dollars in savings is possible in each instance.

## **8 APPENDIX A: Finite Element Analysis of the Galvanic Couple Current and Potential Distribution between Mg and 2024-T351 in a Mg Rich Primer Configuration: Effect of Resistive Pretreatments – FIGURES ONLY**

### **8.1 Abstract**

The distance over which a Mg-rich primer (MgRP) coating provides cathodic protection to scribe exposing bare 2024-T351 (termed as galvanic throwing power) was studied via finite element analysis (FEA) modeling. FEA enabled prediction of spatial distribution of the galvanic current density and potential distribution in a direction perpendicular to the coating/scribe interface. The objective of this current study is to utilize FEA to quantitatively observe the spatial distribution of galvanic current density and galvanic couple potential over a coated/pretreated 2024-T351 with a defect exposing bare/pretreated substrate. Effect of pretreatment resistance, barrier properties of the coatings, anionic species leaching, pretreatment degradation, electrolyte chemistry and electrolyte layer thickness on galvanic throwing power will be investigated. Preliminary experiments for electrochemical boundary condition of bare/pretreated 2024-T351 and Mg are reported herein.

### **8.2 Experimental Procedure**

#### **8.2.1 Materials**

99.9% pure magnesium rod (8.0 mm diam.) and 1.6 mm thick AA2024-T351 sheet were studied in these investigations. The Mg rod was mounted in EpoThin™ epoxy resin manufactured by Buehler in order to make clamping the sample to an electrochemical flat cell easier. The bare electrodes were prepared by alternating polishing with silicon-carbide paper and rinsing with 18.2 MΩ deionized water to a final polishing grit of 1200. AA2024-T351 sheet (1.6 mm thickness) was pretreated with 7 different surface pretreatments for comparison including (i) Non-film forming pretreatment (NFF), (ii) chromate conversion coating (CCC), (iii) trivalent chromium pretreatment (TCP), (iv) non-chromium pretreatment (NCP) (i) Anodization – No Sealing (ANS), (ii)

Anodization with hexavalent chromium sealing (ACS), (iii) Anodization with Trivalent Chromium Pretreatment (TCP) Sealing (ATS). For anodization pretreatments, a thin-film sulfuric acid anodizing, MIL-A-8625F: Type II pretreatment procedure was followed.<sup>36</sup> The electrochemical properties are discussed in chapter 2.

### **8.2.2 Full Immersion Electrochemical Analysis to Establish Boundary Condition**

Potential control during electrochemical experiments was maintained using a potentiostat with computer interface software. Versastat or Gamry Reference 600 potentiostats were utilized for potential control for all electrochemical measurements. Saturated calomel electrode (SCE) and Pt mesh were used as reference and counter electrode, respectively. All full-immersion studies reported herein were conducted in quiescent conditions open to laboratory air.

The potentiodynamic scans were conducted after 1 hour at open circuit potential (OCP) for all chosen systems. For full immersion studies pertinent to pretreatment degradation, OCP was monitored for a longer time (275 h) before potentiodynamic polarization experiments. Cathodic potentiodynamic scans were conducted on bare or pretreated 2024-T351 sheet. The tests were conducted in various bulk solutions of quiescent NaCl and MgCl<sub>2</sub> with and without chromate. A typical cathodic scan started at 0.05 V vs OCP and scanned down to -1.0 V vs OCP at a scan rate of 0.1667 mV/s. Anodic potentiodynamic scans were conducted on 99.9% pure, 8.0 mm diameter bare Mg electrodes. The bare Mg electrodes were polished to 1200 grit silicon carbide paper. The tests were conducted in various bulk solutions of quiescent NaCl and MgCl<sub>2</sub> with and without chromate. A typical anodic scan started at -0.05 V vs OCP up to + 0.5 V vs. OCP and scanned at 0.1667 mV per second.

## 8.3 Results

### 8.3.1 Phenomenological Model

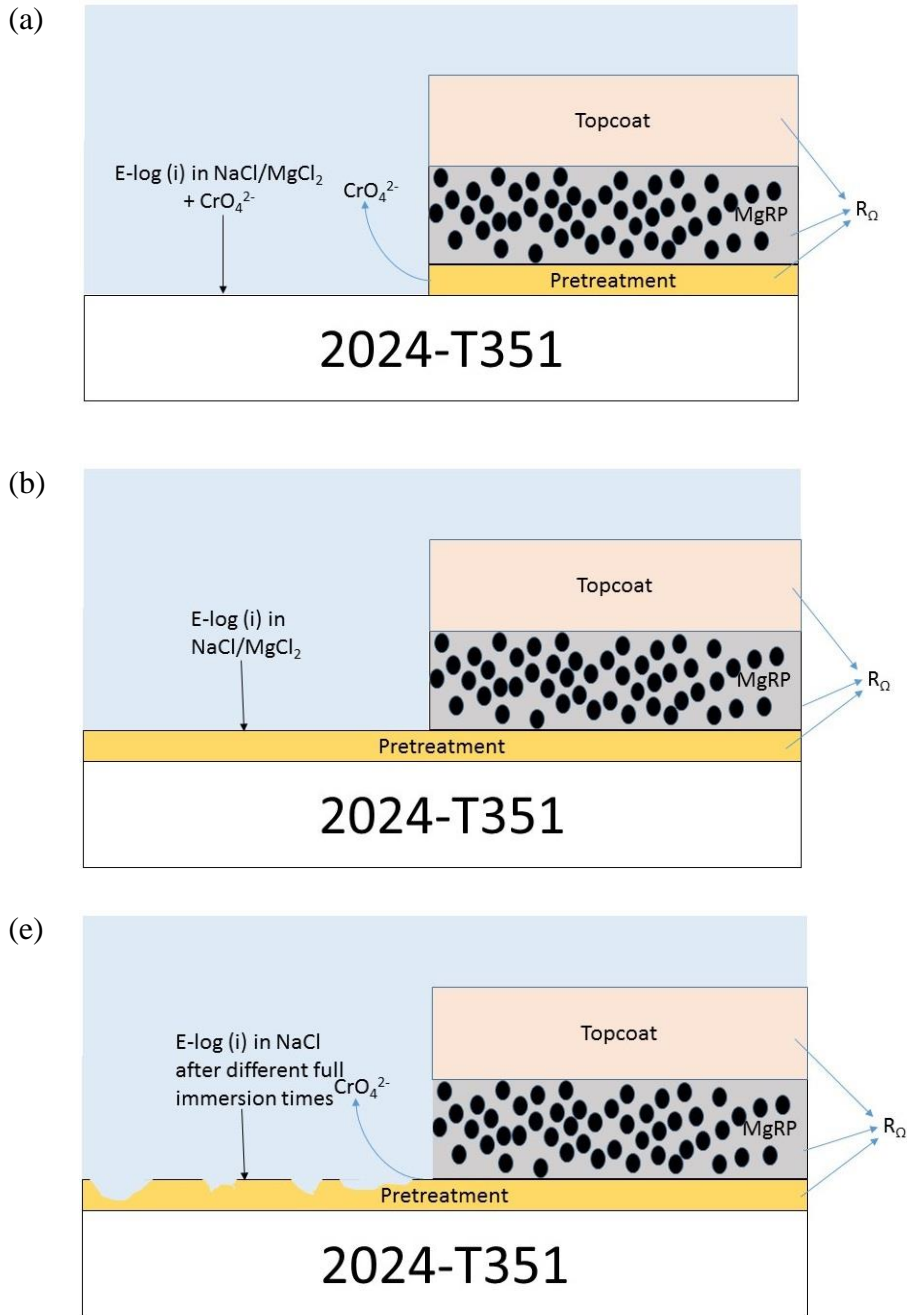


Figure 8.1. Phenomenological model to understand effect of (a) anionic species leaching from pretreatments on cathodic kinetics of bare 2024-T351 and anodic kinetics of Mg (b) resistive effects of pretreatments on cathodic kinetics of bare/pretreated 2024-T351 and (c) pretreatment degradation on cathodic kinetics of pretreated 2024-T351

### 8.3.2 Ionic Effects of Pretreatments

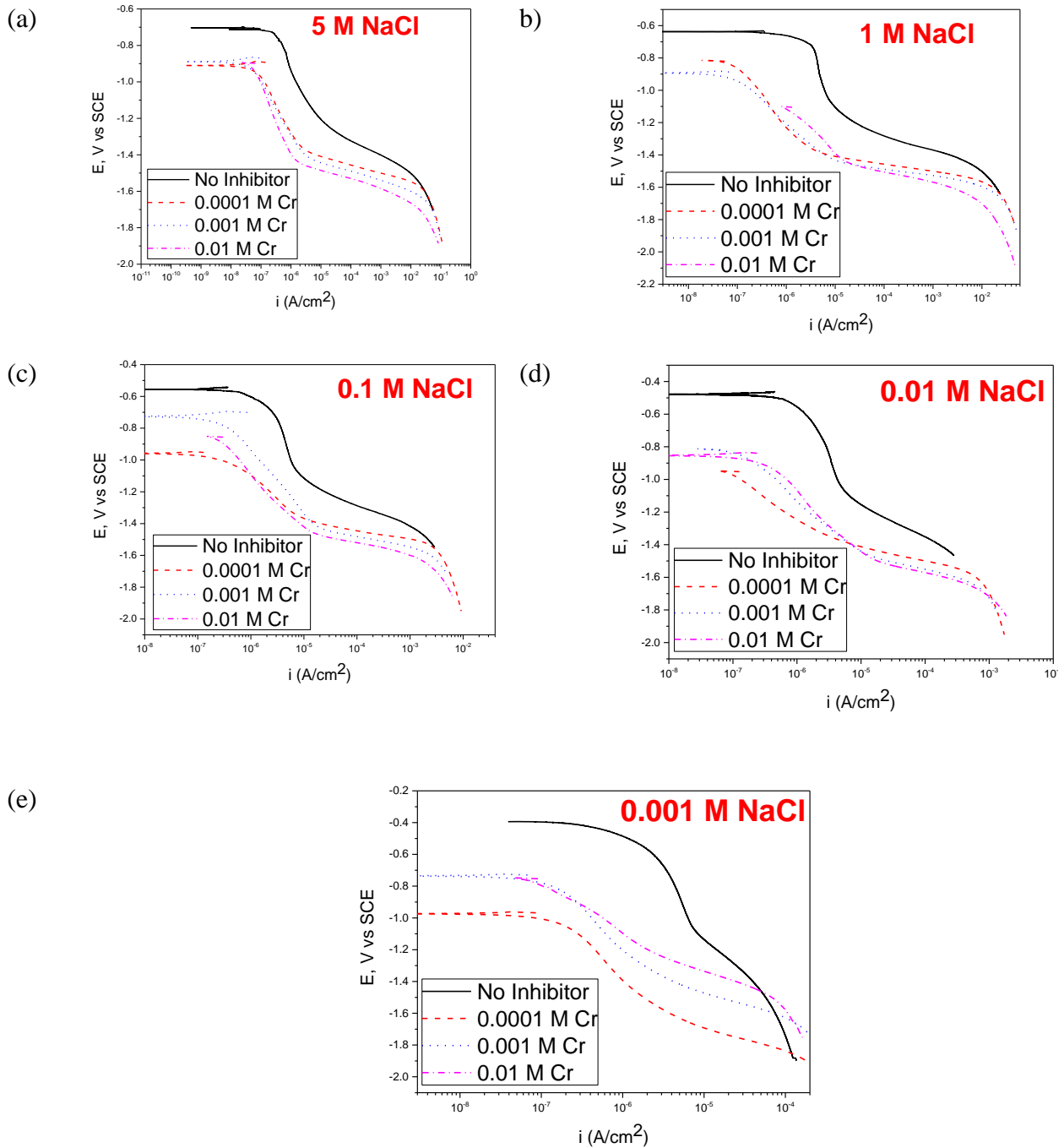


Figure 8.2. E-log (i) data for bare AA2024-T351 in quiescent NaCl solution of different concentration (a) 5 M, (b) 1 M, (c) 0.1 M, (d) 0.01 M and (e) 0.001 M NaCl at 4 inhibitor concentrations

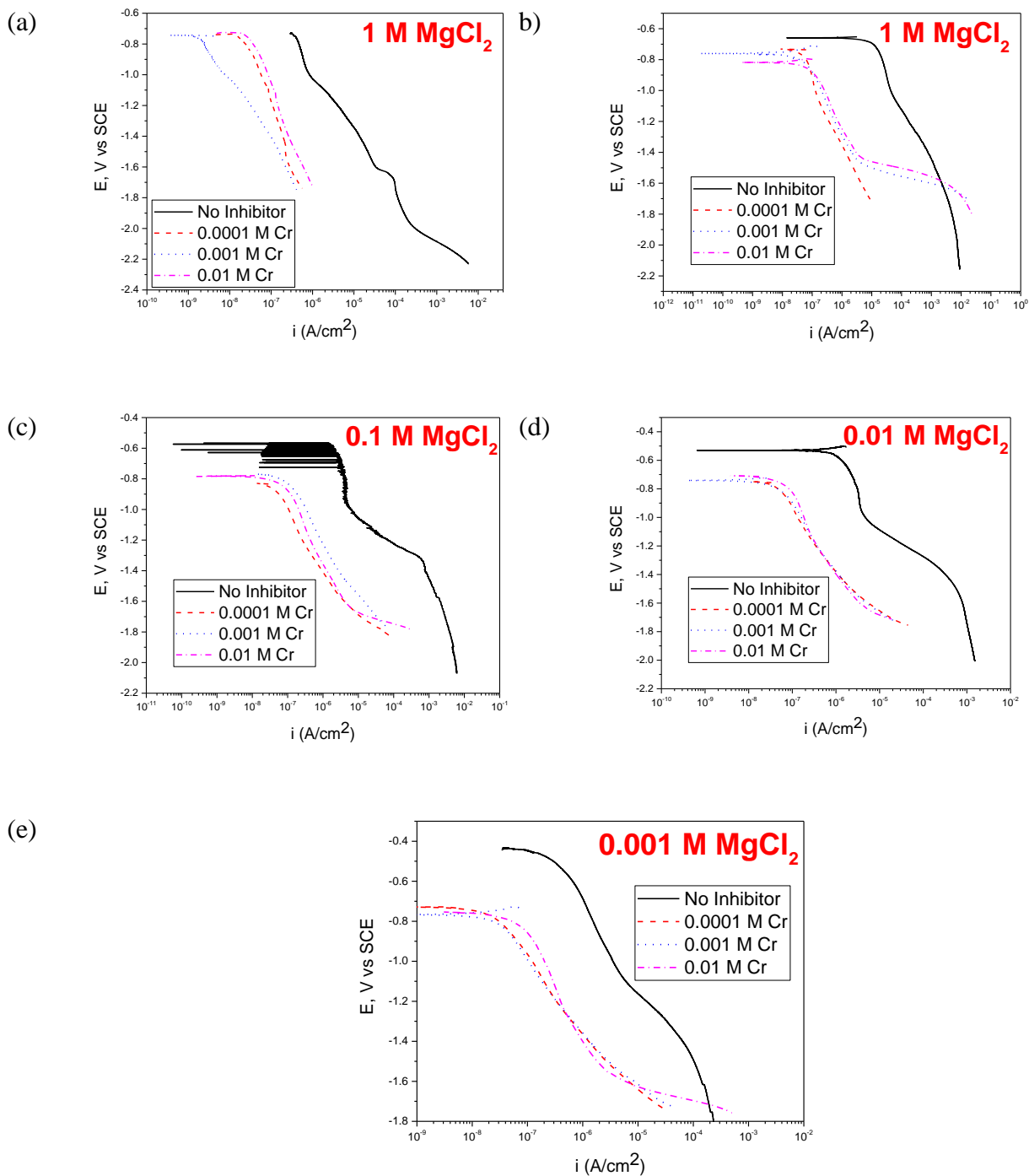


Figure 8.3. E-log (i) data for bare AA2024-T351 in quiescent  $\text{MgCl}_2$  solution of different concentration (a) 5 M, (b) 1 M, (c) 0.1 M, (d) 0.01 M and (e) 0.001 M  $\text{MgCl}_2$  at 4 inhibitor concentrations

### 8.3.3 Resistive Effects of Pretreatments

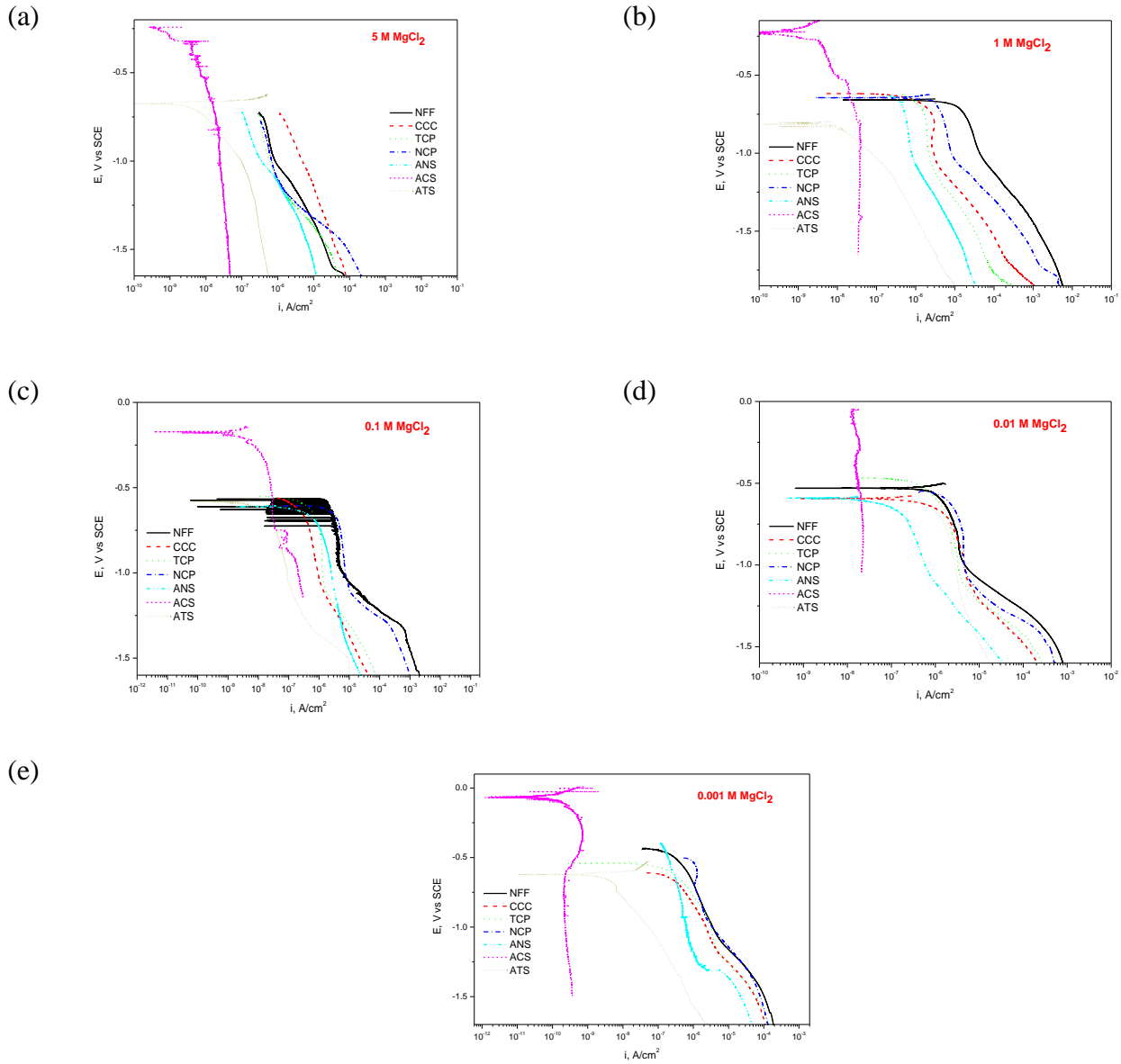


Figure 8.4. E-log (i) data for bare and pretreated AA2024-T351 in quiescent  $\text{MgCl}_2$  solution of different concentration (a) 5 M, (b) 1 M, (c) 0.1 M, (d) 0.01 M and (e) 0.001 M  $\text{MgCl}_2$ . The pretreatments indicated are (a) non-film forming (NFF), (b) chromate conversion coating (CCC), (c) trivalent chromium pretreatment (TCP), (d) non-chromium pretreatment (NCP), (e) anodized no seal (ANS), (f) anodized chromate seal (ACS) and (g) anodized TCP seal (ATS).

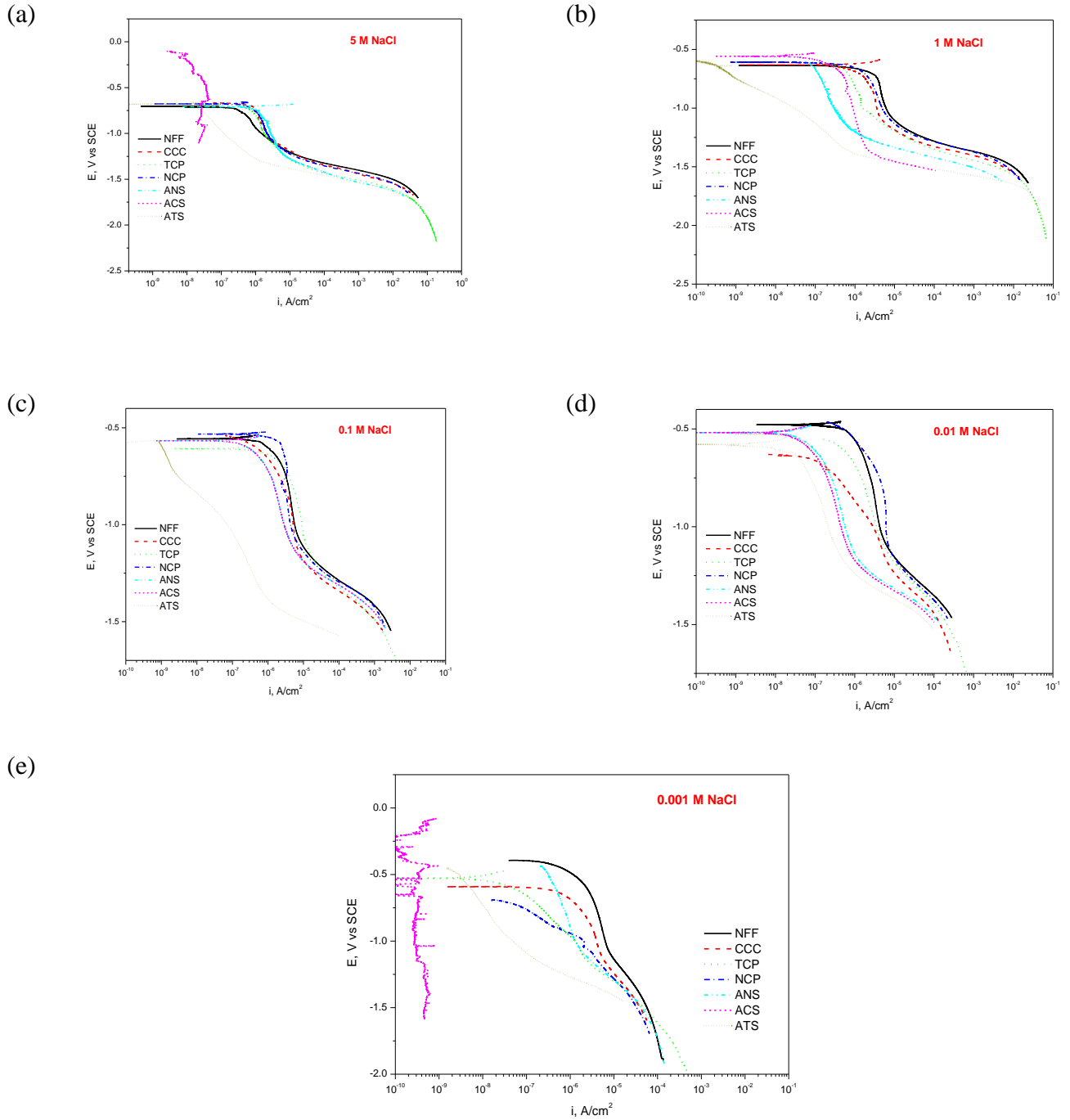


Figure 8.5. E-log (i) data for bare and pretreated AA2024-T351 in quiescent NaCl solution of different concentration (a) 5 M, (b) 1 M, (c) 0.1 M, (d) 0.01 M and (e) 0.001 M NaCl. The pretreatments indicated are (a) non-film forming (NFF), (b) chromate conversion coating (CCC), (c) trivalent chromium pretreatment (TCP), (d) non-chromium pretreatment (NCP), (e) anodized no seal (ANS), (f) anodized chromate seal (ACS) and (g) anodized TCP seal (ATS).

### 8.3.4 Mixed Effects of Pretreatments

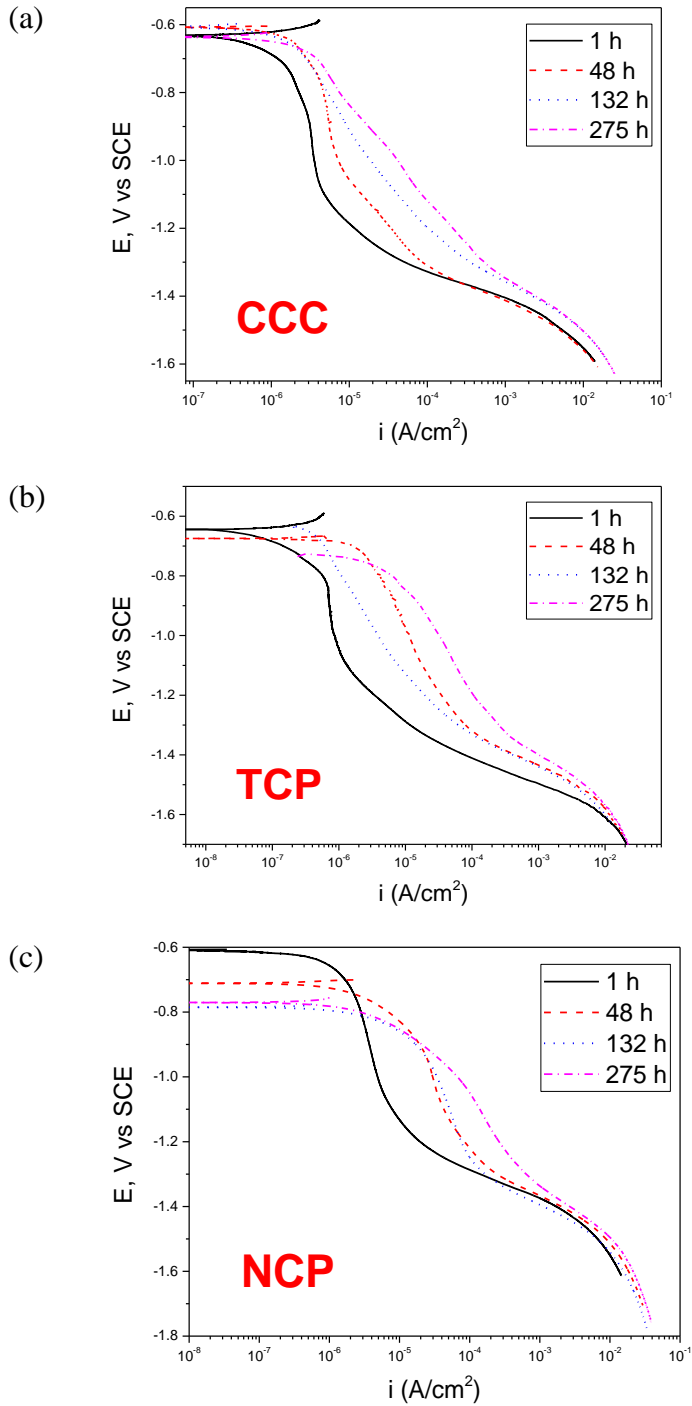


Figure 8.6. E-log (i) data for pretreated AA2024-T351 in quiescent 1 M NaCl solution after different full immersion exposure times for (a) CCC, (b) TCP and (c) NCP

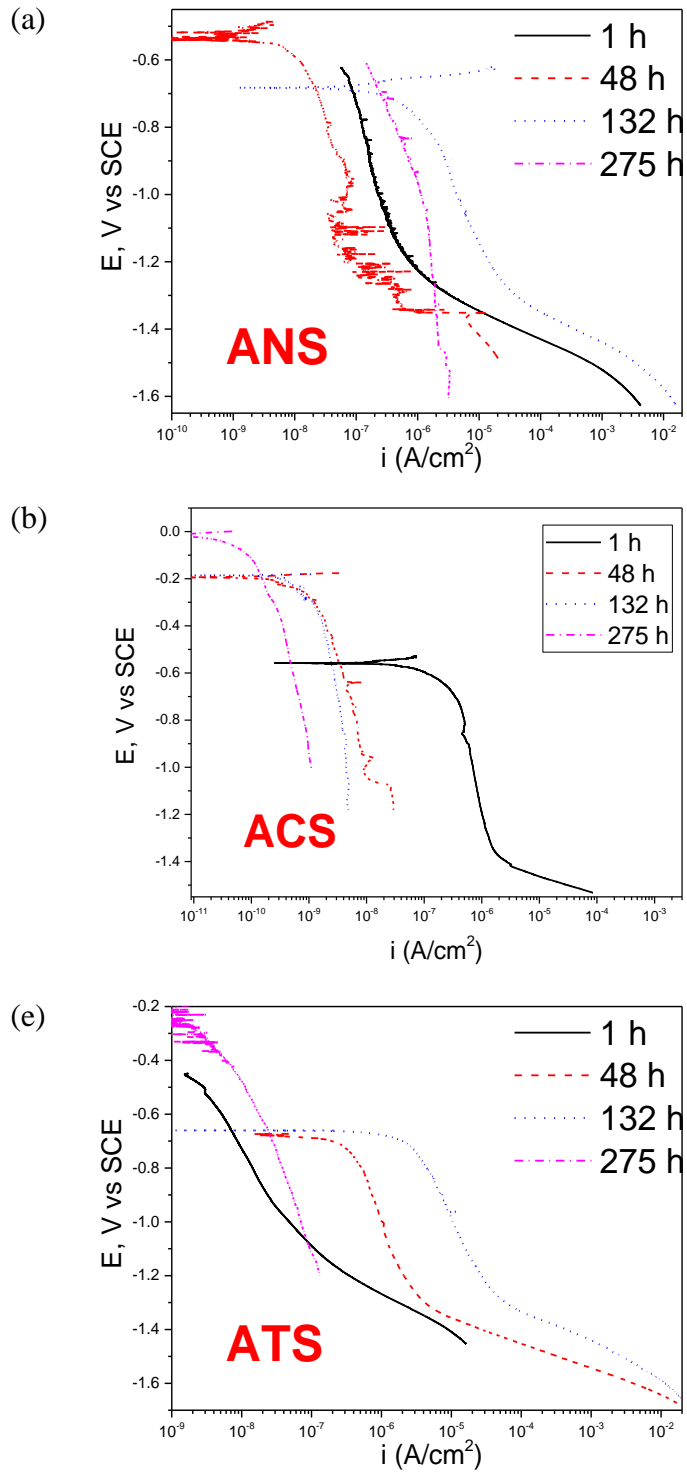


Figure 8.7. E-log (*i*) data for pretreated AA2024-T351 in quiescent 1 M NaCl solution after different full immersion exposure times for (a) ANS, (b) ACS and (c) ATS

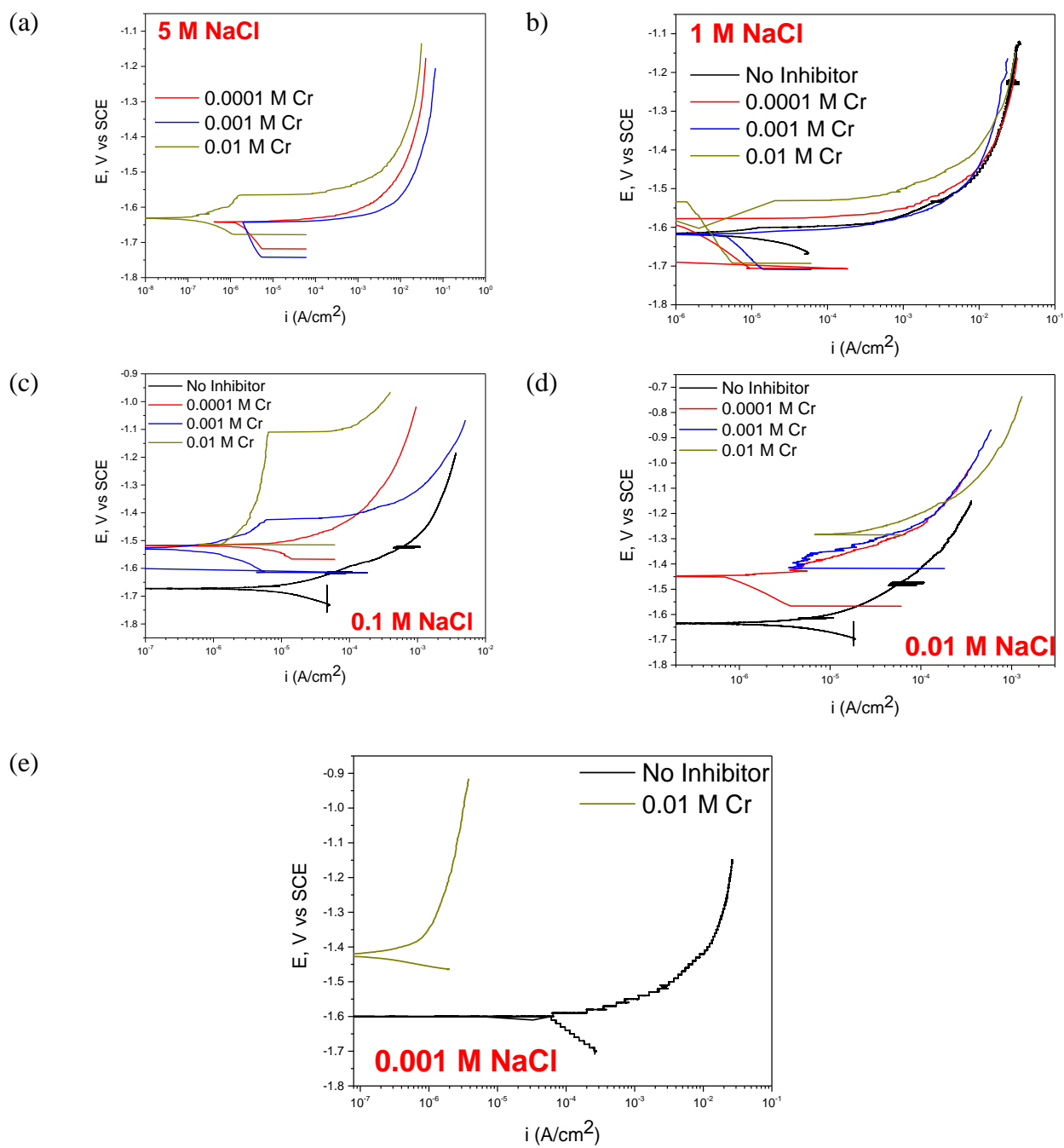


Figure 8.8. E-log ( $i$ ) data for Mg in quiescent NaCl solution of different concentration (a) 5 M, (b) 1 M, (c) 0.1 M, (d) 0.01 M and (e) 0.001 M NaCl at 4 inhibitor concentrations

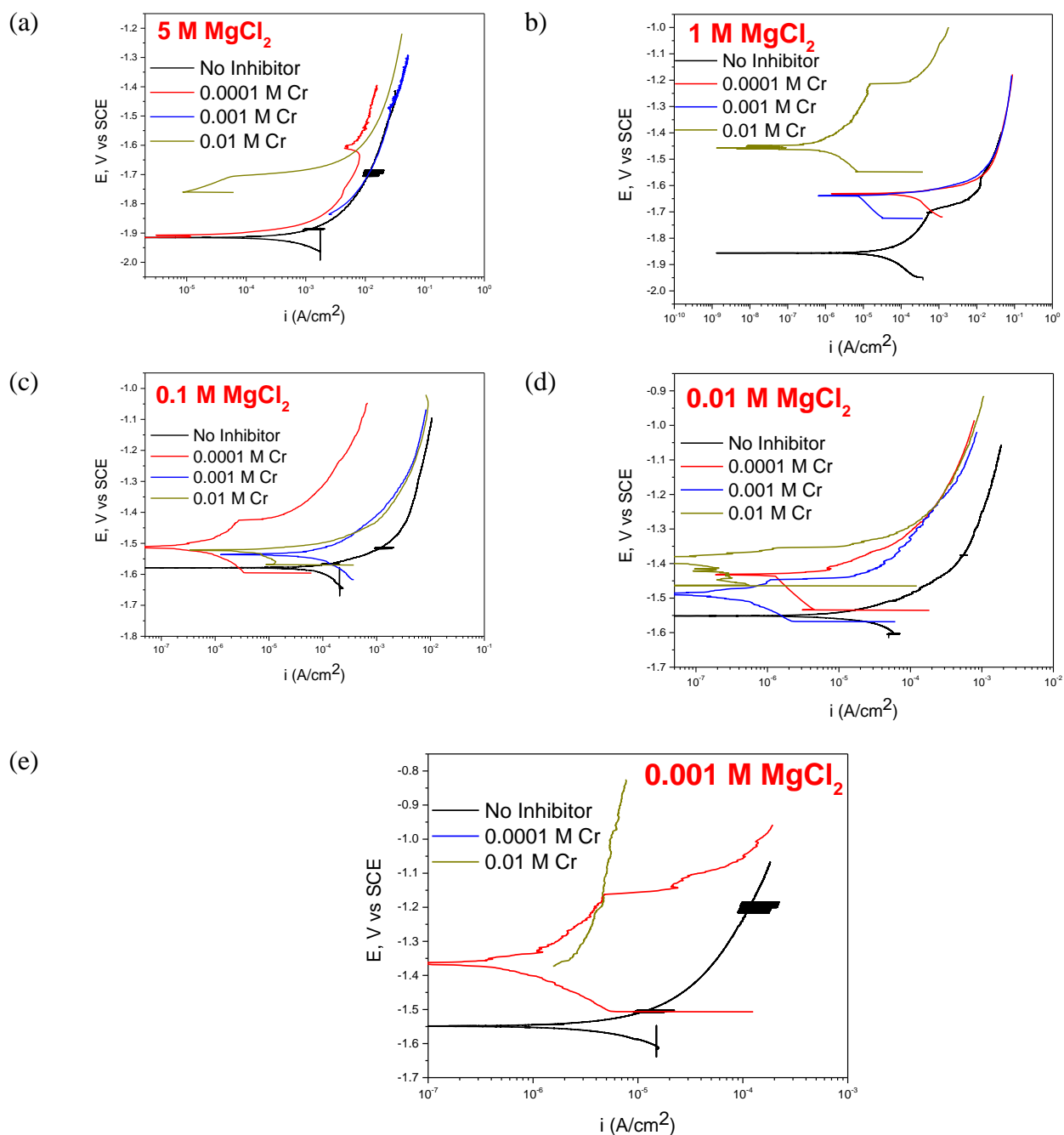


Figure 8.9. E-log (i) data for Mg in quiescent MgCl<sub>2</sub> solution of different concentration (a) 5 M, (b) 1 M, (c) 0.1 M, (d) 0.01 M and (e) 0.001 M MgCl<sub>2</sub> at 4 inhibitor concentrations

### 8.3.5 Solution Conductivity (Based on OLI calculations)

Table 8.1. Solution conductivity for various bulk solutions of NaCl with and without Na<sub>2</sub>CrO<sub>4</sub>

NaCl Concentration	Na <sub>2</sub> CrO <sub>4</sub> Concentration	$\sigma$ (S/m) Calculated by OLI Software
0.001 M	0	0.0123
	0.0001	0.0144
	0.001	0.0339
	0.01	0.2141
0.01 M	0	0.1176
	0.0001	0.1196
	0.001	0.1377
	0.01	0.3113
0.1 M	0	1.0607
	0.0001	1.0606
	0.001	1.0774
	0.01	1.2267
1 M	0	8.4393
	0.0001	8.4391
	0.001	8.4377
	0.01	8.5319
5 M	0	24.0164
	0.0001	24.0161
	0.001	24.0132
	0.01	23.9838

Table 8.2. Solution conductivity for various bulk solutions of MgCl<sub>2</sub> with and without Na<sub>2</sub>CrO<sub>4</sub>

MgCl <sub>2</sub> Concentration	Na <sub>2</sub> CrO <sub>4</sub> Concentration	$\sigma$ (S/m) Calculated by OLI Software
0.001 M	0	0.0245
	0.0001	0.0245
	0.001	0.0249
	0.01	0.2059
0.01 M	0	0.223
	0.0001	0.223
	0.001	0.2237
	0.01	0.2304
0.1 M	0	1.8285
	0.0001	1.8287
	0.001	1.8305
	0.01	1.8486
1 M	0	11.333
	0.0001	11.333
	0.001	11.336
	0.01	11.361
5 M	0	10.6896
	0.0001	10.6901
	0.001	10.6944
	0.01	10.7415

## 8.4 Future Work

The previously used FEA model shown in figure 7a will be modified to account for pretreatment resistances. To simulate an actual scribe the resistance at the vertical edge between Mg and 2024-T351 scribe would be differentiated from the resistance of the topcoat (figure 7b). The edge resistance would account for pretreatment resistance (electrical) and primer polymer (ionic). This would ensure that majority of throwing power effect would be seen from the edge as compared to whole of coating. Effect of pretreatment and polymer resistances, thickness of electrolyte, ionic effects of anionic species leaching and pretreatment degradation on throwing power would be understood.

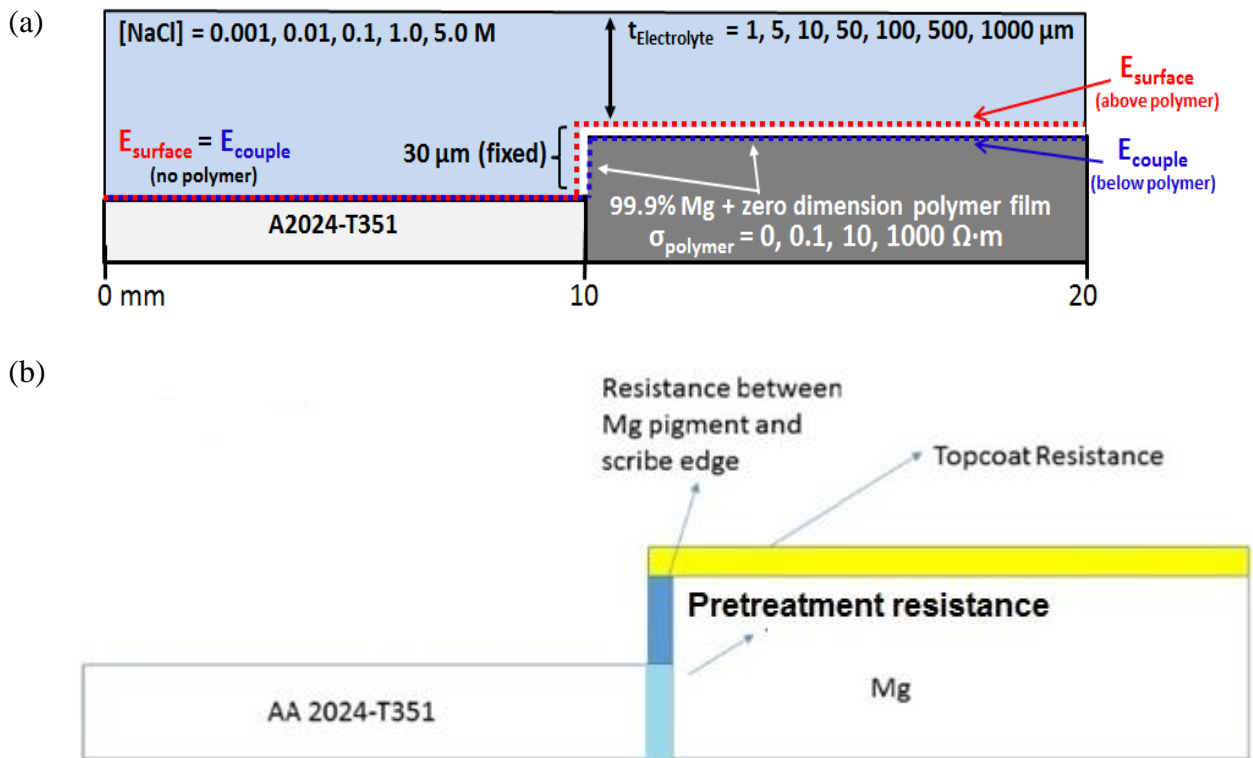


Figure 8.10. Schematic of geometric model developed in FEA software (COMSOL) (a) material and electrolyte conditions studied where the polymer resistance is given and (b) Significant difference in existing model used for throwing power determination

## **9 APPENDIX B: Performance of a Magnesium Rich Primer on Pretreated 2024-T351 in Full Immersion: Throwing Power Investigation Using Optical Profilometry –**

### **FIGURES ONLY**

#### **9.1 Abstract**

The spatial distribution of corrosion volume loss for bare 2024-T351 coupled with a MgRP coating over pretreated 2024-T351 was studied using optical profilometry. The corrosion volume loss distribution over a 2024-T351 scribe was studied after full immersion exposure with three different pretreatments (Non-film forming (NFF), trivalent chromium pretreatment (TCP) and anodization with chromate seal (ACS)) in two different area configurations with coating to scribe area ratios (0.3 and 5). In addition, similar studies were conducted for NFF/MgRP in presence of topcoat for above said coating to scribe area ratios. For a coating to scribe area ratio of 0.3, NFF/MgRP effectively inhibit pitting corrosion of 2024-T351 by sacrificial anode-based cathodic protection. Corrosion volume loss at scribe which is indicative of local sites of pitting were lowered by approximately 2 orders of magnitude adjacent to the coating (< 4mm) in the presence of NFF/MgRP. Scratch protection decreased with increasing distance from the coating edge. Similar experiments conducted for TCP and ACS pretreated MgRP showed very minimal scratch protection. Increase in coating to scribe area ratio did not result in any significant reduction of corrosion volume loss. In case of systems with a polyurethane topcoat, due to heavily mediated galvanic coupling and limited conductive pathways for Mg to couple to 2024-T351, there is no significant scribe protection for non-degraded topcoat.

## 9.2 Experimental Procedures

### 9.2.1 Materials

AA2024-T351 sheet (1.6 mm thickness) was pretreated with 3 different surface pretreatments for comparison including Non-film filming (NFF), trivalent chromium based pretreatment (TCP) and Anodization with hexavalent chromium sealing (ACS). Trivalent chromium pretreatment is a zirconium based conversion coating with trivalent chromium and is developed by NAVAIR. For anodization pretreatments, a thin-film sulfuric acid anodizing, MIL-A-8625F: Type II pretreatment procedure was followed. Thickness of the pretreatments and resistances chosen for this studies is summarized in Table 1.

A 40  $\mu\text{m}$  primer layer of Mg-rich primer and a 50  $\mu\text{m}$  thick topcoat of Aerodur 5000 high-performance advanced coating, both produced by Akzo Nobel Coatings (Waukegan, Illinois) were applied. The Mg rich primer consist of one part epoxy matrix with Mg metal flake pigment of a diameter 20  $\mu\text{m}$  with pigment volume concentration of 45 % (3rd generation 2100P003, Lot: 493-190). Aerodur 5000 (Gloss white finish product: ECM-G7875) is a two component polyurethane topcoat developed for military application in variety of exposure environments.<sup>128</sup>

### 9.2.2 Sample Preparation

A large size defect is created in coated samples by laser ablation. Samples were irradiated with a KrF excimer laser ( $\lambda = 248 \text{ nm}$ , 25 ns full width at half maximum) at a repetition rate of 10 Hz and a fluence of 2 J/cm<sup>2</sup>. All specimens were rastered using a Newport† linear actuator for a total irradiation of 8 PPA for ACS pretreatment only systems, 16-20 laser pulses per area (PPA) for primer only systems and 24-28 PPA for topcoated system and a 90% overlap with a cylindrical shaped spot size of 0.6 mm  $\times$  29 mm. The details of the equipment setup for laser ablation are

reported elsewhere.<sup>163,164</sup> Any effect of laser ablation on microstructure changes is minimal in chosen laser pulse intensity ( $< 10 \mu\text{m}$ ). To further minimize the effect the laser PPA were optimized for each system in such a way that the intact coating was not completely removed. The final few micrometers of the coating and underlying substrate were removed by mechanical polishing so that original microstructure was exposed. The specimens were ground to a 240 grit finish to leave a rough sample to accelerate localized corrosion. An area of ca. 10 mm x10 mm (the exact size of which was noted in each case) was isolated in the center of the bare 2024-T351 for control experiments. The coating/scribe ratio design for coated systems are indicated in Figure 1. Two area ratios were chosen for studies. An insulating extruded PTFE self-adhesive tape was used to isolate the scan area for exposure. For any given test corrosion was observed on the scan area only and not anywhere else on the sample for the entire duration of experiment.

### **9.2.3 Laboratory Full Immersion Exposures Studies**

All full-immersion studies reported herein were conducted in quiescent 2 M NaCl (pH:  $6.9\pm 0.4$ ) open to laboratory air. Two sampled designs with different coating/scribe ratio (0.3 and 5) as indicated in Figure 1 were used for full immersion exposure.

### **9.2.4 Post-mortem Surface Analysis of the Scribe**

Optical profilometry was conducted using a Zygo optical profilometer (Newview 7200/7300 model). The environmentally exposed samples were first exposed to concentrated nitric acid for 15 minutes to remove corrosion products present in the scribe as per the ASTM G-1 Standard.<sup>138</sup> Image refinement and pit volume calculation was performed using MountainsMaps imaging topography software.<sup>142</sup>

### 9.3 Results

#### 9.3.1 Sample Design

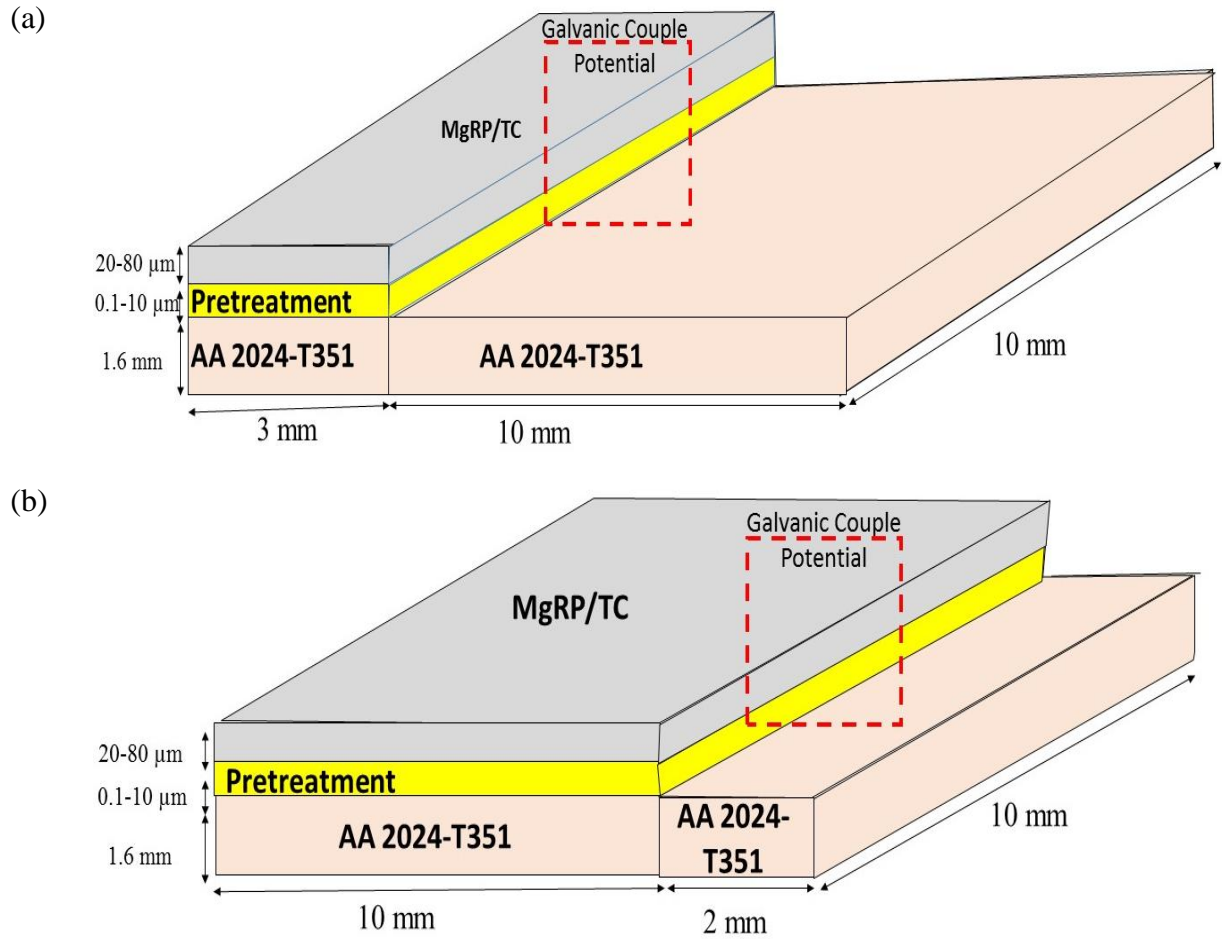


Figure 9.1. Sample design for SVET and optical profilometry measurements. (a) coating/scribe ratio (0.3) and (b) coating/scribe ratio (5)

### 9.3.2 Optical Profilometry Maps

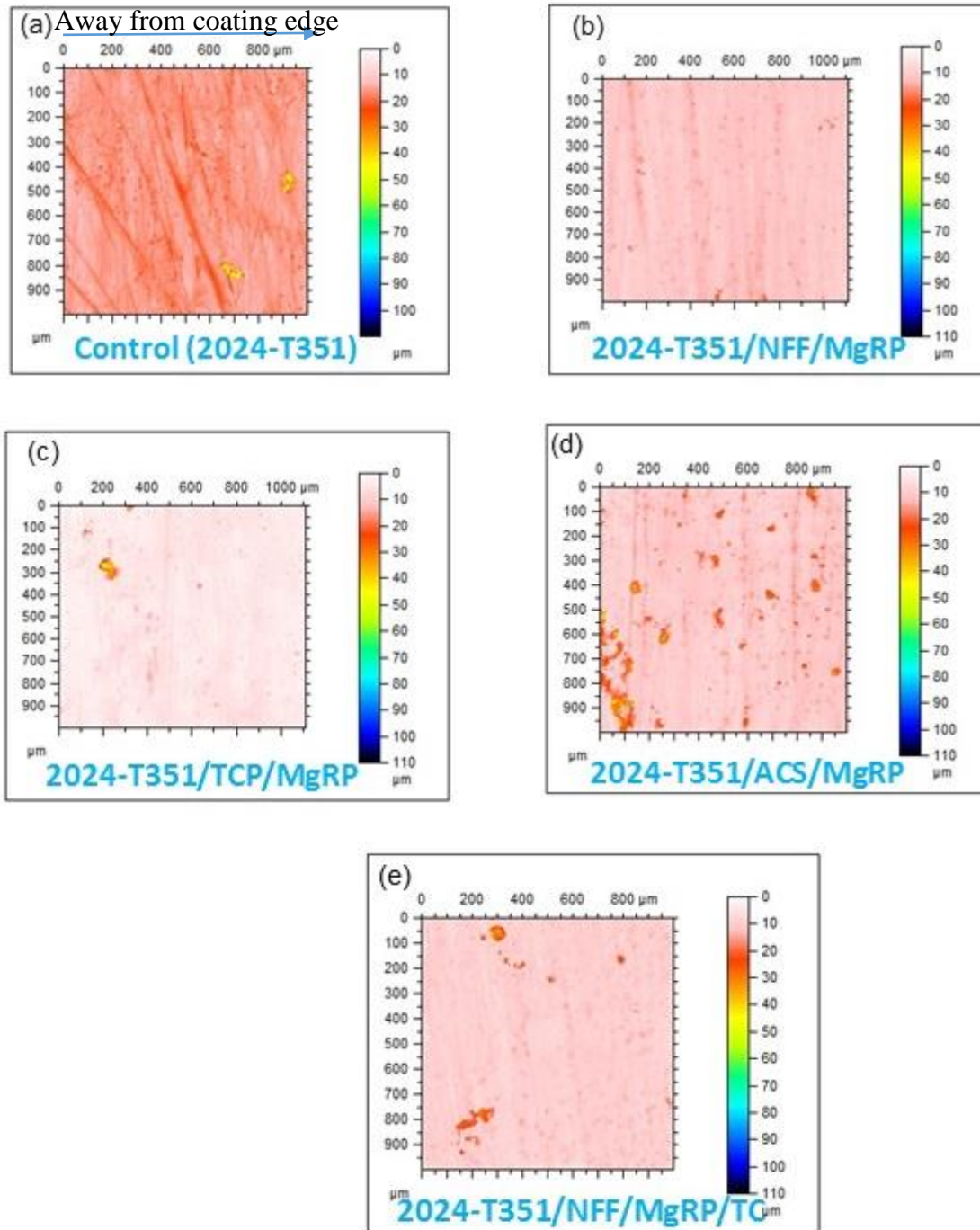


Figure 9.2. Optical profilometry maps indicating depth perpendicular to the plan of the surface for scribe exposing bare 2024-T351 adjacent to the coating ( $< 2$  mm) for selected coating systems indicated after exposure in full immersion for 275 h. (a) no coating, (b) 2024-T351/NFF/MgRP, (c) 2024-T351/TCP/MgRP, (d) 2024-T351/ACS/MgRP and (e) 2024-T351/NFF/MgRP/TC. Coating to scribe area ratio: 0.3.

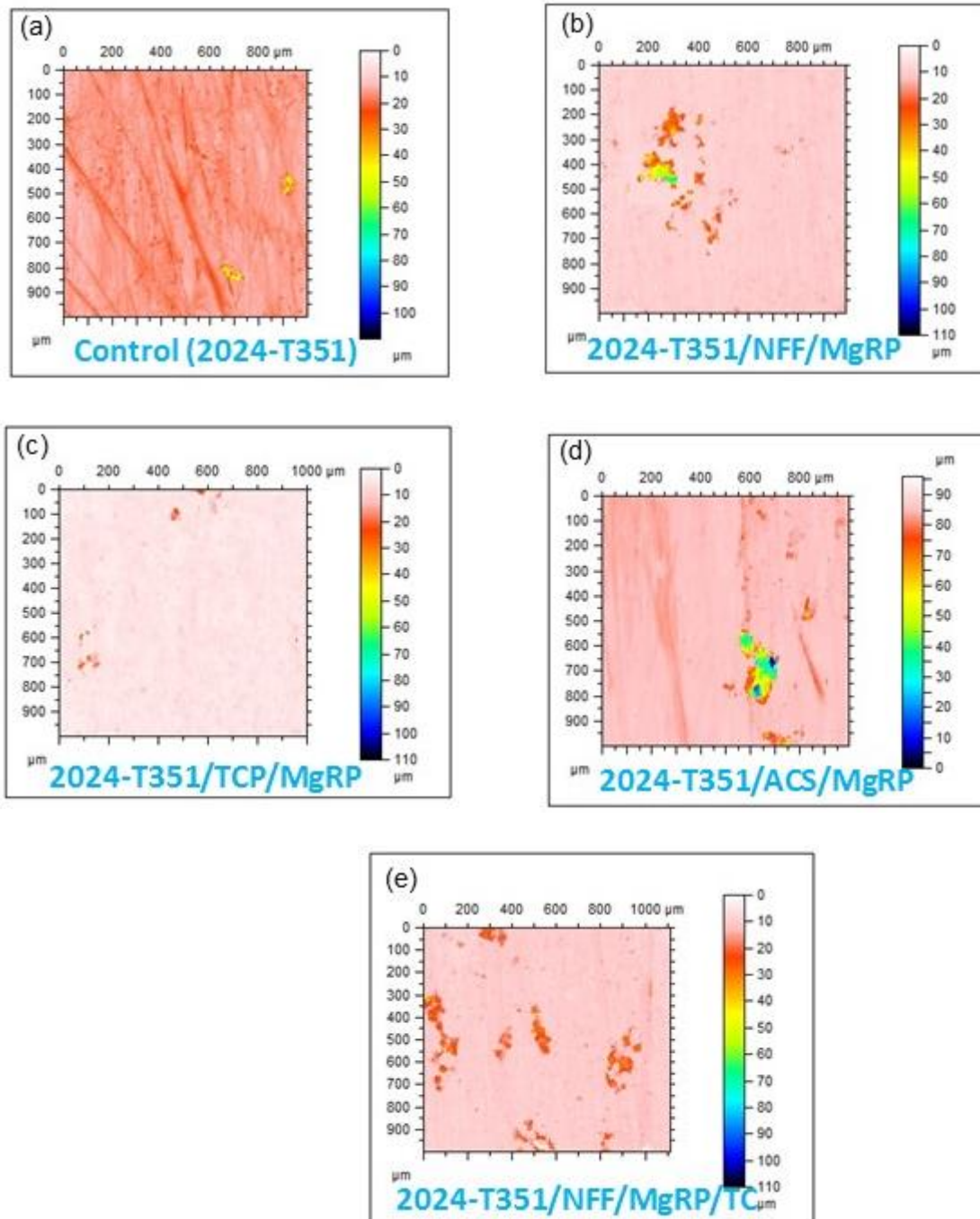


Figure 9.3. Optical profilometry maps indicating depth perpendicular to the plan of the surface for scribe exposing bare 2024-T351 adjacent to the coating ( $< 8$  mm) for selected coating systems indicated after exposure in full immersion for 275 h. (a) no coating, (b) 2024-T351/NFF/MgRP, (c) 2024-T351/TCP/MgRP, (d) 2024-T351/ACS/MgRP and (e) 2024-T351/NFF/MgRP/TC. Coating to scribe area ratio: 0.3.

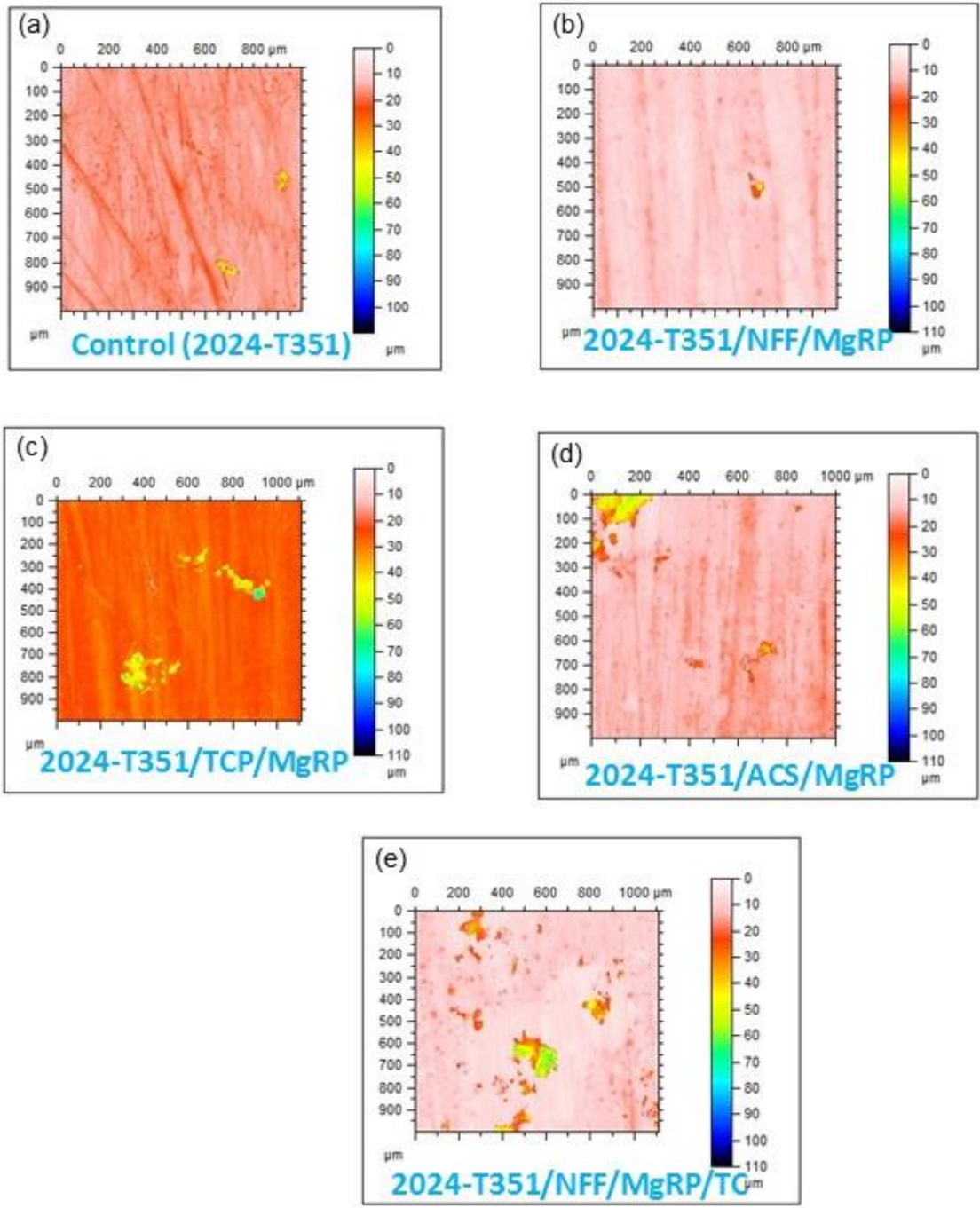


Figure 9.4. Optical profilometry maps indicating depth perpendicular to the plan of the surface of scribe exposing bare 2024-T351 adjacent to the coating (< 2 mm) in selected coating systems indicated after exposure in full immersion for 275 h. (a) no coating, (b) 2024-T351/NFF/MgRP, (c) 2024-T351/TCP/MgRP, (d) 2024-T351/ACS/MgRP and (e) 2024-T351/NFF/MgRP/TC. Coating to scribe area ratio: 5.

### 9.3.3 Effect of Distance from Coating and Coating to scribe area ratio

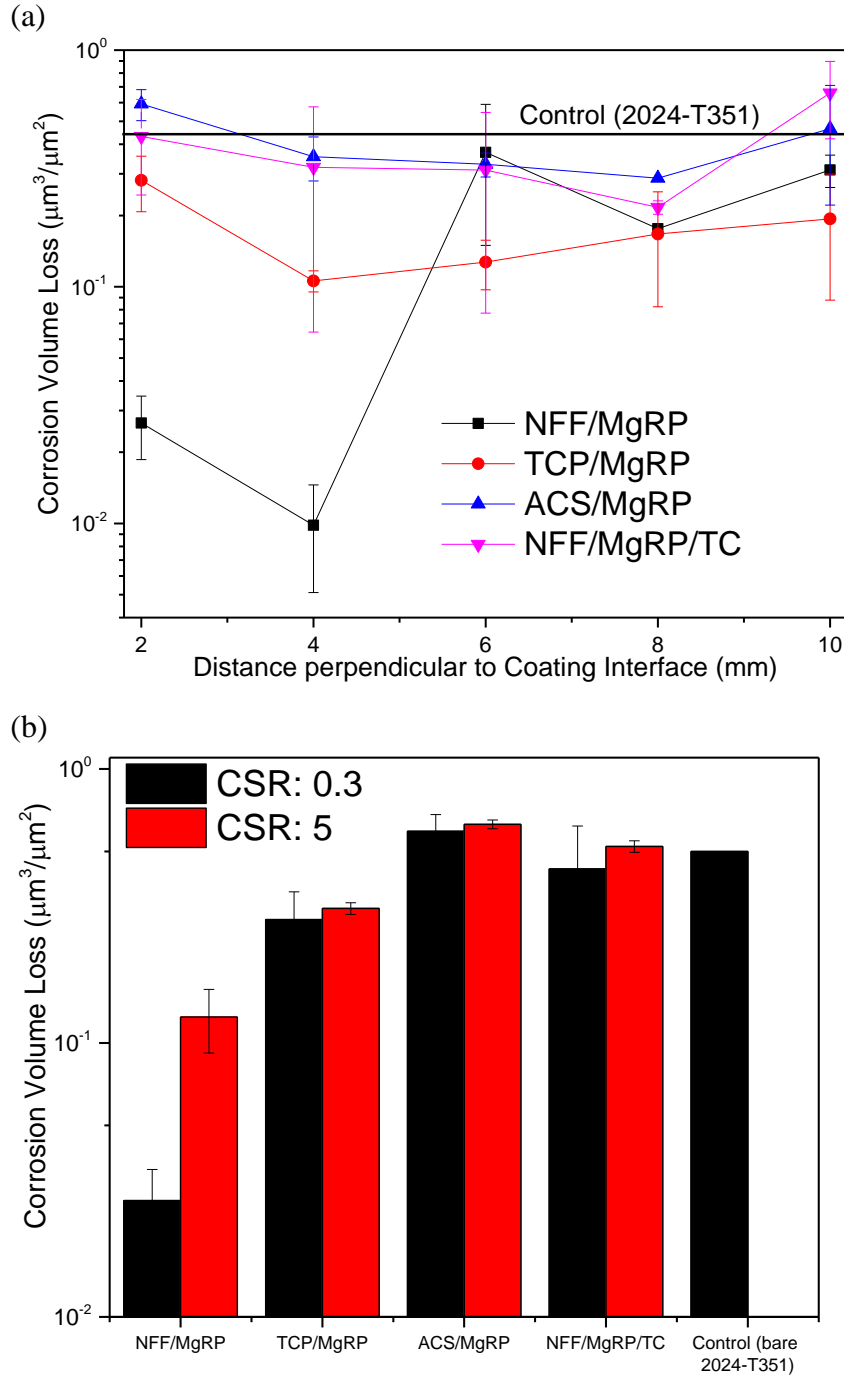


Figure 9.5. Corrosion volume loss of scribe exposing AA2024-T351 adjacent to the coating (< 2 mm) in selected coating systems indicated after exposure in full immersion for 275 h. (a) corrosion volume loss as a function of distance from coating interface. (b) corrosion volume loss as a function of coating to scribe area ratio (CSR)

#### 9.4 Summary and Future Work

- In exposures of the bare 2024-T351 coupled to NFF/MgRP (CSR: 0.3), corrosion volume loss was reduced by 2 orders of magnitude adjacent to the coating (< 4mm) compared to far away from coating (> 4 mm), thus approximating the throwing power of MgRP to be 4 mm.
- TCP and ACS based MgRP systems (CSR: 0.3) exhibited a mediated galvanic protection potential. This resulted in very limited sacrificial anode based protection function. There was no substantial galvanic protection was evident in ACS based systems. The corrosion volume loss in TCP is slightly lower than ACS based systems. This can be correlated to very limited galvanic protection in TCP based system.
- The geometric area ratio of coverage of MgRP to scribe is largely independent of protection function. It is to be noted that the previously reported SVET experiments for short term full immersion exposures showed that large area ratio improved corrosion protection in TCP and ACS based systems. .
- Topcoat significant mediated the galvanic protection potential as well as sacrificial protection function. No galvanic protection function was evident at the scribe as could be deduced from the corrosion volume loss which showed no scribe protection at shorter distances as well as longer coating to scribe area ratio. The secondary modes of corrosion protection such as  $Mg(OH)_2$  redeposition and anionic species leaching might be also considerably limited due to excellent barrier properties of the topcoat.
- Optical profilometry technique utilized for corrosion volume loss analysis in the scribe showed good correlation to throwing power analysis using scanning vibrating electrode technique (SVET).

- Long term full immersion exposures need to be conducted for SVET to understand how galvanic protection function evolves as a function of exposure time. Post-full immersion exposures after SVET would help have good correlation between the anodic current densities in the scribe (from SVET) and corrosion volume loss (from optical profilometry).

## **10 APPENDIX C: Preliminary Investigation of Throwing Power of a Magnesium Rich Primer on 2024-T351 under Thin Films Using Scanning Kelvin Probe – FIGURES ONLY**

### **10.1 Introduction**

The spatial distribution of the galvanic protection potential for a bare 2024-T351 coupled with a MgRP coated 2024-T351 under thin film conditions was investigated using scanning Kelvin probe (SKP). Preliminary characterization of pure Al, Mg, Cu and intermetallic phases in 2024-T351 were performed using scanning electron microscopy and energy dispersive spectroscopy. The chemistry of the bare metal/intermetallic particle can be correlated to their Volta potential. SKP measurements of 2024-T351 coupled to Mg or MgRP was conducted for few selected configuration. The results showed good correlation between the galvanic coupling and the volta potentials.

### **10.2 Experimental Procedures**

#### **10.2.1 Materials**

AA2024-T351, 99.8% pure Mg ribbon, 99.9% pure Mg rod, copper (99.994%) and aluminum (99.9996%) as well as coated, 1.6-mm thick AA2024-T351 panels with MgRP and with/without topcoat were utilized for SKP studies. Bulk synthesized intermetallic phases utilized for the studies are s phase ( $\text{Al}_2\text{CuMg}$ ),  $\text{Al}_7\text{Cu}_2\text{Fe}$ , Al-4 wt% Cu and  $\text{Al}_2\text{Cu}$  ( $\theta$  phase). A 40  $\mu\text{m}$  primer layer of Mg-rich primer and a 50  $\mu\text{m}$  thick topcoat of Aerodur 5000 high-performance advanced coating, both produced by Akzo Nobel Coatings (Waukegan, Illinois) were applied. The Mg rich primer consist of one part epoxy matrix with Mg metal flake pigment of a diameter 20  $\mu\text{m}$  with pigment volume concentration of 45 % (3rd generation 2100P003, Lot: 493-190). Aerodur 5000 (Gloss

white finish product: ECM-G7875) is a two component polyurethane topcoat developed for military application in variety of exposure environments.

### **10.2.2 Surface Analysis of the Intermetallics**

Scanning electron microscopy (SEM) and energy dispersive spectroscopy (EDS) were used for chemical characterization of selected intermetallic phases. A field emission Quanta 650 SEM was used to conduct these investigations. For EDS, Oxford XMax 150 detector was utilized. A working distance of 15 mm and an accelerating voltage of at least 3 times the energy of the maximum characteristic peak of interest were used (~15 kV). At an accelerating voltage of 15 kV, EDS has a penetration depth of roughly 2 to 5  $\mu\text{m}$  into the materials investigated in this study. Elemental maps was collected and EDS analysis was performed using Aztec analysis software. All samples were ground to 1200-grit using SiC paper prior to surface characterization.

### **10.2.3 Sample Preparation for Scribed Coating**

A large size defect (10 mm) was created in coated samples by laser ablation. Samples were irradiated with a KrF excimer laser ( $\lambda = 248 \text{ nm}$ , 25 ns full width at half maximum) at a repetition rate of 10 Hz and a fluence of 2 J/cm<sup>2</sup>. All specimens were rastered using a Newport† linear actuator for a total irradiation of 8 PPA for ACS pretreatment only systems, 16-20 laser pulses per area (PPA) for primer only systems and 24-28 PPA for topcoated system and a 90% overlap with a cylindrical shaped spot size of 0.6 mm  $\times$  29 mm. The details of the equipment setup for laser ablation are reported elsewhere.<sup>163,164</sup> Any effect of laser ablation on microstructure changes is minimal in chosen laser pulse intensity (< 10  $\mu\text{m}$ ). To further minimize the effect the laser PPA were optimized for each system in such a way that the intact coating was not completely removed. The final few micrometers of the coating and underlying substrate were removed by mechanical polishing so that original microstructure is exposed. The specimens were ground to a 240 grit finish

to leave a rough sample to accelerate localized corrosion. An area of ca. 10 mm x10 mm (the exact size of which was noted in each case) was isolated in the center of the bare 2024-T351 for control experiments. The coating/scribe ratio design for coated systems are indicated in Figure 1. Two area ratios were chosen for studies. An insulating extruded PTFE self-adhesive tape was used to isolate the scan area for exposure. For any given test corrosion was observed on the scan area only and not anywhere else on the sample for the entire duration of experiment.

#### **10.2.4 Scanning Kelvin Probe Experiments**

A KP technology ambient advanced SKP with a 50  $\mu\text{m}$  gold coated stainless tip was utilized for SKP measurements. The SKP characterization of bare metals and intermetallic phases were conducted without any electrolyte at 95 % RH conditions in humid air. The SKP characterization of coated 2024-T351 with a scribe were conducted in 650  $\mu\text{L}$  of 5 M NaCl solution at 95 % RH for short-term exposure times. Before atmospheric exposure, the samples were plasma cleaned to reduce the contact angle and ensure a uniform thin layer of electrolyte on the surface. In a separate experiment, the electrolyte film applied over surface using Daisuke method (5 M NaCl, 50 sprays) was allowed to air dry completely and then the relative humidity was ramped up from 45 % RH slowly to higher relative humidity.

## 10.3 Results

### 10.3.1 Chemical Characterization of Intermetallic in 2024-T351

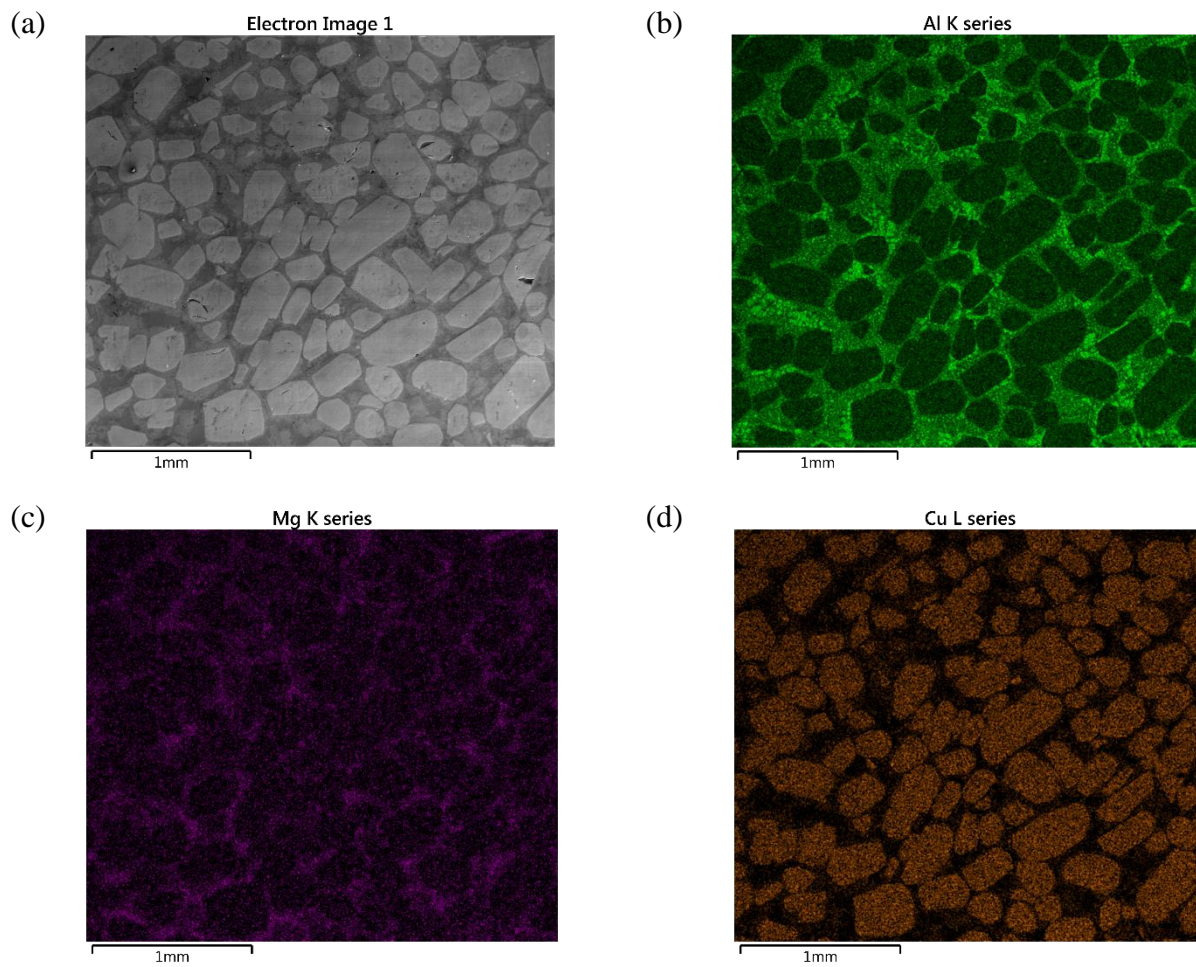


Figure 10.1. Secondary electron image (a) and elemental maps of Al (b), Mg (c) and Cu (d) of bulk synthesized S phase ( $\text{Al}_2\text{CuMg}$ ) intermetallic particle, as cast.

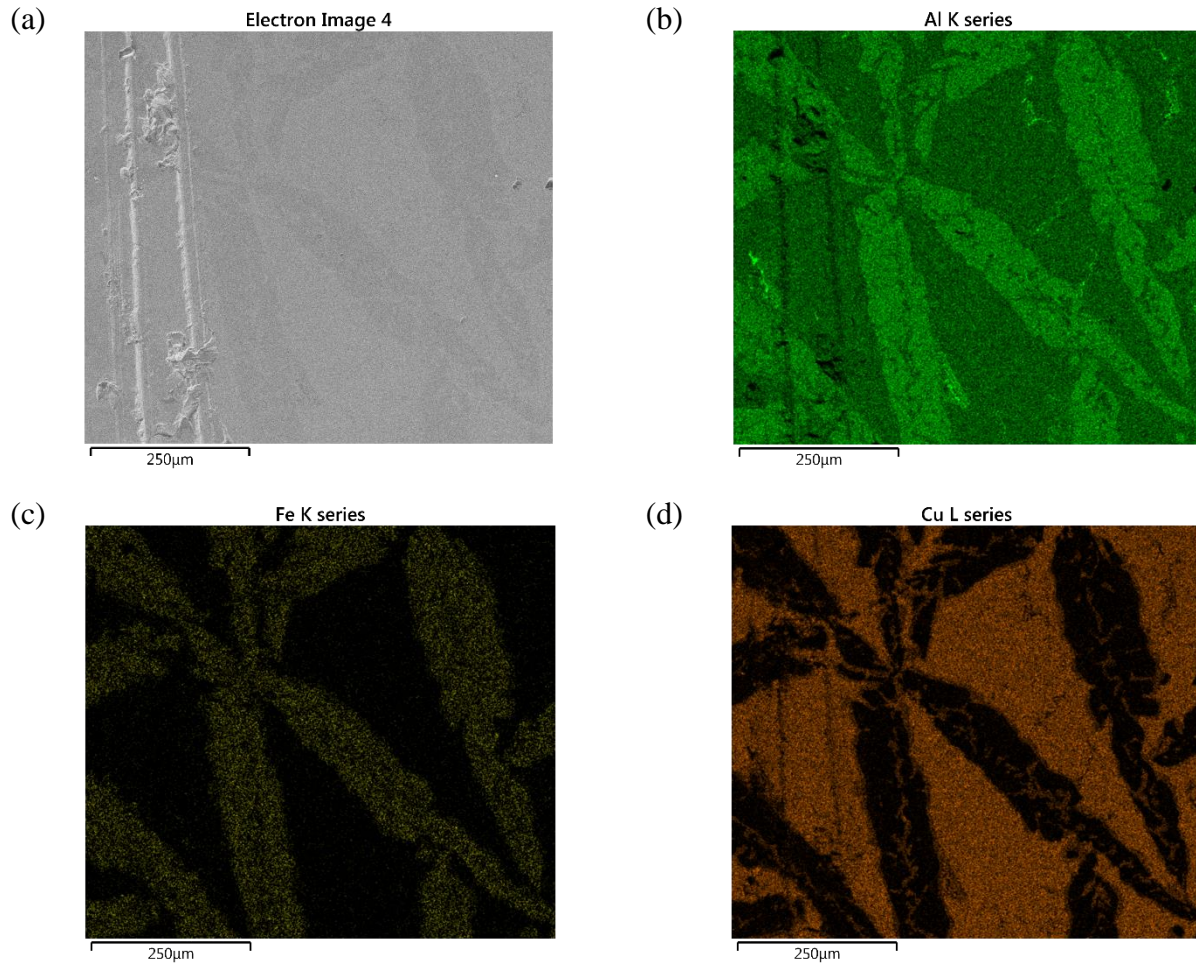


Figure 10.2. Secondary electron image (a) and elemental maps of Al (b), Fe (c) and Cu (d) of bulk synthesized  $\text{Al}_7\text{Cu}_2\text{Fe}$  intermetallic particle, as cast.

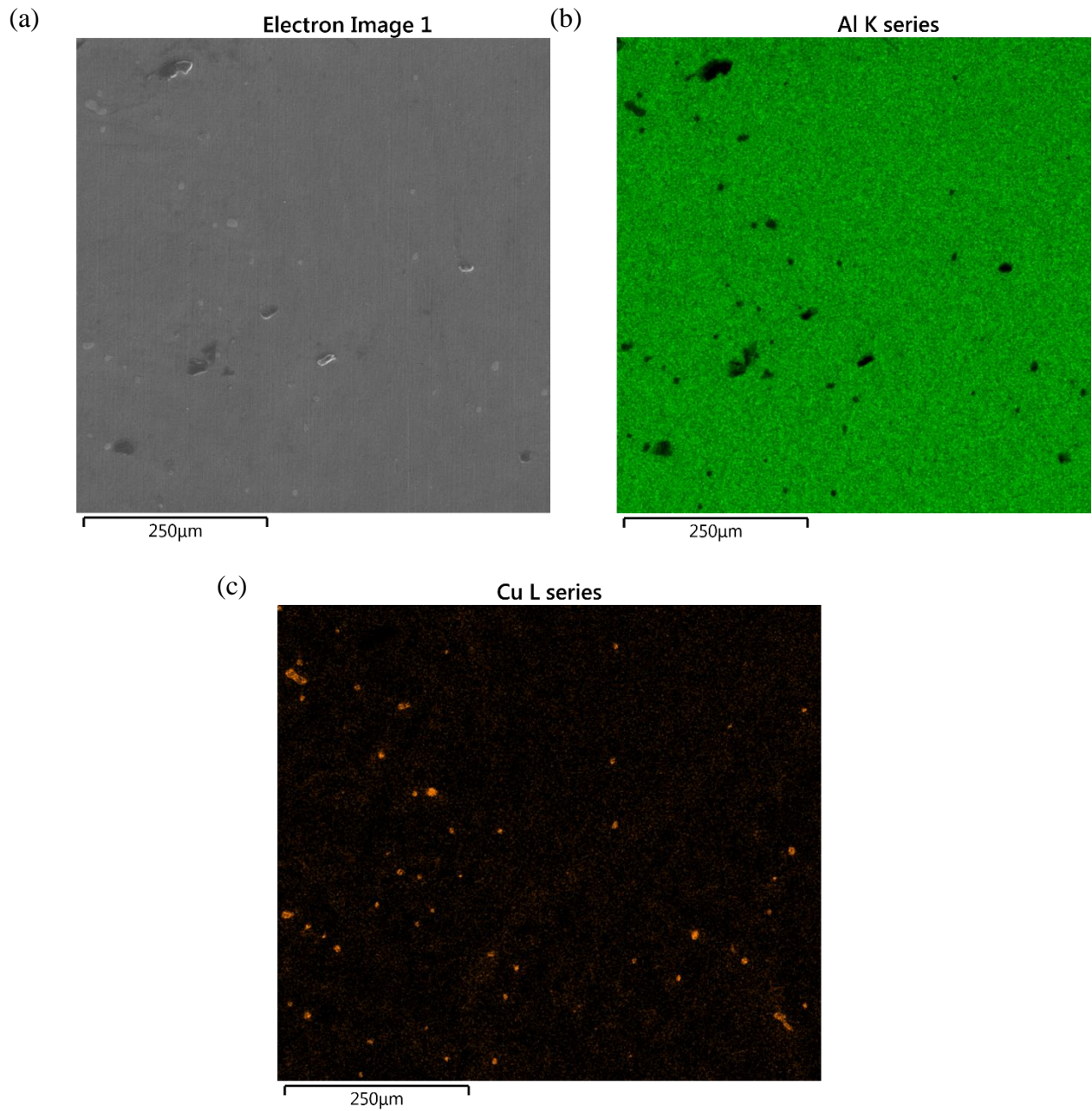


Figure 10.3. Secondary electron image (a) and elemental maps of Al (b), and Cu (c) of bulk synthesized Al – 4 wt % Cu alloy, as cast.

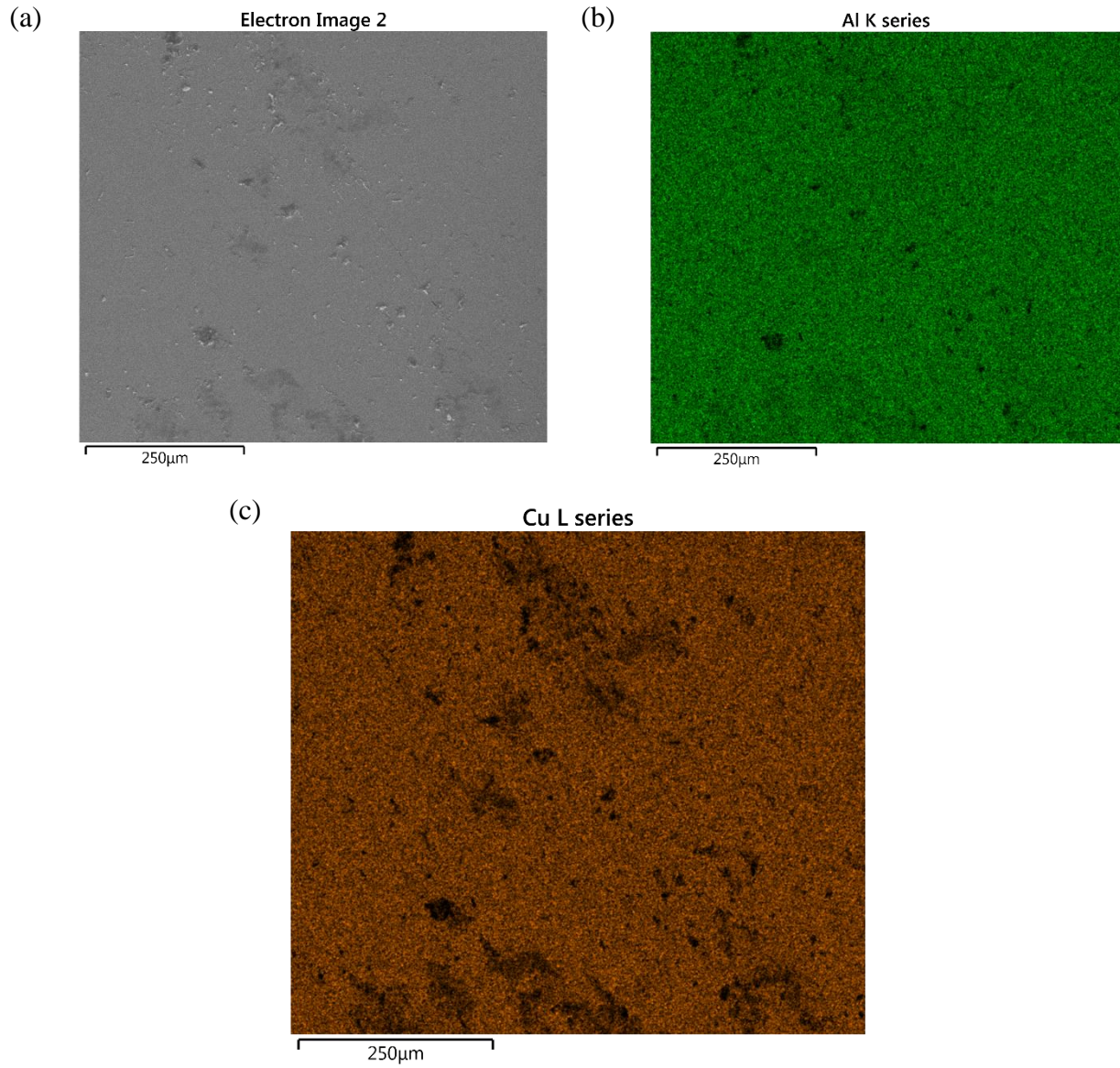


Figure 10.4. Secondary electron image (a) and elemental maps of Al (b), and Cu (c) of bulk synthesized  $\theta$  phase ( $\text{Al}_2\text{Cu}$ ) intermetallic particle, as cast.

### 10.3.2 Characterization of Volta Potentials of Intermetallic Phases

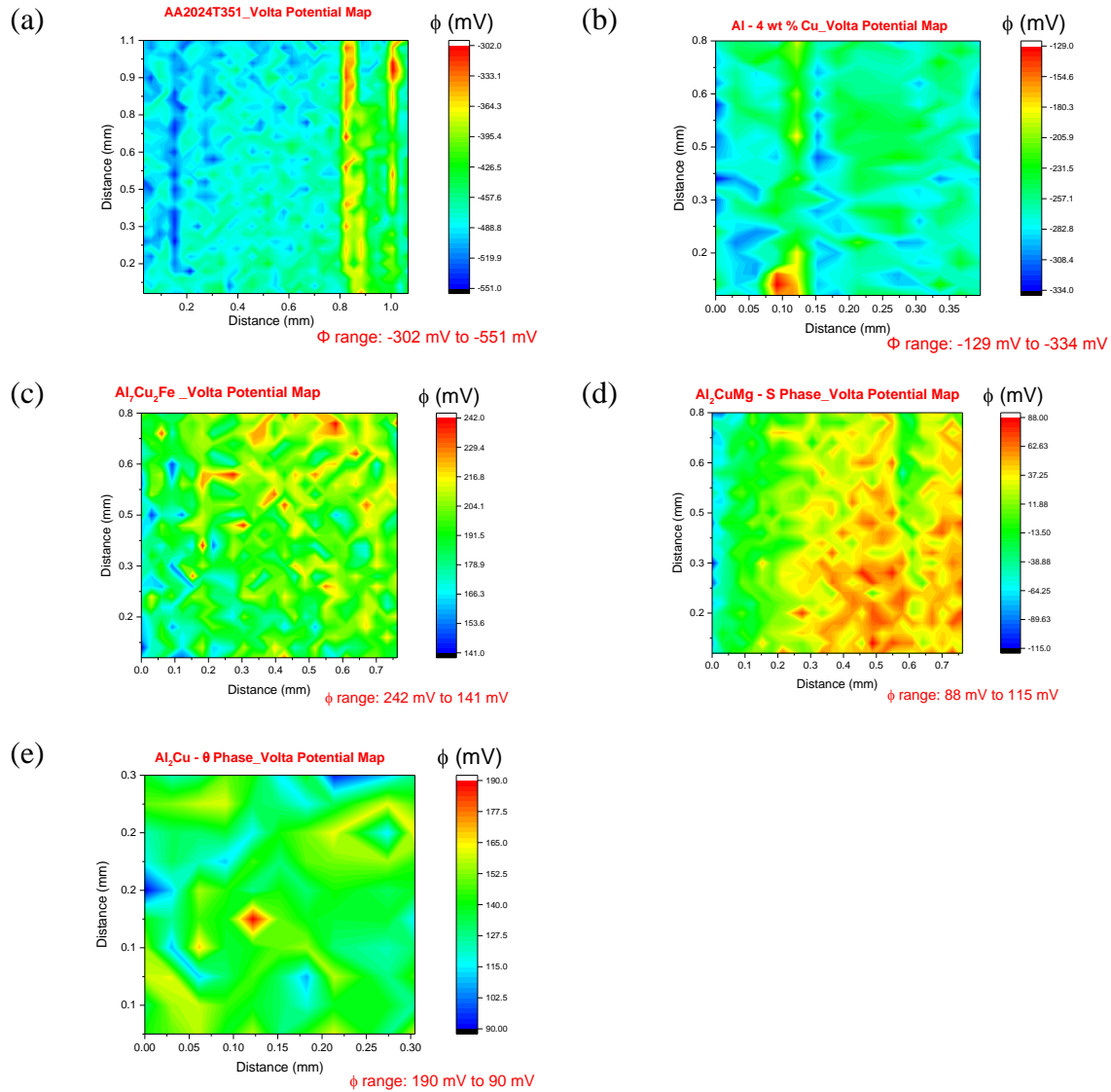


Figure 10.5. Volta potential maps without electrolyte at 95 % RH, ambient temperature for (a) 2024-T351, (b) Al-4 wt. % Cu, (c) Al<sub>7</sub>Cu<sub>2</sub>Fe, (d) Al<sub>2</sub>CuMg and (e) Al<sub>2</sub>Cu of bulk synthesized S phase (Al<sub>2</sub>CuMg) intermetallic particle

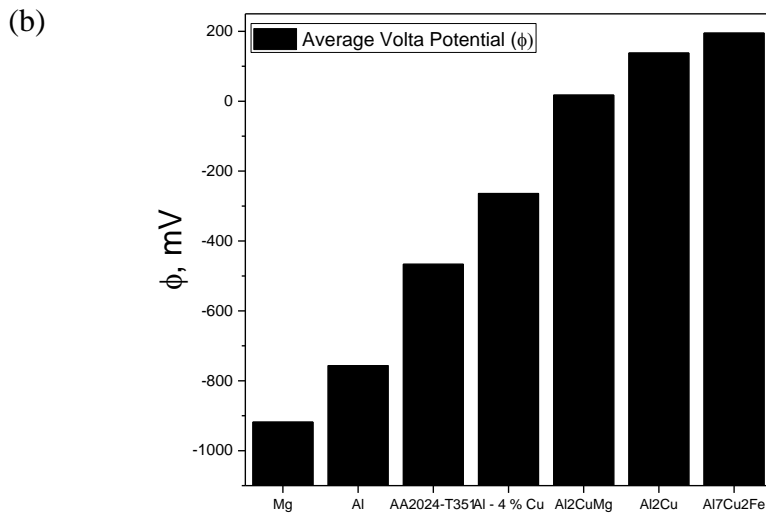
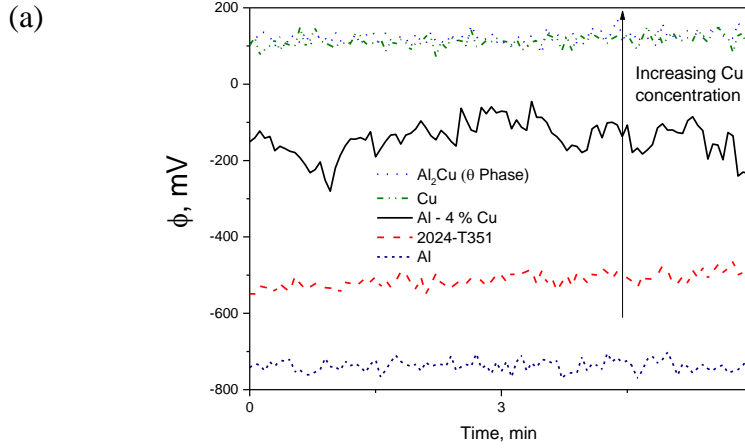


Figure 10.6. Volta potential for bare metals, alloys and bulk synthesized intermetallic phases indicated without electrolyte at 95 % RH, ambient temperature as a function of exposure time (a) and average Volta potential for bare metals, alloys and bulk synthesized intermetallic phases indicated (obtained from Volta potential maps).

### 10.3.3 Galvanic Couple Experiments

(a)

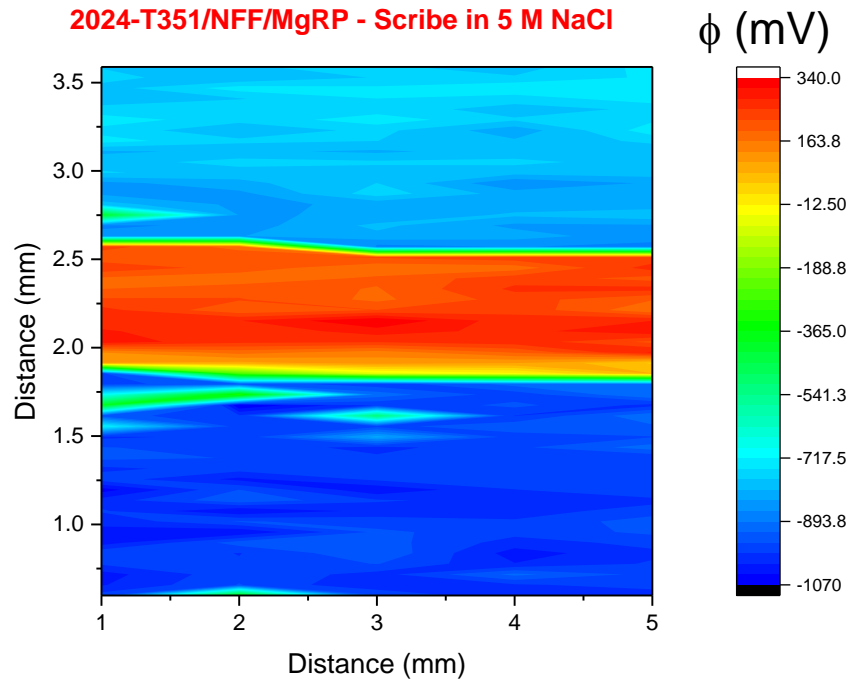


Figure 10.7. Initial Volta potential maps (0-15 min) for 2024-T351/NFF/MgRP exposing a bare scribe (2024-T351) under 5 M NaCl electrolyte at 95 % RH, ambient temperature. The red region in the map indicates the scribe whereas the blue regions indicate the MgRP region. The sample design utilized for the above experiments is same as one utilized for LALT and field exposures (~ 650  $\mu\text{m}$  machine drilled scribe).

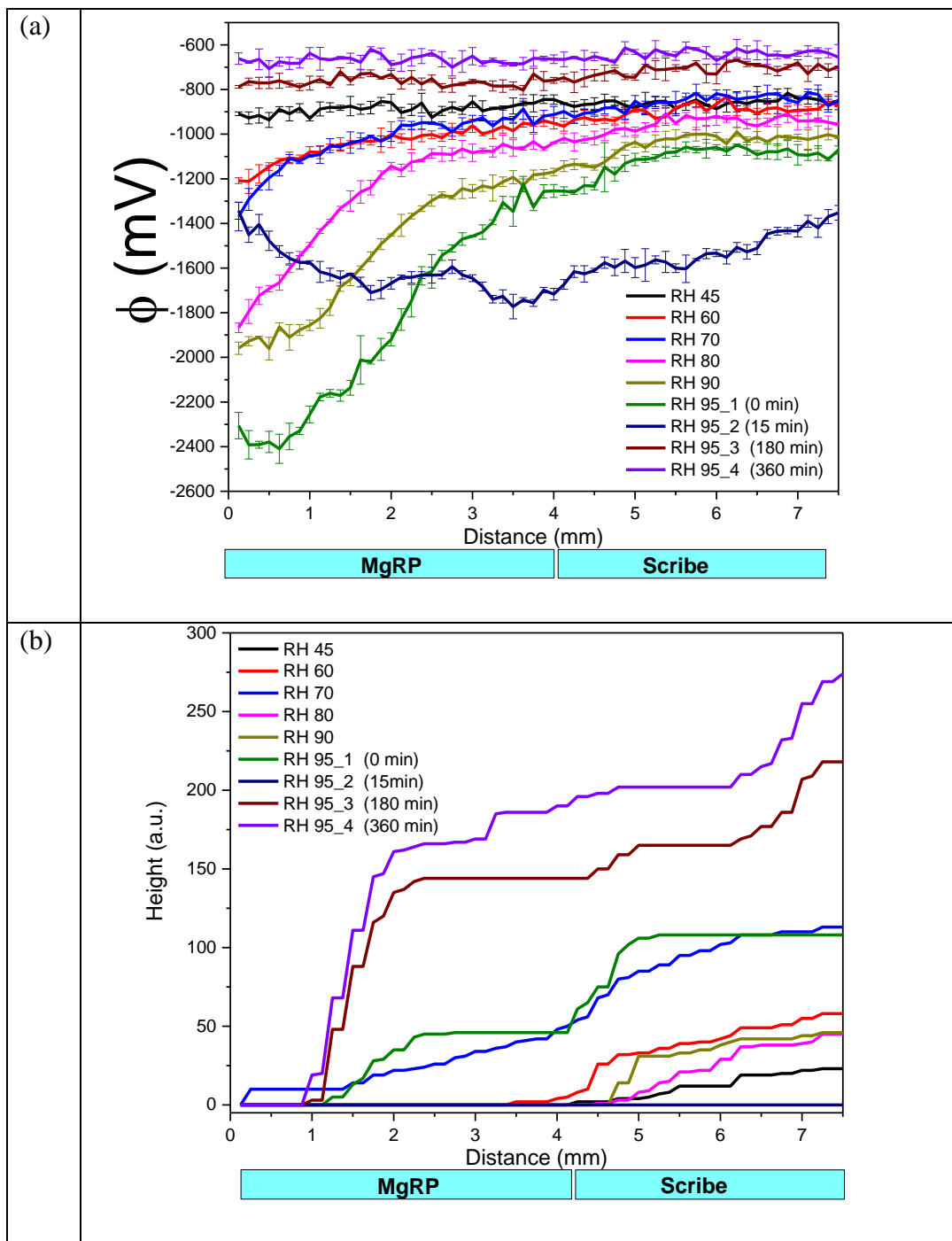


Figure 10.8. Initial Volta potential line profiles (0 – 360 min) (a) and surface topography (b) for 2024-T351/NFF/MgRP exposing a bare scribe (2024-T351) under NaCl electrolyte air dried prior to environmental exposure. Relative humidity was increased in steps from 45 % and held at 95 % RH for 6 h.

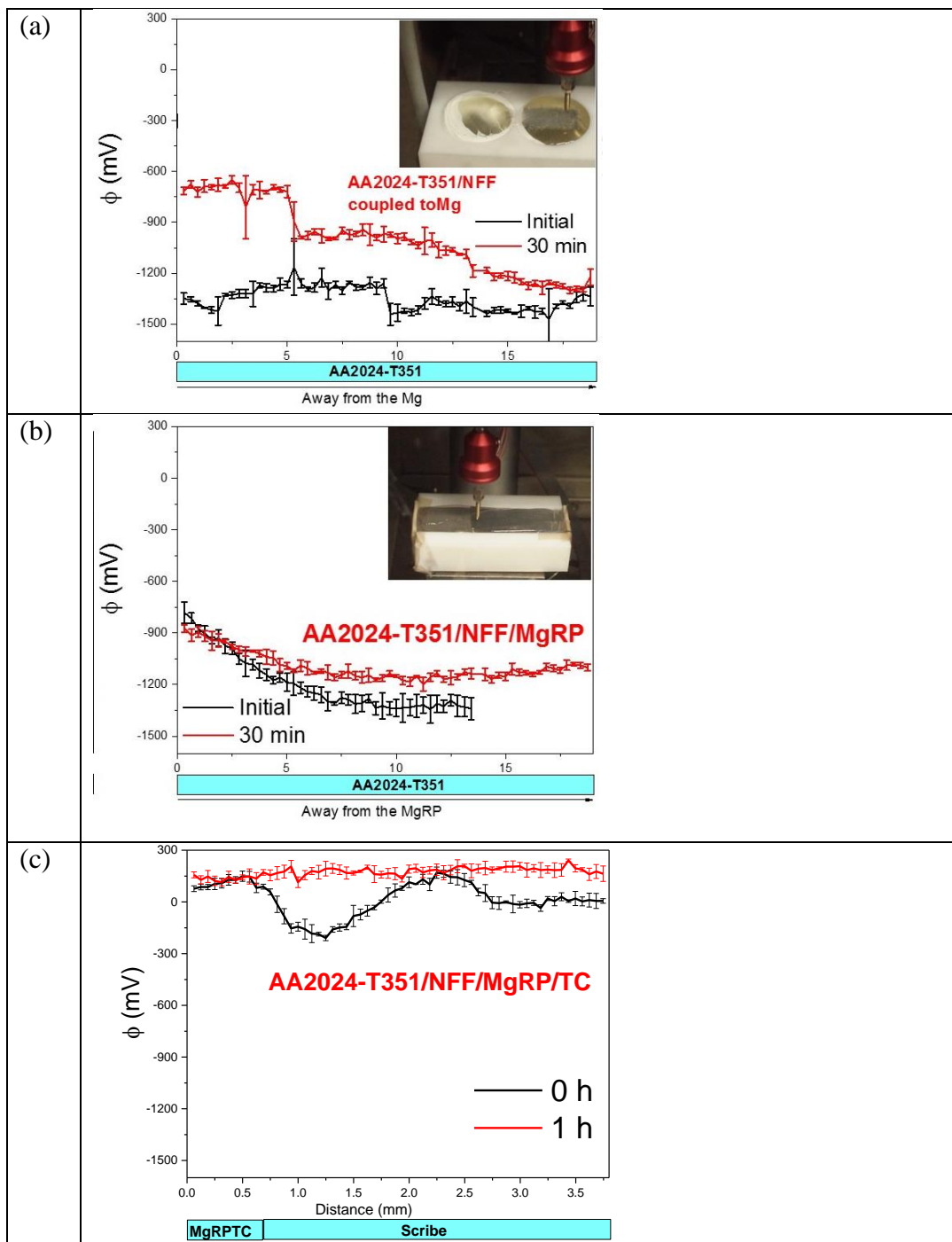


Figure 10.9. Initial Volta potential line profiles for samples indicated under 650  $\mu$ l of 5 M NaCl electrolyte at 95 % RH, ambient temperature. (a) Mg ribbon coupled to bare 2024-T351, (b) 2024-T351/NFF/MgRP coupled to bare 2024-T351 and (c) 2024-T351/NFF/MgRP/TC coupled to bare 2024-T351.

#### **10.4 Summary and Future Work**

The results reported herein confirm that SKP as a technique can be utilized for spatial determination of galvanic protection potential across the scribe which would be indicative of throwing power. Preliminary investigations on Mg or MgRP coupled 2024-T351 indicated that the Volta potentials shifted to more negative values during galvanic coupling of 2024-T351 with Mg indicative of sacrificial anode-based cathodic protection. The spatial resolution of SKP is limited by its probe size, distance of the probe from the surface of metal which varies as a function of electrolyte thickness. While the different segregated regions in the intermetallic phases were not differentiated in SKP by Volta potentials, the average Volta potential of entire region showed good correlation to nobility of the metal or intermetallic phase. The effect of pretreatment resistance on galvanic protection in thin film conditions need to be investigated for future work. The framework utilized for sample design for SVET and optical profilometry studies from previous chapters will be adopted for future SKP studies to study effect of pretreatment resistance, topcoat polymer, coating to scribe area ratio, film thickness on spatially resolved galvanic protection potential.

## **11 APPENDIX D: Extensions of Environmental Degradation of a Mg-rich Primer in Selected Laboratory Environments – Part III. In ASTM B117 Modified with UV Light and Acidified Artificial Sea Water and Selected Full Immersion Exposures – FIGURES ONLY**

### **11.1 Introduction**

Two additional laboratory accelerated life tests (laboratory salt fog exposures and laboratory full immersion exposures) similar to those presented in chapter 3 and 4 were conducted to study the effect of 1) ASTM artificial seawater + UV light and 2) Other aerosol corrosive compounds such as oxalates and nitrates. For salt fog exposures, the standard ASTM B117 salt fog was altered such that the standard 5 % (wt) NaCl solution electrolyte was replaced with ASTM substitute ocean water<sup>135,136</sup> ([SOW] pH = 8.2±0.3) and ultraviolet radiation. The details of the experiments are summarized in Table 1. Artificial seawater was produced according to ASTM D-1141<sup>135</sup> In all salt fog exposures reported in this report, ambient air was supplied to the chamber and to the atomizer for fog production. Ambient concentrations of CO<sub>2</sub> were measured in-situ to be approximately 425 ppm. Other ambient gas concentrations were not measured.

### **11.2 Experimental Procedure**

#### **11.2.1 Materials**

AA2024-T351sheet (1.6 mm thickness) was pretreated with 7 different surface pretreatments for comparison including including (i) Non-film Forming Surface Pretreatment (NFF), (ii) Chromate Conversion Coating (CCC), (iii) Trivalent Chromium Pretreatment (TCP), (iv) Non Chromium Pretreatment (NCP) (v) Anodization – No Sealing (ANS), (vi) Anodization with hexavalent chromium sealing (ACS), (vii) Anodization with Trivalent Chromium Pretreatment (TCP) Sealing (ATS). For anodization pretreatments, a thin-film sulfuric acid anodizing, MIL-A-8625F: Type II

pretreatment procedure was followed. Anodized samples had 3 variants, one without sealing, one with hexavalent chromium sealing and one with trivalent chromium process sealing.

A 40  $\mu\text{m}$  primer layer of Mg-rich primer and a 50  $\mu\text{m}$  thick topcoat of Aerodur 5000 high-performance advanced coating, both produced by Akzo Nobel Coatings (Waukegan, Illinois) were applied. The Mg rich primer consist of one part epoxy matrix with Mg metal flake pigment of a diameter 20  $\mu\text{m}$  with pigment volume concentration of 45 % (3rd generation 2100P003, Lot: 493-190). Aerodur 5000 (Gloss white finish product: ECM-G7875) is a two component polyurethane topcoat developed for military application in variety of exposure environments.

### **11.2.2 Laboratory and Field Exposures of Pretreated AA2024-T351 coated with MgRP and Topcoat**

Mg-rich primer-coated AA2024-T351 panels were exposed to salt spray using a modified ASTM B117 protocol. The standard ASTM B117 salt fog was altered such that the standard 5 % (wt) NaCl solution electrolyte was replaced with ASTM substitute ocean water ([SOW] pH =  $8.2\pm 0.3$ ) and ultraviolet radiation. The details of the experiments are summarized in Table 1. Artificial seawater was produced according to ASTM D-1141. In all salt fog exposures reported in this report, ambient air was supplied to the chamber and to the atomizer for fog production. Ambient concentrations of  $\text{CO}_2$  were measured in-situ to be approximately 425 ppm. Other ambient gas concentrations were not measured. In addition full immersion exposure studies were conducted to study the effect of oxalates and nitrates on coating degradation and sacrificial protection function. 0.1 M sodium nitrate and 0.01 M sodium oxalate were added to 5 % (wt) NaCl (pH:  $6.9\pm 0.4$ ) which was used as control from our previously discussed full immersion studies.

### 11.2.3 Post-mortem Surface Analysis of the Coating and the Scribe

All full-immersion studies as well as post-mortem analysis after salt fog and field exposures reported herein were conducted in quiescent 5 % (wt) NaCl (pH: 6.9±0.4) open to laboratory air. Potential control during electrochemical experiments was maintained using a Gamry Potentiostat (Ref 600/ PCI4)† with computer interface software. A saturated calomel electrode (SCE) and a Pt mesh were used as the reference and counter electrode, respectively. The area tested was far away ( $\geq 2$  cm away) from scribe. A typical EIS scan was acquired in sine sweep mode from 100 kHz to 0.01 Hz with 6 points per decade. MgRP and MgRP/TC coated panels were scanned with an AC amplitude of 80-100 mV to reduce noise. The tests were conducted in quiescent 5 % (wt) NaCl, as discussed above, after 1 hour exposure at open circuit for MgRP coated panels and 12 hour exposure for MgRP/TC coated panels.

X-ray diffraction (XRD) was conducted to characterize global Mg depletion as a function of exposure time in different lab and field environments. A Panalytical X'pert powder diffractometer utilizing a Cu-K $\alpha$  source was utilized for measurements. All samples were scanned continuously from 30 degrees to 50 degrees at 5 degrees per minute. XRD measurements of pristine and environmentally exposed samples were made on panels far away ( $\geq 2$  cm away) from any edge or scribe, presumed to be representative of global coating degradation. XRD obtained from Mg-rich-coated panels were normalized by the face-centered cubic (fcc) Al <200>  $2\theta = 44.74^\circ$  peak from the underlying substrate. Peak normalization and integration was performed with Origin Lab 7.5 software. The lower detection limit for crystalline phases was approximately 3-5 % of the sample by volume.

Scanning electron microscopy (SEM) and energy dispersive spectroscopy (EDS) were used for post-mortem analysis of corrosion products in the scribe. A field emission Quanta 650 SEM was

used to conduct these investigations. For EDS, Oxford XMax 150 detector was utilized. A working distance of 15 mm and an accelerating voltage of at least 3 times the energy of the maximum characteristic peak of interest were used (~15 kV). At an accelerating voltage of 15 kV, EDS has a penetration depth of roughly 2 to 5  $\mu\text{m}$  into the materials investigated in this study. Elemental maps and line profiles were collected and EDS analysis was performed using Aztec image analysis software.

Optical profilometry was conducted using a Zygo optical profilometer (Newview 7200/7300 model). The environmentally exposed samples were first exposed to concentrated nitric acid for 15 minutes to remove corrosion products present in the scribe as per the ASTM G-1 Standard.<sup>138</sup> Image refinement and pit volume calculation was performed using MountainsMaps imaging topography software.<sup>142</sup>

### 11.3 Tables

Table 11.1. Experimental protocol for modified ASTM B117 environmental exposure.

<b>Total Exposure Time</b>	<b>UV exposure (h)</b>	<b>Cycles</b>	<b>ASTM B117 exposure (h)</b>	<b>Cycles</b>
72	12	3	12	3
144	24	3	24	3
384	48	4	48	4
576	72	4	72	4
960	120	5	120	5
1440	120	6	120	6

## 11.4 Figures

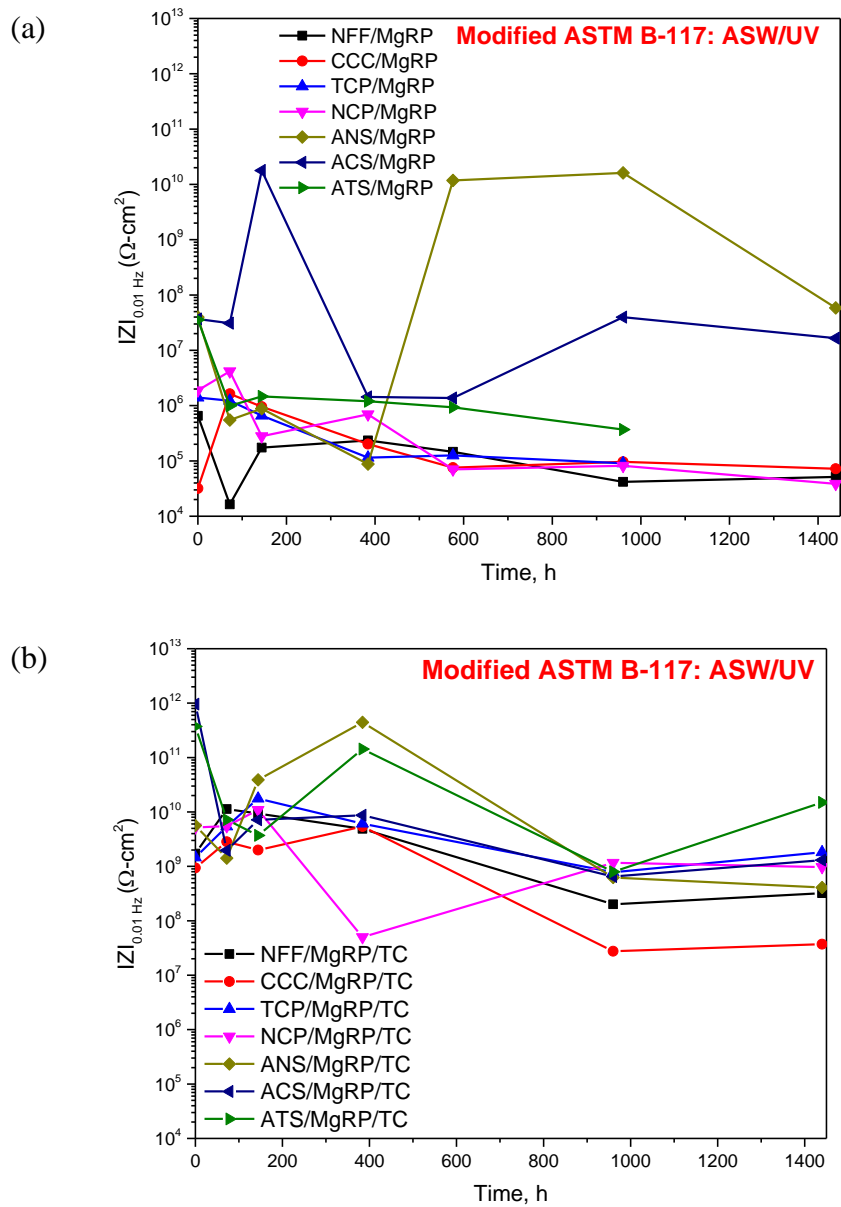


Figure 11.1. Low frequency impedance IZI modulus of intact AA2024-T351/Pretreatment/MgRP at 0.01 Hz vs time in the environments indicated for (a) 2024-T351/Pretreatment/MgRP (b) 2024-T351/Pretreatment/MgRP/TC

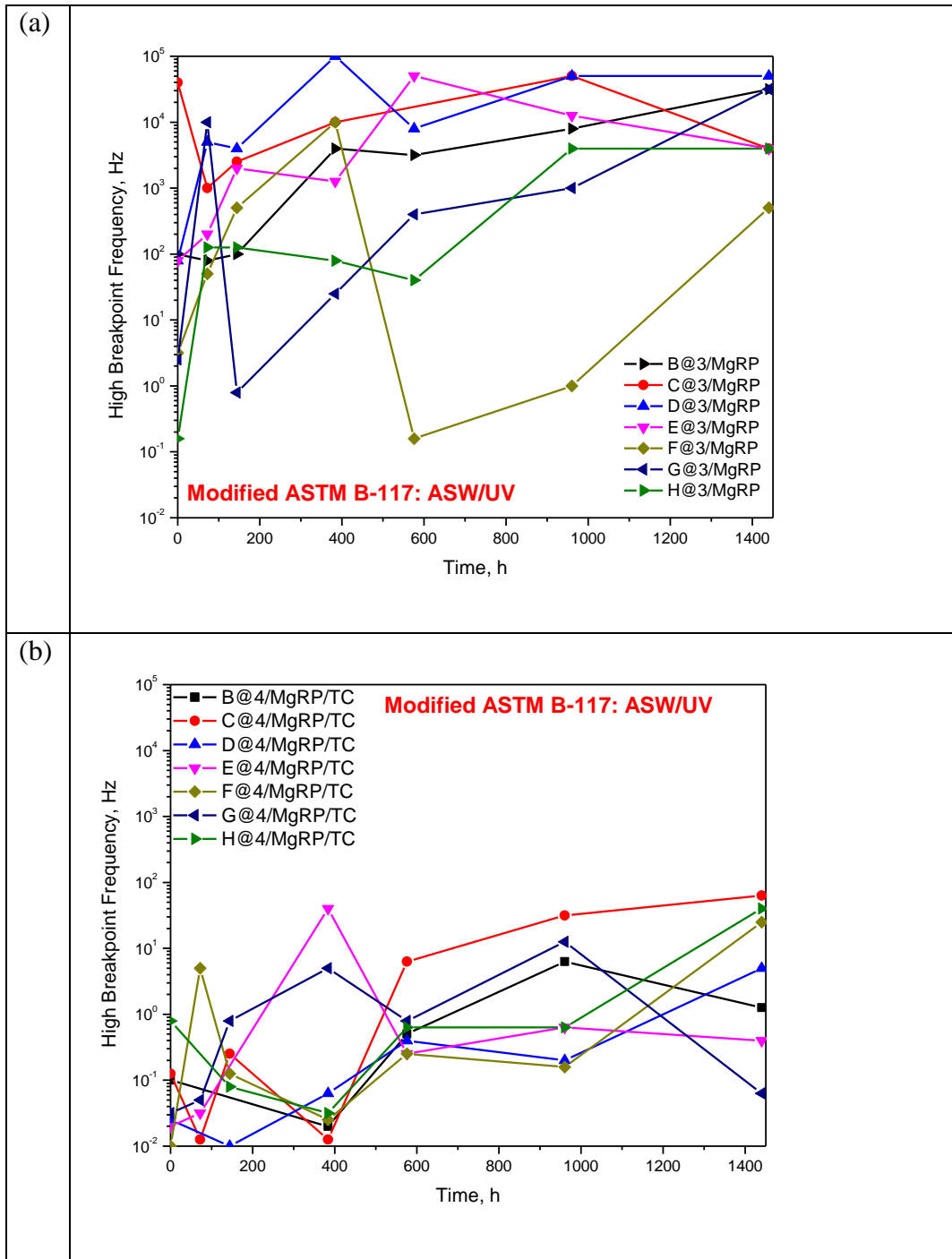


Figure 11.2. High breakpoint frequency ( $F_{bpt}$ ) of intact AA2024-T351/Pretreatment/MgRP at 0.01 Hz vs time in the environments indicated for (a) 2024-T351/Pretreatment/MgRP (b) 2024-T351/Pretreatment/MgRP/TC

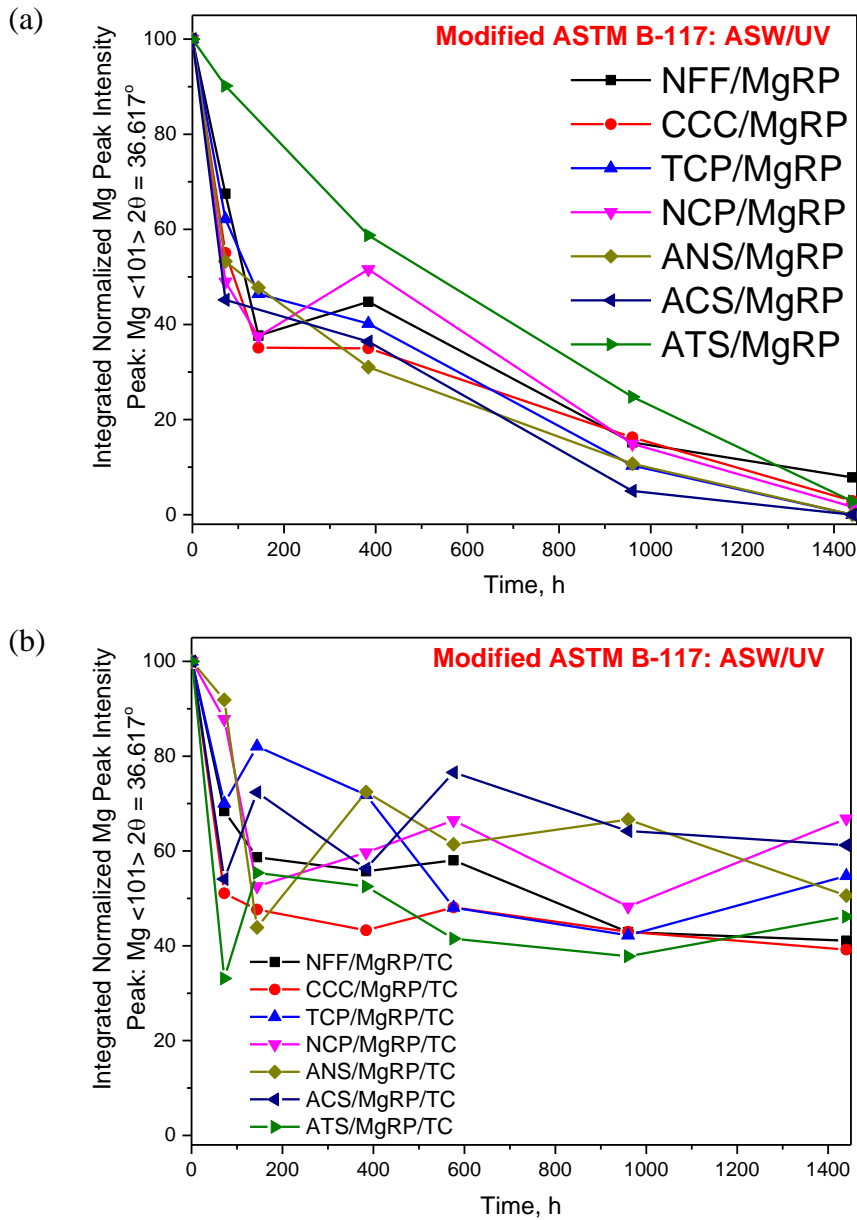


Figure 11.3. The normalized integral XRD intensity for Mg<101> XRD peak of intact AA2024-T351/Pretreatment/MgRP at 0.01 Hz vs time in the environments indicated for (a) 2024-T351/Pretreatment/MgRP (b) 2024-T351/Pretreatment/MgRP/TC

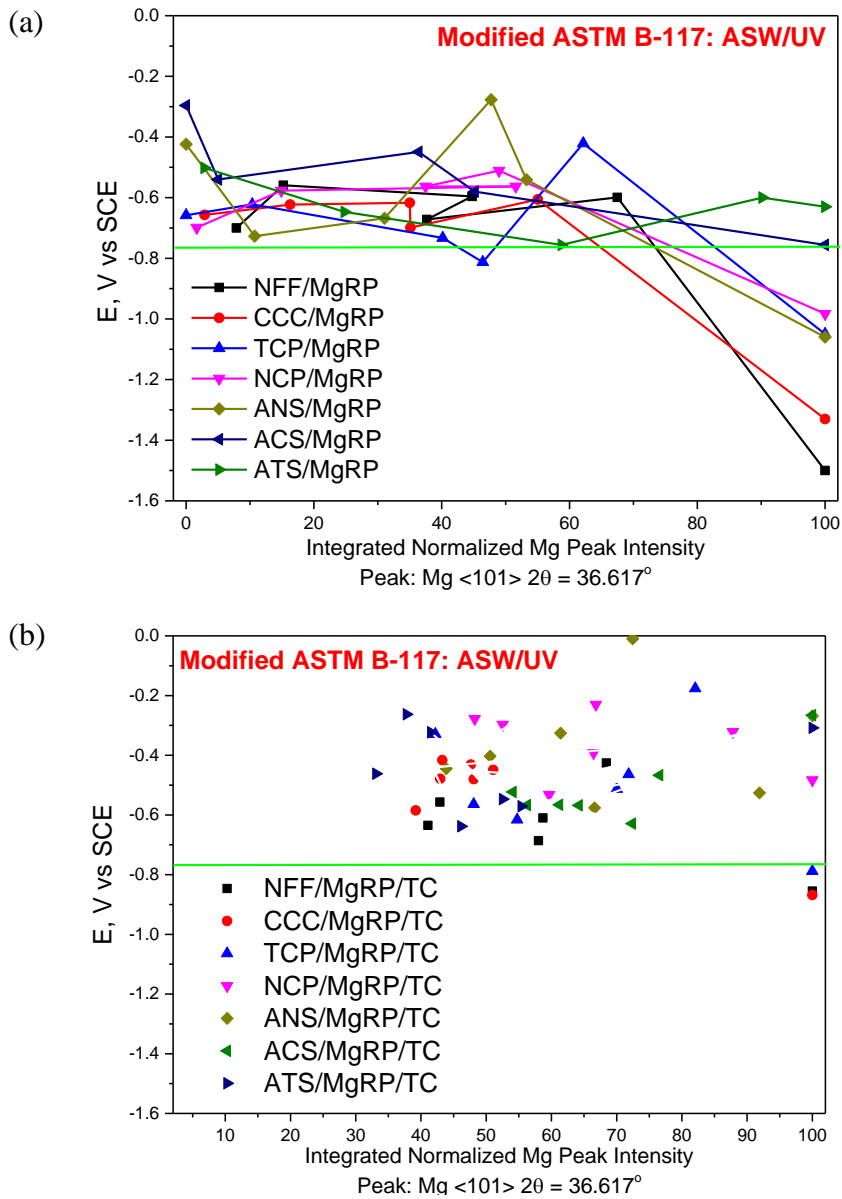


Figure 11.4. Average global galvanic protection potential of intact coating for the last 1 h exposure in 5 % wt NaCl vs the normalized integral XRD intensity for Mg<101>. The time indicates total exposure time in different LALT/Field environments indicated, (a) AA2024-T351/NFF/MgRP after exposure, in Full immersion in 5 % wt NaCl and Field at CHO and (b) AA2024-T351/TCP/MgRP after exposure, in Full immersion in 5 % wt NaCl, ASTM B-117 in 5 % wt NaCl and Field at CHO.

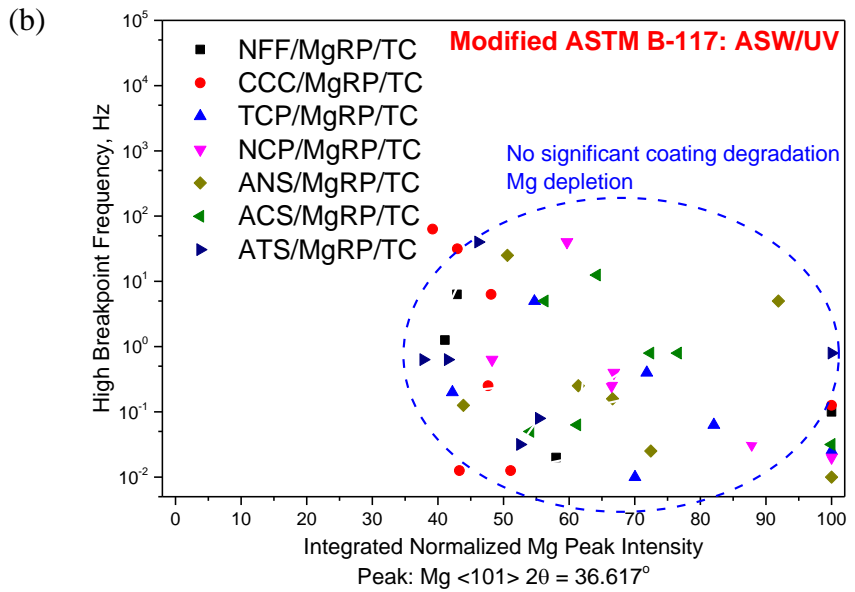
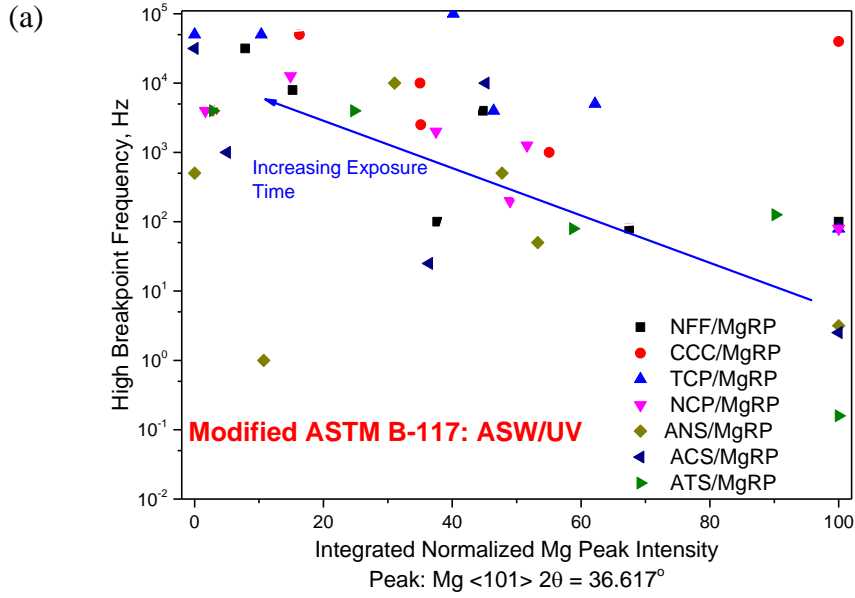


Figure 11.5. High breakpoint frequency of intact coating after 1 h exposure in 5 % wt NaCl vs The normalized integral intensity for Mg<101>. The time indicates total exposure time in different LALT/Field environments indicated,

(a) AA2024-T351/NFF/MgRP after exposure, in Full immersion in 5 % wt NaCl, ASTM B-117 in 5 % wt NaCl, Modified ASTM B-117 with acidified SOW and UV and Field exposure at CHO.

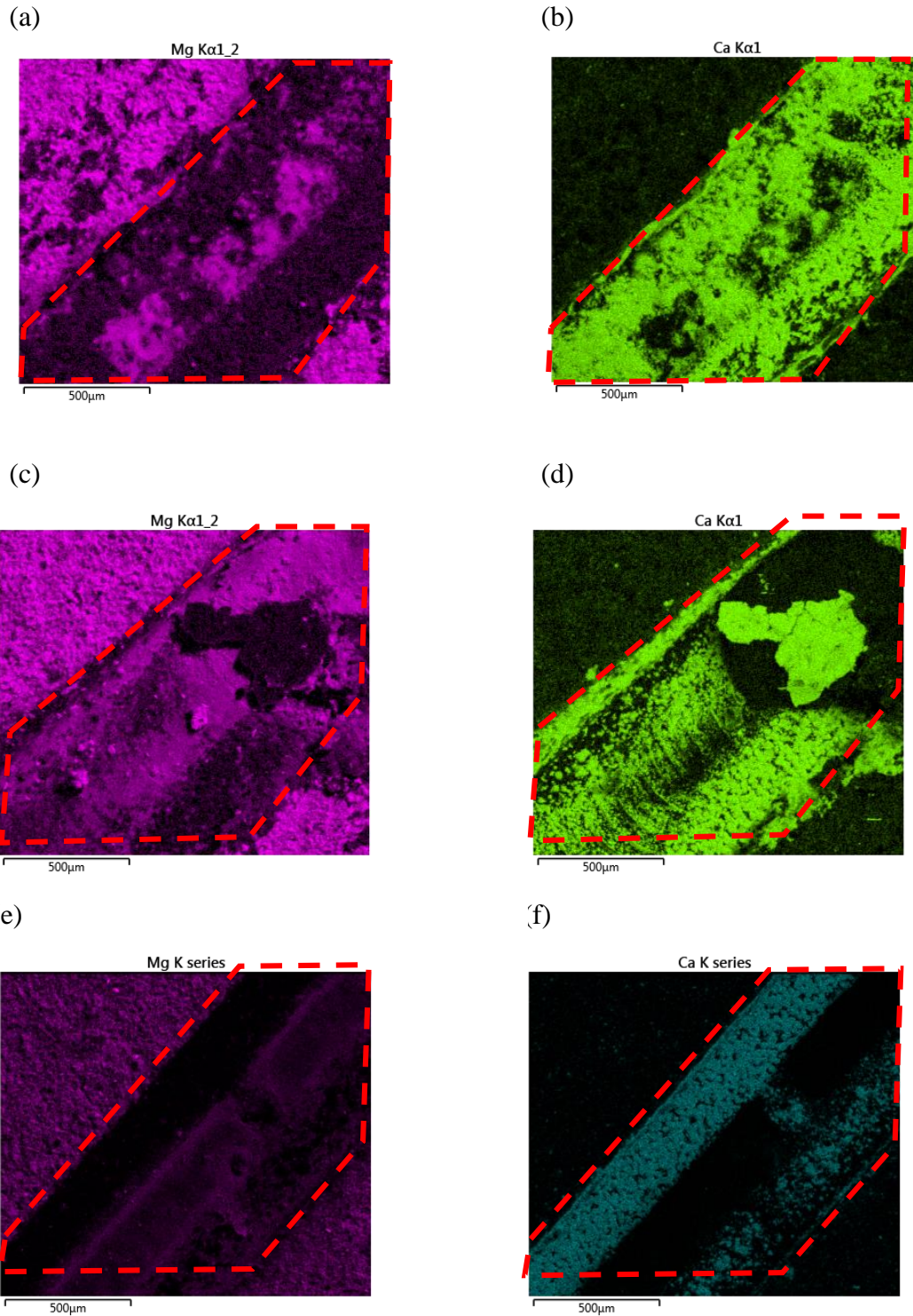


Figure 11.6. EDS maps of elemental Mg and Ca across scribe and adjacent coating pretreated 2024-T351/MgRP after 1440 h exposure in modified ASTM B117 with ASTM SOW and UV (a/b) NFF/MgRP, (c/d) TCP/MgRP and (e/f) ACS/MgRP. (red dash line indicates the borders of the scribe in the figure).

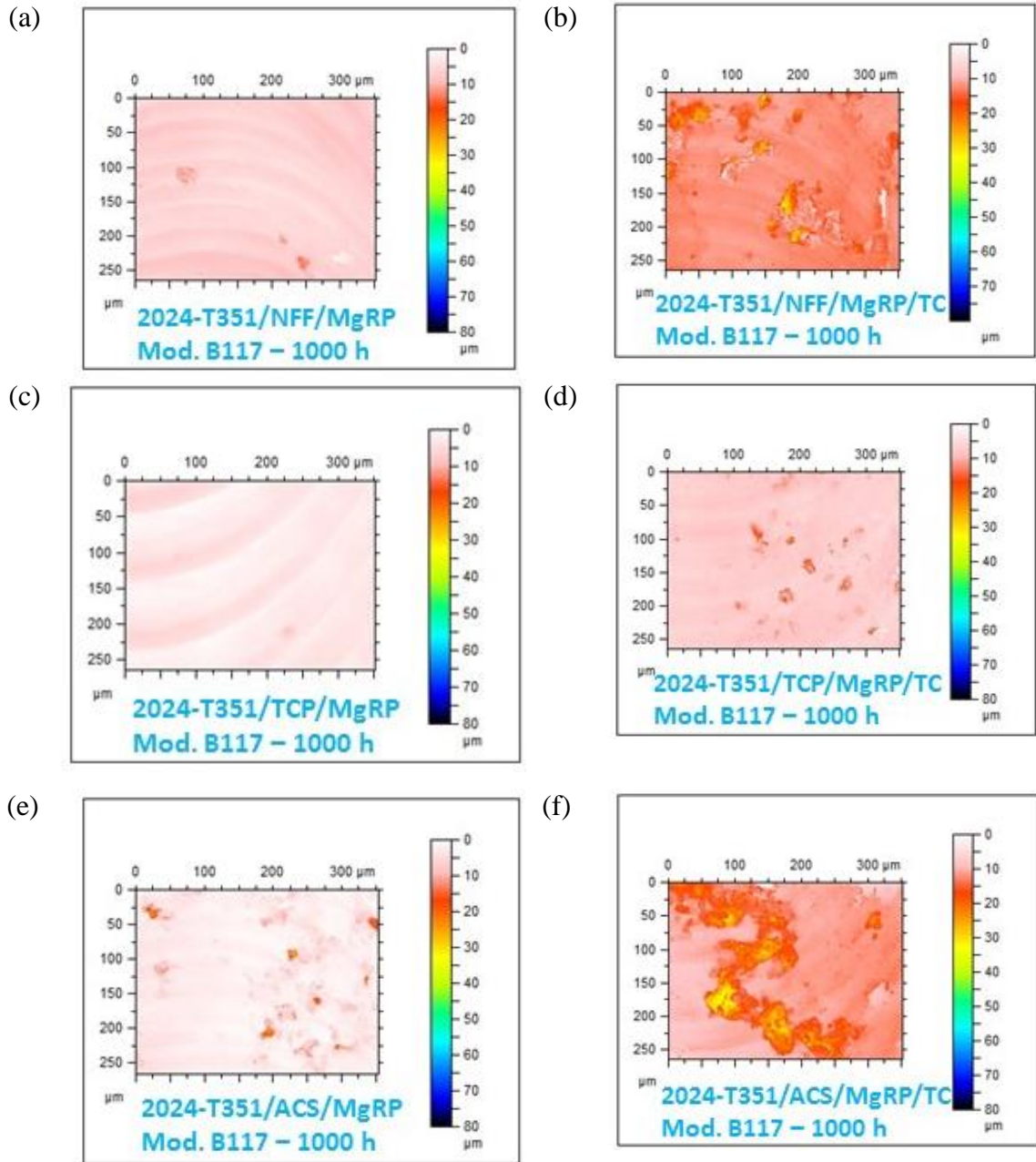


Figure 11.7. Optical profilometry maps of selected AA2024-T351/Pretreatment/MgRP with/without topcoat after exposure in modified ASTM B117 for 1440 h. (a) AA2024-T351/NFF/MgRP, (b) AA2024-T351/NFF/MgRP/TC, (c) AA2024-T351/TCP/MgRP, (d) AA2024-T351/TCP/MgRP/TC, (e) AA2024-T351/ACS/MgRP and (f) AA2024-T351/ACS/MgRP/TC. The 0 μm position (white) on the scale is indicative of the starting material condition before corrosion.

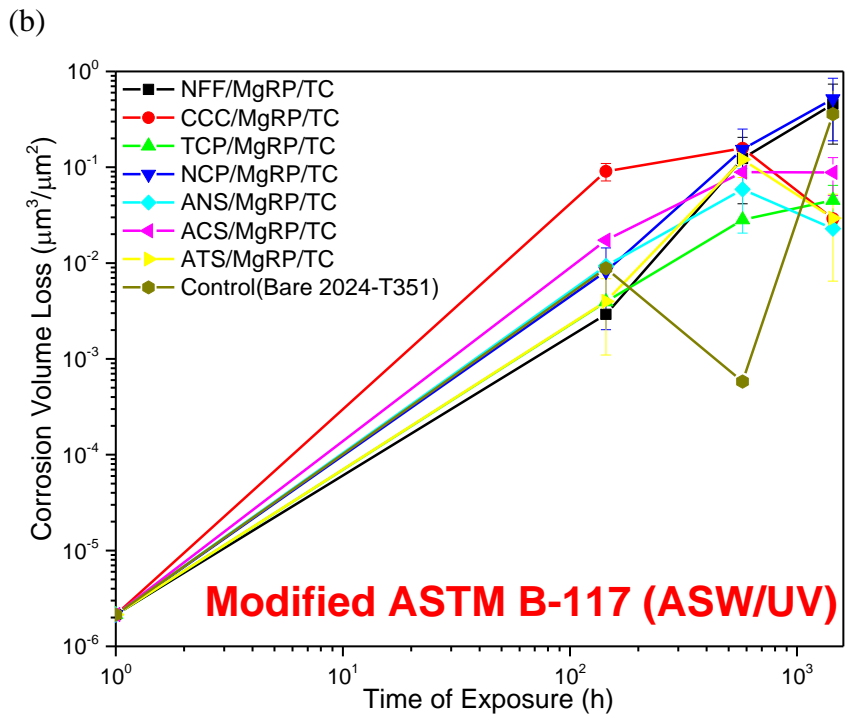
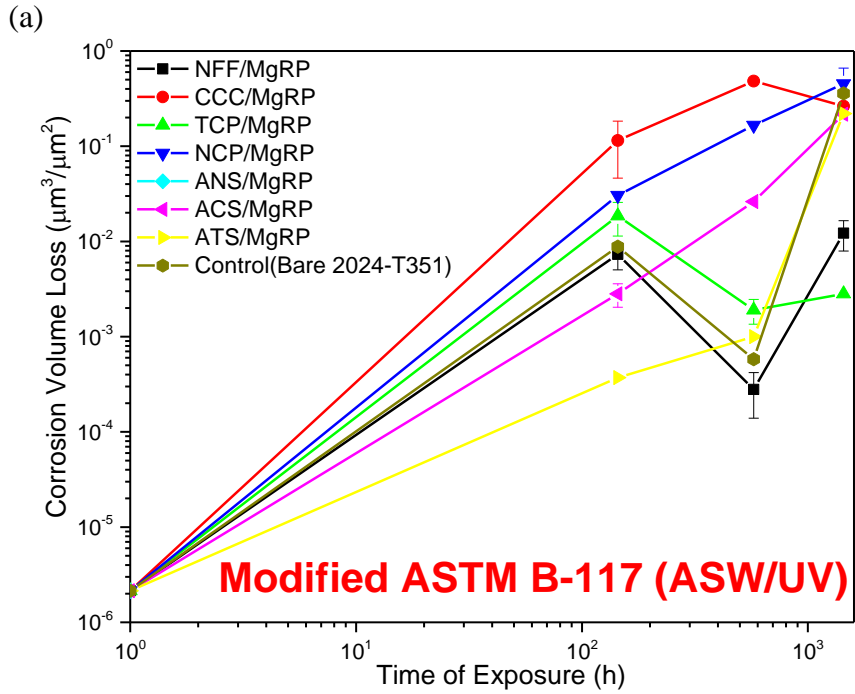
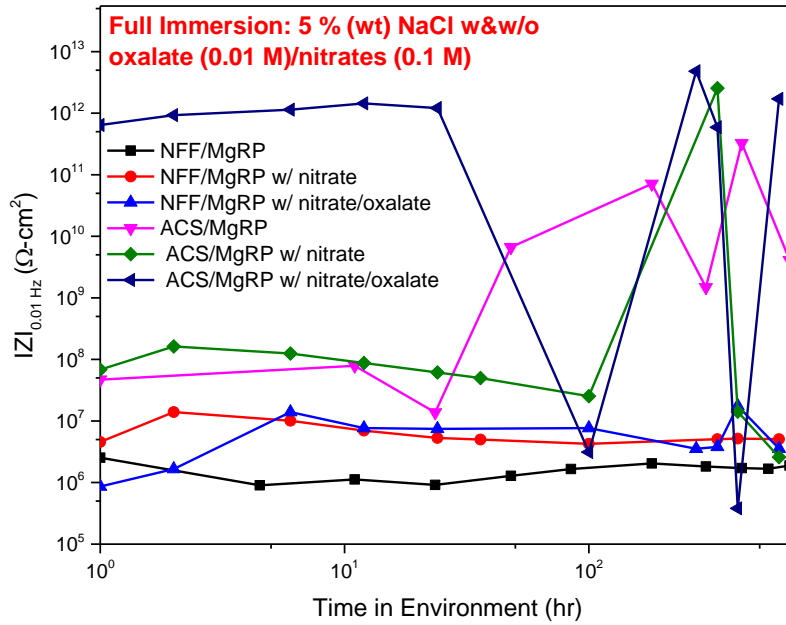


Figure 11.8. Corrosion volume loss of scribe exposing AA2024-T351 in AA2024-T351/Pretreatment/MgRP systems with/without topcoat as a function of exposure time in modified ASTM B117 with ASTM SOW and UV. The baseline data is for uncoated AA2024-T351. (a) 2024-T351/Pretreatment/MgRP and (b) 2024-T351/Pretreatment/MgRP/TC.

(a)



(b)

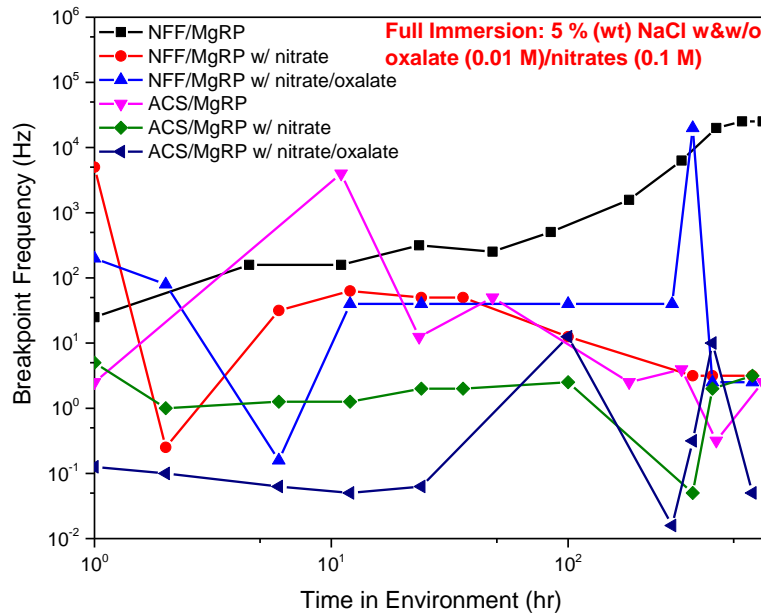


Figure 11.9. Low frequency impedance IZI modulus at 0.01 Hz (a)/High breakpoint frequency ( $F_{bpt}$ ) (b) of intact AA2024-T351/Pretreatment/MgRP vs time in the environments indicated

(a)

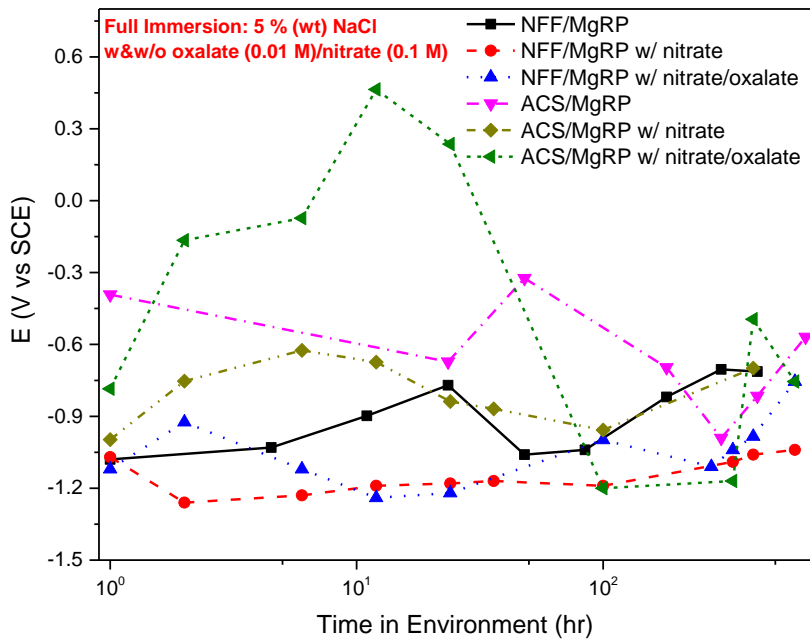


Figure 11.10. Average open circuit potential of last 1 hour of exposure for intact AA2024-T351/Pretreatment/MgRP vs time in the environments indicated

### **11.5 Summary and Future Work**

In addition to previously discussed aspects of coating degradation, sacrificial protection function and scribe protection, modified ASTM B117 is moderate in severity in comparison to standard ASTM B117 exposures. The scribe protection was significantly improved by deposition of calcareous deposits from artificial sea water environment. Full immersion exposures indicated that the barrier degradation and sacrificial protection function of primer is not significantly affected by presence of nitrate or oxalate in addition to chloride indicating that chloride is the main aggressive species resulting in coating degradation and Mg depletion. X-ray diffraction and Raman spectroscopy need to be conducted post-exposure to confirm that Mg depletion trends aren't significantly different and investigate if there are presence of any additional undissolved corrosion product in the surface in new environment.